Cobalt hydride complexes and catalysis

Khanittha Walaijai

PhD

University of York

Chemistry

March 2020

Abstract

This Thesis describes the investigation of cobalt hydride complexes containing PN chelating ligands for cobalt-catalysed H_2 evolution and CO_2 reduction reactions. An overview of strategies for solar and electro-driven fuel production, the development of electrocatalysts for H_2 evolution (HECs) by the natural hydrogenases, synthetic bio-inspired HECs and earth-abundant transition metal complexes are discussed in **Chapter 1**.

Chapter 2 describes synthesis and characterisation of novel cobalt(III) hydride complexes supported by bis PN chelating diisopropylphosphino(2-methylpyridine) ligands: $[Co^{III}(PN)_2(H)(Cl)][PF_6]$ and $[Co^{III}(PN)_2(H)(MeCN)][PF_6]_2$ and related Co^{II} complexes. Their electronic and redox properties as well as mechanistic electron transfers are also discussed.

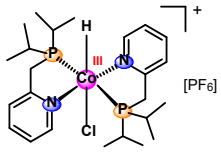

$[Co^{III}(PN)_2(H)(Cl)][PF_6]$

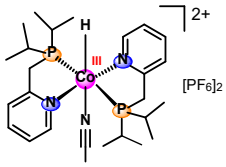

$[Co^{III}(PN)_2(H)(MeCN)][PF_6]_2$

The mechanistic studies for H_2 evolution catalysed by $[Co^{II}(PN)_2(MeCN)][BF_4]_2$, $[Co^{III}cis\text{-}(PN)_2Cl_2][PF_6]$ as well as the corresponding hydride, $[Co^{III}(PN)_2(H)(MeCN)][PF_6]_2$ and $[Co^{III}(PN)_2(H)(Cl)][PF_6]$ via ECEC pathways are discussed in **Chapter 3**. The kinetic information of $[Co^{II}(PN)_2(MeCN)][BF_4]_2$ and $[Co^{III}(PN)_2(H)(MeCN)][PF_6]_2$ as well as comparison of these two catalysts to previously reported HECs are detailed in the **Chapter 3**. Preliminary CV studies of CO_2 reduction activity of $[Co^{III}(PN)_2(H)(Cl)][PF_6]$ and $[Co^{III}cis\text{-}(PN)_2Cl_2][PF_6]$ are also discussed.

Chapter 4 describes synthesis and characterisation of the novel Co(II) complexes containing a tetradentate PNNP 2,9-bis(di-*t*-butylphosphino-methyl)-1,10-phenanthroline ligand as well as their electronic and redox properties. A chemical reduction of the $[Co^{II}(PNNP)Cl_2]$ and $[Co^{II}(PNNP)MeCN][BF_4]_2$ by LiMe or $NaBEt_3H$ suggested an activation mode of H-H bond breaking/making involving metal-ligand cooperation and aromatization–dearomatization processes. Furthermore, the H_2 evolution and CO_2 reaction activity of the $[Co^{II}(PNNP)Cl_2]$ and the $[Co^{II}(PNNP)(MeCN)][BF_4]_2$ is also discussed. Finally, **Chapter 5** summarizes the important findings and suggests future work.

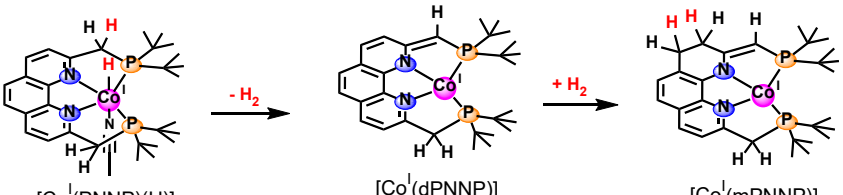

Contents

List of Figures

List of Schemes

List of Tables

List of Charts

Acknowledgements

I would like to acknowledge my research advisors, Prof. Robin N. Perutz and Dr Richard E. Douthwaithe, for their invaluable guidance, excellent support, helpful suggestions throughout my research and the opportunity to work in the great research group. In addition, I would like to thank Dr. Jason Lynam for his guidance and valuable comments as my IPM during the TAP meetings.

I gratefully thank the assistance of Dr Naser Jasim, Dr Emma Dux, Dr Adrian Whitwood, Dr Heather Fish, Mr Karl Heaton and Dr Alexander Heyam for training, technical support and advice. I would like to special thank Dr Barbara Procacci for her great supports and contributions to the NMR experiments, Dr. Joyashish Debgupta and Dr. Mina Anis Amin Ibrahim Meseha for their help on electrochemistry, GC technique and valuable advice and all RNP and RED research groups members.

I would like to acknowledge the Development and Promotion of Science and Technology Talents Project (DPST), Thailand for financial support. Finally, I would like to thank all members of my family, my friends for their love, care, kindness, and encouragement throughout my PhD life.

Khanittha Walaijai

March 2020

Author declaration

I declare that this thesis is a presentation of original work carried out at the university of York between March 2016 and March 2020. This work has never been presented for an award at this or any other university. I confirmed that the work submitted is my own except for the work of others where the references have been given within this thesis and for the following:

- The X-ray crystallographic determination and data analysis were performed by Dr. Adrian Whitwood
- Elemental analyses were performed by Dr Graeme McAllister.
- Mass spectra were recorded by Mr Karl Heaton.

Khanittha Walaijai

March 2020

Chapter 1

Introduction

1.1 Motivation and strategies for solar and electro-driven fuel production

There is an urgent need to find sustainable and clean energy sources due to population growth and economic development in the coming decades.[1, 2] This will inevitably cause a considerable increase in global energy consumption which is expected to increase by over 50% by the mid-2000s.[3] The worldwide energy consumption has been mainly dependent on fossil fuels e.g. coal, oil, and natural gas. However, traditional fossil fuels are non-renewable, regional around the world, and contribute to climate change due to CO_2 emission.[4] Alternative energy sources such as hydro, wind, and solar power are rapidly growing sources of sustainable electricity: however; they are intermittent, and thus require massive energy storage for short and long terms.[5] Renewable electricity also does not provide vehicle fuels for use in transportation particularly long-distant air transport, nor feedstock chemicals for industry such as plastics, fertilizers, and pharmaceuticals. Thus, it is necessary to find new approaches to provide sustainable resources for fuels and commodity productions. Solar energy is the most abundant renewable and clean energy source because the sun's energy shining on earth every hour is greater than the worldwide energy consumption for a whole year.[6-8] Thus, storage and conversion of solar energy into chemical fuels (e.g H_2 or valuable chemicals) or electricity is one of the most promising ways to address a large energy demand. The energy stored in a chemical bond has a higher energy density than electricity stored in battery with respect to weight and volume. Therefore, solar fuels have the potential to store energy in chemical bonds on a large scale. It also an ideal energy source for application in daily life such as long-distance transportation.

Hydrogen is considered as a renewable and environmental-friendly energy source[9, 10], and is a carbon-free fuel. Moreover, it can be converted to liquid compounds such as formate which allows for easier storage and transport. Regarding serious issue from global warming and climate change by CO_2 emission, the sunlight-driven CO_2 reduction into useful fuels such as carbon monoxide, formic acid, methanol or methane provides a more promising approach to alleviate energy shortage as well as global warming.[11-13]

In natural photosynthesis, solar energy is converted to chemical energy by reduction of CO_2 coupled with oxidation of H_2O to produce carbohydrates and oxygen (**Figure 1.1** a). Photosynthesis involves complicated processes where photo-induced water oxidation supplies electrons and protons after a series of physical and chemical reactions in photosystem II (PSII) such as light harvesting, charge-separation and catalytic oxidation of H_2O by Mn cluster.[7, 14, 15] to O_2, generating four protons and four electrons. After photo-excitation of photosystem I (PSI) and the electron and proton transfer processes, the CO_2 is fixed, and separated electrons and protons are finally consumed for CO_2 reduction to produce carbohydrates via the Calvin cycle. Although natural photosynthesis is extremely complicated, the functions and chemical processes can be mimicked by artificial photosynthesis to store energy in synthetic chemical fuels.

For artificial photosynthesis (schematically represented in **Figure 1.1** b), direct use of sunlight for conversion of CO_2 into fuels and more valuable chemicals with water oxidation is considered to have a promising solution for future energy supply and environmental issues.

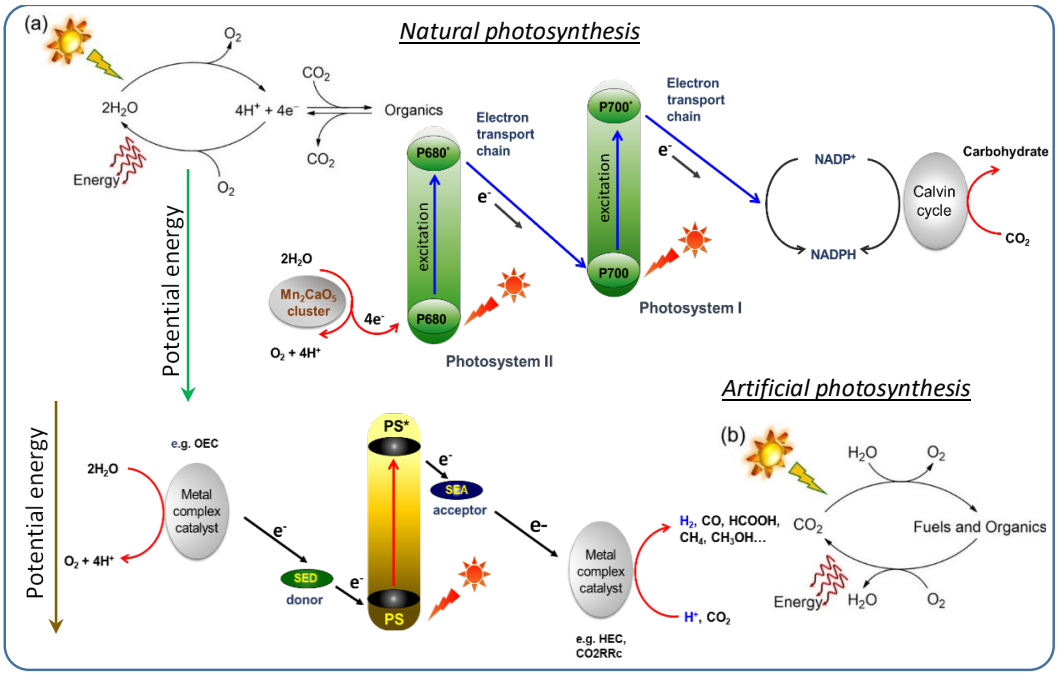

Figure 1.1. Schematic diagrams of a) natural photosynthesis and b) artificial photosynthesis based on molecular systems, and the essential components and sequential processes after light absorption. The abbreviations are photosensitizer or light absorbing unit (PS), oxygen-evolving catalyst (OEC), sacrificial electron donor (SED), sacrificial electron acceptor (SEA), hydrogen evolving catalyst (HEC) and CO_2 reduction catalysts (CO2RRc).[16]

For molecular based artificial photosynthesis, the system comprises three important components for fuel productions which are a photosensitizer or chromophore (PS), redox

mediators (SED for sacrificial electron donor and SEA for sacrificial electron acceptor) and metal complexes as catalysts (e.g. HEC, OEC and CO2RRc). Sequential processes required in the molecular assembly for fuel productions are: light absorption by excitation of a chromophore followed by energy-transfer sensitization of PS* or electron transfer quenching of a donor−chromophore−acceptor (SED−PS−SEA) array by either oxidation process, SED−PS*−SEA → SED−PS^+−SEA^-, or reduction process, SED−PS*−SEA → SED^+−PS^--SEA resulting in a spatial charge separation state. Lastly, electron transfer occurs from SEA^- to a catalyst for reduction, and to SED^+ from a catalyst for oxidation.[17] Based on this approach for light driven fuel production, a dye molecule or semiconductor is typically used as a chromophore for single excitation site attached to an SED and SEA on different side. The electron donor material (SED) requires that the energy level must be more negative than the excited state reduction potential of the chromophore (PS^*), but more positive than the potential of catalyst for oxidation reaction. Similar requirements must also be met for the electron acceptor (SEA): its potential energy level must be between the chromophore excited state oxidation potential and the water reduction potential.

Artificial photosynthesis and Functional devices for solar fuel productions

Solar energy needs to be stored in a robust way in order to use it on demand when the sun is not shining. It can be converted into fuels indirectly via electricity generated by solar energy to drive electrocatalytic reactions as represented in **Figure 1.2** a), route I-II, or it can be converted into chemical fuels by photoelectrocatalytic reactions (**Figure 1.2**, route III). There are two types of devices have been designed for the solar fuels production: the photoelectrochemical (PEC) cell and the photovoltaic-electrochemical (PV-EC) device. For example, solar H_2 production by PEC water splitting cell and/or PV–EC device as schematically depicted in **Figure 1.2** b) and c), respectively. An ideal PEC device consists of a photoanode for the oxidation process and a photocathode for the reduction process. Upon photo-excitation, the generated holes and electrons are transferred to electrocatalysts modified on the surface of photoanode and photocathode to drive photocatalytic reactions for production of chemical fuels. For the PV-EC devices, the light absorption and charge separation are completed by a solar cell which can be isolated from the electrolyzer cell.

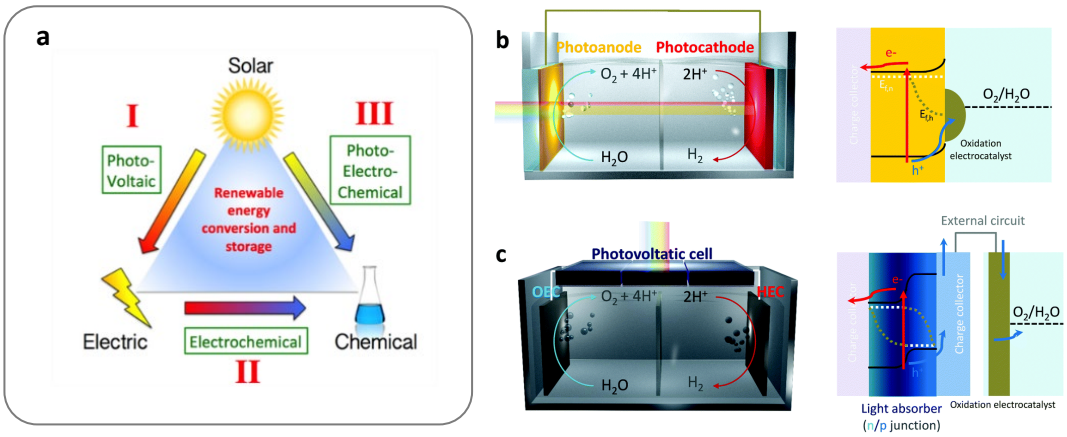

Figure 1.2. Schematic representation[18] of general concept of artificial photosynthesis (a). Types of solar-driven water splitting devices and their charge flows upon light absorption; (b) PEC and (c) PV–EC systems. Reproduced from ref [19] with permission from The Royal Society of Chemistry.

As shown by these two example devices for H_2 fuel production, electrolysis is a promising approach for the energy storage and conversion for hydrogen evolution reaction (HER) or CO_2 reduction reaction (CO2RR). However, a large scale application of electrolysis is restricted by the lack of efficient catalysts. [18, 19] An ideal catalyst should have high activity, high stability and be cost-efficient. Over the last decade, there has been considerable progress in the development of many molecular catalyst-modified electrodes for artificial photosynthesis (AP) devices. [15, 16, 18] Several approaches have been developed for modification of molecular catalysts on different conductive substrates for investigating their electrocatalytic properties.[15, 16]

In order to harness solar energy directly for fuel production, effort has been focused on the development of photoelectrochemical (PEC)[20-22] and photocatalytic water splitting.[23, 24] By this approach, semiconducting materials are generally employed as light-absorbers and modified with molecular catalysts (will be presented in **Section 1.1**) or biocatalysts (as shown in **Section 1.2**) to drive the reduction process (e.g. water splitting, H^+ reduction or CO_2 reduction). Overviews for development of molecular electrocatalysts for H_2 production and CO_2 reduction will be illustrated in **Section 1.3**. This section will summarise challenges and design principles for effective fuel production electrocatalysts including common mechanistic pathways for H^+ and CO_2 reduction. **Section 1.4** will show the early development of electrocatalysts for H_2 evolution (HECs) by the natural hydrogenases, synthetic bio-inspired HECs and earth-abundant transition metal complexes. Some examples of HECs based on various ligand platforms will be presented in **Section 1.5**. Furthermore, some selected examples of molecular CO_2 reduction electrocatalysts with well-defined mechanisms will be shown in **Section 1.6.**

1.2 Semiconductor-molecular catalyst hybrid system for HER and CO2RR

Hybrid systems consisting of a metal complex and a semiconductor are among the most promising systems for artificial photosynthesis because of the excellent electrochemical and/or photocatalytic activity of metal complexes during CO_2 reduction catalysis. Moreover, semiconductors are found to have promise for oxidizing water to O_2. Extensive efforts have been made for constructing metal complex/semiconductor hybrid systems [25, 26], since Honda and Fujita firstly demonstrated a TiO_2 semiconductor for water splitting in the 1970s. [27] For example, hybrid systems as summarized in **Figure 1.3** have been established for visible-light driven photocatalytic and photoelectrochemical CO_2 reduction. The first system **(A)** consists of a metal complex that serves as catalyst for CO_2 reduction and a semiconductor as a light-absorbing unit and oxidation site. In the second system (**B**), the combination of a supramolecular catalyst with an appropriate semiconductor photocatalyst that can absorb visible light can act as an artificial Z-scheme for CO_2 reduction. The artificial Z-scheme photocatalyst that mimics natural photosynthesis consists of two connected semiconductor photocatalysts. This process in green plants looks like the "Z letter" involving with a two-step photoexcitation. This promising strategy is designed to improve photocatalytic activity that is superior to single component photocatalysts by increasing visible light absorption and promoting charge separation and transportation of photoinduced charge carriers. For the Z-scheme system, the photocatalytic activity is strongly dependent on both the metal complex and the semiconductor components. Therefore, development of both metal complexes and semiconductors is very important for light-driven CO_2 reduction by this approach.

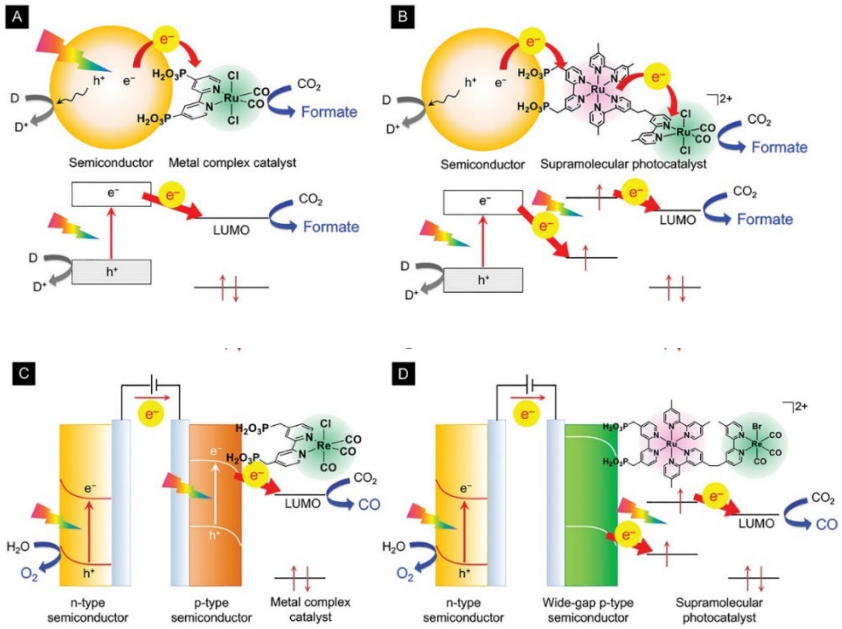

Figure 1.3. Component structure and energy diagram of a hybrid photocatalyst for CO_2 reduction. A) a semi-conductor and a metal complex, B) artificial Z-scheme system composed of a semi-conductor and a supramolecular metal complex for visible-light reduction of CO_2. C) Photoelectrochemical (PEC) system with a metal-complex catalyst. D) Photoelectrochemical system with a supramolecular photocatalyst.[25] Permission is granted subject to an appropriate acknowledgement given to K. Maeda, *Metal-Complex/Semiconductor Hybrid Photocatalysts and Photoelectrodes for CO_2 Reduction Driven by Visible Light*, 2019, **31**, 1808205.

Much effort has been focused on photoelectrochemical cells (PEC)[7-9]; the hybrid photocatalyst concept can be extended to PEC systems as shown in **Figure 1.3** C and D. The single-absorber system (**A**) with p-type visible light absorbing semiconductors (such as InP[27] and Cu_2O[28]) or a molecular dye-sensitized NiO electrode[25] can be applied as a photocathode in a photoelectrochemical cell (**C**). Similarly, a supramolecular metal complex/semiconductor Z-scheme photocatalyst (**B**) can be employed in a two photon light-absorber PEC cell (**D**). In the case of a photoanode, it can be n-type light-absorbing semiconductors with enough driving force for water oxidation[21] for example α-Fe_2O_3, WO_3 and $BiVO_4$ or a dye-sensitized TiO_2 electrode[18-20]. This photoanode supplies electrons through an external circuit. The overall system can be considered as a photoelectrochemical Z-scheme when a visible-light-responsive photoanode is employed.

One of the photocatalyst hybrid systems that have also extensively been investigated is dye-sensitized solar cell (DSPEC) as shown by the general concept for this system in **Figure 1.5**.[28] The DSPEC cells can be modified with molecular catalysts (e.g., WOCs, HECs or CO2RRc) to use the electron flow to produce chemical fuels.[29] The photoexcitation of chromophore (C) generates its excited state C* which is oxidatively quenched by transfer of electrons to the conduction band of the anode to form C^+. The C^+ is reduced by the electrons from the catalyst for the oxidation process (e.g. WOC). Electrons diffuse through the TiO_2 film to the conductive contactor, and then to the cathode, where the electrons are finally transferred to a catalyst for reduction (e.g. HEC or CO2RRc). Accordingly, this approach provides a straightforward theoretical basis for water splitting and CO_2 reduction based on the molecular chromophore and molecular catalyst.

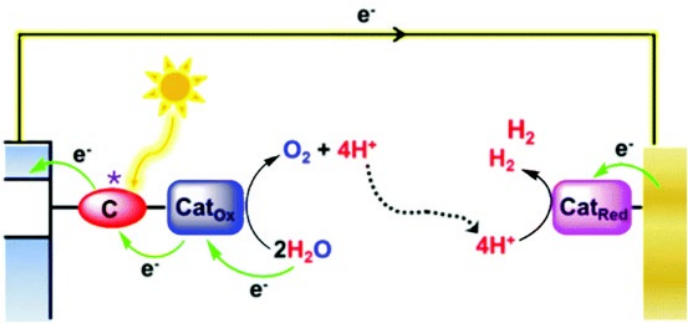

Figure 1.4. Schematic representation of principle of molecular dye-sensitized solar cells.[28]

The development of photocathode modified with HEC or CO2RRc for DSPEC cell

The example of a DSPEC cell (**Figure 1.5** a) with a NiO photocathode consisting of a molecular catalyst and organic dye (the first noble-metal free and covalent dye-catalyst assembly) was reported by Sun et.al in 2012.[30] The cobaltoxime catalyst (as HEC) was immobilized onto the photocathode. This was the first noble metal-free DSPEC cell that can produce hydrogen from mildly acidic aqueous solution driven by sunlight. More recently, the Artero group [31] reported covalently linked organic dye–cobaloxime catalyst assemblies (**Figure 1.5** c). The CV responses (**Figure 1.5** b) of each redox couple in the covalently linked organic dye-cobaloxime catalyst (compound **3**) are similar to those for $\mathbf{2_{Co}}$ and **1** indicating electronic decoupling of light harvesting and electrocatalytic components in the covalent dyad **3**. Moreover, from the redox and photophysical data, the authors could estimate an E_{0-0} value (the HOMO-LUMO energy gap) of 2.40 eV with a redox potential of -1.72 V vs $Fc^{0/+}$ for the **3+/3*** couple (**3*** is the excited state of **3**). This potential could thermochemically drive generation of Co(I) state with driving forces of 0.70 eV via oxidative quenching of **3*** as shown in **Figure 1.5** c.

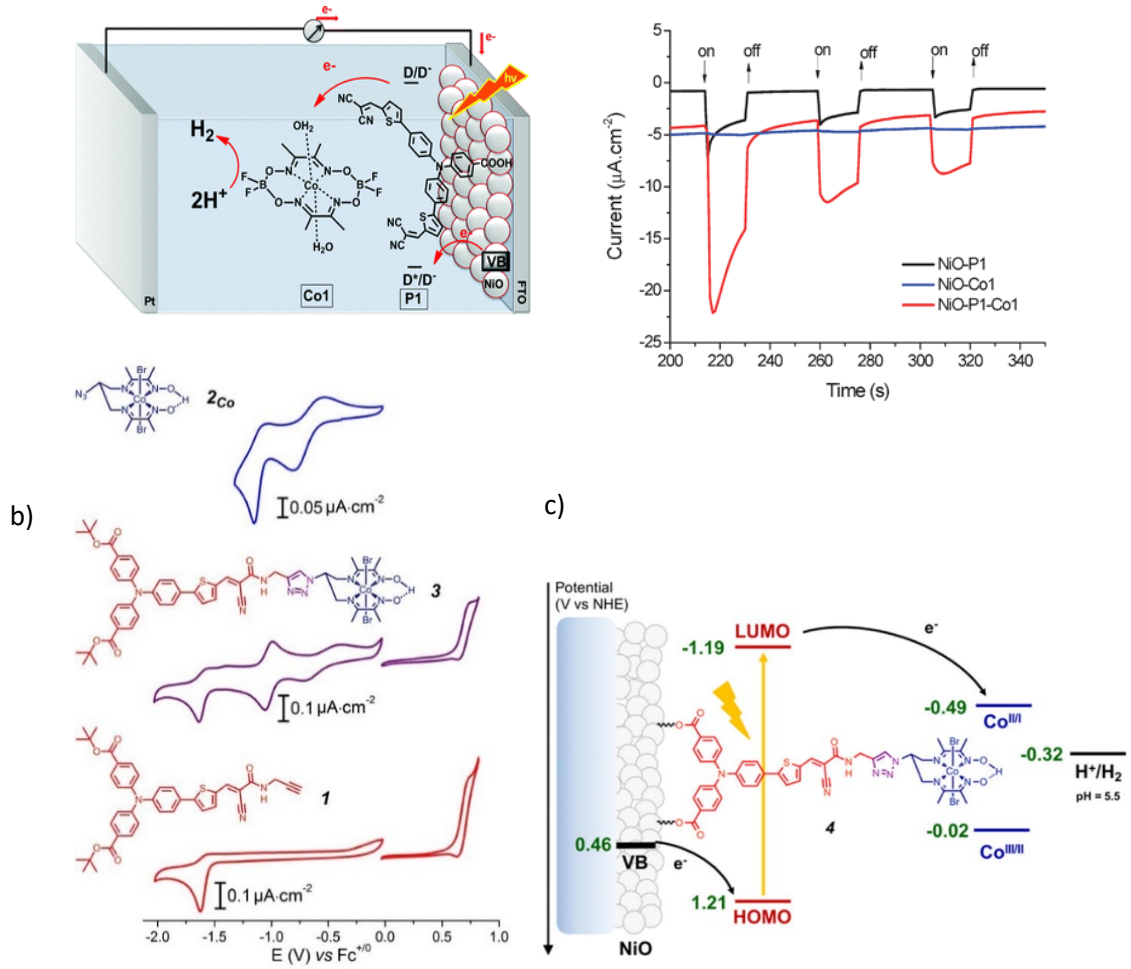

Figure 1.5. a) depiction of PEC devices consisting of a photocathode based on an organic dye sensitized nanostructured NiO film coated with cobaloxime HEC and the photoelectrochemical performance [30], b) CVs of each component: 3 (middle) compared with those of $\mathbf{2}_{Co}$ (top) and of the dye precursor **1** (bottom) and c) energy diagram for covalently linked organic dye-cobaloxime catalyst assemblies (3)-immobilized on NiO photocathode. Reproduced with permission from ref [31]. Copyright 2016 American Chemical Society.

CO2RR molecular-catalyst-modified dye-sensitized photocathode

Ishitani and co-workers [32] have developed a Ru(II)–Re(I) supramolecular photocatalyst-modified NiO p-type semiconductor for light-driven CO_2 reduction in an aqueous electrolyte solution. This system has a bias potential of 1.25 V vs. $Ag/AgNO_3$ under light ($\lambda > 460$ nm) illumination. A TON of 32 and a Faradaic efficiency of 71% were achieved for the reduction of CO_2 into CO by this DSPEC cell. Using a Ru(II)–Re(I) supramolecular photocatalyst-modified $CuGaO_2$ p-type semiconductor ($RuRe/CuGaO_2$) (**Figure 1.6**) instead of the NiO can achieve a 400 mV more positive onset potential for the conversion of CO_2 to CO as compared to the previous system using NiO photocathode [33]. This visible-light-driven catalytic reduction of CO_2 using water as a

reductant without applying any external bias is the first example of a self-driven system constructed with a molecular photocatalyst.

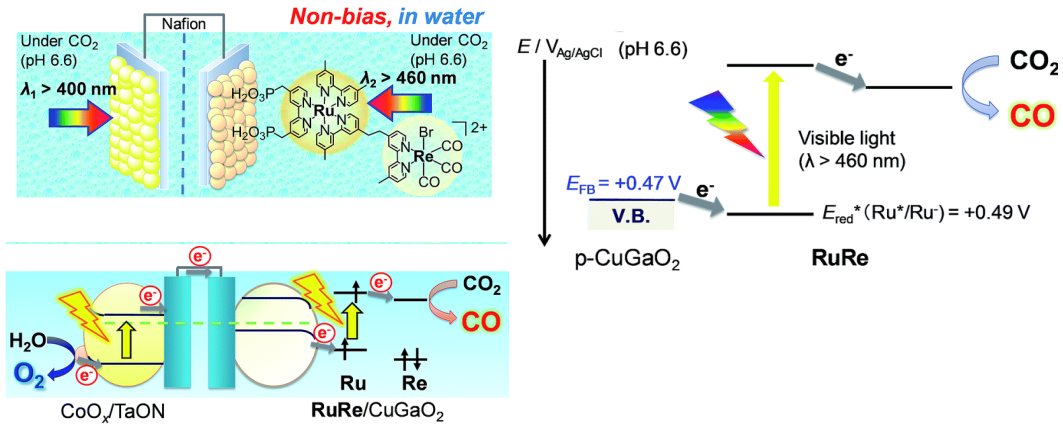

Figure 1.6. a) Schematic depiction of the hybrid photoelectrochemical cell in a Z-scheme configuration, b) reaction scheme of the reduction of CO_2 by the RuRe/$CuGaO_2$ hybrid photocathode. Reproduced from ref [33] with permission from The Royal Society of Chemistry.

A tandem DSPEC cell with visible light absorbing semiconductor (VLA-SC)

In DSPEC cells, organic dyes or molecular complexes are used to absorb light to generate charge separation, and semiconductors with large band gap (TiO_2 and NiO) are typically used to transport charge to catalytic sites. Recently, semiconductors with narrow band gaps, called visible-light-absorbing semiconductors (VLA-SCs), have been used for photoelectrode fabrication without sensitization of dyes. In recent years, p-type VLA-SCs, such as p-Si, InP, GaP, and InGaP have been employed as photocathodes for proton and CO_2 reductions.[18] For example, Ni-based ''DuBois catalysts'' and cobaloxime, which are some of the most efficient and robust complexes for H_2 evolution catalysis, have also been investigated as cocatalysts on the surface of VLA-SCs (**Figure 1.7** a) for photoelectrochemical hydrogen production.[34]

The polymer-modified GaP electrode improves the stability of photocurrent involved with the bare GaP surface by providing a protective layer that inhibits charge recombination at the bare surface. In this work, a cobaloxime species attached to a polyvinylpyridine-modified GaP electrode is photochemically active for H_2 evolution under simulated solar conditions (100 mW cm^{-2}). **Figure 1.7** b shows that the catalyst modified photocathode (red solid) achieves a selected current density at lower potential than the polymer-funtionalized GaP electrode without catalyst modification (grey dash). The photocurrent (**Figure 1.7** c) of the cobaloxime catalysts-polymer-modified electrodes (red solid) is relatively stable compared to unfunctionalized GaP

(black solid): however, the photocurrent does decrease over time due to loss of surface attached Co catalysts.This is a major issue for the reduction of photoperformance during operation.

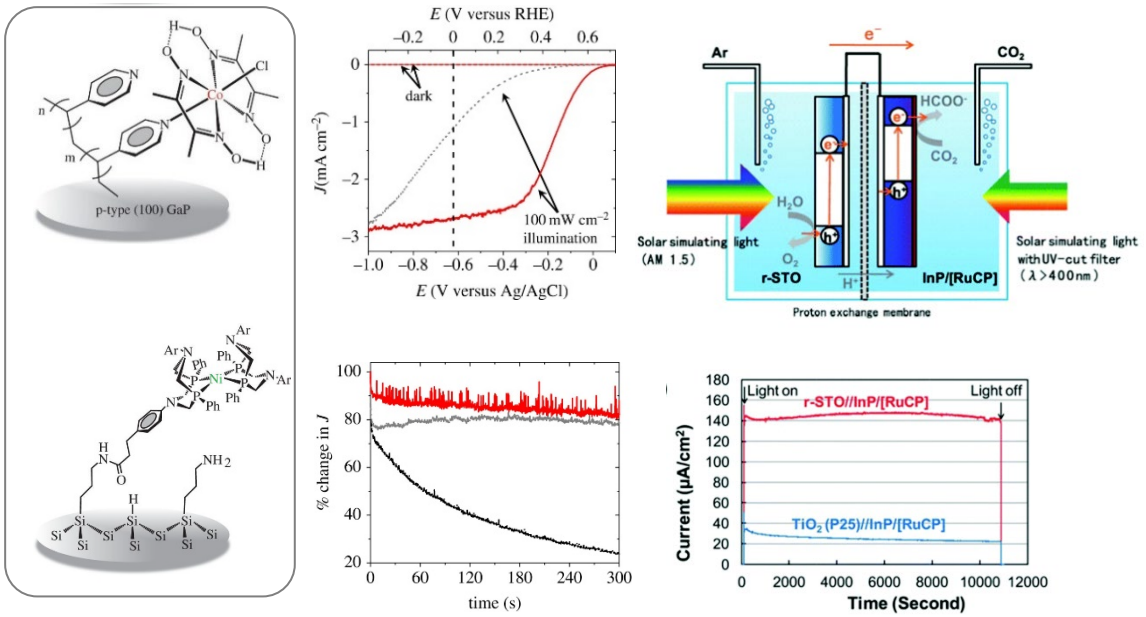

Figure 1.7. (a) cobaloxime-polymer-modified p-type GaP photocathode, the nickel bisdiphosphine-functionalized p-type Si photocathode[34]; (b) linear sweep voltammetry of the photocathode in the Fig. a (red solid), polyvinylpyridine-modified GaP substrate without catalyst modification (grey, dash). (c) electrolysis experiments (E_{app} +0.17 V vs RHE, under solar conditions: 100 mW cm^{-2}) using the photocathode a (red, solid), the polyvinylpyridine-modified GaP substrate with no catalyst modification (grey, dash), and the unmodified GaP electrode (black, solid). Figure d. shows the PEC device for CO_2 reduction consisting of a reduced $SrTiO_3$ photoanode and RuCP as molecular CO_2 reduction catalyst immobilized on InP photocathode, and (e) plots of photocurrent versus time of degradation for the molecular catalyst modified photoelectrodes. Reproduced from ref [35] with permission from The Royal Society of Chemistry.

So far VLA-SC based PEC tandem cells modified by a molecular catalyst have rarely been reported. Arai and co-workers [35] demonstrated a full device for solar formate production from CO_2 and H_2O with no external electrical bias (**Figure 1.7** d). The two half redox reactions were successfully coupled by using the RuCP/p-InP photocathode (RuCP = a ruthenium complex polymer) for CO_2 reduction and a reduced $SrTiO_3$ (r-STO) photoanode for water oxidation. This tandem cell showed a stable photocurrent and selective conversion of CO_2 to formate (**Figure 1.7** e).

Very recently, Souvik Roy and co-workers [36] reported a new three-dimensional MOF that consists of cobaloximes (**Figure 1.8** a), an extensively studied HEC, that act as metallo-linkers between hexanuclear zirconium clusters. This MOF grown on glassy carbon is capable of electrochemical H_2 production with percent faradaic efficiency (% FE) for H_2 production of 84 ±

5% over 5 h (**Figure 1.8** b). Moreover, post-electrolysis studies show that the molecular cobaloxime linkers remain intact. Powder XRD (**Figure 1.8** c) confirmed that the MOF retains its crystalline structure after electrolysis.

Hybrid materials containing cobaloxime catalyst for hydrogen production

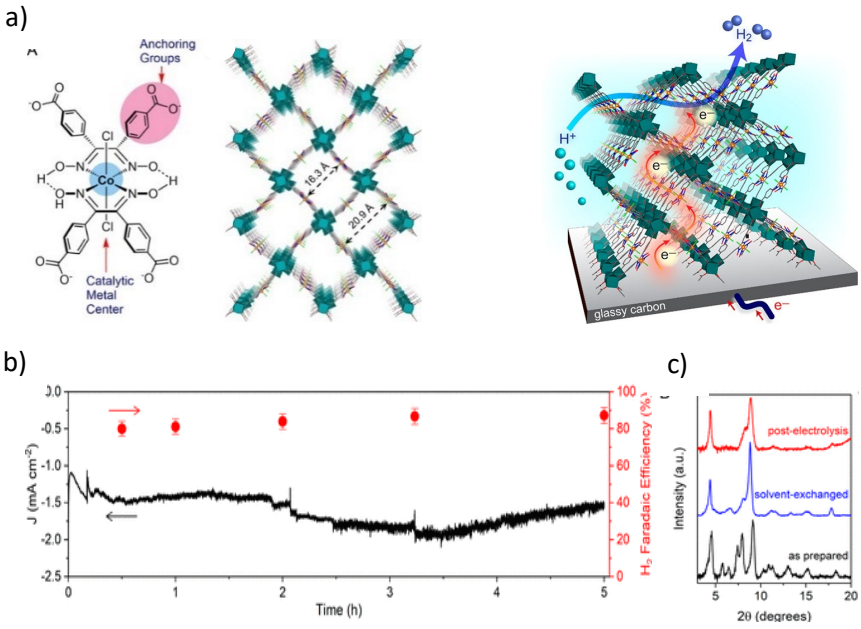

Figure 1.8. a) Structure of the cobaloxime linker and structural model of MOF viewed along [001], b) controlled potential electrolysis by this system at −0.45 V vs RHE in acetate buffer at pH 4 showing current density (black, solid), and faradaic efficiency for H_2 evolution (the red circles), and c) PXRD patterns of the as-synthesized electrodes (black), after solvent exchange with acetone for 24 h (blue), and after 5 h of electrocatalysis (red). Reproduced with permission from ref [36]. Copyright 2019 American Chemical Society.

1.3 Semiconductior modified biocatalyst hybrid system for HER and CO2RR

Biocatalysts are one of the attractive approaches for light-driven fuel productions. Hydrogenase, carbon monoxide dehydrogenase, CODHs and formic acid dehydrogenase FDH are among the most important enzymes used in the visible light driven redox systems.[37] For conversion of CO_2 to CO, the [Ni-Fe]-CODHs type are only recognized as biocatalysts for the reverse reaction of reducing CO_2 to CO at the thermodynamic potential.[38] Hydrogenases are extremely active microbial enzymes that catalyze the oxidation and production of hydrogen with reported turnover frequencies exceeding 9000 s^{-1}.[39, 40] The X-ray structure (**Figure 1.9**) of two main representative FeFe [41] and FeNi [42] clusters were revealed during 1990s. The active site of hydrogenases is deeply buried in the enzyme consisting of a [4Fe-4S] cluster as "electrical wire" to transfer e^- between the active site and protein surface, and a bimetallic [Fe-Fe] and [Ni-Fe] complex. The [Ni-Fe] hydrogenase active site consists of one CO and two CN^- ligands and the [Fe-Fe] hydrogenase contains three CO and two CN^- ligands as well as an aza-propanedithiolate (adt^{2-}) ligand bridging the two metal centres.

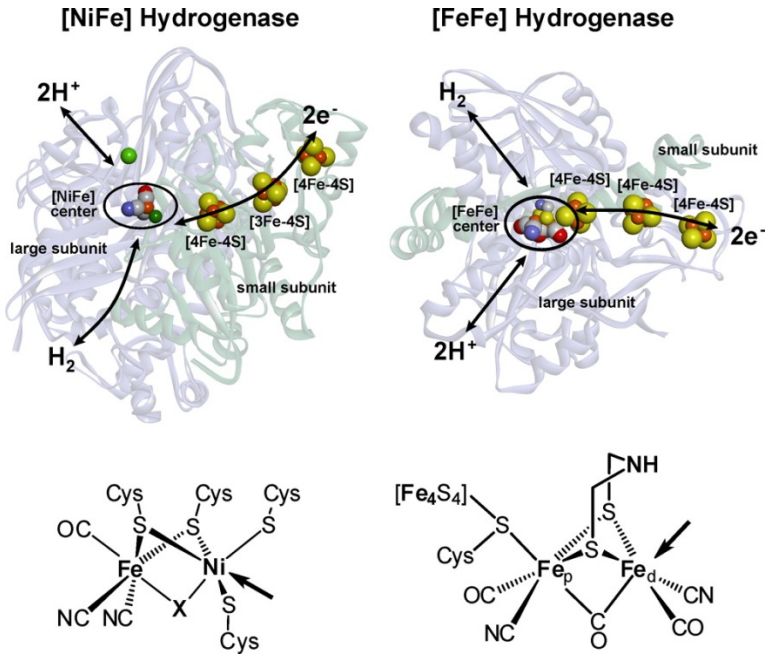

Figure 1.9. Structure of (a) [NiFe]-hydrogenase and (b) [FeFe]-hydrogenase (H-cluster). Fe_d and Fe_p denote the distal and proximal iron, respectively. Schematically indicated are the ET chain (via iron–sulfur centres), and the dihydrogen and the H^+ transfer pathways. The chemical structure of the active sites are shown with the arrows indicating the open metal coordination site. Adapted with permission from ref [39]. Copyright 2014 American Chemical Society.

To date, several detailed reviews on structure of catalytic sites in hydrogenases and their functional roles for H^+/H_2 interconversion have been published. Since 2007, considerably more information of this class of enzyme has been gained by several X-ray crystallographic structures. Furthermore, advanced spectroscopic methods[43, 44] novel electrochemical techniques[45] computational studies[46] were applied together to understand structure of catalytic sites in hydrogenases and the relationships between their structures and functions for H^+ uptake /H_2 production. Moreover, in recent years, detailed information on the H_2 evolution mechanisms has been reported by elucidating the role of hydride intermediate in hydrogenase active sites.[47]

As mentioned previously, the future employment of the hydrogen economy requires processes for producing H_2 from renewable sources (sunlight, water) and low cost techniques. Therefore, substituting a cheap element that can catalyze the reaction at a reasonable potential is a relevant approach as an alternative to the use of platinum electrode. Biocatalysts can fulfil these requirements because they use earth abundant metals in their active site (Fe and Ni), and their catalytic performance is comparable to Pt.[40] Therefore, one of the promising ways for the development of technologies for capturing and storing renewable energy as a fuel is using biocatalysts integrated in fuel cells or artificial devices. However, some problems remain to be faced in this area e.g. their stability under the air, enzyme immobilization.

For example, CODH modified on TiO_2 nanoparticles (**Figure 1.10** a), with ruthenium complex as photosensitizer, can selectively convert CO_2 to CO with a TOF of $\sim$ 0.18 s^{-1}.[48] Very recently, Armstrong group [49] developed the system for CO_2 conversion by the combination of nanoclusters stabilized by polymethacrylic acid (AgNCs-PMAA) as effective photosensitizer (**Figure 1.10** b). This system showed fast and selective, visible-light driven conversion of CO_2 to CO with a TOF of 20 s^{-1} at ambient temperature. Strong coupling of the Ag nanoclusters on TiO_2 facilitates the electron transfer required for CO_2 reduction catalytic activity on CODH. More effective performance of CO_2 conversion by hybrid semiconductor-photosensitizer/enzyme systems could be achieved by increasing the flux of photo-generated electrons.[49]

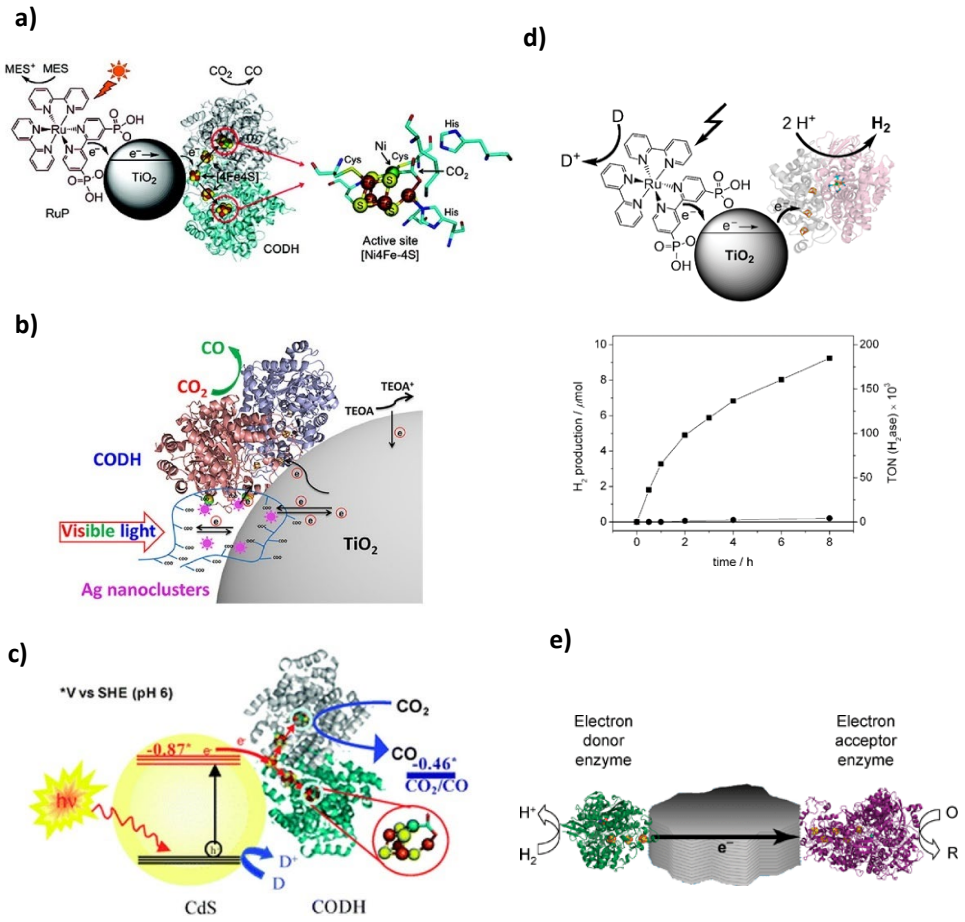

Figure 1.10. Examples of semiconductor-biohybrid systems for CO_2 reduction to CO with CODH immobilised on TiO_2 nanoparticles sensitized with RuP dye (a). Reproduced with permission from ref [48]. Copyright 2010 American Chemical Society. TiO_2 nanoparticles sensitized with silver nanoclusters stabilized by polymethacrylic acid (b) and CdS nanorods (c). Reproduced with permission from ref [49]. Copyright 2018 American Chemical Society. The semiconductor-biohybrid systems (d) for H_2 evolution with hydrogenases immobilized on the same sensitizer as that of a) with time-dependent H_2 evolution profile by irradiation ($\lambda > 420$ nm) at 25 °C in neutral aqueous solution (squares) measured by GC. Reproduced from ref [50] with permission from The Royal Society of Chemistry. A schematic representation (e) of e- flow through a conducting particle modified with a hydrogenase and another enzyme for a reduction process. Reproduced from ref [51] with permission from The Royal Society of Chemistry.

Moreover, the use of this enzyme for visible-light driven CO_2 reduction by sensitized hybrid semiconductor (**Figure 1.10** c) developed by the same group was influenced by the size and shapes of semiconductor particles. By this consideration, CODH attached on CdS nanorods exhibited average TOF of 1.23 s^{-1}, compared to 0.25 s^{-1} observed for the enzyme on CdS quantum dots.[52] The semiconductor biohybrid system for visible-light-driven H_2 production (**Figure 1.10** d) was also acheved by the Armstrong group.[50] This system is constructed by using TiO_2 attached with the photosensitizer, $[Ru^{II}(bpy)_2(4,4'\text{-}(PO_3H_2)_2\text{-}bpy)]^{2+}$(RuP), along with

immobilized O_2-tolerant [NiFeSe]-hydrogenase and using TEOA as a sacrificial electron donor (D). The natural [NiFeSe]-hydrogenase (by changing one of terminal cysteine ligands on the nickel ion to selenocysteine) is found to be more O_2 tolerant than the [Ni-Fe] hydrogenase.[53] This stable hydrogenase also displayed better electrocatalytic performance than that of the [Fe-Fe]- and [Ni-Fe]-hydrogenases by showing higher oxygen tolerance with the retention of high H_2 production. Another new concept (**Figure 1.10** e) for enzymatic catalysis on conducting substrates was developed by this group.[54] Coupling of hydrogenase (electron donor enzyme) and nitrate reductase or fumarate reductase (electron acceptor) to graphite particles can achieve selective reduction of nitrate or fumarate by H_2. In recent years, the development of immobilized biocatalysts on conductive material or semiconductors for photoelectrochemical or electrochemical fuel-forming reactions has demonstrated promising results.[55-57]

1.4 Solar fuel productions by electrocatalysis

1.4.1 Electrocatalytic performance by hydrogenases

Electrocatalysis of hydrogenases for reversible uptake H^+/H_2 production has been extensively studied by "protein film electrochemistry" (PFE). The dynamic cyclic voltammetry technique was first introduced by Armstrong and co-workers[45] and has then been extensively used to investigate catalytic properties of hydrogenases including their mechanisms and kinetics for oxidation and reduction of molecular hydrogen as well as inactivation pathways of the enzymes.[39] In PFE experiments, the hydrogenase has to be immobilized on the electrode surface (**Figure 1.11** a) via the distal [4Fe-4S] cluster to obtain direct ET between protein and electrode. Monitoring current generated by catalytic reaction of hydrogenase in the presence of substrate allows kinetic information (TOF) to be obtained as a function of the electrode potential.

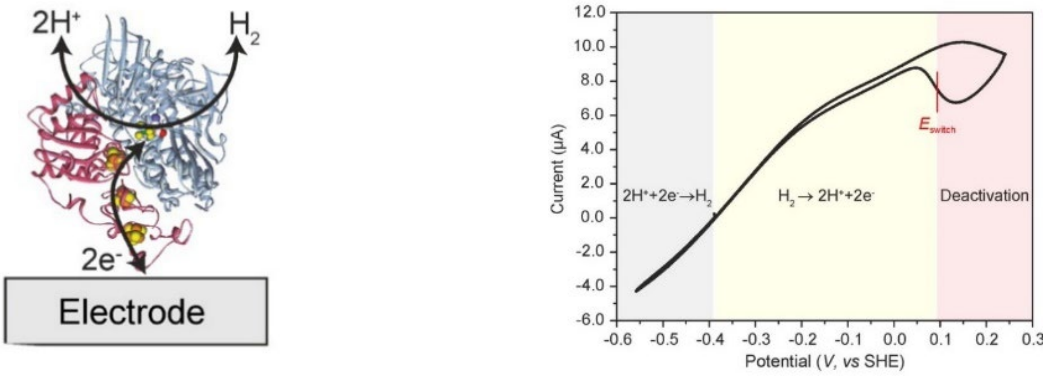

Figure 1.11. a) Schematic representation of the enzyme modified on electrode surface for PFE experiment, b) cyclic voltammogram for reversible H_2 production obtained for the [FeFe] hydrogenase from Dd (*Desulfovibrio desulfuricans*) attached to a pyrolytic graphite electrode (PGE) operating near E^0. Reproduced with permission from ref [39]. Copyright 2014 American Chemical Society.

A well-defined CV response is linked to the catalytic activity of the enzyme modified on the electrode surface. For example, **Figure 1.11** b shows positive currents which correspond to oxidation of H_2 and negative currents to H^+ reduction (H_2 production). In terms of electrode potentials, the three regions in the CV can be typically defined. Scanning to more negative potentials, the higher negative current is obtained due to a H^+ reduction to H_2 and then the direction of the reaction switches to H_2 oxidation at more positive potentials. At higher potentials, the catalytic current starts to drop because the enzyme is oxidized to the inactive states. The deactivation process of the enzyme occurs at higher potentials because the electrode has such a strict redox control on the active site of the hydrogenase. At high potentials, the enzyme is oxidized to the inactive states resulting in the start of current drop. This is a general feature of [NiFe] and [FeFe] hydrogenases. When the potential is swept back to negative direction, the catalytic activity is completely restored. Moreover, inhibition of the activity of hydrogenases by O_2 ,H_2 or CO can be studied by dynamic voltammetry.[39]

1.4.2 Electrocatalysis by small-molecules for H_2 evolution

In an electrocatalytic H_2 production system by a molecular catalyst, at a given potential, heterogeneous electron transfer is directly supplied from an electrode to a homogeneous catalyst in a diffusion-reaction layer near electrode surface to form in situ the active intermediates for H_2 production. Therefore, proton reduction catalysis by molecular catalysts is generally indicated by changes in cyclic voltammetry upon addition of acid HA as illustrated by the CVs of Dubois catalyst in **Figure 1.12** a.

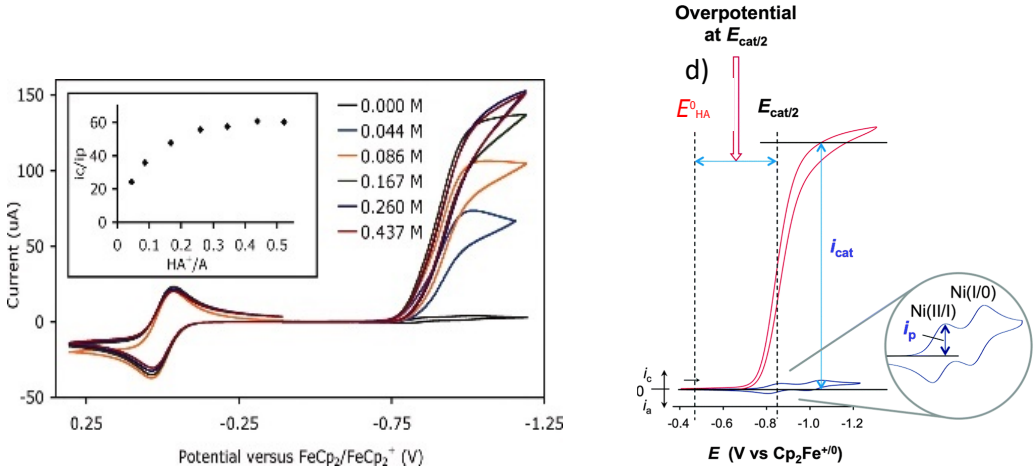

Figure 1.12. a) the CVs of a solution of the $[Ni(P^{Ph}_2N^{Ph}_2)_2(MeCN)]^{2+}$ in MeCN with $TBAPF_6$ upon addition of H^+-DMF(OTF)/DMF up to 437 mM, small inset displays i_{cat}/i_p values *vs.* [H^+-DMF(OTF)/DMF] [58] and b) the CV of $[Ni(P^{Ph}_2N^{Ph}_2)_2]^{2+}$ showing catalytic current enhancement (i_{cat}), non-catalytic current (i_p), thermodynamic potential for proton reduction (E^0_{HA}), half wave potential for catalysis ($E_{cat/2}$), and the resultant overpotential at $E_{cat/2}$. Reproduced from ref [59] with permission from The Royal Society of Chemistry.

An important thermodynamic parameter is the so called "overpotential" which is the difference E_{cat}–E^0_{HA}: overpotential (η) = E_{cat}-$E^0_{HA/H2}$. For accurate determination of the overpotential of a catalysts, the catalytic potential at half of the observed current ($E_{cat/2}$, as shown in **Figure 1.12** b) is preferred to the overpotential calculated by using an onset potential at the base of the wave.[59] In case of using HA acid in particular non-aqeous solvent, $E^0_{HA/H2}$ can be determined by the **eq 1.1** shown below, where $E^0_{H+/H2}$ is the potential of the proton/hydrogen couple[60] and $pK_{a,HA,S}$ is the acid dissociation constant in a particular organic solvent (S).

$$E^0_{HA/H2} = E^0_{H+/H2} - (2.303RT/F)pK_{a,HA,S} \qquad \textbf{eq 1.1}$$

These catalysts are typically investigated in dry organic solvents (e.g. CH_3CN, DMF or CH_2Cl_2) with added acids (HA) as H^+ source for investigating their catalytic activities and mechanistic H_2 evolution pathways. Generally, direct electrochemical reduction of H^+ on electrode surfaces

requires large overvoltages. The direct reduction potential of HA, standard potential $E^0_{HA}$for the HA/A^-, H_2 half-reactions by using glassy carbon electrode, and their $pK_{a,HA}$ values in MeCN are listed by Dempsey.[61] The general concept of current enhancement is illustrated in **Figure 1.12** b which shows data of the $[Ni(P^{Ph}_2N^{Ph}_2)_2]^{2+}$ catalysts for production of H_2. The increase in catalytic current occurs at the Ni(II/I) couple, and. the value of i_{cat}/i_p is related to the observed rate constant (k_{obs}) as described laer in **section1.5.1.**

The example of electrocatalysis by a molecular system for reversible H_2 production is shown in **Figure 1.13**. This is the first example of a synthetic catalyst that shows a similar catalytic role as that observed in natural hydrogenases.[62] The interconversion between H^+ and H_2 could be operated near the thermodynamic potential as indicated by a dotted line, and it catalyzes H_2 production at very low overpotential (68 mV). From the CV response in each experiment, it can be interpreted that the complex in a solution with added H^+ source under N_2 (green trace) showed catalytic H^+ reduction at potentials negative of 0.55 V vs Fc^+/Fc. When the same solution is sparged with H_2 (red trace), an oxidation current is observed, indicating oxidation of H_2. Furthermore, the reductive current is decreased because of product (H_2) inhibition. [62]

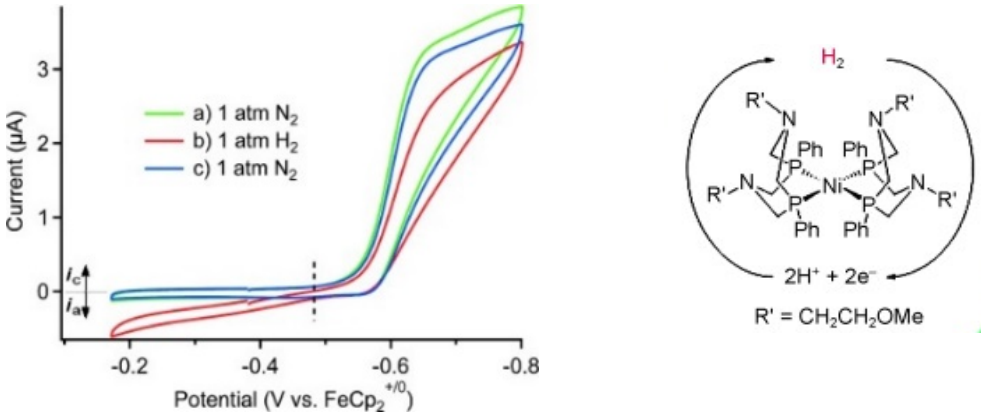

Figure 1.13. CVs obtained from molecular synthetic $[Ni(P^{Ph}_2N^{R'}_2)_2]^{2+}$ displaying reversibly catalytic H_2 production/oxidation. The dotted line indicates the formal reduction potential of the H^+/H_2 couple expected under these conditions.[62] Permission is granted subject to an appropriate acknowledgement given to S. E. Smith, J. Y. Yang, D. L. DuBois and R. M. Bullock, *Reversible Electrocatalytic Production and Oxidation of Hydrogen at Low Overpotentials by a Functional Hydrogenase Mimic*, 2012, **51**, 3152-3155.

1.5 Artificial molecular electrocatalysts for HER and CO2RR

As mentioned above, the development of non-precious metal-based catalysts has gained much attention over the last decade. More recently, the integration of the molecular catalysts in solid-state materials or devices to operate in water has been found to be very promising. The recent review in artificial fuel synthesis [18] commented that the construction of molecule-based devices for the production of fuels from renewable source (sunlight, CO_2 and H_2O) is still far from practical applications. The main issues for molecular catalysts in artificial photosynthesis are long-term stability and lack of effective heterogenization of them in artificial devices.[18] This review emphasized the importance of molecular catalysts, as listed below.

(1) Their active sites are clearly identified with readily characterized structure by conventional spectroscopic and X-ray crystallographic analysis.
(2) Their catalytic mechanisms can be investigated by techniques such as UV-Vis spectroscopy, *in situ* IR spectroscopy, *in situ* NMR spectroscopy and *in situ* MS and spectroelectrochemistry.
(3) Their steric and electronic properties can be properly tuned by specific coordination environment via ligand design.
(4) Their unique structures with single active sites have intrinsic catalytic activity which can be directly improved by a rational design.
(5) Product selectivity is controlled by single, identifiable and adjustable active sites.
(6) Molecular catalysts have high metal-atom economy.

Accordingly, the first stage to achieve a viable AP device is the development of efficient and robust molecular catalysts with high intrinsic activity, low overpotential, and a high catalytic rate.

1.5.1 General concepts for development of molecular electrocatalysts

In general, optimal electrocatalysts must have a good thermodynamic match between the redox potential (E^0) for electron transfer reaction and chemical reaction that is being catalysed as listed in the **Table 1.1**. For example, reduction of substrate CO_2 to CO product requires an electrocatalysts with formal potentials, $E^0(Cat^{n+/0})$ well matched to thermodynamic potential, $E^0(CO/CO_2)$, and appreciable rate constants, k_{cat}, for the chemical reduction of substrates to products at this potential. Thus, both thermodynamic: $E^0(Cat^{n+/0})$, E^0 (products/substrates) and and kinetic parameters (k_{cat}) are important for electrocatalysis. A general approach for substrate conversion by electrocatalysis is represented in **Scheme 1.1**.

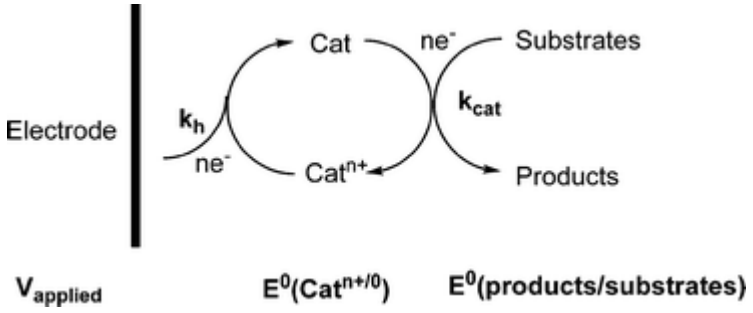

Scheme 1.1. Electrocatalysis by molecular electrocatalysts.[63]

Direct electrochemical reduction of H^+ or carbon dioxide on most electrode surfaces requires large overvoltages. The overvoltage or overpotential ($\eta = E_{app}\text{-}E^0$(products/substrates)) is defined by the difference between the applied electrode potential (E_{app}) and thermodynamic potential, E^0(products/substrates), at a given current density. Therefore, optimal catalysts are expected to minimize overpotential, and their electron transfer and chemical kinetics must be rapid for efficient catalysis. In addition, an electrocatalyst involves heterogeneous electron transfer between the electrode and the catalyst in a solution. The heterogeneous rate constant, k_h, for reduction of the electrocatalyst at the electrode must be high for applied potential near $E^0(Cat^{n+/0})$.

Additionally, the value of i_{cat}/i_p is essentially a measure of the rate of regeneration of the catalyst present in the diffusion layer. For example, H_2 evolution electrocatalyst in the presence of high acid concentration [HA], the catalytic current reaches a plateau value indicating that the current is limited by the rate of the catalytic cycle, not by proton diffusion.[58] Therefore, the i_{cat}/i_p ratios related to the observed rate constant (k_{obs}) as shown in the **eq 1.2** below.

$$\frac{i_{cat}}{i_p} = \frac{n}{0.4463}\sqrt{\frac{RTk_{obs}}{Fv}} \qquad \textbf{eq 1.2}$$

For a two-electron (n = 2) catalytic process at 298 K, this equation can be rearranged to give k_{obs} which is equal to the TOF as shown in the **eq 1.3**

$$k_{obs} = TOF = 0.0497 \times \frac{F\nu}{RT} \times (\frac{i_{cat}}{i_p})^2 \qquad \textbf{eq 1.3}$$

where R = universal gas constant, *T* =the temperature in Kelvin, F= Faraday's constant, and the scan rate (ν) in V s^{-1}. [59] Therefore, the catalytic rate of hydrogen evolution is reflected by TOF value (s^{-1}). For comparison of electrocatalysts, there are typically two parameters (overpotential and TOF values) that are employed for defining a good or bad catalyst.

Savéant [64] introduced a simple method for determining the TOF which is possible by comparing the observed current for a catalyst under catalytic conditions to the current observed under non-catalytic conditions. The more precise benchmarking of electrocatalysts by kinetic analysis called "Foot-of-the-wave analysis" which was subsequently developed by Savéant will be thoroughly described in **chapter 3, section 3.1.2** Moreover, detailed cyclic voltammetry and the electrochemistry of cobalt hydride complexes under non-catalytic condition will be presented in **chapter 2**, **section 2.2** and **2.3.3**, respectively.

1.5.2 Challenges in fuel production by molecular electrocatalysis

The catalysis for H_2 evolution (eq.8) or CO_2 reduction (eq.1-7 in) involves multiple electron and proton transfers, and they are both thermodynamically and kinetically unfavourable.[63] The multielectron reduction of CO_2 with coupled proton transfer occurs at similar thermodynamic potentials (E^0) to H^+ reduction. Therefore, different reactions can compete resulting in poor selectivity particularly aqueous solution. Under the condition with water, proton reduction to H_2 will become a significant competing reaction.[11, 65] However, selectivity for a particular product can be tuned by using molecular catalysts.

Table 1.1. Formal electrochemical redox potentials (pH 7) for the reduction of CO_2 and related compounds in aqueous media.

Reduction potentials of CO_2	E° [V] vs SHE at pH 7
$CO_2 + e^- \rightarrow CO_2^-$	−1.9
$CO_2 + 2H^+ + 2e^- \rightarrow HCOOH$	−0.61
$CO_2 + 2H^+ + 2e^- \rightarrow CO + H_2O$	−0.52
$2CO_2 + 12H^+ + 12e^- \rightarrow C_2H_4 + 4H_2O$	−0.34
$CO_2 + 4H^+ + 4e^- \rightarrow HCHO + H_2O$	−0.51
$CO_2 + 6H^+ + 6e^- \rightarrow CH_3OH + H_2O$	−0.38
$CO_2 + 8H^+ + 8e^- \rightarrow CH_4 + 2H_2O$	−0.24
$2H^+ + 2e^- \rightarrow H_2$	−0.42

Typically, the use of metal complexes to catalyze H_2 evolution or CO_2 reduction involves multi-electron and multi-proton transfer processes. This PCET reaction catalysed by 3d transition metal complexes is much more challenging than the reaction catalysed by noble metal complexes which can efficiently mediate two-electron transfer process as discussed below.[66] Most 3d transition metal complexes require relatively high overpotential to achieve the reaction compared to the activity of noble-metal catalysts[16], and the reaction rate is slower than that mediated by platinum complexes.[67]

1.5.3 Common mechanistic pathways for H^+ and CO_2 reduction

Several research groups [16, 68-71] have investigated the fundamental mechanisms of hydrogen evolution in order to design more rational molecular catalysts for further application to heterogeneous systems and use in fully aqueous condition. The mechanisms for H_2 production by molecular transition-metal complexes have been studied both experimentally and theoretically.[72] In most cases, it is proposed to go via common metal-hydride intermediates (**Scheme. 1.2** a) which are formed by reduction and protonation of a metal centre.[16, 72, 73] The hydride intermediates can subsequently produce H_2 via two possible pathways. For the

homolytic route, bimetallic reaction of metal hydride complexes results in H_2 formation via reductive elimination. Alternatively, an additional reduction of H-$M^{(n+1)+}$ to H-$M^{(n)+}$ followed by protonation can lead to a formation of H_2 by a heterolytic pathway. Both pathways can also occur simultaneously, and the major route depends on the experimental conditions used (e.g. catalysts concentration, proton source, or pH solution).[74]

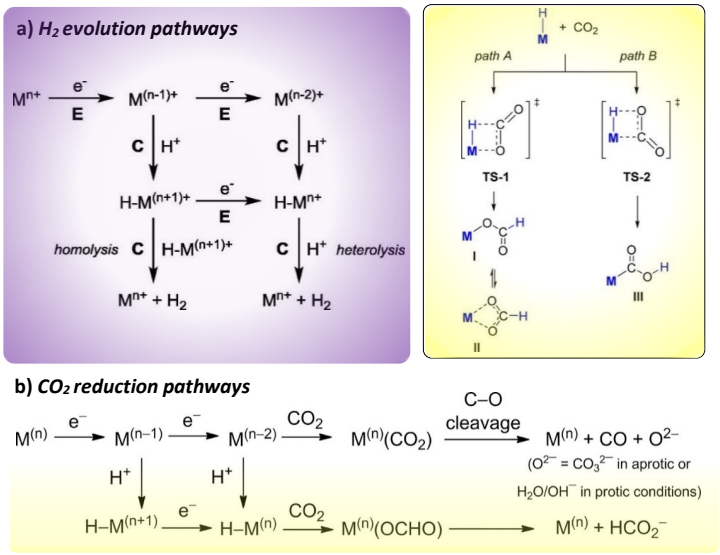

Scheme. 1.2. a) Possible reaction pathways for the HER catalyzed by metal complexes. [65], b) competitive reaction pathways for CO and HCO_2H formation from CO_2 showing the role of the metal-hydride for controlling product distribution.[16] Either of the two hydrides shown can undergo side reactions to form H_2 as shown in a. Inset shows mechanisms for CO_2 insertion into M-H bond.

Reaction of CO_2 with molecular complexes often occurs either by insertion into a metal-hydride bond or by binding to a vacant coordination site at the metal centre (**Scheme. 1.2** b). The common pathway is the CO_2 insertion into a metal-hydride which is believed to be promoted by electrostatic attractions between the polarized $O^{\delta-}$–$C^{\delta+}$ and $M^{\delta+}$–$H^{\delta-}$ bonds, positioning the electrophilic carbon-atom in close proximity to the nucleophilic hydride moiety. The M–H species interacts with CO_2 molecule either **TS-1** or **TS-2** resulting in the formation of a M–OCHO or a M–COOH species (**Scheme. 1.2**, inset). It can also react with H^+ to produce molecular hydrogen (H_2): therefore; the acidity of a solution may influence the product distribution between CO, formate and H_2 the products.

In contrast, electron-rich metal centre with free binding sites favour CO_2 activation through monodentate C-coordination, leading to a metallo-carboxylate species. The η^1-C-bound CO_2 product is readily for protonation in order to facilitate C–O bond cleavage by a push–pull mechanism.[75] In this pathway, the electron-rich metal centre pushes electron density into the

CO_2 ligand while the protons assist the electron transfer by pulling out electron density, ultimately leading to C–O bond cleavage and liberation of water. Based on these two different pathways that vary in the mode of CO_2 activation at metal centres, HCO_2H is generally obtained as a product in the former case, while the CO product formed by the latter pathways is more often observed for electrocatalytic CO_2 reduction by transition metal complexes.

1.5.4 Design principles for effective hydrogen evolution electrocatalysts (HECs)

Mechanistic studies highlight several design considerations (**Scheme 1.3**) that are required for effective catalytic H_2 production mediated by transition-metal complexes that involve formation of hydride intermediates in catalytic cycles. Firstly, an available coordination site and suitable electronic properties of the catalysts are important for a formation of metal-hydride intermediates. Secondly, the overpotential required for proton reduction can be minimized by choosing appropriate ligands that can stabilize reducing metal species. Tuning of their redox potentials can mostly be achieved at the metal or via metal-ligand cooperativity using a non-innocent redox active ligand. Alternatively, tuning of overpotential can be possible by integration of protonation sites into the core structure of catalysts by mimicking the function of hydrogenase (see **section 1.6**). Moreover, the design of catalysts that can function in fully aqueous conditions offers advantages from the maintenance of high local substrate concentration.[72]

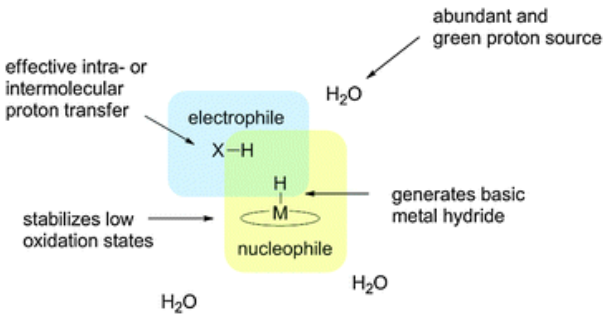

Scheme 1.3. Design parameters for effective HECs that operate via a common metal-hydride intermediate. Reproduced from ref [72] with permission from The Royal Society of Chemistry.

1.5.5 Thermodynamic and kinetic considerations for transition metal hydrides

M-H bond cleavage and reactivity of transition metal hydrides

The metal-hydride bond (M-H bond) in a transition metal hydride can be cleaved via three different modes (**Scheme 1.4**): homolytic dissociation to a hydrogen atom or heterolytic cleavage to a proton with the respective given bond dissociation energy (BDFE) and pKa parameters. The third mode, the heterolytic bond dissociation free energy (ΔG^0_{H-}) of the M-H bond in a $[M\text{-}H]^{(n-1)+}$ to yield the $[M]^{n+}$ and the H^- anion defines hydricity (hydride donor ability)

of the metal hydride intermediate. The *hydride donor ability* is also considered synonymous with the term *thermodynamic hydricity,* ΔG^0_{H-}. The heterolytic clevage of M-H bond to give H^- is endoergic, and the magnitude of ΔG^0_{H-} indicates the amount of energy required for bond cleavage. Therefore, hydrides of metal with lower ΔG^0_{H-} value are better hydride donors. The formal cleavage of M-H can also lead a generation of M^- and H^+. The acidity of metal hydrides is defined by pK_a value and are considered as the same trend as the ΔG^0_{H-} value. The lower pKa values are considered as better H^+ donor.

These three M-H clevage modes are related to one-electron reduction processes of the $[M]^{n+}$ via the thermodynamic cycle (**Scheme 1.4**) showing the relationship between pKa, BDFE, hydricity of a metal hydride and reduction potentails ($E^0(M^{+/\bullet})$ and $E^0(M^{\bullet/-})$) of the parent $[M]^{n+}$.[76]

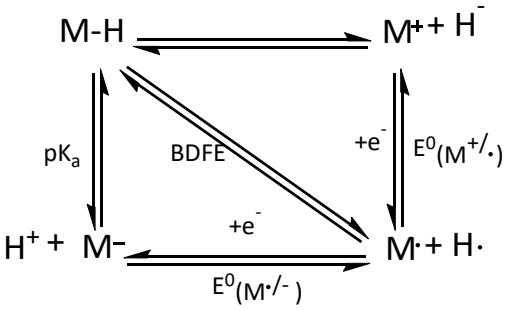

Scheme 1.4. Modes of metal-hydride bond dissociation and related thermodynamic parameters.

Acidity of metal hydrides

The acidity of metal hydrides trends to decrese from first or second row metals to third row congeners: the more acidic of $HMo(CO)_3Cp$ (pka = 8.3) than the $HW(CO)_3Cp$ with the pka of 16.1. The acidity of first-row metal hydride $HMn(CO)_5$ with pka = 14.2 is very different from the third row congener $HRe(CO)_5$ (pKa of 21.1). Furthermore, oxidation of netral hydrides to cationic hydride complexes can greatly increase the acidity.[77]

The electronic effects from ligands can also result in changes of the acidity: for example; changing from electron-withdrawing CO ligand to electron-donating phophine lowers the acidity. The variation of substituents of the two phosphine ligands in the the Ni hydride complexes changing from phenyl group in the $[HNi(dppe)]^+$ (dppe = 1,2-bis(di-phenylphosphino)ethane) to better methyl electron donating moiety in the $[HNi(dmpe)_2]^+$ (dmpe = 1,2-bis(di-methylphosphino)ethane) causes the much higher pKa values from 14.2 to 24.3 in MeCN.[78]

The DuBois group [79] have examined the pKa values of a series of the cobalt hydrides containing two phosphine ligands (dppe) exhibiting a considerable range of about 27 pKa units dependent

on their oxidation states and charges. The neutral hydride $HCo(dppe)_2$ has a low acidity with pKa of 38.1, while the dicationic hydride, $[HCo(dppe)_2(MeCN)]^{2+}$ (pKa = 11.3) is the most acidic species among the compleses in this series.

Hydricity of transition metal hydrides

The hydricity for the well-studied $[HM(diphosphine)_2]^+$ series is dependent on three main factors which are 1) the substituents on the phosphine ligand, 2) the bite angle of the diphosphine ligand and 3) the metal. The hydricity of $[HNi(dmpe)_2]^+$ containing electron-donating Me groups is greater than that of $[HNi(dppe)_2]^+$ by 12 kcal mol^{-1}. The hydrides of Co, Rh, and Pd show the similar trends to the hydricity of the Ni complexes by the same variation of the diphosphine ligands. Remarkably changes in hydricity are found when the metal center is changed. For isoelectronic complexes, the hydricity varies in the order second row > third row > first row.[80] By variation of these structural and electronic parameters, the range of hydricities for metal hydrides spans a range of ΔG^0_{H-} value from 26 to 76 kcal mol^{-1} providing tunable reactivity of metal hydrides in the designed catalyst that may require either strong or weak hydride donor ability for specific H^- transfer reactions.[80]

1.5.6 Hydride transfer reactions of metal hydrides for fuel-forming reactions

A crucial step for the reduction of H^+ to H_2 and conversion of CO_2 to formate catalysed reaction by transition metal hydride intermediates is formal hydride transfer to the H^+ and CO_2 substrate. Accordingly, hydride donor ability is a key descriptor of metal hydride reactivity.[81]

For an electrocatalytic H^+ reduction, the thermodynamic considerations for HER mechanism that involve with a protonation of the hydride intermediate can be described in terms of the hydricity (hydride donor ability) of the metal hydride intermediate (ΔG^0_{H-}), the pKa of acid and the free energy of heterolytic clevage of H_2 (hydricity of dihydrogen, ΔG^0 (H_2) = 76.0 kcal mol^{-1} in acetonitrile (**Scheme 1.5**).[82, 83]

$$[M\text{-}H]^{(n-1)+} \rightleftharpoons [M]^{n+} + H^- \qquad \Delta G^0_{H-} \qquad (1)$$

$$H^+ + H^- \rightleftharpoons H_2 \qquad \Delta G^0_{H-}(H_2) \qquad (2)$$

$$BH \rightleftharpoons B^- + H^+ \qquad 1.364pK_a(BH) \qquad (3)$$

$$[M\text{-}H]^{(n-1)+} + BH \rightleftharpoons M^{n+} + B^- + H_2 \qquad \Delta G^0_{H-}(rxn) \qquad (4)$$

$$\Delta G^0_{H-}(rxn) = \Delta G^0_{H-} - \Delta G^0_{H-}(H_2) + 1.364pK_a(BH) \qquad (5)$$

Scheme 1.5. Free energy for protonation of a metal hydride.

The hydricities of nickel based HECs with diphosphine ligands are systematically evaluated by DuBois and co-workers.[82] The H_2 evolution catalysis by the Ni(diphosphine)$_2^{2+}$complexes can be predicted by the careful evaluation of the factors that affect the thermodynamic hydricity. The well-defined hydricity of a catalytic intermediate lead one to choose acid that will be needed for favourable H_2 release (negative value of ΔG^0_{rxn}). Therefore, rationally chosen of acid as H^+ source (mild acid) for the given hydricity of metal hydride that cause the **eq 5** in **Scheme 1.5** become negative can achive lower overpotential compared to using relative strong acid as H^+ source.

The Kubiak group has reported on the relaionships between the hydricity of transition-metal hydrides to the first reduction potential of the parent d^8 metal complex ($E_{1/2}(M^{n+/(n-1)+})$).[81] These relationships allow for the targeting, tuning, and prediction of metal hydride hydricities and can subsequently be used in the consideration of the pKa values of added acids to match proton sources to hydricities of hydride intermediates in order to favor hydrogen evolution with low overpotentials.[79, 84]A variety of molecular systems based on nickel, iron, and cobalt have been developed, which exhibit excellent activity.[85, 86, 87] However, most of these systems are only studied with strong acid substrates are still operated at high overpotentials, resulting in low energy efficiency.

Thermodynamic and kinetic consideration of PCET for molecular HECs electrocatalysts

The thermodynamic of net multi protons and multi electron transfer processes for HER are illustrated in **Scheme 1.6** a. A metal hydride intermediate [M-H] formed by proton coupled electron transfer (PCET) are often involved in the mechanism for HER.

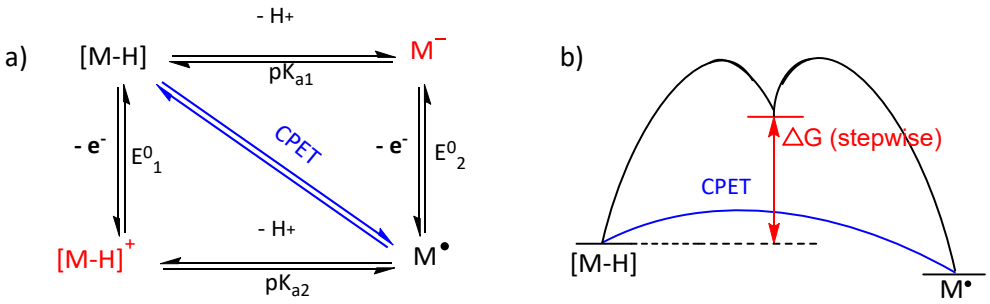

Scheme 1.6. (a) Square scheme representing the thermodynamic factors for stepwise vs. concerted electron-proton transfer and (b) corresponding energy profile for the different pathway.

This PCET process can occur via either stepwise ET-PT, or PT-ET process (black arrows) or concerted proton electron transfer (CPET), blue arrow. [88]The reaction barrier for CPET (**Scheme 1.6** b) is lower than ΔG for stepwise ET-PT or PT-ET process resulting in larger driving force for a formation of the [M-H]. While, the stepwise electron-proton transfer with high intrinsic barrier to form the metal hydride is kinetic challenge for H_2 evolution catalysis which means that reaction can be slow. Therefore, mechanistic and thermochemical studies to understand the factors that influence formation and protonation of metal hydride is critical for improved the catalytic rate. The rates of protonation/deprotonation reactivity involving transition metal complexes or "kinetic acidities" of metal hydride complexes can vary remarkably and are typically much slower than rates of proton transfer to and from oxygen or nitrogen-containing bases and acids with similar driving forces[89] The structural modification of ligands with a positioned pendant base in the second coordination sphere for nickel and cobalt catalysts[90] near the metal centre can overcome the slow kinetics of proton transfer to the metal centre to form hydride intermedites by the proton relay groups.[91, 92] For the nickel based HECs with pendant amines, it has been proved that the catalytic rate is strongly influenced by the ability to deliver protons to the correct location of the pendant amine. Protonation of the amine endo to the metal leads to the N–H being positioned appropriately to favor rapid heterocoupling with the M–H bond for H_2 liberation.[93] The more acidic N-H (protonated amine) and the more hydridic Ni-H bond favor H_2 evolution reaction kinetically.[94]

The next (**section 1.6**) will show the development of HECs and CO2RRCs based on molecular complexes using earth abundant metals. Many molecular based catalysts for proton reduction have been reported but their compatibility and solubility in full aqueous solution remain key challenges. Therefore, the development of a catalyst for hydrogen evolution that use water as H^+ source or substrate is one of important goals to achieve in solar-to-fuel conversion scheme.[69-72] The earth-abundant metal complexes can be potential catalysts for H_2 production because the metal centre exhibits many oxidation states. However, the design and employment of the ligand scaffold is crucial to achieve efficient catalysts.

For CO_2 conversion to CO and HCO_2H with molecular electrocatalysts, proton-assisted multielectron transfer processes can be considered for the design and development of electrocatalysts for CO_2 and H^+ transformation by a combination of appropriate proton donor−acceptor properties in the catalytic site.[63, 66, 74] The development of catalysts with appropriate distance between the proton shuttle moiety and catalytic site can be expected to facilitate multielectron substrate conversions.[66, 74] This approach for design of rational cobalt catalysts will be presented in **chapter 3**, **section 3.1.5.4** for H_2 evolution and **section 3.1.6** for CO_2 reduction.

1.6 The development of molecular electrocatalysts based on earth abundant metals for CO2RR and HER

Overview of molecular CO_2 reduction electrocatalysts

Among the numerous strategies for CO_2 transformation to useful chemical fuels, electrochemical reduction of CO_2 is a promising approach.[95, 96] Consequently, tuning catalytic activity of transition-metal complexes for CO_2 reduction catalysis by application of appropriate ligands has been thoroughly investigated. Nitrogen-donor ligands have been proven to form an important class of molecular electrocatalysts for CO_2 reduction.[97] It has long been known that metal complexes of the second- and third-row transition metals with polypyridyl ligands such as 2,2'-bipyridine or 1,10-phenanthroline are active electrocatalysts for CO_2 reduction. The *fac*-[Re(bpy)$(CO)_3$Cl)] complex and bpy-substituted derivatives have been known as highly active for CO_2-to-CO conversion since Lehn et al's report in the 1980s.[98] This class of molecular catalysts based on polypyridine ligands remains the most promising for the continued development of molecular systems for CO_2 reduction. For this reason, macrocyclic and polycyclic compounds containing nitrogen donors have since been employed as ligands for CO_2 reduction catalysts that include porphyrins,[99 100] polypyridines,[101] cyclam and related unsaturated N4-macrocycles.[102, 103]

1.6.1 Molecular catalysts based on earth-abundant metals for CO2RR

The most frequently studied family of homogeneous Mn analogues of the rhenium catalysts, ***fac*- [Mn(bpy)$(CO)_3$X]** (X = Cl or Br) have been extensively reported. [104-107] The mechanistic study of CO_2 reduction by these complexes was investigated by several groups, and various techniques including CV, IR-SEC, pulse EPR spectroscopy were used. In the case of iron-based catalysts, iron complexes with the porphyrin ligand, [(TPP)Fe^{III}]Cl (TPP = tetraphenylporphyrin), are the best-characterized system. This class of catalyst for CO_2 to CO conversion was reported in the 1980s by Savéant et al [75, 108-110], for example, **FeTPP** [110] (**Chart 1.1).**

It was found that the activity and stability of the catalyst is greatly improved when the mono- or divalent Lewis acids (e.g. Mg^{2+}) or weak Brϕnsted acids (e.*g.*1-propanol, 2-pyrrolidine, and CF_3CH_2OH) were added to the electrolyte solution. Significant progress in this class has been made by Costentin and co-workers [100] by installing phenolic groups in the ortho position of all arene substituents to attain the **FeTDHPP** as illustrated in **Chart 1.1** (TDHPP=5,10,15,20-tetrakis(2',6'-dihydroxyphenyl)-porphyrin). These local proton sources in the complex could stabilize the Fe(0) intermediate leading to enhanced catalytic activity for CO production in the presence of 2 M water. This catalyst operated at an overpotential of 465 mV, and the faradaic efficiency for CO production was greater than 90% through TONs of 50 million over 4 h

electrolysis without degradation. More recently, the same group found that the analogous complex with four cationic trimethylanilinium groups in the ortho position (**Fe-o-PMA**, **Chart 1.1**) [111] has a lower overpotential (η_{cat}) of 220 mV with a concomitant increase of $TOF_{max} = 10^6\ s^{-1}$ in DMF using PhOH as proton donor. The authors proposed that the ionic group at ortho position allows for an efficient coulombic stabilization of the Fe-CO_2 adduct. This design mimics the NiFe active site of CO dehydrogenases (CODHs) from the reduced CO_2 bound state of CODH-II_{Ch} (*Carboxydothermus hydrogenoformans*). The CO_2 binds between Ni and Fe as a bent bridging ligand via η^2, μ_2 coordination mode and is stabilized in the protein pocket by H-bonding with His93 anf Lys 563.[112]

Accordingly, a metal coordinated by a ligand with pendant proton donors is an effective design motif for artificial CO_2 reduction catalysts. [113] Moreover, the kinetics of this catalyzed reaction can be significantly influenced by metal-ligand cooperation. The **Co-macrocycle** with the ligand bearing pendant amines in the second coordination sphere or hydrogen donor moiety could facilitate proton transfer to the metal centre by increasing the local proton concentration and/or stabilization of the M-(η^1-C)CO_2 intermediate via H-bonding as shown the structure in **Chart 1.1**.[114-116] Linehan has developed the cobalt hydride analogue of **Co(dmpe)$_2$** (**Chart 1.1**), dmpe = 1,2-bis(dimethylphosphino)ethane) for production of formate from CO_2 and H_2. The complex exhibits a high catalytic activity with a TOF of 3400 h^{-1} operating at r.t. under low pressure (P = 1 atm) of a mixture of gases of $CO_2 : H_2$. The catalytic activity is comparable to those of noble metal catalysts for CO_2 reduction with hydrogen, however, this catalytic system requires the expensive base for regeneration of the hydride complex to complete the catalytic cycle.[117]

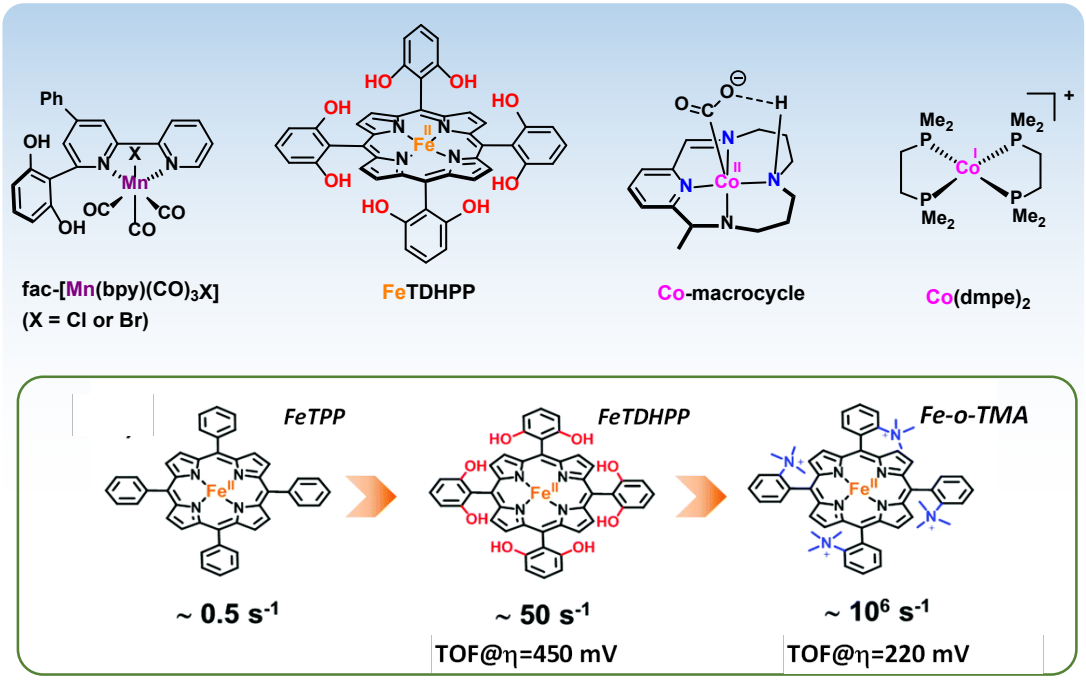

Chart 1.1. Carbon dioxide reduction catalysts with 3d transition metals. Inset shows fine structural adjustments of Fe-porphyrin CO2RRCs with dramatic improvement of their catalytic activities. Reproduced from ref [18] with permission from The Royal Society of Chemistry.

The **Chart 1.1**, inset shows CO_2 reduction catalysts in the Fe-porphyrin class that demonstrate the precise structural modification for achieving new catalysts with high intrinsic properties. It highlights that a slight change in the structure of these molecular complexes may lead to a considerable increase in their catalytic performances. Therefore, the development of efficient catalysts requires a clear understanding of the catalytic mechanism and appropriate design of the structure.

The early development of molecular HECs aimed for structural and functional mimics of the active sites in [Fe-Fe]- and [Ni-Fe]-hydrogenases due to their exceptional catalytic activity for reversible H_2 production as mentioned above.[39, 118, 119] However, the complexes mimicking the hydrogenase active sites show low stability under aerobic conditions and poor catalytic activity with operating at large overpotential (will be described in the next **section 1.6.2**). This led to a search for robust inorganic compounds with various ligand platforms. The design of electrocatalysts with various ligand platforms for complexation with non-precious metals (e.g, Ni, Fe, Co and Mo), as will be described in **section 1.6.3** is found to be a promising strategy for molecular electrocatalysts for H_2 production.

1.6.2 Biomimetic catalysts for electrocatalytic H_2 production

From the striking electrocatalytic activity of two main classes: [Fe-Fe]- and [Ni-Fe]-hydrogenases, over a hundred biomimetic synthetic complexes have been synthesized over the last decade by various modifications of the [Fe-Fe] and [Ni-Fe]-hydrogenase active sites. [120] The early biomimetic diiron complex (FeFe mimic, **Chart 1.2**) was firstly prepared by Rauchfuss and co-workers [29]. It was found that the [Fe-Fe]–H_2ase model complex with only CO bridges, $[Fe_2S_2(CO)_6]$ is inactive for electrocatalytic H_2 evolution at the first reduction event in the presence of weak acid (CH_3COOH) and requires a large overpotential for this catalysis at the second reduction process.[121] The one e^- reduced cluster becomes electrocatalytically active for H_2 production by replacement of one or two CO ligands by strong electron donating non-CO ligands (e.g. PR_3, *N*-heterocyclic carbene).[121] The selected examples such as **FeFe-2** and **FeFe-3** (**Chart 1.2**) can catalyse H_2 evolution at potentials in the range from -1.38 to -2.38 V *vs.* $Fc^{0/+}$.[122] Darensbourg and co-workers [123] proposed their H_2 evolution mechanism via the reduction of the Fe^IFe^I parent complex to Fe^0Fe^I, followed by uptake of protons to generate $(\eta^2\text{–}H_2)Fe^{II}\text{–}Fe^I$. The hydride species is also believed to be a key intermediate in the catalytic cycle for electrochemical H_2 evolution. By comparison of the H_2 evolution pathway between the [Fe-Fe]-hydrogenase and the artificial diiron complexes, the enzyme can achieve H_2 evolution via an $[Fe^IFe^I]$ intermediate ($H_{red}H^+$ and $H_{sred}H^+$, **Chart 1.2**), while the biomimetics generally require the more reduced $[Fe^0Fe^I]$ state resulting in then operating at relatively more negative potential. Moreover, protonation of the mimic complex often generates bridging hydrides [124-127] instead of more reactive terminal hydride species (H_{Hyd}) formed in the catalytic cycle of H_2 evolution by the [Fe-Fe]-enzyme (highlighted inset, **Chart 1.2**).

Subsequent work by Rauchfuss and co-workers[128] revealed the role of a pendant amine positioned near the iron in the structure FeFe-4 (**Chart 1.2**). This basic amine group plays a key role in the production of H_2 which has been proposed as a proton relay for facilitating the formation or cleavage of the H-H bond.[119] The employment of the same concepts for artificial systems by incorporating of appropriate basic groups in a secondary coordination sphere surrounding a metal centre can help intra and intermolecular proton transfer as demonstrated by the Dubois catalysts. This research group has mainly focused on developing mononuclear complexes of Fe, Co, and Ni that contain a basic amine group in the second coordination sphere, close to a vacant coordination site or a hydride ligand on the metal center.[129] Some of these complexes are very effective electrocatalysts for H^+ reduction or H_2 oxidation.[130, 131]

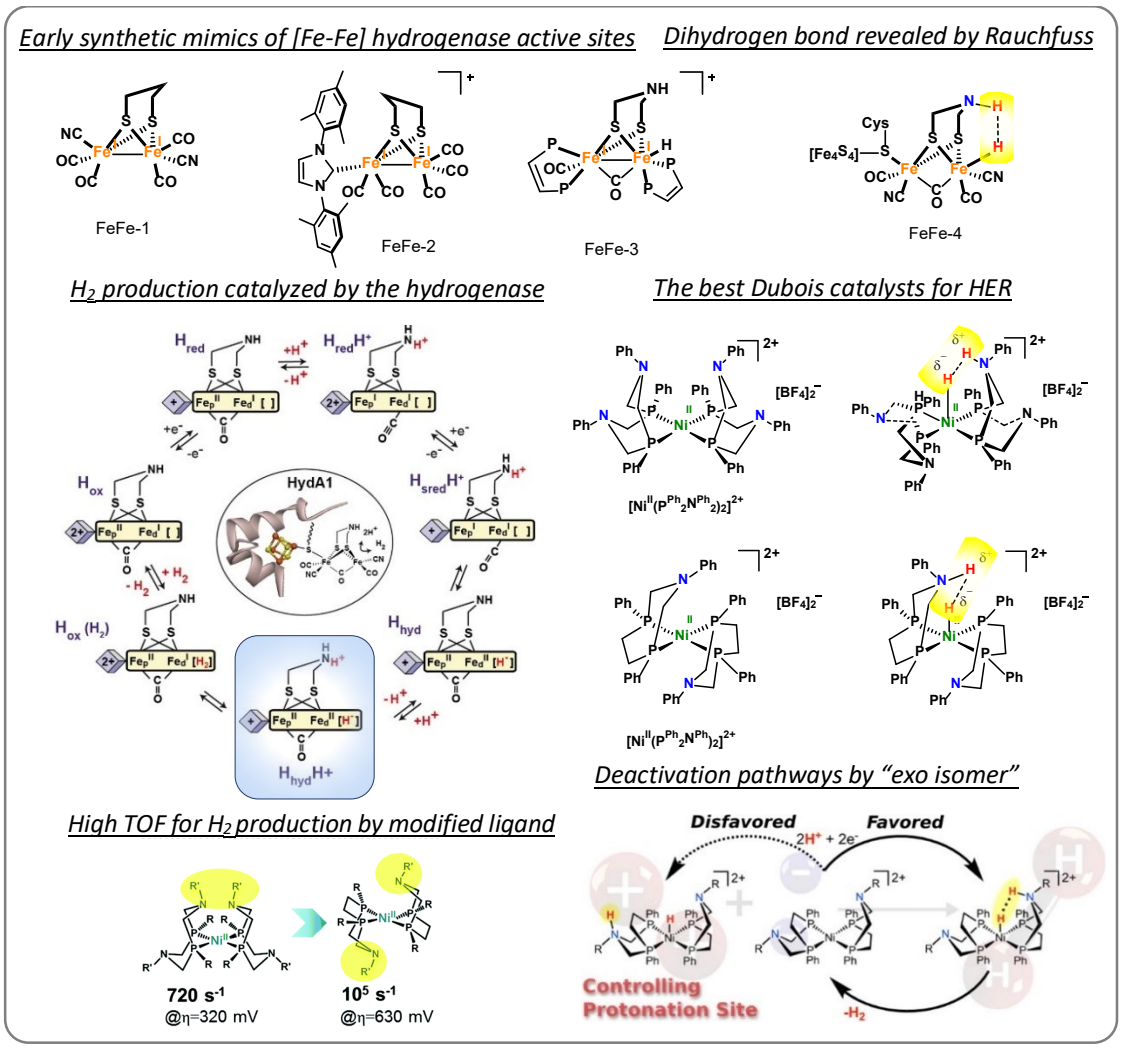

Chart 1.2. The development of early synthetic HECs by mimicking of [Fe-Fe] hydrogenase active site and DuBois HECs by implementing the role of pendant amine in the structure of the H-cluster of [FeFe] hydrogenase with the proposed catalytic cycle for H_2 evolution by this enzyme. Reproduced with permission from ref [132]. Copyright 2017 American Chemical Society. The deactivation pathway of the $[Ni(P^{Ph}_2N^{R'})_2]^{2+}$ by formation of the exo isomer is reproduced with permission from ref [133]. Copyright 2013 American Chemical Society.

The most efficient Dubois catalyst for H_2 production

The Dubois group [134] in 2011 developed nickel diphosphine electrocatalysts with a basic amine group (**Chart 1.2**) to structurally mimic a pendant amine in the structure of the active site of the [FeFe] hydrogenase enzyme as proposed in the structure **FeFe-4**. For example, the selected **$[Ni^{II}(P^{Ph}_2N^{Ph}_2)_2]^{2+}$** from the series of $[Ni^{II}(P^{R}_2N^{R'}_2)_2]^{2+}$can catalyse H_2 evolution at low-overpotential (320 mV), and in this case the proton coupled electron transfer (PCET) mechanism is believed to operate for H^+ reduction catalysis.[135] The in depth mechanistic studies[58, 93, 130] of the $[Ni^{II}(P^{R}_2N^{R'}_2)_2]^{2+}$ series for H_2 evolution proved the crucial role of pendant bases in the second coordination sphere for facilitating proton transfer (**Scheme 1.7**). The reduction of Ni(II) to Ni(I)

is followed by protonation of the pendant amine. This protonation is the key step that either leads to the formation of productive *endo* isomer or inactive *exo isomer (protonation far away from* the metal). The second electron transfer generates a Ni(0) species with a protonated amine. Intramolecular proton transfer from the nitrogen to the nickel leads to formation of the hydride species. It is subsequently protonated to generate the key intermediate with a Ni–H bond and a N–H bond in close proximity (endo) or the deactivated exo isomer. The "dihydrogen bond" between the protic N–H and hydridic Ni–H forms, and a molecular H_2 liberate from this complex resulting in a regeneration the Ni(II) complex completing the catalytic cycle.[59]

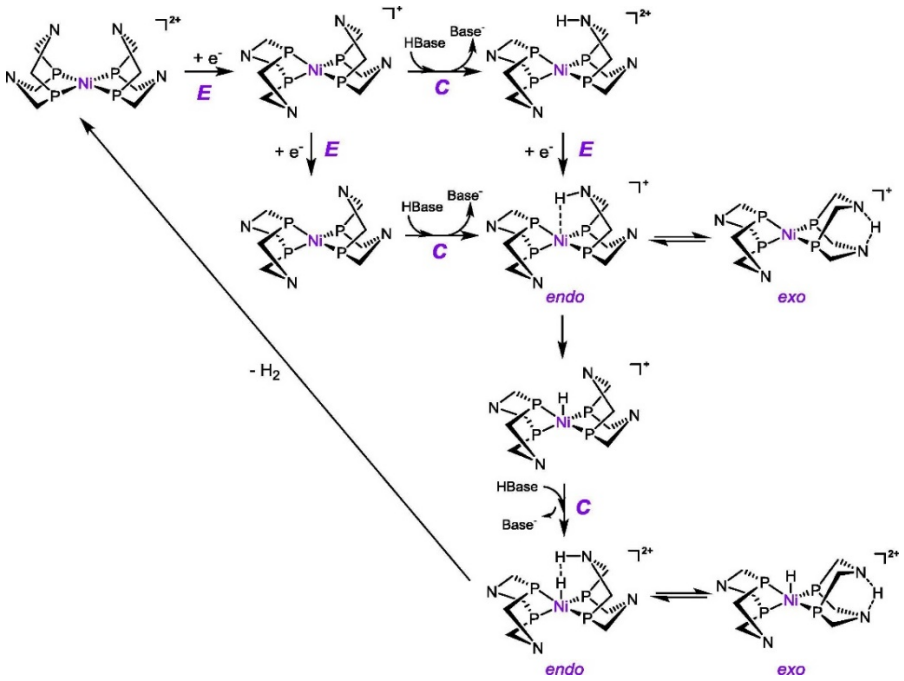

Scheme 1.7. Proposed mechanistic pathway for H_2 production catalysed by $[Ni(P^R_2N^{R'}_2)_2]^{2+}$. R groups on P are not shown, and R' groups on N are not specified for clarify.[65] Permission is granted subject to an appropriate acknowledgement given to J. W. Wang, W. J. Liu, D. C. Zhong and T. B. Lu, *Nickel complexes as molecular catalysts for water splitting and CO_2 reduction*, 2019, **378**, 237-261.

It was later found that the HER activity of the $[Ni(P^R_2N^{R'})_2]^{2+}$ is greatly enhanced by using a $P^R_2N^{R'}$ ligand, a seven-membered analogue of $P^R_2N^{R'}_2$ ligands with only one $N^{R'}$ substituent. The TOF of **$[Ni^{II}(P^{Ph}_2N^{Ph})_2]^{2+}$** for H_2 production of 106,000 s^{-1} at -1.13 V vs $Fc^{0/+}$ was achieved but at a higher overpotential (η = 625 mV) than that of the $[Ni^{II}(P^R_2N^{R'}_2)_2]^{2+}$. [134] The better catalytic activity with high TOF for H_2 production of **$[Ni^{II}(P^{Ph}_2N^{Ph})_2]^{2+}$** can be attributed to its structure. This complex avoids the formation of exo isomer and facilitates formation of the endo isomer when protonated as illustrated in **Chart 1.2**. The subsequent computational studies showed that protonation at the endo isomer is favoured by 6 kcal/mol relative to that of the exo isomer.[133]

To achieve more stable and efficient synthetic HECs compared to the biomimetic [Fe-Fe]-hydrogenases, many other earth-abundant transition complexes by using metals e.g. nickel[65], cobalt[70, 136, 137], iron[138, 139] or molybdenum[16, 122] incorporating various ligand platforms have been designed and synthesized.

1.6.3 Molecular H_2 evolution catalysts (HECs) based on various ligand platforms

The concept of a pendant amine adjacent to a vacant coordination site or hydride ligand has been extended to the development of electrocatalysts for production of H_2. For example, simple mononuclear complexes of Co and Fe with oxime moieties can potentially catalyse H_2 evolution.[72, 87, 140] The first generation cobaloxime developed as a mimic of vitamin B_{12} with the structure shown for **[Co^{III}(dmgH)$_2$(py)Cl]** and **[Co^{II}(dmgBF_2)$_2$(MeCN)$_2$]** in **Chart 1.3**, and various derivatives form one of the most extensively-studied groups of cobalt-based electrocatalysts because of their high activity at low overpotentials for H_2 evolution.[141] Both experimental and theoretical work have been investigated extensively to reveal the catalytic mechanism for H^+ reduction.[142] The same ligand core was employed for complexation with Fe by Gray et al. [143] This work demonstrated that the monometallic Fe complexes with fluorinated diglyoxime ligand, **[(dAr^{F}gBF_2)$_2$Fe(py)$_2$]** (dAr^{F}gBF_2 = 1,2-bis(perfluorophenyl)ethane-1,2-dionedioxime) can act as electrocatalysts for H_2 evolution at −1.28 V *vs.*$Fc^{0/+}$ with a turnover frequency (TOF) of 20 s^{-1}. Moreover, the corresponding monofluoroborated, proton-bridged complex [(dAr^{F}g$_2$H–BF_2)Fe(py)$_2$] displayed an improved TOF of 200 s^{-1} at −1.28 V *vs.*$Fc^{0/+}$. These iron complexes have better catalytic activities and operate at much lower potential than the biomimetic diiron systems (as shown the structure in **Chart 1.2**) and the Savéant complex (**Fe-porphyrin**, **Chart 1.3**).

Many porphyrin-based complexes of earth-abundant metals have been reported as H_2 evolution catalysts including Fe-, [139], Co-[144, 145] and Ni-porphyrins.[146] Nocera and co-workers [145] synthesized a series of "hangman porphyrins" (**Co-hangman porphyrine**, **Chart 1.3**) where the ligand scaffold was modified by incorporating dangling proton-transfer group such as carboxylic acid. The acidic groups located on top of the active metal centre can promote PCET processes by exhibiting a decrease of overpotential and an increase of a TOF for H_2 production.[147] Furthermore, well-designed macrocyclic ligand platforms for example the **Ni-cyclam** (**Chart 1.3**) shows good performance for H_2 evolution electrocatalysis in organic-aqueous media [148] and in fully aqueous solution.[149]

Some examples of non-biomimetic synthetic catalysts such as molybdenum oxo, **[Mo^{IV}(Py5Me)(O)]** (**Chart 1.3**) were reported by Chang et al.[150] This is one of the most efficient electrocatalysts for H_2 evolution from an aqueous medium at neutral pH with high stability and

high turnover frequency. However, it still requires a large overpotential. Bulk electrolysis of a solution of **[Mo^{IV}(Py5Me)(O)]** in phosphate buffer pH 7 for 71 h on a Hg pool electrode with an overpotential of 1,000 mV showed 100% faradaic efficiency and a TOF of 2.4 s^{-1}. Recent studies of dithiolene complex, **[Co^{II}(bdt)$_2$]$^-$** [151] showed that it could efficiently catalyze both electrochemical and photochemical H_2 evolution from water reduction.

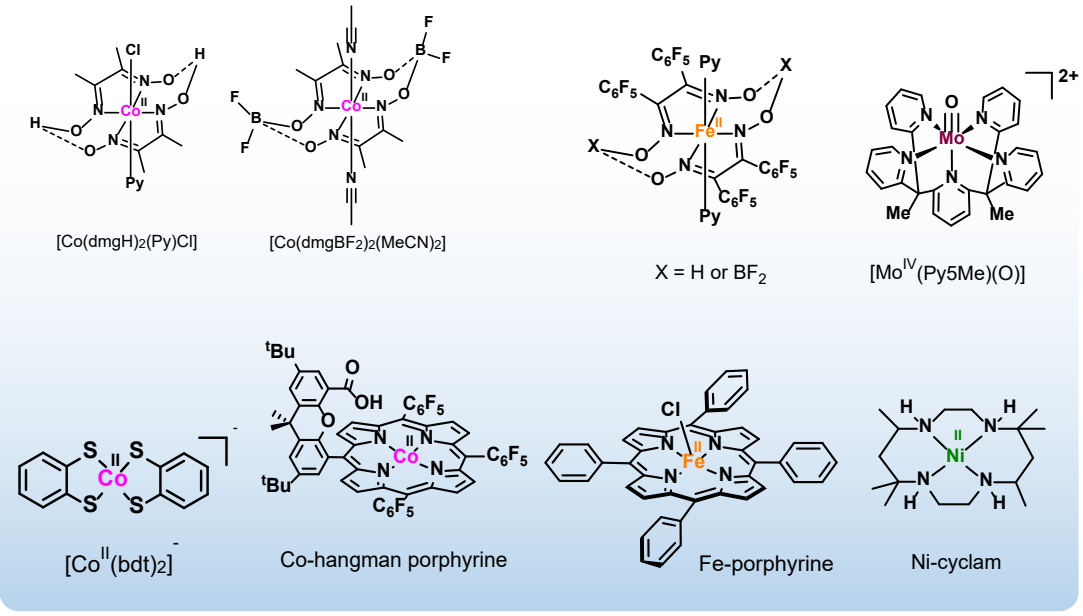

Chart 1.3. Selected molecular electrocatalysts based on eaeth-abundant transition metals with various ligand platforms.

The complexation of 3d-transition metals, especialy cobalt and nickel, with appropriate ligands is found to be a promising way to attain efficient H_2 production catalysts. [65, 67] The ligand with π-back-donating sulfur and phosphine donors can stabilize low-oxidation state metal species. [152] Moreover, the use of redox active ligands can be a promising approach because they can store electrons in the ligand structure facilitating multi-electron transfer. For example, catalysts containing redox active ligands can catalyse H_2 production at low overpotential [68, 153, 154] and also show efficient catalysis for CO_2 reduction.[155, 156]

Chapter 2

Synthesis and characterisation of cobalt complexes with bis PN based pyridine ligands

2.1 Introduction

Bidentate ligands containing soft and hard donor atoms are able to give two different coordination sites which are termed hemilabile by Rauchfuss.[157] These bidentate ligands can potentially stabilize a metal ion in many oxidation states and geometries. Additionally, for catalysis applications, the hard atoms are weakly coordinated to soft metal centre and can be easily dissociated in solution to open an accessible coordination site for binding substrate, while, their chelate effect stabilizes the catalyst precursor in the absence of substrate. [158]. During the past decades, phosphinopyridines and related ligands (P,N ligands) have attracted considerable interest in development of synthetic approaches [159, 160], coordination chemistry [161] and catalysis. The combination of phosphorus (soft donor)- and nitrogen (hard donor)-atoms in pyridyl-phosphines causes them to be among the most important and widely used ligands for the design of unique catalysts for transition-metal homogeneous catalysis.[162-164]. A P,N chelating ligand has general features from P- and N- donor atom as pointed out in **Chart 2.1**

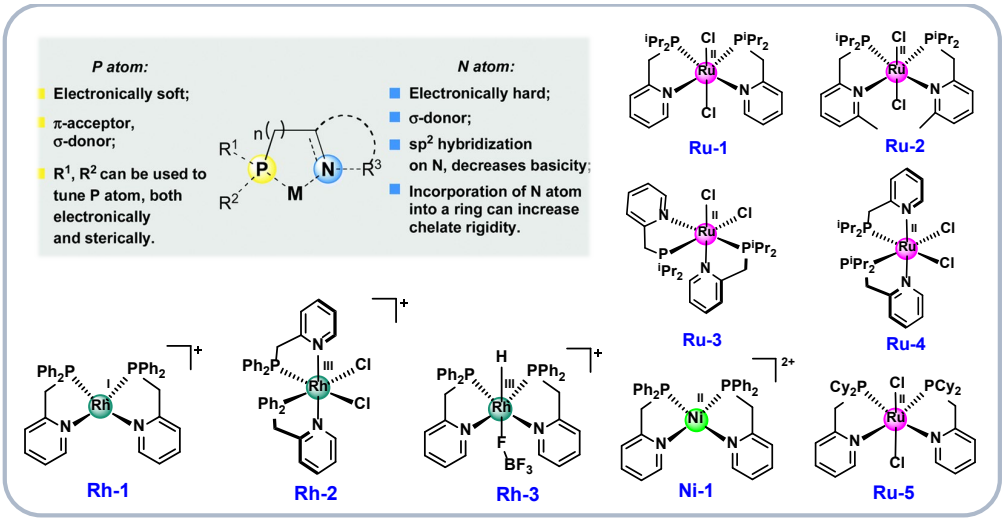

Chart 2.1. Selected examples of transition metal complexes supported by bis-P,N chelating ligands: Ru-1, Ru-2, Ru-3 and Ru-4 from ref. [165], Ru-5 from ref. [166] , Rh-1, Rh-2 and Rh-3 from ref.[167], and Ni-1 from ref [168]. The inset shows general features of a P,N ligand. [162]

The phosphorus acts as the π-acceptor which can stabilize a metal centre in a low oxidation state, while the nitrogen as σ-donor makes the metal more susceptible to oxidative addition

reactions. [162] For example, the DPPMP ligands (DPPMP = diphenylphosphinomethylpyridine) can stabilize the Rh(I) in a low oxidation state in **Rh-1** and a high oxidation state of Rh(III) in **Rh-2** and **Rh-3** as shown the structures in **Chart 2.1**. Moreover, the P-atom of the P,N ligands can be modified with different substituents (e.g. iPr , Cy or Ph) as exemplified in **Chart 2.1**, allowing the development of a highly tuned scaffold both electronically and sterically. Based on the coordination chemistry and structural studies of bidentate P,N ligands, their X-ray crystal structures reported in the literature reveal a *cis* configuration between the two-P and two-N atoms as shown **Chart 2.1**. This *cis* configuration is typical of mononuclear complexes supported by bis-P,N chelating, but complexes with two P,N ligands in the precedent studies are relatively rare compared to transition metal complexes containing a tridentate pincer ligand.

2.1.1 Cobalt complexes supported by PNP, PNN or NPP chelating phosphino pyridines

Cobalt complexes with bis-P,N chelating ligands of pyridine phosphine derivatives have not been reported: however, there are several examples of cobalt complexes (**Chart 2.2**) supported by "pincer type" of a tridentate bis(phosphino)pyridine, PNP [169] and PNN ligand [170-173]. Pioneering works from the Milstein group as well as Chirik and co-workers show that these cobalt pincer complexes containing a PNP ligand are potential catalysts for many reactions such as C-H activation [174], borylation [175], $C(sp^2)$-$C(sp^2)$ Suzuki-Miyaura coupling [176], reduction of CO_2 [177, 178] and hydrogenation of nitriles [179]. Moreover, the studies from other research groups show that the cobalt pincer complexes with a PNP scaffold are also used as catalysts for olefin polymerization [180, 181].

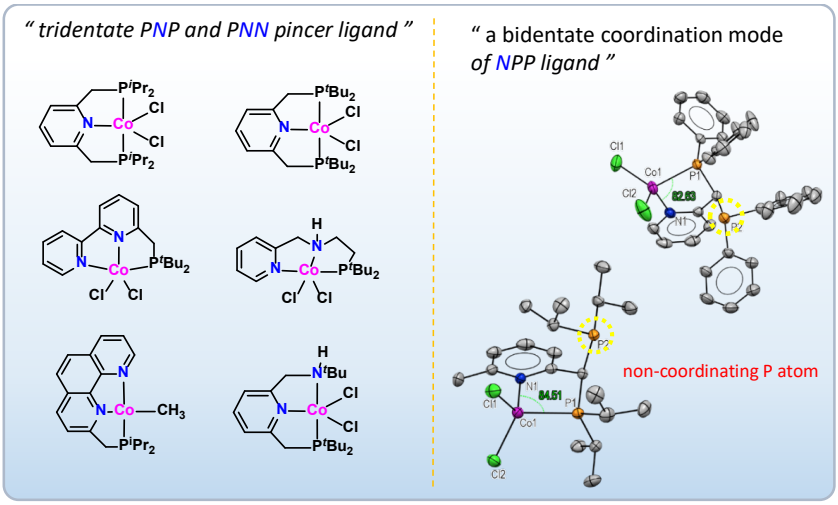

Chart 2.2. Examples of cobalt pincer complexes and coordination mode with a PNP-, PNN- or NPP tridentate ligand.

Although there are numerous cobalt pincer complexes based on PNP and PNN ligands that are well-characterized, the use of cobalt complexes supported by bis-P,N chelating ligands for catalysis has not been reported. There are two examples of the dichloride Co(II) complexes with the tridentate NPP ligand (NPP = 2-pyridylbis(diphenylphosphino)methane) that were characterized by X-ray crystallographic determination (**Chart 2.2**). The coordination mode of the NPP ligand in these two cobalt complexes reveals that only a P,N bidentate coordination mode was formed with the $CoCl_2$ salt.[182, 183]

2.1.2 Electronic properties of cobalt complexes

Electronic properties of cobalt complexes

Cobalt coordination complexes exhibit interesting properties for redox catalysis due to their many oxidation states ranging from Co(-I) to Co(IV). The two main oxidation states are Co(II) and Co(III) complexes which are naturally found in biological system.[184] These two oxidation states display different electronic properties. Co(III), d^6 complexes are typically octahedral and may be low or, very occasionally, high spin. The low spin d^6 (t_{2g}^6) configuration is diamagnetic and inert for ligand substitution reactions.[185] Co(II), d^7 complexes can be four-, five- or six-coordinate and are paramagnetic and substitutionally labile compared to their Co(III) complexes.[186, 187] They may adopt high spin ($t_{2g}^5e_g^2$) or low spin ($t_{2g}^6e_g^1$) configurations.

The one-electron reduction of a six-coordinate, d^6, low spin, Co(III) complex can cause the change in spin state from Co(III), low-spin (LS) to Co(II), high spin state (HS). This change of spin state results in the loss of its axial ligands from the labile Co(II) complex in weakly coordinating solvents. This evidence can be observed in the electrochemical studies of Co(III) schiff base

complexes.[188, 189] and Co(III) complexes with oher ligands.[190, 191] The electrochemical reduction coupled with a chemical reduction (a ligand loss or exchange) results in irreversible Co(III/II) couple with very large ΔEp value.[189] It was generally found in the Co(III/II) reduction for six-coordinate Co(III) complexes which are electrochemically irreversible in nature. It was proved that one electron is added to the antibonding dz^2 orbital of the Co(III) complexes to form the labile Co(II) which is tuned by the field strength of the axial ligands. The variation of σ donor strength of the axial ligands (Cl^-, SCN^-, N_3^-, NO_2^-) in a series of diamagnetic cobalt(III) complexes of bpb and bpc ligands [H2bpb = 1,2-bis(2-pyridinecarboxamido)benzene; H2bpc = 4,5-dichloro-1,2-bis(2-pyridinecarboxamido)benzene] shows a linear spectroelectrochemical correlation between the ligand field strength of the axial ligands and the cathodic peak potential for the Co(III)-Co(II) couple.[191]

Octahedral low-spin Co(II) complexes with $t_{2g}^6e_g^1$ electronic configuration are labile because one electron is partially filled in the antibonding e_g orbital. This electron configuration has unsymmetrical occupancy of the e_g orbital and it is expected to be subject to a ground state Jahn-Teller distortion. [192] This distortion is commonly observed among octahedral complexes where the two axial bonds can be elongated or compressed from those of the equatorial bonds. For example, such distortion is found in the crystal structure of the low-spin complex $K_2Ba[Co^{II}(NO_2)_6]$ which reveals an elongation along one axis. The three different Co-N bond distances in the complex anion are 1.93(6), 1.91(2) and 2.12(2) Å.[193] Alternatively, low spin Co(II) complexes may adopt a 5-coordinate square pyramidal geometry as in $[Co(CN)_5]^{3-}$.

2.2 Cyclic voltammetry

Cyclic voltammetry (CV) is a popular and useful electrochemical technique typically used to study the oxidations and the reductions of molecular species. Furthermore, this technique is powerful to investigate electron transfer-initiated chemical reactions including catalytic processes. [194-197]. CV experiments are performed in a three-electrode cell (**Figure 2.1** a).

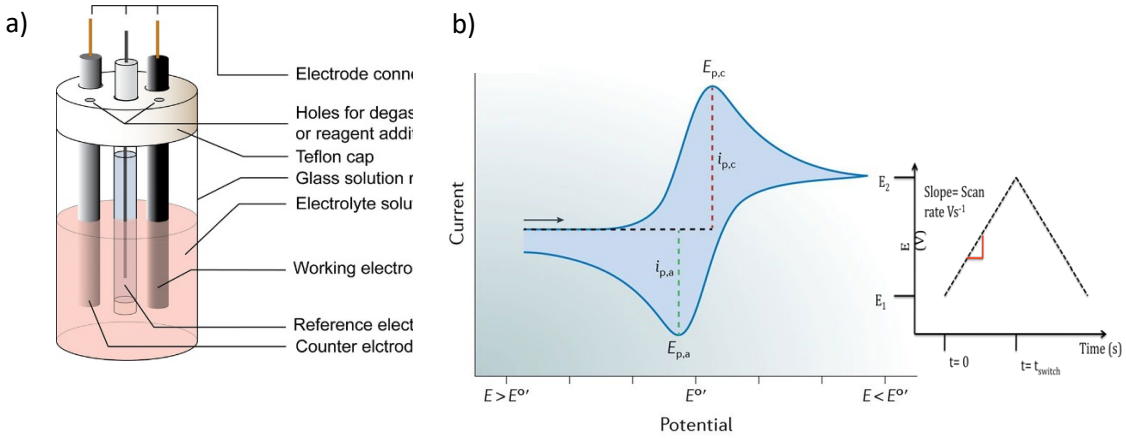

Figure 2.1. Schematic representation of an electrochemical cell for CV experiments (a) and idealized example of a cyclic voltammogram (b), inset showed a triangular waveform.[198]

The fundamentals of CV consist of the sweep of working electrode potential which is immersed in a solution of interest redox species, measuring the resulting current. The potential of the working electrode (WE) is set relative to a reference electrode (RE), e.g. a silver/silver chloride electrode (Ag/AgCl or a saturated calomel electrode (SCE). A counter electrode (CE) completes the circuit allowing current to flow in the cell. The applied potential between the WE and RE electrodes corresponds to the potential versus time (E-t) profile via a linear potential scan versus time which is a triangular waveform (**Figure 2.1** b, inset). The potential of the electrode is swept between two values, sometimes called the switching potentials. At E_2, the scan direction is reversed back to the original potential of E_1. The scan rate is reflected by the slope (red line) of the triangular wave form. A cyclic voltammogram is a display of current (y-axis) versus potential (x-axis) which is called i-E response. The voltammogram is obtained by measuring the current at the working electrode during the potential scan. The x-axis shows the direction in which the potential was scanned to record the data and the arrow represents the beginning and sweep direction of the first segment (forward scan or negative direction). The reduction of a redox species results in a cathodic current with the maximum value ($i_{p,c}$) at a potential $E_{p,c}$. In the backward scan, the potential is swept positively from the switching potential E_2 to the starting potential E_1. This oxidation of the redox species causes an anodic current with the greatest $i_{p,a}$ value at $E_{p,a}$. The formal reduction potential $E^{0'}$ of the redox species is estimated as $E_{1/2} = (E_{p,a} + E_{p,c})/2)$. The reversible redox couple is obtained when the CV is recored in a stationary

solution and this technique can also be used to investigate electron transfer process in other systems (e.g. catalysis, adsorption/desorption). Most of the background information for cyclic voltammetry, summarizing redox processes and elucidating mechanism for homogeneous electron transfer coupled chemical reactions can be found in standard textbooks by "Bard and Faulkner" [196] in chapter 6 and 12, and Savéant.[199] Moreover, a practical guide for CV experiments was published by Dempsey.[200]

IUPAC and US convention for reporting a CV data

There are two conventions (**Figure 2.2**) that are commonly used to report CV data (i-E response): the US convention and the IUPAC convention. Noted that our CV data here in the thesis is reported by using the IUPAC convention.

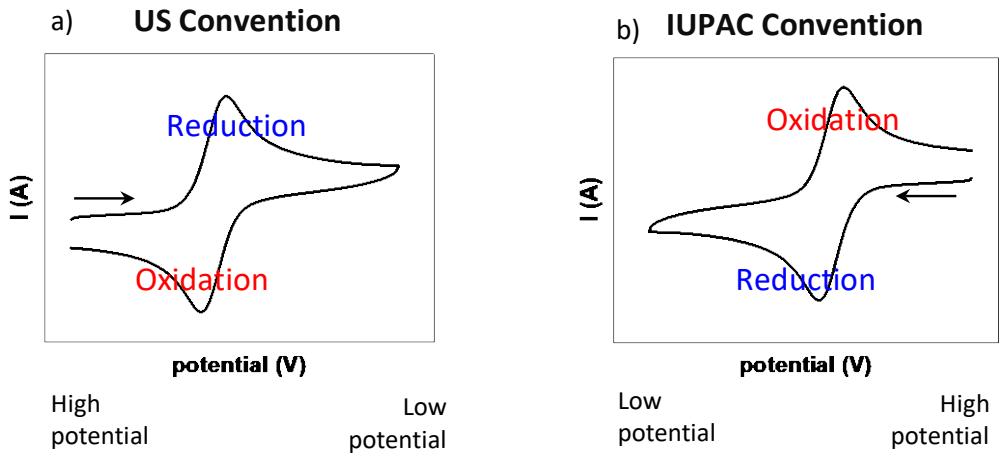

Figure 2.2. CV data reported by the US convention (a) and data reported by the IUPAC convention (b).

The arrow indicates the potential at the beginning and the sweep direction of the first segment (forward scan). Data reported by the two conventions is rotated by 180^0 with respect to one another.

Conversion constants for redox potential measured versus different reference electrodes

The $E_{1/2}$, $E_{cat/2}$ and E_{cat} values reported versus SCE, NHE and SHE is recalculated to the potential measured vs $Fc^{+/0}$ by conversion constants between different reference electrodes at 25°C as shown below:

conversion from SCE to $Fc^{+/0}$ by -380 mV,

conversion from NHE to $Fc^{+/0}$ by -630 mV

conversion from SHE to $Fc^{+/0}$ by -624 mV.[201]

A Nernstian one-electron wave and fast electron transfer kinetics

Considering the equilibrium described by the Nernst equation (**eq 2.1**), the equation relates the potential of an electrochemical cell (E) to the formal potential of a redox species ($E^{0'}$) and the relative concentration of the oxidized (Ox) and the reduced (Red) species in the system at equilibrium.

$$\boldsymbol{E = E^{0'} + \frac{RT}{nF} ln \frac{(Ox)}{(Red)} = E^{0'} + 2.3026 \frac{RT}{nF} log_{10} \frac{(Ox)}{(Red)}} \qquad \textbf{eq 2.1}$$

In the equation, R is the gas constant, T is the temperature, n is the number of electrons and F is Faraday's constant. In experimental conditions, the standard potential is replaced with the formal potential ($E^{0'}$) which is often estimated with the experimentally determined $E_{1/2}$ value ($E_{1/2} = (E_{p,a} + E_{p,c})/2$). For example, the one-electron reduction of Fc^+ to Fc (**Figure 2.3,** H in inset), the $E_{1/2}$ corresponds to the average potential between F and C points. When the potential is scanned over time during the CV experiment, the concentration of the species in solution near the electrode changes following the Nernst equation. This results in attaining the ''Duck"- shaped voltammogram as well as the concentration-distance profiles for Fc^+ (blue) and Fc (green) at different points in the cyclic voltammogram (H, inset).

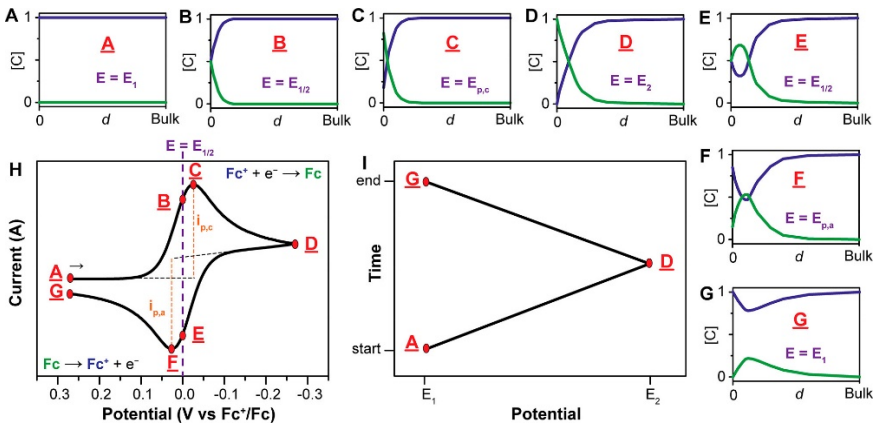

Figure 2.3. (A–G): simulated concentration profiles (mM) for Fc^+ (blue) and Fc (green) as a function of the distance from the electrode (*d*, from the electrode surface to the bulk solution, e.g. 0.5 mm) at various points during the voltammogram. (H): Voltammogram of the reversible reduction of a 1 mM Fc^+ solution to Fc, at a scan rate of 100 mV s^{-1}. (I): Applied potential as a function of time for a generic cyclic voltammetry experiment, with the initial, switching, and end potentials represented (A, D, and G, respectively).[200]

Scanning to negative potentials (cathodically) from point A to D, the Fc^+ is steadily consumed near the electrode because it is reduced to Fc. This results in the increase of current which is governed by the diffusion process of Fc^+ from the bulk solution to the electrode surface. The volume of the solution containing the reduced Fc, called the diffusion layer, continues to grow upon scanning to point C. At this point, the peak cathodic current ($i_{p,c}$) is reached and the decrease in current is observed during scan to more negative potential (from A to D) because the growth of the diffusion layer slows down mass transport of Fc^+ to the electrode. Thus, the rate of diffusion of Fc^+ from bulk solution to the electrode becomes slower. While, [Fc^+] at the electrode surface was depleted, the [Fc] at the electrode increased to reach the equilibrium determined by the Nernst equation. At the switching potential (point D), the scan direction is reversed to positive (anodic) potential. The Fc present at the electrode surface is oxidized back to Fc^+ during scanning to more positive direction. At point B and E, the concentrations of Fc^+ and Fc at the electrode are equal where $E = E_{1/2}$ following the Nernst equation. This is consistent to the halfway potential between the two peaks (C and F) providing the direct way to estimate the $E^{0'}$ for a reversible electron transfer. Therefore, the peak separation is observed as a result of the diffusion of the analyte to and from the electrode. For the chemically and electrochemically reversible reduction (one-electron transfer process), the difference between the anodic and cathodic peak potentials, called peak-to-peak separation (ΔE_p) is 57 mV at 298 K (2.22 RT/F), and the width at half max on forward scan of the peak is 59 mV. [199].

Scan rate variation

The scan rate of CV experiments controls how fast the applied potential is varied. Fast scan rates result in decrease of the thickness of diffusion layer: as a result, higher currents are observed compared to the currents obtained from slow scan rates. [196] For electrochemically reversible (fast) electron transfer processes involving freely diffusing redox species, the Randles-Sevcik (**eq 2.2**) shows how the peak current i_p (A) increases linearly with the square root of the scan rate ν (V s $^{-1}$)

$$i_p = 0.4463nFAC^0\sqrt{\frac{nFD_0}{RT}}\ x\ \sqrt{v} \qquad \textbf{eq 2.2}$$

where, n is the number of electrons transferred, F is the faraday constant, A (cm^2) is the electrode surface area, C^0 (mol cm^{-3}) is the bulk concentration of redox species, and D_0 (cm^{2}s^{-1}) is the diffusion coefficient of the oxidized species. Accordingly, the plot of i_p as a function of $\sqrt{v}$ should be linear for electrochemically reversible redox couple involving diffusion control. Moreover, examination of peak-to-peak separation can help to identify the result of deviation from this linear correlation which can be either an electrochemically quasi-reversible electron transfer process or a deposition of species on the electrode surface. For a quasi-reversible electron transfer process, the peak potentials shift with scan rate variation (described in **section 2.2.3**), while no peak-to-peak separation is observed for a surface-adsorbed species.[200]

2.2.1 Beyond the Nernstian one-electron wave: slow electron transfer, coupled chemical reactions, and multielectron processes

Electron transfer kinetics and electrochemical irreversibility

For fast kinetic one-electron transfer from the electrode to a redox species with diffusion control, a fully reversible Nernstian wave can be obtained following the Nernst equation (**eq 2.1**). This reversible cyclic voltammogram (**Figure 2.4**, black curve) becomes more complicated by several processes. In the simplest cases, the CV response is modified by slow electron transfer or multielectron transfers. In the case of slow electron transfer from the electrode to redox species, the establishment of Nernstian equilibrium will be prevented giving rise to a quasi-reversible (blue curve) or irreversible redox wave with no peak current on a return sweep (red curve). These distinct CV responses of the redox couple with the same formal potential as defined as E_f^0 are observed as a result of slow electron transfer kinetics. The inset shows the triangular potential applied to the working electrode during measurements.[202]

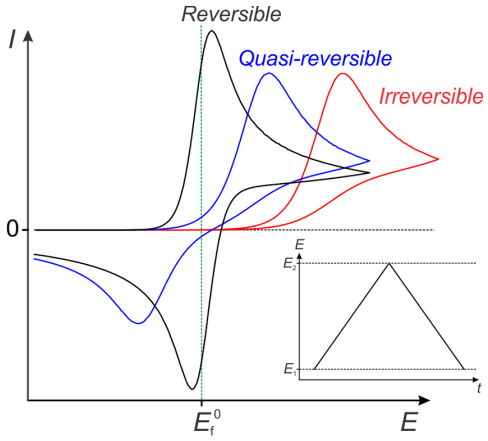

Figure 2.4. Comparison of CVs for reversible, quasireversible, and irreversible electron transfer process with the same formal potential, E_f^0, on a macrodisk electrode. The inset shows the sweep potential applied to the working electrode during measurements.[202]

Thus, this electrochemically reversibility is governed by electron transfer kinetics from the electrode to a redox couple and is completely unrelated to chemically reversibility. If there is a low barrier to electron transfer (electrochemically reversible), the Nernstian equilibrium is immediately established upon any changes in applied potential. When there is a high barrier to electron transfer (electrochemically irreversible), electron transfer is slow and more negative potentials are required. It leads to larger ΔE_p value (> 57 mV) than that for the Nernstian one-electron wave. The apparent electrochemical reversibility of a redox couple can be influenced by changing the scan rate, and an irreversible redox wave can sometimes be forced into a quasi-reversible wave.

The chemical reversibility is used to denote when the redox species is stable upon reduction and can subsequently be reoxidized. The species that react in homogeneous chemical processes after reduction (e.g. degradation or ligand loss) are not chemically reversible. This electron transfer coupled chemical reaction will be described in the following section.

2.2.2 Redox processes in the absence of substrate

As mentioned above, if the electron transfer from the electrode to the redox couple is slow enough to interfere with the Nernstian equilibrium, the cyclic voltammogram becomes quasi-reversible or irreversible. Furthermore, the irreversible shape of CV can also be due to subsequent chemical reaction (**Figure 2.5**), When electron transfers are coupled to chemical reactions, the CV technique can also provide kinetic and mechanistic information. The specific type of mechanism can help to diagnose the homogeneous reaction mechanism as well as the kinetics of these reactions.[203 196, 198, 199].

The notation E indicates an electron transfer step, C refers to a homogeneous chemical reaction (a chemical step). Additionally, the subscript r indicates reversibility, and subscript i indicates irreversibility. Each reaction is described for the reduction of the analyte Ox to Red as represented for each reaction scheme in **Figure 2.5**. The same concept and notations can be readily applied for oxidation processes. The general theory for electrode reactions with coupled homogeneous chemical reaction (EC and CE mechanisms) and analysis methods to determine which processes are occurring in a solution have been described by Bard (chapter 12) [196] and Savéant (chapter 2) [199] as well as the early literature. [204, 205]

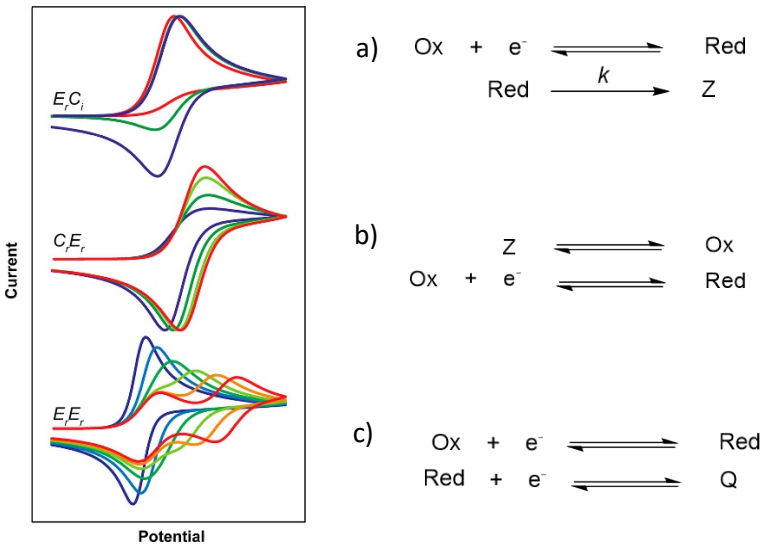

Figure 2.5. Examples of voltammograms modeled using DigiElch simulation software for three common mechanisms. The currents are normalized. E_rC_i mechanism (a): increasing the scan rate (from ν = 0.1 (red) to 1 (green) to 10 V s^{-1} (blue)) restores reversibility (rate constant for the C_i step k= 5 s^{-1}). C_rE_r mechanism (b): the faster the forward rate constant of the C_r step, the more reversible the voltammogram (K_{eq} = 0.1,k_f = 1 (blue), 10 (dark green), 100 (lime green), 1000 s^{-1} (red)). E_rE_r mechanism (c): as the separations between the two reduction potentials ($\Delta E_{1/2}$) decreases, the peaks merge to become a single two-electron peak. $\Delta E_{1/2}$ = −0.05 (dark blue), 0 (light blue), 0.05 (dark green), 0.1 (lime green), 0.15 (orange), and 0.2 V (red), from ref.[200]

Reversible electron transfer followed by an irreversible homogeneous chemical reaction (E_rC_i)

The E_rC_i mechanism (**Figure 2.5** a) is the simple case of a reduction followed by irreversible chemical reaction. The reversible redox Ox/Red couple with a slow homogeneous chemical reaction (k) compared to electron transfer appears in the voltammogram, because the decrease in the amount of Red is negligible.[196] As the rate constant (k) increases, the consumption of Red by the chemical reaction increases, and the equilibrium is interrupted resulting in a non-

Nernstian response. The ratio of the anodic and cathodic peak decrease because the reduced species Red is consumed by the following chemical reaction, leading to lower concentration of species to oxidize on the anodic scan. The CV response can be modified by varying the scan rate, and the raising of scan rate increases the time scale of the CV experiment which competes with the time scale of the chemical step. This results in more Red species for reoxidation on the anodic scan. For fast enough scan rates, the redox wave will become more reversible because oxidation outcompetes the chemical reaction.

Reversible chemical step followed by a reversible electron transfer (C_rE_r)

Another general electrode mechanism is a chemical reaction preceding electron transfer (CE mechanism), and the simple case is the C_rE_r mechanism as shown in **Figure 2.5** b. For this reduction mechanism, the amount of accessible Ox is dependent on the equilibrium constant of the first step. The greater the equilibrium constant, the more reversible redox wave is observed. In the extremely large equilibrium constant value, the voltammogram becomes completely reversible.

Two sequential electron transfer reversible process (E_rE_r)

For the two reversible electrochemical steps (**Figure 2.5** c), the shape of the CV response is dependent on the difference in formal potential of the two electron transfer steps. If the second electron transfer is thermodynamically more favourable than the first, the voltammogram is identical to a Nernstian two-electron wave, and the ΔE_p value will be 28.5 mV instead of 57 mV for the one-electron wave. [196] In a case where the second electron transfer becomes less thermodynamically favourable, a maximum ΔE_p value of just over 140 mV can be reached. At that point, the wave splits into two separated waves, each with ΔE_p = 57 mV.

2.2.3 Peak shift analysis for non-catalytic EC mechanism

For a redox process involving EC coupled reactions, the evolution of peak potentials with scan rate depends on the mechanism.[196, 199, 205] An ideal reversible one-electron redox reaction followed by an irreversible chemical reaction (an ideal E_rC_i mechanism) has a characteristic slope of $E_p/\Delta\log(\nu)$ = 30 mV.

A quasi-reversible electron transfer governed by slow kinetic electron transfer

Kinetic electron transfer between an electrode and a redox couple is governed by two key electrochemical parameters: the standard heterogeneous electron-transfer rate constant, k_s (cm s^{-1}), and the transfer coefficient, α (unitless term). The α parameter describes the symmetry of the energy barrier for electron transfer (α = 0.5 for a perfectly symmetrical barrier). [196, 199] These two parameters correspond to E_{pc} and E_{pa} by **eq 2.3** and **eq 2.4**, respectively.

$$E_{pc} = E^{0'} - \frac{0.78\ RT}{\alpha F} + \frac{2.303RT}{\alpha F}\log\left(k_s\sqrt{\frac{RT}{\alpha F\nu D}}\right) \qquad \textbf{eq 2.3}$$

$$E_{pa} = E^{0'} - \frac{0.78\ RT}{\alpha F} + \frac{2.303RT}{(1-\alpha)F}\log\left(k_s\sqrt{\frac{RT}{(1-\alpha)F\nu D}}\right) \qquad \textbf{eq 2.4}$$

where $E^{o'}$ is the formal reduction potential of the couple, R is the gas constant, T is the temperature (K), F is the Faraday constant, and D is the diffusion coefficient of the redox species ($cm^2\ s^{-1}$). These equations can be rearranged to obtain a linear equation from plotting of E_{pc} and E_{pa} versus $\log\ \nu$ as represented respectively in the **eq 2.5** :and **eq 2.6.**

$$E_{pc} = -\frac{2.303RT}{2\alpha F}\log\ \nu + \left[E^{o'} - \frac{0.78\ RT}{\alpha F} + \frac{2.303\ RT}{\alpha F}log\left(k_s\sqrt{\frac{RT}{\alpha FD}}\right)\right] \qquad \textbf{eq 2.5}$$

$$E_{pa} = \frac{2.303RT}{2(1-\alpha)F}\log\ \nu + \left[E^{o'} - \frac{0.78\ RT}{\alpha F} + \frac{2.303\ RT}{(1-\alpha)F}log\left(k_s\sqrt{\frac{RT}{(1-\alpha)FD}}\right)\right] \qquad \textbf{eq 2.6}$$

There are some examples of Co(III) complexes where the Co(III/II) redox wave exhibits a quasi-reversible voltammogram providing experimental examples of the ErCi mechanism for a redox wave which is governed by slow electron transfer. The peak shift analysis from plotting of E_{pc} versus log ν has a large value for a characteristic slope of $\Delta E_p/\Delta\log(\nu)$ greater than 30 mV for an ideal E_rC_i mechanism which was then denoted as E_qC_i or E_qC_r mechanism standing for quasi-electron transfer (E_q) coupled with reversible (C_r) or irreversible chemical reaction (C_i). For example, the $[HCo^{III}(L2)(CH_3CN)]^{2+}$ has a slope of $\Delta E_p/\Delta\log(\nu)$ = -34 mV and the slope becomes -86-89 mV when raising the scan rate greater than 5 V s^{-1} .[206] The Co(III/II) couple in the $[Co^{II}(P^{tBu}{}_2N^{Ph}{}_2)(CH_3CN)_3]^{2+}$ is also influenced by slow electron transfer kinetics exhibiting the $\Delta Ep/\Delta\log(\nu)$ = -57 mV from the plot of cathodic peak potential E_{pc} versus log ν. [207]

2.3 Overviews of cobalt hydride complexes

In early work, many cobalt hydride complexes supported by phosphine ligands have been reported (**Chart 2.3**). There are some examples of cobalt hydride complexes that could be isolated or generated in situ in a reaction. All of these hydride complexes were supported by phosphine ligands, except for the hydridocobaloxime, and were characterized by spectroscopic techniques without their crystal structures.

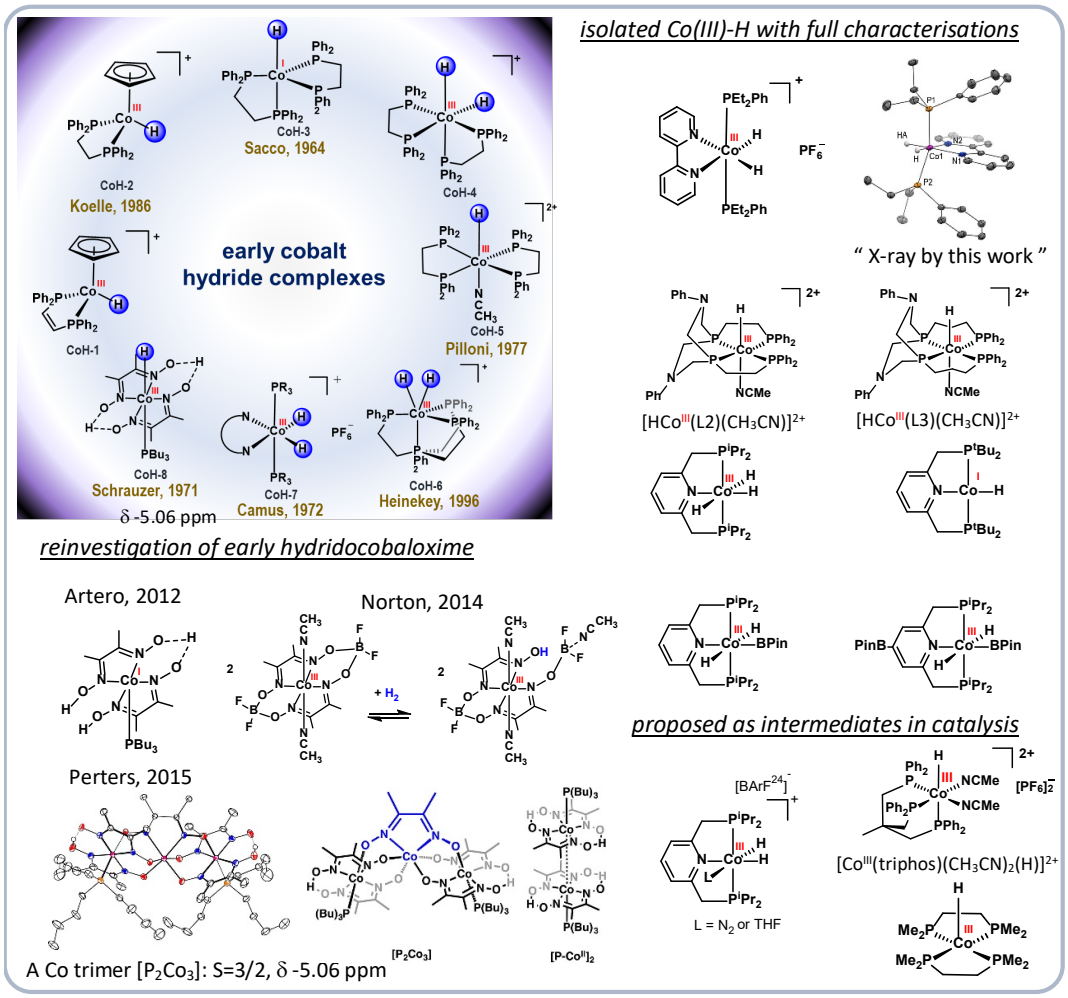

Chart 2.3. Early cobalt hydride complexes and more recent examples for characterisations and application in catalysis.

2.3.1 Synthesis and characterisation of early cobalt hydride complexes

In 1986, Koelle et al.[208] reported that a series of cobalt(III) hydride complexes based on cyclopentadienyl and phosphine derivatives, the $[CpCo^{III}H(PP)]^+$] (PP = $PPh_2CH{=}CHPPh_2$ for **CoH-1** and $PPh_2CH_2CH_2PPh_2$ for **CoH-2**) in **Chart 2.3** were isolated by protonation of $[CpCo^{I}(PP)]^+$ in toluene/methanol solution with NH_4^+ and were characterized by ^1H NMR spectroscopy.

The synthesis of **CoH-3** reported by Sacco was achieved by reduction of the $[Co^{II}(dppe)Br_2]$ (dppe = bis(diphenylphosphino)ethane) with $NaBH_4$ to obtain the Co(I) derivative. A protonation by hydroxylic solvent (EtOH or H_2O) furnished the red plates of **CoH-3**, and subsequent protonation of the cobalt (I), **CoH-3** by perchloric acid resulting in the formation of cobalt(III), **CoH-4** as yellow crystals. Moreover, the electrochemical oxidation of **CoH-3** by exhaustive controlled potential electrolysis resulted in a formation of the **CoH-5**. A bright yellow solid was isolated from the oxidized solution and identified as the **CoH-5** by elemental analysis and IR spectroscopy.[209]. The synthesis of **CoH-5** was first reported by Sacco, and Dubois and coworkers [79] then fully structurally characterized the complex by NMR and X-ray crystallography, and also investigated their redox properties as well as the hydride donor ability of $\mathbf{Co^{I}H\text{-}3}$, $\mathbf{Co^{III}H\text{-}4}$ and $\mathbf{Co^{III}H\text{-}5}$.

A Co(III) hydride supported by a tetrapodal phosphine ligand in **CoH-6** was first prepared by Bianchini[210] in 1988 as the dihydrogen $[(PP3)Co(H_2)]PF_6$ derivative (PP3 = $PhP(CH_2CH_2PPh_2)_3$). The complex was obtained as dark red crystals by protonation of the trigonal bipyramidal monohydride $[Co^{I}(PP3)H]$ derivative in THF with $HOSO_2CF_3$, followed by addition of NH_4PF_6. The dihydrogen complex was identified by IR spectroscopy and elemental analysis. The same group has also reported that the cationic species can have either a dihydrogen or a dihydride structure in the solid state, depending on the counteranion employed. It is reported that the PF_6^- salt crystallizes as the dihydrogen complex, while the BPh_4^- salt adopts the dihydride structure.[211] The further investigation by Heinekey et.al [212] in 1996 showed a modification of synthetic route for the **CoH-6** and a detailed analysis of ^1H and $^1H\{^{31}P\}$ NMR spectra of partially deuterated derivatives and variable temperature NMR experiments. It demonstrated that the **CoH-6** is a highly dynamic dihydride species.

The cationic Co(III) dihydride complex supported by chelating NN and monodentate phosphine ligands (**CoH-7**) was first reported by Camus, Couver and Mestroni in 1972.[213] The series of cationic $[Co(H)_2(NN)(PR_3)_2]^+$ (NN = bpy or phen, R_3 = Bu_3, Pr_3, Et_3 and Et_2 Ph) complexes was prepared by a reaction with $NaBH_4$ together with H_2 bubbling, and followed by adding ammonium salt in MeOH or EtOH solution. The ^1H and ^{31}P NMR characterisation suggested the structure of $[Co(H)_2(NN)(PR_3)_2]^+$ as shown in **Chart 2.3** where the two H^- ligands are in the equatorial plane and are trans to the N-atoms. The two phosphorus atoms in the complex are mutually trans to each other in the axial position. This configuration is consistent with the NMR studies and the X-ray structure of the same cationic $[Co^{III}(H)_2(bpy)(PEt_2Ph)]^+$ in our study.

Hydridocobaloxime by Schrauzer

In 1971, hydridocobaloxime stabilized by axial base trialkylphosphine (**CoH-8**) base was claimed by Schrauzer.[214] The evidence for a Co-hydride bond came from IR spectroscopy showing the stretch of this bond at 2240 cm^{-1} and it was observed at 1680 cm^{-1} for the deuteride analogue. The ^{1}H NMR spectrum showed a chemical shift of the hydride ligand at δ -5.06 which is unusual value for the characteristic of formal hydride ligand. However, this value corresponds with a $Co^{\delta-}$-$H^{\delta+}$ polarization of the metal-hydrogen bond due to the high acidity of this complex ($pK_a \approx 7$) in methanol/water solution by showing the appearance of its conjugate base, Co(I) species with a large absorption band over the 550-650 nm region in the UV-Vis spectrum.

The reinvestigation of hydridocobaloxime by Schrauzer

The reinvestigations of the hydridocobaloxime revealed that the structure of cobalt(III) hydride cobaloxime proposed by Artero and coworkers in 2012 (**Chart 2.3**) contradicts the $[Co^{III}(dmgH)_2(PBu_3)(H)]^+$ discovered by Schrauzer. The NMR structural studies by Peters et al. suggested that the hydride species resonance at δ -5.06 is attributed to a trimeric complex which can be formed by exposure to the air and is a paramagnetic species with the ground spin state S =3/2. Norton and coworkers study the reaction of $[Co^{II}(dmgBF_2)_2(CH_3CN)]$ under high pressure of H_2 (the equation shown in **Chart 2.3**). They found that a slowly reversible reaction of this complex occurs to generate a new species with the exchangeable H atom at the ligand not forming hydride species. This recent study confirmed that the structure of hydridocobaloxime proposed by Schrauzer is unlikely.

2.3.2 Isolable cobalt hydride complexes and their X-ray structures

2.3.2.1 Cobalt hydride supported by a tetraphosphine ligand with pendant amine groups

The isolable $[HCo^{III}(L2)(CH_3CN)]^{2+}$ and $[HCo^{III}(L3)(CH_3CN)]^{2+}$ containing tetradentate phosphine ligands with a pendant amine moiety as shown in **Chart 2.3** were prepared from their cobalt(II) analogues: $[Co^{II}(L2)(CH_3CN)_3]^{2+}$ and $[Co^{II}(L3)(CH_3CN)_3]^{2+}$. These Co(II) complexes supported by the tetradentate phosphine ligand can inhibit ligand exchange and lead to isolable monohydride analogues with well-characterized structures including NMR evidence and also their crystal structures.[206] The $[HCo^{III}(L2)(CH_3CN)]^{2+}$complex was achieved by a reduction of $Co^{II}(L2)(CH_3CN)_3]^{2+}$ with KC_8 in CH_3CN followed by the protonation of the Co^{I} analogue with p-anilinium tetrafluoroborate (**Figure 2.6**). This complex was well characterized by NMR techniques and X-ray crystallography. The hydride ligand appears as a broad signal at δ -21.2 ppm in the ^{1}H NMR. The $^{31}P[^{1}H]$ NMR spectrum also shows very broad peaks of two inequivalent phosphorus at δ 76 and 80 due to quadrupolar relaxation.

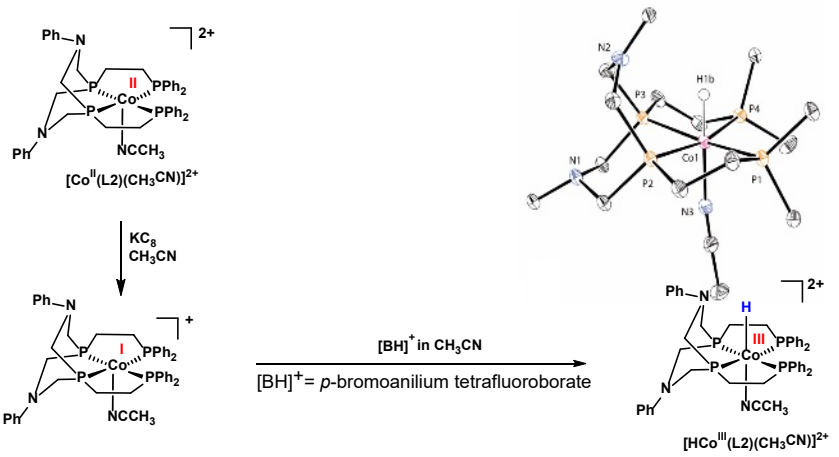

Figure 2.6. Synthetic pathway and the X-ray structure for monohydride $[HCo^{III}(L2)(CH_3CN)]^{2+}$

2.3.2.2 Cobalt hydride with a tridentate bis-(phosphino)pyridine, PNP pincer ligand

The well-defined cobalt complexes supported by a tridentate bis(phosphino)pyridine were reported independently by the groups of Milstein[215] and Chirik.[174, 177, 216] The preparation and structures of selected examples of cobalt hydride pincer complexes with ^{iPr}PNP and ^{tBu}PNP ligands are shown in **Figure 2.7.** All complexes were structurally characterized by ^{1}H NMR, ^{31}P{^{1}H} NMR, IR spectroscopy and X-ray crystallography. The (^{tBu}PNP)Co^{I}H complex exhibited a triplet ($^{2}J_{H,P}$ = 65.3 Hz) at δ −29.0 in the ^{1}H NMR spectrum which was assigned as the cobalt-hydride resonance. A single ^{31}P NMR signal was observed at δ 85.2, indicating formation of a diamagnetic species with C_{2v} symmetry. The medium intensity band in the IR spectrum at 1746 cm^{-1} (KBr disk) was assigned to a terminal cobalt-hydride.

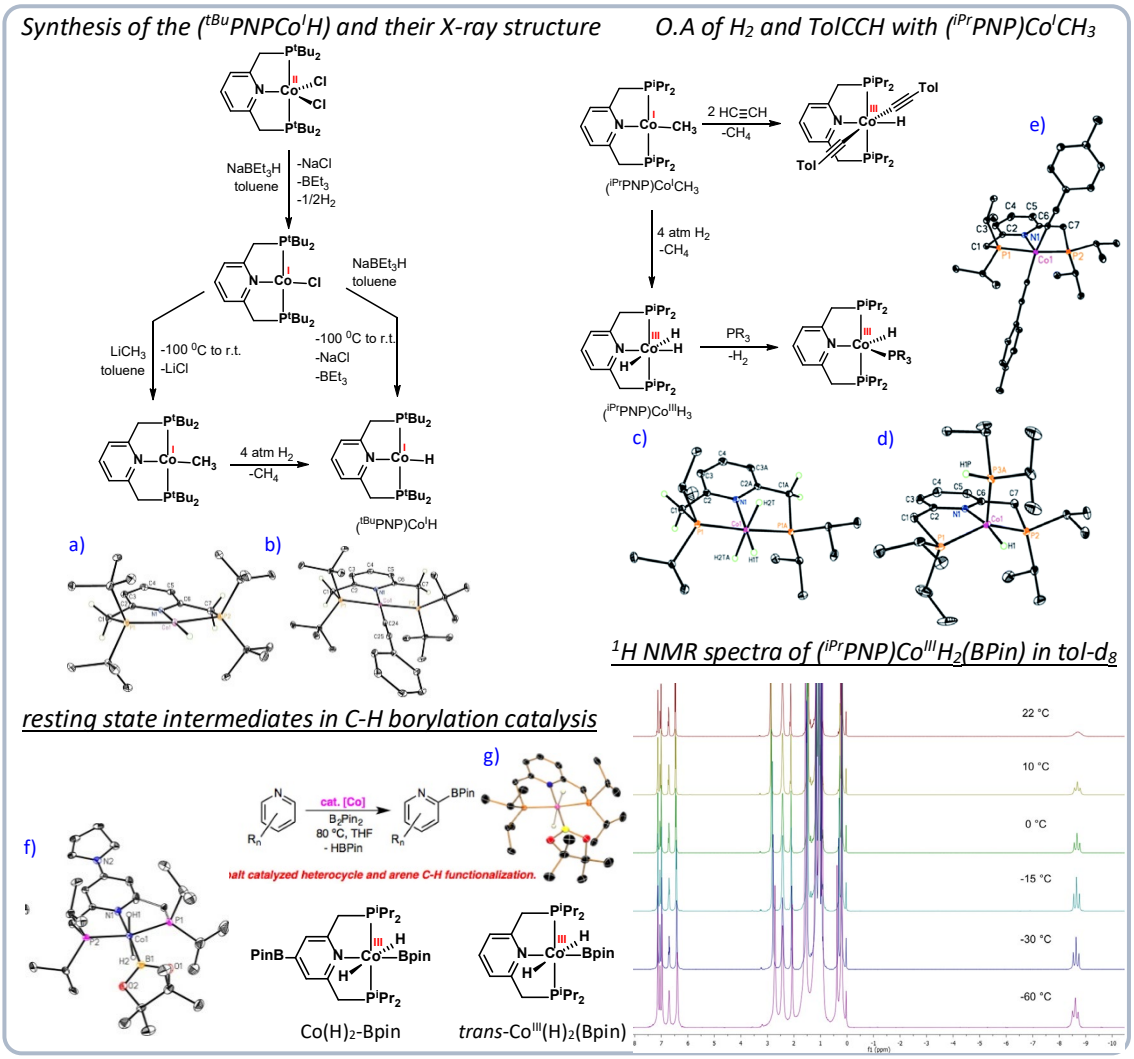

Figure 2.7. Selected examples of the cobalt pincer hydride complexes from Chirik et al.

The Chirik group [174] reported that a cobalt(III) trihydride complex could be prepared by oxidative addition of H_2 to the (^{iPr2}PNP)Co^{I}CH$_3$ (**Figure 2.7** c).The ^{iPr2}PNP electron rich ligand can stabilize the (^{iPr2}PNP)Co^{I}CH$_3$ and enables oxidative addition of H_2 and C-H bond of arene and terminal alkyne to the Co(I) methyl complex. This results in formation of the cobalt(III) trihydride complex and bis(acetylide) complex with the X-ray structure shown in **Figure 2.7** e. Moreover, the same group investigated the mechanism of the C-H borylation of heteroarene catalysed by the cobalt (I) alkyl complex, (^{iPr2}PNP)Co^{I}CH$_2$SiMe$_3$ The catalyst precursor is *trans*-(^{iPr}PNP)Co^{III}H$_2$(BPin) which generates the active species, -(^{iPr}PNP)Co^{I}(BPin) in the cycle by reductive elimination of H_2 via either isomerisation to the cis isomer or by a phosphine dissociation. *Trans*-(^{iPr}PNP)Co^{III}H$_2$(BPin) was fully characterized by NMR and X-ray analysis (**Figure 2.7**, g) and the variable temperature NMR spectra showed a triplet hydride signal at δ -8.7 at 0 ^{0}C. The Co(H)$_2$-Bpin complex was further discovered to be the catalyst resting state for the catalytic C-H borylation via a Co(I)-Co(III) redox couple. This cobalt(III) hydride complex is generated by oxidative addition of HBpin to the corresponding Co(I)-H species

Proposed cobalt hydride intermediate in catalytic reactions

Cobalt has been gaining attention in homogeneous catalysis since it is earth abundant and shows outstanding catalytic activity. The recent review of homogeneous cobalt-catalyzed hydride transfer reactions provides a comprehensive overview of the design, synthesis, and reactivity of cobalt catalysts, their catalytic applications, and reaction mechanisms.[217] The Heinekey group [218] summarized the synthesis, structure and reactivity of cobalt hydride and dihydrogen complexes in early work, and the development of cobalt-catalyzed H_2 production. Moreover, Perutz and Procacci [219] have reviewed the photochemistry of transition metal hydrides across the transition metal groups. Therefore, studies of novel hydride complexes to understand the reactivity of M-H bond are important to the rational development of new catalysts and discovery of their reactivity for new catalytic processes.

2.3.2.3 Cobalt hydrides supported by a tridentate bis-(phosphino)pyridine, PNP pincer ligand

The reactivity and catalytic activity of the cationic cobalt(I) pincer complexes remains limited compared to the catalytic chemistry of cationic Rh and Ir complexes. The Chirik group [169] has recently reported that the oxidative addition of H_2 to $[(^{iPr}PNP)Co^{I}(N_2)]^{+}$ resulted in formation of the cationic cobalt(III) dihydride, $[(^{iPr}PNP)Co^{III}(H_2)L]^{+}$, where L = THF or N_2 (^{iPr}PNP = 2,6-bis((diisopropylphosphaneyl)methyl)pyridine)as shown in **Figure 2.8**). The hydride signals in the ^{1}H NMR spectrum of the cationic dihydride complex at room temperature are broad peaks: however; they become well-resolved signals by displaying two triplets of doublets at δ -22.10 ($^2J_{P,H}$ = 56.6 Hz) and -31.32 ($^2J_{P,H}$ = 63.1 Hz) at -60 ^{0}C. The broad ^{1}H NMR signals of this dihydride species may be a result of rapid and reversible reductive elimination and oxidative addition of H_2 or possibly due to an exchange of the neutral L ligand resulting in a Berry pseuorotation of the five-coordinate intermediate.

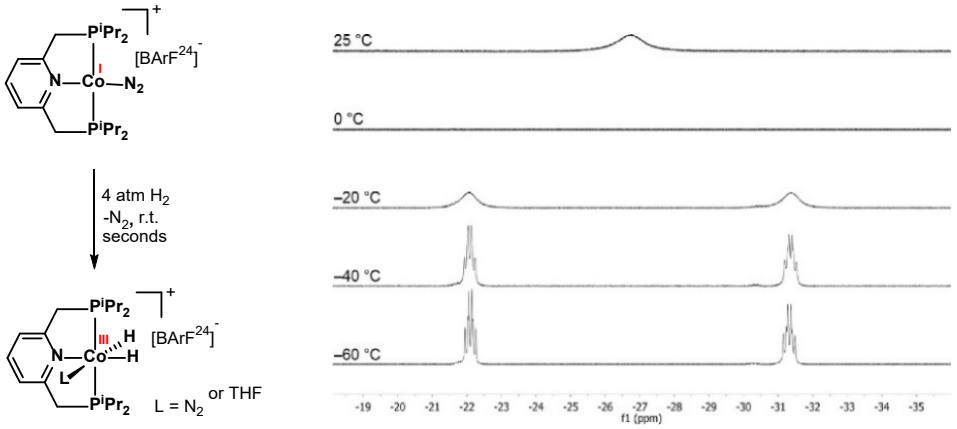

Figure 2.8. Hydride signals of $[(^{iPr}PNP)Co^{III}(H_2)L]^+$ in THF-d_8 from -60 to 25 ^{0}C and the reaction scheme represented oxidation addition of H_2 to the $[(^{iPr}PNP)Co^{I}(N_2)]^+$ cation.[169]

2.3.2.4 Cobalt hydride complexes for CO_2 reduction and hydrogen evolution catalysis

Much effort has been taken to identify cobalt hydride species which are generally considered as intermediates in the homogeneous catalysis of H_2 evolution by cobalt complexes.[72, 87, 140, 151, 220-223] Many molecular cobalt complexes are used as electrocatalysts for H_2 production: however; the key hydride intermediate is frequently difficult to isolate and characterize as a result of high reactivity. Full characterisation of the proposed cobalt (III) hydride intermediates in the HER catalytic cycle with direct evidence of their structure and their redox properties is very scarce.[218]. There are very few examples of Co(III)-H intermediates proposed in the catalytic cycle for hydrogen production that are characterized by NMR techniques and X-ray crystallography. The cobalt hydride complex with a tripodal phosphine ligand, $[Co^{III}(triphos)(CH_3CN)_2(H)]^{2+}$ (**Chart 2.3**) , reported by Gray and co-workers,[224] is generated in situ by protonation of its Co(I) analogue and exhibited a hydride resonance at δ -7.6 (dt $J_{cis\text{-}H\text{-}P}$ = 65 Hz and $J_{trans\text{-}H\text{-}P}$ = 130 Hz). The mechanistic studies of possible pathways for electrocatalytic H_2 production catalyzed by this hydride complex in the presence of acid show reduction of Co^{III}-H intermediate and protonation of the reduced Co^{II}-H species to evolve H_2. Furthermore, the Linehan group [117] showed that $[Co(dmpe)_2H]$ (dmpe = 1,2- bis(dimethylphosphino)ethane) catalyses the reduction of CO_2 to formate. The complex has remarkable turnover frequency of 3400 h^{-1} at room temperature and 1 atm of 1:1 CO_2:H_2 (74 000 h^{-1} at 20 atm) in THF.

Until now, such cobalt(III) hydride intermediates have only been structurally characterized for a few molecular cobalt-based catalysts in a homogeneous catalysis of hydrogen production. Moreover, the electrochemical data was very limited in the literature. For this reason, molecular hydrides of cobalt complexes have been widely investigated to identify and isolate this species in a reaction.

2.3.3 Electrochemistry of cobalt hydride complexes

CV studies of the isolable hydride $[HCo^{III}(L2)(CH_3CN)]^{2+}$ supported by a tetradentate phosphine

Recently, the group of Bullock[206] achieved isolation of a series of Co(III)-H supported by a multidentate phosphine with pendant amines as shown the structure of the $[HCo^{III}(L2)(MeCN]]^{2+}$ in **Figure 2.6**. All of these complexes were fully characterized by ^1H NMR and X-ray crystallographic determination. The CV studies under non-catalytic conditions were also investigated. The interpretation of the CV of $[HCo^{III}(L2)(CH_3CN)]^{2+}$ under non-catalytic conditions (**Figure 2.9**) was supported by digital simulation showing that a reduction of $[HCo^{III}(L2)(CH_3CN)]^{2+}$ proceeds via an $E_rC_rE_r$ reduction mechanism. One electron transfer to the Co(III)-H leads to reversible MeCN dissociation from the Co(II)-H which is further reduced to Co(I)-H. Moreover, reduction of the Co(III)-H also causes cleavage of the H-Co bond from both Co(II)-H and Co(I)-H species resulting in formation of $[Co^{I}(L2)(MeCN)]^{+}$ identified by the anodic peak on the reverse scan in the CV (**Figure 2.9**).

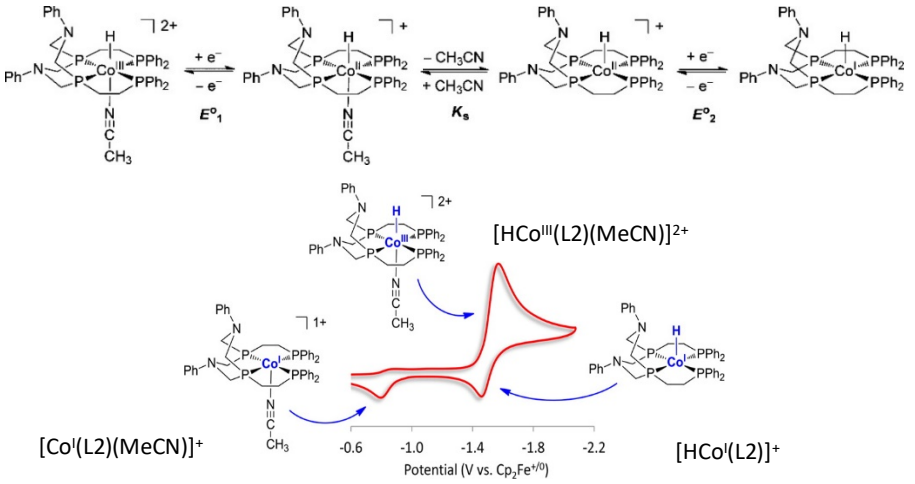

Figure 2.9. Electrochemical reduction mechanism of the $[HCo^{III}(L2)(CH_3CN)]^{2+}$ and CV of this Co(III)-H species at scan rate = 0.1 Vs^{-1} with electrochemically generated species at certain potentials. Adaped with permission from ref [206]. Copyright 2013 American Chemical Society.

The electrochemical studies by the peak shift analysis of the $[HCo^{III}(L2)(CH_3CN)]^{2+}$by varying scan rates between 0.05 and 5 V s^{-1} affords a slope of 34 mV from the plot of E_{pc} values versus log(ν) which supports the $E_rC_rE_r$ mechanism for the reduction of the $[HCo^{III}(L2)(CH_3CN)]^{2+}$. However, raising scan rates (greater than ν = 5 V s^{-1}) caused an increase of the slope to 86–89 mV which corresponded to a transition from reversible to quasi-reversible electron transfer.

Well-tuned redox properties of isolated $[Cp^{R}Co^{III}(P^{tBu2}N^{Ph2})H][BF_4]$complexes

Another series of isolable and well-characterized cobalt hydride complexes, $[Cp^{R}Co^{III}(P^{tBu2}N^{Ph2})H][BF_4]$, where R = H, C_6F_5, C_5F_4N was reported. [225] The structure of these Co(III)-H hydride complexes is shown in **Figure 2.10** by the abbreviations of $[Co^{III}H]^+$, $[Co^{III}H]^+_{C6F5}$, and $[Co^{III}H]^+_{C5F4N}$ indicating subscript R group on each structure. The preparation of these hydride Co(III)-H complexes was achieved by reduction of the Co^{II} analogues by KC_8 leading to the neutral Co(I) species. Subsequent protonation yields the Co^{III} hydrides which were characterized by X-ray crystallography. The well-tuned redox properties as seen in the CVs (**Figure 2.10**) by a positive shift of Co(III/II) and Co(II/I) couples in a series of the $[Co^{II}]^+$, $[Co^{II}]^+_{C6F5}$, $[Co^{II}]^+_{C5F4N}$ were achieved by variation of R group on the Cp ring in this Co(II) series.[225]

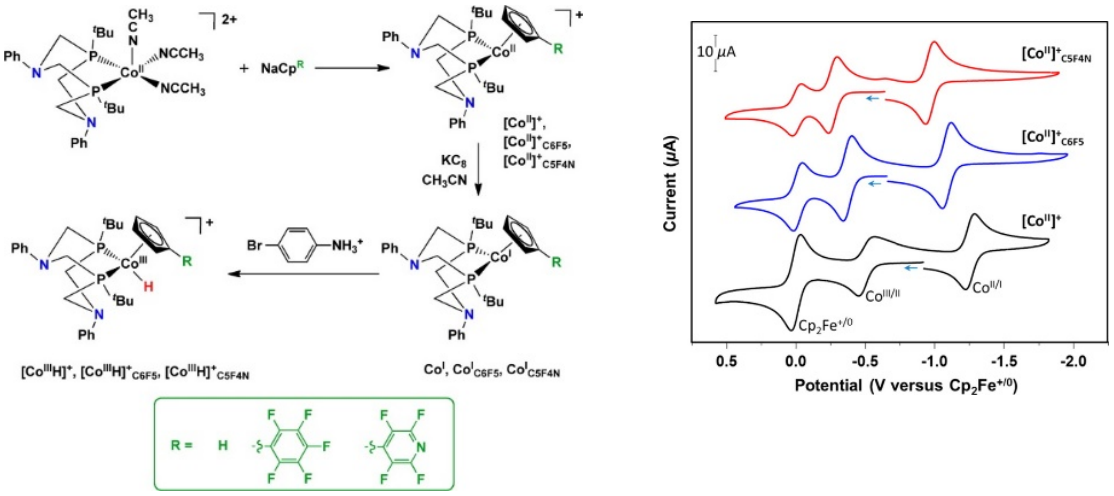

Figure 2.10. Synthesis of $[Cp^{R}Co^{III}(P^{tBu2}N^{Ph2})H][BF_4]$ complexes[225]. Inset shows the CV of $[CpCo^{II}(P^{t}Bu_2N^{Ph}_2)]^+$ ($[Co^{II}]^+$), $[Cp^{C6F5}Co^{II}(P^{t}Bu_2N^{Ph}_2)]^+$ ($[Co^{II}]^+_{C6F5}$), and $[Cp^{C5F4N}Co^{II}(P^{t}Bu_2N^{Ph}_2)]^+$ ($[Co^{II}]^+_{C5F4N}$). Conditions: ν = 0.1 V s^{-1}, 1 mM cobalt complex in MeCN with 0.2 M $TBAPF_6$, 1 mm diameter glassy-carbon working electrode

The Co(III/II)-H couples of each complex in this series shift to more positive potentials as the Cp^R ligand becomes more electron withdrawing. The CVs of $[Co^{III}H]^+$, $[Co^{III}H]^+_{C6F5}$, and $[Co^{III}H]^+_{C5F4N}$ showed an irreversible reduction wave of the Co(III/II)-H couple at E_{pc} of −1.96, −1.73, and −1.61 V vs $Fc^{0/+}$, respectively. These potentials are about 700 mV more negative than the Co(II/I) couples of the corresponding Co^{II} complexes $[Co^{II}]^+$, $[Co^{II}]^+_{C6F5}$, and $[Co^{II}]^+_{C5F4N}$. The CV of each Co(III)-H complex indicates that the reduced Co(II)-H undergoes either a bimetallic or monometallic Co−H bond cleavage reaction by exhibiting a new oxidation wave on the return sweep at a potential near the CoII/I couple. A further study by variable scan rate analysis (0.1−3 V s^{-1}) gave a slope of 18 mV from the plot of E_{pc} versus log ν and supported a bimetallic reaction of the electrochemically reduced Co(II)-H species under non-catalytic conditions.

2.4 Experimental

2.4.1 General Procedures and materials

All compounds were synthesized under an inert atmosphere of N_2 or Ar using standard Schlenk line and glove box techniques unless otherwise noted. Glassware was dried at high temperatures in the oven and evacuated under vacuum and refilled with N_2 at least three times prior to performing a reaction. Dry and deoxygenated solvents were prepared according to standard procedures. Benzene, toluene, hexane and THF, iPr-OH and n-BuOH were dried by refluxing over Na under Ar. Acetonitrile, MeOH, $CHCl_3$ were refluxed and dried over CaH_2. Deuterated solvents (CD_3CN, CD_3OD, acetone-d_6, toluene-d_8, C_6D_6 and $CDCl_3$ were purchased from Aldrich). Acetone-d_6, CD_3CN, CD_3OD were dried over calcium hydride, and toluene-d_8, C_6D_6 were dried over potassium prior to degas by freeze-pump-thawed technique (three times), and stored under Ar atmosphere in a glove box.

Solvents for general use were purchased from Fisher Scientific Ltd. All commercial chemicals were purchased from suppliers as following: Sigma-Aldrich (ammonium hexafluorophosphate, cobalt(II) tetrafluoroborate hexahydrate, chlorodiisopropylphosphine, 96%, tetrabutylammonium hexafluorophosphate ($TBAPF_6$), trifluoroacetic acid, sodium borohydride), Merck (2-methylpyridine, cobalt(II) chloride anhydrous). All of these chemicals were used without further purification.

2.4.2 Characterisation techniques

2.4.2.1 NMR spectroscopy

^1H, $^{13}C\{^1H\}$, ^{19}F, $^{31}P\{^1H\}$ and ^{15}N NMR spectra were recorded on Bruker AV500 (500 MHz) at 298 K unless otherwise noted. The solvent signals were used as internal references for ^1H and $^{13}C\{^1H\}$ spectra and the chemical shifts were reported relative to the tetramethylsilane (TMS) scale in ppm (CD_3CN δH = 1.94 (5), δC = 118.69 (1) and 1.39 (7) ppm; Acetone-d_6 δH = 2.05 (5), δC = 206.68 (1) and 29.92 (7), $CDCl_3$ δH = 7.24 (1), δC = 77.23 (3); C_6D_6 δH = 7.16 (1), δC = 128.39 (3) ppm; THF-d_8 δH = 3.58 (1) and 1.73 (1), δC = 67.57 (5) and 25.37 (5); Toluene-d_8 δH = 2.09 (5), 6.98 (5), 7.00 (1) and 7.09 (m), δC = 20.4 (7), 125.49 (3), 128.33 (3), 129.24 (3), and 137.86 (1); methanol-d_4. δH = 3.31 (5), 4.78 (1), δC = 49.15 (7), $^{31}P\{^1H\}$, ^{19}F and ^{15}N spectra are referenced against an external standard of H_3PO_4, $CFCl_3$ and pyridine, respectively. Multiplicity is abbreviated as: s, singlet; d, doublet; t, triplet; q, quartet; sep, septet; m, multiplet; br, broad.

2.4.2.2 UV-Vis absorption and emission spectroscopy

UV-Vis absorption spectra were recorded at ambient temperature on an Agilent 8453 spectrometer using a quartz cell with 1 cm path length. The emission spectra were measured using a Hitachi F-4500 fluorimeter. All solvents were dried over standard drying agent prior to use and degassed by three freeze-pump-thaw cycles under N_2 or Ar.

2.4.2.3 Mass spectrometry

ESI mass spectra were recorded on a Bruker micrOTOF instrument

2.4.2.4 Magnetic susceptibility measurement

The NMR Evans' method [226, 227] was used to measure the magnetic moment (μ, in Bohr magneton) for the paramagnetic complexes in solution in order to determine the number of unpaired electrons in the complex. Following Evans' method, a solution of the $[Co^{II}(PN)_2(MeCN)][BF_4]_2$ (0.4 mL, 0.0347 M) was prepared by using the same stock solution for pure solvent (1.67% THF in CD_3CN) taken in the inner tube. The ^1H NMR spectra of the reference compound (THF signals) in the two coaxial tubes were recorded on Bruker AV500 (500 MHz) in the temperature range 298-330 K for Δf measurements in Hertz.

$$\mu = 2.84\sqrt{\chi_M T} \qquad \textbf{eq 2.7}$$

$$\chi_M = \left|\frac{-3\,\Delta f}{4\pi f m} \cdot 1{,}000\ \frac{cm^3}{L} \cdot \frac{g}{n}\right| = \left|\frac{-3{,}000\,\Delta f}{4\pi f c}\right| \qquad \textbf{eq 2.8}$$

where
- μ = magnetic moment (Bohr magneton)
- χ_M = molar susceptibility
- T = absolute temperature (K)
- Δf = chemical shift difference (Hz)
- f = spectrometer frequency (Hz)
- m = mass concentration (g/cm^3)
- g = mass of a paramagnetic material
- n = mole of a paramagnetic material
- c = molar concentration

Replacing the χ_M value given in **eq 2.8** by the **eq 2.7** resulted in the relationship between μ and Δf x T as shown in **eq 2.9**

$$\mu = 2.84\sqrt{\frac{3{,}000 \cdot \Delta f \cdot T}{4\pi f c}} \qquad \textbf{eq 2.9}$$

Therefore, plotting of chemical-shift differences (Δf) versus 1/T resulted in the linear correlation with the slope corresponding to (Δf x T) at zero Y-intercept (**eq 2.9**). This slope value is then

taken into **eq 2.9** resulting in obtaining the magnetic moment, μ = 1.64 BM after temperature calibration of the spectrometer. According to the **eq 2.10**,

$$\mu \approx 2\sqrt{S(S+1)} = \sqrt{n(n+2)} \qquad \textbf{eq 2.10}$$

where S = total spin quantum number and n = the number of unpaired electrons. Therefore, the magnetic moment of 1.64 BM corresponded to one unpaired electron in $[Co^{II}(PN)_2(MeCN)][BF_4]_2$ with total spin number of ½ suggesting a d^7, low-spin complex in the solution. It should be noted that this method only probes the temperature-dependent component of the paramagnetic susceptibility.

2.4.2.5 Electrochemistry

The electrochemical studies were performed using a BASi Epsilon-EC potentiostat. EC-Lab software was used to process and analyse the data. All electrochemical experiments were performed in a three-neck single compartment electrochemical cell under Ar atmosphere. A glassy carbon disk electrode (3 mm diameter) was used as the working electrode for cyclic voltammetry (CV) measurements. The auxiliary electrode was a platinum wire for all CV experiments. The reference electrode was a pseudo reference electrode (Ag wire immersed in CH_3CN containing 0.1 M $TBAPF_6$ electrolyte solution) separated from the solution by a Vycor frit and internally referenced to a standard $Fc^{0/+}$redox couple by setting to 0.0 V. All CV measurements for each complex were carried out by using MeCN as solvent, which was dried by distillation over calcium hydride under argon prior to use.

2.4.2.6 UV-Vis spectroelectrochemistry

A standard three-electrode UV-Vis spectroelectrochemical cell with 1 mm path length of a quartz cuvette (BASi) was used. A Pt gauze was used as working electrode, and the counter electrode was a Pt wire. The applied potential for bulk electrolysis of each complex in CH_3CN was referenced to a pseudo reference electrode containing the electrolyte solution and Ag wire separated from the solution by a Vycor frit. The potential was applied using a BASi Epsilon-EC potentiostat, and changes in UV-Vis spectra were measured using an Agilent 8453 spectrometer.

2.4.2.7 X-ray crystallography

Diffraction data were collected at 110.05(10) K using an Agilent **SuperNova** diffractometer with CuKα (λ = 1.54184 Å) or MoKα (λ = 0.71073 Å) radiation. The structures were solved using Olex2[228] with the ShelXT [229] structure solution program using Intrinsic Phasing unless stated otherwise. Refinement was carried out by the ShelXL [230] refinement package using Least Squares minimisation.

$[Co^{II}cis\text{-}(PN)_2Cl][PF_6]$ complex

Refinement Special Details

Three components of the structure exhibited disorder.

Firstly, the hexafluorophosphate was disordered and modelled in two positions with refined occupancies of 0.558:0.442(13). The P-F bond lengths were restrained to be equal and the ADP of the phosphorus atoms constrained to be equal.

Secondly, one tetrahydrofuran was modelled partly in two positions with refined occupancies of 0.748:0.252(11). Three carbons were modelled in two positions. C26, C27 and C28. The C-C bonds adjacent to the oxygen were restrained to be equal length and the C-C opposite the oxygen were similarly restrained to be equal. The ADP of pairs of disordered carbons were constrained to be equal, namely C26 & C26a, C27 and C27a, C28 & C28a.

Finally, there was a site which contained a mixture of THF and pentane. This was located at an inversion centre so there was 0.5 molecules of solvent (either THF or pentane) per asymmetric unit. The ratio of pentane to THF refined to 0.275:0.225(6). For the pentane, the C-C bond lengths were restrained to be 1.52 Å and the C-C-C distance to 2.49 Å. For the THF, the C-C bond lengths were restrained to be 1.52 Å and the C-O bond lengths restrained to be 1.43 Å. C-C-C distances were restrained to be 2.36 Å, the C-O-C distance restrained to be 2.32 Å and the C-C-O distances 2.34 Å. The ADP of proximal atoms were constrained to be equal, namely, C33, C29 & O2, C30 & C35, C36 & C31, C37 & C32. The ADP of all atoms in this mixture were restrained to be approximately isotropic.

Table 2.1. Crystal data and structure refinement for [Co^{II}*cis*-$(PN)_2Cl$][PF_6] (rnp 1903).

Empirical formula	$C_{30.27}H_{53.1}ClCoF_6N_2O_{1.23}P_3$
Formula weight	766.04
Temperature/K	110.00(10)
Crystal system	monoclinic
Space group	$P2_1/n$
a/Å	13.15908(9)
b/Å	12.41713(9)
c/Å	22.29658(17)
α/°	90
β/°	94.0339(7)
γ/°	90
Volume/$Å^3$	3634.19(5)
Z	4
$\rho_{calc}g/cm^3$	1.400
μ/mm^{-1}	6.135
F(000)	1606.0
Crystal size/mm^3	0.244 × 0.171 × 0.035
Radiation	CuKα (λ = 1.54184)
2Θ range for data collection/°	7.576 to 134.146
Index ranges	-15 ≤ h ≤ 14, -14 ≤ k ≤ 14, -25 ≤ l ≤ 26
Reflections collected	33324
Independent reflections	6498 [R_{int} = 0.0351, R_{sigma} = 0.0253]
Data/restraints/parameters	6498/163/507
Goodness-of-fit on F^2	1.253
Final R indexes [I>=2σ (I)]	R_1 = 0.0476, wR_2 = 0.0963
Final R indexes [all data]	R_1 = 0.0499, wR_2 = 0.0971
Largest diff. peak/hole / e $Å^{-3}$	0.73/-0.45

$[Co^{III}$*cis*-$(PN)_2Cl_2][PF_6]$

Single crystals of $[Co^{III}$*cis*-$(PN)_2Cl_2][PF_6]$ (rnp1805) were recrystallized from MeOH/hexane.

Table 2.2. Crystal data and structure refinement for $[Co^{III}$*cis*-$(PN)_2Cl_2][PF_6]$ complex.

Empirical formula	$C_{24}H_{40}Cl_2CoF_6N_2P_3$
Formula weight	693.32
Temperature/K	110.05(10)
Crystal system	monoclinic
Space group	C2/c
a/Å	12.0595(4)
b/Å	11.3567(3)
c/Å	22.3063(7)
α/°	90
β/°	98.322(3)
γ/°	90
Volume/Å^3	3022.82(16)
Z	4
ρ_{calc}g/cm^3	1.523
μ/mm^{-1}	8.077
F(000)	1432.0
Crystal size/mm^3	0.278 × 0.112 × 0.054
Radiation	CuKα (λ = 1.54184)
2Θ range for data collection/°	8.012 to 134.08
Index ranges	-11 ≤ h ≤ 14, -7 ≤ k ≤ 13, -24 ≤ l ≤ 26
Reflections collected	5249
Independent reflections	2700 [R_{int} = 0.0162, R_{sigma} = 0.0227]
Data/restraints/parameters	2700/0/178
Goodness-of-fit on F^2	1.036
Final R indexes [I>=2σ (I)]	R_1 = 0.0245, wR_2 = 0.0620
Final R indexes [all data]	R_1 = 0.0262, wR_2 = 0.0629
Largest diff. peak/hole / e Å^{-3}	0.26/-0.31

$[Co^{III}(PN)_2(H)(Cl)][PF_6]$

Single crystals of $[Co^{III}(PN)_2(H)(Cl)][PF_6]$ were recrystallized in acetone/hexane. Using Olex2 [228], the structure was solved with the Superflip[229] structure solution program using Charge Flipping and refined with the ShelXL[230] refinement package using Least Squares minimisation.

Table 2.3. Crystal data and structure refinement for $[Co^{III}(PN)_2(H)(Cl)][PF_6]$ (rnp1701).

Empirical formula	$C_{24}H_{41}ClCoF_6N_2P_3$
Formula weight	658.88
Temperature/K	110.05(10)
Crystal system	tetragonal
Space group	$P4_32_12$
a/Å	10.81091(11)
b/Å	10.81091(11)
c/Å	24.8859(5)
α/°	90
β/°	90
γ/°	90
Volume/Å^3	2908.57(8)
Z	4
ρ_{calc}g/cm^3	1.505
μ/mm^{-1}	0.903
F(000)	1368.0
Crystal size/mm^3	0.287 × 0.127 × 0.09
Radiation	MoKα (λ = 0.71073)
2Θ range for data collection/°	6.548 to 64.04
Index ranges	-16 ≤ h ≤ 16, -14 ≤ k ≤ 15, -37 ≤ l ≤ 31
Reflections collected	18304
Independent reflections	4725 [R_{int} = 0.0366, R_{sigma} = 0.0330]
Data/restraints/parameters	4725/0/175
Goodness-of-fit on F^2	1.076
Final R indexes [I>=2σ (I)]	R_1 = 0.0268, wR_2 = 0.0572
Final R indexes [all data]	R_1 = 0.0301, wR_2 = 0.0589
Largest diff. peak/hole / e Å^{-3}	0.37/-0.24

$[Co^{II}(PN)_2(MeCN)][BF_4]$

Single crystals of $[Co^{II}(PN)_2(MeCN)][BF_4]$ were recrystallised from CH_3CN/THF**.**

Table 2.4. Crystal data and structure refinement for $[Co^{II}(PN)_2(MeCN)][BF_4]$ complex (rnp1804).

Empirical formula	$C_{26}H_{43}B_2CoF_8N_3P_2$
Formula weight	692.12
Temperature/K	110.00(10)
Crystal system	orthorhombic
Space group	$C222_1$
a/Å	12.6973(5)
b/Å	13.4740(5)
c/Å	18.8166(7)
α/°	90
β/°	90
γ/°	90
Volume/Å^3	3219.2(2)
Z	4
ρ_{calc}g/cm^3	1.428
μ/mm^{-1}	5.730
F(000)	1436.0
Crystal size/mm^3	0.161 × 0.119 × 0.061
Radiation	CuKα (λ = 1.54184)
2Θ range for data collection/°	9.4 to 142.03
Index ranges	-13 ≤ h ≤ 15, -16 ≤ k ≤ 11, -11 ≤ l ≤ 22
Reflections collected	3761
Independent reflections	2492 [R_{int} = 0.0360, R_{sigma} = 0.0584]
Data/restraints/parameters	2492/6/197
Goodness-of-fit on F^2	1.097
Final R indexes [I>=2σ (I)]	R_1 = 0.0534, wR_2 = 0.1324
Final R indexes [all data]	R_1 = 0.0638, wR_2 = 0.1374
Largest diff. peak/hole / e Å^{-3}	0.89/-0.45
Flack parameter	-0.019(9)

2.4.3 Synthesis of 2-(diisopropylphosphino-methyl) pyridine, PN ligand

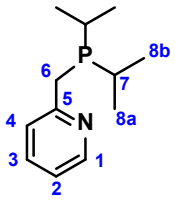

The ligand was synthesized according to the method reported in the literature with a slight change in conditions for reaction and distillation.[159] A solution of 2.5 M ^{n}BuLi in hexane (11.0 mL, 1.1 mmol) was slowly added dropwise to a well-stirred solution of 2-methyl pyridine (2.33 g, 25 mmol) in 50 ml of dry and degassed THF at -78 ^{0}C. Upon adding the ^{n}BuLi solution, the solution changed from colourless to yellow. The solution was brought up to room temperature and left to stir under N_2 atmosphere for 4 h yielding a clear deep red solution. After cooling to -78 ^{o}C, this solution was slowly added via cannula to a stirred solution of chlorodiisopropylphosphine in THF (50 mL) at -78 ^{0}C and was then vigorously stirred under N_2 overnight by allowing to warm up at room temperature. The reaction was quenched by adding 1.0 mL of MeOH to obtain a yellow-brown solution mixture. All volatiles solvents and compounds were subsequently removed under vacuo using standard Schlenk line conditions at 60 ^{0}C to give a yellow-brown oil with a precipitation of LiCl salt. This mixture of products was then purified by distillation at 105 ^{0}C under high vacuum (0.01 mbar) to give the yellow oil (3.0975 g, 59% yield) as the product. The yellow oil was characterized by NMR which was consistent with the literature.[159]

^{1}H NMR (500 MHz,in CD_3CN): δ = 8.40 (ddd, $^{3}J_{H,H}$ = 4.8, $^{4}J_{H,H}$ = 1.8 Hz, $^{5}J_{H,H}$ = 0.9, 1H, **Py-*H*$_1$),** 7.60 (td, $^{3}J_{H,H}$ = 7.9, $^{4}J_{H,H}$ 2.0 Hz, 1H, **Py-*H*$_3$),** 7.27 (ddt, $^{3}J_{H,H}$ = 7.9 Hz, $^{4}J_{H,H}$ = 1.1 Hz, $^{5}J_{H,H}$ = 1.0 Hz, 1H, **Py-*H*$_4$),** 7.09 (ddd, $^{3}J_{H,H}$ = 7.4 Hz, $^{4}J_{H,H}$ = 5.0 Hz, $^{5}J_{H,H}$ = 1.1 Hz 1H, **Py-*H*$_2$),** 2.96 (d, $^{2}J_{H,P}$ = 2.2 Hz, 2H, ***H*$_6$),** 1.79 (dsp, $^{2}J_{H,P}$ = 1.7 Hz, $^{3}J_{H,H}$ = 7.1 Hz, 2H, ***H*$_7$),** 1.05 (dd, $^{3}J_{H,P}$ = 11.3 Hz, $^{3}J_{H,H}$ = 7.0 Hz, 6H, **P-CH-(C*H*$_3$)$_2$),** 1.02 (dd, $^{3}J_{H,P}$ = 13.5 Hz, $^{3}J_{H,H}$ = 7.2 Hz, 6H, **P-CH-(C*H*$_3$)$_2$**).

^{31}P{^{1}H} NMR (202.4 MHz, in CD_3CN): δ = 12.38 (s, **1P**).

^{13}C{^{1}H} NMR (125.7 MHz, in CD_3CN): δ = 162.53 (d, $^{2}J_{C,P}$ = 8.9 Hz, **Py-*C*$_5$),** 150.29 (s, **Py-*C*$_1$),** 137.42 (s, **Py-*C*$_3$),** 124.89 (d, $^{3}J_{C,P}$ = 6.0 Hz, **Py-*C*$_4$),** 121.98 (d, $^{5}J_{C,P}$ = 1.8 Hz, **Py-*C*$_2$),** 33.46 (d, $^{1}J_{C,P}$ = 22.4 Hz ,***C*$_6$),** 24.75 (d, $^{1}J_{C,P}$ = 14.7 Hz, ***C*$_7$),** 20.47 (d, $^{2}J_{C,P}$ = 15.3 Hz, ***C*$_{8a}$,** 19.70 (d, $^{2}J_{C,P}$ = 10.8 Hz, ***C*$_{8b}$**).

^{15}N-^{1}H HMBC (50.66 MHz, in CD_3CN): δ = 1.58 ppm (d,$^{2}J_{N,H}$ = 17 Hz).

2.4.4 Synthesis of $[Co^{II}(PN)_2Cl_2]$

Anhydrous $CoCl_2$ (16.3 mg, 0.125 mmol) was dissolved in dry and degassed n-BuOH (2.0 mL) and then added to a solution of PN ligand (0.0523 g, 0.25 mmol) in n-BuOH (3.0 mL). The solution was left to stir under N_2 for 3 h resulting in a dark red solution. This solution was then collected and filtered via cannula to remove remaining $CoCl_2$ precursor. All volatiles were evaporated under vacuum to obtain a purple solid which was subsequently washed with diethyl ether and dried under vacuum to furnish the dichloro cobalt(II) complex, $[Co^{II}(PN)_2Cl_2]$, as a purple solid (67 mg, 0.122 mmol 97% yield). This complex was characterized by CHN analysis.

Anal. Calcd for $C_{24}H_{40}Cl_2CoN_2P_2$: C, 52.57; H, 7.35; N, 5.11

Found: C, 52.56; H, 7.42; N, 4.95

2.4.5 Synthesis of $[Co^{II}$*cis*$-(PN)_2Cl][PF_6]$ complex

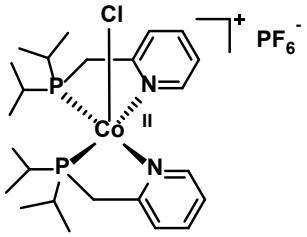

The mono chloride complex, $[Co^{II}$*cis*$-(PN)_2Cl][PF_6]$ was prepared by a reaction of the corresponding cobalt(II) dichloride $[Co^{II}(PN)_2Cl_2]$ complex (53.5 mg, 0.098 mmol) in MeCN solution (3 mL) with NH_4PF_6. A solution of NH_4PF_6 (19.0 mg, 0.12 mmol) dissolved in MeCN (1.0 mL) was added slowly to the solution of the starting complex. An immediate colour change from deep green-blue to a red-brown solution was observed which was then stirred under N_2 overnight resulting in precipitation of a white solid (NH_4Cl) from a deep red-brown solution. After filtration, all volatiles were removed from the filtrate under vacuum to obtain a deep brown oil which was left to dry under vacuum prior to washing with Et_2O. This solution mixture was left to stir under N_2 resulting in precipitation of a red-brown solid (45.3 mg, 0.064 mmol, 65% yield) which was collected to recrystallize in THF layered with pentane. A suitable single crystal for X-ray crystallographic determination as deep red purple block was obtained after leaving it in a J Young NMR tube at room temperature for 3 days.

ESI-MS (THF): m/z 477.1985 $[Co(PN)_2]^+$, calculated for $[C_{24}H_{40}CoN_2P_2]^+$ at 477.1993 (difference 0.8 mDa) and m/z 509.1883 $[Co(PN)_2O_2]^+$, and 509.1891 calculated for $[C_{24}H_{40}CoN_2O_2P_2]^+$.

2.4.6 Synthesis of $[Co^{III}$*cis*-$(PN)_2Cl_2][PF_6]$

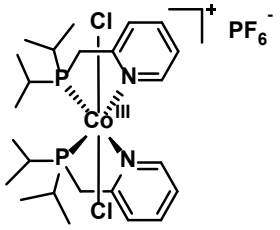

The cobalt(III) dichloro complex, $[Co^{III}$*cis*-$(PN)_2Cl_2][PF_6]$ was successfully synthesized by air oxidation of the corresponding cobalt(II) dichloro complex. The fresh compound of $[Co^{II}(PN)_2Cl_2]$ (140 mg, 0.255 mmol), as prepared by the method mentioned in **section 2.4.4**, was dissolved in MeOH (5.0 mL) to obtain a deep red solution. This solution was bubbled with air as well as vigorously stirred. NH_4PF_6 (41.6 mg, 0.255 mmol) was added as a solid. This mixture was left to stir in air for 3 h resulting in precipitation of the $[Co^{III}$*cis*-$(PN)_2Cl_2][PF_6]$ as a greenish powder. This product was purified by washing with diethyl ether to furnish the clean complex (50 mg, 0.072 mmol, 28% yield) in order to characterize by NMR spectroscopy. A single crystal of the $[Co^{III}$*cis*-$(PN)_2Cl_2][PF_6]$ as a green block was grown from a MeOH solution layered with hexane and the crystal structure was determined by X-ray crystallography.

^{1}H NMR (500 MHz, in acetone-d_6 at 223 K): δ = 8.46 (d, $^3J_{H,H}$ = 5.9 Hz, 2H, **Py-*H*$_1$**), 8.24 (t, $^3J_{H,H}$ = 7.6 Hz, 2H, **Py-*H*$_3$**), 7.97 (d, $^3J_{H,H}$ = 7.7 Hz, 2H, **Py-*H*$_4$**), 7.68 (t, $^3J_{H,H}$ = 6.7 Hz, 2H, **Py-*H*$_2$**), 4.79 (m, $^2J_{H,H}$ +$^2J_{H,P}$, 2H, **C*H*$_{2\ (6a\ or\ 6b)}$-*P***), 4.03 (m (br), $^2J_{H,H}$ +$^2J_{H,P}$, 2H, **C*H*$_{2\ (6a\ or\ 6b)}$-*P***), 3.24 (m, 2H, **P-C*H*$_{(7a\ or\ 7b)}$-(CH$_3$)$_2$**), 2.55 (m, 2H, **P-C*H*$_{(7a\ or\ 7b)}$-(CH$_3$)$_2$**), 1.64 (virtual q, $^3J_{H,H}$ = 6.5 Hz, $^3J_{H,P}$ +$^5J_{H,P}$ = 6.3 Hz, 6H, **P-CH-(C*H*$_{3\ (8a\text{-}8d)}$)$_2$**), 1.53 (virtual q, $^3J_{H,H}$ = 6.7 Hz, $^3J_{H,P}$ +$^5J_{H,P}$ = 6.6 Hz, 6H, **P-CH-(C*H*$_{3\ (8a\text{-}8d)}$)$_2$**), 1.04 (br, 6H, **P-CH-(C*H*$_{3\ (8a\text{-}8d)}$)$_2$**).

^{31}P{^{1}H} NMR (202.4 MHz, in acetone-d_6 at 223 K): δ = 55.13, (s, 2P), -144.37, (sep, $^1J_{P,F}$ = 706.1 Hz, 1PF_6^-)

^{13}C{^{1}H} NMR (125.7 MHz, in acetone-d_6, 223K): δ: 164.23 (s, **Py-*C*$_5$**), 155.37 (s, **Py-*C*$_1$**), 141.25 (s, **Py-*C*$_3$**), 124.50 (t, $^3J_{C,P}$ + $^5J_{C,P}$ = 5.17 Hz**, Py-*C*$_4$**), 124.96 (s, **Py-*C*$_2$**), 37.93 (m, $^1J_{C,P}$ + $^3J_{C,P}$ = 33.76, **Py-*C*$_{(6)}$H$_2$-*P***), 28.72 (m, $^1J_{C,P}$ + $^3J_{C,P}$ = 14.16, **P-*C*$_{(7a\ or\ 7b)}$H-(CH$_3$)$_2$**), 28.31 (m, $^1J_{C,P}$ + $^3J_{C,P}$ = 22.60, **P-*C*$_{(7a\ or\ 7b)}$H-(CH$_3$)$_2$**), 21.47 (br, **P-CH-(*C*$_{(8a\text{-}8d)}$H$_3$)$_2$**)), 19.21 (br, **P-CH-(*C*$_{(8a\text{-}8d)}$H$_3$)$_2$**), 18.52 (br, **P-CH-(*C*$_{(8a\text{-}8d)}$H$_3$)$_2$**).

^{15}N-^{1}H HMBC (50.66 MHz, in CD_3CN): δ = -59.93 (s).

ESI-MS (MeCN): m/z = 547.1385 for $[Co(PN)_2Cl_2)]^+$ (100 %) and m/z 547.1370 calculated for $[C_{24}H_{40}Cl_2CoN_2P_2]^+$ (100 %).

Anal. Calcd for $C_{24}H_{40}Cl_2CoF_6N_2P_3$: C, 41.58; H, 5.82; N, 4.04;

Found: C, 41.11; H, 5.75; N, 3.94.

2.4.7 Synthesis of $[Co^{III}(PN)_2(H)(Cl)][PF_6]$

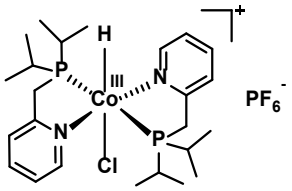

Freshly prepared purple complex, $[Co^{II}(PN)_2C)_2]$ (67 mg, 0.12 mmol) was dissolved in MeOH (5 mL) and allowed to degas by bubbling with N_2 for 10 min before adding $NaBH_4$ (5 mg, 0.132 mmol) as a solid to this solution. The mixture was stirred under N_2 for 1 h prior to adding solid NH_4PF_6 (20.4 mg, 0.125 mmol). This mixture was left to stir for another hour at room temperature to obtain the $[Co^{III}(PN)_2(H)(Cl)][PF_6]$ as product which precipitated as an orange solid. This solid was then washed with a small amount of MeOH and dried under vacuum to obtain an orange solid (39 mg, 0.059 mmol 49% yield). The $[Co^{III}(PN)_2(H)(Cl)][PF_6$ complex was characterized by NMR spectroscopy, ESI-MS and CHN analysis. A single crystal of this complex suitable for X-ray crystallographic determination was obtained by recrystallization in acetone using hexane as layering solvent to furnish orange-red crystals.

^{1}H NMR (500 MHz,in CD_3CN): δ = 8.89 (d, $^3J_{H,H}$ = 5.7 Hz, 2H, **Py-*H$_1$***), 7.71 (td, $^3J_{H,H}$ = 7.8, $^4J_{H,H}$ 1.4 Hz, 2H, **Py-*H$_3$***), 7.35 (d, $^3J_{H,H}$ = 7.8 Hz, 2H, **Py-*H$_4$***), 7.18 (t (br), $^3J_{H,H}$ = 6.7 Hz, 2H, **Py-*H$_2$***), 3.58 (d (br), $^2J_{H,H}$ = 17.2 Hz, 2H, **Py-C*H$_{2\ (6a\ or\ 6b)}$-*P***), 3.36 (d (br), $^2J_{H,H}$ = 17.0 Hz, 2H, **Py-C*H$_{2\ (6a\ or\ 6b)}$-*P***), 2.59 (sep (br), $^3J_{H,H}$ = 7.1 Hz, $^3J_{H,P}$ = 7.0 Hz, 2H, **P-C*H$_{(7a\ 0r\ 7b)}$-(CH$_3$)$_2$**), 2.25 (sep (br), $^3J_{H,H}$ = 7.1 Hz, $^3J_{H,P}$ = 7.0 Hz, 2H, **P-C*H$_{(7a\ or\ 7b)}$-(CH$_3$)$_2$**), 1.62 (virtual q, $^3J_{H,H}$ = 7.1 Hz, $^3J_{H,P}$ + $^5J_{H,P}$ = 7.3, 6H, **P-CH-(C*H$_{3\ (8a\text{-}8d)}$)$_2$**), 1.26 (virtual q, $^3J_{H,H}$ = 7.0 Hz, $^3J_{H,P}$ + $^5J_{H,P}$ = 6.8, 6H, **P-CH-(C*H$_{3\ (8a\text{-}8d)}$)$_2$**), 0.94 (virtual q, $^3J_{H,H}$ = 7.0 Hz, $^3J_{H,P}$ + $^5J_{H,P}$ = 7.1, 6H, **P-CH-(C*H$_{3\ (8a\text{-}8d)}$)$_2$**), 0.67 (virtual q, $^3J_{H,H}$ = 7.1 Hz, $^3J_{H,P}$ = 7.3 + $^5J_{H,P}$, 6H, **P-CH-(C*H$_3$ $_{(8a\text{-}8d)}$)$_2$**), -19.05 (t, $^3J_{H,P}$ = 59.7, 1H, Co-*H*).

^{31}P{^{1}H} NMR (202.4 MHz, in CD_3CN): δ: 66.4, (s, 2P), -144.62, (sep, $^1J_{P,F}$ = 706.6 Hz, 1PF_6^-)

^{13}C{^{1}H} NMR (125.7 MHz,in CD_3CN): δ: 164.88 (virtua t, $^2J_{C,P}$ + $^4J_{C,P}$ = 3.7 Hz, **Py-*C$_5$***), 159.66 (t, $^4J_{C,P}$ + $^6J_{C,P}$ = 4.3 Hz **Py-*C$_1$***), 140.14 (s, **Py-*C$_3$***), 124.95 (br, **Py-*C$_4$***), 124.22 (s, **Py-*C$_2$***), 36.00 (virtual t, $^1J_{C,P}$ + $^3J_{C,P}$ = 15.5 Hz **Py-*C$_{(6)}$*H$_2$-*P***), 28.86 (virtual t, $^1J_{C,P}$ + $^3J_{C,P}$ = 6.3 Hz, **P-*C$_{(7a\ 0r\ 7b)}$*H-(CH$_3$)$_2$**), 22.87 (virtual t, $^1J_{C,P}$ + $^3J_{C,P}$ = 12.0 Hz, **P-*C$_{(7a\ 0r\ 7b)}$*H-(CH$_3$)$_2$**), 19.09 (s, **P-CH-(*C*$_{(8a\text{-}8d)}$H$_3$)$_2$**), 18.34 (s, **P-CH-(*C*$_{(8a\text{-}8d)}$H$_3$)$_2$**), 18.18 (s, **P-CH-(*C*$_{(8a\text{-}8d)}$H$_3$)$_2$**), 18.03 (s, **P-CH-(*C*$_{(8a\text{-}8d)}$H$_3$)$_2$**).

^{15}N-^{1}H HMBC (50.66 MHz, in CD_3CN): δ: -96.48 (s).

ESI-MS (MeCN): m/z 513.1763 $[Co(PN)_2(H)(Cl))]^+$ (100 %) and m/z 513.1760 calculated for $[C_{24}H_{41}ClCoN_2P_2]^+$ (100 %).

Anal. Calcd for $C_{24}H_{41}ClCoF_6N_2P_3$: C, 43.75; H, 6.27; N, 4.25;

Found: C, 43.37; H, 6.03; N, 4.01

2.4.8 Synthesis of $[Co^{II}(PN)_2(MeCN)][BF_4]_2$

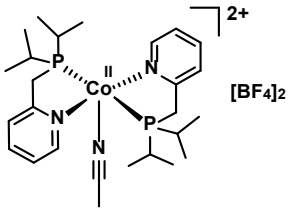

A solution of the PN ligand (167 mg, 0.8 mmol) in acetonitrile (5.0 mL) was added to a solution of $[Co^{II}(CH_3CN)_6][BF_4]_2$ (192 mg, 0.4 mmol)[231] in CH_3CN (30.0 mL) resulting in an immediate colour change from pink to a deep red solution. This mixture was left to stir at room temperature under N_2 overnight prior to concentrating under vacuo to obtain a sticky deep red crude mixture. The crude product was then washed with dry ether with stirring for 30 min to furnish a product as a red-orange solid (249 mg, 0.36 mmol, 90% yield). This solid was then recrystallized by dissolved in a small amount of CH_3CN and layered with THF to obtain deep red crystals suitable for characterization by X-ray crystallography.

ESI-Ms (Acetone): m/z 238.5966 $[Co(PN)_2]^{2+}$ and m/z 238.5971 calculated for $[C_{24}H_{40}CoN_2P_2]^{2+}$.

Anal. Calcd for $C_{24}H_{40}B_2CoF_8N_2P_2$: C, 44.27; H, 6.19; N, 4.30;

Found: C, 43.45; H, 6.12; N, 5.60

2.4.9 Synthesis of $[Co^{III}(PN)_2(H)(MeCN)][PF_6]_2$

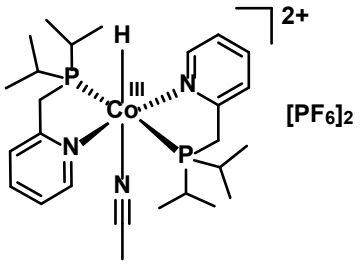

Salts of $[Co^{III}(PN)_2(H)(MeCN)][PF_6]_2$ could be successfully obtained by two different approaches, either via a reaction of the acetonitrile analogue of Co(II) complex, $[Co^{II}(PN)_2(MeCN)][BF_4]_2$ with $NaBH_4$ (**method A**) or by a ligand exchange reaction (**method B**) as described below:

Method A:

The reaction of $[Co^{II}(PN)_2(MeCN)][BF_4]_2$ (56.7 mg, 0.082 mmol) in MeOH (1.0 mL) with 1.3 equiv of $NaBH_4$ (3.8 mg, 0.10 mmol) was performed following the same method as for the preparation of $[Co^{III}(PN)_2(H)(Cl)][PF_6]$ in **section 2.4.7**. The reaction mixture was left to stir for 1 h. Then, 2.0 equiv. of NH_4PF_6 (25.6 mg, 0.157 mmol) was added as a solid resulting in precipitation of the analogous acetonitrile of $[Co^{III}(PN)_2(H)(MeCN)][PF_6]_2$ complex as a yellow powder (25 mg, 0.031 mmol, 38% yield) from a deep brown solution. The yellow solid was then characterized by multi-nuclear NMR spectroscopy, ESI-MS.

Method B:

A solution of $[Co^{III}(PN)_2(H)(Cl)][PF_6]$ (21.2 mg, 0.032 mmol) in MeCN (5.0 mL) was charged with 10.0 equiv of trifluoroacetic acid (25 μl, 0.32 mmol). This solution was heated to 45 ^{0}C and was left to stir under N_2 for 6 h to obtain a greenish solution. All volatiles and excess CF_3COOH were removed under vacuum. A greenish powder was obtained and subsequently washed three times with a small amount of MeOH followed by hexane to afford a dry yellow solid as product (6 mg, 0.007 mmol 23% yield). The product was characterized by NMR spectroscopy.

^{1}H NMR (500 MHz,in CD_3CN): δ: 8.42 (d, $^3J_{H,H}$ = 5.8 Hz, 2H, **Py-*H$_1$***), 7.83 (td, $^3J_{H,H}$ = 7.8, $^4J_{H,H}$ 1.2 Hz, 2H, **Py-*H$_3$***), 7.47 (d, $^3J_{H,H}$ = 7.8 Hz, 2H, **Py-*H$_4$***), 7.30 (t, $^3J_{H,H}$ = 7.0 Hz, 2H, **Py-*H$_2$***), 3.71 (d (br), $^2J_{H,H}$ = 17.6 Hz (in the ^{1}H{^{31}P} spectrum), 2H, **Py-C*H$_{2\ (6a\ or\ 6b)}$-P***), 3.50 (d (br), $^2J_{H,H}$ = 17.5 Hz (in the ^{1}H{^{31}P} spectrum), 2H, **Py-C*H$_{2\ (6a\ or\ 6b)}$-P***), 2.74 (sep (br), $^3J_{H,H}$ = 7.1 Hz, $^3J_{H,P}$ >> 7.3 Hz, 2H, **P-C*H$_{(7a\ 0r\ 7b)}$-(CH$_3$)$_2$**), 2.54 (s, 3H, **C*H$_{3(9)}$*CN**), 2.33 (sep (br), $^3J_{H,H}$ = 7.0 Hz, $^3J_{H,P}$ >> 6.9 Hz, 2H, **P-C*H$_{(7a\ or\ 7b)}$-(CH$_3$)$_2$**), 1.48 (virtual q, $^3J_{H,H}$ = 7.2 Hz, $^3J_{H,P}$ + $^5J_{H,P}$ = 7.4 Hz, 6H, **P-CH-(C*H$_{3\ (8a\text{-}8d)}$)$_2$**), 1.26 (virtual q, $^3J_{H,H}$ = 7.0 Hz, $^3J_{H,P}$ + $^5J_{H,P}$ = 7.0 Hz, 6H, **P-CH-(C*H$_{3\ (8a\text{-}8d)}$)$_2$**), 0.88 (virtual q, $^3J_{H,H}$ = 7.0 Hz, $^3J_{H,P}$ + $^5J_{H,P}$ =

7.0 Hz, 6H, **P-CH-(C*H*$_{3\ (8a\text{-}8d)}$)$_2$**), 0.68 (virtual q, $^3J_{H,H}$ = 7.2 Hz, $^3J_{H,P}$ = 7.4 + $^5J_{H,P}$ Hz, 6H, **P-CH-(C*H*$_{3\ (8a\text{-}8d)}$)$_2$**), -17.12 (t, $^3J_{H,P}$ = 54.3 Hz, 1H, Co-*H*).

^{13}C{^{1}H} NMR (125.7 MHz, in CD_3CN): δ: 164.56 (t, $^2J_{C,P}$ + $^4J_{C,P}$ = 3.2 Hz, **Py-*C*$_5$**), 157.72 (t, $^4J_{C,P}$ + $^6J_{C,P}$ = 4.7 Hz, **Py-*C*$_1$**), 141.11 (s, **Py-*C*$_3$**), 126.18 (t, $^3J_{C,P}$ + $^5J_{C,P}$ = 3.8 Hz, **Py-*C*$_4$**), 125.56 (s, **Py-*C*$_2$**), 35.38 (virtual t, $^1J_{C,P}$ + $^3J_{C,P}$ = 15.4 Hz, **Py-*C*$_{(6)}$H$_2$-*P***), 27.56 (virtual t, $^1J_{C,P}$ + $^3J_{C,P}$ = 6.7 Hz, **P-*C*$_{(7a\ or\ 7b)}$H-(CH$_3$)$_2$**), 23.03 (virtual t, $^1J_{C,P}$ + $^3J_{C,P}$ = 13.2 Hz, **P-*C*$_{(7a\ or\ 7b)}$H-(CH$_3$)$_2$**), 18.61 (s, **P-CH-(*C*$_{(8a\text{-}8d)}$H$_3$)$_2$**)), 18.34 (s, **P-CH-(*C*$_{(8a\text{-}8d)}$H$_3$)$_2$**), 17.96 (s, **P-CH-(*C*$_{(8a\text{-}8d)}$H$_3$)$_2$**), 17.61 (s, **P-CH-(*C*$_{(8a\text{-}8d)}$H$_3$)$_2$**).

^{31}P{^{1}H} NMR (202.4 MHz, in CD_3CN): δ: 72.44, (s, 2P), -144.60, (sep, $^1J_{P,F}$ =706.3 Hz, 1PF_6^-)

ESI-MS (MeCN): m/z 477.1994 $[Co(PN)_2]^+$ and 477.1993 calculated for $[C_{24}H_{40}CoN_2P_2]^+$

Anal. Calcd for $C_{24}H_{41}CoF_{12}N_2P_4$: C, 37.51; H, 5.38; N, 3.65;

Found: C, 37.14; H, 5.27; N, 4.08

2.5 Results and Discussion

2.5.1 Synthesis and characterization of cobalt complexes with bidentate P,N phosphine based pyridine ligands and their corresponding hydride complexes

The preparation of the PN ligand 2-(diisopropylphosphino-methyl) pyridine was performed according to the method reported in the literature[159] with some modifications which gave a yellow oil as product with moderate yield (59% yield). The NMR data including ^{1}H, $^{31}P\{^{1}H\}$, $^{13}C\{^{1}H\}$ and ^{13}C-DEPT NMR spectrum (**Figure A 2.1-2.5**) of the P,N ligand (in CD_3CN solution, 500 MHz) is consistent with the data reported in the literature. The ^{1}H NMR spectrum (**Figure A 2.1-2.2**) showed two equivalent CH_2 (δ 2.96), CH of isopropyl protons and the four doublet signals of methyl groups at chemical shifts around δ 1.0. The $^{31}P\{^{1}H\}$ spectrum (**Figure A 2.3**) displayed a singlet phosphorus signal at δ = 12.38. Moreover, the ^{1}H-^{15}N HMBC of the ligand (**Figure A 2.6**) showed one doublet of the nitrogen in pyridine ring of the ligand at δ 1.58 with $J_{N,H}$ = 17 Hz as referenced to the pyridine ligand (set at δ = 0).

A series of novel cobalt complexes with bis-P,N chelating based phosphine pyridine ligands including the Co(II) complexes: $[Co^{II}(PN)_2Cl_2]$, $[Co^{II}$*cis*$-(PN)_2Cl][PF_6]$ and the corresponding Co(II) acetonitrile complex, $[Co^{II}(PN)_2(MeCN)][BF_4]_2$ were successfully synthesized with moderate to high percent yield as summarized in **Scheme 2.1**. The synthesis of neutral dichloro cobalt(II) complex, $[Co^{II}(PN)_2Cl_2]$ was achieved in high yield (97% yield) by reacting a solution of anhydrous $CoCl_2$ with 2.0 equiv of PN ligand in n-BuOH solution. The corresponding Co(II) acetonitrile complex, $[Co^{II}(PN)_2(MeCN)][BF_4]_2$ as a red-orange solid (90% yield) was prepared from $[Co^{II}(MeCN)_6][BF_4]_2$ and 2.0 equiv. of the PN ligand. Furthermore, the $[Co^{II}(PN)_2Cl_2]$ was used as the starting compound for a synthesis of the chloro complexes in this series including monochloride Co(II) complex, $[Co^{II}$*cis*$-(PN)_2(Cl)]^+$, the corresponding oxidized Co(III) species, $[Co^{III}$*cis*$-(PN)_2(Cl)_2]^+$ and the hydrido, $[Co^{III}(PN)_2(H)(Cl)]^+$ complex. A reaction of the $[Co^{II}(PN)_2(Cl)_2]$ with 1.0 equiv of NH_4PF_6 in MeCN resulted in a formation of the $[Co^{II}$*cis*$-(PN)_2(Cl)][PF_6]$ as red-purple solid (65% yield). The corresponding oxidized $[Co^{III}$*cis*$-(PN)_2Cl_2][PF_6]$ as a green solid with 28% yield was obtained by air oxidation of the $Co^{II}(PN)_2Cl_2$ in MeOH.

The preparation and isolation of cobalt(III) hydride complexes: $[Co^{III}(PN)_2(H)(Cl)][PF_6]$ and $[Co^{III}(PN)_2(H)(MeCN)][PF_6]_2$, were achieved under mild reaction conditions at room temperature using $NaBH_4$ as hydride source. These two hydride complexes could be successfully isolated with a yield of 49% for $[Co^{III}(PN)_2(H)(Cl)][PF_6]$ as an orange solid and 38% for $[Co^{III}(PN)_2(H)(MeCN)][PF_6]_2$ as a nice yellow powder. These two hydride complexes are soluble and stable in common solvents (MeOH, CH_3CN, THF and acetone) under Ar or N_2 atmosphere.

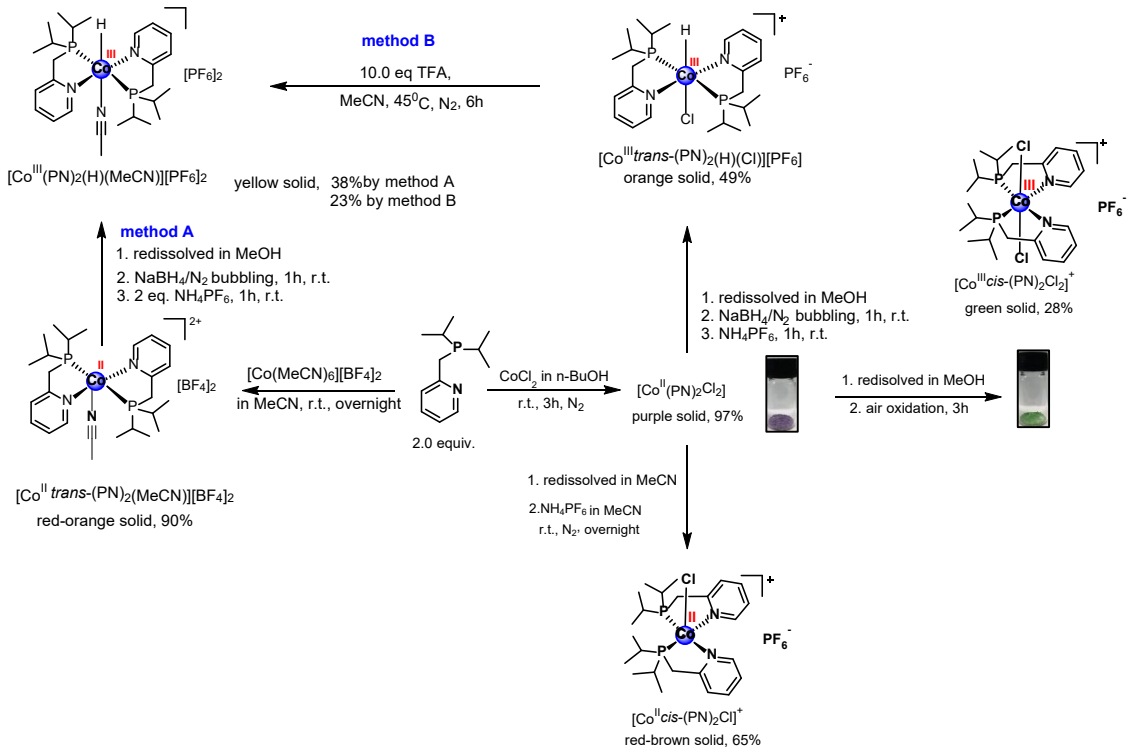

Scheme 2.1. Reaction scheme for preparation of the cobalt(III) hydride complexes with bis-chelating P,N based pyridine ligand, and preparation of the dichloro Co(II) complex, $[Co^{II}(PN)_2Cl_2]$, the monochloride analogue, $[Co^{II}cis\text{-}(PN)_2Cl][PF_6]$ and the corresponding dichloro Co(III) complex, $[Co^{III}cis\text{-}(PN)_2Cl][PF_6]$.

All diamagnetic low-spin d^6 cobalt(III) complexes were characterized by NMR techniques including ^{1}H, $^{31}P\{^{1}H\}$ $^{13}C\{^{1}H\}$, ^{13}C-DEPT, and 2D NMR correlation techniques such as ^{1}H-^{1}H COSY, ^{1}H-$^{31}P\{^{1}H\}$ HMBC, ^{1}H-^{15}N HMBC and ^{1}H-^{13}C-DEPT correlation, as well as by ESI-MS and CHN analysis. Fortunately, single crystals of the complexes $[Co^{II}cis\text{-}(PN)_2Cl][PF_6]$, $[Co^{II}(PN)_2(MeCN)][BF_4]_2$, $[Co^{III}cis\text{-}(PN)_2Cl_2][PF_6]$ and the Cl^- analogue of the hydride complex, $[Co^{III}(PN)_2(H)(Cl)][PF_6]$ could be obtained and were suitable for X-ray crystallographic determination to obtain single crystal X-ray structures. However, the crystal structure of the corresponding acetonitrile hydride complex, $[Co^{III}(PN)_2(H)(MeCN)][PF_6]_2$, was unsuccessful due to decomposition upon data collection for X-ray analysis. These three complexes are air stable in the solid state and did not show a colour change upon leaving the powder in air. The electronic properties and their redox properties of all cobalt complexes were also investigated by UV-Vis spectroscopy (**section 2.5.4**), cyclic voltammetry (**section 2.5.5**) and UV-Vis spectroelectrochemistry (UV-Vis SEC) in **section 2.5.6**) for the Co(III) complexes.

2.5.2 Spectroscopic and crystallographic characterisation

2.5.2.1 Structural characterisation of [Co^{II}cis-(PN)$_2$Cl][PF$_6$]

ESI-Mass spectrometry

The positive mode of ESI-MS of the [Co^{II}*cis*-(PN)$_2$Cl][PF$_6$] (**Figure A 2.7)** showed the molecular ion peaks at *m/z* = 477.1985 and 509.1883 which corresponded to the monocationic [Co^{I}(PN)$_2$]$^+$ and [Co^{I}(PN)$_2$O$_2$]$^+$, respectively. These ion peaks are consistent to the calculated isotopic distribution pattern for [C$_{24}$H$_{40}$CoN$_2$P$_2$]$^+$ at *m/z* = 477.1993 and [C$_{24}$H$_{40}$CoN$_2$O$_2$P$_2$]$^+$ at *m/z* = 509.1891 as shown in **Figure A 2.7** (bottom, b).

X-ray crystal structure of [Co^{II}*cis*-(PN)$_2$Cl][PF$_6$]

The X-ray crystal structure of this complex revealed that one Cl$^-$ anion, two phosphorus and two nitrogen atoms coordinate to the Co(II) centre to furnish a five-coordinate complex which is best described as a distorted square pyramidal geometry (**Figure 2.11**). The crystal structure showed that the two P and N atoms occupy the equatorial plane of the square pyramid with *cis* configuration between these two P atoms and an axial Cl$^-$ ligand. Selected bond distances and bond angles are listed in **Table 2.5**

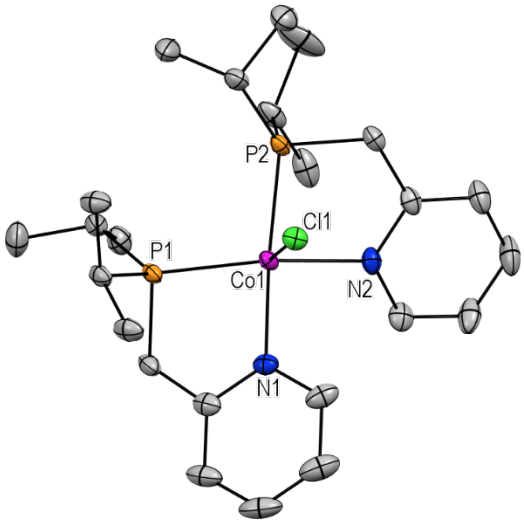

Figure 2.11. X-ray crystal structure of monochloride cobalt(II) complex, [Co^{II}*cis*-(PN)$_2$Cl][PF$_6$]. Selected hydrogen atoms and PF$_6^-$ counter anion were removed for clarity. Thermal ellipsoids shown with probability of 50%.

Table 2.5. Selected bond distances (Å) and bond angles (deg) in the [Co^{II}*cis*-(PN)$_2$Cl][PF$_6$].complex.

atom	atom	bond lengths (Å)	atom	atom	atom	bond angles (deg)
Co1	Cl1	2.4299(9)	P2	Co1	Cl1	87.89(3)
Co1	P2	2.2160(9)	P1	Co1	Cl1	104.46(3)
Co1	P1	2.2156(9)	P1	Co1	P2	101.58(3)
Co1	N1	1.9933(14)	N1	Co1	Cl1	90.78(6)
Co1	N2	2.039(3)	N1	Co1	P2	175.98(6)
			N1	Co1	P1	82.42(6)
			N1	Co1	N2	94.12(10)
			N2	Co1	Cl1	95.53(8)
			N2	Co1	P1	159.72(8)
			N2	Co1	P2	82.24(8)

2.5.2.2 Structural characterisation of [Co^{III}cis-(PN)$_2$Cl$_2$][PF$_6$]

NMR spectroscopy of [Co^{III}cis-(PN)$_2$Cl$_2$][PF$_6$]

In the ^{1}H NMR spectrum at room temperature (**Figure 2.12** a), the isopropyl protons including eight CH_3 groups and CH (H_{7a} and H_{7b}) protons as well as CH_2 (H_{6a} and H_{6b}) as labelled in the structure appeared as a broad signal while while the pyridine resonances are sharp. Moreover, the ^{31}P{^{1}H} NMR spectrum (**Figure 2.12** b) of a solution of this complex in CD_3CN at room temperature also appeared as a broad singlet signal at 55.10 ppm suggesting the two chemically equivalent phosphorus atoms in the structure of [Co^{III}cis-(PN)$_2$Cl$_2$][PF$_6$]. The number of NMR signals is consistent to the structure of this complex containing the C_{2v} symmetry. The solid-state X-ray structure of this complex (**Figure 2.21**) revealed a distorted octahedral geometry where the two P- and two N- atoms are in the equatorial plane and cis to each other. The two Cl$^-$ ligands in the axial position are mutually trans to each other.

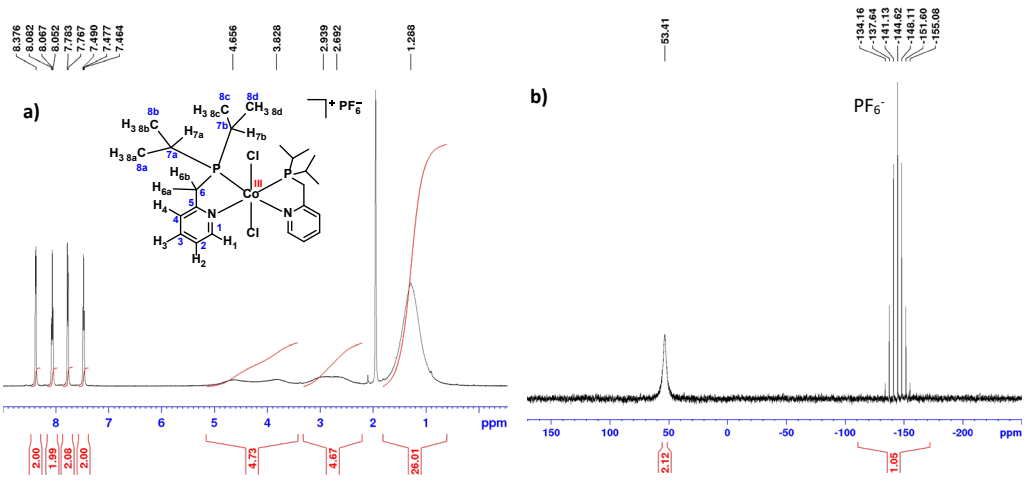

Figure 2.12. ^{1}H NMR spectrum (a) and ^{31}P{^{1}H} NMR spectrum (b) of [Co^{III}*cis*-(PN)$_2$Cl$_2$][PF$_6$] (a) in CD_3CN at room temperature.

According to the appearance of broad signals in the ^{1}H NMR (aliphatic region) at δ 4.66, 3.82, 2.94, 2.69 and 1.29 and broad phosphorus peak of this complex, a dynamic structure of the complex in a solution at room temperature would be expected which might be dissociation of a Cl^- ligand or a change in configuration between the two P atoms in the ligands from *cis* geometry in the solid state to trans configuration in the solution at room temperature or internal rotation of the isopropyl groups. To investigate the fluxional behaviour of this complex, variable temperature NMR experiments were performed in acetone-d_6 solution.

Variable temperature NMR studies of the solution of $[Co^{III}cis\text{-}(PN)_2Cl_2][PF_6]$

By comparison of the NMR measurements (**Figure 2.13**) between the solution of $[Co^{III}cis\text{-}(PN)_2Cl_2][PF_6]$ at 223 K and the spectrum of the solution at room temperature (298K), the $^{31}P\{^1H\}$ NMR signal of the ligands in the complex at low temperature is sharper than that at room temperature (**Figure 2.13** a). Moreover, the isopropyl protons (CH and CH_3 signals) and CH_2 signals in the ^1H NMR spectrum (**Figure 2.13** b) at 223 K became well-separated and much sharper than those signals in the spectrum at room temperature However, the aromatic proton signals of pyridine ring did not show any change**.** This evidence confirmed dynamic behaviour of $[Co^{III}cis\text{-}(PN)_2Cl_2]^+$ in a solution at room temperature which might be dissociation of a Cl^- ligand or a change in configuration between the two P atoms in the ligands from *cis* geometry in the solid state to trans configuration in the solution at room temperature or internal rotation of the isopropyl groups.

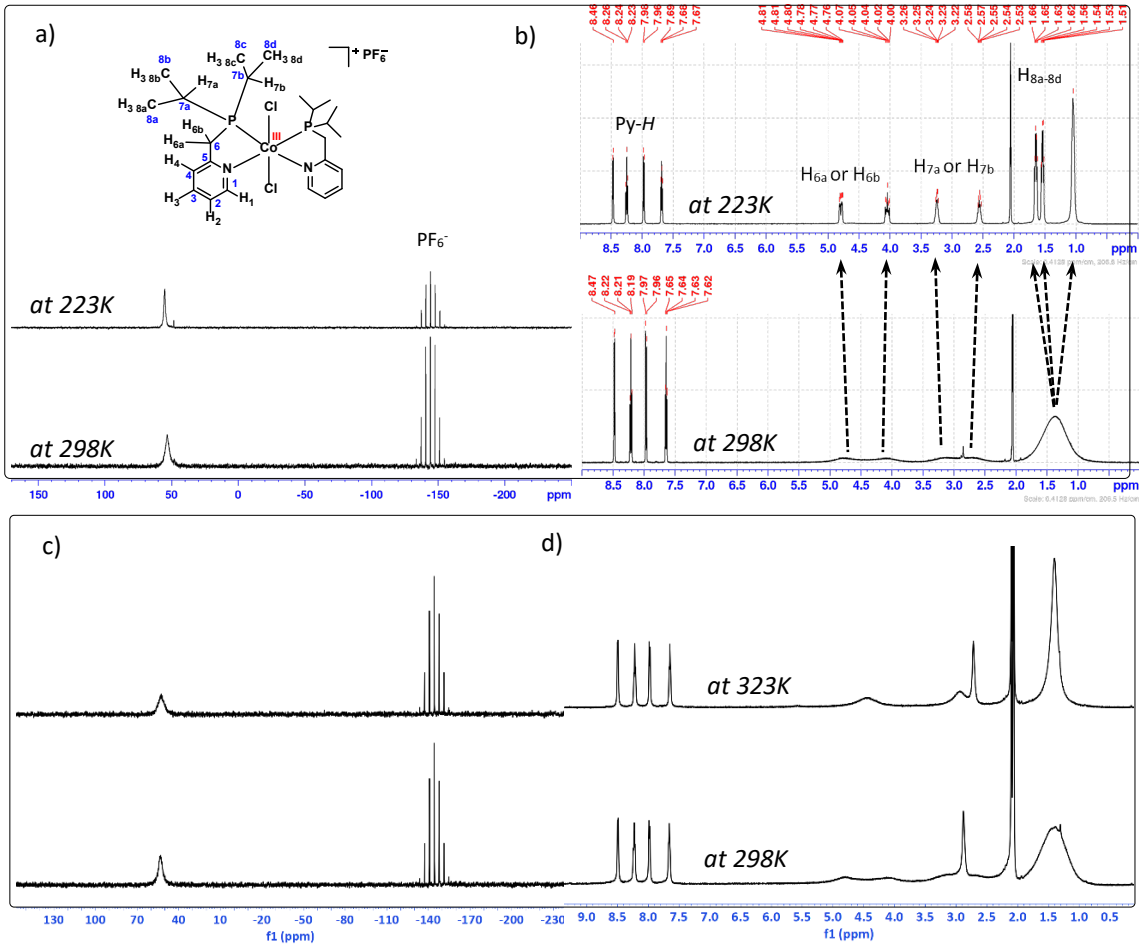

Figure 2.13. $^{31}P\{^1H\}$ NMR spectrum (a) and ^1H NMR spectrum (b) of the $[Co^{III}cis\text{-}(PN)_2Cl_2][PF_6]$ complex in acetone-d_6 at room temperature (bottom) compared to that at 223 K (top), and the $^{31}P\{^1H\}$ NMR spectrum (c) and ^1H NMR spectrum (d) of a solution of this complex at room temperature (bottom) compared to that at 323K (top).

The ^{1}H NMR spectrum (**Figure 2.13** c) and the ^{31}P{^{1}H} NMR spectrum (**Figure 2.13** d) was further recorded at 50 ^{0}C higher than room temperature, and one isopropyl methyl resonance was observed in the ^{1}H NMR spectrum at 323 K. This evidence supported the dynamic behaviour as a result of internal rotation of the isopropyl groups of the complex in the solution.

According to the low-temperature ^{1}H NMR spectrum (**Figure 2.14** a) showed that the protons of isopropyl groups in the complex (H_{6a}, H_{6b}, H_{7a}, H_{7b} and H_{8a-8d}) coupled to the two phosphorus atoms resulting in a complicated signal for these protons. For example, the signal at δ 4.03 for the CH_2 arm (H_{6a} or H_{6b}) as expanded in blue inset appeared as a broad multiplet due to geminal coupling to the proton with $^{2}J_{H,H}$ = 16.9 Hz and to the two P atoms. Additionally, the two signals of CH_3 protons (1.64 and 1.53 ppm as shown in **Figure 2.14** b, inset) exhibited coupling to the two P atoms with respective coupling constants of $^{3}J_{H,H}$ = 6.5, $^{2}J_{H,P}$ + $^{5}J_{H,P}$ = 6.3 and $^{3}J_{H,H}$ = 6.7, $^{2}J_{H,P}$ + $^{5}J_{H,P}$ = 6.6 Hz resulting in virtual quartet peaks.

The ^{1}H{^{31}P} NMR spectrum (**Figure 2.14** c) of the complex in solution at 223 K was much simpler than the ^{1}H NMR spectrum. The CH_2 signals (H_{6a} and H_{6b}) in this complex appeared as well-resolved doublet peaks with $^{2}J_{H,H}$ = 17.0 and 16.9 Hz for CH_2 protons at δ = 4.79 and 4.03, respectively. Moreover, the three separated peaks of methyl protons (H_{8a-8d}) of the P,N ligands at 1.64, 1.53 and 1.04 ppm sharpened in the ^{1}H{^{31}P} NMR spectrum. The overlapping peak at δ = 1.04 for two methyl groups could not be resolved. Coupling constants of $^{3}J_{H,H}$ = 6.5 and $^{3}J_{H,H}$ = 6.7 Hz were obtained for the two separate doublets of the CH_3 groups at δ 1.64 and 1.53, respectively. Furthermore, the isopropyl protons (H_{7a}, H_{7b}) also showed sharper peaks. However, the aromatic protons of pyridine rings in the ^{1}H NMR and ^{1}H{^{31}P} NMR spectrum are similar to each other (**Figure A 2.8**). Moreover, the ^{1}H-^{1}H COSY NMR spectrum in (**Figure 2.15**) showed correlations of geminal protons of the CH_2 group, between H_{6a} and H_{6b}, the coupling between P-C*H*-(CH_3) of H_{7a}, H_{7b} and CH_3 in the isopropyl and also protons in pyridine rings.

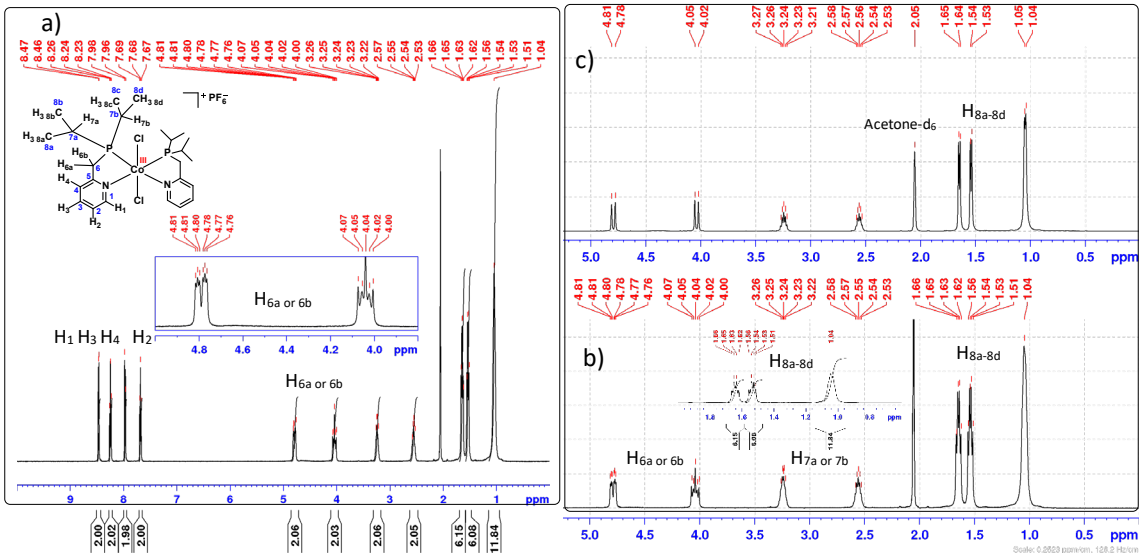

Figure 2.14. ^{1}H NMR spectrum (a) of $[Co^{III}cis\text{-}(PN)_2Cl_2][PF_6]$ in acetone-d_6 at 223 K, blue inset showed the signals of isopropyl protons (H_{6a} and H_{6b}) and the ^{1}H NMR spectrum in aliphatic region (b) with the zoom region of CH_3 signals ($H_{8a\text{-}8d}$) compared to the $^{1}H\{^{31}P\}$ NMR spectrum of this solution at 223 K (c).

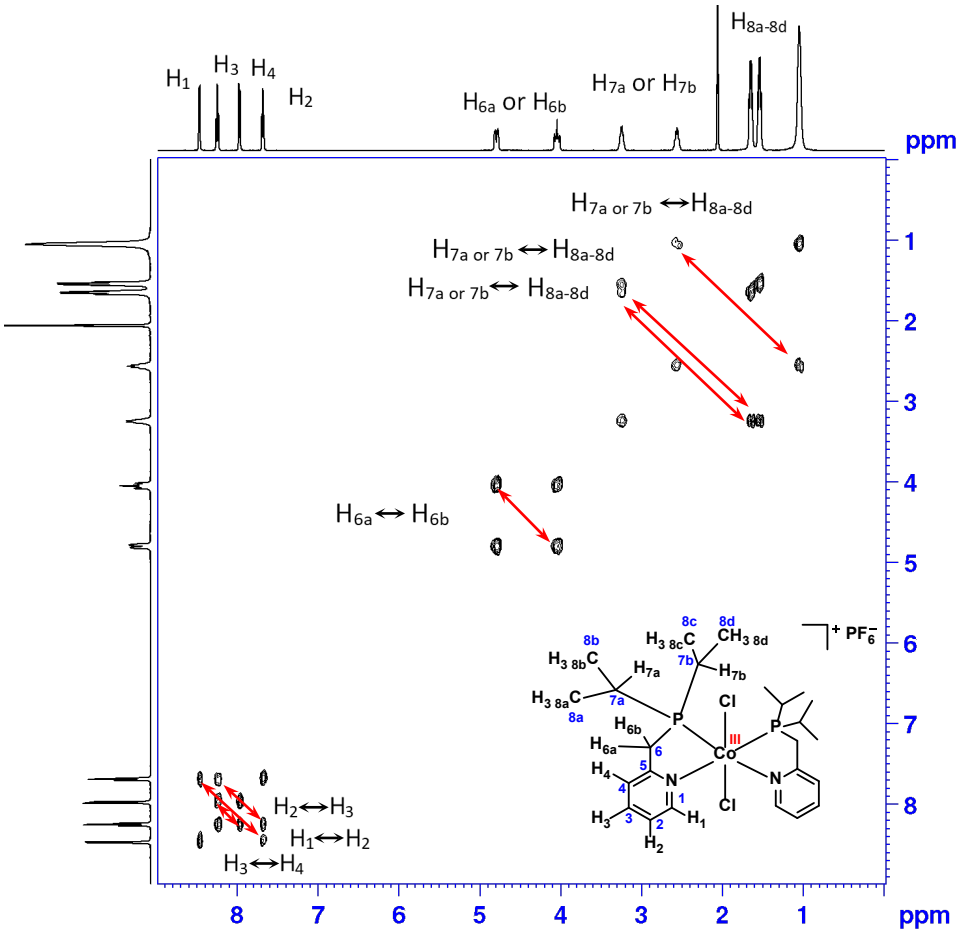

Figure 2.15. ^{1}H-^{1}H COSY NMR spectrum of the $Co^{III}cis\text{-}(PN)_2Cl_2][PF_6]$ in acetone-d_6 at 223 K, the red arrows showed the correlation between two protons as labelled in the spectrum.

The $^{13}C\{^{1}H\}$ spectrum of the solution in acetone-d_6 at 223 K (**Figure 2.16**) showed resonances corresponding to the 12 different carbon atoms as labelled in the structure. The result revealed the characteristic signals of the isopropyl groups in the complex where the two phosphorus atoms are cis to each other and magnetically inequivalent. Therefore, the carbon signals (C_6, C_{7a} and C_{7b}) in the spectrum (**Figure 2.16, top**) of the cis complex showed complicated signals due to the second-order effect of a four-spin $[AX]_2$ system[232] displaying the intense most outer lines (the apparent coupling constants are listed in the **Table 2.6)**. This coupling constant consists of the $J_{C,P} + J_{C,P'}$ as labelled carbon and phosphorus atoms in the structure.

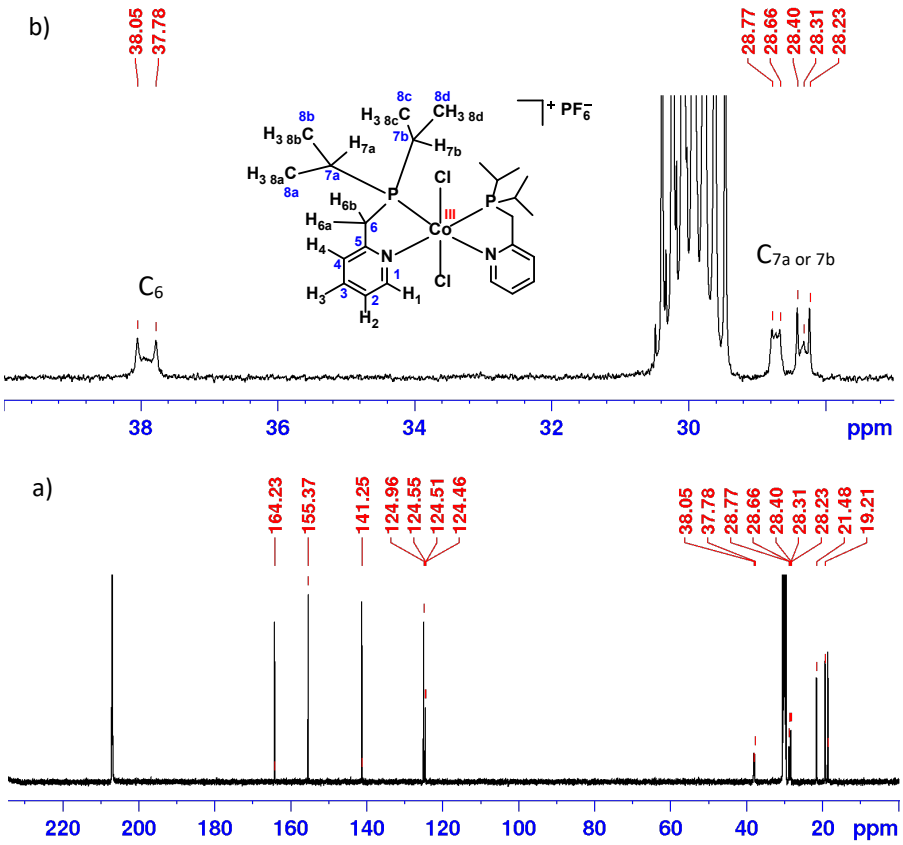

Figure 2.16. $^{13}C\{^{1}H\}$ NMR spectrum of the $[Co^{III}$*cis*-$(PN)_2Cl_2][PF_6]$ in acetone-d_6 at 223 K (a), the isopropyl carbons for C_6 and C_{7a} or C_{7b} (b).

Furthermore, the assignment of each carbon atom was supported by the ^{13}C-DEPT 135 experiment (**Figure A 2.10**) and 2D NMR spectroscopy for ^{1}H-^{13}C-DEPT correlation (**Figure 2.17** and **Figure 2.18**). The signal at δ 38.0 in the ^{13}C-DEPT spectrum with a negative phase corresponded to C_6 with two attached hydrogen atoms (H_{6a} or H_{6b}) which is consistent to the correlation peaks in the ^{1}H-^{13}C-DEPT spectrum (red spots).

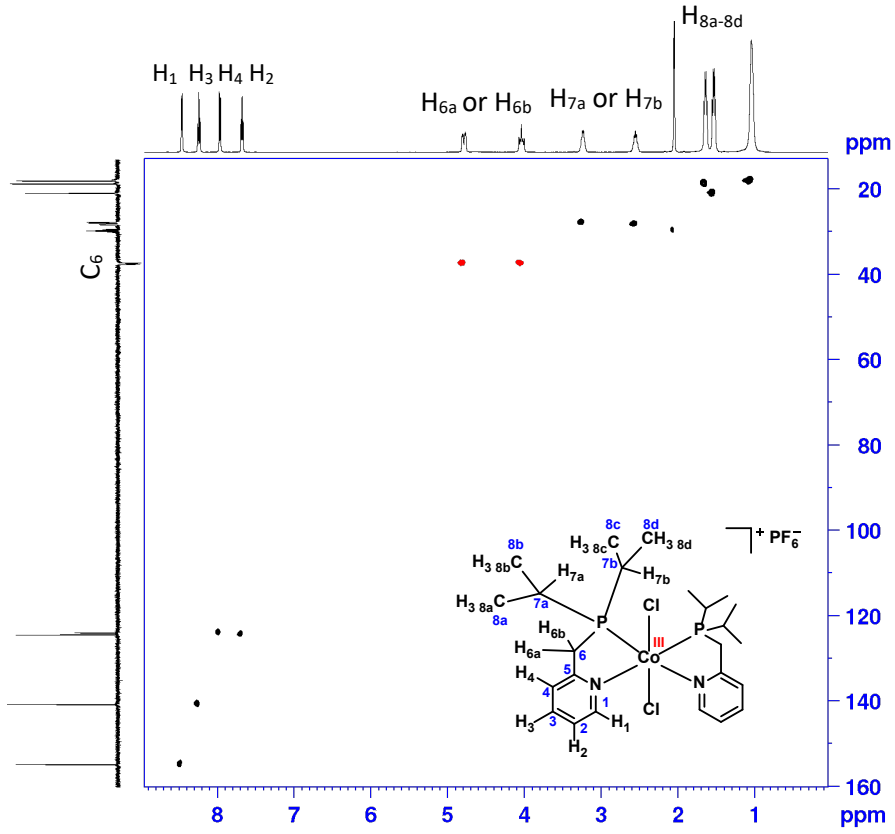

Figure 2.17. ^{1}H-^{13}C DEPT correlation spectroscopy of [Co^{III}*cis*-$(PN)_2Cl_2$][PF_6] in acetone-d_6 at 223K.

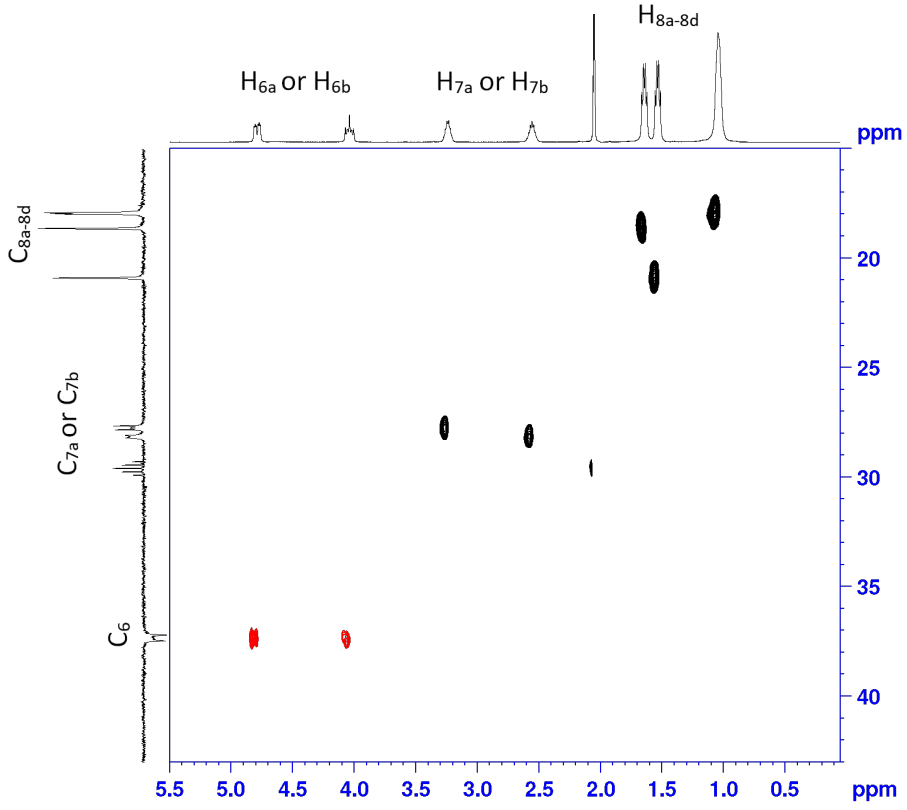

Figure 2.18. ^{1}H-^{13}C DEPT correlation spectroscopy of [Co^{III}*cis*-$(PN)_2Cl_2$][PF_6] in acetone-d_6 at 223K (aliphatic protons).

All NMR characterisation data and assigned atoms in this complex are listed in **Table 2.6**. The assigned atoms in the table correspond to the labelled atoms in the structure of this complex as shown in **Figure 2.19**. Moreover, the ^{1}H-^{15}N HMBC (**Figure A 2.11**) of this complex suggested that the two N atoms in the complex are chemically equivalent since they are observed as a singlet signal at δ –59.93 ppm.

Table 2.6. Assignment of hydrogen, carbon and phosphorus-atoms of the [Co^{III}*cis*-$(PN)_2(Cl)_2$][PF_6] in acetone-d_6 at 223 K.

Assigned atom	δ (ppm)	J (Hz) and multiplicity	Integration
H_1 (C_1)	8.46 (155.37)	$^{3}J_{H,H}$ = 5.9, d (s)	2H
H_3(C_3)	8.24(141.25)	$^{3}J_{H,H}$ = 7.6, t (s)	2H
H_4(C_4)	7.97 (124.50)	$^{3}J_{H,H}$ = 7.7, d ($^{3}J_{C,P}$ +$^{5}J_{C,P}$ = 5.17, t)	2H
C_5	(164.23)	(s)	
H_2(C_2)	7.68 (124.96)	$^{3}J_{H,H}$ = 6.7, t (s)	2H
H_{6a} or H_{6b} (C_6)	4.79 (37.93)	$^{2}J_{H,H}$ = 17.0, d ($^{1}J_{C,P}$ +$^{3}J_{C,P}$ = 33.76, m)	2H
	4.03 (37.93)	$^{2}J_{H,H}$ = 16.9, $^{2}J_{H,P}$ = 17.2, m (br) ($^{1}J_{C,P}$ +$^{3}J_{C,P}$ = 33.76, m)	2H
H_{7a} or H_{7b}	3.24 (28.31)	m ($^{1}J_{C,P}$ +$^{3}J_{C,P}$ = 22.60, m)	2H
(C_{7a} or C_{7b})	2.55 (28.72)	m ($^{1}J_{C,P}$ +$^{3}J_{C,P}$ = 14.16, m)	2H
H_{8a-8d} (C_{8a-8d})	1.64 (19.21)	$^{3}J_{H,H}$ = 6.5,$^{2}J_{H,P}$+$^{4}J_{H,P}$ = 6.3, virtual q (br)	6H
	1.53 (21.47)	$^{3}J_{H,H}$ = 6.7, $^{2}J_{H,P}$+$^{4}J_{H,P}$ = 6.6, virtual q (br)	6H
	1.04 (18.52)	br (br)	12H
P	55.10	S	2P
PF_6^-	-144.36	$^{1}J_{P,F}$ = 706.1, sept	1P
N	-59.93	S	2N

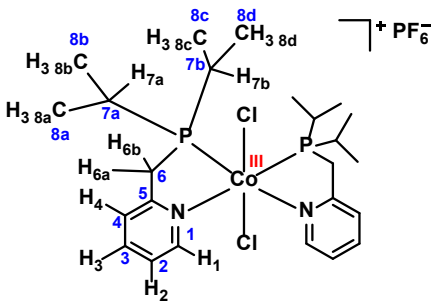

Figure 2.19. labelled atoms in the [Co^{III}*cis*-$(PN)_2Cl_2$][PF_6] complex.

As shown previously in **Figure 2.12**, broad peaks were observed for the isopropyl protons in the ^{1}H NMR spectrum of the solution of [Co^{III}*cis*-(PN)$_2$Cl$_2$][PF$_6$] at room temperature However, the low-temp NMR solution of the complex showed dramatic changes in the isopropyl signals which became sharper and more well separated peaks (**Figure 2.13**, top). The fluxional behaviour could be the result of the configuration change from *cis* to *trans* of the two phosphorus in the complex once the complex was in the solution at room temperature In contrast to this, the isopropyl groups in the [Co^{III}(PN)$_2$(H)(Cl)][PF$_6$] and [Co^{III}(PN)$_2$(H)(MeCN)][PF$_6$]$_2$ where the two phosphorus atoms are *trans* to each other showed well-resolved and sharp peaks in the ^{1}H spectrum (**Figure 2.18** and **Figure A 2.22**). The ^{13}C{^{1}H} NMR spectrum of the [Co^{III}(PN)$_2$(H)(MeCN)][PF$_6$]$_2$ (**Figure 2.20,** top) in CD$_3$CN even at room temperature displayed sharp and well-resolved peaks. This evidence suggested that the hydride complex in a solution has more rigid structure than the [Co^{III}*cis*-(PN)$_2$Cl$_2$][PF$_6$] in the solution at room temperature. Moreover, the ^{13}C{^{1}H} spectrum of the [Co^{III}(PN)$_2$(H)(MeCN)][PF$_6$]$_2$ displayed triplet signals of C$_6$ (δ 35.38), C$_{7a}$ or C$_{7b}$ (δ 27.56 and 23.03) indicating that the carbon couples to two magnetically and chemically equivalent phosphorus atoms in the *trans* complex. These signals were completely different from the C$_6$, C$_{7a}$ or C$_{7b}$ in the [Co^{III}*cis*-(PN)$_2$Cl$_2$][PF$_6$] as shown in **Figure 2.20** (bottom) where the two P atoms are *cis* to each other not only in the chemical shifts but also distinct in the multiplicity. Therefore, these different signals between the [Co^{III}*cis*-(PN)$_2$Cl$_2$][PF$_6$] in the solution at low temperature and those of the peaks in the solution of Co(III) hydride complex at room temperature where two P atoms are *trans* to each other confirmed the distinct configuration of the two phosphorus atoms in the complexes. This analysis supports an alternative explanation of the dynamic broadening of the ^{1}H NMR spectrum of [Co^{III}*cis*-(PN)$_2$Cl$_2$][PF$_6$]. The simplest explanation is that the broadening results from hindered internal rotation of the isopropyl groups. Such hindered rotation is consistent with the observation that the pyridine resonances remain sharp throughout. As a further test, the ^{1}H NMR spectrum was recorded on heating above room temperature, where we observed one isopropyl methyl resonances in the ^{1}H NMR spectrum at 323 K.

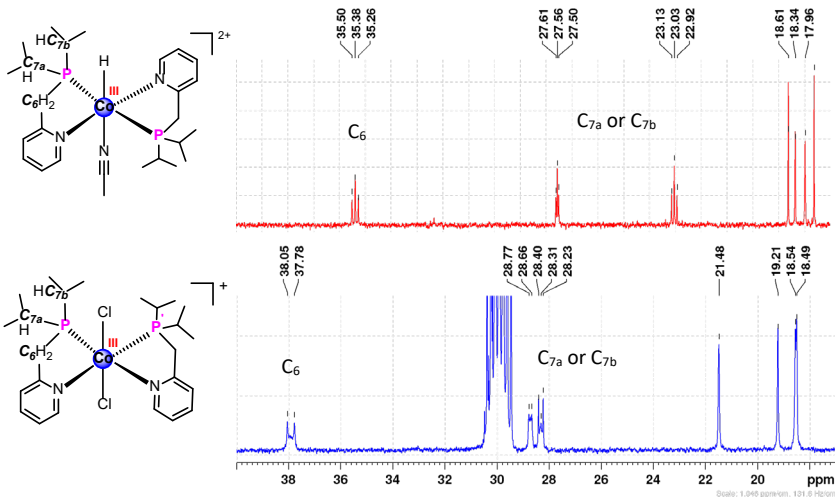

Figure 2.20. The $^{13}C\{^{1}H\}$ NMR spectrum of $[Co^{III}(PN)_2(H)(MeCN)][PF_6]_2$ (top) in CD_3CN at room temperature, and the spectrum of $[Co^{III}$*cis*-$(PN)_2Cl_2][PF_6]$ (bottom) in acetone-d_6 at 223 K.

ESI-Mass spectrometry of the $[Co^{III}$cis-$(PN)_2Cl_2][PF_6]$ complex

The positive mode of ESI-MS of the complex (**Figure A 2.12)** showed the molecular ion peaks at *m/z* = 547.1385 (100%) for $[Co^{III}(PN)_2(Cl)_2]^+$ with isotopic patterns calculated for $[C_{24}H_{40}Cl_2CoN_2P_2]^+$ at *m/z* = 547.1370 (100%).

X-ray crystal structure of [Co^{III}*cis*-$(PN)_2Cl_2$][PF_6]

The crystal structure of the [Co^{III}*cis*-$(PN)_2Cl_2$][PF_6] (**Figure 2.21**) showed a distorted octahedral geometry where the two N-atoms and two P-atoms are *cis* to each other in the equatorial position. It contains two coordinated Cl^- ligands in axial positions which are *trans* to each other**.** The *cis* configuration between the two N- and P-atoms is similar to the crystal structure of the corresponding Co(II) complex containing one Cl^- ligand (**Figure 2.11**). Selected bond lengths and bond angles were listed in the **Table 2.7.**

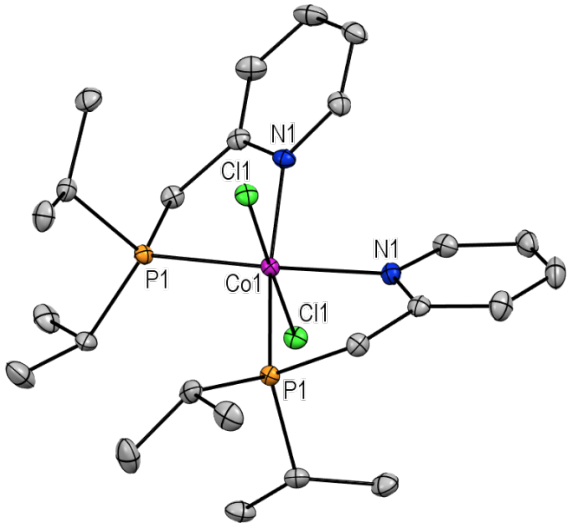

Figure 2.21. X-ray crystal structure of [Co^{III}*cis*-$(PN)_2Cl_2$][PF_6]. Selected hydrogen atoms and PF_6^- counter anion were removed for clarity. Thermal ellipsoids shown with probability of 50%.

Table 2.7. Selected bond distances (Å) and bond angles (deg) for [Co^{III}*cis*-$(PN)_2Cl_2$][PF_6].

atom	atom	bond lengths (Å)	atom	atom	atom	bond angles (deg)
Co1	Cl1	2.2471(4)	Cl1	Co1	$Cl1^1$	179.01(3)
Co1	P1	2.2736(5)	Cl1	Co1	P1	84.614(16)
Co1	N1	2.0366(15)	$Cl1^1$	Co1	P1	95.976(16)
			$P1^1$	Co1	P1	107.59(3)
			N1	Co1	Cl1	93.04(4)
			$N1^1$	Co1	Cl1	86.26(4)
			N1	Co1	$P1^1$	167.78(4)
			N1	Co1	P1	81.43(4)
			N1	Co1	$N1^1$	90.97(8)

2.5.2.3 Structural characterisation of $[Co^{III}(PN)_2(H)(Cl)][PF_6]$

The orange monohydride complex $[Co^{III}(PN)_2(H)(Cl)][PF_6]$ (49% yield) was successfully prepared under mild conditions as shown in **Scheme 2.1**. It should be noted that formation of the hydride species by bubbling H_2 into a solution with $NaBH_4$ in the second step instead of N_2 led to formation of the monohydride complex in similar yield after adding NH_4PF_6. This result suggests that $NaBH_4$ could act as hydride donor for a precursor dichloro cobalt (II) complex to afford a monohydride $[Co^{III}(PN)_2(H)(Cl)]^+$. Another possibility is that $NaBH_4$ could play a role as reducing agent, and the resulting Co(I) species could then be protonated by NH_4PF_6 in MeOH to obtain the monohydride complex. This pathway corresponds to the previous work by Koelle et al [208] which showed that protonation of Co(I) complexes, $[CpCo(P)_2]$ with NH_4PF_6 in toluene/MeOH mixture yielded an isolable Co(III)-H complex.

Structural characterisation of the product was performed by spectroscopic techniques ^1H, $^{13}C\{^1H\}$, ^{13}C-DEPT, $^{31}P\{^1H\}$ spectroscopy and 2D NMR correlation experiments, ESI-MS, CHN analysis, and X-ray crystallography.

NMR spectroscopy of $[Co^{III}(PN)_2(H)(Cl)][PF_6]$

The ^1H NMR spectrum (**Figure 2.22** a) of $[Co^{III}(PN)_2(H)(Cl)]^+$, in solution at room temperature showed sharp and well-resolved peaks for signals of isopropyl protons (H_{6a},H_{6b}, H_{7a}, H_{7b} and $H_{8a\text{-}8d}$) which suggested that this complex can be greatly stabilized by the chelating effect of the bis-P,N ligands in the complex, where the two N- and two P-atoms are *trans* to each other and is a diamagnetic species**.** Therefore, its diamagnetic nature suggested that the $[Co^{III}(PN)_2(H)(Cl)]^+$ in CD_3CN solution is octahedral, low-spin d^6 configuration. In the $^{31}P\{^1H\}$ NMR spectrum (**Figure 2.22** b), the complex showed one phosphorus signal for the two magnetically equivalent phosphorus atoms at δ 66.44 with integral ratio of 2 relative to that of the PF_6^- peak (δ = -144.62). Moreover, the number of resonance peaks in the ^1H, $^{31}P\{^1H\}$ and $^{13}C\{^1H\}$ NMR spectra of the solution of $[Co^{III}(PN)_2(H)(Cl)]^+$ corresponded to the C_2 symmetry axis of the X-ray molecular structure of the complex in solid state as shown in **Figure 2.26**, in set.

A hydride signal appeared at δ -19.04 as a well-resolved triplet peak ($J_{cis\text{-}H\text{-}P}$ = 58.4 Hz) due to coupling with two equivalent phosphorus atoms in the complex. This coupling constant value is consistent with that of cobalt dihydride complexes $[Co^{III}(2,2'\text{-bipy})(PEt_2Ph)_2H_2]^+$ with $J_{cis\text{-}H\text{-}P}$ = 64 Hz and $[Co^{III}(triphos)(H)(MeCN)_2]PF_6$ (triphos = 1,1,1-tris(diphenylphosphinomethyl)ethane) in previous literature which shows $J_{cis\text{-}H\text{-}P}$ = 65 Hz.[224] Moreover, there is virtual coupling between the four signals of different CH_3 protons in isopropyl groups ($H_{8a\text{-}8d}$) and phosphorus atoms leading to virtual quartet signals at δ = 1.62, 1.26, 0.94 and 0.67 in the ^1H NMR spectrum (**Figure 2.22,** inset).

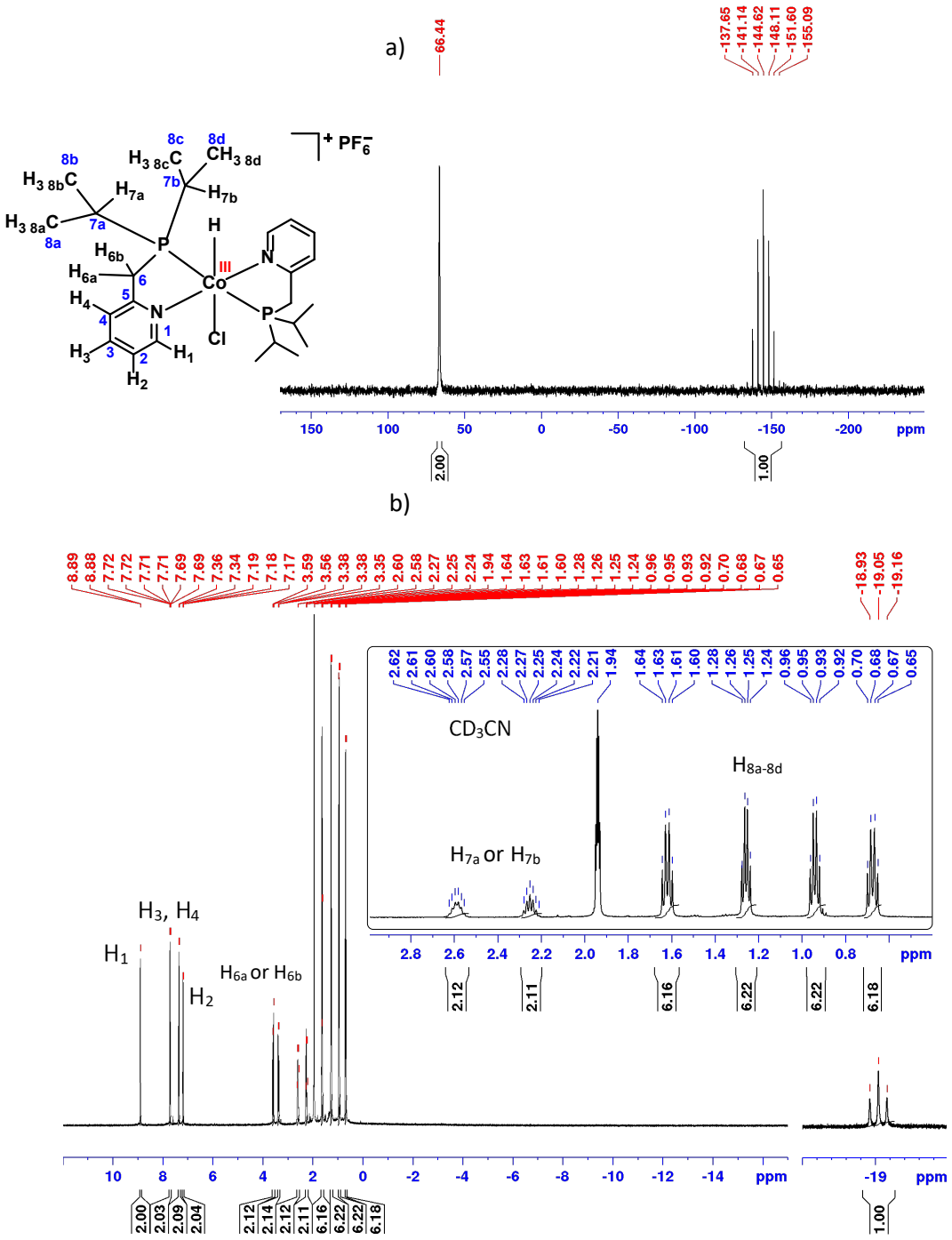

Figure 2.22. $^{31}P\{^{1}H\}$ NMR spectrum (a) and ^{1}H NMR spectrum (b) of $[Co^{III}(PN)_2(H)(Cl)][PF_6]$ in CD_3CN at room temperature.

Moreover, the analysis of the signals in aliphatic region of the ^{1}H NMR spectrum (**Figure 2.23** a) agrees with the $^{1}H\{^{31}P\}$ NMR experiment which showed decoupled phosphorus peaks of H_{6a}, H_{6b}, H_{7a}, H_{7b} and $H_{8a\text{-}8d}$ (**Figure 2.23** b). The hydride signal in the $^{1}H\{^{31}P\}$ NMR spectrum became a singlet, when it was decoupled from the phosphorus. Furthermore, all CH_3 protons (H_{8a}, H_{8b}, H_{8c} and H_{8d}) of isopropyl groups showed the disappearance of two outer lines with the same intensity of four CH_3 protons, and the signals of H_{6a},$H_{6b,}$ H_{7a} and H_{7b} became sharper peaks.

However, the pyridine protons in the complex did not show any change in the $^{1}H\{^{31}P\}$ suggesting no phosphorus coupling (**Figure 2.23** a, top).

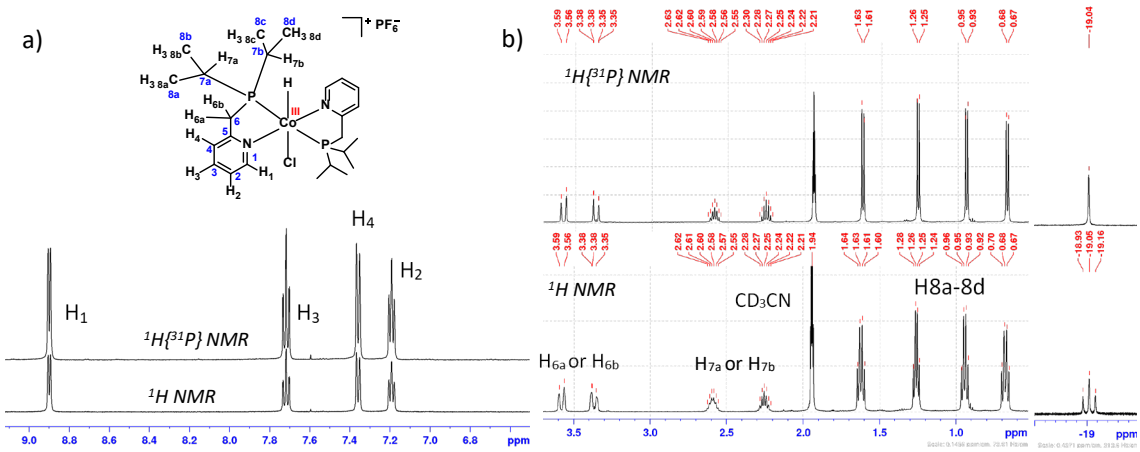

Figure 2.23. ^{1}H NMR spectrum in aromatic region (a) and in aliphatic region (b) compared to the $^{1}H\{^{31}P\}$ NMR spectrum of $[Co^{III}(PN)_2(H)(Cl)][PF_6]$ in CD_3CN at room temperature

The ^{1}H-$^{31}P\{^{1}H\}$ HMBC experiment (**Figure 2.24**) also confirmed that the hydride signal, the CH_2 proton and four peaks of CH_3 showed correlation signals to the two equivalent phosphorus atoms in the complex.

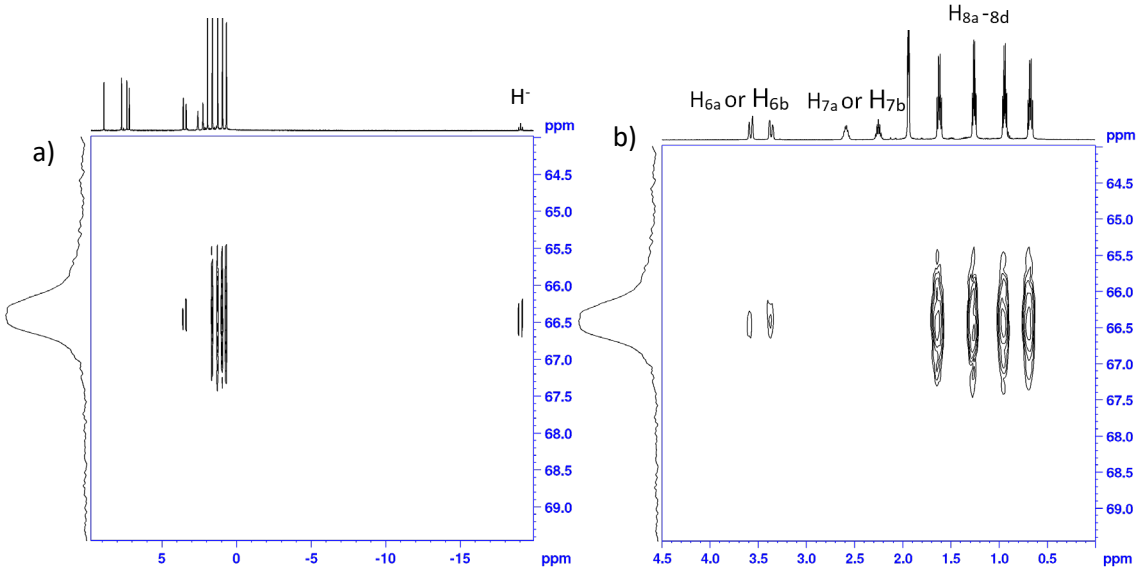

Figure 2.24. ^{1}H-$^{31}P\{^{1}H\}$ HMBC correlation of $[Co^{III}(PN)_2(H)(Cl)][PF_6]$ in CD_3CN at room temperature showing the whole spectrum (a) and aliphatic protons (b).

This evidence supported the postulate that all these aliphatic protons of isopropyl groups can couple to the phosphorus which is strongly coupled to another trans-phosphorus in the same planar equatorial position resulting in an occurrence of the virtual coupling effect. This effect

arises when protons are coupled to a group of other nuclei which are strongly coupled to each other.[233]

The assignments of each atom in the structure of $[Co^{III}(PN)_2(H)(Cl)]^+$ complex including chemical shift, coupling constant, multiplicity and integration ratio are listed in the **Table 2.8**. Each proton peak in the pyridine ring of the complex could be assigned by the information in the ^1H NMR (**Figure 2.22**) and supported by the 2D COSY ^1H-^1H NMR spectrum (**Figure 2.25**). However, the information is insufficient to distinguish the chemical shift of each $H_{7a,7b}$ and the methyl protons (H_{8a},H_{8b},H_{8c} and H_{8d}).

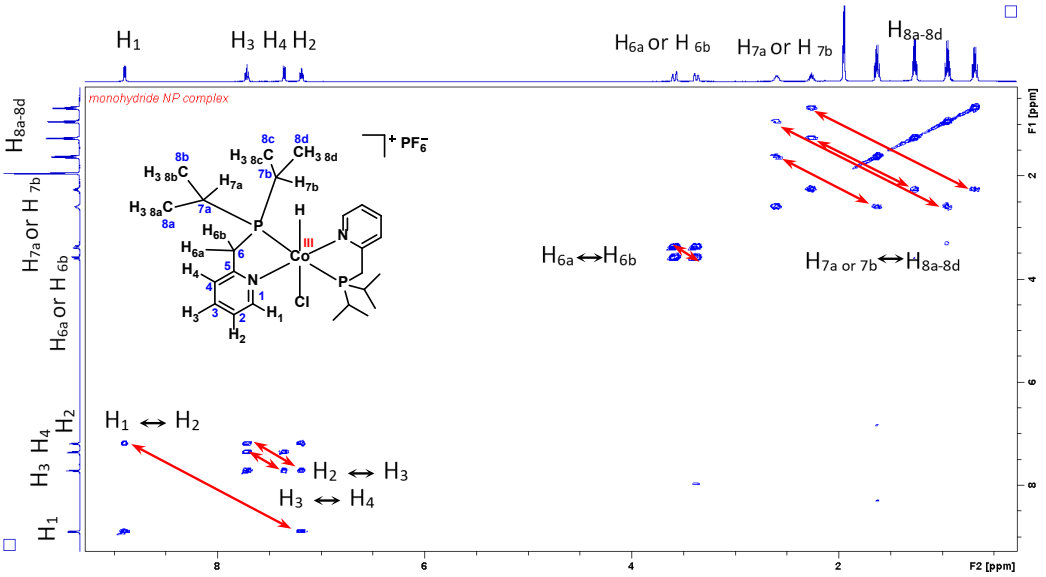

Figure 2.25. ^1H-^1H COSY NMR spectrum of $[Co^{III}(PN)_2(H)(Cl)][PF_6]$ in CD_3CN at room temperature, the red arrows showed the correlation between two protons as labelled in the spectrum.

The structural assignment of carbon atoms in the complex was further characterized by $^{13}C\{^1H\}$ technique (**Figure A 2.13**), ^{13}C DEPT (**Figure A 2.14,** bottom), ^1H-$^{13}C\{^1H\}$ HSQC experiments (**Figure A 2.15** and **Figure A 2.16)** and ^1H-^{13}C DEPT correlation experiments (**Figure A 2.17** and **Figure A 2.18**). The singlet correlation peak in the ^1H-^{15}N 2D NMR of $[Co^{III}(PN)_2(H)(Cl)][PF_6]$ (**Figure A 2.19**) was shifted upfield from the signal of $[Co^{III}$*cis*-$(PN)_2Cl_2][PF_6]$ derivative by 36.55 ppm suggesting greater electron density on the Co(III) centre with the hydride ligand. Based on NMR evidence of this complex in MeCN solution, the assignment of each atom in the structure corresponded to the symmetry element of the crystal structure with C_2 axis rendering the two phosphorus atoms equivalent as shown in **Figure 2.26.**

Table 2.8. Assignment of hydrogen, carbon and phosphorus-atoms of the $[Co^{III}(PN)_2(H)(Cl)][PF_6]$.

Assigned atom	δ (ppm)	J (Hz) and multiplicity	Integration
H_1 (C_1)	8.89 (159.66)	$^3J_{H,H}$ = 5.7, d ($^4J_{C,P}$ +$^6J_{C,P}$ = 4.3, t)	2H
H_3(C_3)	7.71 (140.14)	$^3J_{H,H}$ = 7.8, $^4J_{H,H}$ = 1.4, td (s)	2H
H_4(C_4)	7.35 (124.95)	$^3J_{H,H}$ = 7.8, d (br)	2H
C_5	(164.88)	($^2J_{C,P}$ +$^4J_{C,P}$ = 3.7, virtual t)	-
H_2(C_2)	7.18 (124.22)	$^3J_{H,H}$ = 6.7, t (br) (s)	2H
H_{6a} or H_{6b} (C_6)	3.58 (36.00)	$^2J_{H,H}$ = 17.2, d (br) ($^1J_{C,P}$ +$^3J_{C,P}$ = 15.5, virtual t)	2H
	3.36 (36.00)	$^2J_{H,H}$ = 17.0, d (br) ($^1J_{C,P}$ +$^3J_{C,P}$ = 15.5, virtual t)	2H
H_{7a} or H_{7b} (C_{7a}or C_{7b})	2.59 (28.86)	$^3J_{H,H}$ = 7.1, $^3J_{H,P}$ = 7.0, br sep ($^1J_{C,P}$ +$^3J_{C,P}$ = 6.3, virtual t)	2H
	2.25(22.87)	$^3J_{H,H}$ = 7.1, $^3J_{H,P}$ = 7.0, br sep ($^1J_{C,P}$ +$^3J_{C,P}$ = 12.0, virtual t)	2H
H_{8a-8d} (C_{8a-8d})	1.62 (19.09)	$^3J_{H,H}$ = 7.1, $^3J_{H,P}$+$^5J_{H,P}$ = 7.3, virtual q (s)	6H
	1.26 (18.34)	$^3J_{H,H}$ = 7.0, $^3J_{H,P}$+$^5J_{H,P}$ = 6.8, virtual q (s)	6H
	0.94 (18.18)	$^3J_{H,H}$ = 7.0, $^3J_{H,P}$+$^5J_{H,P}$ = 7.1, virtual q (s)	6H
	0.67 (18.03)	$^3J_{H,H}$ = 7.1, $^3J_{H,P}$+$^5J_{H,P}$ = 7.3, virtual q (s)	6H
Hydride (H)	-19.05	$^3J_{H,P}$ = 59.7, t	1H
P	66.4	S	2P
PF_6^-	144.62	$^1J_{P,F}$ = 706.6 sep	1P
N	-96.48	s	1N

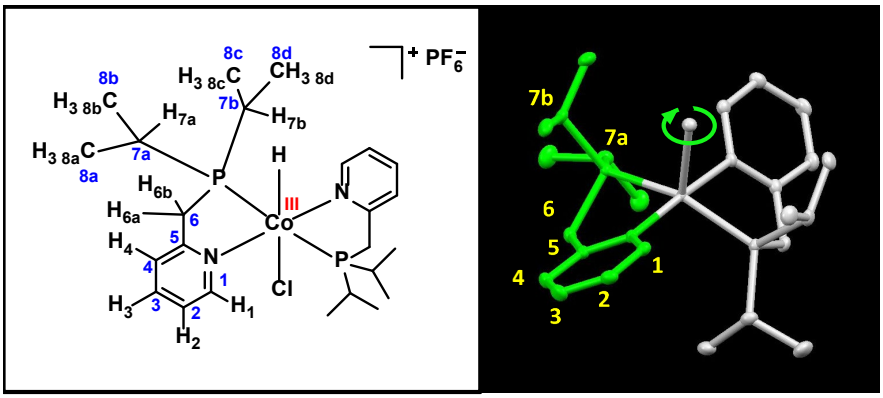

Figure 2.26. Labelled atoms in $[Co^{III}(PN)_2(H)(Cl)][PF_6]$ complex (left) and coloured C_2- rotation axis showing effect of symmetry operation (right).

Accordingly, the phosphorus peak in the $[Co^{III}(PN)_2(H)(Cl)][PF_6]$ is sharper than that of $[Co^{III}$*cis*-$(PN)_2Cl_2][PF_6]$, suggesting that the ligand configuration of the PN ligands in these two complexes are distinct. In the solid state, the X-ray structure of $[Co^{III}$*cis*-$(PN)_2Cl_2][PF_6]$ (**Figure 2.21**) revealed that two bulky isopropyl phosphine groups are located in mutually *cis* positions which contrasts with the trans configuration of the two phosphorus atoms of $[Co^{III}(PN)_2(H)(Cl)][PF_6]$. From the solution NMR studies at room temperature, this structural difference could account for the dynamic behaviour of $[Co^{III}$*cis*-$(PN)_2Cl_2][PF_6]$ which exhibits greater steric congestion than the $[Co^{III}(PN)_2(H)(Cl)][PF_6]$. The hydride complex has the bulky isopropyl groups located far away from each other in the trans position. Therefore, the ^{1}H NMR spectrum of $[Co^{III}(PN)_2(H)(Cl)][PF_6]$ complex in MeCN solution at room temperature showed well-resolved proton signals of Py-C***H***$_2$-P, P-C***H***-$(CH_3)_2$ and P-CH-(C***H***$_3)_2$ groups compared to the broad signals in the ^{1}H NMR spectrum of the $[Co^{III}$*cis*-$(PN)_2Cl_2][PF_6]$. For this reason, the broad signals in the ^{1}H NMR of the *cis* complex in a solution at room temperature would be expected as a dynamic structure due to internal rotation of isopropyl group rather than the contribution from the quadrupolar coupling to Co center with nuclear spin (I = 7/2).

There is one example of d^6 Rh(III) complex supported by bis-chelating DPPMP ($[Rh(DPPMP)_2Cl_2][(benzoate)_2H]$, DPPMP = diphenylphosphinomethylpyridine) ligands reported in the literature.[167] The X-ray structure (**Figure 2.27** c) of this complex showed the *cis*-configuration of the two P- and two N-atoms in the complex which is the same configuration as that of the two PN ligands in the $[Co^{III}$*cis*-$(PN)_2Cl_2][PF_6]$. However, the two Cl^- ligands in $[Rh(DPPMP)_2Cl_2]^+$ are cis to each other, while the two Cl^- ligands in the $[Co^{III}$*cis*-$(PN)_2Cl_2][PF_6]$.located in axial positions and are mutually *trans*. Based on the ^{1}H and $^{31}P\{^1H\}$ NMR evidences, the $[Rh(DPPMP)_2Cl_2]^+$ has relatively more rigid structure than the structure of $[Co^{III}$*cis*-$(PN)_2Cl_2]^+$ in a solution.

ESI mass spectrometry of $[Co^{III}(PN)_2(H)(Cl)][PF_6]$

The positive mode of ESI-MS of the complex (**Figure A 2.20)** displayed the molecular ion peaks for $[Co(PN)_2(H)(Cl))]^+$ at *m/z* = 513.1763 (calcd. 517.1760, difference 0.3 mDaltons) with isotopic distribution patterns calculated for $[C_{24}H_{41}ClCoN_2P_2]^+$ .The ion peaks corresponded to the $[Co^{I}(PN)_2]^+$ at *m/z* = 477.1989 was also observed and calculated for $[C_{24}H_{40}CoN_2P_2]^+$ at m/z 477.1993.

X-ray crystal structure of $[Co^{III}(PN)_2(H)(Cl)][PF_6]$

The crystal structure of hydride complex $[Co^{III}(PN)_2(H)(Cl)][PF_6]$ (**Figure 2.27**) revealed that the molecular structure of this complex in the solid state as a six-coordinate complex which is best described as a distorted octahedral geometry containing a Cl^- ligand trans to a hydride in axial

position and 2N and 2P atoms in the equatorial plane with trans configuration between the two P atoms. Selected bond lengths and bond angles are listed in **Table 2.9**.

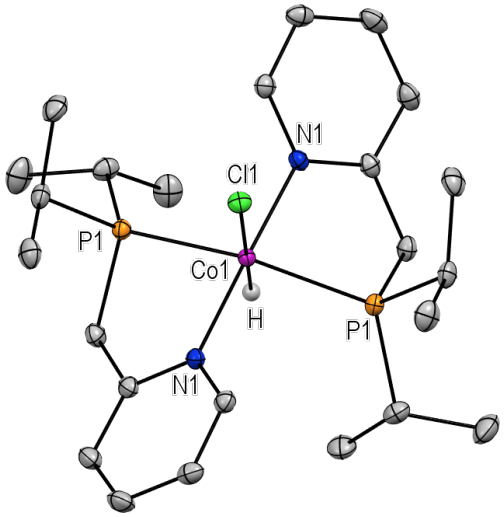

Figure 2.27. X-ray crystal structure of the $[Co^{III}(PN)_2(H)(Cl)][PF_6]$ complex. Selected hydrogen atoms and PF_6^- counter anion were removed for clarity. Thermal ellipsoids shown with probability of 50%.

Table 2.9. Selected bond distances (Å) and bond angles (deg) for the $[Co^{III}(PN)_2(H)(Cl)][PF_6]$ complex

atom	atom	bond lengths (Å)	atom	atom	atom	bond angles (deg)
Co1	N1	1.9528(15)	$N1^1$	Co1	N1	175.35(10)
Co1	P1	2.2425(5)	$N1^1$	Co1	P1	96.43(5)
Co1	Cl1	2.3391(7)	N1	Co1	P1	82.73(5)
Co1	H	1.54(7)	Cl1	Co1	P1	100.339(15)
			Cl11	Co1	N1	92.32(5)
			$P1^1$	Co1	P1	159.32(3)

2.5.2.4 Structural characterisation of $[Co^{II}(PN)_2(MeCN)][BF_4]_2$

The red-orange acetonitrile analogue of the dichloro cobalt(II) complex with bis-P,N chelating pyridine phosphine ligands can be prepared in high yield (90% yield) by a reaction of $[Co^{II}(MeCN)_6][BF_4]_2$ and 2.0 equiv of the PN ligand in dry acetonitrile solution (**Scheme 2.1**). A deep red single crystal grown from CH_3CN/THF was suitable for analysis by X-ray crystallographic determination as shown the structure in **Figure 2.28.** Elemental analysis of the complex showed the experimental values correspond to the calculated values of the $[Co^{II}(PN)_2][BF_4]_2$ complex with no MeCN ligand. It should be noted that the MeCN loss was observed as a result of leaving it dry under vacuum for 3 days.

ESI mass spectrometry of $[Co^{II}(PN)_2(MeCN)][BF_4]_2$

The positive mode of ESI-MS of the complex (**Figure A 2.21)** displayed the molecular ion peaks at m/z = 238.5966 which corresponded to the dicationic $[Co(PN)_2]^{2+}$. The isotopic distribution patterns calculated for $[C_{24}H_{40}CoN_2P_2]^{2+}$ showed at m/z 238.5971 as shown in **Figure A 2.21** (bottom).

X-ray crystal structure of $[Co^{II}(PN)_2(MeCN)][BF_4]_2$

The crystal structure of this complex (**Figure 2.28**) showed five-coordination around the cobalt(II) centre from the two PN ligands and one nitrogen atom from an acetonitrile ligand. The coordination geometry of this complex corresponded to a distorted square pyramid containing the two pyridine phosphine ligands in the equatorial plane and acetonitrile in the axial position. In contrast to the X-ray crystal structure of the $[Co^{II}$*cis*-$(PN)_2Cl][PF_6]$ and $[Co^{III}$*cis*-$(PN)_2Cl_2][PF_6]$ complexes, the molecular structure of this complex revealed that the two phosphorus atoms of the PN ligands are trans to each other which is similar to the configuration of the two P atoms in the octahedral Co(III) hydride, $[Co^{III}(PN)_2(H)(Cl)][PF_6]$ complex with a Cl^- ligand as shown in **Figure 2.27**.

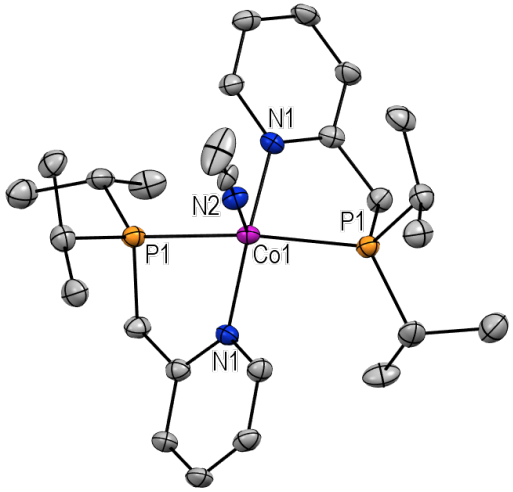

Figure 2.28. X-ray crystal structure of the cation of $[Co^{II}(PN)_2(MeCN)][BF_4]_2$. All hydrogen atoms and BF_4^- are omitted for clarify. Thermal ellipsoids are shown at the 50% probability level.

Table 2.10. Selected bond distances (Å) and bond angles (deg) in the $[Co^{II}(PN)_2(MeCN)][BF_4]_2$ complex.

atom	atom	bond lengths (Å)	atom	atom	atom	bond angles (deg)
Co1	N1	1.967(6)	$N1^1$	Co1	N1	166.8(4)
Co1	N2	2.034(9)	N1	Co1	N2	96.58(19)
Co1	P1	2.2621(18)	N1	Co1	P1	81.53(17)
			N1	Co1	$P1^1$	96.25(17)
			N2	Co1	P1	99.67(6)
			P1	Co1	$P1^1$	160.67(12)

2.5.2.5 Structural characterisation of $[Co^{III}(PN)_2(H)(MeCN)][PF_6]_2$

The acetonitrile derivative of $[Co^{III}(PN)_2(H)(MeCN)][PF_6]_2$ could be prepared by two different methods as shown in **Scheme 2.2**. In the first approach, this complex (method A) is prepared directly with a moderate yield (38%) by treatment of the corresponding cobalt(II) complex, $[Co^{II}(PN)_2(MeCN)][BF_4]_2$ with 1.3 equiv of $NaBH_4$. The addition of 2.0 equiv. NH_4PF_6 caused a precipitation of a yellow solid of the $[Co^{III}(PN)_2(H)(MeCN)][PF_6]_2$. Alternatively, this hydride complex could be synthesized from the chloride analogue of $[Co^{III}(PN)_2(H)(Cl)][PF_6]$ by an exchange reaction between a Cl^- ligand of the complex and MeCN in acetonitrile solution with 10.0 equiv of TFA (method B) with a relatively low yield of yellow solid (23%). The resulting product was then characterized by NMR spectroscopy, ESI-MS and CHN analysis.

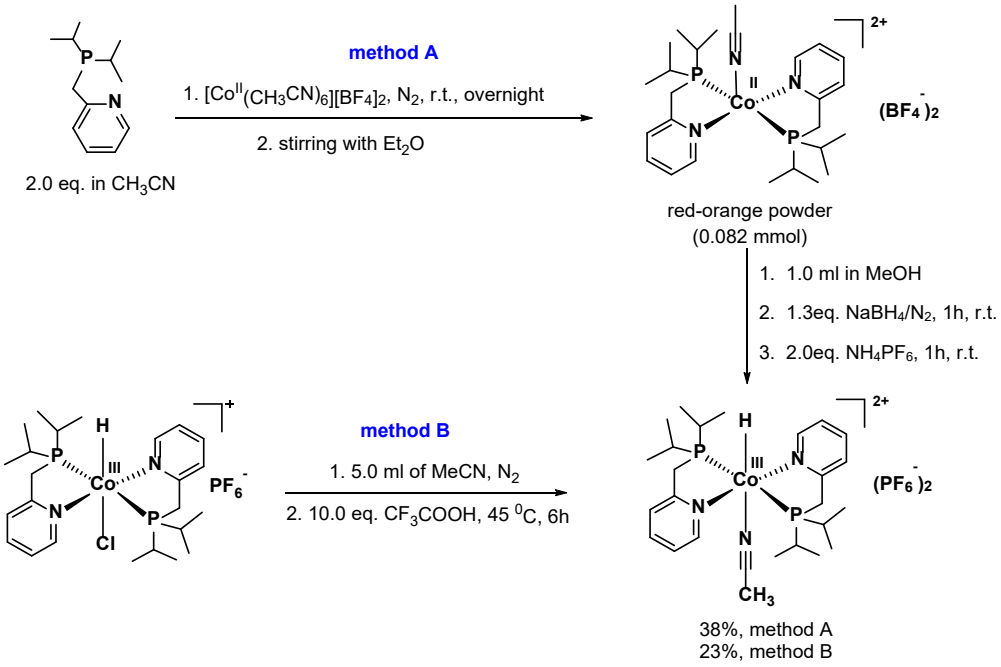

Scheme 2.2. Synthetic pathways for the acetonitrile derivative of cobalt(III) hydride complex, $[Co^{III}(PN)_2(H)(MeCN)]^{2+}$ complex.

A suitable crystal of the $[Co^{III}(PN)_2(H)(MeCN)][PF_6]_2$ prepared by method A could be successfully grown in acetonitrile solution layered with dry diethyl ether to obtain a yellow-brown crystal. Unfortunately, X-ray crystallographic analysis has not been achieved due to a decomposition during recrystallisation. There are five dications of the $[Co^{II}(PN)_2(MeCN)]^{2+}$ and distorted mixtures of ten counter anions (BF_4^- and PF_6^-) in the asymmetric unit.

NMR spectroscopy of $[Co^{III}(PN)_2(H)(MeCN)][PF_6]_2$

The ^1H NMR (**Figure A 2.22 and Figure A 2.23**) and $^{31}P\{^1H\}$ NMR (**Figure A 2.24**) spectra of $[Co^{III}(PN)_2(H)(MeCN)][PF_6]_2$ in CD_3CN at room temperature showed sharp and well-resolved peaks similar to the NMR spectrum of $[Co^{III}(PN)_2(H)(Cl)][PF_6]$ with the same number of peaks and similar multiplicities but at different chemical shifts. As a result, the structural symmetry of this acetonitrile complex was expected to be the same as that of $[Co^{III}(PN)_2(H)(Cl)]PF_6$ with C_2 symmetry and trans configuration of the two P-atoms in the PN ligands (**Figure 2.26**). The sharp NMR spectra indicate that $[Co^{III}(PN)_2(H)(MeCN)]^{2+}$ is also a low spin d^6 complex. The ^1H NMR spectrum (**Figure A 2.25,** bottom) showed that the CH_2 and isopropyl protons coupled to the phosphorus atoms in the complex by exhibiting virtual quartet signals of four methyl groups ($H_{8a\text{-}8d}$), broad septet peaks of H_{7a} , H_{7b}, broad doublet peaks of the methylene protons H_{6a} and H_{6b} and a triplet hydride signal. In the $^1H\{^{31}P\}$ NMR (**Figure A 2.25,** top) the signals for the isopropyl protons, CH_2, and hydride signal which coupled to the phosphorus atoms in the complex became doublet peaks for $H_{8a\text{-}8d}$, sharper peaks of H_{6a}, H_{6b}, H_{7a} and H_{7b} and a singlet signal for the hydride ligand. Furthermore, the $^1H\text{-}^{31}P\{^1H\}$ HMBC experiment (**Figure A 2.26**) confirmed that hydride signal, H_{6a}, H_{6b} and methyl protons of isopropyl groups in complex coupled to the two phosphorus atoms.

To identify a coordinated MeCN peak of this complex in the ^1H NMR spectrum, further characterization of this hydride complex in non-coordinating CD_2Cl_2 was then performed. In the ^1H NMR spectrum (**Figure A 2.27**), the peak at δ = 2.68 with the integral of 3.0 was assigned as the CH_3 proton of the coordinated acetonitrile ligand in this complex, and free acetonitrile in this solution appeared at δ 1.99. The $^{31}P\{^1H\}$ NMR spectrum of this solution (**Figure A 2.28**) showed the ligand in the $[Co^{III}(PN)_2(H)(MeCN)]^{2+}$ resonance at δ 72.44 and an additional small signal which corresponded to the phosphorus signal in the corresponding cobalt(III) hydride complex with Cl^- ligand suggesting activation of C-Cl bond by this complex.

The structure of this complex was also supported by 2D NMR techniques including $^1H\text{-}^1H$ COSY, (**Figure A 2.29-Figure A 2.30**). Furthermore, the assignments of carbon atoms were supported by the $^{13}C\{^1H\}$ NMR spectrum (**Figure A 2.31-Figure A 2.32**), ^{13}C-DEPT NMR spectroscopy (**Figure A 2.33**) and $^1H\text{-}^{13}C$-DEPT correlation experiments (**Figure A 2.34**) The assigned protons, carbon atoms and phosphorus atoms in the structure of $[Co^{III}(PN)_2(H)(MeCN)]^{2+}$ complex as labelled in **Figure 2.29**) corresponded to the NMR spectroscopic data listed in **Table 2.11**

Table 2.11. Assignment of hydrogen, carbon and phosphorus NMR data of $[Co^{III}(PN)_2(H)(MeCN)][PF_6]_2$ complex.

Assigned atom	δ (ppm)	J (Hz) and multiplicity	Integration
H_1 (C_1)	8.42 (157.72)	$^3J_{H,H}$ = 5.8, d ($^4J_{C,P}$ +$^6J_{C,P}$ = 4.7, t)	2H
H_3(C_3)	7.83 (141.11)	$^3J_{H,H}$ = 7.8, $^4J_{H,H}$ 1.2, td (s)	2H
H_4(C_4)	7.47 (126.18)	$^3J_{H,H}$ = 7.8, d ($^3J_{C,P}$ +$^5J_{C,P}$ = 3.8, t)	2H
C_5	(164.56)	$^2J_{C,P}$ +$^4J_{C,P}$ = 3.2, t	-
H_2(C_2)	7.30 (125.56)	$^3J_{H,H}$ = 7.0, t (s)	2H
H_{6a} or H_{6b} (C_6)	3.71 (35.38)	$^2J_{H,H}$ = 17.6, d(br) ($^1J_{C,P}$ +$^3J_{C,P}$ = 15.4, virtual t)	2H
	3.50 (35.38)	$^2J_{H,H}$ = 17.5, d(br) ($^1J_{C,P}$ +$^3J_{C,P}$ = 15.4, virtual t)	2H
H_{7a} or H_{7b} (C_{7a} or C_{7b})	2.74 (27.56)	$^3J_{H,H}$ = 7.1, $^3J_{H,P}$ >> 7.3, sep(br) ($^1J_{C,P}$ +$^3J_{C,P}$ = 6.7, virtual t)	2H
	2.33(23.03)	$^3J_{H,H}$ = 7.0, $^3J_{H,P}$ >> 6.9, sep(br) ($^1J_{C,P}$ +$^3J_{C,P}$ = 13.2, virtual t)	2H
H_{8a-8d}(C_{8a-8d})	1.48 (18.61)	$^3J_{H,H}$ = 7.2, $^3J_{H,P}$+$^5J_{H,P}$ = 7.4, virtual q (s)	6H
	1.26 (18.34)	$^3J_{H,H}$ = 7.0, $^3J_{H,P}$+$^5J_{H,P}$ = 7.0, virtual q (s)	6H
	0.88 (17.96)	$^3J_{H,H}$ = 7.0, $^3J_{H,P}$+$^5J_{H,P}$ = 7.0, virtual q (s)	6H
	0.68 (17.61)	$^3J_{H,H}$ = 7.2, $^3J_{H,P}$+$^5J_{H,P}$ = 7.4, virtual q (s)	6H
H_9 (CH_3CN)	2.54	s	3H
Hydride (H)	-17.12	$^2J_{H,P}$ = 54.3, t	1H
P	72.44	s	2P
PF_6^-	-144.60	$^1J_{P,F}$ = 706.3, sep	1P

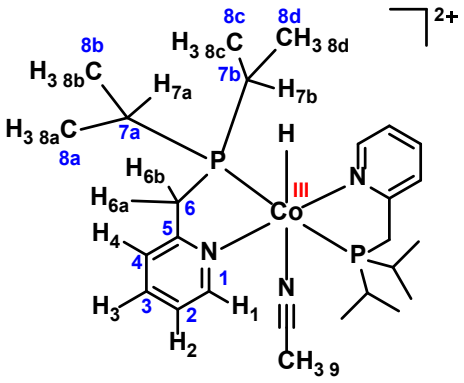

Figure 2.29. Labelled atoms in the structure of $[Co^{III}(PN)_2(H)(MeCN)]^{2+}$complex.

ESI mass spectrometry of $[Co^{III}(PN)_2(H)(MeCN)][PF_6]_2$

The positive mode of ESI-MS of the complex showed molecular ion peaks at *m/z* = 477.1994 which corresponded to the $[Co^{I}(PN)_2]^+$. The isotopic distribution patterns calculated for $[C_{24}H_{40}CoN_2P_2]^+$ showed at m/z 477.1993 as shown in(**Figure A 2.35 bottom)**.

2.5.3 Comparison of X-ray crystallographic data

The X-ray structure (**Figure 2.30**) of $[Co^{II}(PN)_2(MeCN)][BF_4]_2$ (a) and $[Co^{II}$*cis*-$(PN)_2Cl][PF_6]$ (b) shows distorted square pyramidal geometry. The configuration of the two phosphorus atoms of the PN ligands in these two complexes is different. The two P- and two-N atoms in the $[Co^{II}(PN)_2(MeCN)][BF_4]_2$ are mutually trans configuration while the two P atoms are *cis* to each other in the corresponding monochloride Co(II) complex, $[Co^{II}$*cis*-$(PN)_2Cl][PF_6]$. All bond distances of the PN ligands around the Co(II) centre (listed in **Table 2.12**) and the bite angle for P-Co-N angle of the same ligand in these two complexes are comparable. This two bite angles of the same ligands in $[Co^{II}(PN)_2(MeCN)][BF_4]_2$ are the same value of 96.25 (17) deg. However, the bond angles P-Co-P and N-Co-N between the two PN ligands lying in the equatorial plane in the $[Co^{II}$*cis*-$(PN)_2Cl][PF_6]$ complex are considerably distinct by 7.46 deg. The bond angle of the atoms lying trans to each other (P-Co-P and N-Co-N) in the equatorial plane of $[Co^{II}(PN)_2(MeCN)][BF_4]_2$ is slightly different. However, the P-Co-N angles in the equatorial plane of $[Co^{II}$*cis*-$(PN)_2Cl][PF_6]$ are very distinct. The inequivalence of these bond angles between the two ligands in $[Co^{II}$*cis*-$(PN)_2Cl][PF_6]$, where 2P atoms *cis* to each other, is possibly due to non-covalent interactions between the two bulky isopropyl groups. Therefore, it supported a more distorted square pyramidal geometry of the $[Co^{II}$*cis*-$(PN)_2Cl][PF_6]$ than the structure of $[Co^{II}(PN)_2(MeCN)][BF_4]_2$.

The bite angles (P-Co-N) as listed in the **Table 2.12** for $[Co^{II}(PN)_2(MeCN)][BF_4]_2$, $[Co^{II}$*cis*-$(PN)_2Cl][PF_6]$, $[Co^{II}(C_{19}H_{35}NP_2)Cl_2]$, where $C_{19}H_{35}NP_2$ = 2-(bis(diisopropylphosphanyl)methyl)6-methylpyridine, and $[Co^{II}(NPP)Cl_2]$[234] (NPP = 2-pyridylbis(diphenylphosphino)methane) are slightly distinct. These bite angles around 82-84 deg are typical for a five-membered bidentate P,N ligand coordination to a metal center.[165, 234] The different geometry of the complexes, where the different P,N- or N,P,P- ligands in the pseudo-square pyramidal complex for $[Co^{II}(PN)_2(MeCN)][BF_4]_2$ and $[Co^{II}$*cis*-$(PN)_2Cl][PF_6]$ and pseudo tetrahedral $[Co^{II}(C_{19}H_{35}NP_2)Cl_2]$, $[Co^{II}(NPP)Cl_2]$ (NPP = 2-pyridylbis(diphenylphosphino)methane), caused the similar degree of bite angle P-Co-N. It suggested that bidentate P,N ligands has quite unique bite angle for complexation with cobalt (II) center. The investigation of coordination mode of NPP tridentate ligands with different CoX_2 salts (X = Br, Cl and I) showed that only a P,N bidentate coordination mode of this two phosphorus-nitrogen ligand (N,P,P) was formed with these cobalt salts.[182]

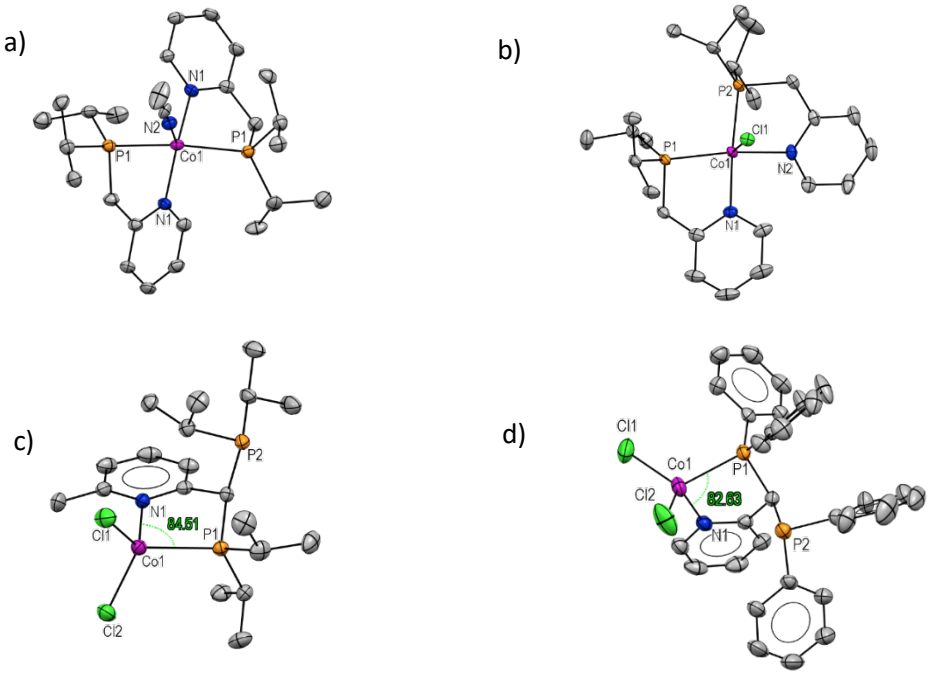

Figure 2.30. X-ray crystal structures of the cation of $[Co^{II}(PN)_2(MeCN)][BF_4]_2$ (a), $[Co^{II}$*cis*-$(PN)_2Cl][PF_6]$ (b), $[Co^{II}(C_{19}H_{35}NP_2)Cl_2]$ (c), and $[Co^{II}(NPP)Cl_2]$ (d). All hydrogen atoms are omitted except for the hydride ligand coordinated to cobalt. The PF_6^- and BF_4^- are omitted for clarity. Thermal ellipsoids are shown at the 50% probability level for all complexes except for the $[Co^{II}(NPP)Cl_2]$ with the 30% probability level.

Table 2.12. Selected bond length (Å) and bond angle (deg) of all complexes.

	$[Co^{II}(PN)_2(MeCN)]^+$	$[Co^{II}$*cis*-$(PN)_2Cl]^+$	$[Co^{II}(C_{19}H_{35}NP_2)Cl_2]$[234]	$[Co^{II}(NPP)Cl_2]$[182]
bond length (Å)				
Co-P1 Co-P2	2.2621(18)	2.2160(9), 2.2156(9)	2.373 -	2.376 -
Co-N1 Co-N2	1.967(6)	1.9933(14), 2.039(3)	2.064 -	2.042 -
Co-NCMe	2.034(9)	-	-	-
Co-Cl	-	2.4299(9)	2.228(Cl1),2.241 (Cl2)	2.203(Cl1), 2.195(Cl2)
bond angles (deg)				
P1-Co-N1 P2-Co-N2	81.53(17)	82.42(6) 82.24(8)	84.51 -	82.63 -
P1-Co-P1	160.67 (12)	101.58(3)		
N-Co-N	166.8(4)	94.12(10)		
P1-Co-N1 P2-Co-N1	96.25(17)	159.72(8) 175.98(6)		

The solid-state X-ray structure (**Figure 2.31**) of $[Co^{III}cis\text{-}(PN)_2Cl_2][PF_6]$ (a) and $[Co^{III}(PN)_2(H)(Cl)][PF_6]$ (b) revealed a distorted octahedral complex with the two axial Cl^- ligands for the $[Co^{III}cis\text{-}(PN)_2Cl_2]^+$,and one axial Cl^- and H^- for the $[Co^{III}(PN)_2(H)(Cl)][PF_6]$. The two P,N ligands in these two Co(III) complexes are occupying in the equatorial position but in different configuration for the two P- and two N-atoms. They are trans to each other for the $[Co^{III}(PN)_2(H)(Cl)][PF_6]$ while mutually cis configuration for the $[Co^{III}cis\text{-}(PN)_2Cl_2]^+$. The cis-configuration in this complex is similar to the coordination mode of bis-P,N chelating ligands in the Rh(III) complexes as shown the X-ray crystal structure in **Figure 2.31**, c) for the $[Rh^{III}(DPPMP)_2Cl_2]^+$ and d) for the $[Rh^{III}(DPPMP)_2(H)FBF_3]^+$. This evidence also supported that a bis-P,N chelating transition metal complex based bidentate pyridine phosphine ligands favoured to coordinating to a metal center with the *cis* configuration rather than the *trans* configuration. Therefore, the trans configuration between the two P-toms in the $[Co^{III}(PN)_2(H)(Cl)][PF_6]$ is rarely observed in a coordination chemistry of bidentate P,N ligands.

Based on comparison of the bond distances as listed in **Table 2.13** between the Co(III) hydride chloride (d) and $[Co^{III}cis\text{-}(PN)_2Cl_2][PF_6]$ (c), the Co-N bond in the $[Co^{III}(PN)_2(H)(Cl)][PF_6]$ is shorter than that in the dichloro analogue by 0.0838 Å, much larger than the esd. Replacement of an axial Cl^- ligand by hydride in the octahedral Co(III) complex resulted in the shortening of the axial Co-Cl bond by 0.132 Å. Moreover, the M-P distance for all complexes as listed in the **Table 2.13** is slightly longer than the M-N bond lengths suggesting a relatively weaker interaction between phosphorus and cobalt(III) center than that of Co-N interaction. It was also observed that the cis-configuration of the two P,N ligand in $[Co^{III}cis\text{-}(PN)_2Cl_2][PF_6]$ and $[Rh^{III}(DPPMP)_2(H)FBF_3]^+$ where the two ligands are in the same equatorial planar caused a more distorted octahedral structure as indicated by the greatly inequivalent of P-M-P and N-M-N by 5.31 deg in $[Rh^{III}(DPPMP)_2(H)FBF_3]^+$ and 16.62 deg in $[Co^{III}cis\text{-}(PN)_2Cl_2]^+$. In contrast to these distinct bond angles, the two P-Co-N angles between the different ligands in the $[Co^{III}(PN)_2(H)(Cl)][PF_6]$ and $[Co^{II}(PN)_2(MeCN)][BF_4]_2$ are equivalent with the respective value of 96.43(5) and 96.25(17) deg. Accordingly, for the Co(III) complexes in the series, the structure of $[Co^{III}cis\text{-}(PN)_2Cl_2][PF_6]$ is more distorted than the $[Co^{III}(PN)_2(H)(Cl)][PF_6]$ possibly due to the repulsion between the two bulky isopropyl groups of the P,N ligands with *cis* configuration. Thus, we postulate that the $[Co^{III}cis\text{-}(PN)_2Cl_2][PF_6]$ in a solution at room temperature exhibited fluxional structure possibly due to hemilabile P,N ligands coordination or might result in a configuration change from *cis* configuration of the two phosphorus atoms in the solid state to the other isomers in solution.

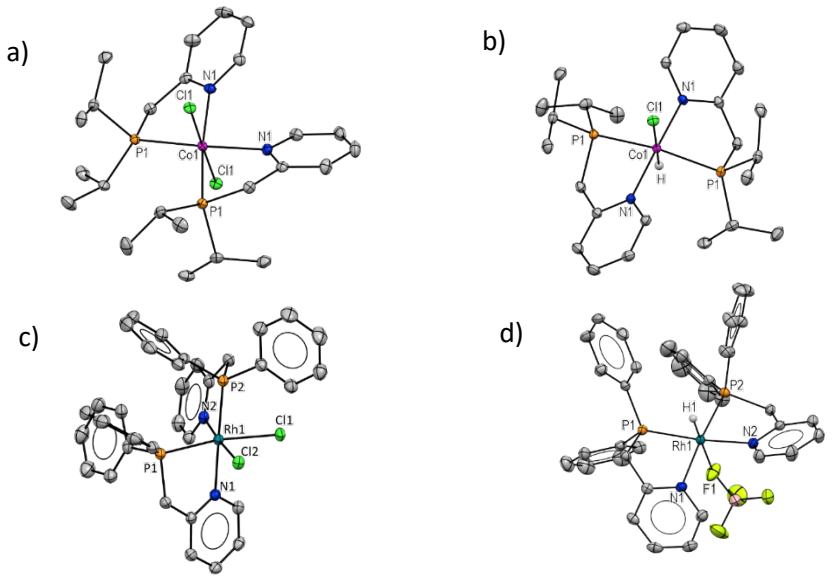

Figure 2.31. X-ray crystal structures of $[Co^{III}cis\text{-}(PN)_2Cl_2][PF_6]$ (a), $[Co^{III}(PN)_2(H)(Cl)][PF_6]$ (b), the cation of $[Rh^{III}(DPPMP)_2Cl_2]^+$ (c), and $[Rh^{III}(DPPMP)_2(H)FBF_3]^+$ (d). All hydrogen atoms are omitted except for the hydride ligand coordinated to cobalt and rhodium. The PF_6^- $PhCOO^-$ and BF_4^- are omitted for clarity. Thermal ellipsoids are shown at the 50% probability level for all complexes.

Table 2.13. Selected bond length (Å) and bond angle (deg) of all complexes.

	$[Co^{III}cis\text{-}(PN)_2Cl_2]^+$	$[Co^{III}(PN)_2(H)(Cl)]^+$	$[Rh^{III}(DPPMP)_2Cl_2]^+$ [167]	$[Rh^{III}(DPPMP)_2(H)FBF_3]^+$ [167]
bond length (Å)				
M-P1	2.2735(5)	2.2425(5)	2.279	2.236
M-P2			2.267	2.246
M-N1	2.0366(15)	1.9528(15)	2.160	2.118
M-N2			2.068	2.132
M-Cl	2.2471(4)	2.3391(7)	2.404(Cl1) 2.344(Cl2)	-
M-H	-	1.54(7)		1.439
bond angles (deg)				
P1-M-N1	81.43(4)	82.73(5)	79.84	82.44
P2-M-N2			83.92	80.59
P1-Co-P1	107.59(3)	159.32(3)		
N-Co-N	90.97(8)	175.35(10)		
P1-Co-N1	167.78(4)	96.43(5)		
P1-Rh-P2				101.57
N1-Rh-N2			93.51	96.26
P2-Rh-N1			176.87	
P1-Rh-N2			95.31	
Cl-Rh-Cl			91.83	

As a result, the solid-state structure of the [Co^{II}*cis*-$(PN)_2Cl][PF_6]$ and the [Co^{III}*cis*-$(PN)_2Cl_2][PF_6]$ with a cis-configuration between the two P- and two-N atoms of the P,N-ligands is common for a coordination mode of other hemilabile bidentate P,N ligands to transition metal complexes. For this study, the bite angle for P-Co-N of the same P,N ligand in all complexes in our study ranging from 79 deg to 85 deg is comparable to this angle in the other transition metal complexes containing P,N ligands with different substituents on phosphorus. [166, 168, 234]

Comparison of the crystal structure data for [Co^{II}*cis*-$(PN)_2Cl][PF_6]$ and [Co^{III}*cis*-$(PN)_2Cl_2][PF_6]$ (**Figure 2.30** c) revealed that, the Co-N, Co-P distances and P-Co-N bite angles in these two complexes are comparable. However, the structure of [Co^{II}*cis*-$(PN)_2Cl][PF_6]$ has the axial Co-Cl bond length of 2.4299 (9), while the Co-Cl bond in the analogous [Co^{III}*cis*-$(PN)_2Cl][PF_6]$ is significantly shorter bond distance (by 0.183 Å). This is in agreement with the empty antibonding orbital of dz^2 orbital for Co(III)- d^6 resulting in the shorter Co-Cl bond in the analogous [Co^{III}*cis*-$(PN)_2Cl][PF_6]$ compared to the Co-Cl bond distance in the corresponding Co(II) complex.[206]

As a consequence, the mutually trans configuration between the two P-atoms of the PN ligands in the $[Co^{II}(PN)_2(MeCN)][BF_4]_2$ and the $[Co^{III}(PN)_2(H)(Cl)][PF_6]$ is clearly unique configuration from other transition metals supported by bis-PN chelating scaffolds. The unique trans configuration of the two P,N ligands in equatorial plane in the $[Co^{III}(PN)_2(H)(Cl)][PF_6]$ caused less distorted from ideal octahedral geometry and resulted in more rigid structure in a solution compared to that of the [Co^{III}*cis*-$(PN)_2Cl_2][PF_6]$. The relatively more rigid structure of the $[Co^{III}(PN)_2(H)(Cl)][PF_6]$ in a solution at room temperature than the [Co^{III}*cis*-$(PN)_2Cl_2][PF_6]$ was observed.

2.5.4 Absorption and emission properties

The electronic properties of the P,N ligand and all complexes in this series including the cobalt(II) complexes $[Co^{II}(PN)_2Cl_2]$, $[Co^{II}$*cis*-$(PN)_2Cl][PF_6]$, $[Co^{II}(PN)_2MeCN][BF_4]_2$, and the Co(III) complexes $[Co^{III}$*cis*-$(PN)_2Cl_2][PF_6]$,: $[Co^{III}(PN)_2(H)(Cl][PF_6]$ and $[Co^{III}(PN)_2(H)(MeCN)][PF_6]_2$ were characterized by UV-Vis absorption spectroscopy. In general, the complexes in this study exhibited absorption bands in the visible region attributed to Co^{2+}/Co^{3+} d-d transition and/or charge transfer (CT) transitions.[235] The UV-Vis absorption properties for each complex in solution are discussed below. The spectroscopic data for the P,N ligand and the Co(II) complexes in MeCN solution are summarized in the **Table 2.14**. The rates of ligand exchange of d^7 Co(II) complexes are typically much greater than those of d^6 Co(III) complexes. As shown below, it was necessary to consider ligand exchange processes in order to understand the UV/vis and electrochemical data.

Table 2.14. UV-Vis spectroscopic data of the P,N ligand, $CoCl_2$, $[Co(MeCN)_6][BF_4]_2$ and Co(II) complexes ($5.75x10^{-4}$ M) in acetonitrile solution.

compound	λ_{max} (nm)	ε (M^{-1} cm^{-1})	Assigned band
P,N ligand	260	4270	π-π^* (L)
$[Co^{II}(MeCN)_6][BF_4]_2$	490	14	d-d transition
$CoCl_2$	571	309	d-d transition: $^4A_2(F)\rightarrow{}^4T_1(P)$ transition[236]
	585	251	
	613	318	
	682	460	
$[Co^{II}(PN)_2(MeCN)][BF_4]_2$	448	902	CT
$[Co^{II}$*cis*-$(PN)_2(Cl)][PF_6]$	479	404	d-d transition + CT
	580	144	d-d transition
	650	107	d-d transition
	688	155	d-d transition
	780	182	d-d transition
$[Co^{II}(PN)_2Cl_2]$	310	1280	CT
	350	802	CT
	487	142	d-d transition
	580	261	d-d transition
	650	278	d-d transition
	688	408	d-d transition
	780	69	d-d transition
	1290 nm (NIR)	-	d-d transition
$[Co^{II}(NPP)Cl_2]$	570, 650 and 694		$^4A_2(F)\rightarrow{}^4T_1(P)$
$[Co^{II}(Me\text{-}NPP)Cl_2]$	562, 588, 675 and 704		$^4A_2(F)\rightarrow{}^4T_1(P)$
	1,000 and 1351 nm		$^4A_2(F)\rightarrow{}^4T_1(F)$

Me-NPP ligand = 2-bis(diphenylphosphino)methyl-6-methylpyridine, and NPP = 2-pyridylbis(diphenylphosphino)methane.

The UV-Vis spectrum of anhydrous $CoCl_2$ (**Figure A 2.36** a) in MeCN displayed the characteristic bands in the range from 570 to 680 nm with ε = 250-460 M^{-1} cm^{-1}. These transitions in the visible region agree with those of $Co^{II}Cl_2 \cdot H_2O$ in MeCN which were assigned to the $^4A_2(F) \rightarrow {}^4T_1(P)$ transition in the tetrahedral Co(II) d^7complex, $[CoCl_4]$.[2-236]

2.5.4.1 UV-Vis absorption properties of the $[Co^{II}(PN)_2(MeCN)][BF_4]$ in CH_3CN solution

The UV-Vis spectrum of $[Co^{II}(PN)_2(MeCN)][BF_4]$ in MeCN showed one absorption band in the visible region centred at λ_{max} 450 nm with ε = 902 M^{-1} cm^{-1} (**Figure 2.32**). This band was assigned as a charge transfer (CT) transition band because the molar absorptivity of this complex was considerably larger than the d-d transition in the centrosymmetric $[Co^{II}(MeCN)_6][BF_4]_2$ precursor at 490 nm with ε = 14 M^{-1} cm^{-1} (**Figure A 2.36** b). Furthermore, the molar absorptivity was also much larger than that for d-d transitions in six- or five-coordinated Co(II) complexes. The ε of d-d transitions of five-coordinated Co^{II} complexes ranges from 50-300 M^{-1} cm^{-1}.[235] For a six-coordinated Co^{II} complex, the molar absorptivity (ε) of d-d transitions is < 50 M^{-1} cm^{-1}.[237, 238] Since $[Co^{II}(MeCN)_6][BF_4]_2$ shows no CT bands in the visible region and the free P,N ligand exhibited no absorption spectrum in the range over 300 nm (**Figure A 2.37** the CT transition of $[Co^{II}(PN)_2(MeCN)][BF_4]$ must involve the PN ligand.

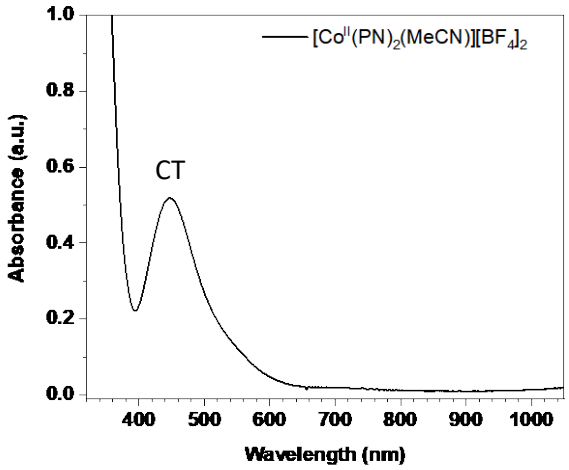

Figure 2.32. The absorption spectrum of the $[Co^{II}(PN)_2MeCN][BF_4]$ complex (5.75×10^{-4} M) in CH_3CN.

2.5.4.2 UV-Vis absorption properties of [Co^{II}cis-(PN)$_2$Cl][PF$_6$] in different solvents

UV-Vis spectra of [Co^{II}*cis*-(PN)$_2$Cl][PF$_6$] recorded in various solvents such as THF, CH_2Cl_2, MeOH, MeCN and acetone were solvent dependent (**Table 2.15**).

Table 2.15. UV/Vis absorption data of [Co^{II}cis-(PN)$_2$Cl][PF$_6$] (5.75x10^{-4} M) in different solvents.

solvents	Wavelengths, nm (ε, $M^{-1}cm^{-1}$)
THF	320 (1,650), 350 (1250), 490 (225), 780 (126)
acetone	360 (965), 490 (112), 580 (51), 650 (44), 690 (101) 780 (69)
CH_3CN	320 (3190), 360 (1984) 490 (397), 580 (144), 650 (107), 690 (157), 780 (182)
CH_2Cl_2	320 (1990), 350 (1460), 490 (258), 780 (124)
MeOH	350 (330), 480 (57), 780 (20)

The spectrum of the complex in each solvent exhibited band/s below 400 nm with high intensity compared to those bands in the visible region above 400 nm suggesting CT transition band at the wavelength lower than 400 nm (**Figure 2.33**). The bands at wavelength above 400 nm with molar absorptivity below 500 M^{-1} cm^{-1} were assigned to Co(II) d-d transitions.

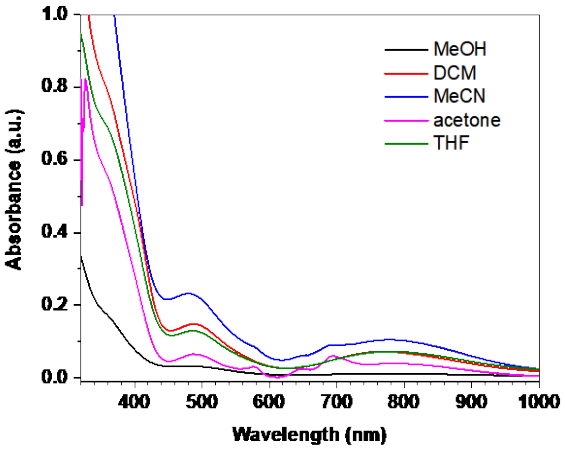

Figure 2.33. UV-Vis absorption of the [Co^{II}*cis*-(PN)$_2$Cl][PF$_6$] complex (5.75x10^{-4} M) in different solvents.

The very weak bands of this complex in MeOH centred at 480 and 780 nm with ε = 57 M^{-1} cm^{-1} and 20 M^{-1} cm^{-1}, respectively could be assigned to Co(II) d-d transition in a distorted octahedral geometry indicating the formation of [Co^{II}(PN)$_2$(MeOH)$_2$]$^{2+}$ in MeOH. This assignment is consistent with the characteristic absorption bands of distorted octahedral Co(II) complexes. For example, the d-d transitions for a six-coordinated [Co^{II}(6Me$_3$TPA)(HSA)][BPh$_4$] (6Me$_3$TPA = tris(6–methyl–2–pyridylmethyl)amine, H_2SA = salicylic acid) in CH_3CN appeared at 476 nm (50

$M^{-1}\,cm^{-1}$), 515 nm (40 $M^{-1}\,cm^{-1}$) and 557 nm (50 $M^{-1}\,cm^{-1}$). The $[Co^{II}(tren)(H_2O)_2]^{2+}$] showed a very weak Co^{2+} d-d transition at 475 nm[239] and the diaqua 6-coordinated Co(II) complex with bis(iminopyridine) displayed band at 450 (60 $M^{-1}\,cm^{-1}$).[240] The d-d transition at around 500 nm with ε = 20 $M^{-1}\,cm^{-1}$ corresponded to the $^4T_{1g}(F)\rightarrow{}^4T_{1g}(P)$ which was observed in the spectrum of $CoCl_2{\cdot}H_2O$ in MeOH.[236]

The UV-Vis spectrum of the complex in other solvents showed two bands at 480 nm and 800 nm with ε = 125-660 $M^{-1}\,cm^{-1}$. These bands showed considerably higher intensity than that of the complex in MeOH which were therefore assigned as d-d transitions in non-centrosymmetric species for 5-coordinated $[Co(PN)_2Cl]^+$. These characteristic bands corresponded to the absorption spectrum of five-coordinated mono-acetonitrile species $[Co^{II}L(MeCN)]^{2+}$ which showed a long wavelength absorption band pattern between 600 and 700 nm.[239, 241, 242] . The $[Co^{II}(TPA)(HSA)][ClO_4]$ in CH_3CN displayed bands at 465 nm (200 $M^{-1}\,cm^{-1}$), 605 nm (160 $M^{-1}\,cm^{-1}$) and 622 nm (140 $M^{-1}\,cm^{-1}$).[243]

Moreover, the spectrum of this complex in MeCN and acetone displayed three additional bands in the range from 580 to 700 nm (**Figure 2.33** red and blue curve). The observation of new absorption bands in the range from 580 nm to 700 nm agrees with the 5-coordinated Co(II) complexes containing Cl^- ligand reported in the literature.[244] The three low-intensity bands reported in the literature at 524 (ε = 100 $M^{-1}\,cm^{-1}$), 570 (ε = 100 $M^{-1}\,cm^{-1}$), and 640 (ε = 100 $M^{-1}\,cm^{-1}$) were assigned as d−d transitions that are partially allowed by d−p orbital mixing, combined with a $Cl \rightarrow Co^{II}$ charge-transfer transition (LMCT). The characteristic bands in this region are also in agreement with the absorption bands of polypyridyl Co(II) complexes containing a Cl^- ligand.[238, 245]

To support the existence of five-coordinated $[Co(PN)_2Cl]^+$ species in solution, the interaction between the independently synthesized $[Co^{II}(PN)_2(MeCN)]^{2+}$ and Cl^- anion was monitored by UV-Vis titration of a solution of the $[Co^{II}(PN)_2(MeCN)]^{2+}$ with tetrabutyl ammonium chloride (TBACl) in MeCN solution.

UV-Vis titrations of $[Co^{II}(PN)_2(MeCN)][BF_4]_2$ in MeCN with TBACl

The addition of 1.0 equiv of Cl^- to a solution of the $[Co^{II}(PN)_2(MeCN)][BF_4]_2$ complex in MeCN resulted in a large decrease of the CT band at λ_{max} 450 nm concomitant with an enhancement of the bands ranging from 580 nm to 800 nm (**Figure 2.34** a). The spectrum of this solution with 1.0 equiv. Cl^- corresponded to the d-d transition bands of the isolated $[Co^{II}$*cis*$-(PN)_2Cl][PF_6]$ in MeCN (**Figure A 2.38**) which supported binding of one Cl^- to form 5-coordinated species containing Cl^- ligand. The addition of Cl^- to this solution up to 2.2 equivalents (**Figure 2.34** b, blue curve) showed further increases in absorption intensity of the three bands at 580, 650, and

688 nm indicating the formation of new species. These bands are not consistent to the absorption bands in the pseudo-octahedral $[Co^{II}(PN)_2Cl_2]$ due to multiple and intense bands. Therefore, the four-coordinated complex, $[Co^{II}(PN)Cl_2]$ was expected to form in the solution by a displacement of the PN ligand with two chlorides upon adding 2.2 equiv of Cl^- to the solution.

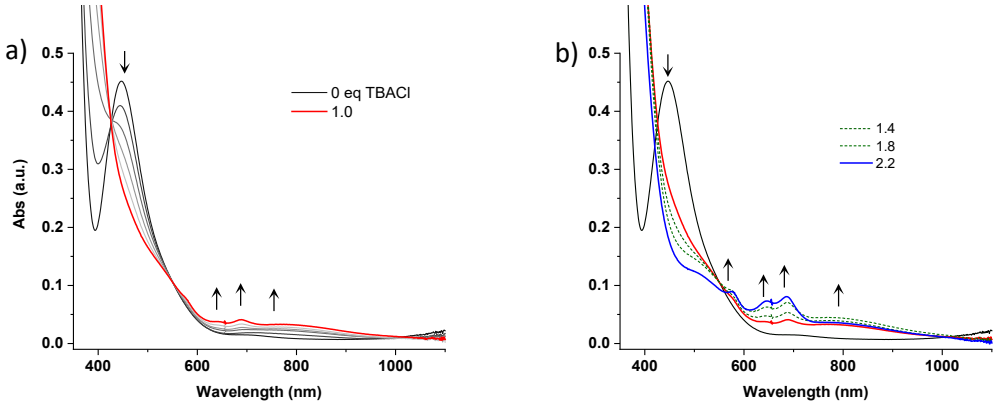

Figure 2.34. UV-Vis spectral changes of the $[Co^{II}(PN)_2(MeCN)][BF_4]_2$ ($5.75x10^{-4}$ M, in CH_3CN) upon addition of TBACl from 0 to 1.0 equiv (a) and adding Cl^- to 2.2 equiv (b).

The addition of large excess Cl^- (15.0 equiv) to the solution of this complex led to the appearance of more intense bands at 580, 650 and 688 nm (**Figure 2.35** a) which is consistent with the spectra of $CoCl_2$ in MeCN solution with 4.0 equiv Cl^- displaying four absorption bands at the similar wavelengths with molar absorptivity in the range of 300-500 M^{-1} cm^{-1} (**Figure 2.35** b). These bands in the visible region are characteristic of $[CoCl_4]^{2-}$ species and they are attributed to the $^4A_2(F)$->$^4T_1(P)$ transition.[235]

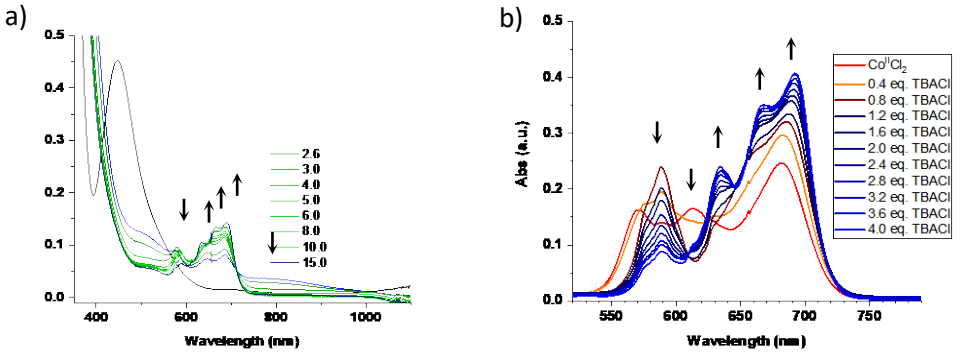

Figure 2.35. UV-Vis spectral changes of the $[Co^{II}(PN)_2(MeCN)][BF_4]_2$ ($5.75x10^{-4}$ M, in CH_3CN) upon addition of TBACl from 2.6 to 15.0 equiv (a) and a solution of $CoCl_2$ upon adding Cl^- up to 4.0 equiv (b).

According to these results, the interaction of the $[Co(PN)_2(MeCN)]^{2+}$ with different equivalents of Cl^- can be proposed in **Scheme 2.3**. The addition of 1.0 equiv Cl^- to the solution of the MeCN

complex resulted in a formation of 5-coordinated complex and two Cl^- ions could replace the PN ligand in the $[Co^{II}(PN)_2(MeCN)]^{2+}$ to form tetrahedral $[Co^{II}(PN)Cl_2]$ upon adding 2.2 eq TBACl. The addition of excess Cl^- to the solution eventually caused displacement of both PN ligands concomitant with the formation of tetrachloride Co(II) dianionic species.

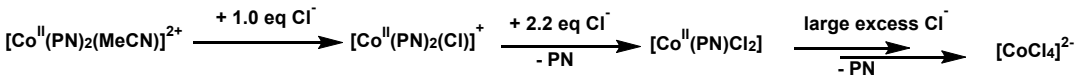

Scheme 2.3. The formation of chloride derivatives by the UV-Vis titration of the $[Co^{II}(PN)_2(MeCN)]^{2+}$ with TBACl in MeCN.

To support a formation of the tetrahedral Co(II) complex, $[Co^{II}(PN)Cl_2]$ for this titration experiment, the $[Co^{II}(PN)Cl_2]$ was prepared by a 1:1 reaction of $CoCl_2$ salt to the P,N ligand in THF solution. The separately synthesized $[Co^{II}(PN)Cl_2]$ is a deep blue which characterized by the UV-Vis measurements in different solutions (THF, MeCN, $CHCl_3$ and MeOH). The UV-Vis spectrum (**Figure A 2.39**) of this complex in THF, MeCN and $CHCl_3$ showed multiple bands ranging from 560 nm to 700 nm. These absorption bands corresponded to d-d transition attributed to $^4A_2(F)$->$^4T_1(P)$ transition in a pseudo-tetrahedral Co(II) complex. The multi absorption bands are consistent to d-d transitions in the four-coordinated Co(II) complexes containing a bidentate P,N coordination mode reported in the literatures for $[Co^{II}(NPP)Cl_2]$ [183] and $[Co^{II}(Me\text{-}NPP)Cl_2]$.[182] The absorption bands of these two complexes with Td symmetry was assigned to $^4A_2(F)$->$^4T_1(P)$ and $^4A_2(F)$->$^4T_1(F)$ transitions as listed in the **Table 2.14**.

Furthermore, another explanation for the observation of the three characteristic bands from 580 to 700 nm in the UV-Vis spectrum of this complex in MeCN and acetone (**Figure 2.33** pink and blue curve) could be that tetrahedral $[Co(PN)Cl_2]$ is formed by a bimolecular ligand exchange reaction between a P,N ligand and Cl^- in the complex. We assumed that a P,N chelating ligand in the complex could exchange with Cl^- in the MeCN solution to form the corresponding 4-coordinated $[Co^{II}(PN)Cl_2]$ and $[Co^{II}(PN)_2]^{2+}$ species as proposed in the **eq 2.11**

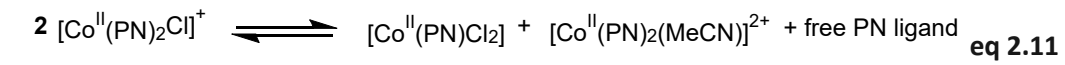

eq 2.11

A bimolecular ligand exchange reaction was evidenced in the cobalt(II) complexes supported by a single bidentate $P^R_2N_2{}^{R'}$ ligand (P_2N_2 = 1,5-diaza-3,7-diphosphacyclooctane), $[Co^{II}(P^R_2N_2{}^{R'})(MeCN)]^{2+}$ diphosphine ligands. This complex undergoes ligand exchange to yield $[Co^{II}(P^R_2N_2{}^{R'})_2(MeCN)]^{2+}$ species.[246, 247]

In general, three transitions, $^4T_2$←$^4A_2$ (ν1), $^4T_1(F)$ ←$^4A_2$ (ν2) and $^4T_1(P)$ ←$^4A_2$ (ν3) may be observed in the absorption spectrum of tetrahedral or pseudo-tetrahedral Co(II) complexes. However, the $^4T_2$←$^4A_2$ (ν1)bands usually lie in the range from 1700 nm to 4000 nm (2500-6000 cm^{-1}) [235, 248 249].

The $^4T_1(F) \leftarrow {}^4A_2$ ($\nu 2$) and $^4T_1(P) \leftarrow {}^4A_2$ ($\nu 3$) transitions appear as multiple absorption bands in the near infrared and visible region. For example, the $[Co^{II}LCl_2]_n$,where L = *N,N*-diisobutylisonicotinamide containing the pseudo tetrahedral $CoNOCl_2$ chromophore showed multiple structured bands in the visible region with maxima at 668 nm (430 M^{-1} cm^{-1}), 624 nm (327 M^{-1} cm^{-1}) and 593 nm (ε = 352 M^{-1} cm^{-1}). The anionic $[CoLBr_3]^-$ species displayed a multiple structured band at 677 nm (ε = 145 M^{-1} cm^{-1}) with a sharp shoulder at 620 nm (ε = 134 $M^{-1}cm^{-1}$) in the visible region corresponding to $^4T_1(P) \leftarrow {}^4A_2$ ($\nu 3$) transition for a tetrahedral Co(II) complex. [250] The splitting of d-d transitions in the visible region in these two chromophores is considered to stem from the lowering in orbital degeneracy due to the difference in the ligand field strength of neutral ligand L and negative halide ligands.[250] Therefore, these characteristic bands corresponding to $^4T_1(P) \leftarrow {}^4A_2$ in the visible region are consistent with the bands at 580 (144 M^{-1} cm^{-1}), 650 (107 M^{-1} cm^{-1}) and 690 (157 M^{-1} cm^{-1}) which supported the formation of $Co^{II}(PN)Cl_2$ as proposed in **Scheme 2.3.**

To investigate the equilibria further, the UV-Vis titration of a solution of the $[Co(PN)_2Cl]^+$ complex with the P,N ligand in MeCN solution was performed. The addition of 1.0-3.0 equiv of the P,N ligand to the solution of this complex led to the disappearance of these three absorptions bands (580, 650 and 688 nm) with the enhancement of absorption intensity at 490 nm and 780 nm (**Figure 2.36**) indicating a conversion of the $Co^{II}(PN)Cl_2$ to the corresponding five-coordinated $[Co(PN)_2Cl]^+$ as proposed in the **eq 2.12**

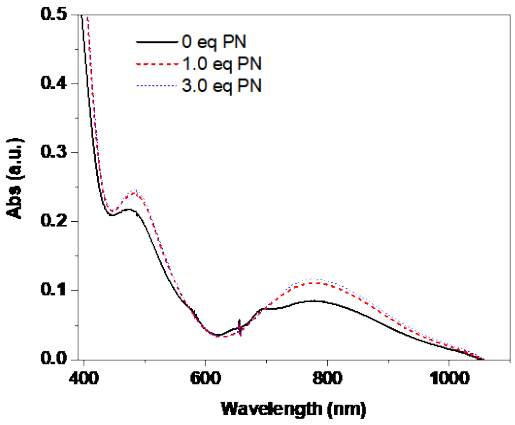

Figure 2.36. UV-Vis spectral changes of the $[Co^{II}$*cis*$-(PN)_2Cl][PF_6]$ ($5.75x10^{-4}$ M, in CH_3CN) upon adding a solution of the P,N ligand in MeCN (0.0-3.0 equiv).

$$2\ [Co^{II}(PN)_2Cl]^+ \xrightleftharpoons{+\ 1.0\ eq\ P,N\ ligand} [Co^{II}(PN)Cl_2] + [Co^{II}(PN)_2(MeCN)]^{2+} + \text{free P,N ligand} \qquad \textbf{eq 2.12}$$

2.5.4.3 UV-Vis absorption properties of the $[Co^{II}(PN)_2Cl_2]$ complex in different solvents

The neutral dichloride $[Co^{II}(PN)_2Cl_2]$ appeared purple in the solid state: however; a colour change was observed upon dissolving in different solvents such as THF, acetone, MeCN, $CHCl_3$, DMF, iPrOH, MeOH and H_2O as shown in **Figure 2.37**, inset. The spectrum of this complex in THF, MeCN, acetone $CHCl_3$ and 2-propanol suggested the formation of $[Co^{II}(PN)Cl_2]$ by showing three absorption bands at 570-700 nm with ε ranging from 250-450 $M^{-1}\,cm^{-1}$ (**Figure 2.37** and listed in the **Table 2.16**). A formation of the $[Co^{II}(PN)Cl_2]$ by dissolving the $[Co^{II}(PN)_2Cl_2]$ in these solvents was confirmed by displaying similar absorption bands to that of the independently synthesized $[Co^{II}(PN)Cl_2]$ as discussed in **section 2.5.4.2**. As a consequence, a loss of PN ligand from the bis-PN coordinated $[Co^{II}(PN)_2Cl_2]$ complex to generate the corresponding four-coordinated $Co(PN)Cl_2$ occurred in the solutions.

In contrast to these solvents, the complex in MeOH and water did not show three characteristic bands of the tetrahedral complex in the range from 590 to 700 nm. Thus, this evidence suggested that two Cl^- dissociated from the complex concomitant with replacement by one or

two of solvent molecule/s in MeOH or aqueous solution to form distorted octahedral complex: $[Co^{II}(PN)_2(Cl)(solv)]Cl$ or $[Co^{II}(PN)_2(solv)_2]Cl_2$ or 5-coordinated $[Co^{II}(PN)_2Cl]^+$ in MeOH. The two weak absorption bands around 480 (230 $M^{-1}\,cm^{-1}$) nm and 770 (98 $M^{-1}\,cm^{-1}$) nm were consistent with the Co^{2+} d-d transition of the monochloride derivative, $[Co^{II}(PN)_2Cl][PF_6]$, and the band at 480 nm corresponded to the distorted octahedral complex as reported in the literature.[251]

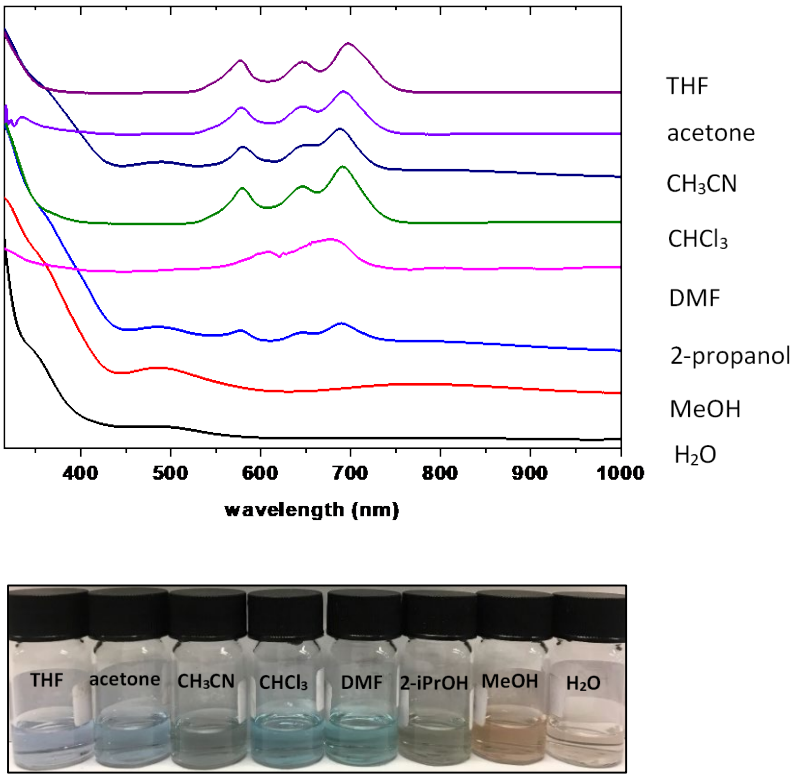

Figure 2.37. Absorption spectra of $[Co^{II}(PN)_2Cl_2]$ at concentrations 5.75x10^{-4} M in different solvents, inset showed different colour of the complex in each solution.

Moreover, the spectrum of this complex in CH_3CN and 2-propanol shows a group of three bands at 688, 650 and 580 nm and the two bands at 490 nm and 780 nm indicating a mixture of tetrahedral $[Co(PN)Cl_2]$ and five- or six-coordinated complexes $[Co^{II}(PN)_2(Cl)]Cl$, $[Co^{II}(PN)_2(Cl)(solv)]Cl$, and $[Co^{II}(PN)_2(solv)_2]Cl_2$. More specifically, the UV-Vis spectrum of the $[Co(PN)_2Cl_2]$ in MeCN suggested the mixture of tetrahedral $[Co(PN)Cl_2]$ and five- and/or six-coordinated complexes of $[Co^{II}(PN)_2Cl]Cl$, $[Co^{II}(PN)_2(Cl)(MeCN)]Cl$, $[Co^{II}(PN)_2(MeCN)_2]Cl_2$ as proposed in the **eq 2.13** to **eq 2.15.**

Dissociation of one P,N ligand from the dichloride complex resulted in the formation of the $[Co(PN)Cl_2]$ (**eq 2.13**). Moreover, this species could possibly be generated by P,N ligand loss from the five-coordinated $[Co^{II}(PN)_2Cl]Cl$ species to form $[Co(PN)Cl_2]$ in **eq 2.14** which was proposed based on similar evidence for the three characteristic bands (580 to 700 nm) observed in the spectrum of isolated $[Co^{II}$*cis*$-(PN)_2Cl][PF_6]$ in MeCN.

$$[Co^{II}(PN)_2Cl_2] \underset{}{\overset{-PN}{\rightleftharpoons}} [Co^{II}(PN)Cl_2] \qquad \textbf{eq 2.13}$$

$$[Co^{II}(PN)_2Cl_2] \underset{}{\overset{-Cl^-}{\rightleftharpoons}} [Co^{II}(PN)_2Cl]Cl \underset{+Cl^-}{\overset{-PN}{\rightleftharpoons}} [Co^{II}(PN)Cl_2] \qquad \textbf{eq 2.14}$$

$$[Co^{II}(PN)_2Cl_2] \underset{-Cl^-}{\rightleftharpoons} [Co^{II}(PN)_2(Cl)(MeCN)]^+ \underset{-Cl^-}{\rightleftharpoons} [Co^{II}(PN)_2(MeCN)]^{2+} \qquad \textbf{eq 2.15}$$

Additionally, the solution of this complex in H_2O, MeOH, 2-iPrOH and MeCN have bands around 310 and 350 nm with larger absorption coefficients indicating charge transfer or intraligand transitions of the cobalt(II) complex containing monodentate anionic ligand in CH_3CN solution reported in the literature.[252] The bands were tentatively assigned to be CT bands.

Table 2.16. UV/Vis absorption data of $[Co^{II}(PN)_2Cl_2]$ ($5.75x10^{-4}$ M) in different solvents.

solvents	**Wavelengths, nm (ε, M^{-1} cm^{-1})**
THF	577 (259.7), 647 (247.5), 697 (395.8)
acetone	578 (230.6), 647(240.4), 692 (358.9)
CH_3CN	310(1280), 350 (802.6) 487(141.6), 580 (261.3), 650 (278.0), 688 (408.0), 780 (79)
$CHCl_3$	320 (730.7), 579 (279.1), 646 (292.1), 691 (450.9)
DMF	320 (126.7), 608 (117.4), 678 (216.0)
2-propanol	308(1904), 486(209.2), 577(181.3), 647 (163.5), 690(237.0), 780 (96)
MeOH	310(1618), 484(229.4), 772(98.02)
H_2O	297 (2408), 342 (754.4), 483 (107.5)

The interaction of $[Co(PN)_2Cl_2]$ with Cl^- in MeCN showed similar UV-Vis spectral changes (**Figure A 2.40**) to that of $[Co^{II}(PN)_2(MeCN)]^{2+}$ solution upon adding Cl^-. These bands corresponded to the spectrum of isolated $[Co^{II}(PN)Cl_2]$ and $[Co^{II}(PN)_2(MeCN)]^{2+}$ with 2.2 equiv. Cl^- (**Figure A 2.41**) which suggested that this solution contained $[Co(PN)Cl_2]$ and $[Co^{II}(PN)_2(Cl)]^+$. Addition of a large excess of Cl^- to the solution of $[Co(PN)_2Cl_2]$ caused the complete decrease of bands at 480 and 800 nm (**Figure A 2.40, bottom**) and appearance of the characteristic bands of the $[CoCl_4]^{2-}$ at 610, 635, 665 and 695 nm (**Figure A 2.40, top**). This result supported complete formation of

$[CoCl_4]^{2-}$ by displacement of PN from all of the PN ligand-containing species to $[CoCl_4]^{2-}$ as proposed in **Scheme 2.3.**

The UV-Vis titration of $[Co(PN)_2Cl_2]$ with the P,N ligand in MeCN solution was performed to monitor the species involving PN ligand loss in the **eq 2.13** and **eq 2.14**. The addition of 10.0 equiv of the P,N ligand to the solution led to the enhancement of intensity at 490 nm and 780 nm (**Figure 2.38**) indicating generation of more five-coordinated $[Co(PN)_2Cl]^+$ (**eq 2.14**). However, residual absorption at 590 and 700 nm showed that $Co^{II}(PN)Cl_2$ could not be completely converted to the $[Co(PN)_2Cl]Cl$ (**Figure 2.38, red**).

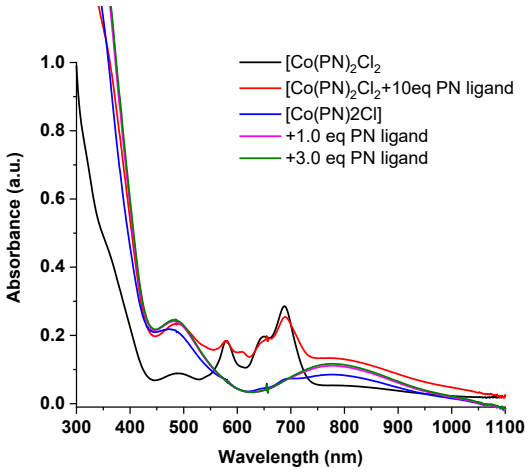

Figure 2.38. UV-Vis spectral change of the $[Co^{II}(PN)_2Cl_2]$($5.75x10^{-4}$ M, in CH_3CN) with adding a solution of the P,N ligand in MeCN (10.0 equiv), compared to the solution of the $[Co^{II}$*cis*-$(PN)_2Cl]^+$ with 1.0 equiv PN ligand (pink) and 3.0 equiv PN ligand (green).

In summary, the Co(II) chloride derivatives showed similar characteristic bands in the visible region at 480 and 780 nm and the bands ranging from 580-700 nm (**Figure 2.39**) which indicated the mixture of $[Co^{II}(PN)_2Cl]^+$, $[Co^{II}(PN)Cl_2]$ and $[Co^{II}(PN)_2(MeCN)]^{2+}$ in MeCN. The electronic spectrum obtained on dissolving dichloride $[Co(PN)_2Cl_2]$ complex displayed three characteristic bands (580, 650 and 688 nm in the visible region with ε = 140-400 M^{-1} cm^{-1}) of the tetrahedral $[Co(PN)Cl_2]$ by a dissociation of one PN ligand. The monochloride, $[Co^{II}$*cis*-$(PN)_2Cl][PF_6]$ complex in MeCN showed the two more intense bands centred at 480 and 780 nm which are consistent with d-d transitions in the 5-coordinated Co(II) species. This evidence suggested that the two P,N ligands are more likely to remain coordinated to the Co(II) centre in the complex containing one anionic Cl^- ligand and a weakly coordinating counterion. In contrast to these chloride analogues, $[Co^{II}(PN)_2(MeCN)]^{2+}$ displayed a CT band at 450 nm with larger ε (ε = 902 M^{-1} cm^{-1}). The charge transfer transition band was observed instead of d-d transition bands indicating that changing axial ligands from a labile Cl^- to a relatively strong coordinating MeCN ligand could

greatly affect the stability and electronic properties of the Co(II) complexes supported by bis P,N pyridine based ligands.

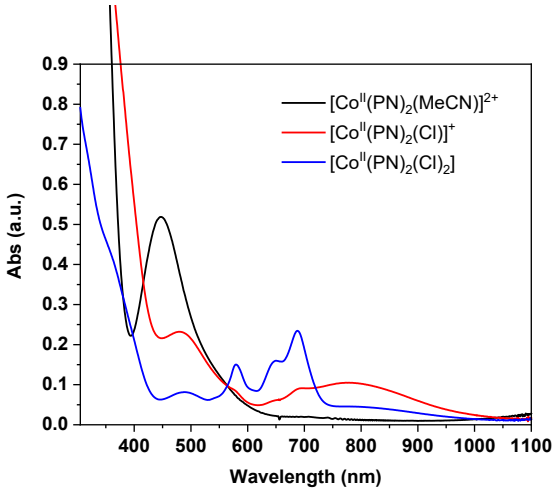

Figure 2.39. UV-Vis spectrum of the Co(II) chloride derivatives ($5.75x10^{-4}$ M, in CH_3CN) for the $[Co^{II}(PN)_2Cl_2]$, $[Co^{II}$*cis*-$(PN)_2Cl][PF_6]$ and the acetonitrile analogue, $[Co^{II}(PN)_2(MeCN)][BF_4]_2$.

UV/vis spectra of Co(III) complexes

The electronic properties of all cobalt(III) complexes such as the dichloro complex $[Co^{III}cis\text{-}(PN)_2Cl_2][PF_6]$ and the two hydride complexes of $[Co^{III}(PN)_2(H)(Cl)][PF_6]$ and $[Co^{III}(PN)_2(H)(MeCN)]^{2+}$ in MeCN solution were also investigated by UV-Vis spectroscopy as discussed below. Generally, the UV-Vis spectrum of all cobalt(III) complexes in this study showed only one absorption band in the visible region at maximum wavelength with molar absorptivity as listed in the **Table 2.17**. Octahedral low spin Co(III) complexes have a d^6 configuration leading to two d-d absorption bands in a perfect octahedron but split into 3 or more components in lower symmetry. For instance, $[Co(en)_2Cl_2]^+$ has bands at 617 (34), 455 (24) and 355 (57) nm with ε given in brackets (M^{-1} cm^{-1})[235] Charge transfer transitions are expected to have much higher absorption coefficients. Chlorine substituents can give rise to LMCT transitions while pyridine substituents are likely to give rise to MLCT transitions.

Table 2.17. UV/vis characterization data of cobalt (III) complexes in acetonitrile solution.

complex	[complex]/M	λ_{max} /nm (ε /M^{-1} cm^{-1})	Assigned band
$[Co^{III}cis\text{-}(PN)_2Cl_2][PF_6]$	$5.75x10^{-4}$	370 (3292)	L or CT
		450 (281),645 (226)	d-d transition
$[Co^{III}(PN)_2(H)(Cl)][PF_6]$	$1.50x10^{-4}$	450 (2,200)	CT
$[Co^{III}(PN)_2(H)(MeCN)][PF_6]_2$	$5.75x10^{-4}$	413 (1,640)	CT
$[Co^{III}(N4Py(X)]^{2+}$ [252]	$1.0x10^{-3}$	496 (877), X=N_3^- 504 (1,140), X=NCS^-	CT

2.5.4.4 UV-Vis absorption properties of $[Co^{III}cis\text{-}(PN)_2Cl_2][PF_6]$

The UV-Vis spectrum (**Figure 2.40**) of $[Co^{III}cis\text{-}(PN)_2Cl_2]^+$ solution in MeCN ($5.75x10^{-4}$ M) suggested a distorted octahedral structure by displaying two d-d transition bands at λ_{max} = 645 nm with ε = 226 $M^{-1}cm^{-1}$ and another band at 450 nm (281 $M^{-1}cm^{-1}$). The latter d-d transition to high energy level band appeared as shoulder which might overlap with CT band at 370 nm (3290 M^{-1} cm^{-1}). These d-d transitions at 645 nm and 450 nm were respectively assigned to $^1T_{1g}$ <- $^1A_{1g}$ and $^1T_{2g}$ <- $^1A_{1g}$, which are typical for d^6.low-spin cobalt(III) complexes. The absorption spectrum of this complex is consistent to the d-d bands (370-540 nm) observed for the $[Co^{III}(N_4Py)X]^+$ cation, where X = MeCN, Cl^- and Br^- with ε value ranging from 200-300 $M^{-1}cm^{-1}$.[252] Moreover, it also agrees with the apparent of two d-d transitions (at 530 and 330 nm) of the hexacoordinated Co(III) complex for $[Co^{III}(L)(N_3)_2]^+$, L = N,N′ -(bis(pyridine-2-yl)benzylidene)-1,4-butanediamine showing a pseudo-octahedral complex reported in the literature.[235, 253]

Moreover, the $[Co^{III}cis\text{-}(PN)_2Cl_2][PF_6]$ as a green powder did not show a colour change between the solid state and solution upon dissolving in different solvents including MeCN, MeOH, $CHCl_3$

and DMSO. This supported that this complex is stable in these solution with no ligand exchange. Accordingly, the UV-Vis spectrum of a solution of $[Co^{III}$*cis*-$(PN)_2Cl_2]^+$ in MeCN indicated that the two P,N ligands and two axial Cl^- ligand stay coordinated at the Co(III) metal center to obtain six-coordinated cation in the solution. This is in contrast to the UV-Vis characterisation of the corresponding 5-coordinated $[Co^{II}$*cis*-$(PN)_2Cl]^+$ and 6-coordinated $[Co^{II}(PN)_2Cl_2]$ in a MeCN solution, these two Co(II) complexes showed the d-d transitions that are attributed to the pseudo-tetrahedral $[Co^{II}(PN)Cl_2]$ formed in the solution by a ligand exchange reaction as discussed in **section 2.5.4.2**.

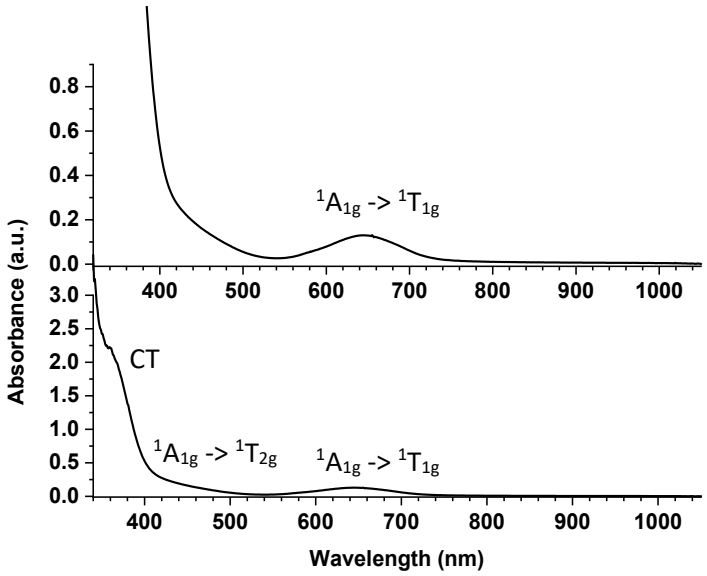

Figure 2.40. UV-Vis spectrum of the $[Co^{III}$*cis*-$(PN)_2Cl_2][PF_6]$ complex ($5.75x10^{-4}$ M) in CH_3CN.

2.5.4.5 UV-Vis absorption properties of $[Co^{III}(PN)_2(H)(Cl)][PF_6]$

The UV-Vis spectrum of $[Co^{III}(PN)_2(H)(Cl)]PF_6$ ($1.5x10^{-4}$ M) in CH_3CN (**Figure 2.41**, black) showed intense absorption bands below 300 nm attributed to ligand-centred transitions, and a band in visible region displaying maximum absorption at λ = 450 nm with molar absorptivity (ε) 2,200 M^{-1} cm^{-1}. This band was tentatively assigned as a charge transfer (CT) transition involving the Co(III) and pyridine ligands as a consequence of higher molar absorptivity compared to that of a forbidden d-d transition for the corresponding Co(III) dichloride complex. This characteristic band was also observed in the visible absorption band of a family of $[Co^{III}(N4Py(X)]^{n+}$, as generally evidenced in d^6 low-spin cobalt(III) complexes.[252]

2.5.4.6 UV-Vis absorption properties of $[Co^{III}(PN)_2(H)(MeCN)][PF_6]_2$

The UV-Vis absorption band of $[Co^{III}(PN)_2(H)(MeCN)]^{2+}$ solution in MeCN (**Figure 2.41**, red) appeared at λ_{max} = 413 nm with ε = 1640 M^{-1} cm^{-1} which was similarly assigned as CT band to that of the corresponding chloro Co(III) hydride complex based on the comparison of molar coefficient value to the dichloride Co(III) analogue. Interestingly, a change of the axial ligand

trans to the hydride from Cl^- to a relative strong field MeCN ligand led to a blue shift by 37 nm from λ_{max} 450 nm of the $[Co^{III}(PN)_2(H)(Cl)][PF_6]$ complex

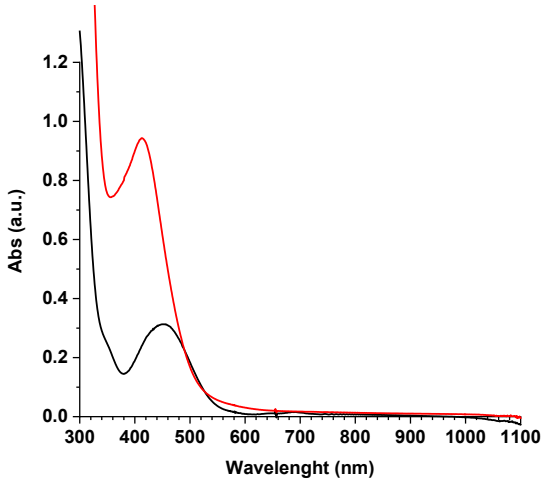

Figure 2.41. The absorption spectrum of the $[Co^{III}(PN)_2(H)(Cl)][PF_6]$ complex ($1.5x10^{-4}$ M), black compared to the spectrum of $[Co^{III}(PN)_2(H)(MeCN)][PF_6]_2$ complex ($5.75x10^{-4}$ M) in MeCN solution.

2.5.4.7 Emission properties of $[Co^{III}(PN)_2(H)(Cl)]PF_6$ complex

The excited state properties of, $[Co^{III}(PN)_2(H)(Cl)]PF_6$, were then investigated, and the steady state emission spectrum of the complex ($1.15x10^{-4}$ M) in CH_3CN was recorded upon excitation at λ_{max} 450 nm. Compared to the absorption properties of the cobalt (III) dihydride, $[Co^{III}$(2,2'-bipy)$(PEt_2Ph)_2H_2][PF_6]$ supported with 2,2'-bipyridine ligand, the UV-Vis spectrum of $[Co^{III}(PN)_2(H)(Cl)]PF_6$ complex showed the band at similar wavelength (450 nm) and molar absorptivity (**Figure 2.42** a). However, the emission band at λ 520 nm for $[Co^{III}(PN)_2(H)(Cl)]PF_6$ is much weaker intensity compared to the band of $[Co^{III}$(2,2'-bipy)$(PEt_2Ph)_2H_2][PF_6]$ upon excitation at maximum absorption wavelength (345 nm) as shown in **Figure 2.42** b. This result indicated that 2,2'-bipyridine moiety plays a significant role in an emission property of the cobalt(III) hydride complex. Substituting it with a pyridine ring resulted in a decrease in emission intensity as observed in the complex $[Co^{III}(PN)_2(H)(Cl)]PF_6$.

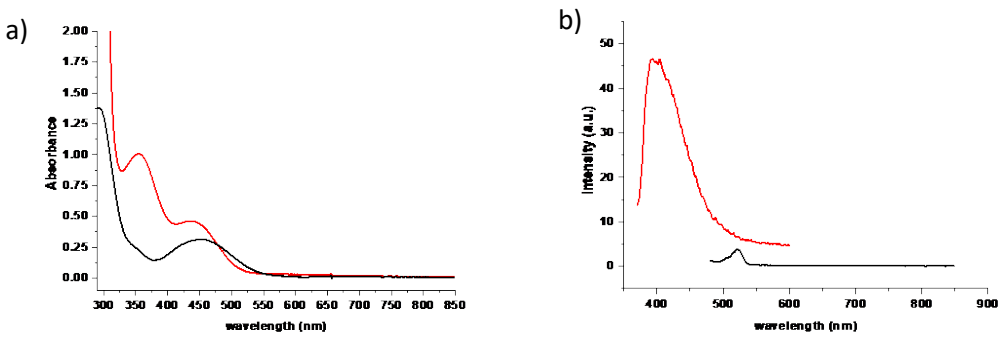

Figure 2.42. Absorption spectra of $[Co^{III}$(2,2'-bipy)$(PEt_2Ph)_2H_2][PF_6]$, (a), red curve and $[Co^{III}(PN)_2(H)(Cl)]PF_6$ ($1.5x10^{-4}$ M) in CH_3CN (black curve), overlay of emission spectra of $[Co^{III}$(2,2'-bipy)$(PEt_2Ph)_2H_2][PF_6]$ ($1.15x10^{-4}$ M), in MeOH at λ_{ex} 345 nm (b, red curve) and $[Co^{III}(PN)_2(H)(Cl)]PF_6$ ($1.15x10^{-4}$ M) in CH_3CN at λ_{ex} 450 nm (black curve).

Because of the lack of emission properties upon excitation of the complex $[Co^{III}(PN)_2(H)(Cl)]PF_6$ at 450 nm in CH_3CN, photochemical properties of this complex in a solution were not investigated further. This led us to start investigating its electrochemical properties in CH_3CN containing 0.1 M tetrabutylammonium hexafluorophosphate ($TBAPF_6$) solution.

2.5.5 Electrochemical properties

Electrochemical characterization of the complexes in this series by cyclic voltammetry (CV) are summarized in **Table 2.18.**

Table 2.18. Electrochemical characterization data of for all cobalt complexes (1mM) in acetonitrile solution containing 0.1M $TBAPF_6$.

complex	$E_{1/2}$/V (ΔE_p, mV)			E_{pc}/V		
	$Co^{III/II}$	$Co^{II/I}$	($Co^{III/II}$-H)	$Co^{I/0}$ or $Co^{I}(L^{\bullet-})$	($Co^{III/II}$-H)	($Co^{II/I}$-H)
$[Co^{II}(PN)_2(MeCN)][BF_4]_2$	-	-1.08 (70)	-	-2.28	-	-
$[Co^{II}$*cis*-$(PN)_2Cl][PF_6]$	-0.12 (109)	-1.2 E_{pa} =-0.15		-2.27		
$[Co^{II}(PN)_2Cl_2]$	-0.40 (150)	-1.32 (143)	-	-2.11	-	-
$[Co^{III}$*cis*-$(PN)_2Cl_2][PF_6]$	-0.42 (146)	-1.30 (110)	-	-2.14	-	-
$[Co^{III}(PN)_2(H)(Cl)][PF_6]$	-	-	-	-	-1.48	-2.02
$[Co^{III}(PN)_2(H)(MeCN)][PF_6]_2$	-	-	-1.10 (110)	-	-	-1.95

2.5.5.1 CV characterisation of $[Co^{II}(PN)_2(MeCN)][BF_4]_2$

The cyclic voltammogram of $[Co^{II}(PN)_2(MeCN)][BF_4]$ was recorded in CH_3CN solution containing 0.1 M $TBAPF_6$. Upon scanning to more negative potential, it showed two reduction processes by exhibiting a fully reversible Co(II/I) wave at $E_{1/2}$ =-1.08 V (ΔE_p=70 mV) and an irreversible wave at E_{pc} = -2.08 (**Figure 2.43** a). The first reversible redox wave was assigned to the Co(II/I) and the latter reduction process at more negative potential was tentatively assigned to the Co(I/0) couple or possibly a ligand-centred reduction of $Co(I)L^{\bullet-}$ couple. Upon scanning to more positive potential, the oxidation peak at + 0.5 V was observed which possibly attributed to the oxidation of PN ligand in the complex or may be Co(III/II) wave (**Figure 2.43** b).

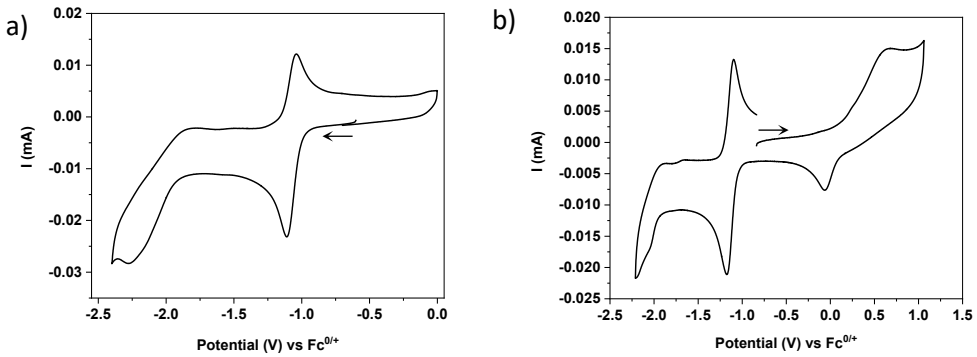

Figure 2.43. Cyclic voltammogram of $[Co^{II}(PN)_2(MeCN)][BF_4]_2$ (1 mM) in CH_3CN with 0.1 M $TBAPF_6$ at scan rate 100 mV s^{-1} (a), scanning to more positive potential (b).

The cathodic and anodic peak currents for the Co(II/I) redox wave in the $[Co^{II}(PN)_2(MeCN)][BF_4]_2$ complex increased linearly with the scan rate $v^{1/2}$ indicating diffusion control (**Figure 2.44**).

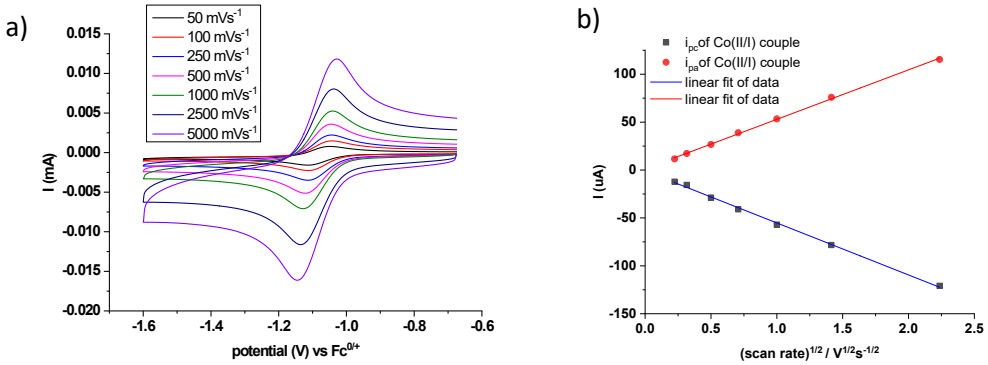

Figure 2.44. Cyclic voltammograms of $[Co^{II}(PN)_2(MeCN)][BF_4]_2$ (1mM) in CH_3CN with 0.1 M $TBAPF_6$ at various scan rates (a) plot of i_{pc} and i_{pa} of Co(II/I) couple versus square root of scan rates (b).

2.5.5.2 CV characterisation of $[Co^{II}cis\text{-}(PN)_2Cl][PF_6]$

The CVs of the monochloride cationic analogue is shown in **Figure 2.45**. The Co(II/I) wave was quasi-reversible and seemed to overlap with another redox wave. According to the characteristic bands in the UV-Vis spectrum of this complex in MeCN solution, there are possible species including $[Co^{II}(PN)_2Cl]^+$, $[Co^{II}(PN)Cl_2]$ and $[Co^{II}(PN)_2(MeCN)]^{2+}$ could be formed in MeCN. Therefore, the overlapping waves were assigned to the Co(II/I) couple in the monocationic $[Co^{II}(PN)_2Cl]^+$ species and the dicationic $[Co^{II}(PN)_2(MeCN)]^{2+}$. The E_{pa} of the Co(II/I) couples in the complex lie close to the E_{pa} of Co(II/I) couple in the independently synthesized $[Co^{II}(PN)_2(MeCN)]^{2+}$ under similar conditions. The reduction process at the most negative potential was assigned to the Co(I/0) or ligand-centred reduction in these Co(II) species which appeared at a similar potential to those of all Co(II) complexes in this study. Additionally, the quasi-reversible Co(III/II) couple was observed at $E_{1/2}$ = -0.12 V (ΔE_p=109 mV) upon scanning to

more positive potential indicating a chemical reaction coupled to one-electron transfer of the Co(III/II) couple in the $[Co^{II}(PN)_2Cl]^+$. Scan rate variation through the Co(II/I) couple showed that peak currents are dependent on the square root of scan rate ($v^{1/2}$) between 0.01 V s^{-1} and 5.0 V s^{-1} **Figure 2.45** c). This result indicated diffusion control of the complex.

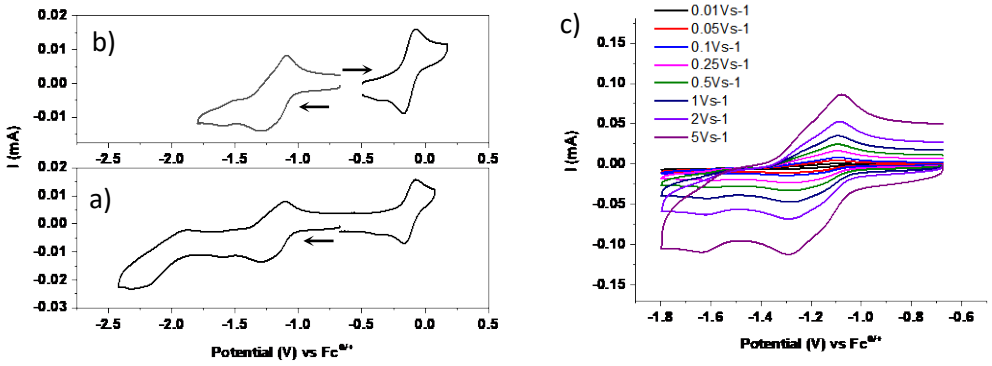

Figure 2.45. Cyclic voltammogram of $[Co^{II}$*cis*$-(PN)_2(Cl)][PF_6]$ (1 mM) in CH_3CN with 0.1 M $TBAPF_6$ (a), the CV of the complex by scanning through the Co(II/I) and the Co(III/II) couple at scan rate 100 mV s^{-1} (b), CVs of the Co(II/II) couple in the complex at various scan rates (c) .

Moreover, the CV of this complex in the presence of 2.0 equiv. of the P,N ligand showed more reversible wave of Co(II/I) redox couple at -1.24 V (ΔE_p = 167) and the disappearance of the small couple at more negative potential (**Figure 2.46**). It suggested a formation of the $[Co(PN)_2Cl]^+$ as a major species in the solution mixture upon adding extra equivalent of P,N ligand to the solution. From the UV-Vis studies (**section 2.5.4.2**), the addition of P,N ligand to the solution of $[Co(PN)_2Cl]^+$ in MeCN caused the disappearance of the bands (580-690 nm) concomitant with the enhancement of the two bands at 490 and 780 nm (**Figure 2.36**). This evidence supported the conversion of $[Co(PN)Cl_2]$ or possible 4-coordinated species in the mixture solution to the five-coordinated $[Co(PN)_2Cl]^+$ under the conditions for CV measurement.

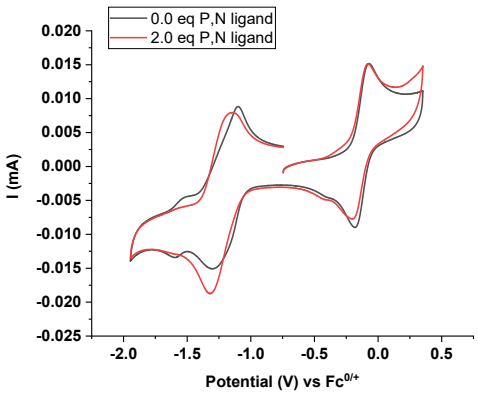

Figure 2.46. Cyclic voltammograms of $[Co^{II}$*cis*$-(PN)_2Cl][PF_6]$ (1mM) in CH_3CN with 0.1 M $TBAPF_6$ and the CV of this solution with 2.0 equiv of the P,N ligand at scan rate 100 mV s^{-1}.

2.5.5.3 CV characterisation of $[Co^{II}(PN)_2Cl_2]$

The CV of $[Co^{II}(PN)_2Cl_2]$ (**Figure 2.47** a) showed three main redox waves as listed in the **Table 2.18**. The first quasi-redox couple at -0.42 V with ΔE_p = 146 mV and the second quasi-reversible wave at -1.32 V (ΔE_p = 143 mV) was assigned to a metal-centred reduction of the Co(III/II) and Co(II/I) couple, respectively. Another irreversible reduction process at E_{pc} = -2.11 V was then assigned to be a redox Co(I/0) couple or possibly a ligand-centred reduction of $Co(I)L^{\bullet-}$ couple. Scan rate variation through the metal-centred reduction of the Co(II/I) couple showed that peak currents are linearly dependent on the square root of scan rate ($v^{1/2}$) between 0.05 V s^{-1} and 5.0 V s^{-1} (**Figure 2.47** b and c). This result indicated diffusion control of the complex from the bulk solution to the surface of working electrode.

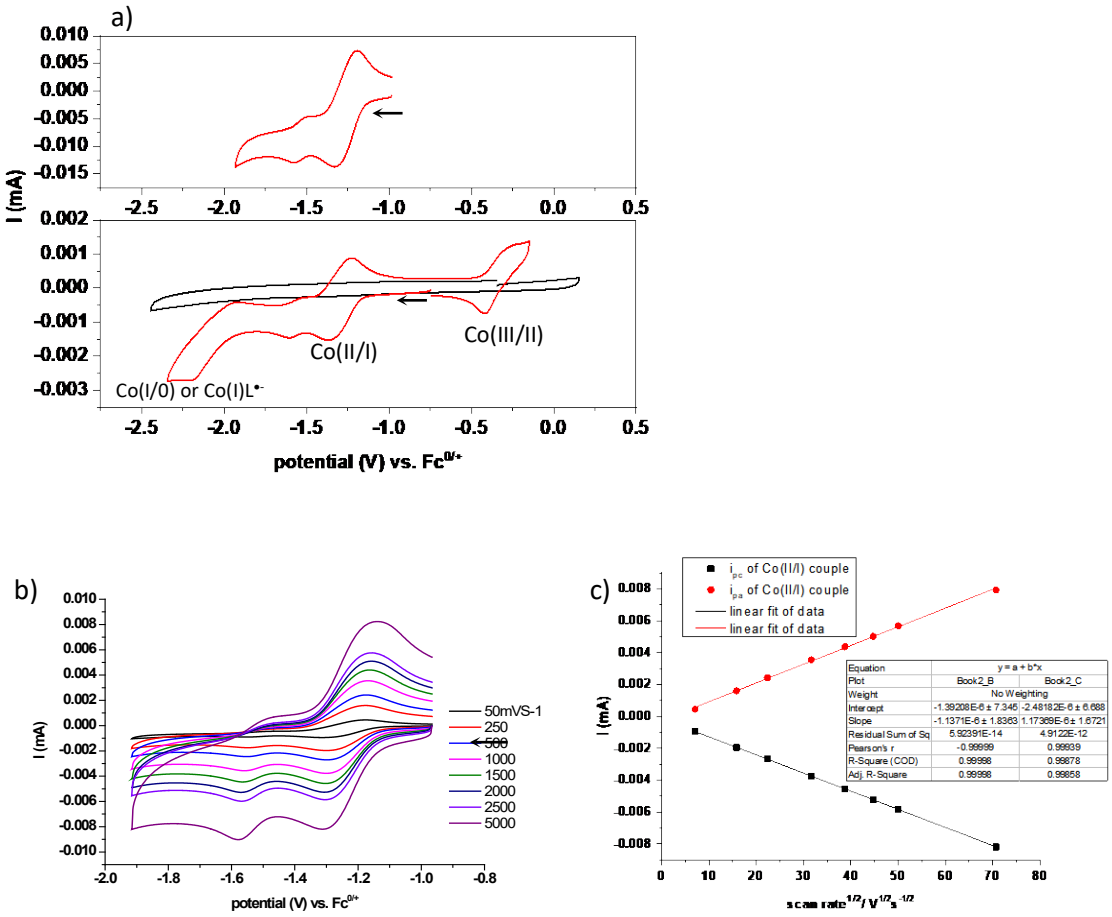

Figure 2.47. Cyclic voltammogram of $[Co^{II}(PN)_2Cl_2]$ (1 mM) in CH_3CN with 0.1 M $TBAPF_6$ and the CV of the complex by scanning through the Co(II/I) couple at scan rate 100 mV s^{-1} (a). The CVs of this complex at various scan rates (b) plot of i_{pc} and i_{pa} of Co(II/I) couple versus square root of scan rates (c).

From the UV-Vis studies (**section2.5.4.3**, **Figure 2.37**), a solution of the $[Co^{II}(PN)_2Cl_2]$ generated a mixture of species in the MeCN solution including the pseudo-tetrahedral $[Co^{II}(PN)Cl_2]$ with the bands at 580, 650 and 688 nm. Therefore, these three main features possibly attributed to

the redox events in the in $[Co^{II}(PN)Cl_2]$ or might be those in other possible Co(II) species formed in the solution. The other possible Co(II) species could be $[Co^{II}(PN)_2Cl]Cl$ and/or $[Co^{II}(PN)_2Cl(MeCN)]Cl$ formed by a Cl^- loss from the $[Co^{II}(PN)_2Cl_2]$ as proposed in **eq 2.14** and **eq 2.15**. A free Cl^- ion in the solution was supported by the oxidation peak of Cl^- in the CV of the $[Co^{II}(PN)_2Cl_2]$ as discussed below.

Evidence of Cl^- loss from the $[Co^{II}(PN)_2Cl_2]$ in MeCN solution by CV studies

Scanning to more positive potential (**Figure 2.48** a, black curve), an oxidation peak at +0.87 V was observed which is in agreement with the oxidation of free Cl^- in a solution.[254] According to this result, it supported the postulate that one chloride ligand could dissociate from the complex to upon dissolving the $[Co^{II}(PN)_2Cl_2]$ in MeCN solution to form $[Co^{II}(PN)_2Cl]^+$ and/or $[Co^{II}(PN)_2Cl(MeCN)]^+$. The addition of TBACl (10 equiv.) to this solution resulted in a shift to more negative potentials in the redox wave of the Co(II/I) couple by 100 mV (from -1.4 V to -1.5 V) as shown in **Figure 2.48** b, red curve. The more negative shift and irreversibility of the Co(II/I) couple were observed by adding 35 equiv. TBACl to the solution. It indicated that new species bearing more anionic Cl^- could possibly be a mixture of the tetrahedral $[Co^{II}(PN)Cl_2]$ and $[CoCl_4]^{2-}$ formed in the solution (**eq 2.16**). Consequently, the changes in Co(II/I) redox couple are consistent with the UV-Vis spectral changes (**Figure A 2.40**) upon titration of the $[Co(PN)_2Cl_2]$ with Cl^- in MeCN.

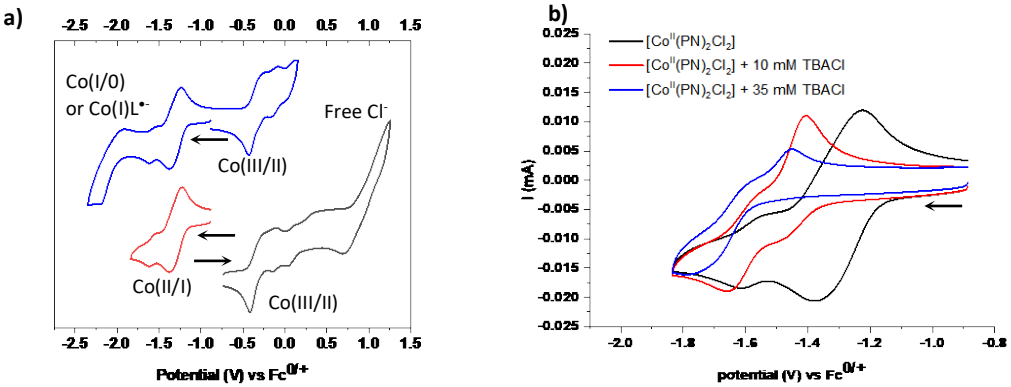

Figure 2.48. Cyclic voltammograms (a) of $[Co^{II}(PN)_2Cl_2]$ (1mM) in CH_3CN with 0.1 M $TBAPF_6$ at 100 mV s^{-1} at different scanning potential windows. CVs of the Co(II/I) couple (b) in this complex (1 mM) upon adding different equiv. of TBACl.

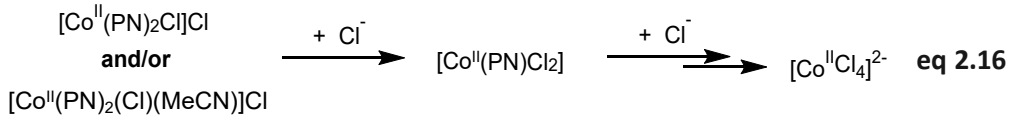

eq 2.16

Furthermore, the CV titration of $[Co(PN)_2Cl_2]$ in MeCN with a solution of the PN ligand (10.0 equiv) suggested formation of the corresponding $[Co(PN)_2Cl]^+$ and/or $[Co^{II}(PN)_2(Cl)(MeCN)]Cl$ by showing the increases of current at Co(II/I) redox couple concomitant with the disappearance of the small couple (**Figure 2.49** a). This result was consistent with the UV-Vis spectral changes (**Figure 2.38**) upon adding PN ligand to the solution of the $[Co(PN)_2Cl_2]$ suggesting the partial conversion to the $[Co(PN)_2Cl]^+$. The release of Cl^- ligands from the $[Co^{II}(PN)_2Cl_2]$ in MeCN solution was also investigated by CVs titration of this complex in MeCN solution with water (**Figure 2.49** b).

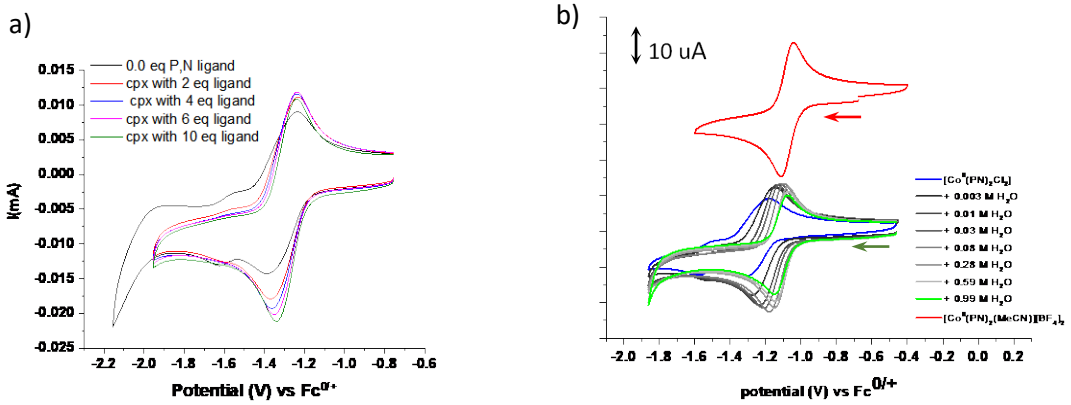

Figure 2.49. Cyclic voltammograms of $[Co^{II}(PN)_2Cl_2]$ (1mM), showing redox wave of Co(II/I), upon titration with the P,N ligand (a).and CV titration of this complex with water (b) in CH_3CN with 0.1 M $TBAPF_6$ at 100 mV s^{-1}. The CV of independently synthesized $[Co^{II}(PN)_2(MeCN)][BF_4]_2$ complex in CH_3CN with 0.1 M $TBAPF_6$ (b, red curve).

CVs titration of $[Co^{II}(PN)_2Cl_2]$ with H_2O in MeCN solution containing 0.1M $TBAPF_6$

The gradual addition of water up to 0.99 M (**Figure 2.49** b) resulted in a more positive shift of the Co(II/I) redox couple by 177 mV concomitant with formation of a fully reversible wave indicating Cl^- loss from $[Co^{II}(PN)_2Cl]^+$ to generate dicationic $[Co^{II}(PN)_2(H_2O)_2]^+$ by adding an excess of water. Moreover, the redox couple of Co(II/I) became more reversible as shown by decreasing peak-to-peak separations (ΔE_p) from 143mV to 73 mV (**Table 2.19)**. Upon titration with water, the Co(II/I) redox couple shifted to more positive potential and is near to the Co(II/I) couple in the $[Co^{II}(PN)_2(MeCN)]^{2+}$ (**Figure 2.49** b, red curve). The result supported the assumption that a Cl^- in the $[Co^{II}(PN)_2Cl]^+$ was replaced by H_2O molecules leading to the formation of

$[Co^{II}(PN)_2(H_2O)_2]^{2+}$ species. The $E_{1/2}$ value and peak-to-peak separation (ΔE_p =73 mV) of the Co(II/I) couple is close to the Co(II/I) wave in the separately synthesized dicationic $[Co^{II}(PN)_2(MeCN)]^{2+}$ complex and also the ΔE_p of Fc $^{0/+}$ couple (76 mV). This result confirmed a fully reversible one-electron transfer to the $[Co^{II}(PN)_2(H_2O)_2]^{2+}$ with no following chemical reaction and also demonstrated that the dicationic $[Co^{II}(PN)_2(H_2O)_2]^{2+}$ and $[Co^{II}(PN)_2(MeCN)]^{2+}$ with no Cl^- ligand displayed reversible redox chemistry for one-electron reduction.

Table 2.19. The values for ΔE and the ratio of i_{pc} to i_{pa} of $[Co^{II}(PN)_2Cl_2]$ complex (1 mM) in CH_3CN with 0.1 M $TBAPF_6$ upon titration with water.

V_{H2O}/µl	$[H_2O]$/M	E_{pc}/V	E_{pa}/V	ΔE/mV	i_{pc}/i_{pa}
0	0.000	-1.196	-1.053	143	0.97
50	0.003	-1.137	-1.034	103	1.03
100	0.01	-1.104	-1.002	102	1.02
150	0.03	-1.079	-0.987	92	1.06
250	0.08	-1.049	-0.963	86	1.08
500	0.28	-1.020	-0.943	77	1.14
750	0.59	-1.017	-0.942	75	1.16
1000	0.99	-1.019	-0.946	73	1.12
$[Co^{II}(PN)_2(MeCN)]^{2+}$		-1.110	-1.040	70	1.08

$\Delta E_p(Fc^{0/+})$ = 76 mV, i_{pc}/i_{pa} = 0.92, ΔE_p of 2-MeCN complex = 70 mV, i_{pc}/i_{pa} = 1.08

In conclusion, the CV of the Co(II) complexes in this study in acetonitrile solution with 0.1 M $TBAPF_6$ was shown in **Figure 2.50**. The acetonitrile derivative exhibited a fully reversible Co(II/I) redox couple at $E_{1/2}$ = -1.08 V with ΔE_p = 70 mV suggesting one-electron transfer reaction with no following chemical reaction. This value was similar to the peak-to-peak separation of ferrocene/ferrocenium redox couple (ΔE_p = 76 mV) which was added as internal reference in the same solution. The redox chemistry of ferrocene is well-known to exhibit a fully reversible one-electron redox couple. This evidence indicated that no ligand loss from the $[Co^{II}(PN)_2(MeCN)]^{2+}$ complex occurred following one electron reduction. In contrast to the redox behaviour of this complex, the cobalt(II) chloride analogue for $[Co^{II}$*cis*-$(PN)_2Cl][PF_6]$ exhibited the quasi-reversible Co(II/I) redox couple appeared around -1.3 V with peak-to-peak separation (ΔE_p > 70 mV). The two waves of Co(II/I) couple at -1.3 V seemed to overlap. Therefore, these two overlapping couples were assigned to the Co(II/I) wave in the $[Co^{II}(PN)_2Cl][PF_6]$ and /or $[Co^{II}(PN)_2(MeCN)]^{2+}$. The Co(II/I) couple in these species is related to the quasi-reversible Co(III/II) and irreversible Co(I/0) or ligand-centred reduction at -0.12 V and -2.27 V, respectively.

In the case of the dichloro $[Co^{II}(PN)_2Cl_2]$ complex, the three main waves were tentatively assigned to the Co(III/II) couple at the most positive potential, the following Co(II/I) couple and the redox Co(I/0) couple or ligand-centred reduction of $Co(I)L^{\bullet-}$ couple. However, these redox events could not be assigned to a certain species because the $[Co^{II}(PN)_2Cl_2]$ generated a mixture of species in a studied by the UV-Vis experiments (**section 2.5.4.3**). Moreover, the quasi-reversible Co(III/II) wave was observed between -0.4 and -0.15 V in the CV of the $[Co^{II}$*cis*-$(PN)_2Cl][PF_6]$ and $[Co^{II}(PN)Cl_2]$, but there was no redox Co(III/II) couple for the $Co^{II}(PN)_2(MeCN)][BF_4]_2$ in the same potential window. It indicated that this complex is harder to oxidize although there is evidence of metal reduction at ca. 0 V. This evidence demonstrated that the chloride ligand in the complex of this series is labile but greatly decreases the Co(III/(II) potential. Moreover, the quasi-reversible Co(II/I) and Co(III/II) redox couple in the $[Co^{II}$cis-$(PN)_2Cl][PF_6]$ or $[Co^{II}(PN)_2Cl]^+$ or $[Co(PN)Cl_2]$ suggested the occurrence of a chemical reaction after one electron transfer (EC mechanism).

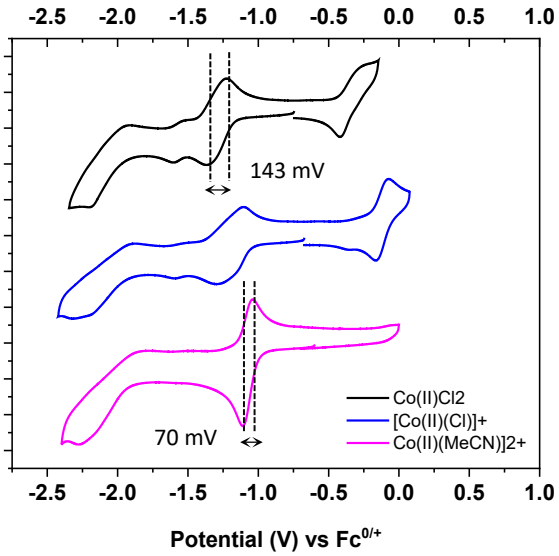

Figure 2.50. Cyclic voltammograms of the Co(II) derivatives (1 mM) in CH_3CN containing 0.1 M $TBAPF_6$ at the scan rate 100 mV/s for the $[Co^{II}(PN)_2Cl_2]$, $[Co^{II}$*cis*-$(PN)_2Cl][PF_6]$ and the acetonitrile analogue, $[Co^{II}(PN)_2(MeCN)][BF_4]_2$.

The redox properties of the Co(III) complexes in this series including dichloro Co(III) complex, $[Co^{III}$*cis*-$(PN)_2Cl_2][PF_6]$ and the Co(III) hydride complexes: $[Co^{III}(H)(Cl)][PF_6]$ and $[Co^{III}(H)(MeCN)][PF_6]_2$ in CH_3CN with 0.1M $TBAPF_6$ were then investigated by CV measurement.

2.5.5.4 CV characterisation of $[Co^{III}$cis-$(PN)_2Cl_2][PF_6]$ complex

In the case of the dichloro cobalt(III) analogue, the CV measurement of $[Co^{III}$*cis*-$(PN)_2Cl_2]PF_6$ in MeCN (**Figure 2.51**) showed the same redox processes as those for the corresponding dichloro cobalt(II) complex, $[Co^{II}(PN)_2Cl_2]$ under similar conditions. The quasi-reversible Co(III/II) and Co(II/I) redox couples appeared at -0.32 V and -1.30 V and the irreversible wave at the most negative reduction potential of -2.14 V was assigned as a Co(I/0) couple or ligand-centred reduction of $Co(I)L^{\bullet-}$. Plotting peak currents (cathodic and anodic currents) of the Co(III/II) redox wave vs $\sqrt{\nu}$, (**Figure 2.51** c) showed the linear dependence indicating diffusion control of the complex from bulk solution to the electrode surface.

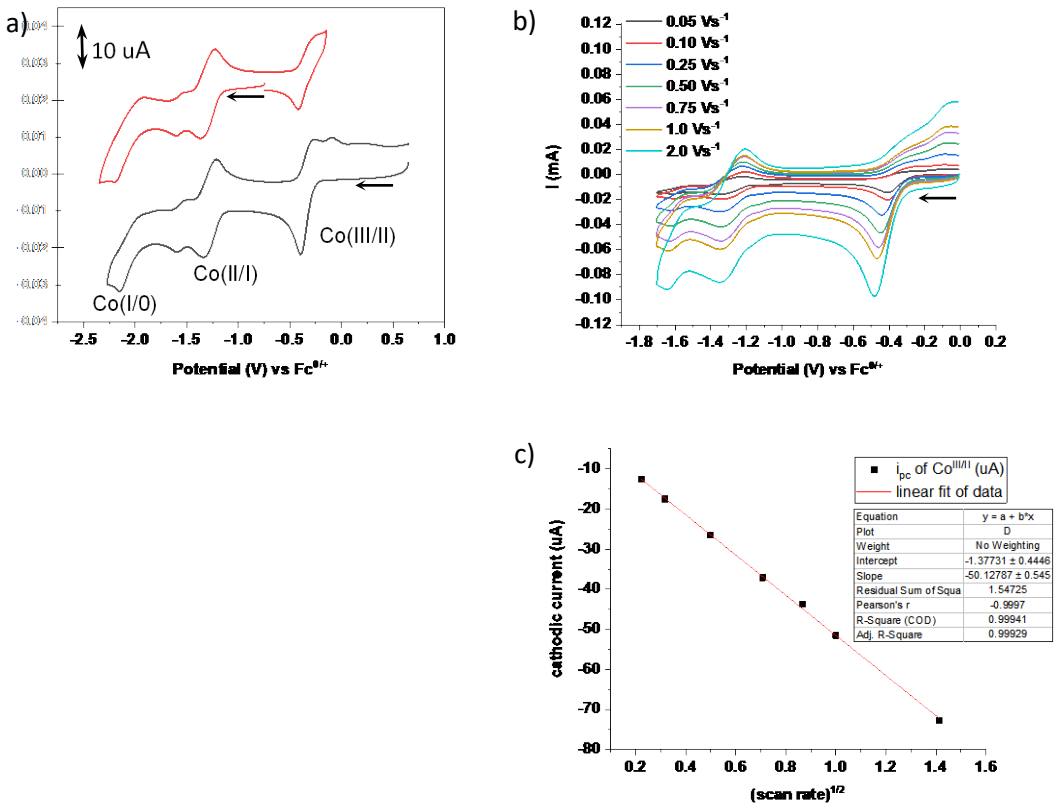

Figure 2.51. Cyclic voltammograms of $[Co^{III}$*cis*-$(PN)_2Cl_2][PF_6]$ complex (1 mM) in CH_3CN containing 0.1 M $TBAPF_6$ at the scan rate 100 mV s^{-1}, black curve compared to the CV of $[Co^{II}(PN)_2Cl_2]$ complex, red curve (a).The CVs of the $[Co^{III}$*cis*-$(PN)_2Cl_2][PF_6]$ with the scan rate between 0.05-2.0 Vs^{-1} (b), plot of i_{pc} of Co(III/II) couple in the CVs of the complex versus square root of scan rates (c).

Moreover, the large peak-to-peak separation (ΔE_p value) of 146 mV for Co(III/II) and 110 mV for Co(II/I) redox couples suggested a chemical reaction. Therefore, the one-electron transfer followed by a chemical reaction (EC mechanism) was assumed for the Co(II/I) in **Scheme 2.4** and the Co(III/II) couple in the $[Co^{III}$*cis*$-(PN)_2Cl_2]^+$ species at -0.32 V (**Scheme 2.5**).

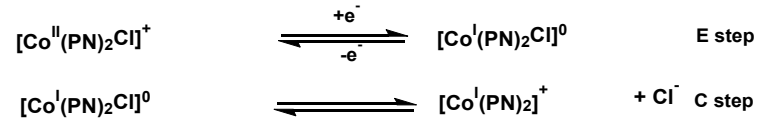

Scheme 2.4. Proposed EC mechanism for an electrochemical reduction of the $[Co^{III}$*cis*$-(PN)_2Cl_2][PF_6]$ complex in acetonitrile solution at -1.30 V for Co(II/I) redox couple.

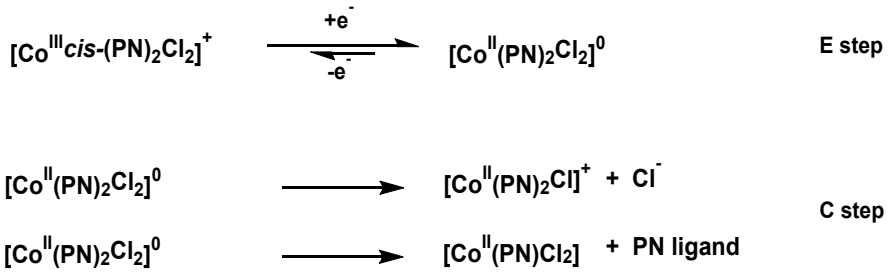

Scheme 2.5. Possible chemical reactions of the reduced $[Co^{II}(PN)_2Cl_2]$ following one-electron reduction of the $[Co^{III}$cis$-(PN)_2Cl_2][PF_6]$ in MeCN at -0.32 V (E_qC_i mechanism).

As shown above, the first reduction process (E step) at Co(III/II) redox couple in the $[Co^{III}$*cis*$-(PN)_2Cl_2][PF_6]$ complex generated the reduced $[Co^{II}(PN)_2Cl_2]$ species prior to a dissociation of coordinated Cl^- ligand and P,N ligand (C step). The UV-Vis characterisation of the independently synthesized $[Co^{II}(PN)_2Cl_2]$ suggested a mixture of $[Co(PN)_2Cl]Cl$ and $[Co(PN)Cl_2]$ species (**section 2.5.4.3**). Therefore, chemical reactions following one-electron reduction of $[Co^{III}(PN)_2Cl_2]^+$ to $[Co^{II}(PN)_2Cl_2]$ would generate $[Co(PN)_2Cl]Cl$ by a release of one chloride and $[Co(PN)Cl_2]$ via a dissociation of P,N ligand.

To support an EC mechanism of Co(III/II) couple by one-electron reduction of the $[Co^{II}$*cis*$-^{I}(PN)_2Cl_2]^+$ species, variation of scan rate of the complex was then performed.

Electrochemical reaction mechanism of $[Co^{III}cis\text{-}(PN)_2Cl_2][PF_6]$

Heterogeneous electron transfer coupled with chemical reaction (EC mechanism)

For an E_rC_i mechanism, an ideal reversible one-electron transfer reaction followed by an irreversible chemical reaction has a slope of $\Delta E_p/\log \nu = \pm 30$ mV from plotting of peak potential (E_p) versus log ν.[199, 255] In our study, plots of experimental values of E_{pc} of Co(III/II) in the complex, $[Co^{III}cis\text{-}(PN)_2Cl_2][PF_6]$, versus log ν between the scan rate 0.05 Vs^{-1} and 2 V s^{-1} gave a slope of -47 mV (**Figure 2.52**).

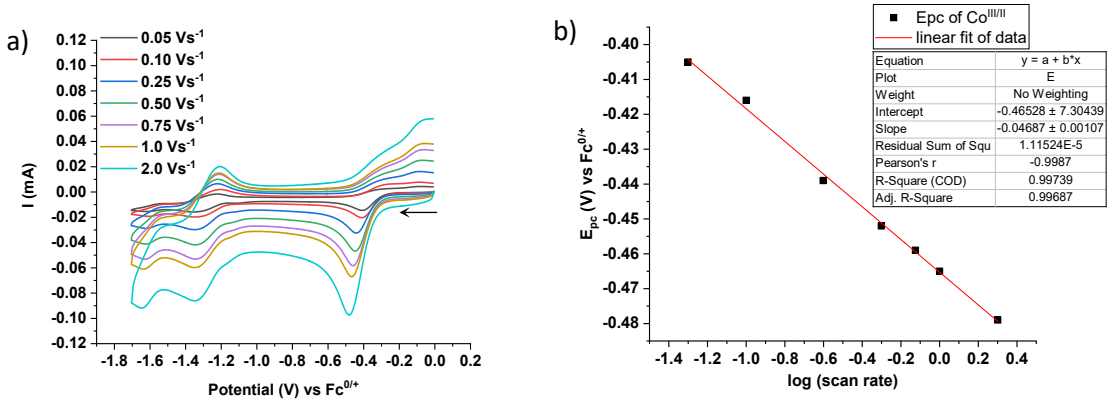

Figure 2.52 Cyclic voltammograms of $[Co^{III}cis\text{-}(PN)_2Cl_2][PF_6]$ (1 mM) in CH_3CN with 0.1 M $TBAPF_6$ at various scan rates (a), plot of E_{pc} versus log(ν) for the E_{pc} of Co(III/II) wave in the CVs of this complex (b).

This slope is larger than the ideal value of -30 mV expected for a cathodic peak potential variation (ΔE_{pc}) due only to a coupled chemical reaction, which further indicated that the Co(III/II) couple is governed by electron-transfer kinetics from the electrode.[199, 256] This value of slope suggested a quasi-reversible electron transfer kinetics followed by an irreversible chemical reaction (E_qC_i mechanism) for the Co(III/II) couple in the complex (**Scheme 2.5**).

This electrode mechanism (E_qC_i mechanism) was previously observed in one-electron reduction of Co(III) complexes containing phosphine ligand with a pendant amine.[225, 257] From scan rate variation analysis of $[Co^{II}(P^{tBu}{}_2N^{Ph}{}_2)(CH_3CN)_3]^{2+}$species, plots of E_{pa} and E_{pc} of the CoIII/II couple versus log(ν) over the range of 0.1–1.0 V s^{-1} resulted in slopes of -57 mV and +57 mV for respective plots of anodic and cathodic peak potential against log ν, which demonstrated quasi-reversible electron transfer kinetics.

2.5.5.5 CV of [Co^{III}(PN)$_2$(H)(Cl)][PF$_6$]

The cyclic voltammogram of [Co^{III}(PN)$_2$(H)(Cl)][PF$_6$] (1 mM) was recorded in CH_3CN containing 0.1 M $TBAPF_6$ exhibited two irreversible reduction peaks at E_{pc} -1.48 V and -2.02 V during the cathodic scan (**Figure 2.53** a). These two irreversible waves with the same cathodic current were tentatively assigned to the stepwise reduction of metal-centred Co$^{(III)/(II)}$-H and Co$^{(II)/(I)}$-H couples, respectively. The reduction potential of Co$^{(III)/(II)}$-H in this complex corresponds to the isolable monohydride complex with a tetradentate phosphine ligand, [HCo^{III}(L2)(CH_3CN)]$^{2+}$ (**Figure 2.6**) exhibiting the quasi reversible wave at scan rate 100 mV s^{-1} with E_{pc} = -1.57 and E_{pa} = -1.47 V vs. $Cp_2Fe^{+/0}$ in CH_3CN containing 0.1 M $TBAPF_6$.[206]

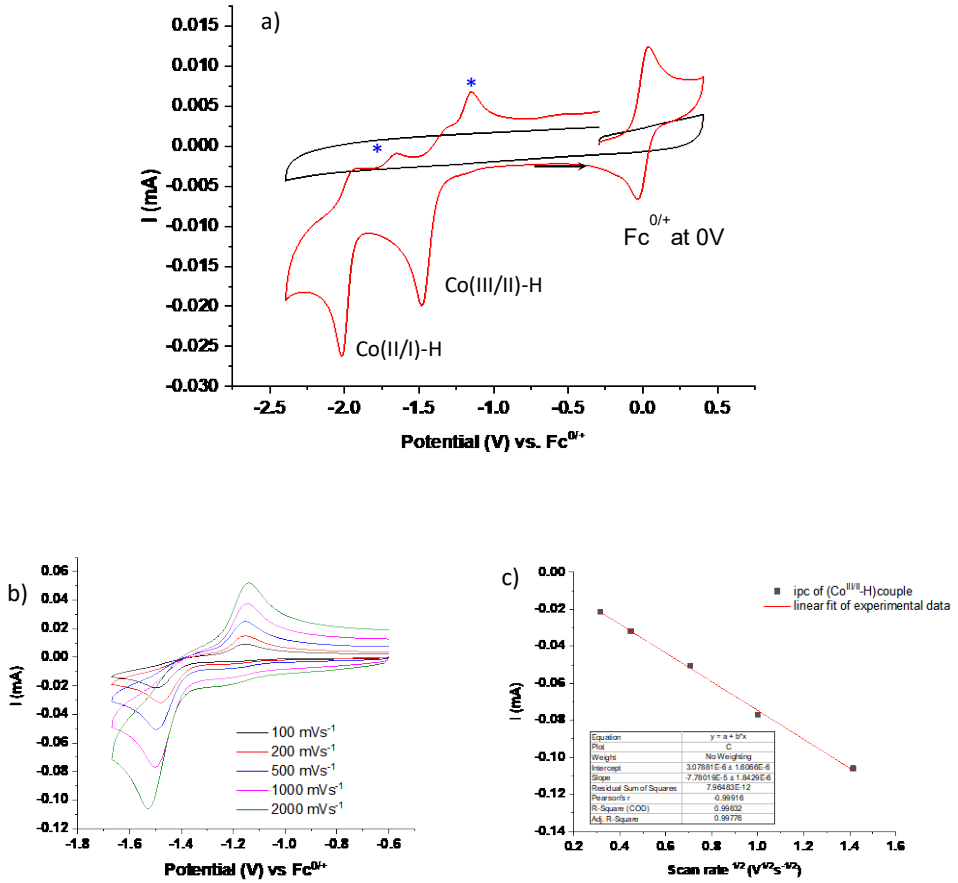

Figure 2.53. Cyclic voltammogram of [Co^{III}(PN)$_2$(H)(Cl)][PF$_6$] (1 mM) in CH_3CN with 0.1 M $TBAPF_6$ at a scan rate of 100 mV s^{-1}. The CVs of this complex at various scan rates (b), plot of i_{pc} of Co$^{(III/II)}$-H couple versus square root of scan rates (c).

The cathodic peak currents at the Co$^{(III)/(II)}$-H potential increased linearly with the scan rate $v^{1/2}$ indicating diffusion control (**Figure 2.53** b and c). The anodic peaks of new species at -1.1 V also increased upon increasing scan rate. This suggested that the new species can then be oxidized by electron transfer with controlled diffusion.

Moreover, the CV of this complex (**Figure 2.53** a) showed that two anodic peaks at $E_{pa'}$ -1.65 V and -1.1 V (blue asterisk) were observed upon the anodic scan which indicated a formation of new species possibly resulting from a cleavage of H^- or Cl^- from the respective reduced Co^{I}-H and Co^{II}–H species. This characteristic is consistent with the reduction of the $[HCo^{III}(L2)(CH_3CN)]^{2+}$ complex which showed the oxidation peak on a reverse scan at $E_{pa'}$ = -0.8 V. This new peak was assigned to the oxidation of $[Co^{I}(L2)(MeCN)]^+$, which could be formed by net loss of either H• or H^- in a H−Co bond cleavage reaction.[206].

Table 2.20. CV characterisation data of the $[Co^{III}(PN)_2(H)(Cl)][PF_6]$ and $[Co^{III}(PN)_2(H)(MeCN)][PF_6]_2$ (1mM) in CH_3CN with 0.1 M $TBAPF_6$ at a scan rate of 100 mV s^{-1}.

Assignment		This work		Literature
		$[Co^{III}(PN)_2(H)(Cl)][PF_6]$	$[Co^{III}(PN)_2(H)(MeCN)][PF_6]_2$	$[HCo^{III}(L2)(CH_3CN)]^{2+}$[206]
($Co^{III/II}$-H)	E_{pc} (V)	-1.48	-1.14	-1.57
	E_{pa} (V)	-	-1.03	-1.47
($Co^{II/I}$-H)	E_{pc} (V)	-2.02	-1.95	-
	E_{pa} (V)	-	-	-
($Co^{III/II}$-H)	$E_{pa'}$(V)	-1.10	-	-
($Co^{II/I}$-H)	$E_{pa'}$(V)	-1.65	-1.65	-
($Co^{II/I}$-NCMe)	$E_{pa'}$(V)	-	-	-0.8

Electrochemical reaction mechanism of $[Co^{III}(PN)_2(H)(Cl)][PF_6]$

The cyclic voltammogram of $[Co^{III}(PN)_2(H)(Cl)][PF_6]$ exhibited an irreversible wave with E_{pc} = -1.48 V at the scan rate 0.1 V s^{-1} which was assigned to the one-electron reduction of Co(III/II)-H couple followed by an irreversible chemical reaction (EC mechanism) via a cleavage of H^- or Cl^- from the resulting reduced species. The CV studies by scan rate variation of this complex showed that the cathodic peak potential of Co(III/II)-H wave at -1.48 V also depended on the scan rate by showing a negative shift of E_{pc} upon increase of scan rate between 0.05 V s^{-1} and 10 V s^{-1} (**Figure 2.54** a). Plots of experimental values of E_{pc} versus log ν gave a slope of -49 mV (**Figure 2.54** b) which is greater than that of an ideal slope of $\Delta E_p/\log \nu$ = -30 mV.[255] for an E_rC_i mechanism. Therefore, the electron transfer to the Co(III/II) couple was assigned as an quasi-reversible electron transfer followed by irreversible Cl^- dissociation ($E_qC_i$mechanism).

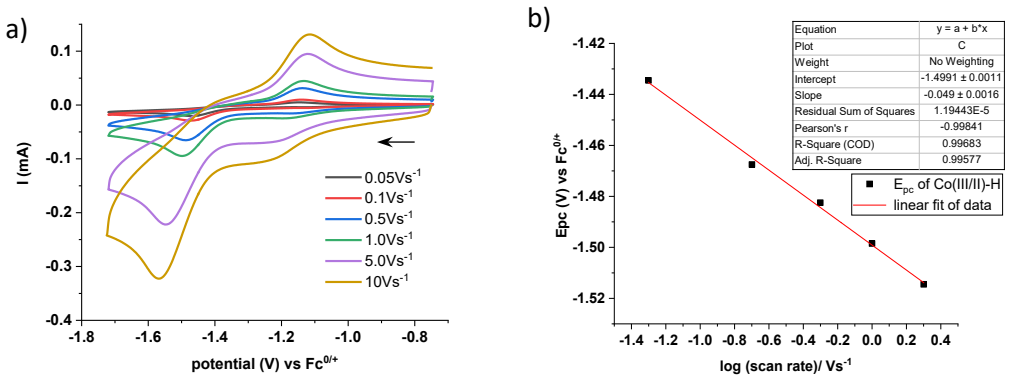

Figure 2.54. Cyclic voltammograms of Co(III/II)-H couple in $[Co^{III}(PN)_2(H)(Cl)][PF_6]$ (1mM) in CH_3CN with 0.1 M $TBAPF_6$ at various scan rates (a), plot of E_{pc} versus log(ν) for the cathodic peak potential of Co(III/II)-H wave in this complex (b).

This result supported the quasi-reversible electron transfer (E_qC_i pathways) for the Co(III/II)-H wave in the $[Co^{III}(PN)_2(H)(Cl)][PF_6]$ complex which is similar to the reduction of the dichloro Co(III) complex at the Co(III/II) wave with a slope of -47 mV from the plot of E_{pc} versus log (ν). For this reason, the quasi-reversible electron transfer coupled with an irreversible Cl^- dissociation (E_qC_i mechanism as shown in **Scheme 2.6**) is proposed for a reduction through a Co(III/II)-H peak at -1.48 V.

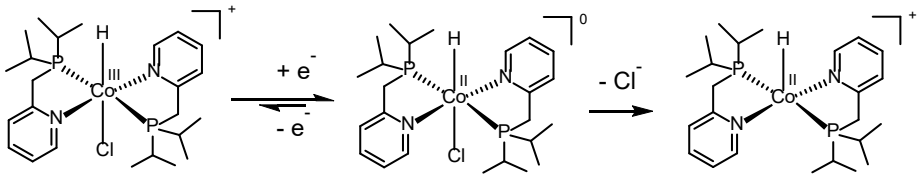

Scheme 2.6. E_qC_i mechanism for a reduction of $[Co^{III}(PN)_2(H)(Cl)][PF_6]$ in CH_3CN at -1.48 V

According to the CV of $[Co^{III}(PN)_2(H)(Cl)]^+$, a reverse scan through the Co(III/II)-H couple showed an anodic peak at E_{pa}' = -1.11 V which was assigned to the oxidation of the resulting product from a chemical reaction following one-electron reduction of the Co(III) hydride complex. Moreover, the corresponding cathodic peaks at E_{pc}' around -1.20 V, which appeared at more positive reduction potential compared to the Co(III/II)-H couple in the original $[Co^{III}(PN)_2(H)(Cl)]^+$ species, were more clearly observed in the CV at relatively high scan rates between 0.5 and 10 V s^{-1} (**Figure 2.54** a). This new reduction peak at E_{pc}' around -1.2 V also obviously showed in the CV of $[Co^{III}(PN)_2(H)(Cl)][PF_6]$ (2 mM in MeCN) which had been left in a solution for 10 h prior to recording the CV at the scan rate 0.1 V s^{-1} (**Figure 2.55,** blue curve). This new reduction peak related to the anodic wave at potential (E_{pa}') with peak-to-peak separation (ΔE_p) of 120 mV. As shown previously, the new reduction peak was more clearly observed in the CV of this complex at the higher scan rate of 0.5 V s^{-1} (**Figure 2.55,** red curve) than that at 0.1 V s^{-1} (black). Compared

to the CV of a solution of the independently synthesized MeCN analogous of the cobalt(III) hydride complex, the peak at E_{pc}' appeared at the potential between the E_{pc} value of the Co(III/II)-H couple in the analogous Cl^- and MeCN complex.

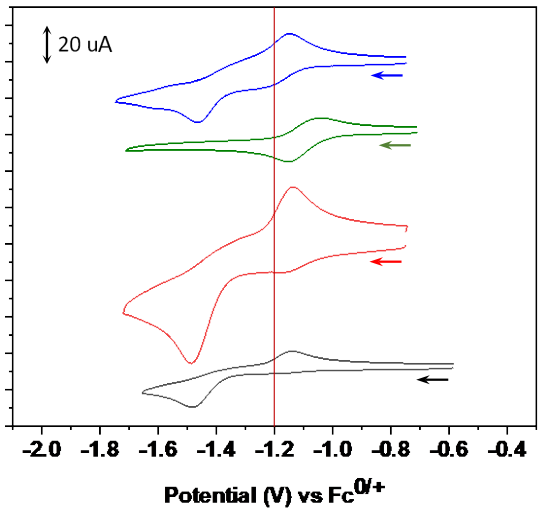

Figure 2.55. CV of the Co(III/II)-H couple in $[Co^{III}(PN)_2(H)(Cl)][PF_6]$ (2 mM) after leaving in solution for 10 h prior to recording the CV (blue), freshly prepared solution of $[Co^{III}(PN)_2(H)(Cl)][PF_6]$ at the scan rate 0.1 V s^{-1} (black) and 0.5 V s^{-1} (red), compared to the Co(III/II)-H couple in $[Co^{III}(PN)_2(H)(MeCN)]^{2+}$ at the scan rate 0.1 V s^{-1} (green) at the scan rate 0.1 V s^{-1}.

These results indicated that slow exchange between Cl^- ligand in the Co(III) complex, $[Co^{III}(PN)_2(H)(Cl)][PF_6]$, and CH_3CN solvent could occur upon leaving the complex in a solution concomitant with formation of the analogous Co(III) acetonitrile complex as shown in **Scheme 2.7**

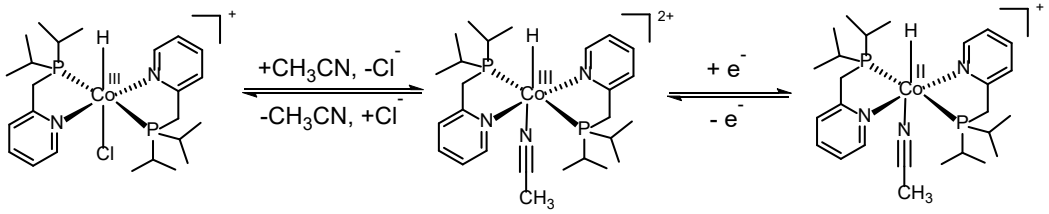

Scheme 2.7. Proposed mechanism for a reduction of $[Co^{III}(PN)_2Cl_2][PF_6]$ in MeCN for the new redox wave at $E_{pc'}$ of -1.23 V and $E_{pa'}$ of -1.11 V.

Upon recording 5 cycles through the Co(III/II)-H couple of a fresh $[Co^{III}(PN)_2(H)(Cl)][PF_6]$ solution at scan rate 1 V s^{-1} (**Figure 2.56**), the cathodic peak current, i_{pc} of Co(III/II)-H redox couple decreased concomitantly with slight increases in peak currents ($i_{pa'}$ and $i_{pc'}$) of the redox wave at $E_{pc'}$ = -1.22 V and $E_{pa'}$ = -1.13 V with ΔE_p of 90 mV at 1 V s^{-1}.

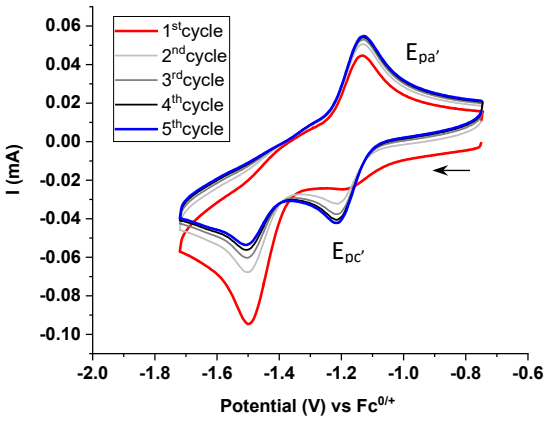

Figure 2.56. CVs (5 cycles) of $[Co^{III}(PN)_2(H)(Cl)][PF_6]$, 0.5 mM in CH_3CN at scan rate 1 V s^{-1}.

2.5.5.6 CV studies of $[Co^{III}(PN)_2(H)(MeCN)][PF_6]_2$

The electrochemical properties of $[Co^{III}(PN)_2(H)(MeCN)]^{2+}$ were then investigated under the same conditions as those for $[Co^{III}(PN)_2(H)(Cl)]^{+}$. The dicationic acetonitrile analogue, $[Co^{III}(PN)_2(H)(MeCN)]^{2+}$ also showed two reduction processes: however, the first reduction event of the Co(III/II)-H couple became a quasi-reversible process with $E_{1/2}$ -1.1 V and ΔE_p of 110 mV at 0.1 V s^{-1} and appeared at much less negative reduction potential than that of chloride bound $[Co^{III}(PN)_2(H)(Cl)]^{+}$ complex (E_{pc} -1.48 V) as shown in **Figure 2.57** (blue curve) and listed in the **Table 2.20**. Moreover, the first reduction potential of Co(III/II) couple and the latter Co(II/I) wave in the monocationic $[Co^{III}$*cis*-$(PN)_2Cl_2]^{+}$ species appeared at considerably more positive potential (red curve) compared respectively to the Co(III/II)-H couple and Co(II/I)-H of the $[Co^{III}(PN)_2(H)(Cl)]^{+}$ (black) by 1.06 V. This suggested that the hydride ligand in the two Co(III)-H complexes make more electron density in the Co(III) metal center compared to the corresponding $[Co^{III}$*cis*-$(PN)_2Cl_2]^{+}$ resulting in easier to oxidize the $[Co^{III}(PN)_2(H)(Cl)]^{+}$ cation.

The Co(II/I)-H couple in the $[Co^{III}(PN)_2(H)(MeCN)]^{2+}$ and the $[Co^{III}(PN)_2(H)(Cl)]^{+}$ appeared at a similar potential around -2.0 V. It indicated the second electron transfer to the same species formed in a solution after one-electron reduction which could possibly be a $[Co^{II}(PN)_2H]^{+}$.

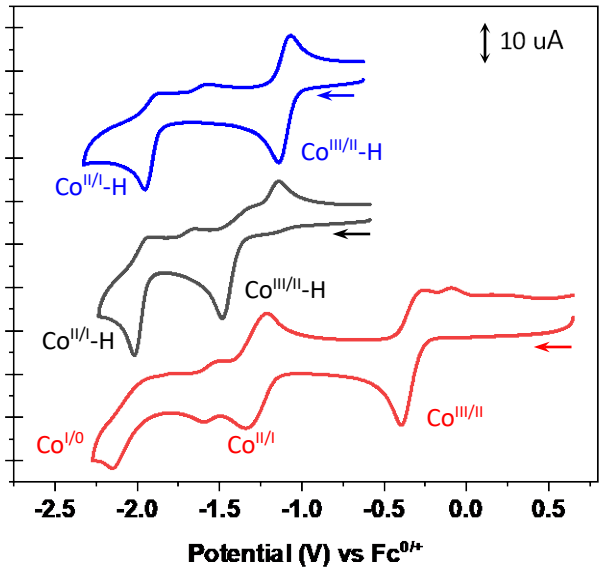

Figure 2.57. Cyclic voltammogram of the $[Co^{III}(PN)_2(H)(MeCN)]^{2+}$ complex (1 mM) in CH_3CN with 0.1 M $TBAPF_6$ (blue), compared to the hydride chloride derivative, $[Co^{III}(PN)_2(H)(Cl)][PF_6]$ (black) and dichloro Co(III) complex, $[Co^{III}$*cis*-$(PN)_2Cl_2]^{+}$ at the scan rate 100 mV s^{-1}.

Plots of i_{pc} and i_{pa} of this Co(III/II)-H couple in the $[Co^{III}(PN)_2(H)(MeCN)]^{2+}$ complex as a function of the square root of the scan rate showed a linear dependence of peak currents (i_p) to $\nu^{1/2}$ (**Figure 2.58** b) suggesting a diffusion-controlled migration of this species from bulk solution to the electrode.

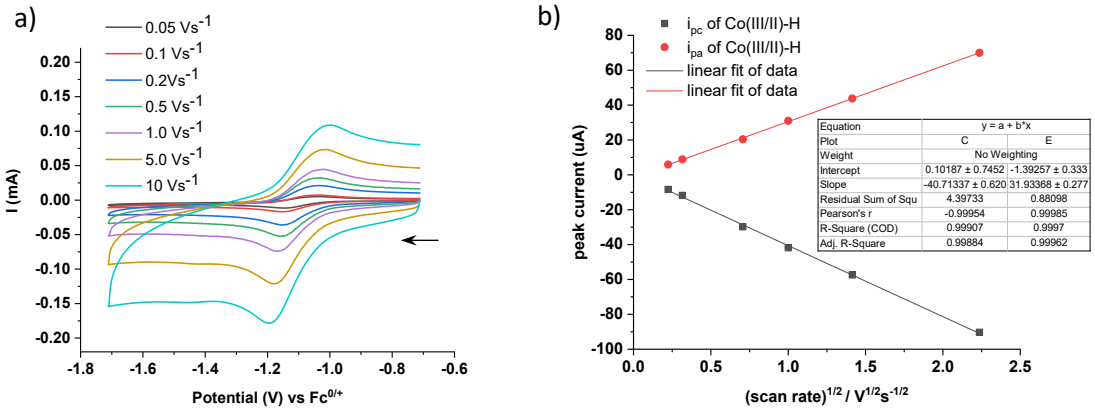

Figure 2.58. Cyclic voltammograms of the Co(III/II)-H couple for $[Co^{III}(PN)_2(H)(MeCN)][PF_6]_2$ complex (1 mM) in CH_3CN with 0.1 M $TBAPF_6$ at various scan rates (a), plots of i_{pc} and i_{pa} of Co(III/II)-H couple versus square root of scan rates (b).

Electrochemical reaction mechanism of the $[Co^{III}(PN)_2(H)(MeCN)][PF_6]_2$ complex

According to an ideal reversible one-electron transfer reaction, the shifts of peak potentials with scan rate depend on the mechanism.[205, 255] For an ideal reversible one-electron transfer reaction followed by an irreversible chemical step (E_rC_i mechanism), a characteristic slope of $\Delta E_p / \Delta \log(\nu)$ has to be ±30 mV for plotting of E_{pa} or E_{pc} against $\log(\nu)$. From the CVs of $[Co^{III}(PN)_2(H)(MeCN)]^{2+}$at different scan rates (**Figure 2.58** a), slopes of -31 mV and +29 mV were respectively obtained from the plot of E_{pc} vs $\log(\nu)$ and E_{pa} against $\log(\nu)$ for the scan rate from 0.5 to 10 V s^{-1} (**Figure 2.59** a and b). This result indicated the reduction of $[Co^{III}(PN)_2(H)(MeCN)]^{2+}$ species to the $[Co^{II}(PN)_2(H)(MeCN)]^{+}$ by reversible electron transfer kinetics followed by a reversible chemical reaction (E_rC_r mechanism) as shown in **Scheme 2.8**.

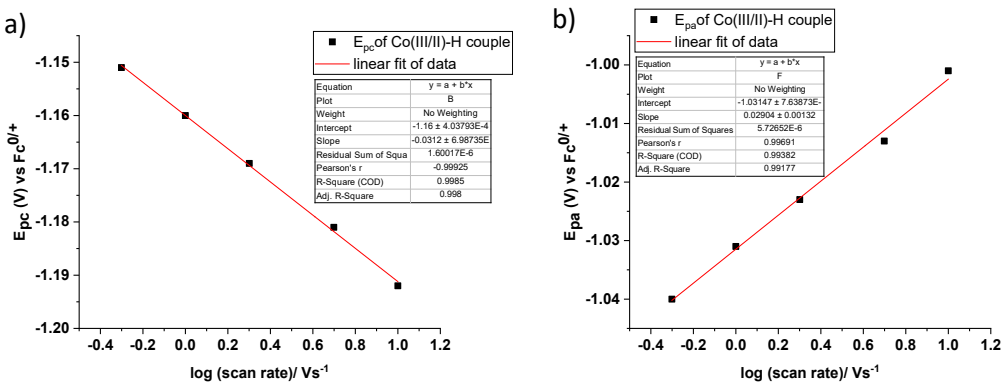

Figure 2.59. (a), plot of E_{pc} (b) and E_{pa} (c) for the cathodic peak potential of Co(III/II)-H wave in the $[Co^{III}(PN)_2(H)(MeCN)][PF_6]_2$ complex versus log(ν). Conditions: 1 mM, in CH_3CN with 0.1 M $TBAPF_6$

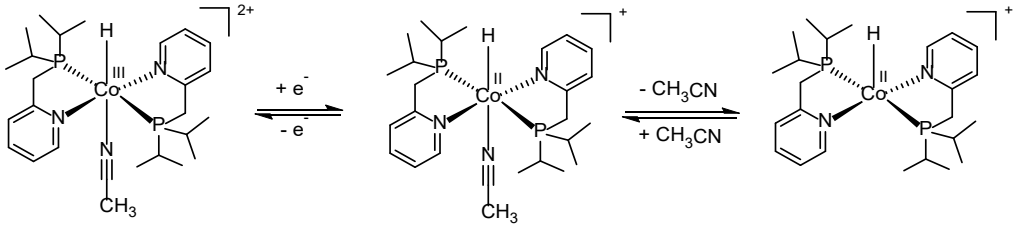

Scheme 2.8. E_rC_r mechanism for a reduction of $[Co^{III}(PN)_2(H)(MeCN)][PF_6]_2$ in CH_3CN at -1.10 V.

Consequently, the electrochemical mechanism is consistent with a reversible redox wave of Co(III/II)-H at $E_{1/2}$ = -1.10 V with a large ΔE_p of 112 mV in the CV at 0.1 V s^{-1} (**Table 2.18**) which is much greater than that of ideal ΔE_p = 57 mV expected for a Nernstian one-electron wave. This evidence further indicated that one-electron reduction at the Co(III/II)-H couple in the acetonitrile analogue of cobalt(III) hydride, $[Co^{III}(PN)_2(H)(MeCN)]^{2+}$ species resulted in a dissociation of the MeCN ligand from the reduced Co(II)-H species as displayed in **Scheme 2.8.**

In summary, the scan rate variation analysis for the cobalt(III) complex containing Cl^- ligand/s in this series yielded slopes of -47 mV and -49 mV from plotting of experimental values of E_{pc} versus log ν for $[Co^{III}(PN)_2(Cl_2)][PF_6]$ and $[Co^{III}(PN)_2(H)(Cl)][PF_6]$ (**Table 2.21**). These results supported quasi-reversible electron transfer kinetics coupled with an irreversible chemical reaction (E_qC_i mechanism) for the reduction of Co(III) complexes. In the case of $[Co^{III}(PN)_2(H)(MeCN)]^{2+}$, the reduction mechanism exhibited a different pathway by showing the slope of $\Delta E_p / \Delta \log(\nu) \sim \pm 30$ which supported an E_rC_r mechanism.

Table 2.21. Electron transfer kinetic parameters obtained from plots of E_p versus log(ν).

Complex	couple	peak	Slope (mV)	Mechanism	$E^{0'}$(V)
$[Co^{III}cis\text{-}(PN)_2Cl_2][PF_6]$	$Co^{III/II}$	E_{pc}	-43	E_qC_i	-0.42
$[Co^{III}(PN)_2(H)(Cl)][PF_6]$	$Co^{III/II}$-H	E_{pc}	-49	E_qC_i	-
$[Co^{III}(PN)_2(H)(MeCN)][PF_6]_2$	$Co^{III/II}$-H	E_{pc}	-31	E_rC_r	-1.10
		E_{pa}	+29		
$[Co^{II}(P^{tBu}{}_2N^{Ph}{}_2)(CH_3CN)_3]^{2+}$ [207]	$Co^{III/II}$	E_{pc}	-57		+0.33
		E_{pa}	+57	E_qC_r	+0.33
$[HCo^{III}(L2)(CH_3CN)]^{2+}$ [206]	$Co^{III/II}$-H	E_{pc}	-34	E_qC_r	-
$[HCo^{III}(L3)(CH_3CN)]^{2+}$ [206]	$Co^{III/II}$-H	E_{pc}	-41	E_qC_r	

2.5.6 UV-Vis spectroelectrochemistry

Following the studies of the electron transfer mechanism of the Co(III) complexes by scan-rate variation analysis in acetonitrile solution, the proposed electrochemical reaction mechanism was further investigated by the UV-Vis spectroelectrochemistry (UV-Vis SEC). The in-situ UV–visible spectroscopic characterization a reduced species was then carried out by bulk electrolysis of the initial Co(III) complexes in MeCN solution containing 0.1 M $TBAPF_6$.

2.5.6.1 UV-Vis SEC characterization of $[Co^{III}cis\text{-}(PN)_2(Cl)_2][PF_6]$

As summarized in the **Table 2.21**, a mechanism of the electron transfer for the Co(III/II) couple in the $[Co^{III}cis\text{-}(PN)_2Cl_2][PF_6]$ complex was proposed as an E_qC_i pathway due to the appearance of quasi-reversible Co(III/II) redox wave with a large value of peak-to-peak separation (ΔE_p = 146 mV) at 0.1 V s^{-1} in the CV of this complex. The characterisation of the in situ generated species following one-electron reduction of $[Co^{III}(PN)_2Cl_2]^+$ by bulk electrolysis was monitored by UV-Vis spectroscopy.

Exhaustive electrolysis of a 1 mM solution of $[Co^{III}cis\text{-}(PN)_2(Cl)_2][PF_6]$ in MeCN at 0.04.V was carried out leading to the spectral changes. The evolution of new absorption bands over the course of electrolysis (**Figure 2.60**, a) is in agreement with the UV-Vis absorption spectrum of the independently synthesized dichloro cobalt(II) complex, $[Co^{II}(PN)_2Cl_2]$ in CH_3CN solution as shown in **Figure 2.37**.

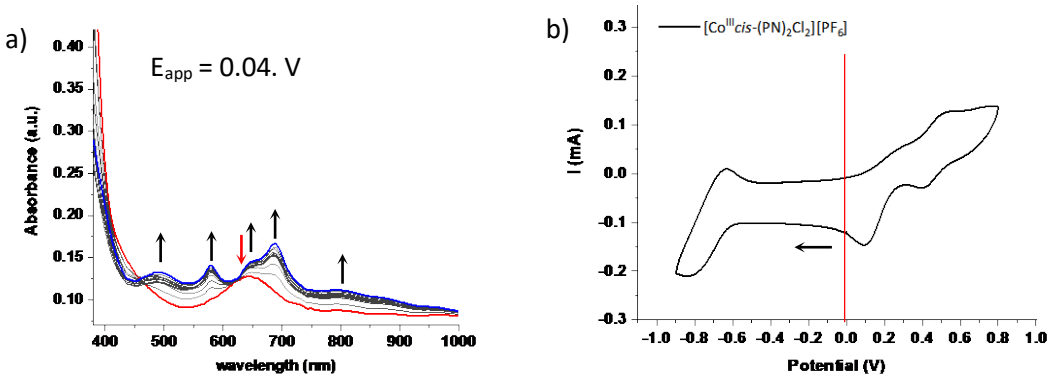

Figure 2.60. UV-Vis Spectral changes recorded during bulk electrolysis of $[Co^{III}cis\text{-}(PN)_2Cl_2][PF_6]$, 2 mM solution in MeCN under an Ar atmosphere at E_{app} = 0.04 V (a), CV of the complex measured under similar conditions before electrolysis using Pt gauze as working electrode (b).

Therefore, this evidence suggested the formation of the $[Co(PN)_2Cl]Cl$ and $[Co^{II}(PN)Cl_2]$ which confirmed the chemical steps as shown in **Scheme 2.5**. However, the configuration of the resulting product could not be determined; the two phosphorus atoms of the P,N ligands in equatorial plane of the Co(II) complex could be *trans* or *cis* to one another. The characteristic bands of the $[Co^{II}(PN)Cl_2]$ were observed at λ_{max} = 580, 650 and 688 nm, and the bands at 487

nm and 780 nm corresponded to the formation of $[Co^{II}(PN)_2Cl]^+$. These new bands agree with the absorption spectrum of the independently synthesized $[Co^{II}(PN)_2Cl_2]$ complex upon dissolving in MeCN as listed in the **Table 2.16**.

2.5.6.2 UV-Vis SEC characterization of $[Co^{III}(PN)_2(H)(Cl)][PF_6]$

The electrochemical generation of a reduced species from the cobalt(III) hydride complexes by one-electron reduction of $[Co^{III}(PN)_2(H)(Cl)]^+$ in MeCN solution and their in situ UV-Vis characterization was also performed. A significant blue shift of the absorption spectrum (**Figure 2.61** a) of the original $[Co^{III}(PN)_2(H)(Cl)]^+$complex by 25 nm occurred during the course of electrolysis at E_{app} = -1.10 V. This evidence agrees with an irreversible chemical reaction following one-electron reduction of the $[Co^{III}(PN)_2(H)(Cl)][PF_6]$ solution which confirmed a dissociation of chloride ligand from the reduced species subsequent to one-electron reduction of the Co(III)-H species. Moreover, the result corresponded to the appearance of an irreversible Co(III/II)-H wave at -1.10 V in the CV of $[Co^{III}(PN)_2(H)(Cl)][PF_6]$ complex (**Figure 2.61**, b). The evidence from this study also revealed that the axial chloride ligand dissociated from the complex after one electron reduction of the$[Co^{III}(PN)_2(H)(Cl)][PF_6]$ complex resulting in the formation of the pentacoordinated, $[Co^{II}(PN)_2H]^+$ species as shown previously in **Scheme 2.6**.

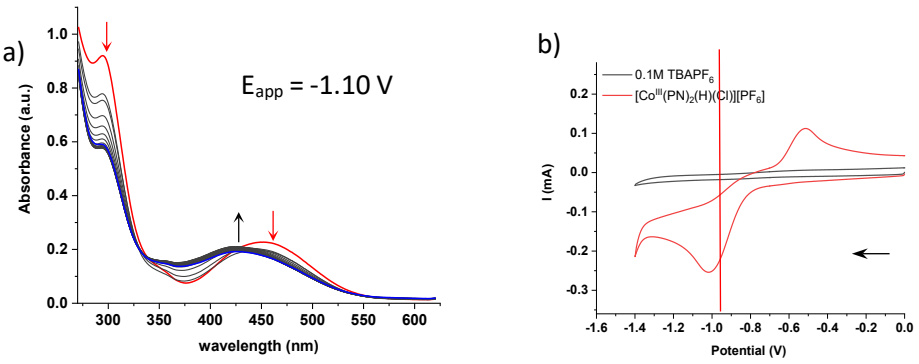

Figure 2.61. UV-Vis Spectral changes during bulk electrolysis of $[Co^{III}(PN)_2(H)(Cl)][PF_6]$, 1 mM solution in MeCN under an Ar atmosphere at E_{app} = -1.10 V (a), CV of the complex under similar conditions measured before electrolysis using Pt gauze as working electrode at 0.05 V s^{-1} (b).

2.5.6.3 UV-Vis SEC characterization of $[Co^{III}(PN)_2(H)(MeCN)][PF_6]_2$ complex

The in situ UV-Vis characterization of the reduced species by one-electron reduction of the $[Co^{III}(PN)_2(H)(MeCN)]^{2+}$ in MeCN solution from bulk electrolysis at -0.78 V under similar conditions to the corresponding chloro derivative was then performed. The UV-Vis absorption spectrum of the reduced Co(II)-H complex showed a slight increase in absorption intensity around 450 nm upon exhaustive electrolysis of the $[Co^{III}(PN)_2(H)(MeCN)]^{2+}$ solution (**Figure 2.62,** a). This spectral change corresponded to a quasi-reversible wave of the Co(III/II)-H couple in the CV of $[Co^{III}(PN)_2(H)(MeCN)]^{2+}$ solution (**Figure 2.62**, b) which indicated a reversible chemical reaction involving a dissociation of the MeCN ligand after one-electron reduction of the Co(III)-H complex as shown in **Scheme 2.8**.

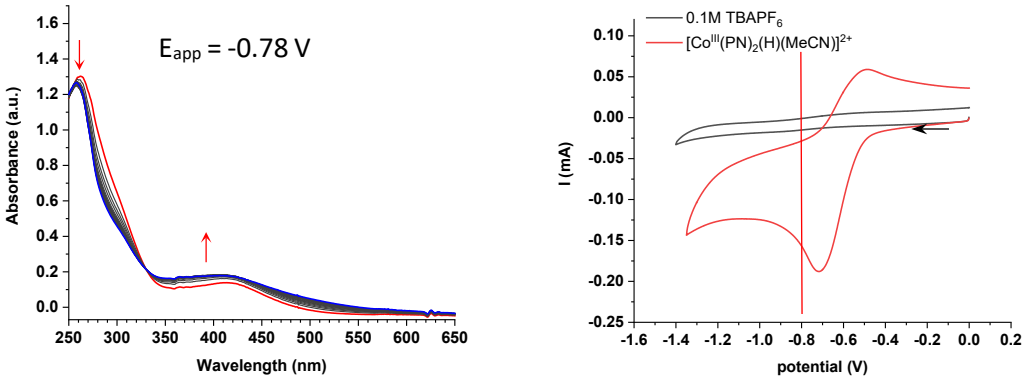

Figure 2.62. UV-Vis Spectral changes recorded during bulk electrolysis of $[Co^{III}(PN)_2(H)(MeCN)][PF_6]_2$, 1 mM solution in MeCN under an Ar atmosphere at E_{app} = -0.78 V (a), CV of the complex using Pt gauze as working electrode at scan rate 0.05 V s^{-1} under similar conditions measured before electrolysis (b).

Moreover, species generated over the course of electrolysis of $[Co^{III}(PN)_2(H)(MeCN)][PF_6]_2$ in MeCN solution exhibit one visible absorption band at wavelength around 425 nm in a similar manner to the spectra observed on bulk electrolysis of $[Co^{III}(PN)_2(H)(Cl)][PF_6]$ (**Figure 2.63**). This evidence confirmed dissociation of chloride from the reduced $[Co^{II}(PN)_2(H)(Cl)]^0$ species and release of a MeCN ligand from the reduced $[Co^{II}(PN)_2(H)(MeCN)]^+$ complex to form the same product of pentacoordinated $[Co^{II}(PN)_2(H)]^+$ species (**Scheme 2.9**).

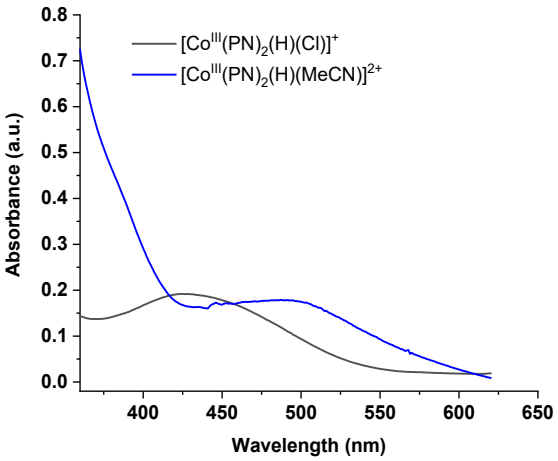

Figure 2.63. UV-Vis spectrum of $[Co^{III}(PN)_2(H)(Cl)][PF_6]$ complex (1 mM), black, and $[Co^{III}(PN)_2(H)(MeCN)][PF_6]_2$ (blue) recorded after bulk electrolysis for 2 min in MeCN under an Ar atmosphere.

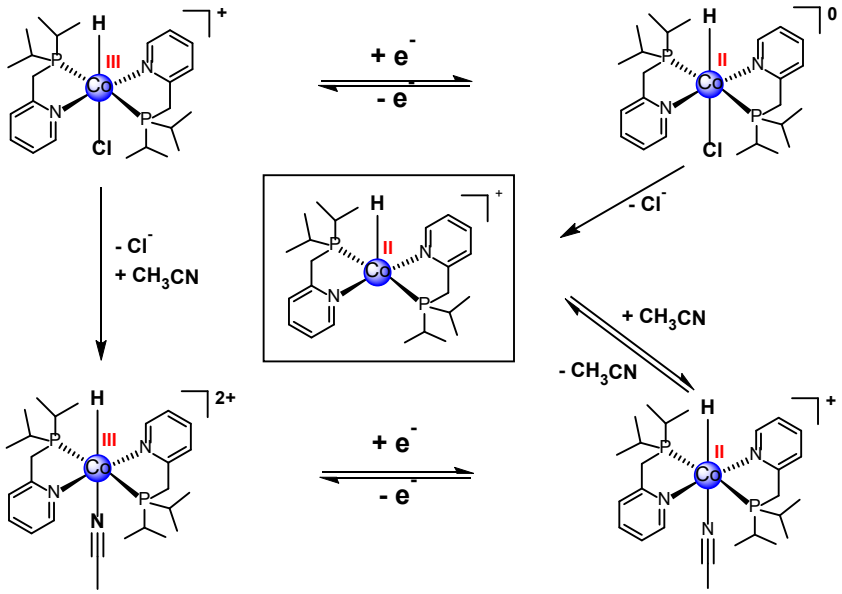

Scheme 2.9. Proposed electrochemical reaction mechanism of one-electron reduction of the cobalt(III) hydride complexes with bis P,N pyridine based ligands.

2.6 Conclusion

2.6.1 Synthesis and characterisation

A new series of cobalt (III) hydride complexes, $[Co^{III}(PN)_2(H)(Cl)]^+$and $[Co^{III}(PN)_2(H)(MeCN)]^{2+}$ with bis pyridine phosphine (PN = 2-((diisopropylphosphaneyl)methyl)pyridine) ligands and their corresponding cobalt dichloride, $[Co^{III}$*cis*$-(PN)_2Cl_2]^+$, $[Co^{II}$*cis*$-(PN)_2Cl][PF_6]$, $[Co^{II}(PN)_2Cl_2]$ and acetonitrile analogues $[Co^{II}(PN)_2(MeCN)]^{2+}$, were successfully synthesized. A mild reaction for the preparation of the hydride complexes at room temperature was achieved by reacting the starting cobalt(II) analogue with $NaBH_4$ as hydride source together with N_2 bubbling in MeOH. We also found that NH_4PF_6 is a suitable salt for a precipitation of the hydride complexes which allowed the isolation of $[Co^{III}(PN)_2(H)Cl]^+$ or $[Co^{III}(PN)_2(H)(MeCN)]^{2+}$ species from a reaction mixture as a solid containing a PF_6^- counter anion. Furthermore, this $[Co^{III}(PN)_2(H)(MeCN)]^{2+}$ hydride species could alternatively be prepared by an exchange between a Cl^- ligand in the $[Co^{III}(PN)_2(H)(Cl)]^+$ analogue and MeCN in acidified MeCN solution at 60^0C.

The diamagnetic nature of the low-spin d^6 Co(III) complexes in this series including the $[Co^{III}(PN)_2(H)(Cl)]^+$, $[Co^{III}(PN)_2(H)(MeCN)]^{2+}$ and $[Co^{III}$*cis*$-(PN)_2Cl_2]^+$ allowed characterization by NMR spectroscopy such as ^{1}H, ^{13}C{^{1}H}, ^{13}C-DEPT, ^{31}P{^{1}H} spectroscopy and 2D NMR experiments including ^{1}H-^{1}H COSY, ^{1}H-^{31}P{^{1}H} HMBC and ^{1}H-^{13}C-DEPT correlation. Moreover, their structural characterisations were supported by ESI-MS and CHN analysis. The structures of the hydride chloride $[Co^{III}(PN)_2(H)(Cl)][PF_6]$, the $[Co^{III}$*cis*$-(PN)_2Cl_2][PF_6]$, $[Co^{II}$*cis*$-(PN)_2Cl][PF_6]$ and $[Co^{II}(PN)_2(MeCN)][BF_4]_2$ were determined by X-ray crystallography which revealed the difference in configuration of the PN ligands by showing the cis-configuration of the two phosphorus atoms in the $[Co^{III}$*cis*$-(PN)_2(Cl)_2][PF_6]$ and the $[Co^{II}$*cis*$-(PN)_2Cl][PF_6]$ complex, and the trans-configuration in $[Co^{III}(PN)_2(H)(Cl)]^+$ and $[Co^{II}(PN)_2(MeCN)][BF_4]_2$. The distinct configuration of these two Co(III) complexes also resulted in a different degree of fluxionality in their structures by showing broad signals of isopropyl protons in the ^{1}H NMR solution of $[Co^{III}$*cis*$-(PN)_2(Cl)_2]^+$ at room temperature In contrast to this, the $[Co^{III}(PN)_2(H)(Cl)]^+$ and $[Co^{III}(PN)_2(H)(MeCN)]^{2+}$ cation in a solution has more rigid structure displaying sharp and well-separated peaks in the NMR spectra. The variable temperature NMR studies of $[Co^{III}$*cis*$-(PN)_2Cl_2]^+$ at 223, 298K and 323K indicated a dynamic structure from the hindered internal rotation of the isopropyl groups of the *cis* complex with C_{2v} symmetry. The separated two broad peaks for CH_2 arm and CH of the isopropyl in the ^{1}H NMR spectrum at room temperature become one broad peak. The one broad CH_3 protons is shaper peak at higher temperature above room temperature Moreover, it also supported that the cis-structure was adopted in solution at low temperature.

2.6.2 Electronic properties

The UV-Vis studies of the Co(III) complexes in this series reveal that the lowest energy charge-transfer bands follow the wavelength order $[Co^{III}(PN)_2(H)(Cl)]^+$, $[Co^{III}(PN)_2(H)(MeCN)]^{2+}$, $[Co^{III}$*cis*-$(PN)_2Cl_2]^+$ at 450, 413 and ca. 370 nm respectively. Of these ions, only the dichloride exhibits clear d-d bands. It indicated that H^- and/or MeCN ligands in the $[Co^{III}(PN)_2(H)(Cl)]^+$ and $[Co^{III}(PN)_2(H)(MeCN)]^{2+}$ greatly alter the electronic properties which leads to a large red shift of the absorption spectrum and more negative shift of the Co(III/II)-H couple compared to a redox Co(III/II) couple in the corresponding $[Co^{III}$*cis*-$(PN)_2(Cl)_2][PF_6]$. Therefore, the UV-Vis evidence in this study demonstrated that a modification of an axial ligand (changing from Cl^- to a CH_3CN and/or H^- ligand) in the octahedral Co(III) hydride complexes considerably affected their electronic properties by causing a red shift of CT transition. For example, substitution of an axial ligand from Cl^- to H^- led to a large red shift of 80 nm (0.60 eV) in the CT transition band of $[Co^{III}$*cis*-$(PN)_2(Cl)_2][PF_6]$, from 370 nm (3.351 eV) to 450 nm (2.755 eV). However, a change in configuration of P,N ligands from *cis* to *trans* geometry between the two phosphorus atoms could also possibly play a role in this spectral change. Moreover, this absorption change corresponded to their redox properties which showed a dramatic negative shift by 1.06 V of the first reduction potential of Co(III) to Co(II) in the CV displaying E_{pc} = -0.42 V for monocationic $[Co^{III}$*cis*-$(PN)_2Cl_2]^+$ species and -1.48 V for $[Co^{III}(PN)_2(H)(Cl)]^+$ species.

From the UV-Vis absorption studies of cobalt(II) complexes it is apparent that ligand exchange processes occur in solution. The dichloro derivative, $[Co^{II}(PN)_2Cl_2]$ in coordinating solvents exhibited a dramatic difference in the UV-Vis spectrum from that in non-coordinating solvents due to replacement of Cl^- ligand/s by a solvent molecule or a P,N ligand exchange. It leads to a generating of four- and five- coordinated $[Co^{II}(PN)Cl_2]$ and $[Co^{II}(PN)_2Cl]^+$ as a mixture in the solution resulting in a multi structed absorption in the UV-Vis spectrum. In contrast to this, the $[Co^{II}(PN)_2(MeCN)][BF_4]_2$ analogue displayed only one CT band at 448 nm with ε = 902 M^{-1} cm^{-1}, suggesting a strong binding between the Co(II) centre and the MeCN ligand.

2.6.3 Redox and electrochemical reaction mechanism

The redox properties by consecutive one-electron reduction of the cobalt complexes were investigated by cyclic voltammetry. A first reduction process of $[Co^{II}cis\text{-}(PN)_2Cl][PF_6]$, $[Co^{II}(PN)_2Cl_2]$, $[Co^{III}cis\text{-}(PN)_2Cl_2][PF_6]$, $[Co^{III}(PN)_2(H)(Cl)][PF_6]$ and $[Co^{III}(PN)_2(H)(MeCN)][PF_6]_2$ is quasi-reversible with ΔE_p value greater than that observed for a fully reversible Co(II/I) couple in monocationic $[Co^{II}cis\text{-}(PN)_2Cl]^+$ and the $[Co^{II}(PN)_2Cl_2]$ appeared at more negative potential than the reduction of $[Co^{II}(PN)_2(MeCN)]^{2+}$ by 120-240 mV. The $[Co^{III}(PN)_2(H)(Cl)][PF_6]$ complex showed an irreversible Co(III/II)-H couple concomitant with an oxidation process of the resulting product formed after one-electron reduction. While, the CVs of $[Co^{III}cis\text{-}(PN)_2Cl_2][PF_6]$ and $[Co^{III}(PN)_2(H)(MeCN)][PF_6]_2$ display a quasi-reversible wave of Co(III/II) and Co(III/II)-H couple with ΔE_p = 146 and 110, respectively.

The variable scan rate analysis of $[Co^{III}cis\text{-}(PN)_2Cl_2]^+$ and the $[Co^{III}(PN)_2(H)(Cl)]^+$ suggested that the one-electron reduction of these two complexes shows a quasi-electron transfer coupled with an irreversible chemical reaction (E_qC_i mechanism). The UV-Vis spectroelectrochemical studies supported the chemical step after one-elecron reduction of the $[Co^{III}cis\text{-}(PN)_2Cl_2]^+$ by the generation of a mixture of Co(II) species: because; the reduced $Co^{II}(PN)_2Cl_2$ is labile in a solution and undergoes P,N ligand exchange or a Cl^- loss in the solution. For the one-electron reduction of $[Co^{III}(PN)_2(H)(Cl)]^+$, the Cl^-dissociation from the reduced $[Co^{II}(PN)_2(H)(Cl)]^0$ species resulting in a formation of the penta coordinated $[Co^{II}(PN)_2(H)]^+$ species was observed. Moreover, the same $[Co^{II}(PN)_2(H)]^+$ species is formed via E_rC_r pathway for the first reduction of the $[Co^{III}(PN)_2(H)(MeCN)]^{2+}$ complex as a result of a reversible release of MeCN from the reduced $[Co^{II}(PN)_2(H)(MeCN)]^+$ species (**Scheme 2.9**.).

Chapter 3

Electrocatalytic H_2 evolution and electroreduction of CO_2 by cobalt complexes with bis-chelating PN ligands

3.1 Introduction

Cobalt has been emerging over the last decade as the most versatile non-precious metal for catalysts for electrocatalytic hydrogen evolution [67, 121, 122, 218, 220]. Apart from the development of exceptional Dubois catalysts containing Ni metal centre as HECs (presented in **Chapter 1**), the H^+ reduction catalysed by cobalt complexes was revealed a long time ago. A first generation of H_2-evolving cobalt-based catalysts with diglyoxime ligands is known as cobaloximes and will be illustrated in **section 3.1.5.1**. Over the past decade, numerous examples of cobalt-based complexes have emerged as electrocatalysts for H_2 evolution, including cobalt diglyoximes [87], cobalt diimine-dioximes [141, 258], Co-porphyrins[145], cobalt based polypyridine ligands [68, 259-261]and cobalt dithiolate systems.[153, 222] Mechanisms of homogeneous catalyzed H_2 evolution by cobalt-based catalysts have been extensively investigated. In most cases, generation of a Co(III)-hydride intermediate by protonation of a basic Co(I) species is considered as a key step in the proposed mechanism of this catalytic reaction.

3.1.1 General H_2 evolution pathways catalyzed by cobalt complexes

Cobalt-catalyzed hydrogen evolution has been studied extensively both experimentally [136, 140, 262-265] and theoretically [266-268]. The H_2 evolution pathways are proposed to proceed via common cobalt hydride intermediates, and all of the proposed mechanisms start with a reduction of Co(II) to Co(I) with a subsequent protonation to form Co(III)-H. Hydrogen evolution can occur through two distinct pathways: a bimolecular reaction of Co(III)-H leading to reductive elimination of H_2 (homolytic pathway, **Scheme 3.1**) or a protonation of Co^{III}–H to evolve H_2. Alternatively, it can be further reduced to form Co(II)-H which subsequently produces H_2 via similar homolytic or heterolytic pathways.[122]

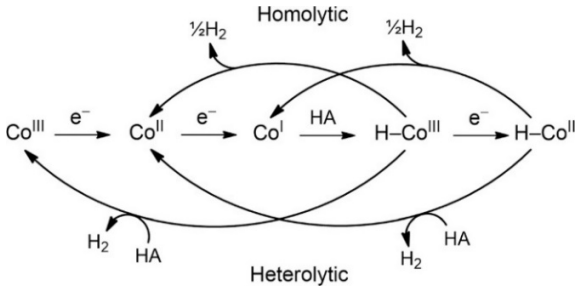

Scheme 3.1 Reaction pathways for the evolution of H_2 from the reaction of a Co^{I} complex with acid (HA).[16]

3.1.2 Benchmarking molecular H_2-evolving electrocatalysts by cyclic voltammetry

Electrocatalytic cyclic voltammetry has been a useful tool for investigation of catalytic mechanism, overpotential (η) and understanding overall rates (k_{cat}) for molecular catalysis.[197, 257] A rational comparison of molecular catalysts does not only require overpotential which is defined as the potential where catalysis occur but also the catalytic rate at this electrode potential. The determination of overpotential (η) and catalytic rate constant for an electrocatalytic multi electron transfer process will be described in the next section.

3.1.2.1 Overpotential

Overpotential (η) is defined as the additional potential that required to drive a reaction at a certain rate beyond thermodynamic requirement. This parameter is calculated as the difference between the applied potential and the standard potential for the production of hydrogen from acid HA as shown in **eq 3.1.**[269]

$$\text{Overpotential } (\eta) = E_{cat} - E^0_{HA/H2} \qquad \textbf{eq 3.1}$$

Determination of the thermodynamic potential for H_2 evolution in non-aqueous solvent ($E^0_{HA/H2}$) based on the Nernst equation was defined by Evans following **eq 3.2.**[60]

$$E^0_{HA/H2} = E^0_{H+/H2} - (2.303RT/F)pK_{a,HA,S} \qquad \textbf{eq 3.2}$$

The most recently reported value of $E^0_{H+/H2}$ (-0.028 V vs. $Fc^{0/+}$) in acetonitrile was determined by the open-circuit-potential (OPC) method by Bullock et al.[270] On this basis, the thermodynamic potential ($E^0_{HA/H2}$) for acids used in my work such as $TsOH{\cdot}H_2O$, CF_3COOH and CH_3COOH with pKa = 8.6, 12.65 and 23.51 in CH_3CN [61], respectively, was calculated with the following equations (**eq 3.3**-**eq 3.5**).

$E^0_{HA/H2}$ value of $TsOH{\cdot}H_2O$ = -0.028-(0.059x8.6) = -0.54 V vs. $Fc^{0/+}$ **eq 3.3**

$E^0_{HA/H2}$ value of CF_3COOH = -0.028-(0.059x12.65) = -0.77 V vs. $Fc^{0/+}$ **eq 3.4**

$E^0_{HA/H2}$ value of CH_3COOH = -0.028-(0.059x23.51) = -1.42 V vs. $Fc^{0/+}$ **eq 3.5**

Using $E_{cat/2}$ as catalytic potential in stead of E_{cat} (**eq 3.1**) was recommended for less-ideally behaved systems or a non-ideal catalytic waves as shown in **Figure 3.1.**[271]

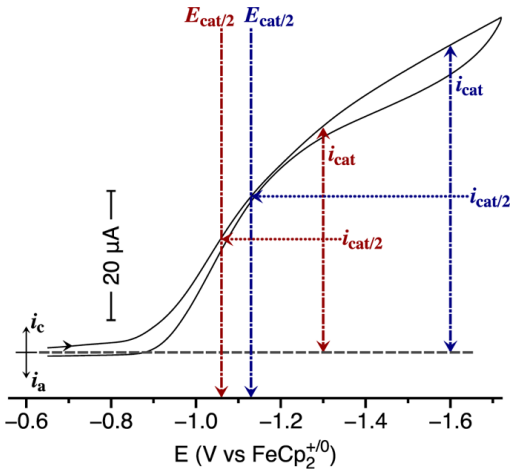

Figure 3.1. Experimental wave illustrating non-ideal catalytic behaviour, showing two possible selections for i_{cat} and their corresponding $E_{cat/2}$ values.

3.1.2.2 Kinetics analysis of H_2 evolution electrocatalyst

Savéant and co-workers' [272] simulated CV responses for the one-electron electrocatalytic process for reduction of substrate A to C by a redox catalyst P/Q (EC' mechanism) as shown below

Electrocatalytic one-electron reduction process (E_rC_i' mechanism) and Idealized CV Responses.

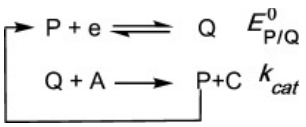

The different CV responses for this simple electrocatalytic process are dependent on the parameters in the **eq. 3.6** and **eq. 3.7**, where λ is the kinetic parameter, γ represents the excess factor, k_e is the rate constant of electron transfer from the reduced catalyst Q to substrate A, C_p^0 is the bulk concentration of redox catalyst P, and C_A^0 is the bulk concentration of substrate A.

$$\lambda = \left(\frac{RT}{F}\right)\left(\frac{k_e C_p^0}{\nu}\right) \qquad \textbf{eq 3.6}$$

$$\gamma = \frac{C_A^0}{C_p^0} \qquad \textbf{eq 3.7}$$

A plot of log λ versus log γ can be constructed by dividing into various zones with distinct CV responses (**Figure 3.2**).[269] All of CV waveforms with the short description are shown in the **Figure 3.2**). Some of these zones that generally are mentioned in derivation of kinetic data such as k_{obs} from FOWA will be described in more detail. The compass rose in the kinetic zone diagram suggests how different CV responses and zones may be accessed by varying λ (e.g scan-rate variation) and γ

For zone D (No Catalysis), the CV observed is that of the reversible-one electron reduction of P/Q couple under non-catalytic conditions. In zone KS, there are many descriptions that used to refer to the CV response in this zone (e.g. S-Shaped, plateau-shape, pure kinetic conditions, no substrate consumption). An S-shaped response is observed where the forward and reverse scans are exactly superimposed. This region is characterized by the situation where the substrate concentration at the electrode surface is equal to the bulk concentration. A peaked CV shape is observed in zone K because there is competition between consumption of the substrate by the rate-determining step, with diffusion of a new substrate to the electrode. No reverse anodic wave is seen because any reduced catalyst is oxidized through catalytic turnover.

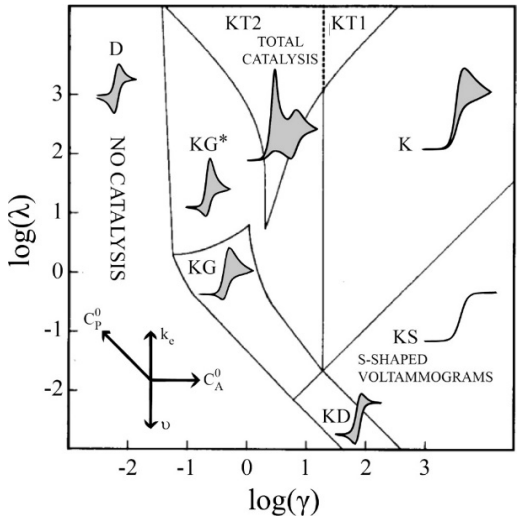

Zone	Waveform	Description
D		No catalysis
K		Substrate is depleted near the electrode
KS		Substrate not depleted at electrode; forward/reverse traces overlay
KD		Substrate concentration is not depleted; 'S' shape not observed due to reduced kinetic parameter (λ)
KG		Substrate near electrode is consumed; kinetic parameter small
KG*		See KG description
KT2		All substrate is consumed by a small amount of active catalyst
KT1	—	See KT2; catalytic wave and redox wave overlap

Figure 3.2. Kinetic zone diagram and simulated CV waveforms for the one-electron reduction of substrate A via redox catalyst mediator P, where λ is the kinetic parameter and γ is the excess. factor (see the text). The compass rose visually depicts how catalysis may move between zones (C_P^0 is the initial concentration of the catalyst, C_A^0 is the initial concentration of the substrate, ν is the scan rate, and k_e is the rate constant for homogeneous electron transfer from the reduced catalyst to the substrate). The CV waveforms follow the convention of negative potentials to the right and cathodic current upward. Scans are started from positive potentials. [269]

Experimentally, the S-shaped CV response can be obtained from peak-shaped CV (zone K) by increasing the scan rate (decreasing λ) as suggested in the compass rose. Therefore, the overall time required to record the CV is short and substrate consumption is limited. Alternatively, the S-shaped CV response may be achieved by increasing the substrate concentration (increasing γ). Moreover, the fast chemical reaction, as compared to the timescale of the voltammogram (Fν/RT), is required to access to the pure kinetic zones requires. Thus, in the case of slow catalysis (small k_e), scan rate may be decreased to increase the value of λ. However, caution must be exercised because slow scan rates (and very large λ) may lead to substrate consumption within the diffusion layer.[269]

Determination of k_{obs} for a fast catalytic reaction from CV

For the electrocatalytic H_2 evolution involving two-electron catalytic process, more complicated CV responses may be observed while the wave forms shown in **Figure 3.2** are relatively general. However, the concepts of catalytic rate and substrate diffusion by simple electrocatalytic process are applied for many cases of H_2-evolving electrocatalysts. For example, the fast Dubois catalysts [133] demonstrate that S-shaped or plateau CV can be achieved by raising the scan rate.

By extension, the concepts of an electrocatalytic process (EC' mechanism) to two-electron catalytic reaction (ECEC mechanism), it is assumed that all electron transfers occur at the electrode (n=2) where the second reduction is easier than the first, only 1 equiv of P is necessary for catalytic turnover (n'=1). Accordingly, the catalytic plateau current (i_{cat}) can be represented by the general, **eq 3.8**.

$$\boldsymbol{i_{cat} = nFSC_p^0\sqrt{Dn'k_{obs}}} \qquad \textbf{eq 3.8}$$

where S = the surface area of electrode in the unit of cm^2, C_p^0 = the concentration of catalyst in bulk solution (M), D = the diffusion coefficient (cm^2s^{-1}), F is faraday's constant and k_{obs} is the appearent catalytic rate constant (s^{-1}). The catalytic plateau current (i_{cat}) is given by **eq 3.8** is independent of the scan rate. Therefore, an ideal S-shaped CV response (in zone KS) (**Figure 3.2**) with a fixed plateau current and a scan rate independent would be expected for a fast catalytic reaction as compared to Fν/RT under pure kinetic conditions. [269]

For a catalytic H^+ reduction to H_2, n=2 and n'=1 are replaced in the **eq 3.8** affording **eq 3.9.**

$$\boldsymbol{i_{cat} = 2FSC_p^0\sqrt{Dk_{obs}}} \qquad \textbf{eq 3.9}$$

When a reversible non-catalytic wave can be observed in the absence of substrate, dividing **eq 3.9** by the non-catalytic peak current (i_p^0) as expressed by Randles-Sevcik in **eq 3.10** leads to **eq 3.11** with a cancellation of A, C_p^0 and D.

$$\boldsymbol{i_p^0 = 0.4463FSC_p^0\sqrt{\frac{F\nu D}{RT}}} \qquad \textbf{eq 3.10}$$

$$\boldsymbol{\frac{i_{cat}}{i_p^0} = 0.448\sqrt{\frac{RTk_{obs}}{F\nu}}} \qquad \textbf{eq 3.11}$$

According to the **eq 3.11**, the ratio of i_{cat}/i_p^0 depends on a function of k_{obs} and the scan rate. Thus, k_{obs} can be directly calculated from the measured parameters i_{cat} and i_p^0 yielding **eq 3.12.**

$$\boldsymbol{k_{obs} = 0.0497 \times \frac{F\nu}{RT} \times \left(\frac{i_{cat}}{i_p^0}\right)^2} \qquad \textbf{eq 3.12}$$

Moreover, the second-order catalytic rate constant, k_{cat} (M^{-1} s^{-1}) and the TOF (s^{-1}) can be determined by i_{cat}/i_p as defined in the **eq 3.13**

$$\boldsymbol{TOF = k_{cat}C_p^0 = \frac{F\nu n_p^3}{RT}\left(\frac{0.4463}{n_{cat}}\right)^2\left(\frac{i_{cat}}{i_p}\right)^2} \qquad \textbf{eq 3.13}$$

where, D is diffusion constant of catalytically active species; k_{cat} is the rate constant of catalytic reaction, n_{cat} = number of electrons required for the catalytic reaction.

Practically, the peak-shaped catalytic wave is usually observed. An S-shaped or plateau-shape CV could not be obtained as result of side-phenomena such as consumption of substrate,

degradation of catalysts and inhibition by product. [273] Competition from side phenomena cannot always be described through experimental parameters. To manage this problem, Savéant and Costentin developed a new method so-called "Foot of the wave analysis" (FOWA).[273] as discussed below. One of side phenomena, that is usually observed in catalytic CV responses of molecular H_2-evolving electrocatalysts, is H^+ consumption as described below.

FOWA plots from unperturbed catalytic responses vs consumption of the H^+ substrate

The catalytic CV response shown in **Figure 3.3** a is obtained with no competition between side-phenomena and the catalytic reaction. Therefore, an ideal S-shaped CV gives an ideal straight line over the whole range of the X-axis from FOWA plot (**Figure 3.3** a') with the starting point and Y-intercept at zero. While the peak-shaped catalytic waves are observed if H^+ consumption interrupts the catalytic reaction. **Figure 3.3** b shows that the decrease of substrate concentration results in more deviation from the S-shape response because of an increasing contribution of substrate diffusion toward the electrode. Use of FOWA analysis (**Figure 3.3** b') allows the observation of a straight line near the foot of the wave for all cases with different acid concentrations. By FOWA analysis, it is demonstrated that the interference by H^+ consumption near the peak of a catalytic wave can be limited and at the foot of the wave and catalysis occurs under pure kinetic conditions (KS zone).

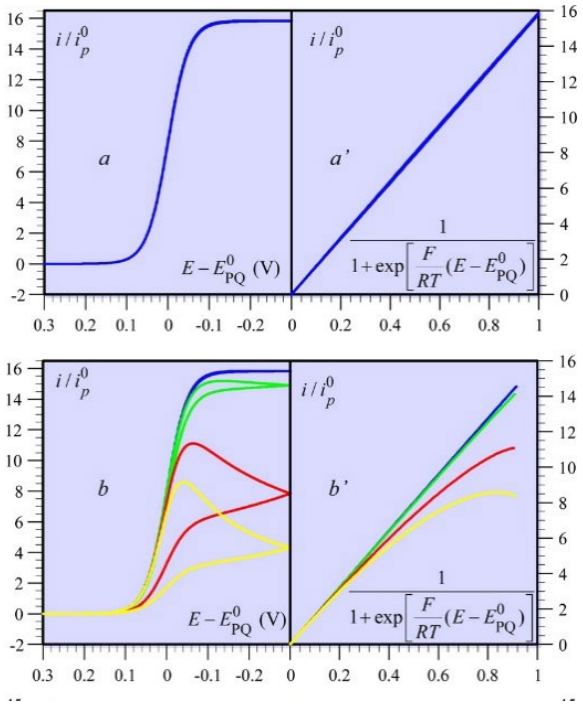

Figure 3.3. (a) Simulated catalytic CV responses (no side-phenomenon), with ν = 0.1 V s^{-1} , D_P = 10^{-5} cm^2 s^{-1} , C_P^0 = 1 mM, T = 298 K, n' = 2, and C_A^0 = 50 s^{-1};(a') FOWA analyses for the same CV response C_A^0 = 1 M, $2k$= 100 M^{-1} s^{-1}. (b) Simulated catalytic CV responses (substrate consumption) with various concentrations of substrate (decreasing from blue to yellow:C_A^0= 1, 0.1, 0.01, and 0.005 M; (b') FOWA plots for the same CV response.[273]

Application of FOWA for Determining a Rate Constant from a peaked-shape catalytic CV response for a Multistep Catalytic Reaction

As mentioned above, side phenomena interfere with the catalytic reaction resulting in peak-shaped catalytic waves. This peak-shaped CV response precludes the straightforward calculation of k_{obs} from the experimental ratio of $i_{cat}/(i_p^0)$ as given in **eq 3.12.** Therefore, the estimation of pseudo-first order rate constant (k_{obs}) in the unit of s^{-1} by FOWA can be the rational choice for analysing a catalytic reaction under pure kinetic conditions occurring at the foot of the wave. [269]

3.1.2.3 Foot of the wave analysis (FOWA)

For a two-electron electrocatalytic process where all electron transfers take place at the electrode and the second reduction step is easier than the first, the expression of current is given by the **eq 3.14** for an ECEC and EECC mechanism for H_2 evolution[274]:

$$\boldsymbol{i} = \frac{\boldsymbol{2FSC_p^0\sqrt{Dk_{obs}}}}{\boldsymbol{1+e^{[\frac{F}{RT}(E-E_p^0)]}}} \qquad \textbf{eq 3.14}$$

where k_{obs} is the apparent rate constant, and E_p^0 is the standard potential of the redox couple mediating catalysis.[274] This equation explains a catalytic current response for a two-electron electrocatalytic reaction as a function of the potential obtained under the conditions of zone KS and the case in which the first chemical step is rate determining. Dividing **eq 3.14** by i_p^0 as defined in the **eq 3.10** yields the **eq 3.15** which allows for determination of k_{obs} by plotting i/i_p^0 as a function of $1/1 + e^{[\frac{F}{RT}(E-E_p^0)]}$ near the foot of the wave to attain a linear function at a certain scan rate. The observed rate constant can then be extracted from the slope of the linear fit.

$$\frac{\boldsymbol{i}}{\boldsymbol{i_p^0}} = \frac{\boldsymbol{2\sqrt{k_{obs}}}}{\boldsymbol{0.4463}}\sqrt{\frac{\boldsymbol{RT}}{\boldsymbol{F\nu}}} \times \frac{\boldsymbol{1}}{\boldsymbol{1+e^{[\frac{F}{RT}(E-E_p^0)]}}} \qquad \textbf{eq 3.15}$$

In the absence of competing side phenomena, plotting i/i_p^0 versus $1/1 + e^{[\frac{F}{RT}(E-E_p^0)]}$ leads to a straight line with an intercept at zero. This linear relationship requires that one of the electron transfer processes for catalysis should occur at a much more positive potential than the other and the first chemical step (k_1) is rate-limiting. To overcome these limitations, using $E_{cat/2}$ instead of E_p^0 as the expression in **eq 3.16** is fulfilled for all kinetic regimes, not only where k_1 is rate limiting.[257, 274]

$$\frac{\boldsymbol{i}}{\boldsymbol{i_p^0}} = \frac{\boldsymbol{i_{cat}/i_p^0}}{\boldsymbol{1+e^{[\frac{F}{RT}(E-E_{cat/2})]}}} \qquad \textbf{eq 3.16}$$

Where, i_p^0 is the peak current of the reversible wave in non-catalytic condition, i_{cat} is the steady-state catalytic plateau current, $E_{cat/2}$ is the potential at $i_{cat/2}$, and the expression $1/\{1+\exp[(F/RT)(E-E_{cat/2})]\}$ describes the fraction of catalyst that is reduced at a given potential.

Thus, in our study, FOWA as expressed in the **eq 3.16** was used to analyse the electrocatalytic wave.

3.1.2.4 Turnover frequency and catalytic Tafel plot

The turnover frequency is generally defined as the time derivative of turnover number, which is considered when a catalyst is stable obtaining from the ratio:

$$TOF = \frac{N_{product}}{N_{active\ cat}}$$

of the number of moles of product, produced per unit of time to the number of active catalysts in the reaction-diffusion layer. In a homogeneous electrocatalytic process, turnover frequency is defined by the **eq 3.17**.[274]

$$\boldsymbol{TOF = \frac{TOF_{max}}{1+exp\left[\frac{F}{RT}(E-E_{cat/2})\right]}} \qquad \boldsymbol{TOF_{max} = k_{cat}C_p^0} \qquad \textbf{eq 3.17}$$

According to this equation, TOF is dependent on the applied potential E and becomes independent of potential when the applied potential is significantly negative of $E_{cat/2}$ leading to reach the TOF_{max} value. This value is simply given as $TOF_{max} = k_{cat}C_p^{\pi}$ Σ ØKŜℕŜ ¢*hC*$_{Y'l\cdot È}$ łă úĺKŜ 2ōăŜℕØŜŘ ℕIּúŜ Ŏ2yãűIּyű óƖ$_{2ōă}$ú ₸ℕ2Y Ch ² !Σ łyˇă™ Iּű Iּ Ŏ2yØŜyűł2yIּf м a IּŎłŘ Ŏ2yŎŜyűℕIּűł2y^{H75} LyűℕŘdzŎűł2yˇ2₸ űKŜ η where $\eta = E^0_{H^+/H_2} - E$ provides a TOF-η relationship which can be expressed as the **eq 3.18** below.

$$\boldsymbol{TOF = \frac{TOF_{max}}{1+exp\left[\frac{F}{R}\left(E^0_{H^+/H_2}-E_{cat/2}\right)\right]exp(-\frac{F}{RT}\eta)}} \qquad \textbf{eq 3.18}$$

3.1.3 Early investigation of cobalt hydride complexes for HER

Reactive Co(III)-H and/or Co(II)-H intermediates are often involved in HER catalysed by cobalt complexes (previously metioned in **section 3.1.1**), and early mechanistic studies of cobalt-catalysed H_2 production suggested that a pathway for H_2 evolution depended on experimental conditions such as concentration of active catalyst or pH as described in the selected cases. A stable hydridocobaloxime (**CoH-8**, **Chart 2.3**) was claimed in 1971. Early kinetics studies of this complex for hydrogen evolution in aqueous and non-aqueous solution were also reported in 1978 by Chao and Espenson.[276] However, it was proved later that the CoH-8 was not the $[Co^{III}(dmgH)_2(PBu_3)(H)]$.

A series of cobalt(III) hydrides based on cyclopentadienyl and phosphine derivatives: **CoH-1**, **CoH-2**, $[CpCo^{III}(P)_2(H)]^+$ (P = PPh_3, PEt_3, $P(OMe)_3$) were isolated by protonation of their cobalt(I) $[CpCo^{I}(P)_2]$ precursors using ammonium salts. These complexes were characterized by ^1H NMR spectroscopy. The activity of the cobalt(I) complexes for electrocatalytic H_2 evolution: for example: $[CpCo^{I}(P)_2]$ and their cobalt(III) hydride analogues, $[CpCo^{III}(P)_2(H)]^+$, were examined in aqueous solution at pH 5. It was found that a reduction of $[CpCo^{III}(P)_2(H)]^+$ to $[CpCo^{II}(P)_2(H)]$ afforded $[CpCo^{I}(P)_2]$ and H_2 via bimetallic reaction of $[CpCo^{II}(P)_2(H)]$ or could give H_2 via a protonation of $[CpCo^{II}(P)_2(H)]$. The resulting $[CpCo^{I}(P)_2]$ is reprotonated to repeat a catalytic cycle for hydrogen evolution in the presence of acid. [208]

As mentioned previously in Chapter 2, cobalt hydride complexes have been much investigated due to their efficiency in many catalyzed reactions. Many cobalt hydride complexes containing phosphine ligands have been reported as intermediates involved in H_2 evolution catalysis.[122] More recent studies of hydride complexes that are evoked as intermediates for catalytic H_2 production will be illustrated in **section 3.1.4**.

3.1.4 Recent studies of cobalt hydride intermediates in catalytic HER

All of the selected cobalt hydride complexes shown in **Figure 3.4** are intermediates for the H_2 evolution reaction. Most of them were generated in situ in a solution under catalytic conditions, and some of them were isolated for mechanistic and/or kinetic studies for H_2 evolution catalysis. For example, the in-situ generation of the hangman porphyrin, [HCo^{III}(HMP)] (HMP = hangman porphyrin) by electrochemical reduction of the Co(II) analogue in acidified MeCN solution using strong acid as H^+ source was reported by Nocera et al [145] in 2011. The evidence for the Co(III)-H and Co(II)-H hydride intermediates was obtained by CV under catalytic conditions as will be discussed below. In the same year, Gray and co-workers [263] reported generation of $HCo^{III}(dmgBF_2)$ by protonation of the Co(I) precursor with a photo-acid monitored by laser transient techniques. The same group in 2012 reported direct evidence for $[Co^{III}(triphos)(CH_3CN)_2(H)]^{2+}$ under catalytic conditions by NMR spectroscopy as discussed below.[224]

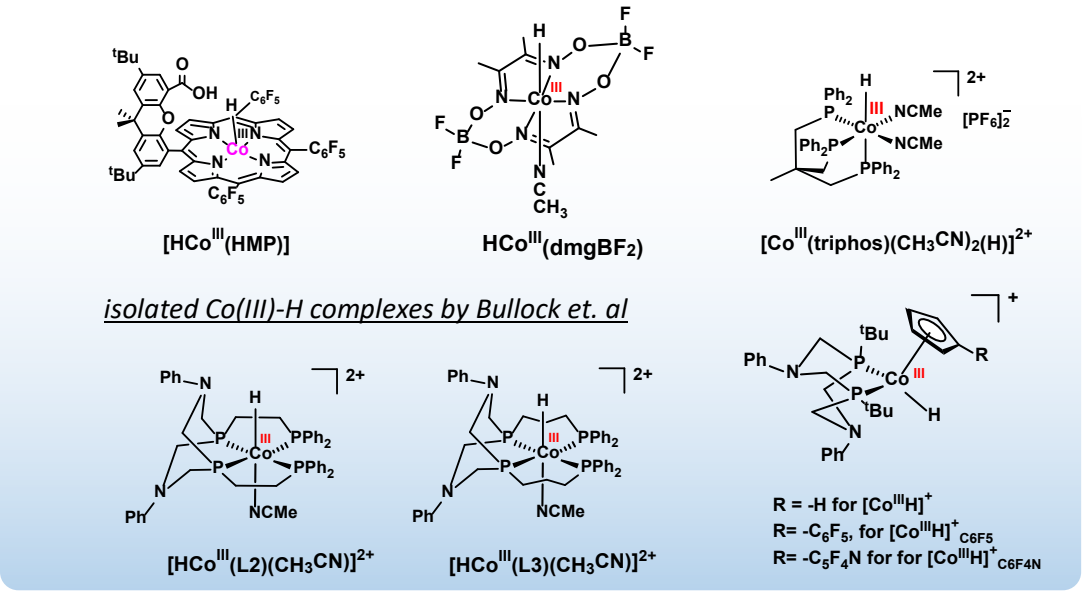

Figure 3.4. Structure of recent cobalt hydride catalysts for H_2 production.

In situ generation of [HCo^{III}(HMP)] hydride complexes monitored by CV

The CVs of **1-Co** and **2-Co** solution with no acid (**Figure 3.5** a) showed Co(I/0) couple redox couples at similar potential around -2.0 V but displayed distinct reversibility. The irreversible Co(I/0) couple in the **1-Co** is due to a protonation of Co(0) species by the pendant COOH to form a Co(II)-H intermediate. The irreversible Co(I/0) in the **2-Co** with no pendant COOH was also observed when weak acid was added to the solution (**Figure 3.5** a, green trace). This confirmed that Co(II)-H is required for HER catalysis by these two complexes.

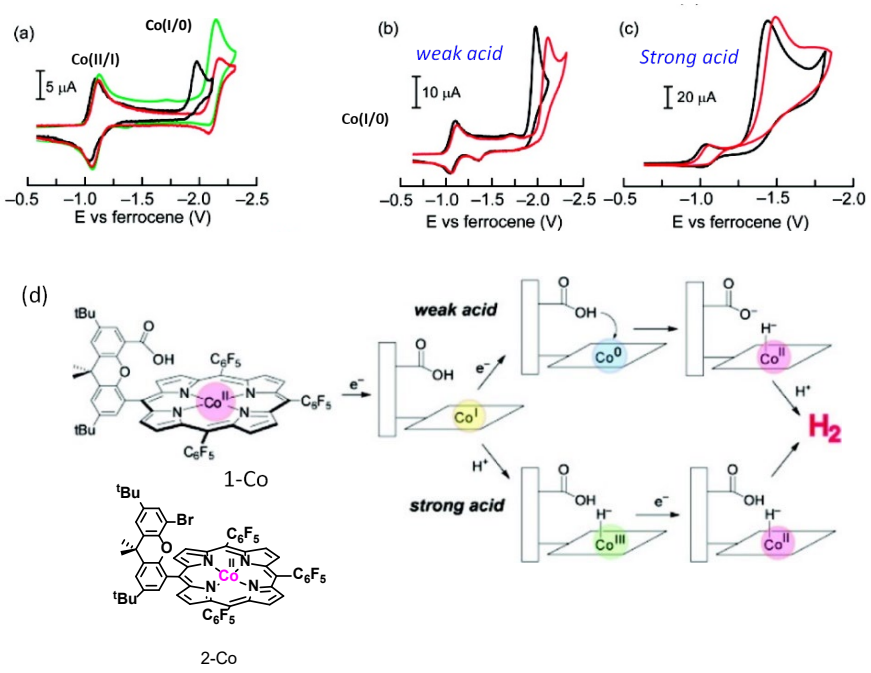

Figure 3.5. (a) CVs of 0.5 mM 1-Co (black line), 2-Co (red line), and 2-Co with 0.5 mM benzoic acid (green line). (b) CVs of 0.5 mM 1-Co with 2.5 mM benzoic acid (black line) and 0.5 mM 2-Co with 3.0 mM benzoic acid (red line). (c) CVs of 0.8 mM 1-Co (black line) and 2-Co (red line) with 10 mM tosic acid. Condition: scan rate 100 mV/s; 0.1 M $TBAPF_6$ in acetonitrile. Glassy carbon working electrode. d) Schematic representation of electrochemical generation of the Co(III)-H intermediate under catalytic conditions.[145]

The CVs (**Figure 3.5** b) of **1-Co** and **2-Co** solution acidified with weak acid (benzoic acid) showed catalytic current near Co(I/0) couple without a loss of reversibility at Co(II/I) couple. It was proposed that H_2 evolution mechanism catalyzed by the **1-Co** and **2-Co** requires a protonation of Co(II)-H formed by a protonation of Co(0) as shown in **Figure 3.5** d**.** Moreover, the hangman effect by installing carboxylic acid group in the **1-Co** improved their catalytic activity by showing catalytic peak at lower reduction potential compared to that of **2-Co** (**Figure 3.5** b). By using strong acid, the Co (II/I) wave in both **1-Co** and **2-Co** becomes irreversible (**Figure 3.5** c). This indicates that the Co(I) analogue is protonated by the tosic acid. But the higher catalytic currents

occurs at more negative potential than the Co(II/I) reduction event. It indicated that a Co(III)-H species formed in a solution needs to be further reduced to Co(II)-H for H_2 generation.

From the proposed H_2 evolution pathway (**Figure 3.5** d), the electrocatalytic H_2 evolution of **1-Co** in MeCN by using strong acid (tosic acid as H^+ source) occurs via a reduction of Co^{III}-H intermediate with a subsequent protonation of the reduced Co^{II}-H species to evolve H_2. In the case of using weak acid as H^+ source (benzoic acid), **1-Co** requires a protonation of Co(II)-H formed by a protonation of the doubly reduced Co(0) for H_2 production.

In-situ generation of $HCo^{III}(dmgBF_2)$ complex monitored by transient absorption spectroscopy

Recent work by Gray et al. [122] revealed the mechanism of H_2 evolution from a photogenerated **$HCo^{III}(dmgBF_2)$** suggesting that reaction *via* a protonation of Co^{II}–H is more favorable under certain experimental conditions: for example; in solutions where Co^{III}–H is in low concentrations and reducing equivalents are in excess. Co(III)-H is generated by protonation of Co(I) with a photo acid monitored by laser transient techniques to investigate proton-transfer and electron transfer kinetics. **Scheme 3.2** shows that excited-state proton transfer from ^{Br}NaphOH to $[Co^{I}(dmgBF_2)]^-$ produces **$HCo^{III}(dmgBF_2)$** with a rate constant of 4×10^9 $M^{-1}s^{-1}$. The Co(III)-H is then reduced by excess Co(I) diglyoxime in solution to produce Co(II)-H (k_{red} = 9.2x10^6 M^{-1} s^{-1}). A heterolytic H_2 evolution by protonation of the Co(II)-H then occurs concomitant with generation of Co^{II}-diglyoxime.

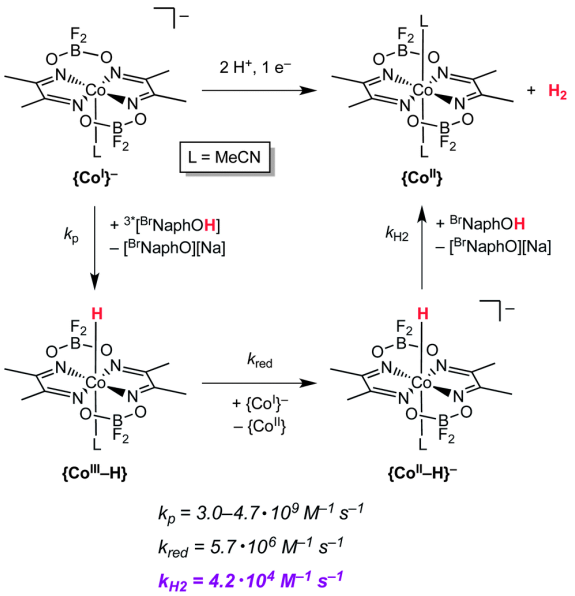

Scheme 3.2. Kinetics parameters for reactions leading to hydrogen evolution from a cobaloxime.[122]

Direct evidence of in situ generation of $[Co^{III}(triphos)(CH_3CN)_2(H)]^{2+}$ by ^1H NMR

In 2012, Gray et al.[224] prepared a series of cobalt complexes with a tripodal phosphine. The hydride **$[Co^{III}(triphos)(CH_3CN)_2(H)]^{2+}$** (**Figure 3.6** a) is generated in situ by protonation of its Co(I) analogue, and direct evidence of the Co(III)-H hydride species hydride signals at δ -7.6 are observed in the ^1H NMR spectrum. The CV studies (**Figure 3.6** b) of the Co(I) species in MeCN with increasing *p*-toluenesulfonic acid monohydrate ($TsOH \bullet H_2O$, pK_a=8.7) display enhancement of currents near the $Co^{II/I}$couple. However, the much higher currents are observed at more negative potential (close to Co(I/0) couple) and at higher acid concentrations. Based on the evidence from the NMR, CV and kinetic studies, the Co(III)-H intermediate produces hydrogen (**Figure 3.6** c) via two competing bimolecular pathways including a slower homolytic route by two species of Co(III)-H and a faster heterolytic cleavage of a highly reactive Co(II)-H. This intermediate is formed after reduction of Co(III)-H by Co(I) analogue and is then rapidly protonated to produce H_2 [224].

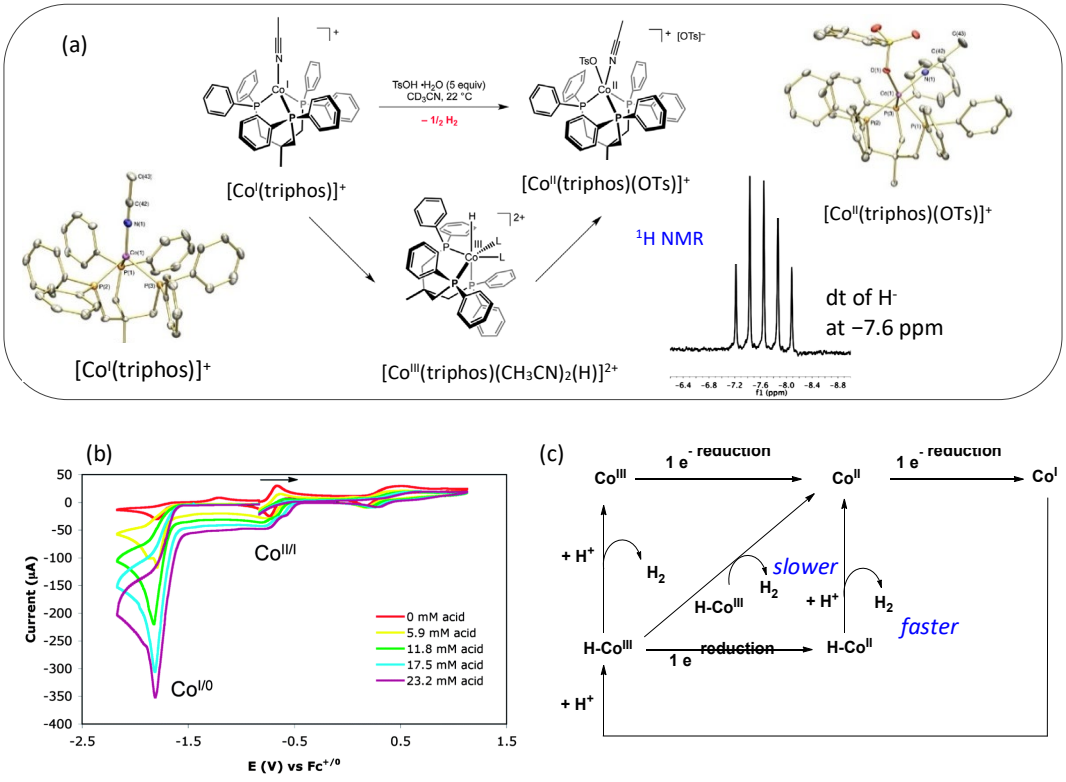

Figure 3.6. a) H_2 evolution from a cationic $[Co^I(triphos)]^+$ via the Co(III)-H intermediate monitored by ^1H NMR. [122], b) CVs of $[Co^I(triphos)]^+$ in MeCN solution with 0.1 M $TBAPF_6$ in the presence of $TsOH \cdot H_2O$ [224] and c) possible pathways to hydrogen production by the fast protonation of Co^{II}-H or slow bimolecular reaction of Co^{III}-H.

Although the reduction of these Co(III)-H complexes in the presence of acid results in catalytic H_2 evolution, they were generated in situ and have not been investigated under non-catalytic conditions (with no acid in a solution). The Bullock group achieved the isolation of the $[HCo^{III}(L2)(CH_3CN)]^{2+}$ supported by a tetradentate phosphine (**Figure 3.4**) This hydride complex was fully characterized with well-defined redox properties (described previously in **section 2.3.2** and **2.3.3**). The mechanism for H_2 production under electrocatalytic conditions is proposed to proceed via both a heterolytic pathway by protonation of HCo(II) or HCo(I) and a homolytic pathway by the bimetallic reaction of HCo(II) or HCo(I) as described in **section 3.1.1**.

A reduction of Co(III)-H to Co(II)-H identified by cyclic voltammetry

In 2016, Bullock et al. [207] reported the mechanism of H_2 evolution electrochemically catalyzed by **$[Co^{II}(P_2N_2)(CH_3CN)_3]^{2+}$** using cyclic voltammetry by the combination of variable scan rate analysis and foot-of-the-wave analysis (FOWA). Transient hydride intermediates can be formed by reduction of Co^{II} to Co^{I} in the presence of acid. The CV (**Figure 3.7** a) of **$[Co^{II}(P_2N_2)(CH_3CN)_3]^{2+}$** with 4.0 equiv *p*-bromoanilinium (pK_a = 9.43) at 0.1 V s^{-1} displays a catalytic wave at E_{pc} = −0.98 V which is shifted to negative potential from the Co(II/I) couple by 110 mV. The anodic peak on the return scan is consistent with the oxidation of Co(I). Raising the scan rate up to 2 Vs^{-1} results in more negative shifts of catalytic peak potential (E_{pc}), and the catalytic waves become separated from the Co(II/I) couple. This separation between the Co(II/I) and Co(III/II)-H couples was also observed in the CVs of the complex at ν =2 V s^{-1} with increasing amounts of p-bromoanilinium (**Figure 3.7** b). The current at the Co(II/I) couple remains constant while the catalytic current at E_{pc} = −1.04 V continues to enhance with the acid concentration indicating that a reduction from Co(III)-H to Co(II)-H must occur prior to liberation of H_2.

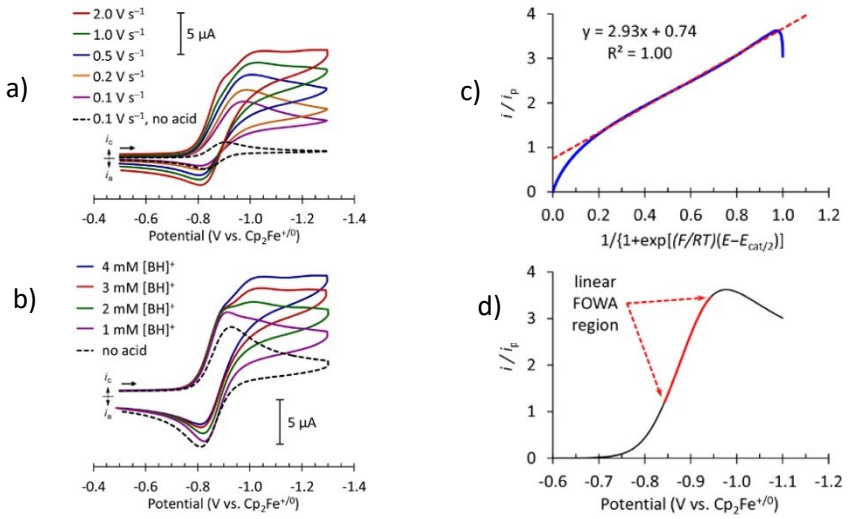

Figure 3.7. Cvs of $[Co^{II}(P^{tBu}{}_2N^{Ph}{}_2)(CH_3CN)_3]^{2+}$ (1 mM) and *p*-bromoanilinium tetrafluoroborate (4 mM) (a) at different scan rates, and (b) varying concentrations of *p*-bromoanilinium tetrafluoroborate (1–4 mM) at scan rate = 2 V s^{-1}; (c) FOWA plot (blue) of $[Co^{II}(P^{tBu}{}_2N^{Ph}{}_2)(CH_3CN)_3]^{2+}$ showing the linear fit (dash line, red); (d) normalized CV (black) showing the potential window that gives a linear FOWA plot (red portion). ν = 0.1 V s^{-1}.[207]

Moreover, a plot of E_{pc} versus log(ν) from the CV in **Figure 3.7** a gave a slope of −54 mV suggesting the formation of Co(III)-H hydride intermediate with quasi-reversible electron transfer kinetics which corresponded to their previous studies on the Co(III/II)-H couples of isolated **$[HCo^{III}(L2)(CH_3CN)]^{2+}$** and **$[CpCo^{III}(P^{tBu2}N^{Ph2})H]^{+}$**. By using foot-of-the-wave analysis FOWA (**Figure 3.7** c), a deviation from linearity at the foot of the wave indicates that the $Co^{III/II}H$ couple is close to and slightly more negative than the $Co^{II/I}$ couple. A plot of i/i_p versus $1/\{1+\exp[(F/RT)(E-E_{cat/2})]\}$ should give a straight line at small values of $1/\{1+\exp[(F/RT)(E-E_{cat/2})]\}$ with an intercept of zero if one of the electron transfers for catalysis occurs at a much more positive potential than the other, i.e. a large ΔE°'. Therefore, FOWA confirmed that the Co(II/I) and Co(III/II)-H couples in $[Co^{II}(P^{tBu}{}_2N^{Ph}{}_2)(CH_3CN)_3]^{2+}$ appear at similar potentials under catalytic conditions. This is in agreement with scan rate analysis by suggesting a reduction of Co(III)-H to Co(II)-H hydride intermediate via quasi-reversible electron transfer kinetics.

Moreover, the FOWA plot (**Figure 3.7** c) also showed a rapid decrease in i/i_p at high $1/\{1+\exp[(F/RT)(E-E_{cat/2})]\}$ indicating acid depletion. The linear region in **Figure 3.7** c corresponds to the red trace in the CV shown in **Figure 3.7** d.

Until now, direct evidence from the spectroscopic and crystallographic characterisations of Co(III) hydride complexes was very limited.[122, 218] In-depth understanding of H_2 evolution pathways catalysed by cobalt complexes requires a straightforward mechanistic and kinetic investigation of cobalt hydride complexes which can lead to rational design of cobalt based

HECs. The next **section 3.1.5** will show examples of cobalt complexes that catalyse H_2 evolution via some of the cobalt hydride intermediates shown previously, other cobalt catalysts and examples of cobalt catalysts for selective CO_2 conversion to CO or HCOOH in **section 3.1.6**.

3.1.5 Molecular cobalt catalysts for H_2 production

Apart from the development of exceptional Dubois catalysts containing Ni metal centre as HECs (presented in Chapter 1), cobalt complexes also have been extensively investigated as efficient catalysts due to their intrinsic high activity in the HER.[65, 67] This section will introduce the development of cobalt based HECs separated into four classes based on their structures with different ligand platforms: diglyoxime derivatives (**section 3.1.5.1**), polypyridyl ligands (**section 3.1.5.2**), dithiolene complexes (**section 3.1.5.3**) and catalysts containing basic amine groups (**section 3.1.5.4**).

3.1.5.1 Cobalt complexes with diglyoxime derivatives

The early cobalt complexes with diglyoxime ligands known as cobaloximes were initially designed as structural mimics of vitamin B_{12}.[141] Cobaloximes were recognized early as efficient catalysts for H_2 evolution from an acidic aqueous solution and could catalyze hydrogen evolution at low overpotentials.[67] For example, The $Co^{III}(dmgH)_2pyCl$ (dmgH = the dimethylglyoximato anion, py = pyridine), **Co-dmg-1** as shown the structure in **Chart 3.1** electrochemically catalyzed H_2 evolution at a $Co^{II/I}$ potential of -1.44 V vs $Fc^{0/+}$ in DMF with $[Et_3NH^+]Cl$ (pK_a = 10.75). The analogous (**Co-dmg-2**) behaves similarly.[87] Replacing the bridging H-atoms by $-BF_2$ groups (**Co-dmg-3** and **Co-dmg-4**) can improve the stability of the catalysts in acidic solutions. However, most of these cobaloxime derivatives still have limited stability in acidic conditions. For this reason, the next generation catalysts as another class of B_{12} mimics, cobalt diimine-dioxime complexes (**Co-dmg-5**-**Co-dmg-7**) have been developed by Artero et al.[141] Changing one oxime bridge to a propane tether also enhances stability by inhibiting hydrolysis of the complexes. [277] Bulk electrolysis of **Co-dmg-3** and **Co-dmg-7** for 2 h in acidic aqueous solution (pH 2.2) using GC as WE at E_{app} = -1.31 V vs $Fc^{0/+}$ results in TON for H_2 production of 16 and 23, respectively, with FE_{H2} of around 80%.[278] DFT calculations of **Co-dmg-7**, suggested that the dioxime moiety may be involved in facilitating catalysis through proton transfer.[268] Moreover, cobaloxime derivatives are also widely combined in photocatalytic systems for H_2 production and used as catalysts in the presence of photosensitizer and sacrificial electron donor.[220]

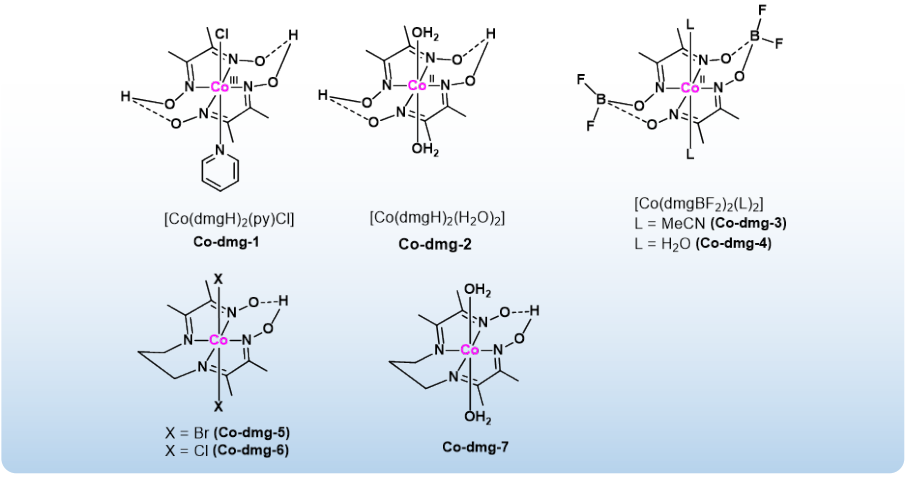

Chart 3.1. Selected examples of cobaloxime derivatives and cobalt diimine-dioxime complexes.

3.1.5.2 Cobalt(II) catalysts with polypyridyl ligands

Polypyridyl-cobalt complexes form a diverse class of HECs, incorporating pyridine- and bpy-derived tetra- and penta-dentate ligands with a Co(II) ion.[70] Molecular metal-polypyridyl catalysts have been extensively studied for hydrogen evolution or water reduction (**Chart 3.2**). A series of water-compatible polypyridine cobalt complexes for hydrogen evolution catalysis has been investigated by C.J. Chang and J.R. Long groups [69, 279]. This class of catalysts are highly stable in water with high rates of conversion and selectivity for proton reduction. Moreover, reactivity of these scaffolds can be tuned by molecular design including altering supporting ligand electronics, denticity and/or incorporating redox-active elements. The pyridine ligands can also stabilize first-row transition metals including cobalt(I) oxidation state in aqueous solution.[280, 281]

The earliest HECs for electrocatalytic H_2 production among this class was developed with bipyridyl derived tetradentate ligand, **Co-Py4-1**. The CV in 1:1 H_2O:MeCN with TFA showed catalytic current at the potential of the Co(II)/Co(I) couple, and bulk electrolysis with a GC WE produced H_2 with FE of 99% at E_{app}-1.40 V vs $Fc^{0/+}$ [282]

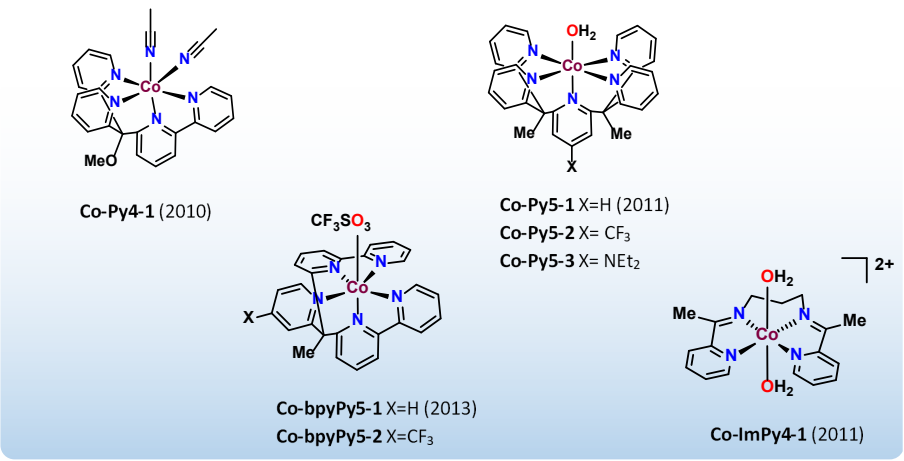

Chart 3.2. Examples of cobalt(II) based polypyridyl catalysts for H_2 evolution.

However, this complex is not soluble at higher water content. To achieve the development of water soluble and resistant catalysts, the pentadentate $Py5Me_2$ ligands [259] were then used for the next generation of cobalt catalysts, **Co-Py5-1, Co-Py5-2** and **Co-Py5-3**, for water reduction in fully aqueous solution. The CVs of these complexes were collected in water with 1 M phosphate buffer, pH 7 at a Hg pool electrode which showed an irreversible wave of the Co(II/I) couple as shown in **Figure 3.8**. Modification of the ligand scaffold at the 4-position of the central pyridine in complex **Co-Py5-1** by introduction of electron withdrawing CF_3 or donating NEt_3 groups affords the complexes **Co-Py5-2** and **Co-Py5-3**, respectively. Electron withdrawing CF_3 in **Co-Py5-2** leads to a positive shift of the Co(II/I) couple compared to the Co(II/I) couple in the **Co-Py5-1**, while a negative shift of the Co(II/I) wave in **Co-Py5-3** is observed by incorporating a donating NEt_3 group. An increase of current at more negative potential than the Co(II/I) couple in each complex indicates subsequent catalytic water reduction at this potential. This finding allows the investigation of electronic effects on the catalytic activity for H_2 production and also demonstrates the ability to tune potentials in a rational molecular design.

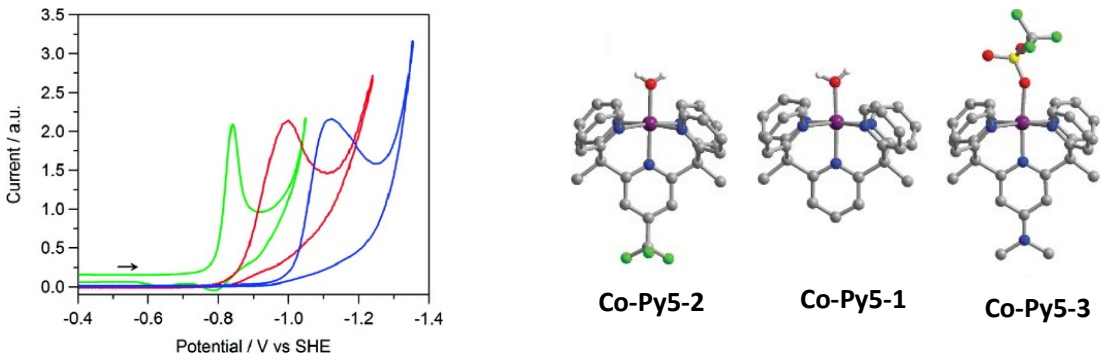

Figure 3.8. Normalized CVs of Co-Py5-1 (red), Co-Py5-2 (green), and Co-Py5-3 (blue) in 1 M phosphate buffer at pH 7 at a Hg pool electrode.[259]

A neutral ligand scaffold in these active and water tolerant catalysts has been widely used for many reasons. First, positively charged complexes can be obtained so that a suitable charge-balancing anion may provide water solubility. Secondly, water-resistant properties are expected by strong bonding interaction between the aromatic pyridine ring and the cobalt metal centre. Finally, the strong σ donor abilities of the pyridines and their metal to ligand π back bonding ability should stabilize low-valent reduced metal species.

H_2 evolution catalysis by Co-based pyridine catalysts with a redox-active ligand

In 2013, Chang and co-workers [279] designed a series of cobalt complexes containing 2,2'-bipyridine moieties, **Co-bpyPy5-1** and **Co-bpyPy5-2** which are expected to be not only redox-active ligands but also provide a robust framework assuming no hydrogenation of these complexes. The hydrogenation of the complexes during catalysis could deactivate H^+ reduction as observed in a reaction of cobalt-bisglyoximato.[283] The CV of complex, **Co-bpyPy5-1** showed a metal-centred Co(II/I) reduction at -1.20 V vs $Fc^{0/+}$ followed by two ligand-centred reductions of $bpy^{0/\bullet-}$ at -1.79 V and -1.94 V. The redox wave of Co(II/I) couple is 230 mV more positive than that in acetonitrile derivative of **Co-Py5-1** [260] which indicated stabilization of Co^{I} via π backbonding to bpy ligand. The introduction of CF_3 electron withdrawing group in **Co-bpyPy5-2** results in positive shifts of Co(III/II) and Co(II/I) couples by 75 and 61 mV, respectively. Interestingly, the two ligand-centred reductions are shifted more positive (80 mV) than the metal redox couples. This evidence suggested that the reduced Co(I) complex can be highly stabilized by redox-active bpy ligands. The **Co-bpyPy5-2** can catalyze proton reduction in CH_3CN with weak acetic acid by showing catalytic waves at two potentials between the Co(II/I) couple and ligand-centred $bpy^{0/\bullet-}$. The authors concluded that it could possibly operate via two different mechanisms depending on the applied potential.

A cobalt bis(iminopyridine) complex, **Co-ImPy4-1** as shown the structure in **Chart 3.2** was synthesized by Gray et al.[240] This complex is a highly active electrocatalyst for water reduction with %FE up to 87% (E_{app}-1.4 V vs SCE) which is proposed to facilitate proton reduction catalysis by a contribution from ligand-centred redox activity. The CV data collected in aqueous solution displays irreversible reduction waves near potentials of the Co(II/I) wave and a slightly more negative ligand-centred catalytic wave. The much higher peak current of this wave is tentatively ascribed to a ligand centred-reduction of the putative cobalt(III) hydride intermediate.[284] The mechanisms for the H_2 evolution catalyzed by this complex were postulated via slightly different pathways depending on pH of solution.

At pH ≤ 6, it starts with a single electron reduction of the complex **Co-ImPy4-1**, (denoted as $[Co^{II}(L)]^{2+}$) to the corresponding reduced $[Co^{I}(L)]^{+}$ in **eq 3.19**. A protonation of the reduced Co(I) species is then likely to occur leading to generation of $[Co^{III}\text{-}H\ (L)]^{2+}$ (**eq 3.20**). A further reduction of the cobalt(III) hydride intermediate is required for H_2 production. This may operate by metal-centred reduction (**eq 3.21**) or ligand-centred of $[Co^{III}\text{-}H\ (L)]^{2+}$ to generate $[Co^{III}\text{-}H(L^{\bullet -})]^{+}$ (**eq 3.22**), which could not be ruled out. Additionally, ligand-centred reduction pathways as shown below (**eq 3.23**-**eq 3.24**) were also proposed at high proton concentration where hydrogen evolution is presumably faster than ligand decomposition.

metal-centred reduction pathway

$$[Co^{II}(L)]^{2+} + e^{-} \rightarrow [Co^{I}(L)]^{+} \quad \textbf{eq 3.19}$$

$$[Co^{I}(L)]^{+} + H^{+} \rightarrow [Co^{III}\text{-}H\ (L)]^{2+} \quad \textbf{eq 3.20}$$

$$[Co^{III}\text{-}H(L)]^{2+} + e^{-} \rightarrow [Co^{II}\text{-}H(L)]^{+} \quad \textbf{eq 3.21}$$

ligand-centred reduction pathway

$$\mathbf{[Co^{III}\text{-}H(L)]^{2+} + e^{-} \rightarrow [Co^{III}\text{-}H(L^{\bullet -})]^{+}} \quad \textbf{eq 3.22}$$

$$\mathbf{[Co^{I}(L)]^{+} + e^{-} \rightarrow [Co^{I}(L^{\bullet -})]^{0}} \quad \textbf{eq 3.23}$$

$$\mathbf{[Co^{I}(L^{\bullet -})]^{0} + H^{+} \rightarrow [Co^{III}\text{-}H\ (L^{\bullet -})]^{+}\ or\ [Co^{II}\text{-}H\ (L)]^{+}} \quad \textbf{eq 3.24}$$

At pH ≥ 7, a protonation of Co(I), as shown in **eq 3.20,** is not a major route to evolve hydrogen and is slow on the CV time scale. The electrolysis experiment at E_{app} near the metal-centred Co(II/I) redox couple (-1.0 V vs SCE) results in minimal hydrogen production. This suggested that H_2 production under low H^{+} concentration possibly occur via a ligand-centred pathway. At low $[H^{+}]$, a doubly reduced $[Co^{I}(L^{\bullet -})]^{0}$ complex is formed by a further reduction of $[Co^{I}(L)]^{1+}$ (via **eq 3.19** and **eq 3.23**) prior to reacting with H^{+} resulting in formation of the $[Co^{III}\text{-}H(L^{\bullet -})]^{1+}$ or $[Co^{II}\text{-}H(L)]^{1+}$ (**eq 3.24**) which are responsible for H_2 evolution.

3.1.5.3 Cobalt catalysts with dithiolene ligands

The dithiolene ligands are attractive ligand scaffold for H_2 evolution catalysis because it is less susceptible to possible hydrogenation due to the 1,2-unsaturated configuration and exhibits reversible electron transfer. This class of cobalt-based HECs (**Chart 3.3**) can catalyze H^+ reduction in aqueous solutions both photochemically and electrochemically.[151] For example, the CV of **Co-S-1** showed a reversible couple consistent with one electron transfer in H_2O:MeCN (1:1). This complex can catalyse H_2 evolution in solution by using strong acid TsOH. Bulk electrolysis at E_{app}= -1.00 V vs SCE using a GC WE gave a FE_{H2} > 99% over 1 h.[153]

Related HECs **Co-S-1Me**, **Co-S-1Cl**, and **Co-S-2** were subsequently investigated; the **Co-S-2** with electron-withdrawing nitrile moieties showed the best photocatalytic activity over this HEC group but electrochemical H_2 evolution catalysis operates at the largest negative potential. A theoretical study revealed a different catalytic H_2 evolution pathway between **Co-S-2** and **Co-S-1** with its derivatives.[285] The latter form undergoes double protonation at the S-atoms following one-electron reduction, giving neutral species which enter the catalytic cycle after receiving a further electron at similar potentials to the first reduction. In contrast, the less basic **Co-S-2** takes up only one proton upon initial reduction forming an anionic intermediate which is less favourable for a further reduction. Formation of a Co^{III}–H active species is then believed to occur via intramolecular H^+ transfer in all cases.[285]

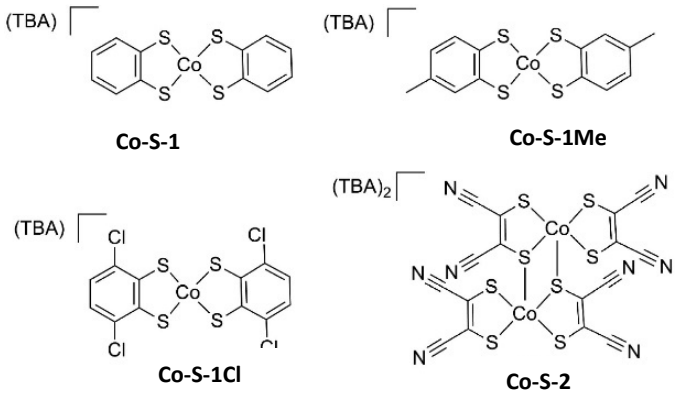

Chart 3.3. Structures of various cobalt dithiolene catalysts.

3.1.5.4 Cobalt complexes containing a basic amine group

H_2 evolution catalysis facilitated by a basic pendant amine in the second coordination sphere

- *The fastest catalytic rate for HER by the $[Co^{II}(L2)(CH_3CN)]^{2+}$*

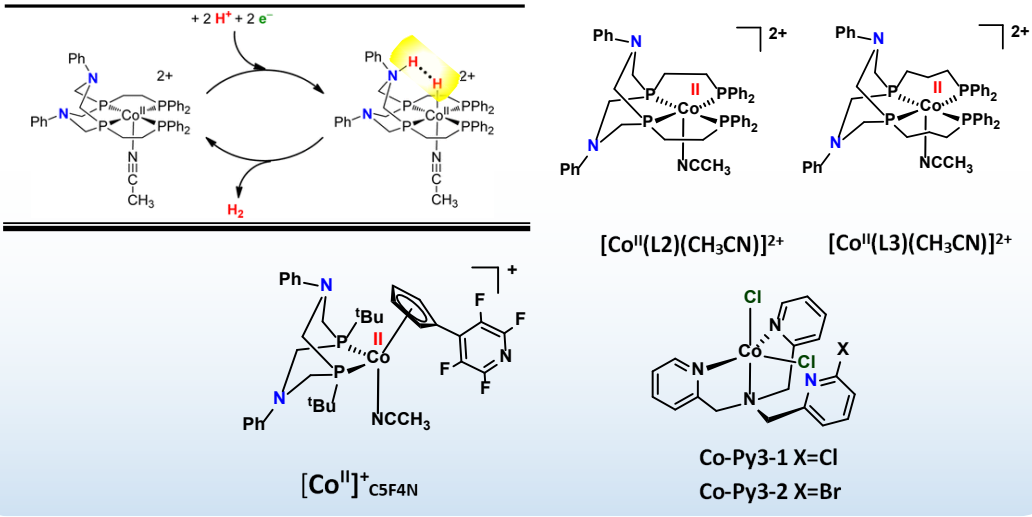

Chart 3.4. Examples of HECs based on-cobalt(II) complexes containing a basic amine group.

The Bullock group previously reported the electrochemical reduction mechanism of $[Co^{III}(L2)(CH_3CN)H]^+$ and $[Co^{III}(L3)(CH_3CN)H]^+$ via $E_rC_rE_r$ pathways (as shown in **Figure 2.9**). Very recently, the same group [286] studied the mechanism and kinetics for H_2 evolution catalysed by the Co(II) analogue, $[Co^{II}(L2)(CH_3CN)]^{2+}$. The CVs of $[Co^{II}(L2)(CH_3CN)]^{2+}$ and $[Co^{II}(L3)(CH_3CN)]^{2+}$in MeCN solution acidified with 1:1 $[(DMF)H]^+$:DMF display catalytic currents at the reduction potential of the corresponding Co(III)-H complex suggesting that the Co(II)-H intermediate is required for H_2 evolution. The mechanism of $[Co^{II}(L2)(CH_3CN)]^{2+}$ for H_2 production in acidic CH_3CN solution was experimentally and theoretically studied suggesting formation of H_2 via the active *endo*-HCo^{II} intermediate with a protonated pendant amine (**Chart 3.4**). The kinetic studies of $[Co^{II}(L2)(CH_3CN)]^{2+}$ gave a TOF of 980 s^{-1} for H_2 production with an overpotential at $E_{cat/2}$ = 1020 mV. The catalytic performance with a TOF up to 1800 s^{-1} for H_2 production by this complex can be improved by addition of water. The authors claimed that $[Co^{II}(L2)(CH_3CN)]^{2+}$ catalyses H^+ reduction with the fastest rate among H_2-evolving Co-based molecular electrocatalysts. However, the H_2 evolution catalysed by $[Co^{II}(L2)(CH_3CN)]^{2+}$ was studied at much higher acid concentration (>400 mM) than that of other cobalt(bisiminopyridine) catalysts.[240]

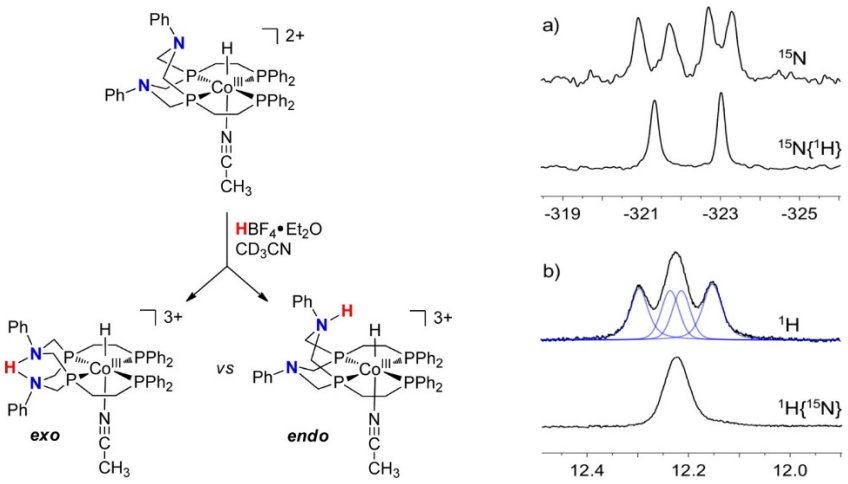

Figure 3.9. Protonation of $[HCo^{III}(L2)(CH_3CN)]^{2+}$ to form exo versus endo isomer and NMR spectra of ^{15}N-labeled *exo*-$[HCo^{III}(^{15}N\text{-}L2\text{-}H)(CH_3CN)]^{3+}$. Figure (a) ^{15}N NMR (top) and $^{15}N\{^1H\}$ NMR (bottom) spectra, and (b) ^{1}H NMR (top) and $^1H\{^{15}N\}$ NMR spectra (bottom) of the NHN resonance.[286]

The rate determining step for H_2 evolution catalysed by the by $[Co^{II}(L2)(CH_3CN)]^{2+}$ was proposed to be an intramolecular isomerisation of the protonated pendant amine from the exo- to endo-isomer. The protonation of ^{15}N labelled-$[HCo^{III}(L2)(CH_3CN)]^{2+}$ in MeCN acidified with HBF_4Et_2O result in a formation of protonated exo isomer of $[HCo^{III}(^{15}N\text{-}L2\text{-}H)(CH_3CN)]^{3+}$ as a major species. This was confirmed by the ^{1}H and ^{15}N NMR spectrum as shown in **Figure 3.9**. This evidence proved the role of pendant amine in the complex for facilitating H^+ transfer to the hydride ligand in the metal centre of the hydride intermediate for H_2 evolution.

Lowering overpotential by electron withdrawing group on ligand scaffold

Another series of cobalt(II) complexes with pendant amines is represented by the **$[Co^{II}]^{+}_{C5F4N}$** complexes in **Chart 3.4**. The CV titration (**Figure 3.10** b) of the complex with the most electron withdrawing group on Cp ring, **$[Co^{II}]^{+}_{C5F4N}$** showed catalytic current near the Co(II/I) couple upon adding acid. It can operate at lower overpotential (860 mV at $E_{cat/2}$) with a lower turnover frequency of 350 s^{-1} compared to the overpotential of 1020 mV with a TOF of 1800 s^{-1} for H_2 production catalysed by $[Co^{II}(L2)(CH_3CN)]^{2+}$ containing pendant amine (as shown above). The proposed mechanism for H_2 evolution catalyzed by the $[Co^{II}]^{+}_{C5F4N}$ is the same as the H_2 evolution pathways catalysed by the $[Co^{II}(L2)(CH_3CN)]^{2+}$, where the pendant amine plays the same role for assisting proton transfer.

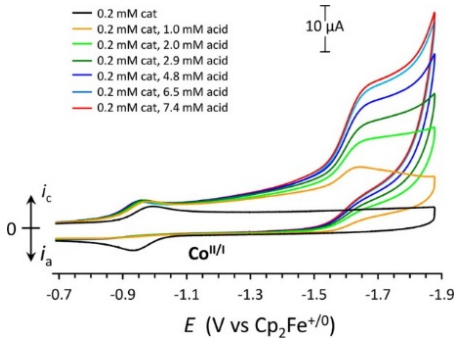

Figure 3.10. CVs of the $[Co^{II}]^{+}_{C5F4N}$ upon increasing the acid concentration (*p*-anisidinium as H^+ source). Conditions: 0.2 mM of $[Co^{II}]^{+}_{C5F4N}$ complex in MeCN with 0.2 M $TBAPF_6$, scan rate 5 V s^{-1}, 1 mm diameter glassy-carbon working electrode.[225]

H_2 evolution catalysis facilitated by non-coordinating pyridine ring

In 2016, Junfei and co-worker [245] reported photocatalysts for water reduction based on cobalt(II) complexes, **Co-Py3-1** and **Co-Py3-2** supported by a tetradentate pyridyl ligand. The possible mechanisms of photocatalytic H_2 evolution were proposed in **Figure 3.11**. Interestingly, the dangling pyridyl ligand with a Br or Cl act as both redox-active ligands and a protonation site facilitating electron and proton transfers. As a result, their photocatalytic H_2 evolution with a TON of 20 000 (6 h irradiation) can be achieved. This is the highest TON value reported to date among the TON for polypyridyl Co-based photocatalytic water reduction catalysts. For the **Co-Py3-1** (Cl substituted pyridyl group), the non-coordinating pyridyl in the complex may catalyse H_2 evolution by itself resulting in the double catalytic H_2 evolution sites of **Co-Py3-1**. This example provides a new strategy to design more effective WRCs.

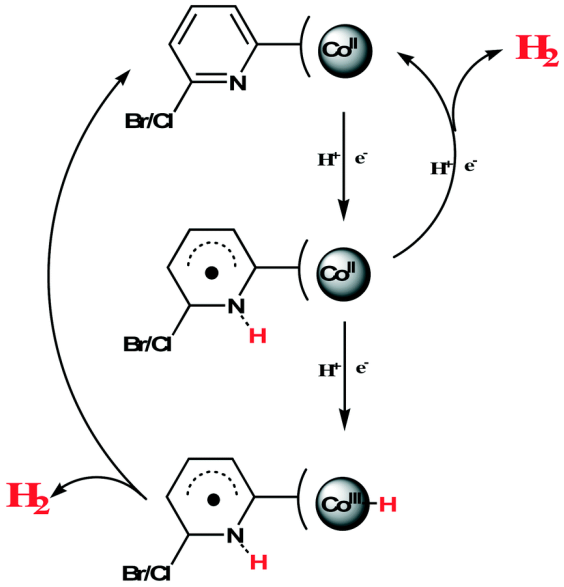

Figure 3.11. Possible photocatalytic H_2 evolution mechanisms of Co-Py3-1 and Co-Py3-2. [245]

3.1.6 Electrochemical conversion of CO_2 by cobalt complexes

Compared to the CO_2 reduction catalysts containing Mn, Fe and Ni as metal centre, there are few efficient homogeneous cobalt catalysts for CO_2 electroreduction due to slow reaction and lack of selectivity for product formation. There are some examples of cobalt catalysts that prefer CO_2 reduction to H^+ reduction as demonstrated by Peters and co-workers[155] and recently reported by Artero et al.[287] Moreover, the mechanistic pathways were proposed based on experimental evidence and density functional theory (DFT) calculations.

In 2014, Peters et al. [155] reported CO_2 reduction activity by the cobalt(III) complexes, $[Co^{III}N_4H(Br)_2]^+$ supported by redox-active ligand with pyridyldiimine (PDI) moiety as shown in **Figure 3.12**. This complex is known as a competent H_2 evolution catalyst: however; it can electrochemically catalyse CO_2 reduction in MeCN using H_2O as proton source. It showed a preferential CO_2 reduction to CO relative to H_2 evolution with faradaic efficiency of 45± 6.4% for CO and 30 ± 7.8 % for H_2. The CV shows an increase of current near to the formal Co(I/0) redox couple (**Figure 3.12**). There is no increase in catalytic current at the redox couple of Co(II/I), thus the $[Co^{I}N_4H)(MeCN)]^+$ was initially assumed as precatalyst for CO_2 reduction. According to DFT calculation for $[Co^{I}N_4H)(MeCN)]^+$ complex, the authors concluded that the stability of the $N_4H^{\bullet-}$ ligand and ability to accommodate a second electron possibly contribute to favouring CO_2 reduction over H^+ reduction in the presence of large concentrations of water. This promising evidence has confirmed that polypyridine ligands can store an electron during electrocatalytic reduction of CO_2.[288] For this reason, redox noninnocence of the ligand could possibly play a significant role in substrate activation and product selectivity.[289]

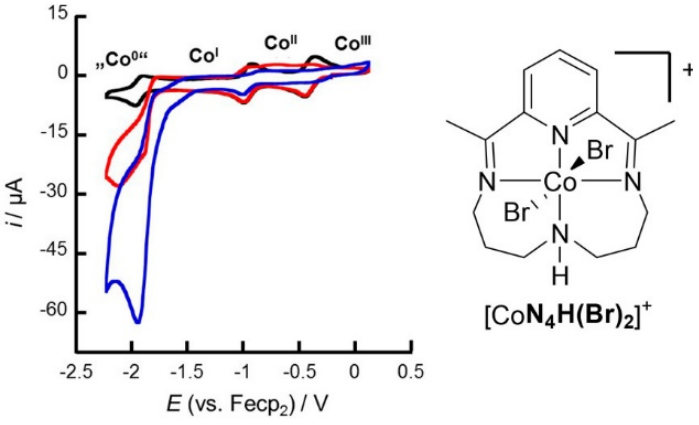

Figure 3.12. CV of 0.3 mM $[Co^{III}N_4H(Br)_2]^+$ in CH_3CN/0.1 M NBu_4PF_6 under Ar (black line), after saturation with CO_2 (red line), and after adding 10 M H_2O to the same solution; ν = 0.1 V s^{-1}, glassy carbon as working electrode.[155]

Cobalt-based catalysts for CO_2 reduction with pendant basic groups

In the last few years, cobalt catalysts with polypyridylamino with a basic pendant group have gained attention for CO_2 reduction (**Chart 3.5**). [115] [114, 290, 291] For example, Marinescu et al [114] studied the role of secondary pendant amine in CO_2 reduction catalysis by **Co-CO_2-1**. CV studies reveal that their activity depends strongly on the number of secondary amines incorporated in the ligand scaffold. DFT calculations shows the CO_2 reduction pathways by the intermediate with pendant amines (**Co-CO_2-1**) that facilitate the intermolecular proton transfer via hydrogen bonding to a weak acid (TFE). This role of pendant amine for assisting the rate-limiting H^+ transfer result in a linear correlation between the catalytic rate and the number of pendant NH groups. Another study by Dey and co-workers[292] show exceptional and selective CO_2-to-CO reduction catalyzed by the 2,6-dithiomethylpyridino Co(dppe) (dppe = bis(diphenylphosphino)ethane) complex (**Co-CO_2-2**). CV studies suggest that the protonated thiolate group may assist the CO_2 binding to the Co^I intermediate. Moreover, this catalyst can mediate CO_2 reduction via the Co(I) intermediate which is different from most of the transition-metal-based systems that require reduction of the metal to its formal zerovalent state for CO_2 reduction.

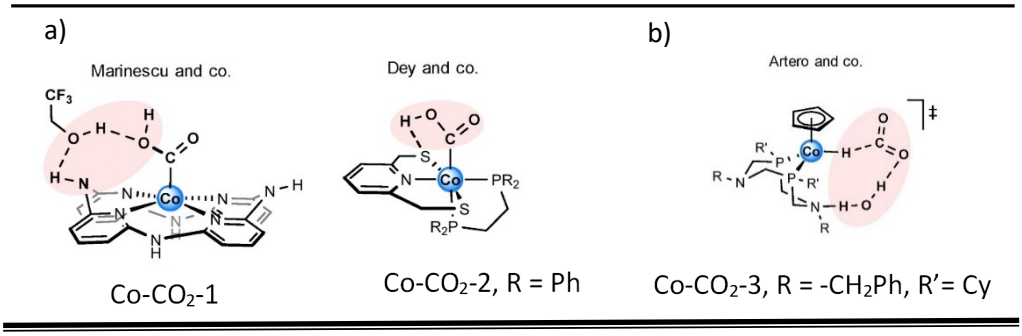

Chart 3.5. Selected examples of cobalt catalysts with pendant basic group for selective CO_2 conversion to CO (a) and HCOOH (b).[291]

The cobalt hydride derivatives (**Co-CO_2-3**) of cyclopentadienyl cobalt complexes containing a pendant amine can selectively catalyse CO_2 reduction to formic acid as reported by Artero et al.[287]. They are very selective for CO_2 conversion to formic acid in DMF/water mixture with faradaic efficiency of 90±10% at moderate overpotential (500-700 mV). This is also considered as the most promising CO_2-to-formic acid cobalt electrocatalyst developed to date. From mechanistic studies and DFT calculations, the authors revealed that the pendant amine moieties are able to stabilize key intermediates (**Co-CO_2-3**) via hydrogen bonding with H_2O during H^- transfer from the Co^{II}-H intermediate to CO_2 molecule. This confirms the key step for the selective conversion of CO_2 to formic acid. The proposed CO_2 reduction mechanism is shown in **Scheme 3.3.**

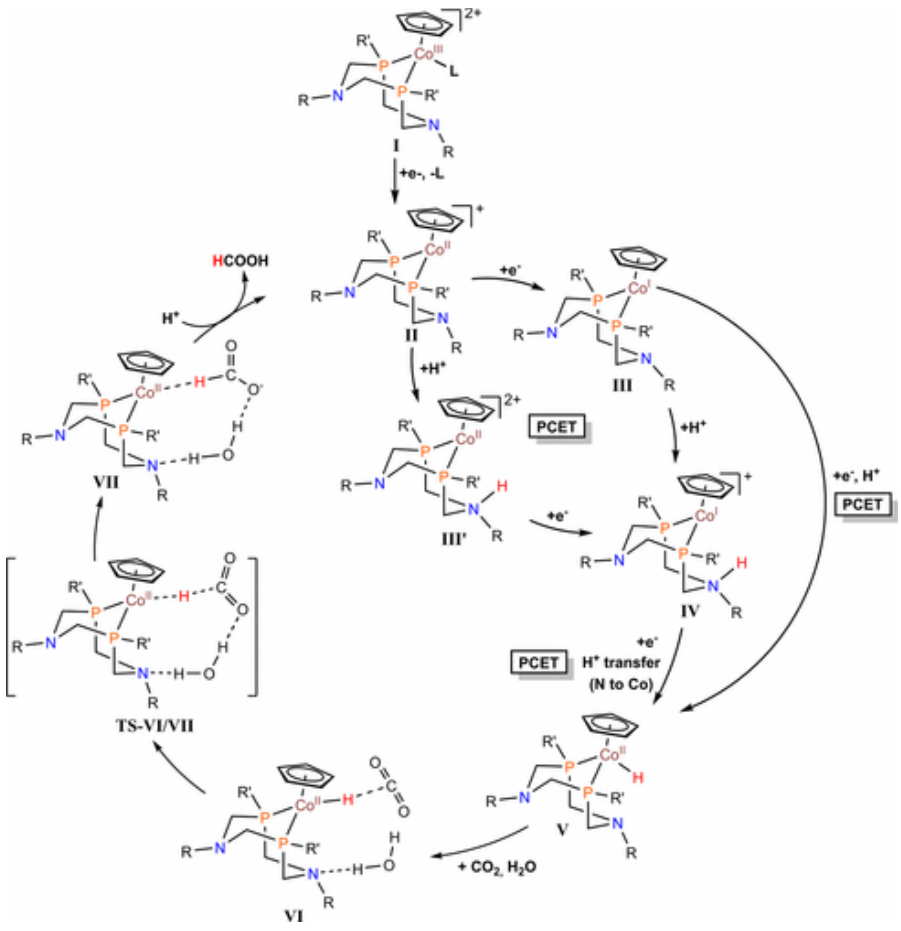

Scheme 3.3. Postulated mechanism for electrocatalytic CO_2 reduction. [287]

3.2 Experimental

3.2.1 General procedure for electrochemical studies

All cyclic voltammetry experiments were performed in a three-neck single compartment electrochemical cell under Ar atmosphere. A commercial glassy carbon disc electrode with 3 mm diameter from Basi® was used as working electrode. The auxiliary electrode was a platinum wire for all CV experiments. The silver wire pseudo-reference was constructed by attaching a Vycor porous glass to glass tube via heat-shrink tubing consisting of silver wire immersed in electrolyte solution (0.1 M tetrabutylammonium hexafluorophosphate, $TBAPF_6$, in acetonitrile). Thus, this pseudo-reference electrode was separated from an analyte solution by the Vycor glass. Ferrocene (Fc) was added to an analyte solution for the last measurement of each experiment in order to use as internal reference compound to measure redox potential. All experiments were carried out in 0.1 M $TBAPF_6$ in dry and degassed acetonitrile as the supporting electrolyte solution, and potentials were reported with respect to the ferrocene/ferrocenium (Fc^+/Fc) couple at 0 V. Before each scan, a solution was degassed with Ar for 5 min, and the working electrode was thoroughly cleaned prior to using for each measurement by polishing with wet alumina powder on polishing pad and then sonicating in Millipore water for 3 min. The electrode was subsequently rinsed with millipore water followed by acetone prior to get it dry by N_2 blowing.

3.2.2 Bulk electrolysis experiment

The electrochemical studies were performed by using a BASi Epsilon-EC potentiostat and EC-Lab software was used for process and analysis of the data. All bulk electrolysis experiments were performed in a 50 mL three-neck round bottom flask equipped with suba seals containing 20 mL of 0.1 mM of each complex in MeCN containing 0.1 M $TBAPF_6$ under Ar atmosphere. A glassy carbon disk electrode was used as working electrode for cyclic voltammetry (CV), and carbon plates (10 x 10 x 1 mm) were used as a working and a counter electrode. The silver wire immersed in acetonitrile containing 0.1 M tetrabutylammonium hexafluorophosphate ($TBAPF_6$) was used as the pseudo-reference electrode, and ferrocene was used as internal reference which was added to the solution after electrolysis.

The carbon plate as working electrode was polished on all edges and two faces on sand paper with a few drops of Millipore water prior to polish with wet alumina powder on polishing pad. The electrode was then rinsed by Millipore water to eliminate alumina on the surface and then sonicated in the water for 30 min to get rid of all residual alumina. The electrode was rinsed by water, and acetone (analytical grade) before allowing it to dry in the air or blowing with N_2 stream

3.2.3 Gas chromatography

Gas analysis was performed using a Shimadzu Corporation GC-2014 equipped with molecular sieve column and a thermal conductivity detector (TCD). Gas samples were analyzed by the following conditions; 20 mL min^{-1}, 90°C column temperature and 120 °C detector temperature. Under these conditions, the retention time of H_2 is 1.0 min and the air peak is at 2.0 min. 200 μL of gas was withdrawn from the headspace of the cell using a sample lock gas-tight syringe.

3.2.4 Determination of H_2 and calculation of Faradaic efficiency for H_2 evolution

The experimental number of moles of H_2 produced from the system in the headspace can be obtained by using a calibration curve for determination of H_2 as shown in **Figure A 3.22.** This calibration curve was built by injecting a known amount of 50% H_2/CO to obtain peak area of H_2 by GC analysis. The gaseous products in the headspace after bulk electrolysis for 2 h were analyzed by sampling 200 μL using a gas-tight syringe. The sample was then manually injected into the GC instrument. The peak area of H_2 analyzed by the GC technique from the direct injection of head space gas for each complex was plotted against times of electrolysis (**Figure A 3.23**). The peak area of H_2 at 2h of electrolysis was taken and then fitted to the linear equation obtained through the calibration curve to obtain the experimental number of moles of H_2.

The bulk electrolysis of $[Co^{II}(PN)_2(MeCN)][BF_4]_2$ under the conditions given in **Table 3.2**, gave 32.5 μmol. the area of 96,732 can be collected directly from injection 200 μL of head space gas at 2 h of electrolysis. The resulting value was then placed to the linear fit equation obtained through the calibration curve with the linear equation:

$$y = 145838x-28582$$

$$x = (96,732 + 28582)/145838$$

$$= 0.859 \text{ μmol}$$

From this value, the total number of moles H_2 produced from the experiment can be calculated by multiplying by the headspace volume of the cell with 63.8 mL.

$$nH_2 \text{ (exp)} = (63,800 \text{ μL}/200 \text{ μL}) \times 0.859 \text{ μmol}$$

$$= 274.1 \text{ μmol}$$

The theoretical moles of H_2 (nH_2 (cald)), were determined from the area of the I-t plot (**Figure 3.29** b) giving 53 C equating to 273.6 μmol of H_2. From this calculation, the plot of charge versus time of electrolysis (**Figure 3.29** c) which showed the charge passed through a solution over 1 h of applying constant potential was obtained.

Therefore, the plot of charge versus time was converted to the plot of theoretical number of moles of H_2 versus time (**Figure 3.29** d) by applying to the **eq 3.25**. According to the bulk electrolysis at constant applying potential (-1.33 V) for 2 h, the charge passed (Q) of 53 C and theoretical number of moles of H_2 (273.6 μmol) can be obtained as shown below:

$$\mathbf{nH_2 \text{ (cald)} = Q/FE = [53/(96485 \text{ C x } 2)]} \qquad \textbf{eq 3.25}$$

$$= 273.6 \text{ μmol}$$

This value allowed determination of the percent faradaic efficiency by using **eq 3.26**:

$$\text{percent faradaic efficiency, \% FE } (H_2) = [nH_2 \text{ (exp)}/nH_2 \text{ (cald)}] \times 100 \qquad \textbf{eq 3.26}$$

$$= (274.1/273.6)x100$$

$$\mathbf{= 100\ \%}$$

3.3 Results and discussion

The electrochemical characterisation of each complex was discussed in **chapter 2** (**section 2.5.5**). The CVs of $[Co^{II}(PN)_2(MeCN)][BF_4]_2$ and $[Co^{III}(PN)_2(H)(MeCN)][PF_6]_2$ are shown in **Figure 2.43** and **Figure 2.57** electrochemical data are summarized in **Table 3.1**. The first one-electron reduction of the hydride complex through Co(III/II)-H couple at -1.1 V resulted in a reversible MeCN loss from the Co centre (E_rC_r mechanism). However, the Co(II) complex showed a fully reversible Co(II/I) couple. Moreover, the Co(III/II)-H in the hydride complex is very close to the reversible Co(II/I) couple of $[Co^{II}(PN)_2(MeCN)][BF_4]_2$ indicating that the hydride ligand greatly stabilized the Co(III) oxidation state. Moreover, the second one-electron reduction in these two complexes displayed irreversible electron transfer. The irreversible Co(II/I)-H couple appeared at a potential comparable to the reduction through the Co(I/0) redox couple (-2.0 V).

The CV of $[Co^{III}(PN)_2(H)(Cl)][PF_6]$ (**Figure 2.57**) showed two irreversible reduction processes at E_{pc} = -1.48 V and -2.02 V for the Co(III/II)-H and Co(II/I)-H couples, respectively. Similarly to $[Co^{III}(PN)_2(H)(MeCN)][PF_6]_2$, the cathodic peak of the Co(III/II)-H couple appeared at slightly more negative potential and is close to the Co(II/I) redox couple of $Co^{II}(PN)_2Cl_2$ (red line), $[Co^{II}$*cis*-$(PN)_2Cl][PF_6]$ (blue), and $[Co^{III}$*cis*-$(PN)_2Cl_2][PF_6]$ (pink), under similar conditions. Moreover, the Co(II/I)-H wave of $[Co^{III}(PN)_2(H)(Cl)][PF_6]$ is near to the Co(I/0) couple of $Co^{II}(PN)_2Cl_2$ and $[Co^{II}$*cis*-$(PN)_2Cl][PF_6]$, and electron transfers at these couples are all irreversible processes.

The assigned redox couples of each complex in this series agree with the cobalt (II) and Co(III) based molecular electrocatalysts reported in the literature as summarized in **Table 3.1** and the structures are shown in **Chart A 3.1**. All complexes can catalyse H^+ reduction where H_2 evolution catalysis occurred near to the Co(II/I) couple and most of these complexes are reported to catalyse HER via a formation of Co(III)-H and/or Co(II)-H hydride intermediates.

Table 3.1. Electrochemical data for the cobalt complexes (in acetonitrile solution with 0.1M $TBAPF_6$ in this study and in the literature).

Complex, this work	$E_{1/2}$/V (ΔE_p, mV) vs $Fc^{0/+}$			E_{pc} /V vs $Fc^{0/+}$	
	$Co^{III/II}$	$Co^{II/I}$	$(Co^{III/II}$-H)	$Co^{I/0}$or Co^{I} ($L^{\bullet-}$)	$(Co^{II/I}$-H)
$[Co^{II}(PN)_2(MeCN)][BF_4]_2$	-	-1.08 (70)	-	-2.28	-
$[Co^{III}(PN)_2(H)(MeCN)][PF_6]_2$	-	-	-1.10 (110)	-	-1.95
$[Co^{III}(PN)_2(H)(Cl)][PF_6]$	-	-	-1.48 (E_{pc})	-	-2.02
$[Co^{II}$*cis*-$(PN)_2Cl][PF_6]$	-0.12 (109)	-1.2 (E_{pc}) -0.15 (E_{pa})		-2.27	
$[Co^{II}(PN)_2Cl_2]$	-0.40 (150)	-1.32 (143)	-	-2.11	-
literature					
Complex, literature	**Ref.**	$E_{1/2}$/V (ΔE_p, mV) vs $Fc^{0/+}$			E_{pc} /V vs $Fc^{0/+}$	
		$Co^{III/II}$	$Co^{II/I}$	$(Co^{III/II}$-H)	$Co^{I/0}$or Co^{I} ($L^{\bullet-}$)	$(Co^{II/I}$-H)
$[HCo^{III}(L2)(CH_3CN)]^{2+}$	206	-		-1.57 (E_{pc}) -1.47 (E_{pa})	-2.28	-0.82, -0.80 $E_{pa}'(Co^{I})$
$[Co^{II}(L2)(CH_3CN)]^{2+}$	286	-	-0.82		-2.20	
$[Co^{II}(triphos)(OTs)]^{+}$	224	-	-0.16	-	-1.87	
$[Co^{I}(triphos)(MeCN)]^{+}$	224	+0.66	-0.68		-1.81 -2.73 ($Co^{0/-1}$)	
$[Co^{III}(dppe)_2(MeCN)(H)][PF_6]_2$	79	-0.83				-1.16
$[Co^{II}(dppe)_2(MeCN)][BF_4]_2$	293	+1.2(E_{pc}) -0.13(E_{pa})	-0.71 (60)		-1.56(70) -2.03 ($Co^{0/-1}$)	
$[Co^{II}(P^{Ph}{}_2N^{Ph}{}_2)_2(MeCN)][BF_4]_2$	246	-	-0.58 (71)		-2.04 $Co^{(I/-I)}$ (100 mV)	
$[Co^{II}(P^{tBu}{}_2N^{Ph}{}_2)(MeCN)_3][BF_4]_2$	247	+0.34 (114)	-0.87 (63)			
$[Co^{II}(P^{tBu}{}_2N^{Bz}{}_2)(MeCN)_3][BF_4]_2$	247	+0.26 (161)	-0.94 (82)			
$[Co^{II}(P^{Ph}{}_2N^{Ph}{}_2)(MeCN)_3][BF_4]_2$	246	-	-0.99 (70)			
$[Co^{II}(PNP)(MeCN)_3][BF_4]_2$	246		-1.15 (150)			
$[Co^{II}(dppp)(MeCN)_3][BF_4]_2$	246		-0.91 (72)			
$[Co^{II}(MeCN)_6][BF_4]_2$	246		-1.21 (95)			
Hangman porphyrin 1-Co	145		-1.08			
Hangman porphyrin 2-Co	145		-1.11	-	-2.14	-
Cobalt bis iminopyridine	240	-0.48	-1.00			

L2 = 1,5-diphenyl-3,7-bis((diphenylphosphino)alkyl)-1,5-diaza- 3,7-diphosphacyclooctane; alkyl = $(CH_2)_2$, n = 2 (L2); $(CH_2)_3$, n = 3 (L3)

The redox properties of the two hydride complexes are significantly different from one another. $[Co^{III}(PN)_2(H)(MeCN)]^{2+}$ showed a quasi-reversible Co(III/II)-H couple, whereas the first reduction of $[Co^{III}(PN)_2(H)(Cl)]^{+}$ through the Co(III/II)-H couple became irreversible at E_{pc}-1.48 V and appeared at much more negative potential (by 380 mV) than that of MeCN bound complex (**Figure A 3.1**). It indicates that one-electron transfer to the monocationic $[Co^{III}(PN)_2(H)(Cl)]^{+}$ bearing anionic Cl^{-} ligand is more difficult than the one-electron reduction of the dicationic $[Co^{III}(PN)_2(H)(MeCN)]^{2+}$ containing neutral MeCN. However, a similar second reduction process of Co(II/I)-H couple to that of the MeCN analogue was observed displaying an irreversible process around -2.0 V.

H^+ reduction activity of $[Co^{II}(PN)_2(MeCN)]BF_4]_2$ and $[Co^{III}(PN)_2(H)(MeCN)][PF_6]_2$ with trifluoroacetic acid (TFA)

The electrocatalytic H^+ reduction activity of the complexes in this study was examined by CV techniques. The CV titration experiment of each complex with trifluoroacetic acid (TFA with pKa = 12.6 in MeCN) as H^+ source was performed in MeCN solution containing 0.1 M $TBAPF_6$.

3.3.1 CV studies of $[Co^{III}(PN)_2(H)(MeCN)][PF_6]_2$ using TFA as H^+ source

The CV response of this complex upon adding TFA showed increases in current on reduction of $[Co^{III}(PN)_2(H)(MeCN)][PF_6]_2$ at the Co(III/II)-H couple at -1.14 V (**Figure 3.13**). The enhancement of current near this couple suggests that the one-electron reduction of the Co(III)-H to the Co(II)-H is required for HER catalysis. Therefore, a subsequent protonation of the reduced Co(II)-H species or a bimolecular reaction of the Co(II)-H species could occur for H_2 evolution. Plots of the ratio i_{cat}/i_p versus acid concentration showed a linear increase of the current ratios up to ca. 0.03 M indicating a first order catalytic rate constant on acid concentration for HER catalysis by the hydride complex. At higher concentrations, the current ratio was slightly lower than expected from the initial line.

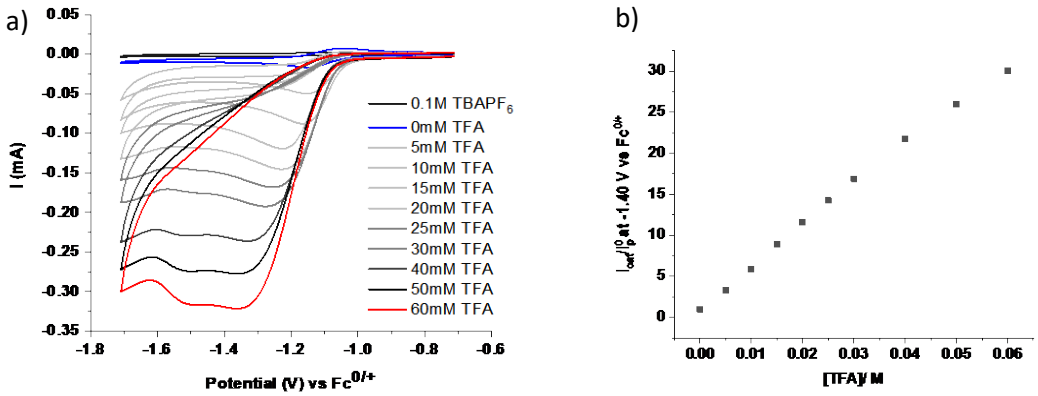

Figure 3.13 (a) CVs of $[Co^{III}(PN)_2(H)(MeCN)][PF_6]_2$ with the addition of TFA acid. (b) Plot of i_{cat}/i_p of the complex versus concentration of TFA acid. Conditions: 1 mM of the complex in CH_3CN with 0.1 M $TBAPF_6$ at scan rate of 100 mV s^{-1}.

3.3.2 CV studies of $[Co^{II}(PN)_2(MeCN)][BF_4]_2$ using TFA as H^+ source

The CV response of the independently synthesized Co(II) derivative to TFA acid was then examined under the same catalytic conditions. Upon the addition of TFA to a solution of this complex, the fully reversible Co(II/I) couple of the complex became irreversible, and the enhancement of a catalytic current near to the Co(II/I) couple was observed (**Figure 3.14**). This CV response suggested the occurrence of H^+ reduction catalysis could be feasible by a protonation of the reduced Co(I) following one-electron transfer to the $[Co^{II}(PN)_2(MeCN)]^{2+}$ to form the Co(III)-H hydride intermediate. From the CV response of the $[Co^{III}(PN)_2(H)(MeCN)]^{2+}$ under catalytic conditions (**Figure 3.13** a), the additional one-electron transfer to the Co(III)-H species was required to form the reduced Co(II)-H intermediate for H_2 liberation. As a consequence, the Co(II)-H species would be involved in the H_2 evolution step and could be regenerated to repeat the same catalytic cycle. The current ratio (i_{cat}/i_p) also linearly depended on acid concentrations (**Figure 3.14** b) by showing the enhancement of the current ratio with i_{cat}/i_p = 27 at 60 mM TFA.

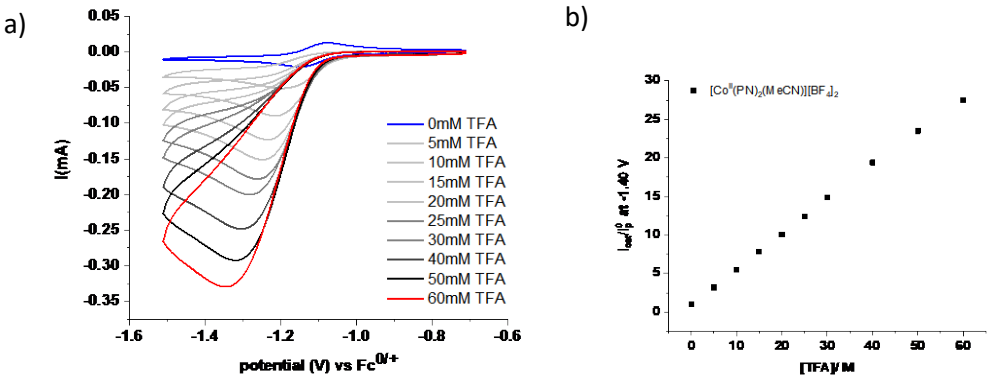

Figure 3.14. (a) CVs of $[Co^{II}(PN)_2(MeCN)][BF_4]_2$ with the addition of TFA acid. (b) Plot of i_{cat}/i_p at -1.40 V of the complex versus concentration of TFA acid . Conditions: 1 mM of the complex in CH_3CN with 0.1 M $TBAPF_6$ at scan rate of 100 mV s^{-1}.

Based on the CV studies of $[Co^{III}(PN)_2(H)(MeCN)][PF_6]_2$ and $[Co^{II}(PN)_2(MeCN)]^{2+}$ under catalytic conditions, the catalytic wave near to the Co(III/II)-H couple for $[Co^{III}(PN)_2(H)(MeCN)]^{2+}$ overlapped with the catalytic wave (CW) close to the Co(II/I) potential for $[Co^{II}(PN)_2(MeCN)]^{2+}$ in MeCN with 10 mM TFA (**Figure 3.15**). This suggests that the starting Co(II) complex catalysed HER by an ECEC mechanism as proposed in **Scheme 3.4**. The GC analysis of the gaseous product in the head space of the electrochemical cell during bulk electrolysis (E_{app} ~ -1.4 V vs $Fc^{0/+}$) for a solution of the $[Co^{II}(PN)_2(MeCN)][BF_4]_2$ and the $[Co^{III}(PN)_2(H)(MeCN)][PF_6]_2$ confirmed formation of H_2 gas (with ~ 100 %FE for H_2 production) in the headspace of the cell (**section 3.3.9**).

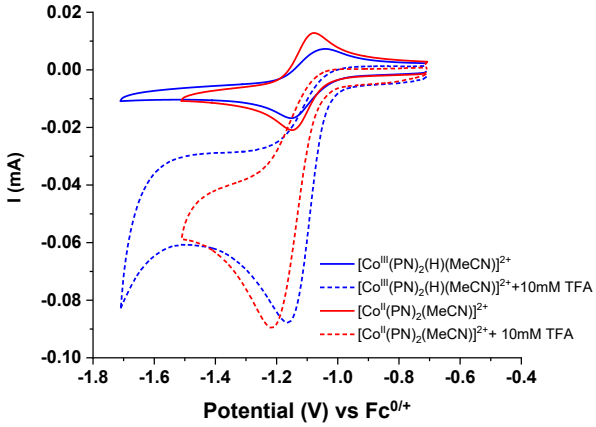

Figure 3.15. Cyclic voltammograms of $[Co^{III}(PN)_2(H)(MeCN)][PF_6]_2$ (1 mM) in the absence and presence of 10 mM TFA in CH_3CN containing 0.1 M $TBAPF_6$ at a scan rate of 100 mV s^{-1}, compared to the CV of $[Co^{II}(PN)_2(MeCN)][BF_4]_2$ under the same conditions.

The proposed H_2 evolution mechanism catalysed by $[Co^{II}(PN)_2(MeCN)][BF_4]_2$ via metal-centred reduction

According to the proposed mechanism, the H_2 evolution pathway by the starting Co(II) complex occurs via an ECEC mechanism. The reduced Co^{I} species is formed by one-electron transfer (E_1 step) from the electrode to $[Co^{II}(PN)_2(MeCN)][BF_4]_2$. A subsequent protonation of this species (C_1 step) then occurs resulting in a formation of the Co(III)-H intermediate. The hydride species takes up an additional electron from the electrode (E_2 step) to generate the reduced Co(II)-H intermediate which is responsible for the H_2 evolution step by a protonation (C_2 step, heterolytic pathway) or via bimolecular reaction of the two Co(II)-H intermediates (homolytic pathway).

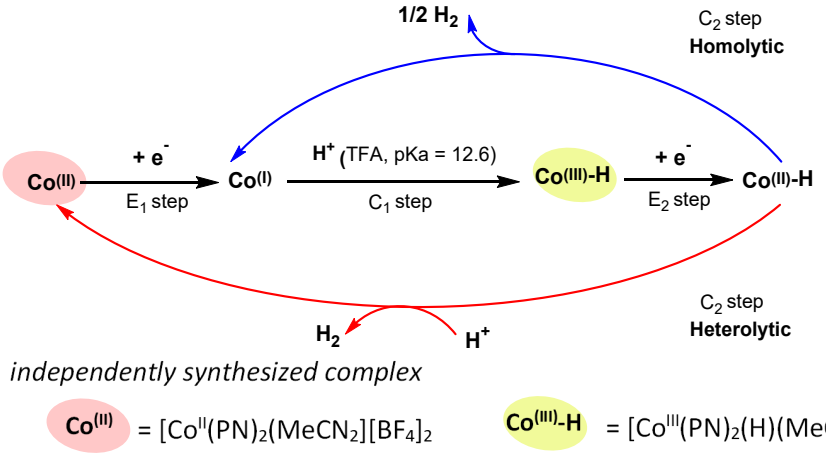

Scheme 3.4. Proposed catalytic H_2 evolution mechanism based on metal-centred reduction of $[Co^{II}(PN)_2(MeCN)][BF_4]_2$ and the Co(III) hydride derivative, $[Co^{III}(PN)_2(H)(MeCN)][PF_6]_2$.

To confirm that the catalytic wave at –1.4 V originated from metal-centred reduction of Co(II/I) couple in the $[Co^{II}(PN)_2(MeCN)][BF_4]_2$, control experiments were then carried out under the same conditions. CV measurements (**Figure A 3.2** a) of solutions of the Co(II) precursor $[Co(CH_3CN)_6][BF_4]_2$ and the PN ligand in the presence of 170 mM TFA were performed. The CV response of the Co(II) precursor and the free PN ligand showed a negligible increase of current around -1.4 V where the catalytic waves of the $[Co^{II}(PN)_2(MeCN)][BF_4]_2$ were found. This result confirmed that the catalytic wave at -1.4 V originated from HER catalysis by the complex. However, it also showed that free PN ligand was able to catalyze proton reduction but that required more negative potential of -1.8 V to be applied as shown in **Figure A 3.2** b.

H^+ reduction activity of $[Co^{II}(PN)_2Cl_2]$ and $[Co^{III}(PN)_2(H)(Cl)][PF_6]$ with different H^+ sources.

In this study, cyclic voltammetry measurements of $[Co^{III}(PN)_2(H)(Cl)][PF_6]$ and $Co^{II}(PN)_2Cl_2$ were carried out in MeCN solution containing 0.1 M $TBAPF_6$ using different acids as H^+ source such as tosylic acid monohydrate ($TsOH{\cdot}H_2O$), trifluoroacetic acid (CF_3COOH) and acetic acid (CH_3COOH) with pKa in CH_3CN of 8.6, 12.65 and 23.51, respectively.[61]

3.3.3 CV studies of $[Co^{II}(PN)_2Cl_2]$ and $[Co^{III}(PN)_2(H)(Cl)][PF_6]$ using TFA as H^+ source

The CV titration of $[Co^{III}(PN)_2(H)(Cl)][PF_6]$ (**Figure A 3.3)** and $[Co^{II}(PN)_2Cl_2]$ with TFA acid (**Figure A 3.4**) showed catalytic currents near to the respective Co(III/II)-H and Co(II/I) couple which is similar to the CV response of $[Co^{III}(PN)_2(H)(MeCN)][PF_6]_2$ and $[Co^{II}(PN)_2(MeCN)][BF_4]$ These two complexes also displayed catalytic current enhancement close to the Co(II/I) and Co(III/II)-H reduction potentials (**Figure 3.15**). The overlap of catalytic current in the CV of $[Co^{II}(PN)_2Cl_2]$ and the $[Co^{III}(PN)_2(H)(Cl)][PF_6]$ (**Figure 3.16**) indicated that the $[Co^{II}(PN)_2Cl_2]$ catalyse H^+ reduction via formation of a Co(III)-H intermediate. The further reduction of Co(III)-H to form a Co(II)-H species is required for subsequent protonation for H_2 evolution. Therefore, the $[Co^{III}(PN)_2(H)(Cl)][PF_6]$ and $[Co^{II}(PN)_2Cl_2]$ complexes catalyse H^+ reduction via the similar H_2 evolution pathway (ECEC) to that of the MeCN analogues, $[Co^{III}(PN)_2(H)(MeCN)][PF_6]_2$ and $[Co^{II}(PN)_2(MeCN)][BF_4]_2$ (**Scheme 3.4**).

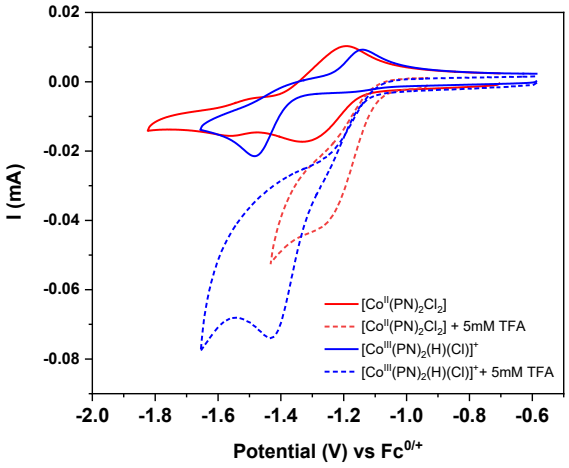

Figure 3.16. Cyclic voltammograms of $[Co^{III}(PN)_2(H)(Cl)][PF_6]$ (1 mM) in the absence and presence of 5 mM TFA in CH_3CN containing 0.1 M $TBAPF_6$ at a scan rate of 100 mV s^{-1}, compared to the CV of $[Co^{II}(PN)_2Cl_2]$ under the same conditions.

3.3.4 CV studies of $[Co^{II}(PN)_2Cl_2]$ and $[Co^{III}(PN)_2(H)(Cl)][PF_6]$ with $TsOH{\cdot}H_2O$

According to the previous literature[224], tosylic monohydrate acid ($TsOH{\cdot}H_2O$) with pK_a 8.6 in CH_3CN was used as proton source for H_2 evolution catalyzed by a triphos cobalt(I) complex in CH_3CN. By using this acid as H^+ source, the hydride signal in the Co(III)-H intermediate generated in situ by a protonation of the Co(I) species could be monitored by ^1H NMR. For this reason, in our work, the activity of this complex for electrocatalytic proton reduction was performed by using $TsOH{\cdot}H_2O$ as proton source in CH_3CN containing 0.1 M $TBAPF_6$. The cyclic voltammograms of $[Co^{III}(PN)_2(H)(Cl)][PF_6]$ (**Figure 3.17** a and b) and the CVs of $[Co^{II}(PN)_2Cl_2]$ (**Figure 3.18**) in the presence of increasing amounts of $TsOH{\cdot}H_2O$ showed similar enhancement of catalytic current near to the Co(III/II)-H and Co(II/I) couple, respectively.

This result indicated that these two complexes catalyse H^+ reduction via a similar H_2 evolution pathway (ECEC) to that of using TFA as H^+ source. However, complicated CV responses of these two complexes under the same conditions (**Figure 3.18**) with additional reduction processes at more negative potential than the Co(III/II)-H couple and the Co(II/I) wave were observed by using $TsOH{\cdot}H_2O$ as H^+ source. Based on the cobalt catalysts for HER, the additional reduction events suggested decomposition of the starting Co(II) complex or the intermediates during catalysis. Alternatively, a reductive degradation of the complex resulting in a formation of particles at the surface of the working electrode (glassy carbon) could be possible.[294, 295]

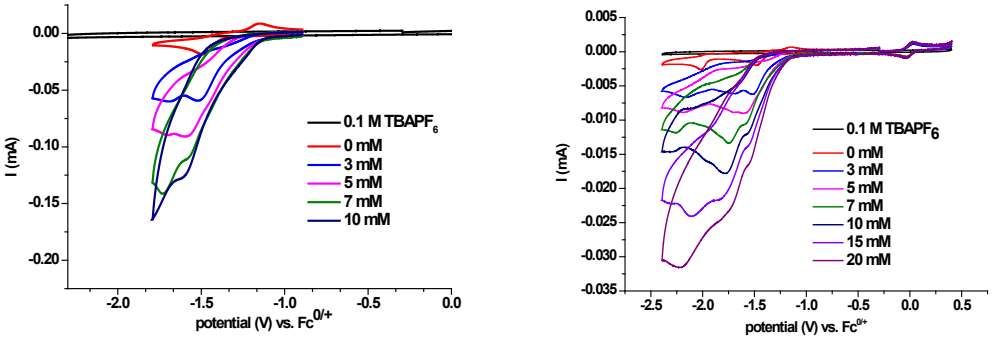

Figure 3.17. (a) CVs of $[Co^{III}(PN)_2(H)(Cl)][PF_6]$ (1 mM) in CH_3CN with 0.1 M $TBAPF_6$ at 100 mV s^{-1} in the presence of various concentrations of $TsOH{\bullet}H_2O$ showing the Co(III/II)-H couple. (b) Cvs scanning to more negative potentials.

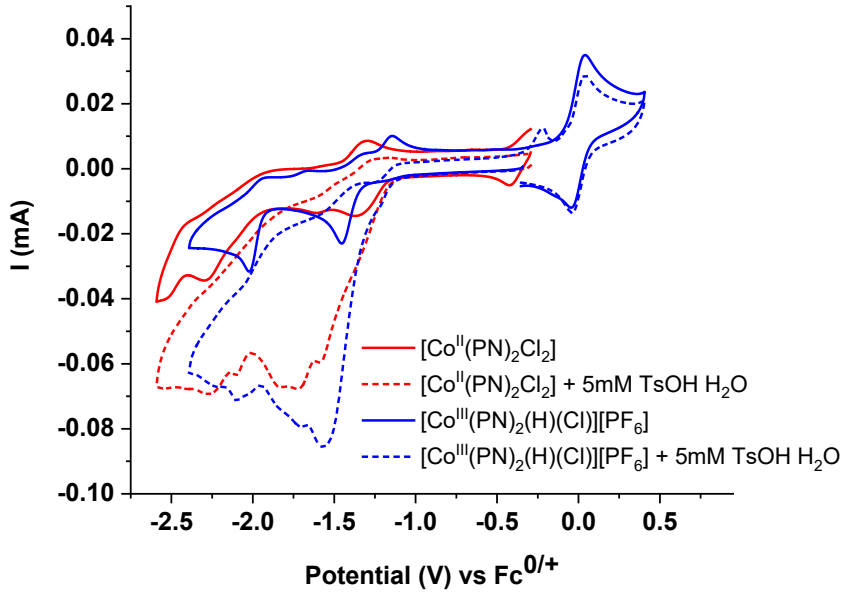

Figure 3.18. Cyclic voltammograms of $[Co^{III}(PN)_2(H)(Cl)][PF_6]$ (1mM) in the absence and presence of 5mM TsOH•H_2O in CH_3CN containing 0.1 M $TBAPF_6$ at a scan rate of 100 mV s^{-1}, compared to the CV of $[Co^{II}(PN)_2Cl_2]$ as the same conditions.

By comparison between TFA acid and TsOH·H_2O as H^+ sources for H_2 evolution catalysis by these two complexes, the CV studies suggested that the complexes are more stable in the solution acidified by relatively weak TFA acid by showing the increase of catalytic current near to the Co(III/II)-H at -1.4 V with no complicated CV response.

Furthermore, a stability of the $[Co^{III}(PN)_2(H)(Cl)][PF_6]$ in MeCN solution with TFA acid and TsOH·H_2O was examined by ^1H and $^{31}P\{^1H\}$ NMR studies as discussed in the **section 3.3.5.**

3.3.5 NMR studies of the $[Co^{III}(PN)_2(H)(Cl)][PF_6]$ solution in acidified CD_3CN

The solution of $[Co^{III}(PN)_2(H)(Cl)][PF_6]$ with 10.0 equiv TsOH·H_2O

$^{31}P\{^1H\}$ NMR spectra were recorded upon addition of 2.0, 5.0 and 10.0 equiv of TsOH•H_2O to a solution of $[Co^{III}(PN)_2(H)(Cl)][PF_6]$ in CD_3CN at r.t. (**Figure 3.19**). The solution in the presence of 5.0 and 10.0 equiv of TsOH•H_2O showed a new phosphorus signal at δ 32.2 (blue square) which was assumed to be due to the two equivalent P atoms in the product Co(III) complex (shown inset, blue). The starting $[Co^{III}(PN)_2(H)(Cl)][PF_6]$ remained in the solution with the phosphorus signal at δ = 66.4 and the hydride signal at δ -19.0 as indicated by orange labels (**Figure 3.19**, inset). Signals due to $[Co^{III}(PN)_2(H)(Cl)][PF_6]$ are also present in in the aromatic and aliphatic region of the ^1H NMR spectrum (**Figure 3.20**). The peak at δ 1.36 ppm was assigned to overlapping peaks of CH_3 protons in the product Co(III) complex which are consistent with eight

equivalent methyl signals and the two equivalent pyridine rings. Moreover, a relatively very weak triplet hydride peak around δ -17.1 ($^{2}J_{H,P}$ = 54 Hz) was also observed in the ^{1}H NMR spectrum of the solution with 5.0 and 10.0 eq of TsOH (**Figure 3.19** b and c, respectively). This signal corresponded to the hydride peak in the separately synthesized $[Co^{III}(PN)_2(H)(MeCN)]^{2+}$ in CD_3CN (**Figure A 2.22**).

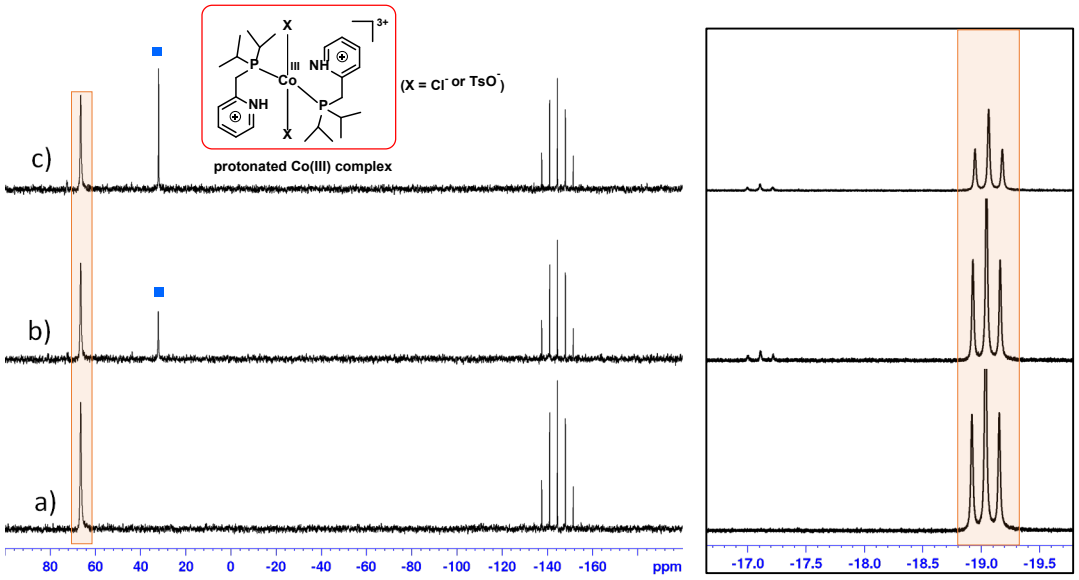

Figure 3.19. $^{31}P\{^{1}H\}$ NMR spectra of $[Co^{III}(PN)_2(H)(Cl)][PF_6]$ at room temperature (in CD_3CN), in the presence of a) 0.0 equiv, b) 5.0 equiv and c) 10.0 equiv $TsOH\bullet H_2O$. Inset shows the ^{1}H NMR of these solutions in hydride region and the orange labels indicate the signals of the $[Co^{III}(PN)_2(H)(Cl)][PF_6]$.

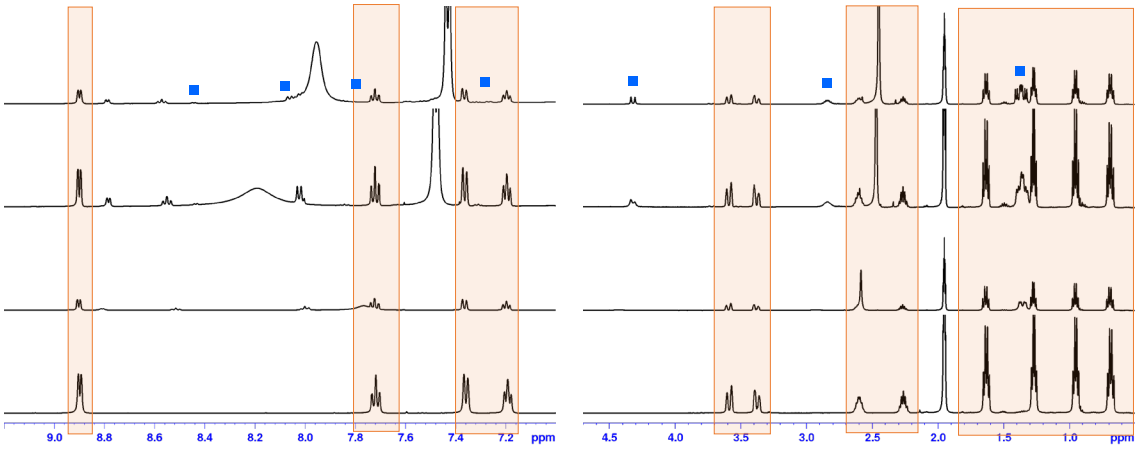

Figure 3.20. ^{1}H NMR spectra of $[Co^{III}(PN)_2(H)(Cl)][PF_6]$ at room temperature (in CD_3CN), a) in the presence of 0.0 equiv, b) 2.0 equiv c) 5.0 equiv and d) 10.0 equiv $TsOH\bullet H_2O$.

Moreover, heating the solution of the $[Co^{III}(PN)_2(H)(Cl)][PF_6]$ with 10.0 equiv. $TsOH\cdot H_2O$ in CD_3CN at 45 ^{0}C for 150 min led to an obvious colour change from orange to a green solution. The $^{31}P\{^{1}H\}$ NMR spectrum (**Figure 3.21** d) and the ^{1}H NMR spectrum of this green solution in hydride region (**Figure 3.21** d, inset) and the proton signals in aromatic and aliphatic region (**Figure 3.22** d) indicated full conversion of $[Co^{III}(PN)_2(H)(Cl)][PF_6]$ to $Co^{III}(PN)_2(H)(MeCN)]^{2+}$ and also the protonated Co(III) complex as proposed in **Scheme 3.5**.(**2-b**). In the ^{1}H NMR spectrum (**Figure 3.22** a-d), the shift of the broad peak in the aromatic region around δ 8.0-8.2 was observed which

would be the due to proton exchange involving the protonated Co(III) complex and TsOH. The proton exchange between TsOH and H_2O in CD_3CN was ruled out because this exchange process was observed as broad signal at δ 6.24 in the ^1H NMR spectrum (**Figure 3.23**).

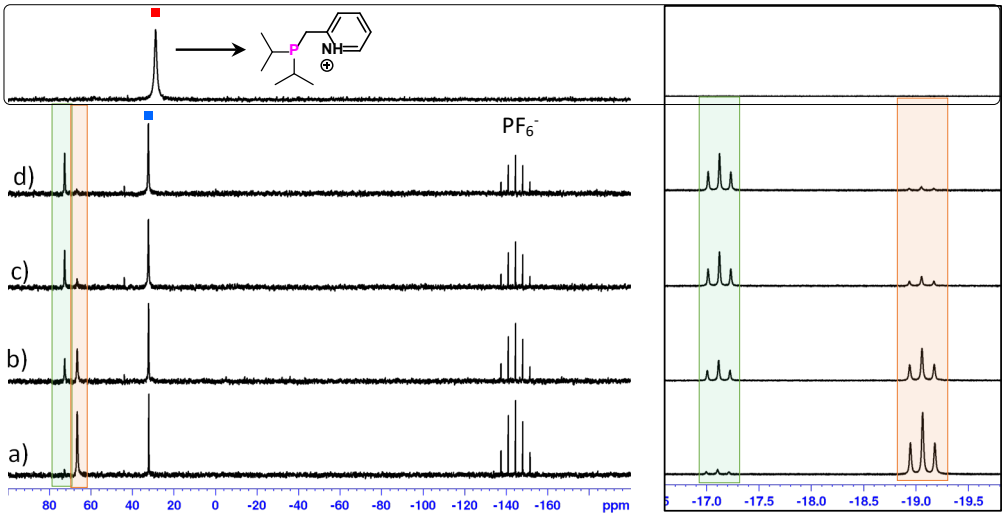

Figure 3.21. $^{31}P\{^1H\}$ NMR spectra of $[Co^{III}(PN)_2(H)(Cl)][PF_6]$ in CD_3CN, in the presence of 10.0 equiv TsOH•H_2O a) at room temperature, b) heated at 45^{0}C for 30 min c) for 90 min and d) for 150 min. The box at right shows the ^1H NMR spectra of these solutions in the hydride region where the orange and green labels indicate the signals of the $[Co^{III}(PN)_2(H)(Cl)][PF_6]$ and $[Co^{III}(PN)_2(H)(MeCN)]^{2+}$, respectively. The box at the top shows a solution of free PN ligand with 10.0 equiv TsOH•H_2O for comparison.

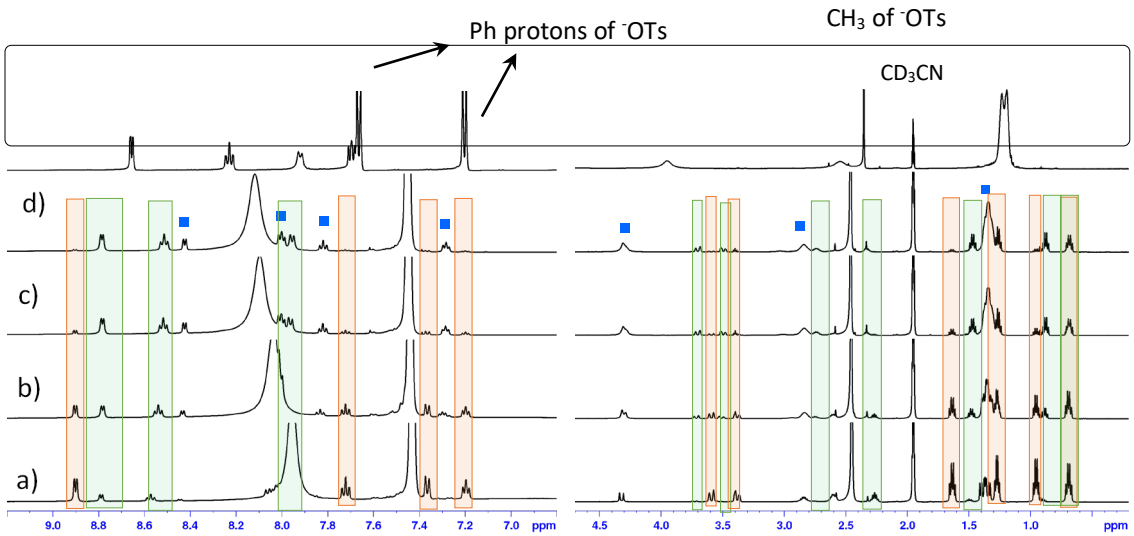

Figure 3.22. ^1H NMR spectra of $[Co^{III}(PN)_2(H)(Cl)][PF_6]$ in CD_3CN, in the presence of 10.0 equiv TsOH•H_2O **a)** at room temperature, **b)** heated at 45^{0}C for 30 min **c)** for 90 min and **d)** for 150 min. The box at the top compares these spectra to a solution of free PN ligand with 10.0 equiv TsOH•H_2O. The orange and green labels indicate the signals of the $[Co^{III}(PN)_2(H)(Cl)][PF_6]$ and $[Co^{III}(PN)_2(H)(MeCN)]^{2+}$, respectively.

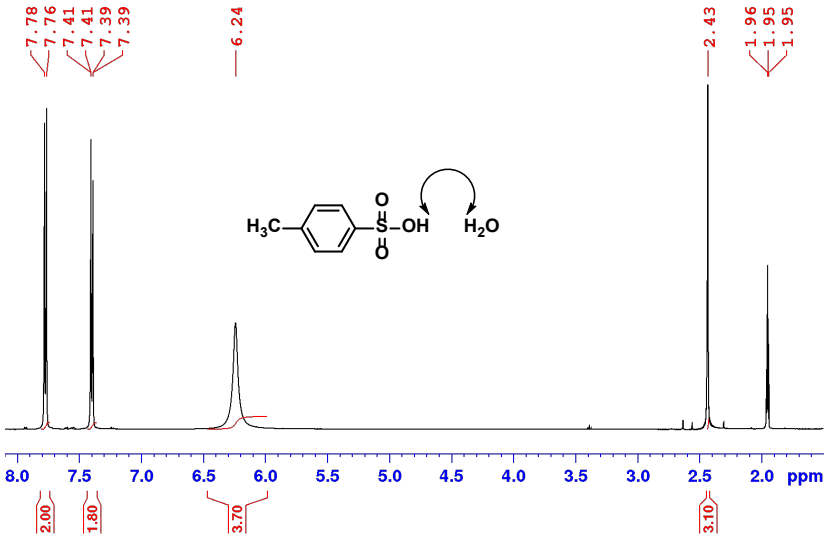

Figure 3.23. ^{1}H NMR spectrum of 10.0 equiv TsOH•H_2O in CD_3CN at room temperature. The arrow indicates a proton exchange between the -SO_3H and H_2O in the TsOH•H_2O solution.

To sum up this section, the NMR studies of the solution of hydride complex in CD_3CN with TsOH•H_2O at r.t. suggested the decomposition of the $[Co^{III}(PN)_2(H)(Cl)][PF_6]$ to the protonated Co(III) complex with a small amount of $[Co^{III}(PN)_2(H)(MeCN)]^{2+}$ as proposed in **Scheme 3.5**. However, heating the solution to 45 ^{0}C with 10.0 eq TsOH H_2O could suppress the formation of the protonated Co(III) complex but accelerated the exchange reaction between coordinated Cl^- and MeCN solvent to form $[Co^{III}(PN)_2(H)(MeCN)]^{2+}$ (**Scheme 3.5** (2-b)).

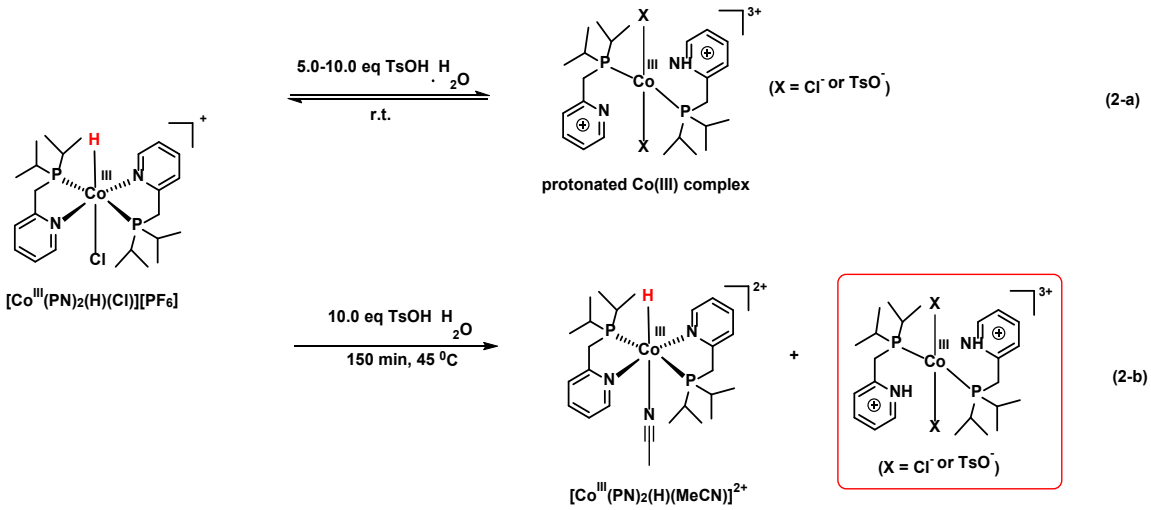

Scheme 3.5. Proposed reactions for $[Co^{III}(PN)_2(H)(Cl)][PF_6]$ in the presence of 5-10.0 equiv TsOH•H_2O at r.t. (2-a) and for the reaction with 10.0 equiv TsOH·H_2O in CD_3CN at 45 ^{o}C**.**

The solution of $[Co^{III}(PN)_2(H)(Cl)][PF_6]$ with 10.0 equiv TFA

After leaving a solution of $[Co^{III}(PN)_2(H)(Cl)][PF_6]$ with 10.0 eq TFA in CD_3CN for 30 min, the $^{31}P\{^1H\}$ NMR spectrum did not show any change (**Figure A 3.5** b). However, leaving the solution at r.t. for 2 days showed only the generation of $[Co^{III}(PN)_2(H)(MeCN)]^{2+}$ identified by the phosphorus peak at δ 72.4. In the ^1H NMR spectrum, the proton signals as labelled by green squares in the hydride region (**Figure A 3.5** c, inset), aromatic and aliphatic region (**Figure A 3.6** c) also corresponded to the ^1H NMR data of the isolated $[Co^{III}(PN)_2(H)(MeCN)]^{2+}$. From this evidence, the $[Co^{III}(PN)_2(H)(MeCN)]^{2+}$ with the negligible amount of the doubly protonated Co(III) complex was formed in a solution of $[Co^{III}(PN)_2(H)(Cl)]^{+}$ with 10.0 equiv TFA in CD_3CN upon leaving it at r.t. for 2 days. Moreover, the formation of $[Co^{III}(PN)_2(H)(MeCN)]^{2+}$ could be accelerated by heating the solution to 45 ^{0}C for 6 h under N_2 as shown in **Scheme 3.6**.

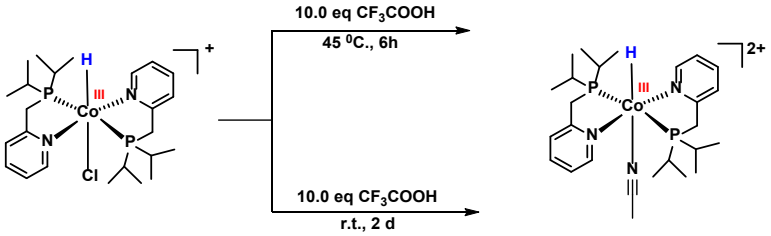

Scheme 3.6. Reaction of $[Co^{III}(PN)_2(H)(Cl)][PF_6]$ in the presence of 10 equiv CF_3COOH in CD_3CN upon leaving it at room temperature for 2 days and heated at 45 ^{0}C for 6 h**.**

In contrast, acidification of $[Co^{III}(PN)_2(H)(Cl)][PF_6]$ with 5.0 eq $TsOH{\cdot}H_2O$ at r.t. led to formation of a considerable amount of the doubly Co(III) protonated species (**Scheme 3.5**, red in set) with a relatively small amount of the $[Co^{III}(PN)_2(H)(MeCN)]^{2+}$. However, the generation of the Co(III)-H species could also be mediated by heating at 45 ^{0}C with 10.0 eq of TsOH H_2O. Based on the NMR studies of the solution of $[Co^{III}(PN)_2(H)(Cl)][PF_6]$ in acidified CD_3CN solution, it can be concluded that the $[Co^{III}(PN)_2(H)(Cl)][PF_6]$ and the resulting $[Co^{III}(PN)_2(H)(MeCN)]^{2+}$ are more stable in the solution with TFA acid than that with $TsOH{\cdot}H_2O$.

3.3.6 CV studies of $[Co^{II}(PN)_2Cl_2]$ and $[Co^{III}(PN)_2(H)(Cl)][PF_6]$ with CH_3COOH

The CV response of $[Co^{III}(PN)_2(H)(Cl)][PF_6]$ upon addition of relatively weak acetic acid (pK_a= 23.5 in MeCN) to a solution resulted in no current increase near to the Co(III/II)-H couple: however; the current is enhanced at more negative reduction potential near to the Co(II/I)-H couple (-2.2 V vs. $Fc^{0/+}$) (**Figure A 3.7**). Moreover, the hydride complex and the $[Co^{II}(PN)_2Cl_2]$ showed similar current responses under the same catalytic conditions (**Figure 3.24**). This CV response of $[Co^{III}(PN)_2(H)(Cl)][PF_6]$ at Co(II/I)-H corresponded to the catalytic wave of the $Co^{II}(PN)_2Cl_2$ which is close to a redox couple of Co(I/0) or ligand-centred $Co(I)L^{\bullet-}$ (**Figure A 3.8** a). This evidence suggested that the two stepwise-electron reduction processes of the starting Co(II) complex to

form the doubly reduced Co(0) species would require reaction with relatively weak CH_3COOH whereas catalysis with TFA acid with pK_a = 12.6 occurs at less negative potential. Therefore, a protonation of Co(0) or $Co(I)L^{\bullet-}$ species led to a generation of Co(II)-H intermediate which required one more e^- to form reactive Co(I)-H species for H_2 evolution step. However, the first electron reduction of the Co(III)-H and the $Co^{II}(PN)_2Cl_2$ did not show an increase in current and remained reversible Co(II/I) couple with no shift in the redox potential (**Figure A 3.8** b).

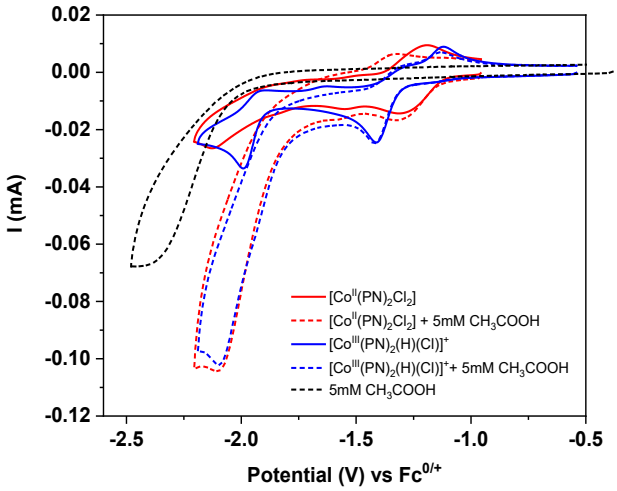

Figure 3.24. Cyclic voltammogram of $[Co^{II}(PN)_2Cl_2]$ (1 mM) in CH_3CN containing 0.1 M $TBAPF_6$, in the presence of 5 mM CH_3COOH, compared to $[Co^{III}(PN)_2(H)(Cl)][PF_6]$ under the same conditions at scan rate 100 mV s^{-1}.

To further support the hypothesis that reactivity at the cobalt centre of the hydride intermediate depended on the basicity of the metal centre and the pK_a of acid used as H^+ source, the CV titration experiments of the complex with H_2O (pK_a = 38-41 in MeCN[61] was then carried out. The titration of a solution of the $[Co^{III}(PN)_2(H)(Cl)][PF_6]$ complex with water showed no current increases at both reduction potentials of the Co(III/II)-H and Co(II/I)-H couple (**Figure A 3.9**). Based on the result from this study, the reduced Co(I)-H species for $[Co^{III}(PN)_2(H)(Cl)]^+$ or the doubly reduced Co(0) or $Co(I)L^{\bullet-}$ for $[Co^{II}(PN)_2Cl_2]$ would be required for a protonation by using a relative weak CH_3COOH acid as H^+ source for HER catalysis. This result suggested that the mechanism for hydrogen evolution depended on strengths of acids that were used as the proton source. According to the result in this study, the HER catalysis of the $[Co^{III}(PN)_2(H)(Cl)][PF_6]$ and $[Co^{II}(PN)_2Cl_2]$ with CH_3COOH as H^+ source would require more electron density or more basicity of the cobalt centre to react with H^+ than that by using relatively strong TFA acid as H^+ source. Consequently, the distinct mechanisms for electrocatalytic H_2 evolution by the complexes in this study were proposed based on metal-centred reduction and depended on the pK_a of acid used as H^+ source as discussed below.

The proposed H_2 evolution mechanism catalysed by $[Co^{II}(PN)_2Cl_2]$ via metal-centred reduction

The current responses of starting $Co^{II}(PN)_2Cl_2$ with TFA as H^+ source near to the Co(II/I) couple indicated that one-electron transfer (E1 step, the first electron transfer) to the starting $[Co^{II}(PN)_2Cl_2]$ led to a formation of the reduced Co(I) species which subsequently reacted with H^+ (C1 step, the first chemical reaction) to form the Co(III)-H intermediate. The additional one-electron reduction (E2 step, the second electron transfer) of this Co(III)-H was required for generation of the active Co(II)-H hydride intermediate (black arrows, **Scheme 3.7**). This reduced Co(II)-H species could either react with H^+ for H_2 production (C2 step, the second chemical reaction) via a heterolytic pathway (red arrows) or evolve H_2 via bimetallic reaction of two Co(II)-H intermediate (homolytic pathway, blue arrows). The CV response of $[Co^{II}(PN)_2Cl_2]$ corresponded to the increase of catalytic current of the independently synthesized and $[Co^{III}(PN)_2(H)(Cl)]^+$ near to the Co(III/II)-H. This confirmed that the reduced Co(II)-H species formed by one-electron transfer to the Co(III)-H is necessary for HER catalysis. The liberation of H_2 could be repeated by E1C1 step to regenerate Co(III)-H species followed by a protonation or a bimetallic reaction of Co(II)-H intermediate via E2C2 step. Consequently, overall mechanism for H_2 evolution catalysed by the complexes in this series was proposed via $E_1C_1E_2C_2$ pathway.

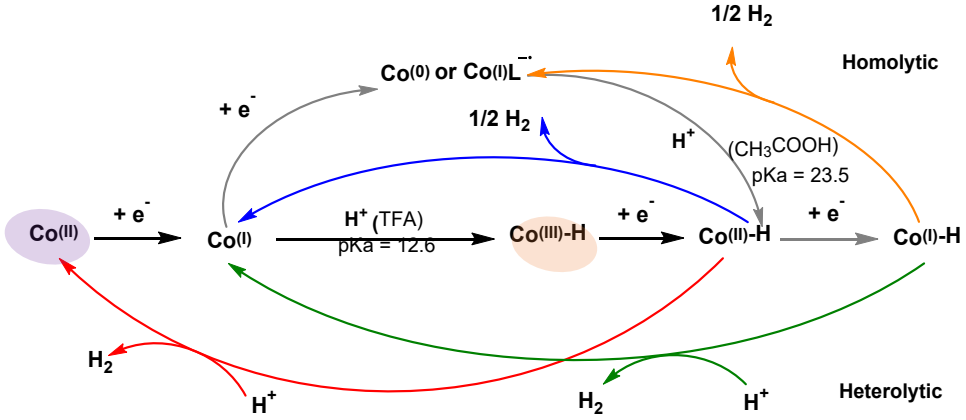

Scheme 3.7. Proposed acid dependent catalytic H_2 evolution mechanisms based on metal-centred reduction of isolated $[Co^{II}(PN)_2Cl_2]$ and, $[Co^{III}(PN)_2(H)(Cl)][PF_6]$.

In the case of using CH_3COOH as H^+ source, generation of Co(0) or $Co(I)L^{\bullet-}$ species via the two steps of single electron transfer to $[Co^{II}(PN)_2Cl_2]$ followed by a protonation of the doubly reduced species resulted in formation of Co(II)-H intermediate (**Scheme 3.7**, grey arrows). A further one-electron reduction of the Co(II)-H followed by a protonation of the Co(I)-H (green arrows) or a bimolecular reaction of Co(I)-H species (orange arrows) caused a liberation of H_2. The proposed

mechanism for HER is consistent with the observation of a catalytic wave near the Co(II/I)-H couple in the Co(III)-H hydride complex and the Co(I/0) wave in $[Co^{II}(PN)_2Cl_2]$.

This proposed mechanism for HER catalysis demonstrated that the pK_a for acids used as proton source caused the difference in the mechanism for hydrogen evolution. More basic Co(I)-H species generated by applying more negative potential around -2.0 V would be needed to react with H^+ using relatively weak acid. This result corresponds to electrocatalytic behaviour of $[Co^{II}(dmgBF_2)_2L]$, where dmg^{2-} = dimethylglyoximato dianion; L = CH_3CN or N,N-dimethylformamide, in the presence of different strengths of acid used.[140] Different mechanisms for electrocatalytic hydrogen production by this complex were proposed depending on the strengths of acid used. Moreover, the $[Co(bapbpy)Cl]^+$ (bapbpy = 6,6'-bis(2-aminopyridyl)-2,2'-bipyridine) complex containing both a redox-active bipyridine ligand and pendant proton relays can electrochemically catalyse H_2 evolution in DMF.[296] The different catalytic mechanisms studied by cyclic voltammetry and bulk electrolysis experiments were found to be dependent on the strength of acid used as H^+ source and the applied potential. These identified pathways for H_2 evolution involved either metal-centred and/or ligand-assisted process.

From the CV studies of the complexes in this series under catalytic conditions with TFA as H^+ source, the H_2 evolution mechanism of $[Co^{II}(PN)_2(MeCN)][BF_4]_2$ and $[Co^{III}(PN)_2(H)(MeCN)][PF_6]_2$ (**Scheme 3.4**) and the H_2 evolution pathways for $[Co^{II}(PN)_2Cl_2]$ and isolated $[Co^{III}(PN)_2(H)(Cl)][PF_6]$ (**Scheme 3.7**) were proposed via an ECEC mechanism. The more detailed mechanistic investigation of HER by these complexes was supported by UV-Vis and NMR techniques and bulk electrolysis experiments as discussed below.

From the CVs responses under catalytic conditions and the stability of the $[Co^{III}(PN)_2(H)(Cl)][PF_6]$ and $[Co^{III}(PN)_2(H)(MeCN)][PF_6]_2$ in acidified MeCN solution, TFA with pK_a=12.6 (in MeCN) was the most suitable acid as H^+ source. The NMR studies (**section 3.3.5**) of an acidic solution of the $[Co^{III}(PN)_2(H)(Cl)][PF_6]$ suggested that the $[Co^{III}(PN)_2(H)(Cl)][PF_6]$ and the resulting $[Co^{III}(PN)_2(H)(MeCN)]^{2+}$ are more stable in the solution with TFA acid than that with $TsOH{\cdot}H_2O$. Furthermore, using TFA as H^+ source involved only metal-centred reduction at less negative potential than required for generation of doubly reduced Co(0) or $Co(I)L^{\bullet-}$ for $[Co^{II}(PN)_2Cl_2]$ species. Therefore, a ligand-centred-reduction could be excluded from the singly reduced species by one-electron transfer to the starting Co(II) complex. However, the conclusions for the chlorinated species need to be treated more cautiously than those for the species with coordinated MeCN because of the issues with speciation described in **chapter 2**, **section 2.5.4.3**.

3.3.7 The H_2 evolution mechanism for $[Co^{II}(PN)_2(MeCN)][BF_4]_2$ and $[Co^{III}(PN)_2(H)(MeCN)][PF_6]_2$

According to the mechanism proposed in **Scheme 3.4**, the first step is one-electron transfer to $[Co^{II}(PN)_2(MeCN)]^{2+}$ to form the reduced Co(I) species. However, the solution changed colour in the presence of TFA acid in MeCN suggesting protonation. The UV-Vis spectrum of the complex showed a decrease of the CT absorption band at 450 nm upon adding 2.0 eq of TFA (**Figure A 3.10** a). To test this hypothesis, deprotonation of the protonated complex by NEt_3 up to 3.2 equiv. was carried out. Partial recovery of the original complex (**Figure A 3.10** b) was observed by adding NEt_3 to the solution with 2.0 equiv. TFA. In contrast to these spectral changes, addition of relatively weak CH_3COOH acid (2.0 eq) to a solution of $[Co^{II}(PN)_2(MeCN)][BF_4]_2$ showed a negligible UV-Vis spectral change. There was a slight decrease in the CT band on adding a large excess of CH_3COOH (40.0 equiv) as shown in **Figure A 3.11.**

This evidence confirmed that $[Co^{II}(PN)_2(MeCN)]^{2+}$ was protonated prior to one-electron transfer under electrocatalytic conditions using TFA as H^+ source (**Scheme 3.8**). Therefore, we assumed that the protonated complex (intermediate A-MeCN) was reduced by one-electron reduction (E_1 step) to form the Co(I) species (intermediate B-MeCN), and the Co(III)-H intermediate was subsequently formed by a H^+ transfer reaction (C_1 step) from bulk solution or from a protonated pyridine ring of a PN ligand. For the second electron and proton transfer (E_2 and C_2 step) in the catalytic cycle, the bimetallic pathway of the reduced Co(II)-H for H_2 liberation was ruled out as a result of the CV and UV-Vis SEC studies of the isolated $[Co^{III}(PN)_2(H)(MeCN)][PF_6]_2$ under non-catalytic conditions. The variable scan rate analysis with a slope of $\Delta E_{pc}/\log \nu$ = -31 mV obtained from plotting E_{pc} versus log ν of the Co(III)-H intermediate (**Figure 2.59** a) indicates reversible MeCN loss from the reduced species. The theoretical slope ($\Delta E_p/\log \nu$) of 20 mV from plotting between E_{pc} versus log ν is expected for an ideal bimolecular reaction following one-electron transfer.[225] Therefore, a bimolecular reaction of the $[Co^{II}(PN)_2(H)(MeCN)]^+$ to form the resulting $[Co^{I}(PN)_2(MeCN)]^+$ and H_2 was ruled out. Moreover, the UV-Vis SEC result supported the hypothesis that one-electron transfer to the $[Co^{III}(PN)_2(H)(MeCN)]^{2+}$ concomitant with a MeCN loss led to a generation of the pentacoordinated $[Co^{II}(PN)_2(H)]^+$ (E_2 step). Based on this result, a subsequent protonation of $[Co^{II}(PN)_2(H)]^+$ intermediate was more likely to occur for H_2 evolution step concomitant with a regeneration of the starting $[Co^{II}(PN)_2(MeCN)]^{2+}$ complex (C_2 step).

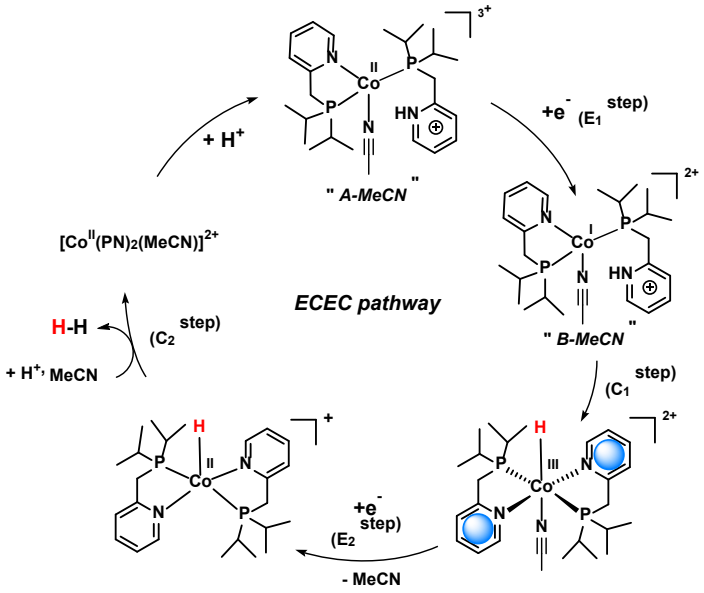

Scheme 3.8. Proposed mechanism for electrocatalytic hydrogen evolution catalyzed by the starting $[Co^{II}(PN)_2(MeCN)][BF_4]_2$ complex.

Furthermore, protonation of the reduced Co(I) complex (C_2 step) was confirmed by a chemical reduction of $[Co^{II}(PN)_2(MeCN)][BF_4]_2$ with KC_8 followed by a protonation by $TsOH{\cdot}H_2O$ acid in MeCN solution (**Scheme 3.9**).

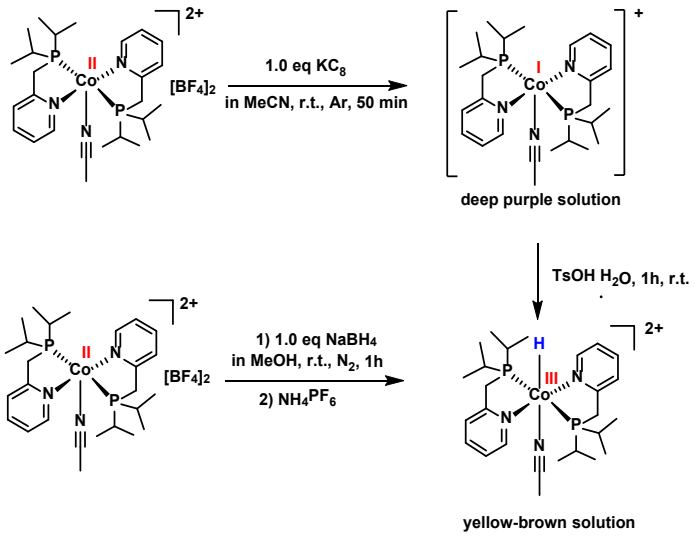

Scheme 3.9. The formation of $[Co^{III}(PN)_2(H)(MeCN)]^{2+}$via chemical reduction using KC_8 followed by a protonation and a reaction with $NaBH_4$ in MeOH.

Formation of the hydride intermediate in this reaction was confirmed by the ^1H NMR (**Figure A 3.12**) and $^{31}P\{^1H\}$ NMR studies (**Figure A 3.13**) which agree with the NMR signals of isolated $[Co^{III}(PN)_2(H)(MeCN)][PF_6]_2$. However, $[Co^{III}(PN)_2(H)(MeCN)][PF_6]_2$ was not the major product and unidentified paramagnetic and diamagnetic species were observed in solution. The standard route to $[Co^{III}(PN)_2(H)(MeCN)][PF_6]$ involves reacting $[Co^{II}(PN)_2(MeCN)][BF_4]_2$ with $NaBH_4$ in

MeOH followed by addition of NH_4PF_6. In this case, $NaBH_4$ could act as reducing agent for a reduction of the Co(II) to Co(I) complex which was then protonated by NH_4^+ to form the hydride species.

3.3.8 H^+ reduction activity of $[Co^{III}$*cis*-$(PN)_2Cl_2][PF_6]$ and $[Co^{II}$*cis*-$(PN)_2Cl][PF_6]$ with TFA

The CV responses of $[Co^{III}(PN)_2(H)(Cl)][PF_6]$ and the separately synthesized $[Co^{II}(PN)_2Cl_2]$ under electrocatalytic conditions using different proton sources, suggested that H^+ reduction activity of these two complexes operates via metal-centred reduction (**Scheme 3.7**). The CV responses of $[Co^{II}$*cis*-$(PN)_2Cl]^+$ and $[Co^{III}$*cis*-$(PN)_2Cl_2]^+$ using TFA acid as H^+ source were investigated in order to compare their H_2 evolution reactivity to that of the $[Co^{II}(PN)_2(MeCN)][BF_4]_2$ under the same catalytic conditions.

The CV response of $[Co^{II}$*cis*-$(PN)_2Cl]^+$ (**Figure A 3.14 a)** and $[Co^{III}$*cis*-$(PN)_2Cl_2]^+$ (**Figure A 3.14 b**) displayed current increases dependent on TFA concentration near to the Co(II/I) couple which is similar to the CV response of the $[Co^{II}(PN)_2(MeCN)][BF_4]_2$ (**Figure 3.14**). The plots of current ratio (i_{cat}/i_p) at -1.40 V (**Figure 3.25**), showed that the current responses of the Co(II/I) couple in the $[Co^{III}$*cis*-$(PN)_2Cl_2]PF_6$, $[Co^{II}$*cis*-$(PN)_2Cl]PF_6$ and $[Co^{II}(PN)_2(MeCN)][BF_4]_2$ were similar upon adding TFA acid up to 30 mM. The catalytic wave of $[Co^{III}$*cis*-$(PN)_2Cl_2][PF_6]$ was also observed at a potential near to the Co(II/I) redox couple, and the current ratios were acid concentration dependent with a saturation point at 40 mM of acid (blue triangle). However, the enhancement of catalytic currents for $[Co^{II}(PN)_2(MeCN)][BF_4]_2$ and $[Co^{II}$*cis*-$(PN)_2Cl]PF_6$ analogue showed no saturation current upon adding TFA acid up to 60 mM. Moreover, at high acid concentrations (40-60 mM), the values of the current ratio are in the order $[Co^{II}(PN)_2(MeCN)][BF_4]_2$ > $[Co^{II}$*cis*-$(PN)_2Cl][PF_6]$ > $[Co^{III}$*cis*-$(PN)_2Cl_2][PF_6]$.

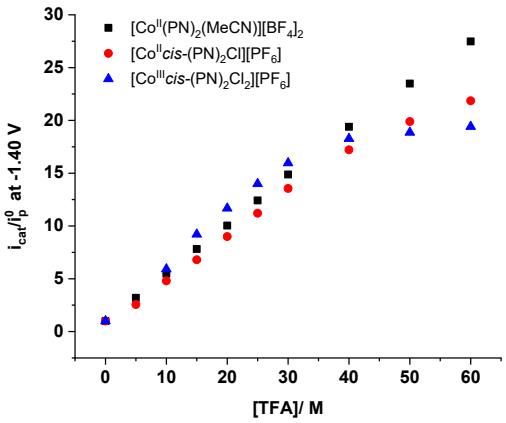

Figure 3.25. Plot of i_{cat}/i_p ratio at -1.40 V versus [TFA] at scan rate of 100 mV s^{-1} for $[Co^{II}(PN)_2(MeCN)][BF_4]_2$, black squares, $[Co^{II}$*cis*-$(PN)_2Cl]PF_6$, red dots, and $[Co^{III}$*cis*-$(PN)_2Cl_2]PF_6$ blue triangles.

It can be inferred that $[Co^{II}(PN)_2(MeCN)]^{2+}$ with 60 mM TFA exhibited the highest reactivity among the complexes as compared in **Figure 3.25**. Therefore, the Cl^- in these complexes could possibly inhibit or deactivate the active species for the HER reaction. The more detailed pathway for H_2 evolution of the chloride derivatives with lowering activity was then proposed and discussed in **section 3.3.8.1.**

3.3.8.1 The H_2 evolution mechanism using $[Co^{III}cis\text{-}(PN)_2Cl_2][PF_6]$, $[Co^{II}cis\text{-}(PN)_2Cl][PF_6]$ and $[Co^{III}(PN)_2(H)(Cl)][PF_6]$ with TFA as the H^+ source

The CV titration of $[Co^{III}cis\text{-}(PN)_2Cl_2]^+$ with TFA showed increases of currents near the Co(II/I) couple as shown in **Figure A 3.14** a. However, the H_2 evolution mechanism using $[Co^{III}cis\text{-}(PN)_2Cl_2][PF_6]$ as precursor is expected to be complicated by the presence of multiple species in solution. Based on the CV (**section 2.5.5.4**) and UV-Vis SEC (**section 2.5.6.1**) result of the $[Co^{III}cis\text{-}(PN)_2Cl_2][PF_6]$ in the absence of H^+ substrate, one-electron transfer to this complex caused generation of $[Co^{II}(PN)_2Cl_2]^0$ which underwent a subsequent PN ligand loss to produce $[Co^{II}(PN)Cl_2]^0$ (red arrows, **Scheme 3.10**) and one Cl^- release to attain the $[Co^{II}cis\text{-}(PN)_2Cl]^+$ (blue arrows, **Scheme 3.10**). Therefore, $[Co^{II}cis\text{-}(PN)_2Cl]^+$ was formed by electrochemical reaction of the $[Co^{III}cis\text{-}(PN)_2Cl_2]^+$ via an EC mechanism. The UV-Vis spectrum of a solution of the isolated $[Co^{II}cis\text{-}(PN)_2Cl][PF_6]$ in MeCN indicated the presence of a mixture of $[Co^{II}cis\text{-}(PN)_2Cl]^+$, $[Co^{II}(PN)Cl_2]^0$ and also the $[Co^{II}(PN)_2(MeCN)]^{2+}$ formed by the exchange reaction between Cl^- and MeCN. Therefore, $[Co^{II}(PN)_2(MeCN)]^{2+}$ was also formed upon one-electron reduction of the $[Co^{III}cis\text{-}(PN)_2Cl_2]^+$ as indicated by the black equilibrium, **Scheme 3.10**.

Under catalytic conditions, the CV response of $[Co^{III}cis\text{-}(PN)_2Cl_2]^+$ was observed near to the Co(II/I) couple which is similar to catalytic potential of the isolated $[Co^{II}(PN)_2Cl_2]$, $[Co^{II}cis\text{-}(PN)_2Cl][PF_6]$ (**Figure A 3.14** b) and $[Co^{II}(PN)_2(MeCN)][BF_4]_2$. Therefore, it can be inferred that the one-electron reduction of $[Co^{III}cis\text{-}(PN)_2Cl_2]^+$ generated a mixture of the $[Co^{II}cis\text{-}(PN)_2Cl]^+$ and $[Co^{II}(PN)_2(MeCN)]^{2+}$ which are involved with HER catalysis (**Scheme 3.10**). This MeCN species generated in the solution under catalytic conditions can then catalyse H_2 evolution through a similar pathway to that of the isolated $[Co^{II}(PN)_2(MeCN)][BF_4]_2$ complex. Therefore, the same pathway for H_2 evolution (**Scheme 3.10,** black cycle) as that of the separately synthesized $[Co^{II}(PN)_2(MeCN)]^{2+}$ complex (**Scheme 3.8**) was also proposed as a parallel H_2 evolution pathway in the catalytic cycle for HER by $[Co^{II}cis\text{-}(PN)_2Cl]^+$ (**Scheme 3.10**, blue cycle). The proposed mechanism for HER catalysis by the starting $[Co^{III}cis\text{-}(PN)_2Cl_2][PF_6]$ leads to a considerable amount of $[Co^{II}(PN)Cl_2]^0$ (red arrow). We assumed that the $[Co^{II}(PN)Cl_2]^0$ generated in the catalytic cycle of the $[Co^{III}cis\text{-}(PN)_2Cl_2]^+$ could be the least active species for H^+ reduction among the catalytic activity of other complexes containing one Cl^- and no Cl^- ligand for the respective $[Co^{II}cis\text{-}(PN)_2Cl]^+$ and $[Co^{II}(PN)_2(MeCN)]^{2+}$. This assumption was confirmed by the comparison of

current ratio (i_{cat}/i_p) for these three complexes under the same catalytic conditions at the same potential of -1.4 V (**Figure 3.25**). The dichloride $[Co^{III}cis\text{-}(PN)_2Cl_2]^+$ showed the least current ratio (i_{cat}/i_p) value at high TFA concentration (60 mM) indicating the lowest H^+ reduction activity.

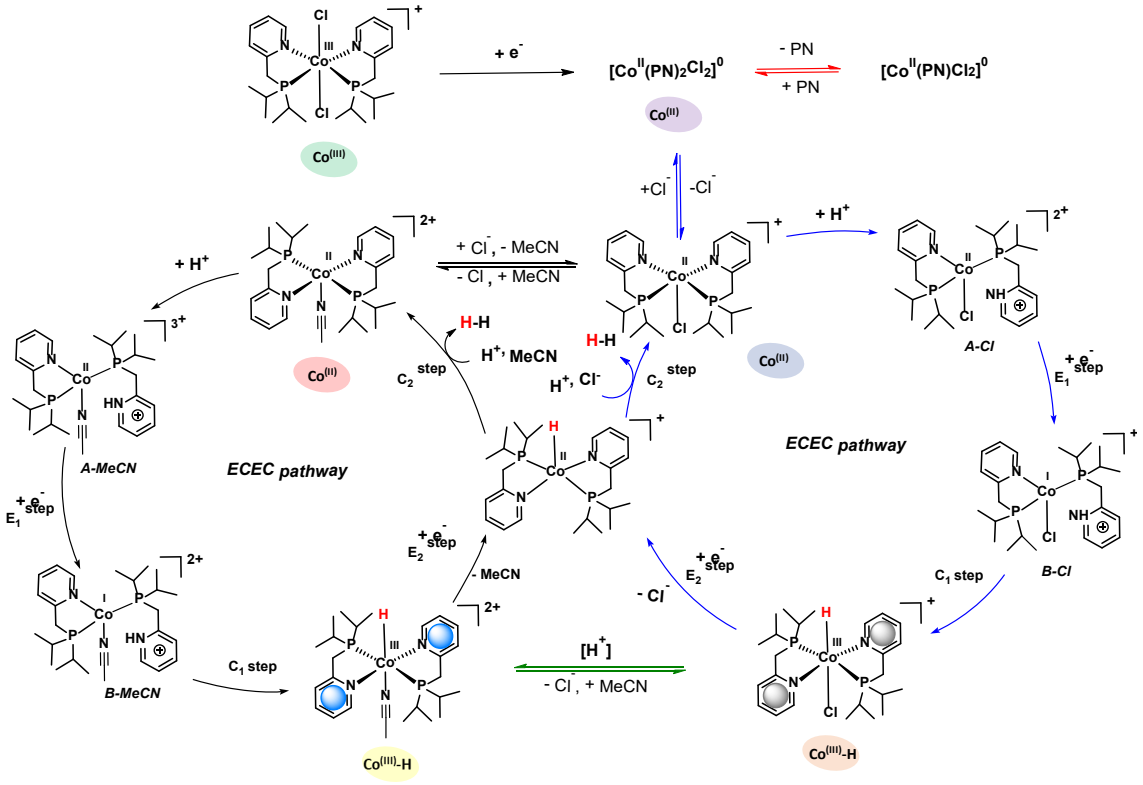

independently synthesized complex

$Co^{(III)}$-H	= $[Co^{III}(PN)_2(H)(MeCN)][PF_6]_2$	$Co^{(III)}$-H	= $[Co^{III}(PN)_2(H)(Cl)][PF_6]$
$Co^{(II)}$	= $[Co^{II}(PN)_2(MeCN)][BF_4]_2$	$Co^{(II)}$	= $[Co^{II}(PN)_2Cl_2]$
$Co^{(III)}$	= $[Co^{III}cis\text{-}(PN)_2Cl_2][PF_6]$	$Co^{(II)}$	= $[Co^{II}cis\text{-}(PN)_2Cl][PF_6]$

Scheme 3.10. Proposed mechanism for electrocatalytic HER reaction catalyzed by the isolated $[Co^{III}cis\text{-}(PN)_2Cl_2]PF_6$ $[Co^{II}cis\text{-}(PN)_2Cl]PF_6$ and $[Co^{III}(PN)_2(H)(Cl)][PF_6]$ complexes using TFA acid as H^+ source.

In the presence of TFA, we assume that $[Co^{II}cis\text{-}(PN)_2Cl]^+$ is protonated to form intermediate A-Cl prior to entering the $E_1C_1E_2C_2$ pathway for H_2 evolution which is similar to that of the isolated Co(II) MeCN analogue. This protonated complex (A-Cl) could then take up one-electron (E_1 step) to form a Co(I) intermediate (B-Cl) followed by the Co(III) hydride intermediate $[Co^{III}cis\text{-}(PN)_2(H)(Cl)]^+$ formed by H^+ transfer via a pyridinium ligand or from TFA (C_1 step). The additional one-electron reduction of the $[Co^{III}(PN)_2(H)(Cl)]^+$ leads to dissociation of the axial Cl^- to form the active penta-coordinated $[Co^{II}(PN)_2(H)]^+$. The generation of this species following one-electron transfer to the $[Co^{III}(PN)_2(H)(Cl)]^+$ was confirmed by the scan rate variation analysis (**chapter 2, section 2.5.5.5**) and UV-Vis SEC (**section 2.5.6.2**) studies of the isolated $[Co^{III}(PN)_2(H)(Cl)][PF_6]$.

The plotting of E_{pc} of Co(III/II)-H couple versus log ν over the scan rate in the range of 0.05-10 V s^{-1} gave a slope $\Delta E_{pc}/\log \nu$ = -49 mV indicating an E_qC_i mechanism via irreversible Cl^- loss following one-electron reduction of the $[Co^{III}(PN)_2(H)(Cl)][PF_6]$. For this reason, the bimetallic reaction of the two Co(II)-H species with an ideal slope of $\Delta E_{pc}/\log \nu$ = -20 mV[196] was ruled out for H_2 evolution pathways catalysed via the $[Co^{III}(PN)_2(H)(Cl)]^+$. Therefore the H_2 evolution step was proposed to occur via protonation of $[Co^{II}(PN)_2(H)]^+$ (C_2 step) by a heterolytic pathway with concomitant Cl^- recoordination. Finally, the regeneration of protonated complex (intermediate A-Cl) could then occur to repeat the catalytic cycle for evolving H_2 via this ECEC mechanism.

Based on the mechanistic studies of cobalt complexes in the literature,[203, 263]; for example: the most commonly proposed H_2 evolution mechanism for the well-known cobaloximes is a protonation of Co(II)H. This accepted mechanism is supported by theoretical studies [142, 267] and transient spectroscopic studies of the hydride of cobaloxime using a very strong photoacid. [263] Moreover, as shown in **section 3.1.4**, all cases for H_2 evolution catalysed by cobalt-based electrocatalysts generate the Co(III)-H intermediate which is commonly formed by protonation of the reduced Co(I) analogue, and a further reduction of Co(III)-H to Co(II)-H is required for the catalysis. Most cases produce H_2 via protonation of Co(II)-H by heterolytic pathways.[145, 207, 263] However, in some cases for cobalt-catalyzed H_2 evolution, it was reported Co(II)-H species can produce hydrogen by both homolytic pathway and heterolytic mechanisms depending on experimental conditions such as concentration of H^+ or pH.[206, 208]

3.3.8.2 Protonation behaviour for $[Co^{III}cis\text{-}(PN)_2Cl_2]PF_6$, $[Co^{II}(PN)_2Cl_2]^0$ and $[Co^{II}(PN)_2(MeCN)][BF_4]_2$

The NMR studies of $[Co^{III}cis\text{-}(PN)_2Cl_2]PF_6$, in CD_3CN with 10.0 equiv of TFA acid (**Figure A 3.15** and **Figure A 3.16**), showed no spectral change. This evidence confirmed that the starting Co(III) complex does not react with H^+ and is not able to be protonated under catalytic conditions. However, one-electron reduction of the Co(III) complex generated the reduced Co(II) species which was subsequently protonated prior to H_2 production via an ECEC mechanism. The proposed protonated species (A-MeCN and A-Cl) in **Scheme 3.10** were evidenced in the UV-Vis spectral changes upon titration of the isolated $[Co^{II}(PN)_2Cl_2]$ and $[Co^{II}(PN)_2(MeCN)][BF_4]_2$ in MeCN solution with TFA acid as shown in **Figure A 3.17** and **Figure A 3.10** a, respectively. An immediate colour change from grey-blue to pale blue occurs with decreases in absorbance at wavelengths 490, 580, 660, 690 and 800 nm. Moreover, deprotonation of the protonated species by adding NEt_3 to the solution showed a partial regeneration of these bands suggesting that some of the $[Co^{II}cis\text{-}(PN)_2Cl]^+$ and $[Co^{II}(PN)Cl_2]$ was restored (**Figure A 3.17** b). However, an increase of absorption intensity at λ 290 nm was observed possibly because NEt_3 might react with the metal centre to form new species.

The addition of 10.0 equiv CF_3COOH to a solution of the precursor $CoCl_2$ anhydrous salt under the same conditions did not cause a spectral change (**Figure A 3.18**). This result suggested that pyridine phosphine ligand in the complex $[Co^{II}(PN)_2Cl]^+$ could be responsive to H^+. In the ^1H NMR spectrum, a solution of the $[Co^{II}(PN)_2Cl_2]$ showed a downfield shift of broad signals in the presence of CF_3COOH as shown in **Figure A 3.20.**

In the case of using CH_3COOH as H^+ source, there was no significant change in the absorption spectrum for the $[Co^{II}(PN)_2Cl_2]$ (**Figure A 3.21**) and $[Co^{II}(PN)_2(MeCN)][BF_4]_2$ upon adding a solution of CH_3COOH up to 40.0 equivalents (**Figure A 3.11**). This suggests that the PN ligands in $[Co^{II}$*cis*$-(PN)_2Cl]^{2+}$ and $[Co^{II}(PN)_2(MeCN)]^{2+}$ were not protonated by weak CH_3COOH acid in MeCN solution.

3.3.8.3 Evidence of exchange between Cl^- in $[Co^{III}(PN)_2(H)(Cl)]^+$ and MeCN in acidic conditions

The CV studies of the $[Co^{III}(PN)_2(H)(Cl)][PF_6]$ in MeCN solution under non-catalytic conditions clearly showed that there is a slow exchange between Cl^- ligand and MeCN solvent. The CV of 2 mM solution of $[Co^{III}(PN)_2(H)(Cl)][PF_6]$ was recorded when a solution was left in the electrolyte solution for 10 h exhibiting a new redox wave at more positive reduction potential compared to the Co(III/II)-H couple in the original $[Co^{III}(PN)_2(H)(Cl)]^+$. This wave was more clearly observed upon raising the scan rate from 0.1 to 0.5 V s^{-1} (**Figure 3.26** a). Upon adding 10 mM TFA acid to this solution which had been left for 10 h, an immediate colour change occurred from orange to pale yellow that further suggested formation of the $[Co^{III}(PN)_2(H)(MeCN)]^{2+}$. This complex displayed a yellow solution in acetonitrile with λ_{max} = 413 nm and ε = 1640 M^{-1} cm^{-1}. It can be assumed that the exchange between Cl^- ligand in $[Co^{III}(PN)_2(H)(Cl)]^+$ and MeCN to form $[Co^{III}(PN)_2(H)(MeCN)]^{2+}$ is accelerated in acidic conditions at room temperature. This exchange reaction corresponds to the conversion of $[Co^{III}(PN)_2(H)(Cl)]^+$ to $[Co^{III}(PN)_2(H)(CD_3CN)]^{2+}$ by heating a solution of the $[Co^{III}(PN)_2(H)(Cl)]^+$ complex in CD_3CN with 10 equiv. TFA at 45 ^0C (**Scheme 3.6**).

Under catalytic conditions, the CV of $[Co^{III}(PN)_2(H)(Cl)][PF_6]$ which had been left for 10 h in the presence of 10 mM TFA showed two separate catalytic waves at scan rate 0.1 V s^{-1} (**Figure 3.26** b), and the current increased upon raising the scan rate to 0.5 V s^{-1} suggesting a diffusion controlled process (**Figure 3.26** c). Moreover, comparison of the catalytic wave of $[Co^{III}(PN)_2(H)(Cl)]^+$ species (red solid line) in this solution to the non-catalytic (blue dots) and catalytic wave (red dots) of the independently synthesized $[Co^{III}(PN)_2(H)(MeCN)]^{2+}$ complex in acetonitrile solution with 30 mM TFA acid showed identical CWs at similar potential (**Figure 3.26** d). Therefore, the $[Co^{III}(PN)_2(H)(MeCN)]^{2+}$ was formed in the solution of $[Co^{III}(PN)_2(H)(Cl)][PF_6]$ complex when it was left for 10 h. This evidence supported the equilibrium as proposed in

Scheme 3.10 (indicated by green arrow) that the coordinated Cl^- ligand in the $[Co^{III}(PN)_2(H)(Cl)]^+$ complex dissociates chloride in acidified MeCN to form $[Co^{III}(PN)_2(H)(MeCN)]^{2+}$. The catalytic wave originating from this MeCN analogue was then observed at less negative potential than that by $[Co^{III}(PN)_2(H)(Cl)]^+$.

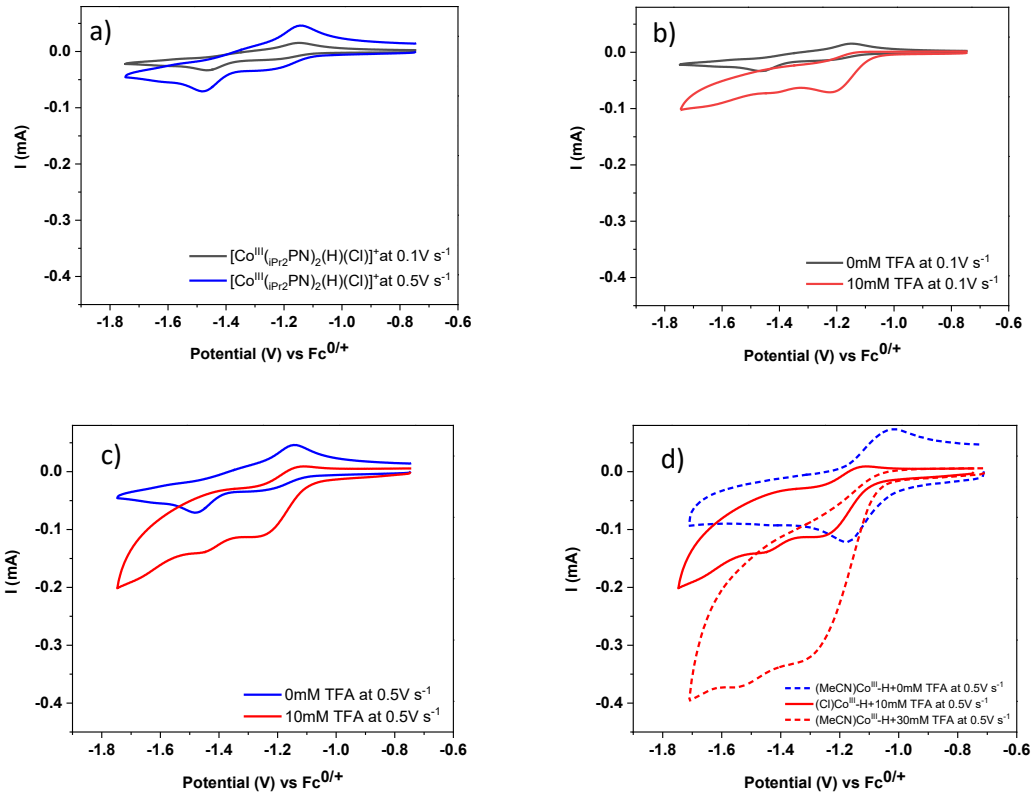

Figure 3.26. CVs of the Co(III/II)-H couple of $[Co^{III}(PN)_2(H)(Cl)][PF_6]$ (2 mM) left in solution for 10 h before CV measurement at (a) a scan rate of 0.1 V s^{-1} (black) and 0.5 V s^{-1} (blue), (b) the CV of this solution with 10 mM TFA acid at scan rate 0.1 V s^{-1} and (c) the same at 0.5 V s^{-1}. (d) the catalytic wave at scan rate 0.5 V s^{-1} of the CV of independently synthesized $[Co^{III}(PN)_2(H)(MeCN)][PF_6]_2$ with 30 mM TFA (red dot) and the non-catalytic wave of this complex at scan rate 0.5 V s^{-1} (blue dot). The catalytic wave for $[Co^{III}(PN)_2(H)(Cl)]^+$ with 10 mM TFA left for 10 h is shown for comparison (red line).

Furthermore, at relatively high proton concentration, the catalytic waves for $[Co^{III}cis\text{-}(PN)_2Cl_2][PF_6]$ and $[Co^{II}(PN)_2(MeCN)][BF_4]_2$ overlapped more because of shifts in the half-wave potential. The value of $\Delta E_{cat/2}$ was 30 mV on adding 60 mM TFA (**Figure 3.27** top) compared to $\Delta E_{cat/2}$ = 60 mV and $\Delta E_{1/2}$ = 220mV with 10 mM TFA and no TFA acid, respectively. The more positive shift in catalytic half-wave potential of $[Co^{III}cis\text{-}(PN)_2Cl_2][PF_6]$ at higher acid concentration is attributed to the exchange between Cl^- in the hydride intermediate, formed after the first one-electron and proton transfer, and MeCN.

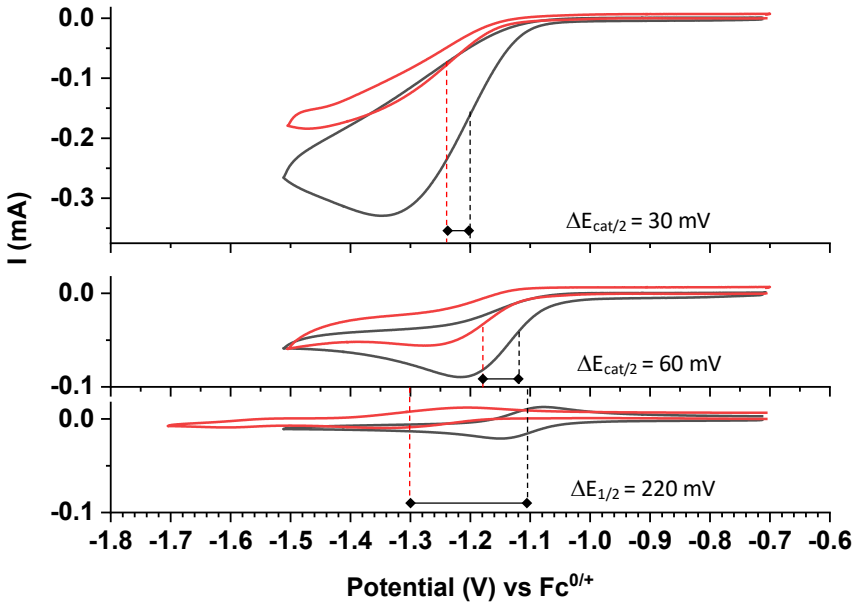

Figure 3.27. CVs of Co(II/I) couple for [Co^{III}*cis*-(PN)$_2$Cl$_2$]PF$_6$, (red) and [Co^{II}(PN)$_2$(MeCN)][BF$_4$]$_2$ (black) at scan rate 100 mV s^{-1}. Conditions: 1 mM in CH$_3$CN containing 0.1 M TBAPF$_6$, in the presence of 0 mM TFA (bottom), 10 mM TFA (middle) and 60 mM TFA (top).

3.3.8.4 The effect of Cl$^-$ on H$^+$ reduction activity of [Co^{II}(PN)$_2$(MeCN)][BF$_4$]$_2$ and [Co^{III}(PN)$_2$(H)(MeCN)][PF$_6$]$_2$

The MeCN complex [Co^{II}(PN)$_2$(MeCN)][BF$_4$]$_2$ in the presence of 60 mM TFA showed much higher catalytic current than [Co^{III}cis-(PN)$_2$Cl$_2$][PF$_6$] under similar conditions. This evidence suggests that Cl$^-$ ligands in [Co^{III}cis-(PN)$_2$Cl$_2$][PF$_6$] could inhibit the catalytic activity possibly by formation of deactivated [Co^{II}(PN)Cl$_2$]^0 complex after one-electron reduction of the [Co^{III}cis-(PN)$_2$Cl$_2$][PF$_6$] followed by one PN ligand loss as proposed in **Scheme 3.10** (red arrow). To test this hypothesis, CV titrations of a solution of the [Co^{II}(PN)$_2$(MeCN)][BF$_4$]$_2$ and [Co^{III}(PN)$_2$(H)(MeCN)][PF$_6$]$_2$ with Cl$^-$ in MeCN solution (TBACl in 0.1 M TBAPF$_6$) were carried out.

The addition of Cl$^-$ to a solution of [Co^{II}(PN)$_2$(MeCN)][BF$_4$]$_2$ and a solution of the [Co^{II}(PN)$_2$(H)(MeCN)][PF$_6$]$_2$ caused decreases in the catalytic currents indicating (**Figure 3.28** a and b, respectively) that Cl$^-$ could suppress HER catalytic activity. Therefore, this evidence confirmed that the interaction between Cl$^-$and [Co^{II}(PN)$_2$(MeCN)]$^{2+}$ and [Co^{III}(PN)$_2$(H)(MeCN)]$^{2+}$ under catalytic conditions generates the deactivated [Co^{II}(PN)Cl$_2$]^0 complex.

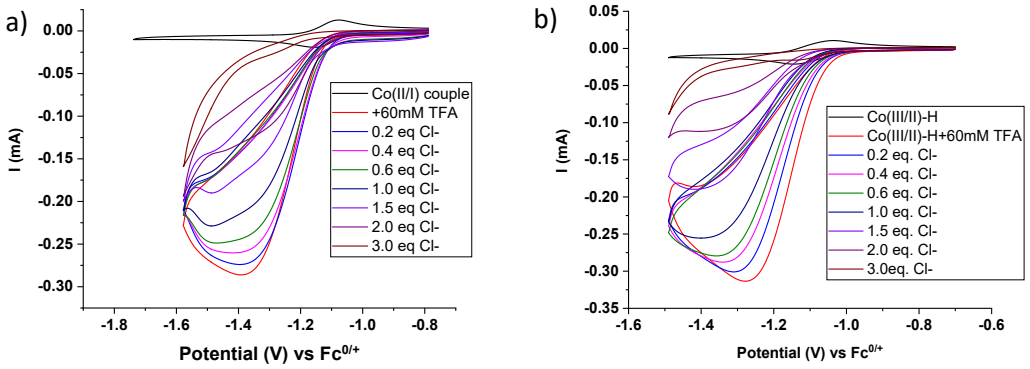

Figure 3.28. CVs of with 60 mM of TFA acid upon addition of TBACl from 0.0 to 3 equiv. (a) $[Co^{II}(PN)_2(MeCN)][BF_4]_2$ and (b) $[Co^{III}(PN)_2(H)(MeCN)][PF_6]_2$. Conditions: 1 mM of the complex in CH_3CN with 0.1 M $TBAPF_6$ at scan rate of 100 mV s^{-1}.

The considerable decreases in catalytic current at -1.4 V by adding Cl^- agree with the deactivation pathway as proposed in the HER catalysed by $[Co^{II}$*cis*$-(PN)_2Cl]PF_6$ and $[Co^{III}(PN)_2(H)(Cl)][PF_6]$ (**Scheme 3.10**, blue arrows). Therefore, the liberation of H_2 concomitant with recoordination of Cl^- (C_2 step) in the catalytic cycle would lead to differences in activity between $[Co^{III}(PN)_2(H)(Cl)][PF_6]$ and $[Co^{III}(PN)_2(H)(MeCN)][PF_6]_2$ for H_2 evolution catalysis.

3.3.9 The production of H_2 by bulk electrolysis

To confirm that the catalytic wave around –1.4 V originated from H_2 evolution catalysis, bulk electrolysis experiments of each complex were performed in acetonitrile (**Table 3.2**).

Table 3.2. Conditions for bulk electrolysis of each complex (0.9 mM) in acetonitrile containing 0.1 M $TBAPF_6$ acidified with TFA acid.

Complexes	[TFA] mM	E_{cat} (V)	$E_{cat/2}$ (V)	E_{app} (V)	% FE (H_2)
$[Co^{III}$*cis*-$(PN)_2Cl_2][PF_6]$	60	-1.70	-1.29	-1.48	99
$[Co^{II}(PN)_2(MeCN)][BF_4]_2$	60	-1.47	-1.21	-1.33	100
$[Co^{III}(PN)_2(H)(MeCN)][PF_6]_2$	60	-1.46	-1.22	-1.40	91
$[Co^{III}(PN)_2(H)(Cl)][PF_6]$	30	-1.55	-1.34	-1.50	101

3.3.9.1 Bulk electrolysis of $[Co^{II}(PN)_2(MeCN)][BF_4]_2$ and H_2 determination by GC

Bulk electrolysis of $[Co^{II}(PN)_2(MeCN)][BF_4]_2$ was carried out to obtain the area of I-t plot (**Figure 3.29** a) which showed the current passed through a solution over 2 h of electrolysis at constant potential (-1.33 V). The CV of the complex under catalytic conditions was recorded before applying constant potential (**Figure 3.29** b). The sampling of H_2 produced in the head space of the cell during bulk electrolysis of the solution was quantified by GC. The increase in experimental number of moles of H_2 produced from the system over the course of electrolysis (**Figure 3.29** c) indicated that the complex can catalyse H_2 evolution upon applying the potential without a loss of its catalytic activity over 2 h. The percent faradaic efficiency for H_2 evolution (% FE(H_2)) of 100 % was achieved suggesting that all of charge passed through the system was consumed by the catalysts for H_2 evolution over 2 h of electrolysis (see experimental **section 3.2.4**). The data for CV measurements before bulk electrolysis, I-t plots from controlled potential experiment and the experimental number of mole of H_2 produced from the system over the course of electrolysis for $[Co^{III}$*cis*-$(PN)_2(H)Cl_2]^+$, $[Co^{III}(PN)_2(H)(Cl)]^+$ and $[Co^{III}(PN)_2(H)(MeCN)]^{2+}$ are shown in **Figure A 3.24**, **Figure A 3.25** and **Figure A 3.26**, respectively. All complexes in this study showed 90-100 % FE for H_2 evolution.

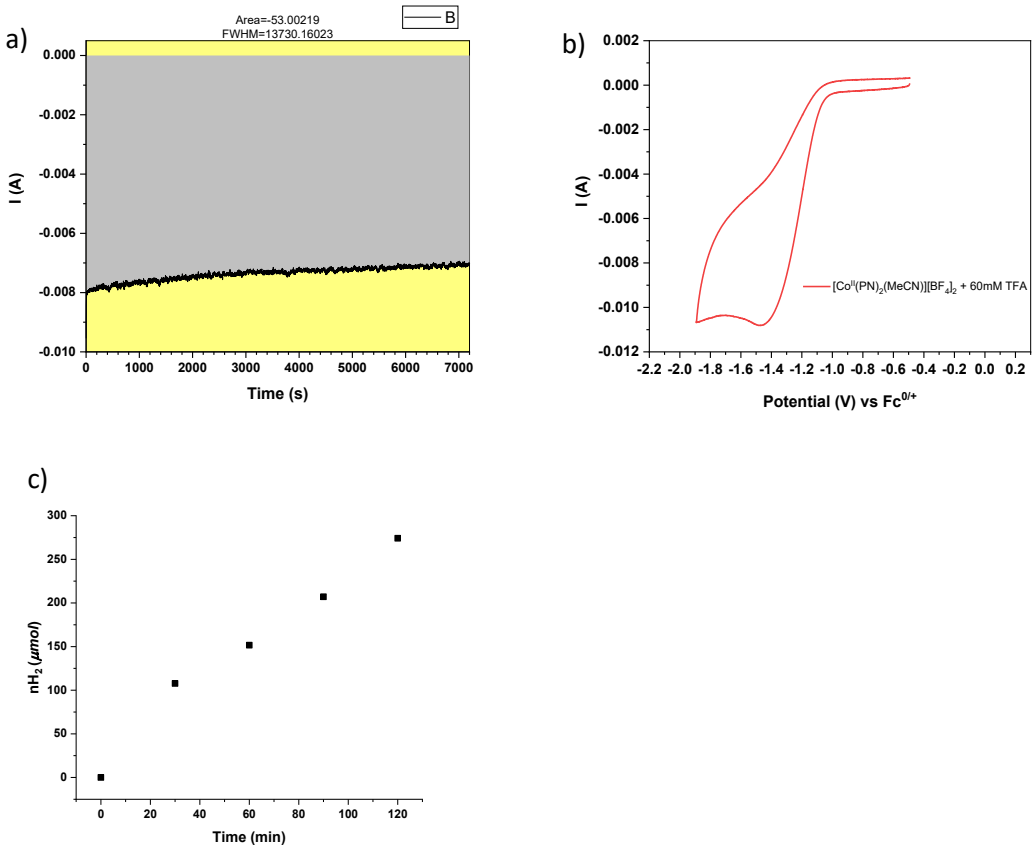

Figure 3.29 (a) I-t plot from controlled potential electrolysis of this complex in the solution with 60 mM of TFA by applying constant potential at -1.33 V vs $Fc^{0/+}$ for 2 h. (b) The CV of $[Co^{II}(PN)_2(MeCN)][BF_4]_2$ (0.9 mM) in CH_3CN solution containing 0.1 M $TBAPF_6$ in the presence of 60 mM of TFA; (c) the experimental number of moles of H_2 against time of electrolysis.

3.3.9.2 Dipping test

Furthermore, to prove that there is no deposition of particles at the surface of the carbon plate used as the working electrode during bulk electrolysis, a dipping test was performed by rinsing the electrode after electrolysis prior to using this electrode as a WE for CV measurement of the electrolyte solution with no catalyst. The cyclic voltammograms from the dipping test of the catalyst **Figure 3.30 .** show that catalytic activity is not increased consistent with homogeneous catalysis and the absence of Co nanoparticle deposition. In some cases, cobalt complexes can catalyze the H_2 evolution reaction in a heterogeneous manner by electrodeposition of cobalt particles at the working electrode upon extended catalytic H^+ reduction.[203, 294]

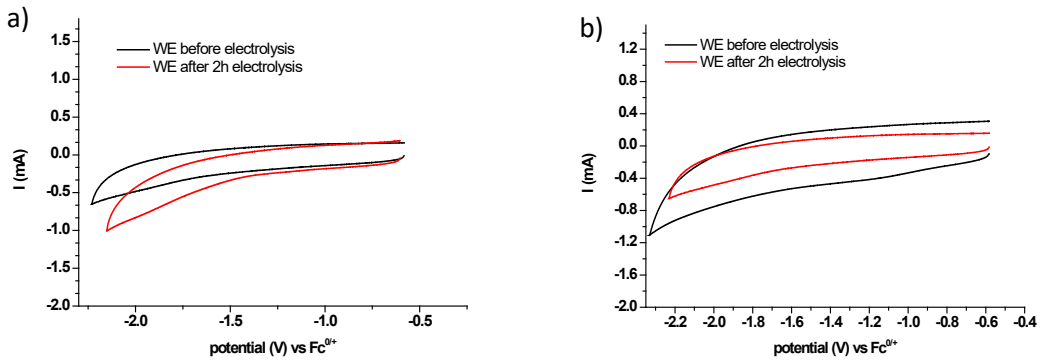

Figure 3.30. The CVs of electrolyte solution (0.1 M $TBAPF_6$) using carbon plate as the working electrode (WE) (a) before electrolysis (black), and after use for electrolysis of the $[Co^{II}(PN)_2(MeCN)][BF_4]_2$, (b) $[Co^{III}$*cis*-$(PN)_2Cl_2][PF_6]$. Conditions: in CH_3CN solution (0.5 mM) containing 0.1 M $TBAPF_6$ in the presence of 60 mM of TFA solution.

3.3.10 Benchmarking HER catalysts and comparison to other catalysts

3.3.10.1 Overpotential determination

In this work, the overpotential (η) of each catalyst as listed in **Table 3.3** was determined using the potential at the half-current on the catalytic wave ($E_{cat/2}$) as the expression shown below.

$$\text{Overpotential } (\eta) = E_{cat/2} - E^0_{HA/H2},\ E^0_{HA/H2} \text{ for TFA acid in MeCN} = -0.77 \text{ V}$$

The calculation of overpotentials for $[Co^{III}(PN)_2(H)(Cl)][PF_6]$ by using different acids as H^+ source is described in the **Appendix** with the data as listed in **Table A 3.1.**

Table 3.3. Overpotentials (vs. $Fc^{0/+}$) and %FE for hydrogen evolution of each complex in this work and literature example.

Complexes	Acids (pK_a)	E_{cat} (V)	η (mV)	E_{app} (V)	% FE(H_2)
$[Co^{III}$*cis*-$(PN)_2Cl_2][PF_6]$	TFA (12.6)	-1.70	520	-1.48	99
$[Co^{II}(PN)_2(MeCN)][BF_4]_2$	TFA (12.6)	-1.47	440	-1.33	100
$[Co^{III}(PN)_2(H)(MeCN)][PF_6]_2$	TFA (12.6)	-1.46	450	-1.40	91
$[Co^{III}(PN)_2(H)(Cl)][PF_6]$	TFA (12.6)	-1.55	570	-1.50	101
literature					
$[Co^{II}(L2)(CH_3CN)]^{2+}$	$[(DMF)H]^+$:DMF (6.1)		1210		
	[*p*-bromoanilinium]$^+$ (9.43)		930		
$[Co^{II}(L3)(CH_3CN)]^{2+}$	[*p*-bromoanilinium]$^+$ (9.43)		710		
Co-Py4-1	TFA (12.6)	-	620	-1.40	99
Co-Py5-1	CH_3COOH(23.5)	-	500	-1.1	100
Co-bpyPy5-1	CH_3COOH(23.5)	-1.80	460	-1.1	90
Co-Py3-1	CH_3COOH(23.5)	-1.35	-	-2.38	95
Co-Py3-2	CH_3COOH(23.5)	-1.45	-	-2.38	94
$[Co(bdt)_2]^-$	TFA (12.6)		240	-1.01	>99

3.3.10.2 Kinetic analysis of H_2 evolution catalysts by FOWA

The peak-shaped CV responses of $[Co^{III}(PN)_2(H)(MeCN)][PF_6]_2$ and $[Co^{II}(PN)_2(MeCN)][BF_4]_2$ and the effect of increasing acid concentration (**Figure 3.13** a and **Figure 3.14** a) indicated that these two complexes catalyse H_2 evolution catalysis under pure kinetic conditions with substrate consumption.[269] Therefore, FOWA analysis is applied for determination of observed catalytic rate constant (k_{obs}), overall catalytic rate constant (k_{cat}) and *TOF* for H_2 production. Moreover, a catalytic Tafel plot for those three complexes was constructed based on the corresponding kinetic data (k_{obs}) obtained from FOWA in order to reliably compare their catalytic activity and efficiency to other HER catalysts

FOWA of the $[Co^{II}(PN)_2(MeCN)][BF_4]_2$ complex with 60 mM TFA

The catalytic currents of $[Co^{II}(PN)_2(MeCN)]^{2+}$with TFA concentrations of 25 mM (**Figure 3.31** a) and 60 mM (**Figure 3.31** b) were scan rate dependent suggesting competition between catalytic reaction and substrate consumption (under zone K). A more plateau-like catalytic wave was observed upon raising the scan rate up to 1.0 Vs^{-1} at these two acid concentration. This suggested that H^+ consumption is more limited at high scan rate. [274] A plot of the current ratio (i_{cat}/i_p) against [TFA] as shown in **Figure 3.14** b confirmed that catalytic current is dependent on acid concentrations.

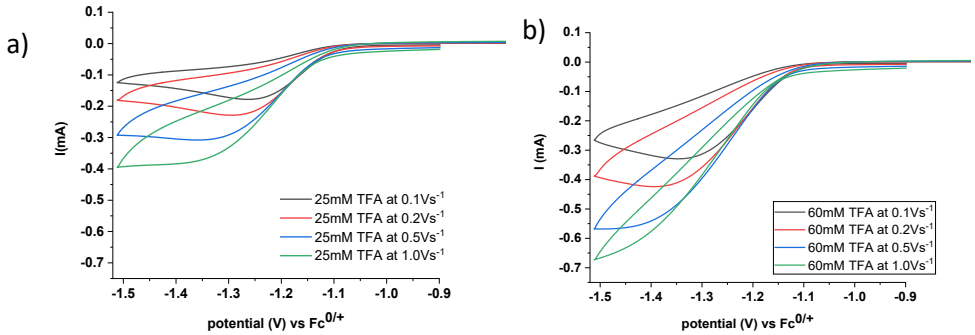

Figure 3.31. CVs of $[Co^{II}(PN)_2(MeCN)][BF_4]_2$ (1 mM) in CH_3CN containing 0.1 M $TBAPF_6$ with 25 mM TFA acid (a) and 60 mM TFA (b) at various scan rates from 0.1 to 1.0 V s^{-1}.

In order to more accurately estimate the observed catalytic rate (k_{obs}) for H_2 evolution by the $[Co^{II}(PN)_2(MeCN)][BF_4]_2$ catalyst, foot of the wave analysis (FOWA) from electrocatalytic cyclic voltammograms was performed, by plotting normalized current (i/i_p^0) versus $1/\{1+\exp[(F/RT)(E-E_{cat/2})]\}$ as shown in the **eq 3.27**.

$$\frac{i}{i_p^0} = \frac{2\sqrt{k_{obs}}}{0.4463}\sqrt{\frac{RT}{Fv}} \times \frac{1}{1+e^{\left[\frac{F}{RT}(E-E_{cat/2})\right]}} \qquad \textbf{eq 3.27}$$

where experimental $\frac{i}{i_p^0}$ and $E_{cat/2}$ values are obtained from the catalytic wave of $[Co^{II}(PN)_2(MeCN)][BF_4]_2$ with 60 mM TFA (**Figure 3.32**).

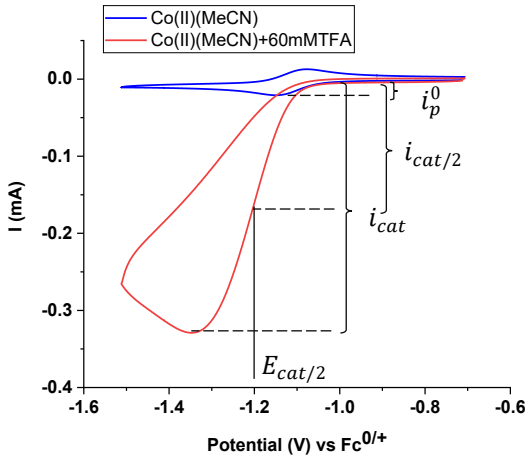

Figure 3.32. Experimental determination of i/i_p from CVs of $[Co^{II}(PN)_2(MeCN)][BF_4]_2$ (1 mM) in CH_3CN containing 0.1 M $TBAPF_6$ (black), and with an addition of 60 mM TFA acid (red) at scan rate 0.1 V/s.

Thus, these experimental data from the CV response of $[Co^{II}(PN)_2(MeCN)]^{2+}$ with 60 mM TFA acid were used to obtain FOWA plots with varying scan rates at 0.1, 0.5 and 1.0 V s^{-1} (**Figure 3.33**).

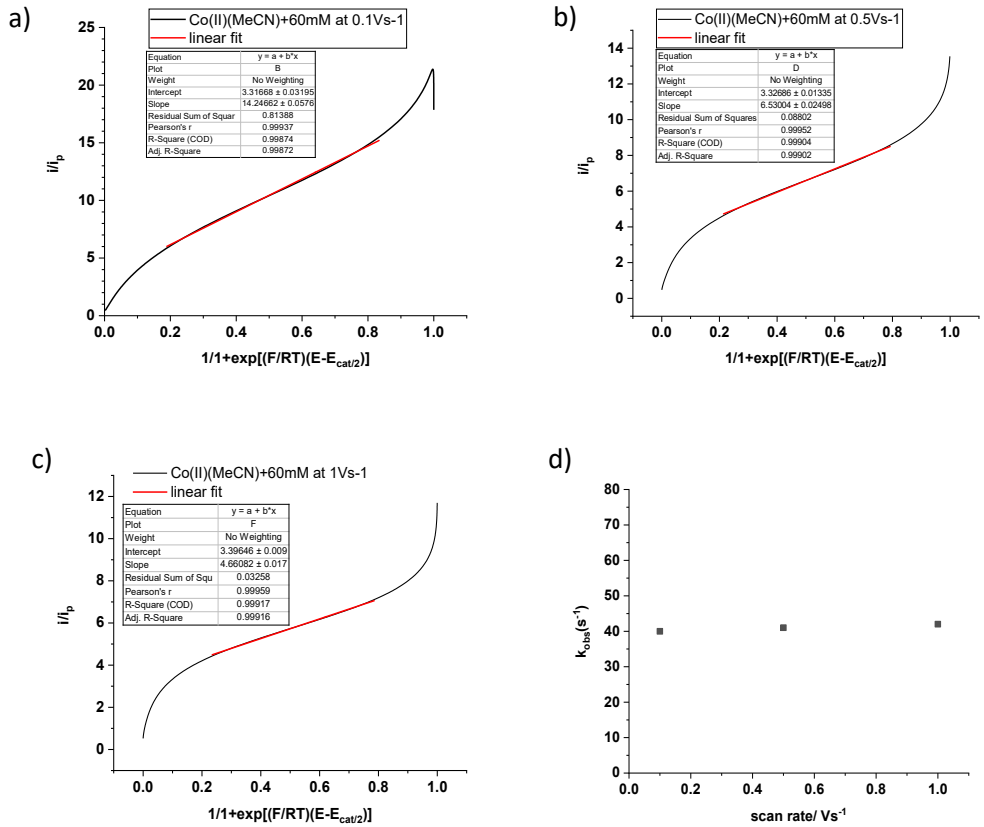

Figure 3.33. FOWA plots and linear fit for $[Co^{II}(PN)_2(MeCN)][BF_4]_2$ complex (1 mM in MeCN with 0.1 M $TBAPF_6$) with 60 mM TFA at different scan rates: (a) 0.1, (b) 0.5, (c) 1 V s^{-1}, (d) k_{obs} values for the complex at different scan rates.

The slope of the linear region in FOWA plot was used to determine an observed catalytic rate constant (k_{obs}) for catalytic HER using the **eq 3.28**:

$$k_{obs} = \frac{(m)^2(0.4463)^2 F v}{4RT} \qquad \textbf{eq 3.28}$$

where m is the slope of the linear fit curve as shown inset, F is the Faraday constant = 96,485 C mol^{-1}, R is the gas constant = 8.314 J mol^{-1} K^{-1} and T is the temperature at 298 K. Inserting a slope of 14.2 with the scan rate of 0.1 V s^{-1} and all constant values to the equation above gives a value of k_{obs} = 40 s^{-1}. From the k_{obs} value (**eq 3.29**), a catalytic rate constant can be retrieved by dividing by the bulk concentration of acid. This yields a k_{cat} value in M^{-1} s^{-1}:

$$k_{cat} = \frac{k_{obs}}{[H^+]} \qquad \textbf{eq 3.29}$$

Thus, k_{cat} = 710 M^{-1} s^{-1} was obtained from FOWA plot for a solution of the catalyst with 60 mM TFA acid at scan rate 0.1 V s^{-1}. Similar determination of k_{obs} from FOWA plots at the two other

scan rates were then performed to yield the k_{cat} values at different scan rates as shown in **Figure 3.34** and enumerated in **Table 3.4.**

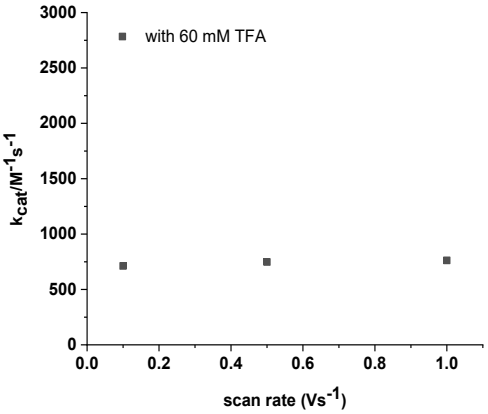

Figure 3.34. k_{cat} values for the $[Co^{II}(PN)_2(MeCN)][BF_4]_2$ complex at different scan rates.

From this analysis, the linear portion in FOWA plot (**Figure 3.35,** a) corresponds to the ideal portion (red region) in the catalytic wave (i-E curve) of a solution of $[Co^{II}(PN)_2(MeCN)]^{2+}$ complex with 60 mM TFA acid as shown in **Figure 3.35** b.

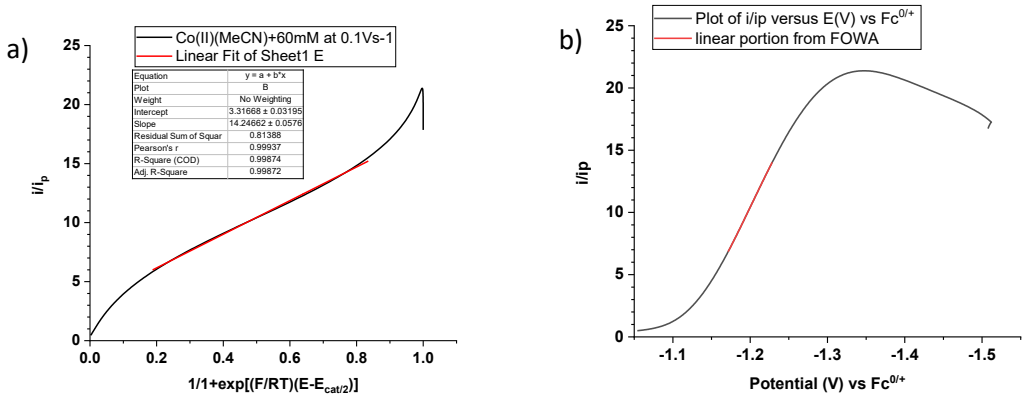

Figure 3.35. (a) Linear fit for FOWA for $[Co^{II}(PN)_2(MeCN)][BF_4]_2$, (b) portions of the catalytic current response of this complex used for FOWA. The region shown in red represents the linear portion of the foot-of-the-wave.

This FOWA plot (**Figure 3.35** a) is a non-ideal case as observed in $[Co^{II}(P_2N_2)(CH_3CN)_3]^{2+}$ as presented in **Figure 3.7** c [207]. It displays three different regions, first a rapid increase of the normalized current at small values of $1/\{1+\exp[(F/RT)(E-E_{cat/2})]\}$, second a linear increase with a constant slope at intermediate values of $1/\{1+\exp[(F/RT)(E-E_{cat/2})]\}$ which is in agreement with the ideal FOWA analysis. Finally, the currents fall rapidly at high $1/\{1+\exp[(F/RT)(E-E_{cat/2})]\}$ because of acid consumption at the electrode near the peak of the catalytic wave.

The mechanistic H_2 evolution studies of $[Co^{II}(P_2N_2)(CH_3CN)_3]^{2+}$ by FOWA and scan rate variation for detecting transient hydride species suggested that potential of Co(II/I) and Co(III/II) couple are close. The Co(III/II)-H wave is slightly more negative than the Co(II/I), and a reduction from Co(III)-H to Co(II)-H must occur prior to liberation of H_2. These findings agree with the catalytic pathways of the $[Co^{II}(PN)_2(MeCN)][BF_4]_2$. Its Co(III)-H analogue requires a further reduction to form Co(II)-H for H_2 evolution via protonation of the reduced Co(II)-H. We also observed that the potential of Co(III/II)-H in $[Co^{III}(PN)_2(H)(MeCN)]^{2+}$ is slightly more negative than the Co(II/II) couple in $[Co^{II}(PN)_2(MeCN)]^{2+}$ which does not fulfill the requirement for the ideal FOWA analysis. For the ideal FOWA plot, a linear increase of the normalized current near the foot of the wave at a small value of $1/\{1+\exp[(F/RT)(E-E_{cat/2})]\}$, requires that one of the electron transfers for catalysis should occur at a much more positive potential than the other, i.e. a large $\Delta E^{\circ\prime}$.[257]

The FOWA plot for estimation of k_{obs} and k_{cat} for H^+ reduction catalysis by $[Co^{II}(PN)_2(MeCN)][BF_4]_2$ with 25 mM TFA acid was also performed using FOWA to gain more reliable k_{cat} values at different scan rates: 0.5 V s^{-1} and 1 V s^{-1}. FOWA plots (**Figure A 3.27**) gave a k_{obs} about half of that measured with 60 mM TFA (summarized in the **Table 3.4**). However, the k_{cat} values are similar to the k_{cat} from FOWA plots for a solution of the complex with 60 mM TFA acid as shown in the plot of k_{cat} versus the scan rate (**Figure 3.36**).

Table 3.4. Conditions for CV studies of $[Co^{II}(PN)_2(MeCN)][BF_4]_2$ (1 mM) and kinetic data from FOWA.

[TFA]/ M	Scan rate/ Vs^{-1}	FOWA plot		
		slope	k_{obs} (s^{-1})	k_{cat} (s^{-1} M^{-1})
0.025	0.1	9.9	19	765
	0.5	4.7	21	860
	1.0	3.5	24	960
0.06	0.1	14.3	40	710
	0.5	6.53	41	750
	1.0	4.66	42	760

FOWA of $[Co^{III}(PN)_2(H)(MeCN)][PF_6]_2$ complex with 30 mM TFA.

The catalytic CV response of the hydride $[Co^{III}(PN)_2(H)(MeCN)]^{2+}$ complex also displayed a peak-shaped CV upon adding TFA acid up to 60 mM and did not reach a saturated catalytic current (**Figure 3.13**). Plots of i_{cat}/i_p versus acid concentration showed a linear increase of the current ratio indicating a first order catalytic rate constant. The catalytic response also depends on the scan rate (**Figure A 3.28**) which is similar to that of $[Co^{II}(PN)_2(MeCN)][BF_4]_2$.

FOWA plots for $[Co^{III}(PN)_2(H)(MeCN)][PF_6]_2$ with 30 mM TFA at different scan rates (**Figure A 3.29**) yield k_{obs} and k_{cat} values enumerated in **Table 3.5**. The plot of k_{cat} versus scan rates are shown in **Figure A 3.29** d).

Table 3.5. Conditions for CV studies of $[Co^{III}(PN)_2(H)(MeCN)][PF_6]_2$ (1 mM) and kinetic data from FOWA.

[TFA]/ M	Scan rate/V s^{-1}	FOWA plot		
		slope	k_{obs} (s^{-1})	k_{cat} (s^{-1} M^{-1})
0.03	0.1	14.8	43	1550
	0.5	6.77	45	1560
	1.0	4.8	45	1560

In conclusion, FOWA for the complexes in this study gave reliable k_{obs} and k_{cat} with the values enumerated in **Table 3.6**

Table 3.6. Conditions for CV studies and observed rate constant (k_{obs}) from FOWA plots with the corresponding catalytic rate constant (k_{cat}) values for all complexes.

complex	*FOWA*			*Thermodynamic data*	
	[TFA]/ M	k_{obs} (s^{-1})	k_{cat} (M^{-1} s^{-1})	$E_{cat/2}$ (V)	η (mV)
$[Co^{II}(PN)_2(MeCN)][BF_4]_2$	0.06	41±1	740±26	-1.20	430
	0.025	21±2.5	862±98	-1.16	390
$[Co^{III}(PN)_2(MeCN)(H)][PF_6]_2$	0.03	44±6	1557±6	-1.13	360

$\eta = E^0_{H^+/H_2} - E_{cat/2}$, $E^0_{H^+/H_2}$ = -0.77 V vs $Fc^{0/+}$

A plot of k_{cat} for hydrogen evolution catalysis against the scan rates for all complexes at different concentrations of TFA is shown in **Figure 3.36**

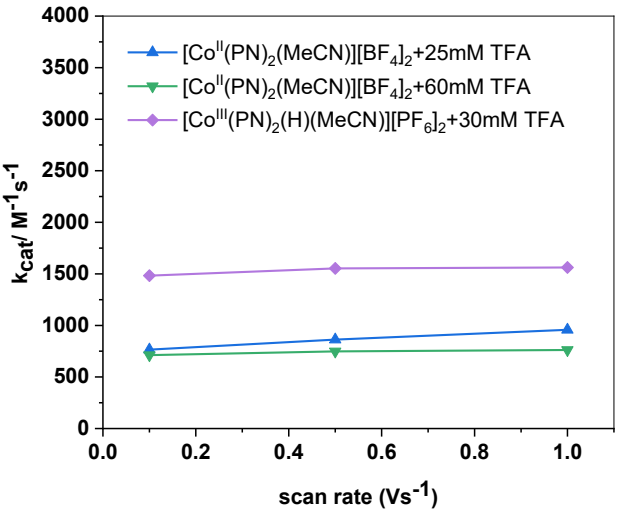

Figure 3.36. k_{cat} values for all complexes from the FOWA plots at different scan rates.

According to the kinetic analysis of $[Co^{II}(PN)_2(MeCN)][BF_4]_2$ and the corresponding $[Co^{III}(PN)_2(H)(MeCN)][PF_6]_2$ by FOWA, the k_{cat} values showed no significant change upon increasing the scan rate between 0.1 to 1.0 V s^{-1}. The k_{cat} value by FOWA for $[Co^{III}(PN)_2(H)(MeCN)][PF_6]_2$ with k_{cat} = 1560±6 M^{-1} s^{-1} is about double that of 800±92 M^{-1} s^{-1} for $[Co^{II}(PN)_2(MeCN)][BF_4]_2$. This suggests that protonation of the Co(I) species to form a Co(III)-H intermediate (C_1 step in the proposed mechanism) would be a rate-determining step for HER catalysis of the starting $[Co^{II}(PN)_2(MeCN)]^{2+}$. By consideration of the first catalytic turnover of the proposed HER mechanism (**Scheme 3.8**), $[Co^{II}(PN)_2(MeCN)]^{2+}$ needs to electrochemically generate the Co(III)-H intermediate by protonation of the Co(I) species, while the isolated $[Co^{III}(PN)_2(H)(MeCN)]^{+}$ acts as Co(III)-H intemediate by itself and is readily accessible in bulk solution. Therefore, the relatively slow formation of Co(III)-H from $[Co^{II}(PN)_2(MeCN)]^{2+}$ by protonation of the reduced Co(I) species could affect the overall catalytic rate constant.

3.3.10.3 Catalytic Tafel plot for $[Co^{II}(PN)_2(MeCN)][BF_4]_2$ and $[Co^{III}(PN)_2(H)(MeCN)][PF_6]_2$

The FOWA plot of the catalytic CV response allows the determination of the turnover frequency (*TOF*) as described in **section 3.1.2.4**. The equation **eq 3.30** [274] shows that *TOF* is dependent on the applied potential E and becomes independent of potential when the applied potential is significantly more negative than $E_{cat/2}$ tending toward TOF_{max}.

$$TOF = \frac{TOF_{max}}{1+\exp\left[\frac{F}{RT}\left(E^0_{H^+/H_2}-E_{cat/2}\right)\right]\exp\left(-\frac{F}{RT}\eta\right)} \qquad \textbf{eq 3.30}$$

where TOF_{max} is the observed rate constant (k_{obs}) from FOWA, in s^{-1} at 1 M acid .[275]

This *TOF* value can be linked together to overpotentials (η) by the log *TOF*-η relationship. This Tafel plot allows the determination of TOF_0 (*TOF* at zero overpotential) which depends on the intrinsic properties of a catalyst of interest.

To benchmark the electrocatalysts in this series, the data enumerated in **Table 3.7** includes k_{obs} from FOWA, k_{cat} and $E_{cat/2}$ from the catalytic CV wave of each catalyst which were used to construct catalytic Tafel plots.

Table 3.7. Conditions for CV studies and the kinetic data obtained from FOWA plot to construct Tafel plot for each complex.

complex	*FOWA at ν = 0.1 Vs^{-1}*			*Data for Tafel plot*	
	[TFA]/ M	k_{obs} (s^{-1})	k_{cat} (s^{-1} M^{-1})	TOF_{max} (s^{-1})	$E_{cat/2}$ (V)
$[Co^{II}(PN)_2(MeCN)][BF_4]_2$	0.06	45	750	750	-1.20
$[Co^{III}(PN)_2(MeCN)(H)][PF_6]_2$	0.03	45	1500	1500	-1.13

A theoretical turnover frequency (TOF_{max}) in a 1 M solution of acid with values of 600, 750 and 1500 s^{-1}, respectively, corresponded to k_{cat} in the unit of M^{-1} s^{-1} multiplied by 1 M solution of TFA acid. It should be noted that the experimental *TOF* would be equivalent to k_{obs} in s^{-1}. The plots of log *TOF* against overpotential (log TOF-η plot) for all catalysts are shown in **Figure 3.37**.

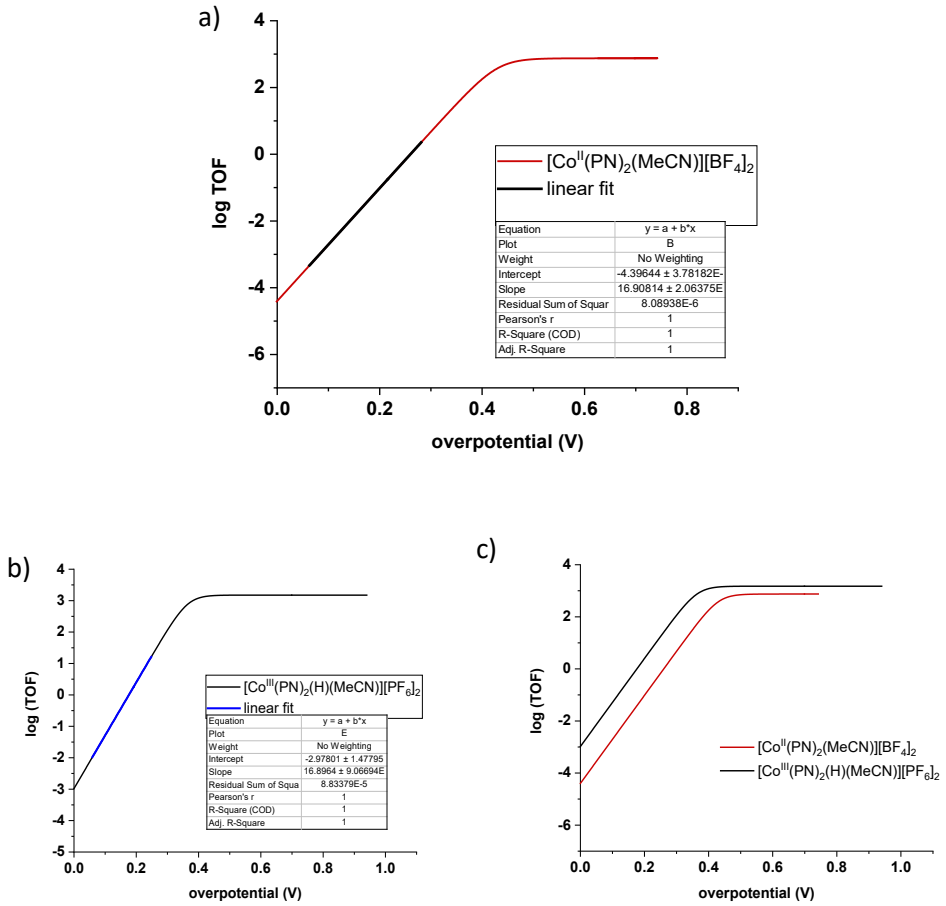

Figure 3.37. Catalytic Tafel plots at scan rate 0.1 V s^{-1} for (a) [Co^{II}(PN)$_2$(MeCN)][BF$_4$]$_2$ with 60 mM TFA, (b) [Co^{III}(PN)$_2$(H)(MeCN)][PF$_6$]$_2$ with 30 mM TFA, (c) comparison of Tafel plots for the two complexes.

These catalytic Tafel plots allow calculation of the catalytic rate at zero overpotential (TOF_0) which is more reliable to benchmark our catalysts against others (**Table 3.8)**. Moreover, the slope of each curve is F/(RT)ln10 =16.9 at 298 K which further supports the ECEC pathway for catalytic H_2 evolution by all complexes in this study.[274] Kinetic analysis of HER catalysts in this study demonstrated that FOWA allows construction of catalytic Tafel plots to compare the intrinsic properties of electrocatalysts under different experimental conditions such as solvent and proton source. Thus, this approach is independent of experimental factors including electrochemical cell configuration, and the amount of active catalyst in only the diffusion-reaction layer is used for TOF calculation. As a result, this method provides a rational benchmarking of intrinsic catalytic activity. An efficient catalyst will show high TOF value at low overpotential, which is located in the top left corner of the log TOF-η plot. [275]

Table 3.8. Conditions for CV studies and the kinetic data obtained from FOWA plot and catalytic Tafel plot for each complex.

complex	*FOWA*				*Tafel plot at $\nu = 0.1$ Vs^{-1}*		
	[TFA]/ M	k_{obs} (s^{-1})	k_{cat} ($M^{-1}\,s^{-1}$)	TOF_{exp} (s^{-1})	TOF_{max} (s^{-1})	TOF_0 ($x10^{-3}\,s^{-1}$)	slope
$[Co^{II}(PN)_2(MeCN)][BF_4]_2$	0.06	41±1	740±26	41±1	750	0.004	16.9
$[Co^{III}(PN)_2(MeCN)(H)][PF_6]_2$	0.03	44±6	1557±6	44±6	1500	1.05	16.9

The hydride $[Co^{III}(PN)_2(H)(MeCN)][PF_6]_2$ showed better catalytic activity with the TOF_0 value of 1.05 $x10^{-3}$ s^{-1}, which is 20 times larger than that of $[Co^{II}(PN)_2(MeCN)][BF_4]_2$. This result showed that $[Co^{III}(PN)_2(H)(MeCN)][PF_6]_2$ is a more efficient catalyst because it reached the maximum *TOF* (TOF_{max}) at significantly lower overpotential than that of $[Co^{II}(PN)_2(MeCN)][BF_4]_2$ by 70 mV. Again, the data suggest that the formation of the Co(III) hydride intermediate (E_1C_1 step) could be a rate determining step for H_2 production proposed in **Scheme 3.8**.

3.3.11 Comparison to other hydrogen evolution electrocatalysts

The Tafel plots for all complexes in this work (**Figure 3.38**) can readily be used to compare to previously reported HER electrocatalysts shown in **Chart 3.6**. The kinetic data which is available from the literature for constructing the Tafel plot is enumerated in **Table 3.9.**

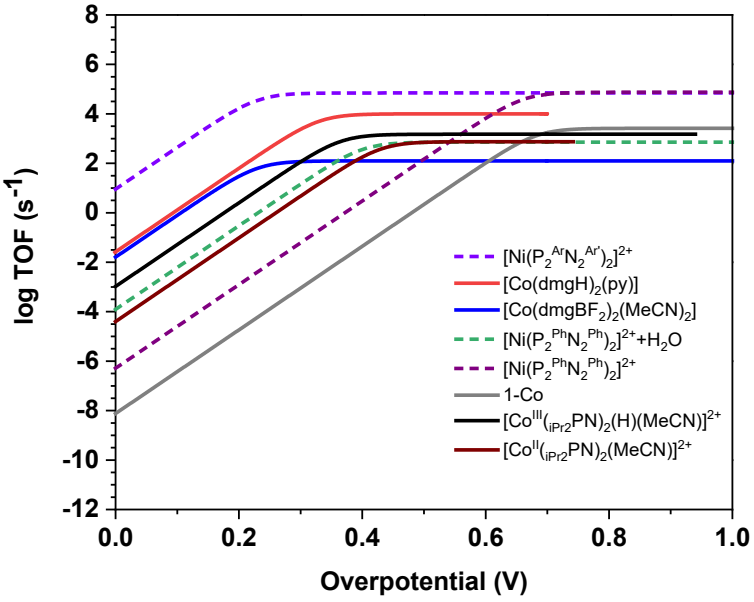

Figure 3.38. Catalytic Tafel plots for selected electrocatalysts for H_2 evolution.

Table 3.9. Data for catalytic Tafel plots for comparison of the complexes in this thesis with other electrocatalysts for H_2 evolution.

complex	solvent+acids	$E^0_{H^+/H_2}$	$E_{cat/2}$ (η) V	TOF_{max} (s^{-1}) ([H^+ = 1 M)	TOF_0 (s^{-1}) (x10 $^{-3}$)
$[Co^{II}(PN)_2(MeCN)][BF_4]_2$	CH_3CN+TFA	-0.77	-1.20 (0.43)	750	0.04
$[Co^{III}(PN)_2(H)(MeCN)][PF_6]_2$	CH_3CN+TFA	-0.77	-1.13 (0.36)	1500	1.05
$Co(dmgH)_2(py)$[275]	DMF+Et_3NH^+	-1.20	-1.53 (0.33)	10^4	26.2
$Co(dmgBF_2)_2(MeCN)$[297]	CH_3CN+4-trifluoromethoxyanilinium	-0.58	-0.81 (0.23)	125	16.1
$[Ni(P^{Ph}_2N^{Ph}_2)_2(MeCN)]^{2+}$ [297]	CH_3CN+[DMF(H)]$^+$ +water	-0.43	-0.83 (0.40)	720	$5.17x10^{-4}$
$[Ni(P^{Ph}_2N^{Ph}_2)_2(MeCN)]^{2+}$[275]	CH_3CN+[DMF(H)]$^+$	-0.5	-1.16 (0.66)	75,000	0.12
$[Ni(P^{Ar}_2N^{Ar'}_2)_2]^{2+}$[297]	Hexanedinitrile+[DMF(H)]$^+$+water	-0.49	-0.72 (0.23)	70,000	9024
1-Co[298]	CH_3 CN+TFA	-0.62	-1.30 (0.68)	2600	$7.6x10^{-6}$
[Fe-Fe]-hydrogenase [275, 299]	-	-	(0.09)	-	630

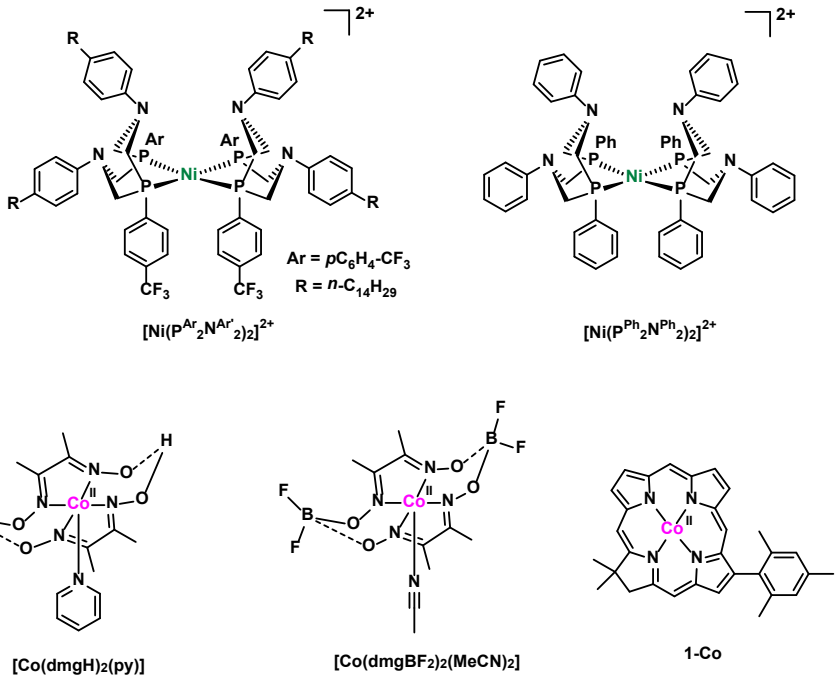

Chart 3.6. Molecular structures of each catalyst in the Tafel plot.

According to the Tafel plot, $[Ni(P^{Ar}_2N^{Ar'}_2)_2]^{2+}$ is the most efficient electrocatalyst among the leading HER electrocatalysts shown in **Chart 3.6** including cobaloximes: $Co(dmgH)_2(py)$, $Co(dmgBF_2)_2(MeCN)$, and the parent $[Ni(P^{Ph}_2N^{Ph}_2)_2]^{2+}$ electrocatalyst. The $[Ni(P^{Ar}_2N^{Ar'}_2)_2]^{2+}$ can operate at the lowest overpotential of 230 mV and shows the highest catalytic activity with TOF_{max} of 70,000 s^{-1} . The rational design structure of this complex by incorporating electron-withdrawing ligands and long alkyl chains in to the parent $[Ni(P^{Ph}_2N^{Ph}_2)_2]^{2+}$ HER electrocatalyst

improved the catalytic activity by lowering overpotential by ~200 mV with an increase of TOF_0 by 5 orders of magnitude compared to the parent Ni(II) complex.

The overpotential is lowered by using an electron-withdrawing ligand, while the structural dynamics of this catalyst are controlled by both long alkyl chains on the pendant amines and viscous dinitrile solvents. By this structural modification of the catalysts and operating in the suitable solvent, the formation of the inactive "exo-isomer" that arises from exo protonation at a single pendant amine, can be avoided.[297]

All complexes in our study are also more efficient than the $[Ni(P^{Ph}_2N^{Ph}_2)_2]^{2+}$ catalysts by comparison of the TOF_0 value in the catalytic Tafel plot. However, the catalytic activity of all catalysts in this series are lower than that of the cobaloxime family which is one of the most studied classes of molecular electrocatalysts for H_2 evolution with pioneering works by Artero et al.[141, 220, 300] It was found that the ligand oxygen atoms in cobaloximes can play a role as proton relays during electrocatalytic production of H_2 similar to that of pendant amine in the $[Ni(P^{R}_2N^{R'}_2)_2]^{2+}$ catalysts.

In our study, protonation of the pyridine ligand in the $[Co^{II}(PN)_2(MeCN]^{2+}$ occurs before the first electron transfer step to form the corresponding protonated Co(I) species (**Scheme 3.8**). Then, a ligand-assisted proton transfer to the Co(I) and/or direct reaction with a proton in bulk solution could possibly occur to generate the Co(III)-H intermediate. This evidence might result in their catalytic activity where the TOF_0 values in the Tafel plot are in between the TOF_0 of cobaloximes and the $[Ni(P^{Ph}_2N^{Ph}_2)_2]^{2+}$ HER electrocatalysts containing a pendant amine arm as a proton relay group.

CO_2 reduction activity studied by cyclic voltammetry

The electrocatalytic CO_2 reduction activity $[Co^{III}(PN)_2(H)(Cl)]^+$and $[Co^{III}$*cis*-$(PN)_2Cl_2]^+$ in CO_2-saturated acetonitrile solution was studied by the CV technique as discussed below.

3.3.12 CV studies of the $[Co^{III}$*cis*-$(PN)_2Cl_2]PF_6$ and $[Co^{III}(PN)_2(H)(Cl)]PF_6$ in saturated CO_2 MeCN solution

The CO_2 reduction activity of the $[Co^{III}$*cis*-$(PN)_2Cl_2]PF_6$ and $[Co^{III}(PN)_2(H)(Cl)]PF_6$ was examined in MeCN solution saturated with CO_2 containing 0.1 M $TBAPF_6$. The CV of the $[Co^{III}$*cis*-$(PN)_2Cl_2]PF_6$ (**Figure 3.39** a) showed a large positive shift of Co(I/0) redox couple by 150 mV from the Co(I/0) couple in this complex under Ar. There was no increase of current at shifted Co(I/0) couple in the $[Co^{III}$*cis*-$(PN)_2Cl_2]PF_6$. In contrast, the two-fold enhancement of current at the potential near to a metal-centred reduction of Co(II/I)-H in $[Co^{III}(PN)_2(H)(Cl)]PF_6$ was observed. This result indicated that the doubly-reduced Co(0) intermediates generated by two stepwise reduction of the $[Co^{III}$*cis*-$(PN)_2Cl_2]PF_6$ could strongly bind with CO_2 in a saturated CO_2 solution. In contrast to this, the Co(III)-H complex show chemical reaction with CO_2 by exhibiting current increase near the potential of Co(II/I)-H. This evidence proved the role of Co-H bond which is responsible for CO_2 reduction activity.

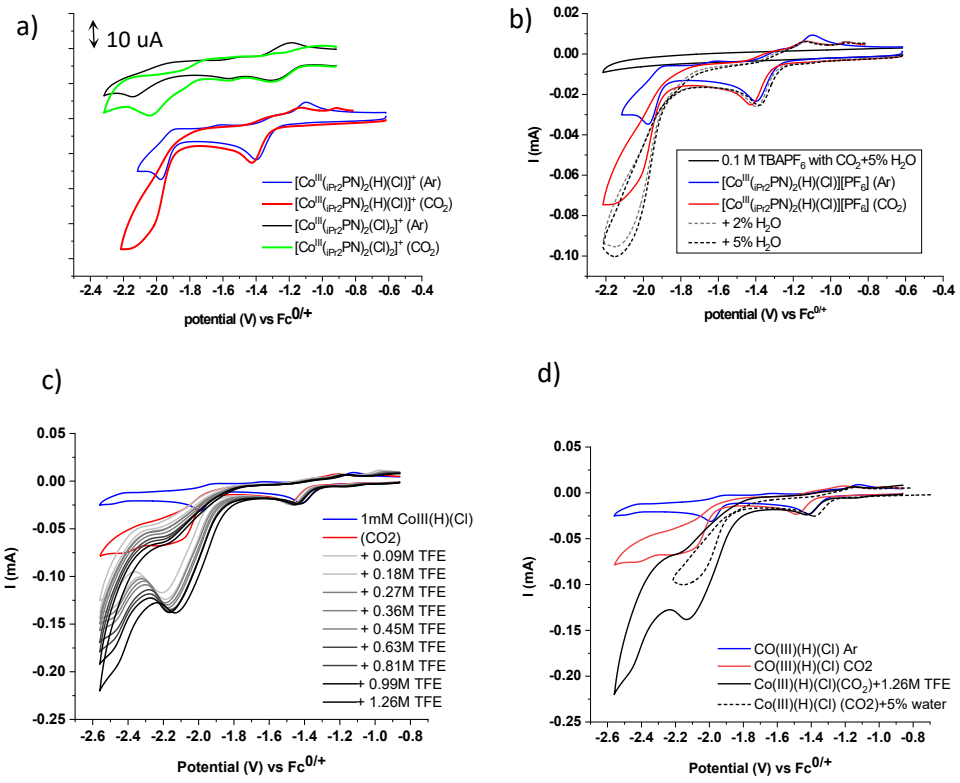

Figure 3.39. a) CVs of $[Co^{III}$*cis*-$(PN)_2Cl_2]^+$ (1 mM) in CH_3CN containing 0.1 M $TBAPF_6$ under Ar (black) and in CO_2-saturated MeCN solution (green) compared to the CVs of $[Co^{III}(PN)_2(H)(Cl)]^+$ under similar conditions, b) the CVs of $[Co^{III}(PN)_2(H)(Cl)]^+$ in CO_2-saturated MeCN solution with varying concentrations of acid H_2O as H^+ source, c) TFE as H^+ source, and d) comparison of CVs of $[Co^{III}(PN)_2(H)(Cl)]^+$ in CO_2-saturated MeCN solution with 1.26 M TFE (solid black) and 5% H_2O (dash line, black). Condition: the scan rate at 0.1 Vs^{-1}.

CO_2 reduction activity of $[Co^{III}(PN)_2(H)(Cl)]PF_6$ using H_2O or TFE as H^+ source

The CVs (**Figure 3.39** b) of the Co(III)-H complex in CO_2-saturated MeCN solution with H_2O showed a slight enhancement of the peak currents near Co(II/I)-H potential around -2.15 V vs $Fc^{0/+}$ with a positive shift by 70 mV from the Co(II/I)-H in the CV of this solution with no H^+ source. By using TFE as H^+ source, the CV responses (**Figure 3.39** c) were similar to the solution upon adding water but with slight increase in the currents as comparison of the CVs in **Figure 3.39** d. This suggested relatively more conversion of CO_2 to possible CO or HCOO-/HCOOH products in the presence of H^+ source compared to the solution without H^+ source.

The controlled experiments by CV measurements of a solution of this complex with no CO_2 by varying concentrations of water (**Figure A 3.9** a) showed no significant increase in the currents near reduction potential of Co(II/I)-H. It can be assumed that the increase in current near Co(II/I)-

H couple in the CV of the $[Co^{III}(PN)_2(H)(Cl)]^+$ with 5% H_2O (**Figure 3.39** b) was due to the CO_2 conversion with negligible amount of H_2 production from common side reaction (H^+reduction).

Proposed mechanism for conversion of CO_2 to formate/formic acid by the Co(III)-H

The increase in current without the addition of proton source to a solution indicated that CO_2 might insert into Co-H bonds to form the corresponding formato complex or formate/formic acid in a solution. It clearly showed that the reduced Co(I)-H hydride species formed by stepwise $2e^-$ reduction is required prior to the occurrence of a following chemical reaction. This result is consistent with previous reports that showed CO_2 insertion into Co-H bonds of the Co(I) complex supported by PN(Py)P pincer ligand.[177] As a result, the mechanism for conversion of CO_2 to formate or formic acid by the $[Co^{III}(PN)_2(H)(Cl)]PF_6$ was assumed to proceed via insertion of CO_2 into Co^I-H bond (**Scheme 3.11**) or other pathways to give possible CO or H_2 as products (not shown in the scheme).

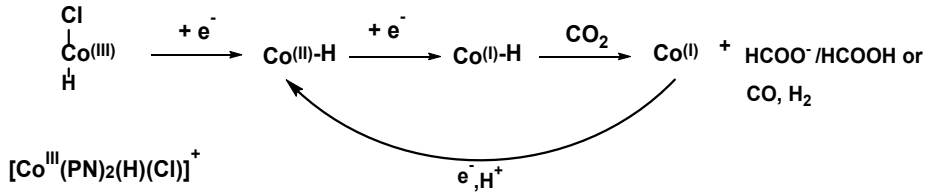

Scheme 3.11. Proposed mechanism of the cobalt(III) hydride complex for CO_2 reduction activity.

For a typical pathway for transformation of CO_2 to CO by transition metal complexes, It has been proposed that conversion of CO_2 to CO proceeds via the direct coordination of CO_2 to the metal centre before being reduced to form CO as product.[301] A presence of proton source in catalytic system could facilitate C–O bond cleavage in a metallo-carboxylate species resulting in liberation of CO and H_2O.

CV studies of $[Co^{III}$*cis*-$(PN)_2Cl_2][PF_6]$ in saturated CO_2 acetonitrile solution with different H^+ sources

The CV titration of the $[Co^{III}$*cis*-$(PN)_2Cl_2][PF_6]$ with H_2O (**Figure 3.40** a) displayed positive shifts of the redox Co(II/I) and Co(I/0) couples, and a stoichiometric current at these two redox waves was observed. This evidence suggested that H^+ or water could facilitate the interaction between metal centre and CO_2 in the singly- Co(I) and doubly-reduced Co(0) intermediate. Interestingly, in case of using MeOH or TFE as proton source (**Figure 3.40** b and **Figure 3.40** c, respectively), increases in currents with i_{cat}/i_p about 7.6 were observed at the potential near to the redox Co(I/0) couple indicating electrocatalytic activity for CO_2 reduction. In addition, positive shifts

and irreversibility of Co(II/I) wave also indicated the binding event between the reduced Co(I) metal centre in the complex with CO_2 and conversion to a possible reduced product by a further reduction of the CO_2 bound Co(I) intermediate.

The CV of the complex in CO_2-saturated MeCN solution with 5% v/v MeOH showed the increase of current near the Co(I/0) couple in the complex, and this peak current disappeared after degassing with CO_2. This evidence supported a conversion of CO_2 by the complex at a reduction potential around -2.1 V. Therefore, the H^+ reduction of this complex in the absence CO_2 under similar condition appeared at the onset potential around -2.25 V (**Figure 3.40** b, dash line, black).

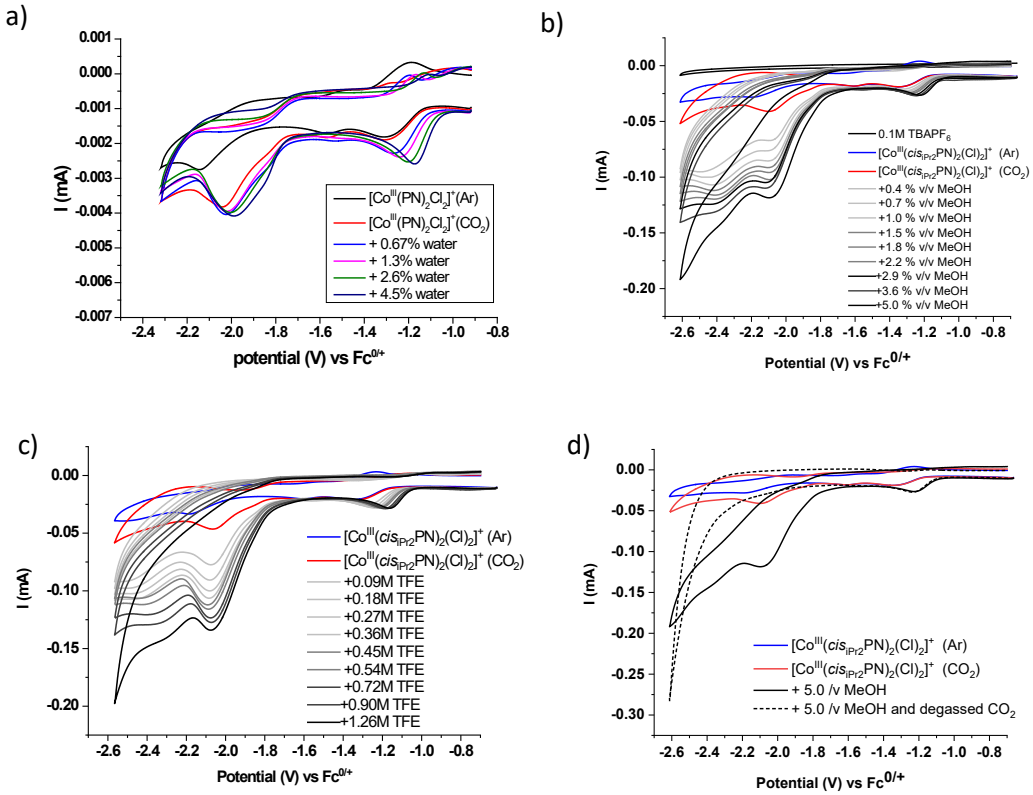

Figure 3.40. CVs titration of $[Co^{III}cis\text{-}(PN)_2Cl_2]^+$ with a) H_2O, b) MeOH, and c) TFA as H^+ source and d) comparison of CVs of $[Co^{III}cis\text{-}(PN)_2Cl_2]^+$ in MeCN under Ar (blue), in saturated CO_2 MeCN solution (red) with 5.0% v/v MeOH (solid black) and the solution with MeOH after degassed CO_2 by bubbling with Ar (dash line, black). Conditions for a), b) and c): 1 mM of the $[Co^{III}cis\text{-}(PN)_2Cl_2]^+$in saturated CO_2 MeCN solution containing 0.1 M $TBAPF_6$, at the scan rate 0.1 V s^{-1}.

Table 3.10. Electrochemical data from CV measurements and conditions for the studies of electrocatalytic CO_2 reduction activity of each complex.

H^+ source	$[Co^{III}(PN)_2(H)(Cl)][PF_6]$			$[Co^{III}$*cis*$-(PN)_2Cl_2][PF_6]$		
	[acid]	E_{cat} (V)	i_{cat}/i_p	[acid]	(E_{cat}) (V)	i_{cat}/i_p
TFE	1.26 M	-2.13	6.05	1.26 M	-2.07	7.6
H_2O	5% v/v	-2.15	3.7	4.5% v/v	-1.99	1.9
MeOH	-	-	-	5.0% v/v	-2.10	8.0

3.4 Conclusion

3.4.1 H_2 evolution catalysis

H^+ reduction activity by CV studies

All complexes in this study can electrochemically catalyse H^+ reduction with high %FE (90-100%) for H_2 evolution at moderate overpotential (400-600 mV) in MeCN using TFA as H^+ source. The H_2 evolution mechanism catalysed by $[Co^{II}(PN)_2(MeCN)][BF_4]_2$ (**Scheme 3.4**) and $[Co^{II}(PN)_2Cl_2]$ (**Scheme 3.7**) proceeds via an ECEC mechanism. The metal-centred reduction activity involved for this catalysis was confirmed by CV studies of the complex with different strength of acids. The relatively strong acid (TFA in this work) showed the catalytic current near a singly reduced Co(II/I) couple but the weak CH_3COOH acid caused catalytic currents near the doubly reduced Co(0) or $Co(I)L^{\bullet-}$ as observed in the CVs studies of the of $[Co^{II}(PN)_2Cl_2]$ under catalytic conditions. Therefore, large negative potential is required by using weak acetic acid as H^+ source, while relatively strong acid, TsOH H_2O than TFA and CH_3COOH causes a decomposition of the catalysts. Thus, TFA is the most suitable acid for using as H^+ source to undertake mechanistic H_2 evolution studies. It was found the catalytic rate constant for H_2 evolution catalysed by the $[Co^{III}(PN)_2(H)(MeCN)]^{2+}$.and $[Co^{II}(PN)_2(MeCN)]^{2+}$.is first-order reaction respect to TFA concentration.

The mechanism studies for H_2 evolution

The H_2 evolution pathway catalysed by the $[Co^{II}(PN)_2Cl_2]$ complex in MeCN using TFA as H^+ source via ECEC mechanism is shown **Scheme 3.7**. The stepwise one-electron metal-centred reduction of the Co(II) to the reduced Co(I) with a subsequent protonation resulted in a formation of $[Co^{III}(PN)_2(H)(Cl)]^+$ intermediate (E1C1). The NMR studies suggest that Cl^- ligand in the $[Co^{III}(PN)_2(H)(Cl)]^+$ can exchange with MeCN under catalytic conditions with high concentration of TFA to generate the $[Co^{III}(PN)_2(H)(MeCN)]^{2+}$ analogue. The further one-electron reduction of the Co(III)-H is required to produce active Co(II)-H intermediate prior to evolving H_2. The UV-Vis SEC studies and scan-rate variation analysis of the $[Co^{III}(PN)_2(H)(Cl)]^+$ and $[Co^{III}(PN)_2(H)(MeCN)]^{2+}$ indicate formation of $[Co^{II}(PN)_2H]^+$ following one-electron transfer. The slope of $\Delta E_{pc}/\log \nu$ = -31 mV obtained from plotting E_{pc} versus log ν of Co(III/II)-H couple in $[Co^{III}(PN)_2(H)(MeCN)]^{2+}$ is not consistent with a bimolecular pathway for Co(II)-H, thus it supported H_2 evolution by a protonation of the reduced Co(II)-H via heterolytic pathways.

The more detailed mechanistic H_2 evolution studies of the $[Co^{III}$*cis*-$(PN)_2Cl_2)][PF_6]$ showed a complicated H^+ reduction mechanism because the labile nature of the corresponding $[Co^{II}(PN)_2Cl_2]$ after one-electron reduction of the $[Co^{III}$*cis*-$(PN)_2Cl_2)][PF_6]$ results in a mixture of

various Co(II) species formed in the solution and they contributed to the catalytic H_2 evolution as shown in **Scheme 3.10**.

However, $[Co^{II}(PN)_2(MeCN)][BF_4]$ with TFA as H^+ source shows a simpler catalytic cycle for H_2 evolution (**Scheme 3.8**). Protonation of this starting Co(II) complex at one of the pyridine ligands monitored by the UV-Vis experiments was proposed in the mechanism prior to entering the E1C1E2C2 cycle for H_2 evolution. The protonated pyridine in the intermediate (A-MeCN) might play an important role in assisting H^+ transfer from bulk solution to the reduced Co(I) metal centre to form the corresponding $[Co^{III}(PN)_2(H)(MeCN)]^{2+}$ intermediate. A reduced Co(II)-H species is necessary for H_2 evolution by a protonation (E2C2) via heterolytic pathway.

Kinetic studies by FOWA and Tafel plot

The kinetic studies reveal that the k_{cat} of 1560±6 M^{-1} s^{-1} for $[Co^{III}(PN)_2(H)(MeCN)]^{2+}$ is about double that of k_{cat} of 740±26 for $[Co^{II}(PN)_2(MeCN)][BF_4]_2$. The catalytic Tafel plot suggested that $[Co^{III}(PN)_2(H)(MeCN)][PF_6]_2$ is a more efficient catalyst than the corresponding Co(II) by reaching the maximum *TOF* (TOF_{max}) at significantly lower overpotential than that of $[Co^{II}(PN)_2(MeCN)][BF_4]_2$ by 70 mV. Moreover, the catalytic Tafel plot allows comparisons to the reported HECs catalysts and it was found that the TOF_0 values are in between the TOF_0 of cobaloximes and the $[Ni(P^{Ph}_2N^{Ph}_2)_2]^{2+}$ HER electrocatalyst containing a secondary pendant amine arm as a proton relay. This supports the hypothesis that the intrinsic properties of the pyridine rings in $[Co^{II}(PN)_2(MeCN)][BF_4]_2$ and $[Co^{III}(PN)_2(H)(MeCN)][PF_6]_2$ facilitate H^+ transfer. We suggested that protonation of the reduced Co(I) species to generate Co(III)-H species might be the catalytic rate-determining step as suggested by the higher k_{cat} value of $[Co^{III}(PN)_2(H)(MeCN)][PF_6]_2$ than that for $[Co^{II}(PN)_2(MeCN)][BF_4]_2$

3.4.2 CO_2 reduction activity

The preliminary studies of CO_2 reduction activity of the $[Co^{III}$*cis*-$(PN)_2Cl_2)][PF_6]$ and the $[Co^{III}(PN)_2(H)(Cl)][PF_6]$ show a promising result for electroreduction of CO_2. The current increase near reduction potential of Co(II/I)-H in the CV of CO_2-saturated solution of the Co(III)-H complex without H^+ source suggested an insertion of CO_2 into the Co-H bond in the doubly reduced Co(I)-H intermediate (as proposed in **Scheme 3.11**). This pathway is expected to yield formate or formic as product. It was also observed that adding H^+ (from H_2O, MeOH or TFE) can increase the peak current. For example, much higher current density was achieved when MeOH or TFE was added to a saturated CO_2 solution of the $[Co^{III}$*cis*-$(PN)_2Cl_2)][PF_6]$. The stabilisation of the Co(I) intermediate demonstrated by a positive shift of the Co(II/I) couple upon adding H^+ source was found for all complexes.

Chapter 4

Metal-ligand cooperation of cobalt complexes with tetradentate PNNP based phenanthroline ligand

4.1 Introduction

Traditionally, the noble transition-metals catalysts have largely been used for activation of a wide variety of chemical bonds particularly for a H_2 molecule such as the utilization of Ir, Pd, Rh, Ru and others. [302-304] Catalytic (de)hydrogenation reactions are found in any part of chemical synthesis and in the modern chemical industry with large-scale chemical production. Recently, the remarkable development of base metal catalysts for this major class of reaction has been made using 3d transition metal complexes as summarized in the review. [305] This review describes the rapid development of the Fe, Co and Mn-based catalysts that occurred from last three years, and they also mentioned the ligand systems utilized for the first row transition metal catalysts which often similar to or fully mimic those successfully used for Ru-based catalysis. It was pointed out that tridentate or pincer ligands are the most promising ligands and featured in a vast majority of active catalysts regardless of metal used.

In respect of noble-metal free catalysts, many cobalt complexes, in the form of either molecular or in situ-formed complexes, are gaining attention in the field of homogeneous hydrogenations. The most recently review of emerging cobalt catalysts for homogeneous hydrogenations by Beller et al.[306] noted that the stability and reactivity of the complexes have been greatly assisted by multidentate ligands under steric and/or electronic effects. For example, tridentate or tetradentate phosphine ligands indirectly tune the reactivity of the metal centre to accelerate the overall process, whereas the elementary steps in the catalytic cycle catalyzed by pincer-type complexes are controlled by direct participation of the ligand via metal-ligand cooperation (MLC). Moreover, this group recently reported that Co(I) and Co(II) pincer complexes with an appropriate tridentate or tetradentate phosphine ligand result in the desired activity for hydrogenation of aromatic, aliphatic and cyclic esters, while monodentate and bidentate phosphine ligands showed no reactivity for this catalytic reaction.[307]

Metal-ligand cooperation

During the last decade, the bulky phosphorus-containing tridentate pincer ligand system based monoanionic scaffold was mostly applied in coordination and organometallic chemistry.[308] The unique reactivity of the pincer complexes with lutidine- and picoline-based ligands with one or two CH_2 groups in the ortho-position(s) of a central pyridine unit were first demonstrated by Milstein in 2015.[309]

Upon deprotonation by strong bases, this type of complex can undergo dearomatization of the heteroaromatic core to produce an exocyclic double bond, thus generating a reactive centre for metal-ligand cooperation as shown in (**Scheme 4.1**).

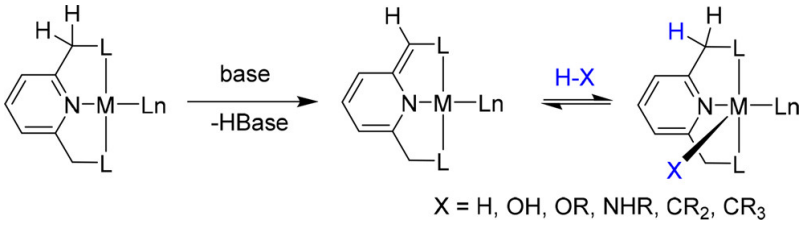

Scheme 4.1. Bond activation by MLC reactivity involving ligand aromatization–dearomatization.[309]

This new mode of activation of chemical bonds involving ligand aromatization–dearomatization processes of transition metal complexes supported by bis(phosphino) pyridine-based PNP pincer ligand has led to unusual bond activation processes and new catalytic reactions.[310-312] In this type of reactivity, chemical bonds are broken reversibly across the metal centre and the pincer-ligand arm leading to new bond making and -breaking processes. A large number of tridentate pincers with different types of ligands and their metal complexes have been developed as a result of the thermal stability, robustness and interesting reactivity. For this reason, they are particularly attractive for hydrogenation-related catalysis, which involves heterolytic H_2 activation by ligand-assisted reactivity as a key step in the overall processes. This unique feature of pincer ligands in turn allows a wider range of activity than that traditionally obtained by metal-based catalysis alone.[313] Furthermore, pyridine-based pincer complexes have been attractive for metal-ligand cooperative catalysis due to their ease of deprotonation of the methylene spacer group resulting in switching charge from a neutral- to monoanionic ligand. This particular unique of pyridine-derived neutral ligands with non-innocent behavior could potentially facilitate metal catalyzed organic transformation.[314]

More recently, MLC reactivity involving ligand aromatization–dearomatization have been investigated by employing heteroaromatic ligands with more conjugated π-electron system such as acridine [315, 316], bipyridine [171, 317], and phenanthroline [170, 318]-derived pincer ligands (**Scheme 4.2**).

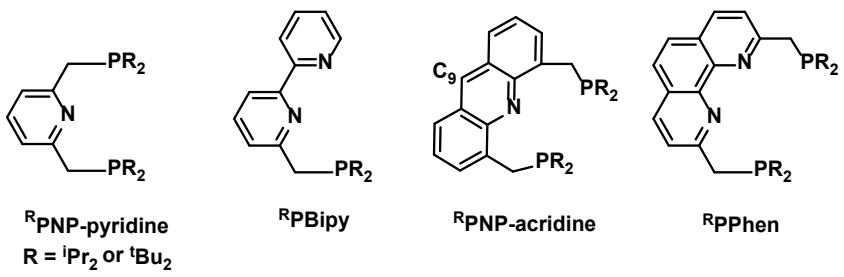

^{R}PNP-pyridine
R = $^{i}Pr_2$ or $^{t}Bu_2$ ^{R}PBipy ^{R}PNP-acridine ^{R}PPhen

Scheme 4.2. A well-defined pyridine and its derivatives based on pincer ligands involving aromatization-dearomatization MLC.

For example, in 2013, Milstein and coworkers [318] discovered that the hydride of ruthenium complexes supported by a tetradentate phenanthroline-based ligand, [Ru($_{t}$Bu2PNNP)(H)(Cl)], offers facile dearomatization upon deprotonation of the benzylic proton by LiN($SiMe_3$)$_2$ to give the corresponding dearomatized complex **1** (**Scheme 4.3**). NMR studies of complex **1** with H_2 resulted in the appearance of a low intensity of singlet phosphorus at 118.91 ppm in the ^{31}P NMR spectrum which correlates to a triplet hydride signal at -8.65 ppm in ^{1}H NMR. Therefore, they strongly suggested that the trans-dihydride complex **2** is an intermediate to form complex **3**. The formation of the dihydride intermediate was then proved by the reaction of dichloro complex, [Ru($_{t}$Bu2PNNP)(Cl)$_2$], with two equivalents of $NaBEt_3H$ in [D_8]-toluene. It was found that the dihydride complex **2** was initially formed in low concentrations followed by the formation of complexes **1** and **3**. After warming to room temperature, a mixture of two products containing 68% of complex **1** and 32% of complex **3** was observed by NMR studies. This evidence corresponded to the generation of **1** and **3** in the absence of H_2 by liberation of H_2 to form **1** and hydrogenation of the phenanthroline backbone to give complex **3** as proposed in **Scheme 4.3**.

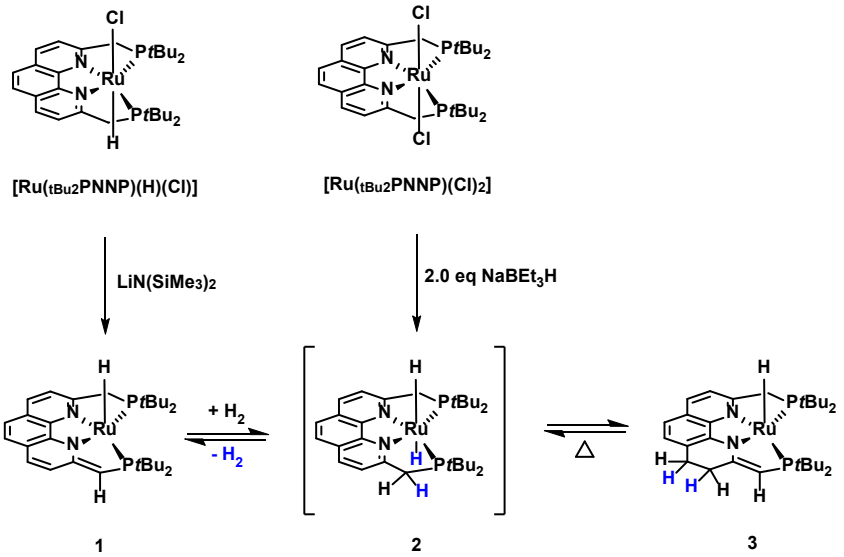

Scheme 4.3. A unique mode of stepwise MLC by an aromatization/deconjugation sequence for H_2 activation by the complex **1**.

These aromatization/deconjugation steps of the ligand backbone were demonstrated to be reversible which led to the discovery of an unprecedented mode of stepwise cooperation between the metal centre and the coordinated ligand. The modification of this planar ligand in the ruthenium complex also exhibited the concept of long-range cooperation which was previously observed in acridine[315] and diazafluorene[319] based ruthenium complexes. A unique mode of cooperation involving a long range interaction between the acridine C9 position of the ligand (**Scheme 4.2**) and the metal centre was found in these complexes.

Cobalt-based pincer complexes by Chirik et. al.

In regard of noble metal-free complexes based on bis(phosphino)pyridine pincer ligands, several classes of four-coordinate cobalt complexes supported by tridentate pincer-type ligands were investigated by Chirik et al.[216] (**Scheme .4.4**).

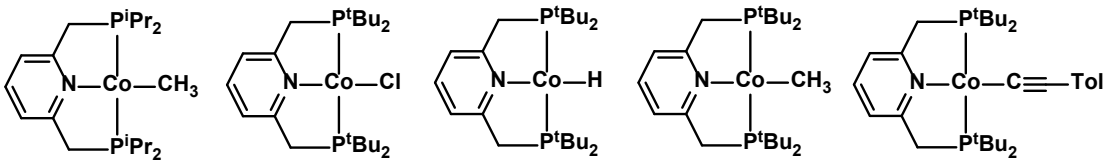

Scheme 4.4. Thermally stable cobalt complexes with ^{R}PNP ligands.

Chirik et al[216] reported the synthesis and crystallographic characterization of ($^{i}Pr_2$PNP)$CoCH_3$ as well as its reactivity as a platform for oxidative addition of non-polar substrates including H_2, C-H bonds of arene and terminal alkynes in 2014 (**Scheme 4.5**). They reasoned that the thermal

stable methyl cobalt(I) complex, ($^{i}Pr_2$PNP)CoCH_3 was stable with no modification of the ligand because of complexation with a sufficiently electron donating ^{R}PNP-pyridine ligand. Moreover, this electron-rich ligand enables oxidative addition of H_2 and C-H bonds to the Co(I) methyl complex which resulted in the formation of a cobalt(III) trihydride complex and a bis(acetylide) hydride complex.

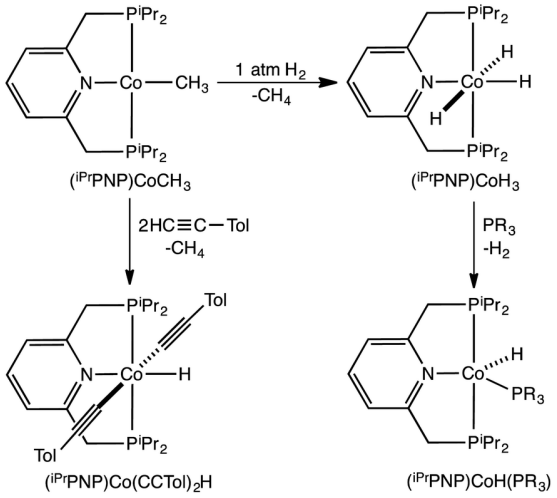

Scheme 4.5. Oxidative addition of H_2 and TolCCH with (^{iPr}PNP)CoCH_3.[216]

However, the crystal structure of ($^{i}Pr_2$PNP)CoCH_3 complex obtained in this work contradicted the structures of the complexes reported by Milstein and coworkers in the previous year. [320] The attempt to synthesize (^{R}PNP)Co(I)methyl as a diamagnetic complex (R_2 = $^{i}Pr_2$ and $^{t}Bu_2$) was not successful because H atom loss from the benzylic position of the chelate to form Co(I), $[PNP]^0$ with ligand-centred radical or Co(II), $[PNP]^{1-}$ with a cobalt-centred radical as proposed in **Scheme 4.6**.

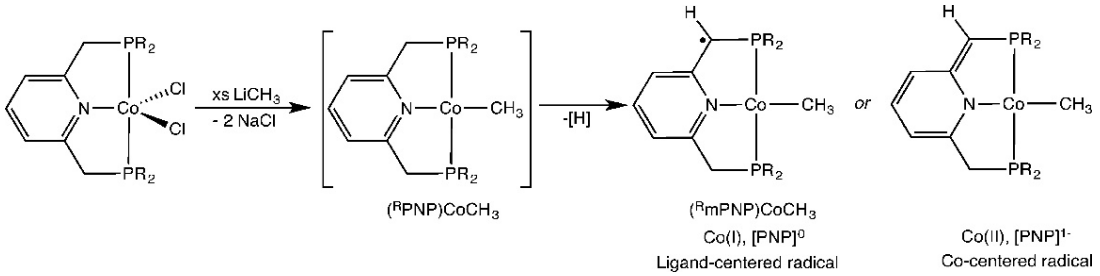

Scheme 4.6. Ligand modification via proposed H-atom loss from (^{R}PNP)CoCH_3 complexes as previously reported (R = $^{i}Pr_2$ and $^{t}Bu_2$).[320]

Subsequently, the analogue of ($^{i}Pr_2$PNP)CoCH_3 complex with the $^{t}Bu_2$ substituents at the phosphine arms was prepared by the Chirik group.[216] A series of ($^{t}Bu_2$PNP)CoX (X = H, CH_3, Cl, CCPh) was isolated and their electronic structures and thermal stability were then examined. Importantly, a modification at the benzylic position of all pincer complexes was observed in this

series by treatment with the stable nitroxyl radical, TEMPO (2,2,6,6-tetramethylpiperidin-1-yloxidanyl). Moreover, the hydride and methyl derivative in this series also exhibited a thermal modification of the pincer ligand at 110 ^{0}C. Based on this evidence, they proposed that the modification of pincer ligand could be feasible by deprotonation pathway of the benzylic proton via homolytic or heterolytic cleavage. The electronic structure of the modified pincer cobalt complexes could be identified as low-spin cobalt(II) complexes with a closed shell anionic form of the modified chelate proved by EPR spectroscopy, magnetometry and computational studies. The energetically accessible one-electron Co(II/I) redox couple led to a weakening of C-H bond relative to the Rh analogue which showed a much higher thermodynamic barrier to one-electron chemistry resulting from a stronger C-H bond.

This finding from Chirik et al. demonstrated that a suitable pairing of a strong ligand field with the cobalt centre could enable two-electron oxidative addition chemistry with the first row transition metal. In this chapter, we report the chemistry of cobalt complexes with the tetradentate bis(di-*t*-butylphosphino-methyl)-1,10-phenanthroline ligand (**Scheme 4.7**), chosen in order to avoid problems of ligand loss observed with the bidentate ligands described in Chapter 2. Interestingly, in our work, a reduction of the cobalt(II) complex, Co^{II}(PNNP)Cl_2 with tridentate coordination mode of this ligand resulted in a unique ligand-based reactivity which resulted in the dearomatized and deconjugated complex. This MLC reactivity was similar to that observed in the ruthenium analogue as described above by the Milstein group.

4.2 Experimental

4.2.1 General Procedures and materials

General procedures for synthesis of all complexes were carried out under inert atmosphere with standard Schenk line technique as mentioned in the experimental section in **Chapter 2**. Benzene, toluene, hexane and THF, were dried by refluxing over Na under Ar. Deuterated solvents (toluene-d_8, C_6D_6 were purchased from Aldrich and were dried over potassium prior to degassing by freeze-pump-thaw technique (three times), and stored under Ar atmosphere in a glove box.

Solvents for general use were purchased from Fisher Scientific Ltd. All commercial chemicals were purchased from suppliers as follows: Sigma-Aldrich (ammonium hexafluorophosphate, cobalt(II) tetrafluoroborate hexahydrate, tetrabutylammonium hexafluorophosphate ($TBAPF_6$), trifluoroacetic acid, sodium borohydride), Alfa-Aesar (2,9-dimethyl-1,10-phenanthroline), Merck (cobalt(II) chloride anhydrous), Acros (di-tert-butylchlorophosphine, 2.5M n-butyllithium in hexane). All of these chemicals were used without further purification.

4.2.2 Characterisation techniques

X-ray crystallographic determination and spectroscopic techniques such as multi-nuclear NMR techniques, UV-Vis spectrophotometry including mass spectrometry, and X-ray crystallographic determination were generally used for structural characterisation. Evans' NMR measurements for paramagnetic species were performed to investigate their magnetic properties. The plots of Δf (Hz) for the reference compound (THF signals) versus 1/T (K^{-1}) for $[Co^{II}(PNNP)(MeCN)][BF_4]_2$, $[Co^{II}(PNNP)Cl][BArF^4]$ and $[Co^{I}(PNNP)][PF_6]$ are shown in **Figure A 4.19**. Cyclic voltammetry (CV) was carried out in order to study their redox properties. All of these techniques with detailed information were described in the experimental section in Chapter 2 otherwise noted.

4.2.2.1 X-ray crystallography

[Co^{II}(PNNP)Cl_2] complex

Single crystals of $C_{30}H_{46}Cl_2CoN_2P_2$ were recrystallized from CH_2Cl_2/pentane.

Table 4.1. Crystal data and structure refinement for [Co^{II}(PNNP)Cl_2] (rnp 1807).

Empirical formula	$C_{30}H_{46}Cl_2CoN_2P_2$
Formula weight	626.46
Temperature/K	110.05(10)
Crystal system	monoclinic
Space group	Ia
a/Å	11.5536(4)
b/Å	13.8764(4)
c/Å	19.7451(8)
α/°	90
β/°	103.215(4)
γ/°	90
Volume/$Å^3$	3081.75(19)
Z	4
$\rho_{calc}g/cm^3$	1.350
μ/mm^{-1}	7.102
F(000)	1324.0
Crystal size/mm^3	0.292 × 0.18 × 0.099
Radiation	CuKα (λ = 1.54184)
2Θ range for data collection/°	7.858 to 142.166
Index ranges	-13 ≤ h ≤ 13, -16 ≤ k ≤ 16, -24 ≤ l ≤ 23
Reflections collected	10352
Independent reflections	4322 [R_{int} = 0.0482, R_{sigma} = 0.0492]
Data/restraints/parameters	4322/16/480
Goodness-of-fit on F^2	1.026
Final R indexes [I>=2σ (I)]	R_1 = 0.0507, wR_2 = 0.1238
Final R indexes [all data]	R_1 = 0.0562, wR_2 = 0.1293
Largest diff. peak/hole / e $Å^{-3}$	0.57/-0.22
Flack parameter	0.140(8)

$[Co^{II}(PNNP)Cl][BAr^{F}_4]$

Single crystals of $C_{62}H_{58}BClCoF_{24}N_2P_2$ were recrystallized from THF/Pentane.

Table 4.2. Crystal data and structure refinement for $[Co^{II}(PNNP)Cl][BAr^{F}_4]$ (rnp1811).

Identification code	rnp1811
Empirical formula	$C_{62}H_{58}BClCoF_{24}N_2P_2$
Formula weight	1454.33
Temperature/K	110.05(10)
Crystal system	triclinic
Space group	P-1
a/Å	12.7861(5)
b/Å	14.3291(6)
c/Å	18.3248(6)
α/°	70.055(3)
β/°	88.097(3)
γ/°	83.611(3)
Volume/Å^3	3136.3(2)
Z	2
ρ_{calc}g/cm^3	1.540
μ/mm^{-1}	4.040
F(000)	1478.0
Crystal size/mm^3	0.178 × 0.127 × 0.087
Radiation	CuKα (λ = 1.54184)
2Θ range for data collection/°	6.846 to 134.154
Index ranges	-15 ≤ h ≤ 15, -17 ≤ k ≤ 15, -18 ≤ l ≤ 21
Reflections collected	21246
Independent reflections	11189 [R_{int} = 0.0243, R_{sigma} = 0.0359]
Data/restraints/parameters	11189/177/1027
Goodness-of-fit on F^2	1.066
Final R indexes [I>=2σ (I)]	R_1 = 0.0493, wR_2 = 0.1214
Final R indexes [all data]	R_1 = 0.0583, wR_2 = 0.1272
Largest diff. peak/hole / e Å^{-3}	1.24/-0.64

$[Co^{II}(PNNP)(MeCN)][BF_4]_2$ complex

Single crystals of $C_{34}H_{52}B_2CoF_8N_4P_2$ were recrystallized from MeCN/THF.

Table 4.3. Crystal data and structure refinement for $[Co^{II}(PNNP)(MeCN)][BF_4]_2$ (rnp1810).

Empirical formula	$C_{34}H_{52}B_2CoF_8N_4P_2$
Formula weight	811.28
Temperature/K	109.95(10)
Crystal system	monoclinic
Space group	$P2_1/c$
a/Å	17.1644(3)
b/Å	21.2787(5)
c/Å	41.7856(7)
α/°	90
β/°	93.8035(15)
γ/°	90
Volume/Å^3	15228.0(5)
Z	16
ρ_{calc}g/cm^3	1.415
μ/mm^{-1}	0.605
F(000)	6768.0
Crystal size/mm^3	0.199 × 0.138 × 0.11
Radiation	MoKα (λ = 0.71073)
2Θ range for data collection/°	6.208 to 54.206
Index ranges	-15 ≤ h ≤ 22, -27 ≤ k ≤ 25, -53 ≤ l ≤ 41
Reflections collected	68439
Independent reflections	33514 [R_{int} = 0.0565, R_{sigma} = 0.0793]
Data/restraints/parameters	33514/30/1943
Goodness-of-fit on F^2	1.040
Final R indexes [I>=2σ (I)]	R_1 = 0.0862, wR_2 = 0.2164
Final R indexes [all data]	R_1 = 0.1280, wR_2 = 0.2506
Largest diff. peak/hole / e Å^{-3}	1.94/-1.02

$[Co^{I}(PNNP)][PF_6]$ complex

Single crystals of $C_{30}H_{46}CoF_6N_2P_3$ were recrystallized from THF/pentane.

Table 4.4. Crystal data and structure refinement for $[Co^{I}(PNNP)][PF_6]$ (rnp1809).

Empirical formula	$C_{30}H_{46}CoF_6N_2P_3$
Formula weight	700.53
Temperature/K	110.05(10)
Crystal system	monoclinic
Space group	C2/c
a/Å	29.7069(6)
b/Å	15.8314(2)
c/Å	22.4989(4)
α/°	90
β/°	107.176(2)
γ/°	90
Volume/Å^3	10109.4(3)
Z	12
ρ_{calc}g/cm^3	1.381
μ/mm^{-1}	5.828
F(000)	4392.0
Crystal size/mm^3	0.234 × 0.157 × 0.056
Radiation	CuKα (λ = 1.54184)
2Θ range for data collection/°	7.086 to 134.144
Index ranges	-35 ≤ h ≤ 26, -18 ≤ k ≤ 17, -25 ≤ l ≤ 26
Reflections collected	22587
Independent reflections	9009 [R_{int} = 0.0217, R_{sigma} = 0.0234]
Data/restraints/parameters	9009/51/628
Goodness-of-fit on F^2	1.038
Final R indexes [I>=2σ (I)]	R_1 = 0.0360, wR_2 = 0.0949
Final R indexes [all data]	R_1 = 0.0398, wR_2 = 0.0980
Largest diff. peak/hole / e Å^{-3}	0.65/-0.48

[Co^{I}(dPNNP)] complex

Single crystals of $C_{30}H_{45}CoN_2P_2$ were recrystallized from THF/pentane.

Table 4.5. Crystal data and structure refinement for [Co^{I}(dPNNP)] (rnp2004).

Empirical formula	$C_{30}H_{45}CoN_2P_2$
Formula weight	554.55
Temperature/K	104(1)
Crystal system	monoclinic
Space group	$P2_1/n$
a/Å	11.2155(2)
b/Å	12.5221(2)
c/Å	19.8059(4)
α/°	90
β/°	96.084(2)
γ/°	90
Volume/Å^3	2765.91(9)
Z	4
ρ_{calc}g/cm^3	1.332
μ/mm^{-1}	0.758
F(000)	1184.0
Crystal size/mm^3	0.133 × 0.084 × 0.064
Radiation	Mo Kα (λ = 0.71073)
2Θ range for data collection/°	6.652 to 58.35
Index ranges	-14 ≤ h ≤ 14, -13 ≤ k ≤ 16, -26 ≤ l ≤ 13
Reflections collected	13420
Independent reflections	6461 [R_{int} = 0.0286, R_{sigma} = 0.0439]
Data/restraints/parameters	6461/0/328
Goodness-of-fit on F^2	1.034
Final R indexes [I>=2σ (I)]	R_1 = 0.0341, wR_2 = 0.0761
Final R indexes [all data]	R_1 = 0.0483, wR_2 = 0.0826
Largest diff. peak/hole / e Å^{-3}	0.41/-0.25

[Co^{II}(mPNNP)Cl]

Single crystals of $C_{30}H_{47}ClCoN_2P_2$ were recrystallized from toluene/pentane.

Table 4.6. Crystal data and structure refinement for [Co^{II}(mPNNP)Cl] (rnp1812).

Empirical formula	$C_{30}H_{47}ClCoN_2P_2$
Formula weight	592.01
Temperature/K	109.95(10)
Crystal system	monoclinic
Space group	$P2_1/c$
a/Å	9.02445(15)
b/Å	18.5073(3)
c/Å	18.6275(3)
α/°	90
β/°	101.6780(16)
γ/°	90
Volume/$Å^3$	3046.74(9)
Z	4
$\rho_{calc}g/cm^3$	1.291
μ/mm^{-1}	6.364
F(000)	1260.0
Crystal size/mm^3	0.225 × 0.082 × 0.056
Radiation	CuKα (λ = 1.54184)
2Θ range for data collection/°	9.558 to 134.146
Index ranges	-9 ≤ h ≤ 10, -22 ≤ k ≤ 21, -22 ≤ l ≤ 19
Reflections collected	11144
Independent reflections	5451 [R_{int} = 0.0200, R_{sigma} = 0.0284]
Data/restraints/parameters	5451/0/356
Goodness-of-fit on F^2	1.029
Final R indexes [I>=2σ (I)]	R_1 = 0.0290, wR_2 = 0.0697
Final R indexes [all data]	R_1 = 0.0352, wR_2 = 0.0727
Largest diff. peak/hole / e $Å^{-3}$	0.39/-0.29

4.2.3 Synthesis of 2,9-bis(di-*tert*-butylphosphino)-methyl)-1,10 phenanthroline, PNNP ligand

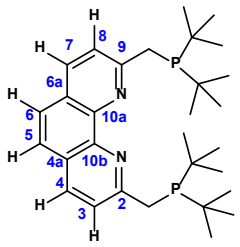

The ligand was synthesized following the previous literature [318] as a pale yellow powder (1.086 g, 33.8% yield) after precipitating with MeOH and hexane. This compound was characterized by ^{1}H, ^{31}P{^{1}H} and ^{13}C{^{1}H} NMR spectroscopy. All NMR data were in agreement with those reported in the literature. [318]

^{1}H NMR (500 MHz, in C_6D_6): δ =1.16 (d, 36 H, ^{3}J(H,P)=11.0 Hz, **PC(C*H*$_3$)$_3$**), 3.45 (d, $^{2}J_{H,P}$ = 2.8 Hz, 4H, **C*H*$_2$P*t*Bu$_2$**), 7.29 (s, 2H, **Phen-*H*$_{5,6}$**), 7.66 (d, $^{2}J_{H,P}$ = 8.3 Hz, 2H, **Phen-*H*$_{3,8}$**), 7.75 (d, $^{2}J_{H,P}$ = 8.2 Hz, 2H, **Phen-*H*$_{4,7}$**).

^{31}P{^{1}H} NMR (202.4 MHz, in C_6D_6): δ = 35.61 ppm, (s).

^{13}C{^{1}H} NMR (125.7 MHz, in C_6D_6): δ = 30.34 (d, 12C, $^{2}J_{C,P}$ = 13.7 Hz **PC(*C*H$_3$)$_3$**), 32.57 (d, 4C, $^{1}J_{C,P}$ = 23.6 Hz **PC(CH$_3$)$_3$**), 33.90 (d, 2C, $^{1}J_{C,P}$ = 25.8 Hz ***C*H$_2$**P*t*Bu$_2$), 124.21 (d, 2C, $^{3}J_{C,P}$ = 9.5 Hz **Phen-*C*$_{3,8}$**), 125.91 (s, 2C**, Phen-*C*$_{5,6}$**), 127.41 (d, 2C, $^{5}J_{C,P}$ = 1.0 Hz **Phen-*C*$_{4a,6a}$**), 135.89 (s, 2C, **Phen-*C*$_{4,7}$**), 146.54 (s, 2C, **Phen-*C*$_{10a,10b}$**), 163.20, (d, $^{2}J_{C,P}$ = 14.8 Hz, 2C, **Phen-*C*$_{2,9}$**).

4.2.4 Synthesis of [Co^{II}(PNNP)Cl$_2$]

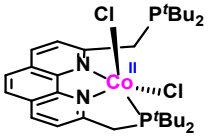

A solution of PNNP ligand (150 mg, 0.302 mmol) in 4.0 mL of n-BuOH was slowly added to a solution of 1.1 equiv. of $CoCl_2$ (43.1 mg, 0.332 mmol) in 2.0 mL of n-BuOH leading to a rapid colour change to a deep red-purple solution. The reaction mixture was left to stir under Ar for 3 h to obtain a purple powder that precipitated from the solution. The product was washed with THF prior to drying under vacuum to provide a clean product in high yield (135 mg, 71% yield). A suitable single crystal for X-ray crystallographic analysis was obtained by recrystallization in a J Young NMR tube of a DCM solution layered with pentane (**Figure 4.1** and the X-ray data in **Table 4.7**).

4.2.5 Synthesis of $[Co^{II}(PNNP)Cl][BAr^{F}_4]$

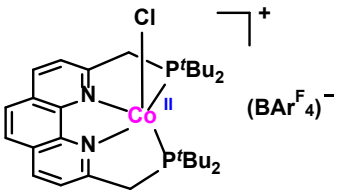

A solution of the $[Co^{II}(PNNP)Cl_2]$ in dry CH_2Cl_2 was mixed with a solution of $NaBAr^F_4$ by dropwise addition resulting a colour change to a deep green-purple solution. The reaction mixture was stirred under N_2 at room temperature. for 5 h and subsequently filtered via cannula to collect a filtrate solution. All volatiles were removed under vacuum and was recrystallized in a J Young NMR tube by dissolving in THF layered by pentane. This complex was left in the glove box at room temperature overnight to obtain deep purple plates suitable for single crystal X-ray crystallographic determination.

ESI-MS (THF): m/z = 555.2468 (25%) $[Co(PNNP)]^+$. Calcd for $C_{30}H_{46}CoN_2P_2$ 555.2463.

4.2.6 Synthesis of $[Co^{II}(PNNP)(MeCN)][BF_4]_2$

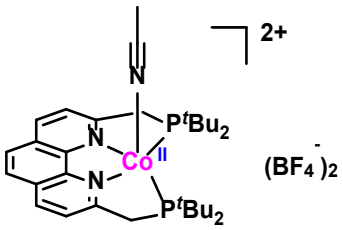

A suspension of PNNP ligand (150 mg, 0.239 mmol) was added to a solution of $[Co(MeCN)_6][BF_4]_2$ in acetonitrile to obtain a total volume of 50 mL of solution resulting in an immediate colour change from a pink solution to a dark yellow-brown colour. This reaction mixture was left to stir at 50 ^{0}C under N_2 for 3 h. Subsequently, the solution was concentrated by evaporating solvent under vacuum until about 1 mL remained. Et_2O (30 mL) was then added to precipitate the expected product as a yellow-brown powder (140 mg, 0.182 mmol, 76.15%)

ESI-Ms (MeCN): m/z 277.6222 for $[Co(PNNP)]^{2+}$ and 277.6229 calculated for $[C_{30}H_{46}CoN_2P_2]^{2+}$

4.2.7 Synthesis of [Co^{I}(PNNP)][PF$_6$]

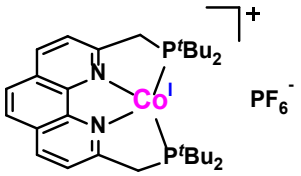

Solid $NaBH_4$ (5.0 mg, 0.13 mmol) was added to a solution of [Co^{II}(PNNP)Cl$_2$] (52 mg, 0.08 mmol) in 5.0 mL of methanol resulting in a colour change from purple-brown to deep green. The mixture was left to stir under N_2 for 1h before adding NH_4PF_6 (13.5 mg, 0.08 mmol). After stirring at room temperature for 1h, all volatiles were evaporated under vacuum to obtain the product as a dark green solid (33.6 mg, 0.048mmol, 60% yield). A concentrated THF solution of this complex was layered by pentane to form a crystal suitable for X-ray crystallographic determination. No NMR spectrum could be obtained because the complex is paramagnetic.

4.2.8 Synthesis of [Co^{I}(PNNP)(Me)]

LiMe in Et_2O (1.6 M, 0.048 mmol, 0.03 mL) was slowly added dropwise to a suspension of the [Co(PNNP)Cl$_2$] (30 mg, 0.048 mmol) in toluene at -77 ^{0}C (using acetone/dry ice bath). The reaction mixture was allowed to warm up with stirring to room temperature., stirred for ~ 30 s and then cooled in acetone/dry ice bath and stirred for ~ 2 min. This warming up and cooling down process was repeated again until a deep black solution was obtained indicating formation of the [Co^{I}(PNNP)(Me)]. All volatiles were subsequently removed under vacuum to furnish a deep black solid as product. This solid was then dissolved in C_6D_6, and the solution was filtered through cotton and celite prior to NMR measurement.

^{1}H NMR (500 MHz, in C_6D_6): δ (ppm) = 0.03 (s, 3H, **Co-C*H*$_3$**), 1.25 (br, overlap), 36H, **PC(C*H*$_3$)$_3$**), 3.61 (br, 4H, **C*H*$_2$P*t*Bu$_2$**), 8.37 (d, 2H, $^3J_{H,H}$ = 7.32 Hz, **Phen-*H***), 10.31 (d, 2H, $^3J_{H,H}$ = 7.36 Hz, **Phen-*H***).

^{31}P{^{1}H} NMR (202.4 MHz, in C_6D_6): δ (ppm) = 64.01, (s, 1P).

4.2.9 Synthesis of [Co^{I}(dPNNP)]

The selective formation of [Co^{I}(dPNNP)] was achieved by leaving a solution of the [Co^{I}(PNNP)(Me)] in toluene for 2-3 days. A colour change from deep black to deep green solution suggested that the dearomatized complex was formed in a solution mixture. A conversion of this complex to dearomatized [Co^{I}(dPNNP)] was monitored by NMR spectroscopy.

Alternatively, the [Co^{I}(dPNNP)] was prepared by the similar approach for the synthesis of [Co^{I}(PNNP)(Me)], but the solution mixture was left to further stir at -77 ^{0}C until the deep green color solution was obtained (~ 5 min after adding LiMe). All volatiles were then removed under vacuum leading to attain a deep green solid as product. This solid was extracted with pentane and then characterized by NMR techniques and mass spectrometry. Moreover, the deep green solid was recrystallized from a pentane solution layered with Et_2O in a J Young NMR tube to obtain a single crystal as deep green needle for X-ray crystallographic determination.

^{1}H NMR (500 MHz, in C_6D_6): δ (ppm) = 1.30 (d, 18H, ^{3}J(H,P)= 9.61 Hz, **PC(C*H*$_3$)$_3$**), 1.42 (d, $^{3}J_{H,P}$ = 9.71 Hz, **PC(C*H*$_3$)$_3$**), 2.06 (d, 2H, $^{2}J_{H,P}$ = 5.89 Hz, **C*H*$_2$P*t*Bu$_2$**), 4.17 (s, 1H, **C*H*P*t*Bu$_2$**), 6.34 (d, 1H, $^{3}J_{H,H}$ = 17.8 Hz, **Phen-*H*$_8$**), 6.57 (d, 1H, $^{3}J_{H,H}$ = 8.88 Hz, **Phen-*H*$_4$**), 6.58 (d, 1H, $^{3}J_{H,H}$ = 7.59 Hz, **Phen-*H*$_6$**), 6.73 (d, 1H, $^{3}J_{H,H}$ = 7.93 Hz, **Phen-*H*$_5$**), 6.85 (d, 1H, $^{3}J_{H,H}$ = 8.92 Hz, **Phen-*H*$_3$**), 8.55 (d, 1H, $^{3}J_{H,H}$ = 7.94 Hz, **Phen-*H*$_7$**)

^{31}P{^{1}H} NMR (202.4 MHz, in C_6D_6): δ (ppm) = 48.67, (s, 1P), 66.83, (s, 1P).

^{13}C{^{1}H} NMR (125.7 MHz, in C_6D_6): δ (ppm) = 30.89 (br, **PC(*C*H$_3$)$_3$**), 31.30 (br, **PC(*C*H$_3$)$_3$**), 35.57 (br, **P*C*(CH$_3$)$_3$**), 35.67 (br, **P*C*(CH$_3$)$_3$**), 41.12 (d, $^{1}J_{C,P}$ = 14.54 Hz, ***C*H$_2$P*t*Bu$_2$**), 78.36 (d, $^{1}J_{C,P}$ = 45.98 Hz, **C*H*P*t*Bu$_2$**), 109.92 (s, **Phen-C$_6$**), 118.92 (s, **Phen-C$_{4a}$**), 120.62 (d, $^{3}J_{C,P}$ = 12.17 Hz, **Phen-C$_3$**), 123.40 (s, **Phen-C$_7$**), 124.96 (d, $^{3}J_{C,P}$ = 6.32 Hz, **Phen-C$_8$**), 126.17 (s, **Phen-C$_5$**), 132.17 (s, **Phen-C$_4$**), 138.22, 144.67, 150.89, 154.84 (**Phen-C$_{6a}$, Phen-C$_9$, Phen-C$_{10a}$, Phen-C$_{10b}$**), 169.34 (d, $^{2}J_{C,P}$ = 18.50 Hz **Phen-C$_2$**).

LIFDI-MS: m/z = 554.23742 for [Co^{I}(dPNNP)] (100 %) and m/z 554.23845 calculated for [Co^{I}(dPNNP)] $C_{30}H_{45}CoN_2P_2$ (100 %).

4.2.10 Synthesis of [Co^{II}(mPNNP)Cl] and the [Co^{I}(mPNNP)]

A suspension of a purple powder of [Co^{II}(PNNP)Cl_2] (11.6 mg) in C_6D_6 was placed in the fridge of the glove box (-30 ^{0}C). $NaBEt_3H$ (1.0 M solution in THF), 37 μl (2.0 equiv) was slowly added to a cold suspension of the complex. This resulted in an immediate colour change to a deep purple solution which then rapidly changed to a deep orange-brown color solution after warming to room temperature. The solution mixture was left overnight in the glove box to evaporate the solvent. A solid residue was redissolved in a small amount of toluene and then filtered through cotton and celite prior to layering with pentane. This solution was left to recrystallize in J young NMR tube for two months to obtain a suitable crystal for single crystal X-ray diffraction.

The solution of the deep brown solid in C_6D_6 solution formed by a conversion of the [Co^{I}(dPNNP)] under 4 bar of H_2 was characterized by the NMR techniques.

^{1}H NMR (500 MHz, in C_6D_6): δ (ppm) = 1.38 (d, 18H, ^3J(H,P)= 10.23 Hz, **PC(C*H*$_3$)$_3$**), 1.48 (d, 18H, $^3J_{H,P}$ = 10.23 Hz, **PC(C*H*$_3$)$_3$**), 1.94 (d, 2H, $^2J_{H,P}$ = 7.21 Hz, **C*H*$_2$P*t*Bu$_2$**), 2.53 (t, 2H, $^3J_{H,H}$ = 7.10 Hz, **Phen-C*H*$_2$**), 2.92 (t, 2H, $^3J_{H,H}$ = 7.15 Hz, **Phen-C*H*$_2$**), 4.24 (s, 1H, **C*H*P*t*Bu$_2$**), 6.38 (d, 1H, $^3J_{H,H}$ = 8.20 Hz, **Phen-*H*$_8$**), 6.82 (d, 1H, $^3J_{H,H}$ = 7.69 Hz, **Phen-*H*$_6$**), 6.98 (d, 1H, $^3J_{H,H}$ = 7.77 Hz, **Phen-*H*$_5$**), 8.35 (d, 1H, $^3J_{H,H}$ = 8.25 Hz, **Phen-*H*$_7$**).

^{31}P{^{1}H} NMR (202.4 MHz, in C_6D_6): δ (ppm) = 55.12, (s, 1P), 71.98, (s, 1P).

^{13}C{^{1}H} NMR (125.7 MHz, in C_6D_6): δ (ppm) = 27.58 (d (overlap), **Phen-*C*H$_2$**), 27.72 (d (overlap), **Phen-*C*H$_2$**), 31.15 (br, **PC(*C*H$_3$)$_3$**), 31.39 (br, **PC(*C*H$_3$)$_3$**), 35.09 (d, $^1J_{C,P}$ = 9.37 Hz **P*C*(CH$_3$)$_3$**), 35.59 (d, $^1J_{C,P}$ = 6.25 Hz **P*C*(CH$_3$)$_3$**), 40.46 (d, $^1J_{C,P}$ = 13.51 Hz, ***C*H$_2$P*t*Bu$_2$**), 87.25 (d, $^1J_{C,P}$ = 40.40 Hz, **C*H*P*t*Bu$_2$**), 108.98 (s, **Phen-C$_6$**), 118.22 (s, **Phen-C$_{4a}$**), 121.94 (d, $^3J_{C,P}$ = 6.12 Hz, **Phen-C$_8$**), 124.71 (s, **Phen-C$_5$**), 127.47 (s, **Phen-C$_7$**), 130.62 (s, **Phen-C$_{6a}$**), 143.63 (s, **Phen-C$_{10b}$**), 149.57 (s, **Phen-C$_{10a}$**), 154.53 (s, **Phen-C$_9$**), 165.72 (d, $^2J_{C,P}$ = 12.72 Hz, **Phen-C$_2$**).

4.3 Results and discussion

One of our research aims was to prepare cobalt hydride complexes based on a tetradentate phosphine phenanthroline ligand (PNNP ligand), with the structure shown in **Chart 4.1**. A preparation method for the synthesis of $[Co^{III}(PN)_2(H)(Cl)][PF_6]$ was developed by reacting $[Co^{II}(PN)_2Cl_2]$ with $NaBH_4$ in MeOH under N_2. Although $Co(PNNP)Cl_2$ could be prepared, this method could not be successfully applied to the preparation of the desired hydride complex containing the phosphino-based phenanthroline system.

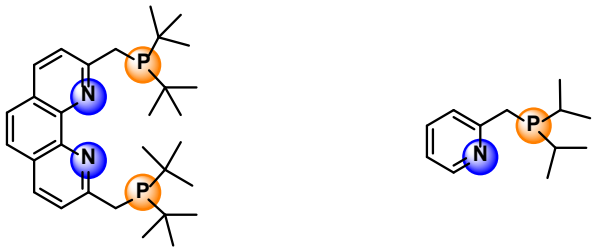

PNNP ligand PN ligand

Chart 4.1. The structure of the tetradentate PNNP ligand compared to the bidentate PN ligand.

As a result, new preparation routes using $NaBEt_3H$ as a stronger hydride source were tried. These experiments led to the discovery of interesting metal-ligand cooperativity (MLC reactivity) in the cobalt complexes in this series. Chirik suggested that Co(CH3) complexes would be more stable than cobalt hydrides and could exhibit useful reactivity. For this reason, we attempted to synthesize a $Co(PNNP)(CH_3)$. Based on the evidence from Chirik et al.[216], the thermally stable cobalt(I) methyl complex, $(^{i}Pr_2PNP)CoCH_3$ could be synthesised with no modification of the ligand because of the complexation with a sufficiently electron donating ^{R}PNP-pyridine ligand. Moreover, this electron rich ligand enables oxidative addition of H_2 and reductive elimination of methane from the Co(I) methyl complex which resulted in the formation of a cobalt(III) trihydride complex and also the cobalt(I) hydride.[216] **Section 4.3.5-4.3.9** in this chapter will show the results and discussion for the reaction of $[Co^{II}(PNNP)Cl_2]$ and $[Co^{II}(PNNP)(MeCN)][BF_4]_2$ with different hydride and methylating reagents such as $NaBH_4$, $NaBEt_3H$ and $LiCH_3$. The X-ray structure of the dearomatized $[Co^{I}(dPNNP)]$ and the hydrogenated $[Co^{II}(mPNNP)Cl]$ were discussed in **section 4.3.10**. Moreover, the electronic structure and redox properties (**section 4.3.11**) of $[Co^{II}(PNNP)Cl_2]$ and $[Co^{II}(PNNP)(MeCN)][BF_4]_2$ were investigated by UV-Vis spectroscopy and cyclic voltammetry. The electrocatalytic H_2 evolution and electroreduction of CO_2 were also examined which will be discussed later in **section 4.3.12.**

Synthesis and characterisation of cobalt complexes with tetradentate PNNP phosphine based phenanthroline ligand

A new series of cobalt complexes based on the tetradentate phosphino phenanthroline ligand, $[Co^{II}(PNNP)Cl_2]$, $[Co^{II}(PNNP)Cl][BAr^F{}_4]$ and $[Co^{II}(PNNP)(MeCN)][BF_4]_2$ were prepared by complexation of the PNNP ligand with $CoCl_2$ or $[Co(MeCN)_6][BF_4]_2$ as metal precursor (**Scheme 4.7**). These cobalt complexes were successfully prepared in high yield (> 70%). The monochloride, $[Co^{II}(PNNP)Cl][BAr^F{}_4]$ was obtained by reaction of the dichloro complex with $NaBAr^F{}_4$. Fortunately, a suitable single crystal for all complexes was obtained and the structures were characterized by X-ray crystallography. The X-ray crystal structures of $[Co^{II}(PNNP)Cl_2]$, $[Co^{II}(PNNP)Cl][BAr^F{}_4]$ and $[Co^{II}(PNNP)(MeCN)][BF_4]_2$ are illustrated in **Figure 4.2** and **Figure 4.3**, respectively.

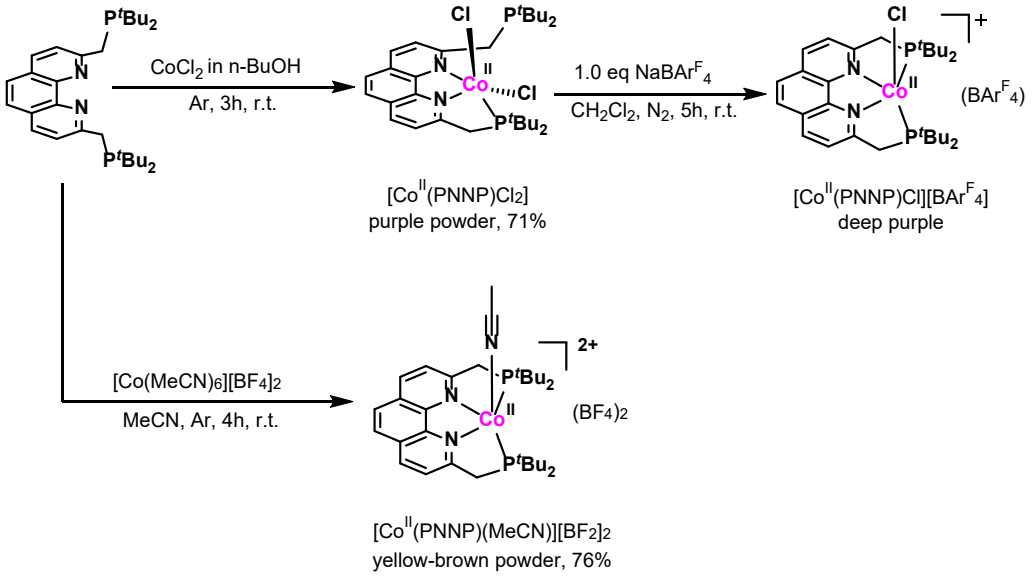

Scheme 4.7. Synthesis of the Co(II) complexes: $[Co^{II}(PNNP)Cl_2]$, $[Co^{II}(PNNP)Cl][BAr^F{}_4]$ and $[Co^{II}(PNNP)(MeCN)][BF_4]_2$.

4.3.1 Synthesis and characterisation of the PNNP ligand

The ligand was characterized by ^1H, $^{31}P\{^1H\}$ and $^{13}C\{^1H\}$ NMR spectroscopy (in C_6D_6 solution, 500 MHz). The NMR spectra of PNNP ligand corresponded to the data reported in the literature.[318] The ^1H NMR spectrum (**Figure A 4.1**, black in set) showed two equivalent CH_2 (δ 2.96), CH of isopropyl protons and the four doublet signals of methyl groups at chemical shifts around δ 1.0. The $^{31}P\{^1H\}$ spectrum (**Figure A 4.1,** red inset) displayed a singlet phosphorus signal at δ = 35.61 ppm.

4.3.2 Synthesis and characterisation of [Co^{II}(PNNP)Cl_2]

[Co^{II}(PNNP)Cl_2] was prepared by complexation of anhydrous $CoCl_2$ with 1.0 equiv. of the PNNP ligand in n-BuOH at room temperature. The purple powder was obtained with high yield (71 %). The X-ray crystal structure of this complex (**Figure 4.1**) revealed a distorted square pyramidal geometry around the Co(II) centre with tridentate PNN coordination mode of the ligand with the two chloride ligands located in cis to one another. The characterization of the complex in solution state was performed using ESI-MS as described below.

X-ray crystal structure of [Co^{II}(PNNP)Cl_2]

The X-ray structure of this complex (**Figure 4.1**) showed a square pyramidal geometry with five coordinate cobalt. The molecule was found in two positions in the structure and there is also the presence of a racemic twin. The major component is illustrated (86%). The minor component (14%) was modelled on the major component. The diagram shows the major component only. The P,N,N atoms of the PNNP ligand and one chlorine atom (Cl1) are located in the basal plane with the other chlorine (Cl2) occupying the apical position. The square pyramidal geometry is supported by values of τ (the shape-defining parameter for five-coordinate structures) which is defined as $\tau = I\beta\text{-}\alpha I/60$ (the angles refer to a 5-coordinate complex, M(ABCDE) with ligand A in the axial position).[321] For a perfectly square-pyramidal geometry with $\alpha = \beta = 180°$ (α and β are the two equally greatest angles in a basal plane, B-M-C defined as α and D-M-E defined as β), τ is equal to zero. The parameter τ becomes unity for a perfectly trigonal-bipyramidal geometry where β is the greater value = 180° between the three atoms in the equatorial plane and α = 120°. For intermediate cases, β is defined as the greater angle in a basal plane of a five-co-ordinate system which corresponded to the N2-Co-P1 (155.51(16)). The smaller α parameter is defined as Cl1-Co1-N1 bond angle of 129.6(3). The values of β = 155.51 and α = 129.6 afforded the geometric parameter τ of 0.43 for the five-coordinated [Co^{II}(PNNP)Cl_2]. Accordingly, it is best described as a distorted square pyramidal geometry.

The molecular geometry of this complex is consistent with the cobalt dichloride complexes supported with NNN pincer.[171, 322] This [Co^{II}(PNNP)Cl_2] complex demonstrated a similar coordination mode to that for tridentate pincer ligands in many cobalt complexes. For example, the molecular geometry of the four-coordinate cobalt complex with ^{iPr}PNN-Phen ligand, [$CH_3Co(^{iPr}$PNN-Phen)] is described as distorted planar. The P-Co-C bond angle is nearly linear with the large distortion of 160.80 degree due to a slight lifting of the metal above the plane.[170] In the [Co^{II}(PNNP)Cl_2] complex, the bond angle of P1A-Co1A-N2A is 155.51(16) deg which indicates a larger distortion than that in [$CH_3Co(PNN^{iPr}$Phen)] containing relatively small iPr group. This result corresponds to the greater steric demand of the *t*Bu group.

Compared to the ruthenium dichloride complex containing the same PNNP ligand, the Ru(II) analogue [Ru^{II}(PNNP)Cl_2] showed a distorted octahedral coordination geometry around the Ru(II) centre. The two chloride ligands are located trans to each other (Cl-Ru-Cl angle = 167.51(3) and perpendicular to the plane of the tetradentate PNNP ligand.[318] The relatively smaller cobalt(II) centre shows a tridentate coordination mode to the PNNP ligand with one non-coordinating phosphine arm. This coordination mode maintains the planarity of remaining PNNCo group due to complexation of the smaller size of Co(II) metal centre with constraint from bulky *t*Bu groups. Moreover, the nature of Co(II)-d^7 ion generally favours a low-spin five-coordinated complex affording a $17e^-$ complex.

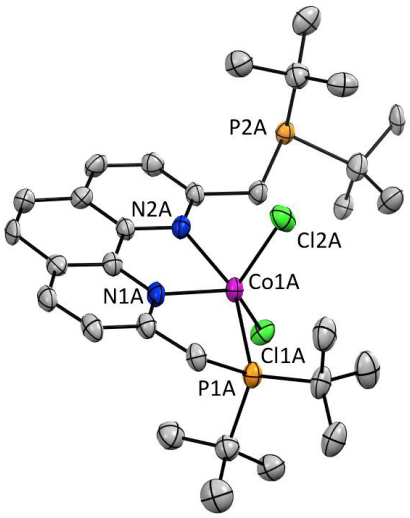

Figure 4.1. X-ray crystal structure of [Co^{II}(PNNP)Cl_2]. Selected hydrogen atoms were removed for clarity. Thermal ellipsoids shown with probability of 50%.

Table 4.7. Selected bond lengths (Å) and angles (deg) in the $[Co^{II}(PNNP)Cl_2]$.

atom	atom	bond lengths (Å)	atom	Atom	atom	bond angles/deg
Co1A	Cl1A	2.297(2)	Cl1A	Co1A	Cl2A	126.07(11)
Co1A	Cl2A	2.301(3)	Cl1A	Co1A	P1A	96.11(9)
Co1A	P1A	2.506(2)	Cl2A	Co1A	P1A	102.03(9)
Co1A	N2A	2.218(6)	N2A	Co1A	Cl1A	91.04(17)
Co1A	N1A	2.091(8)	N2A	Co1A	Cl2A	92.42(17)
			N2A	Co1A	P1A	155.51(16)
			N1A	Co1A	Cl1A	129.6(3)
			N1A	Co1A	Cl2A	103.5(3)
			N1A	Co1A	P1A	80.0(3)
			Cl	Co	Cl	126.07
			N1A	Co1A	N2A	77.4(3)

4.3.3 Synthesis and characterisation of $[Co^{II}(PNNP)Cl][BAr^F_4]$

The monochloride analogue of $[Co^{II}(PNNP)Cl_2]$ was obtained by reaction of the dichloro complex with $NaBAr^F_4$ in CH_2Cl_2. A dechlorination reaction of $[Co^{II}(PNNP)Cl_2]$ resulted in a formation of the monocationic $[Co^{II}(PNNP)Cl]^+$ and precipitation of NaCl from the reaction mixture. The solid state structure of $[Co^{II}(PNNP)Cl][BAr^F_4]$ was characterized by single crystal X-ray analysis as shown in **Figure 4.2**.

ESI mass spectrometry of $[Co^{II}(PNNP)Cl][BAr^F_4]$

The positive mode of ESI-MS of the complex (**Figure A 4.20**) showed molecular ion peaks of $[Co^{I}(PNNP)]^+$ at *m/z* = 555.2468 (calculated for $C_{30}H_{46}CoN_2P_2$ 555.2463) with dissociation of a Cl^- ligand. The calculation for the monocationic $[C_{30}H_{46}CoN_2P_2Cl]^+$ yields m/z = 591.2229.

X-ray crystal structure of $[Co^{II}(PNNP)Cl][BAr^{F}_4]$

The X-ray crystal structure of the complex (**Figure 4.2**) displayed distorted square pyramidal geometry where 2P2N coordination occupied in the equatorial plane and one Cl^- located in the axial position. The selected bond distances and bond angles were listed in the **Table 4.8.**

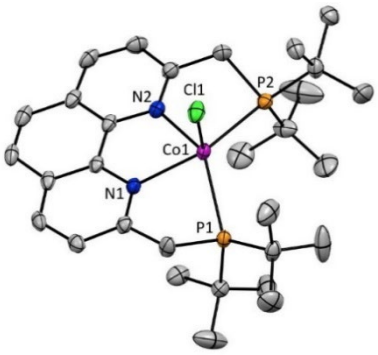

Figure 4.2. X-ray crystal structure of $[Co^{II}(PNNP)Cl][BAr^{F}_4]$. Hydrogen atoms and $BAr^{F}_4{}^-$ counter anion were removed for clarity. Thermal ellipsoids shown with probability of 50%.

Table 4.8. Selected bond lengths (Å) and angles (deg) for $[Co^{II}(PNNP)Cl][BAr^{F}_4]$ complex.

atom	atom	bond lengths (Å)	atom	atom	atom	bond angles/deg
Co1	Cl1	2.2665(8)	Cl1	Co1	P1	103.41(3)
Co1	P1	2.5502(8)	Cl1	Co1	P2	103.88(3)
Co1	P2	2.5119(9)	P2	Co1	P1	120.20(3)
Co1	N1	2.151(2)	N1	Co1	Cl1	92.65(7)
Co1	N2	2.126(2)	N1	Co1	P1	75.76(6)
			N1	Co1	P2	152.43(7)
			N2	Co1	Cl1	101.53(7)
			N2	Co1	P1	142.90(7)
			N2	Co1	P2	79.07(7)
			N2	Co1	N1	76.07(9)

4.3.4 Synthesis and characterisation of $[Co^{II}(PNNP)(MeCN)][BF_4]_2$

The yellow-brown solid from the reaction of $[Co(NCMe)_6][BF_4]_2$ with PNNP was recrystallized in MeCN/THF layered with Et_2O in a J Young NMR tube to obtain a single crystal as a brown block for X-ray crystallographic determination. The X-ray crystal structure (**Figure 4.3**) of $[Co^{II}(PNNP)(MeCN)][BF_4]_2$ revealed a distorted square pyramidal geometry for the PNNP ligand in the equatorial plane and MeCN ligand in the axial position. Selected bond distances and bond angles are listed in **Table 4.9**.

ESI mass spectrometry of $[Co^{II}(PNNP)(MeCN)][BF_4]_2$

The positive mode of ESI-MS of the complex (**Figure A 4.2**) showed molecular ion peaks of $[Co^{II}(PNNP)]^{2+}$ at *m/z* = 277.6222 with no MeCN ligand which corresponded to the calculation for the dicationic $[C_{30}H_{46}CoN_2P_2]^{2+}$at m/z = 277.6229.

X-ray crystal structure of $[Co^{II}(PNNP)(MeCN)][BF_4]_2$

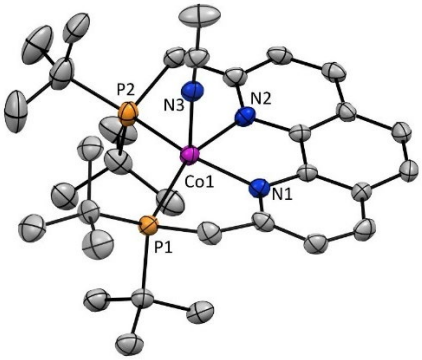

Figure 4.3. X-ray crystal structure of $[Co^{II}(PNNP)(MeCN)][BF_4]_2$. Hydrogen atoms and BF_4^- counter anion were removed for clarity. Thermal ellipsoids shown with probability of 50%.

Table 4.9. Selected bond lengths (Å) and angles (deg) for $[Co^{II}(PNNP)(MeCN)][BF_4]_2$ complex.

atom	atom	bond lengths (Å)	atom	Atom	atom	bond angles/deg
Co1	N1	1.967(4)	N1	Co1	N3	90.73(16)
Co1	N2	1.964(4)	N1	Co1	P1	80.99(12)
Co1	N3	2.043(4)	N1	Co1	P2	159.81(12)
Co1	P1	2.3724(14)	N2	Co1	N1	81.30(16)
Co1	P2	2.3208(15)	N2	Co1	N3	91.91(17)
			N2	Co1	P1	159.89(12)
			N2	Co1	P2	80.66(12)
			N3	Co1	P1	97.75(12)
			N3	Co1	P2	98.85(12)
			P2	Co1	P1	114.91(5)

4.3.5 Synthesis and characterization of $[Co^{I}(PNNP)][PF_6]$

A reaction of the $[Co^{II}(PNNP)Cl_2]$ with 1.6 equiv $NaBH_4$ and NH_4PF_6 in MeOH under N_2 generated the cobalt(I) complex with no formation of the desired hydride complex. The resulting $[Co^{I}(PNNP)][PF_6]$ was recrystallized in THF/pentane to obtain single crystals as deep green needles. A single crystal was suitable for X-ray crystallographic analysis, and the crystal structure of this complex was shown in **Figure 4.4.** with selected bond lengths and bond angles listed in **Table 4.10**. The sum of the angles around Co is 364.49° indicating that the coordination geometry is nearly planar. It was found that the $[Co^{I}(PNNP)][PF_6]$ is not stable in $CDCl_3$ showing

a colour change from deep green to a purple solution upon dissolving a deep green solid in this solvent for NMR sample preparation. Moreover, the reaction of this complex under H_2 under the similar reaction conditions did not generate a hydride complex.

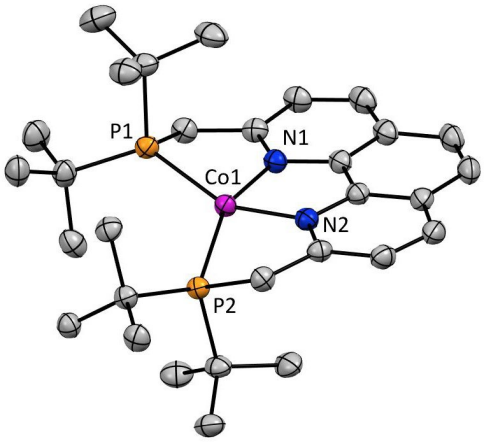

Figure 4.4. X-ray crystal structure of [Co^{I}(PNNP)][PF_6] complex. Hydrogen atoms and PF_6^- counter anion were removed for clarity. Thermal ellipsoids shown with probability of 50%.

Table 4.10. Selected bond lengths (Å) and angles (deg) for [Co^{I}(PNNP)][PF_6] complex (RNP 1809).

atom	atom	bond lengths (Å)	atom	atom	atom	bond angles/deg
Co1	N1	1.9091(17)	N1	Co1	P1	81.24(6)
Co1	N2	1.9013(18)	N1	Co1	P2	156.30(6)
Co1	P1	2.2518(6)	N2	Co1	N1	82.82(8)
C9	C10	1.490(3)	N2	Co1	P1	155.46(6)
Co1	P2	2.2674(6)	N2	Co1	P2	81.70(6)
			P1	Co1	P2	118.73(2)

4.3.6 Synthesis and characterization of [Co^{I}(dPNNP)]

A reaction of [Co^{II}(PNNP)Cl$_2$] with 1.0 eq of LiMe led to a formation of the [Co^{I}(PNNP)(Me)] as a deep black solid. The NMR studies of a solution of the [Co^{I}(PNNP)(Me)] showed a selective conversion into the dearomatized [Co^{I}(dPNNP)] complex when the solution was left at room temperature. The formation of the [Co^{I}(dPNNP)] was proposed via a loss of CH_4 through metal-ligand cooperation of the Co(I) methyl intermediate (**Scheme 4.8**).

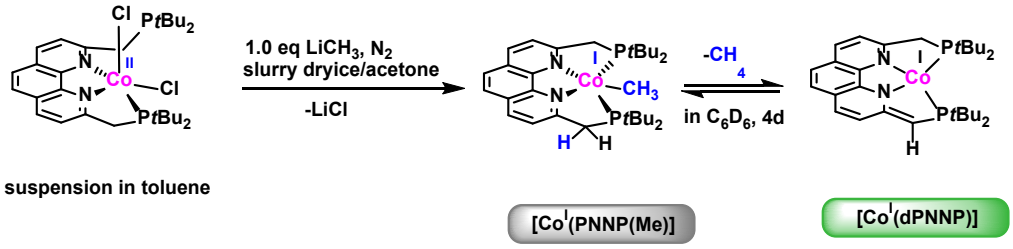

Scheme 4.8. The formation of dearomatized [Co^{I}(dPNNP)] via a loss of CH_4 from the [Co^{I}(PNNP)(CH$_3$)] intermediate.

4.3.6.1 The NMR studies of a conversion of [Co^{I}(PNNP)(CH$_3$)] to [Co^{I}(dPNNP)]

The ^{1}H and ^{31}P{^{1}H} NMR spectra of a solution of [Co^{I}(PNNP)(CH$_3$)] under Ar were recorded after leaving it at room temperature. for 30 min (**Figure 4.5** a). The two chemically equivalent phosphorus atoms in the [Co^{I}(PNNP)(CH$_3$)] corresponded to the phosphorus signal at 64.01 ppm as labelled by black dot in the ^{31}P{^{1}H} spectrum which is consistent with the signals (black dots) in the ^{1}H NMR spectrum. The assignments of the protons and phosphorus atoms as labelled in the structure (**Figure 4.5**, inset) were supported by 2D ^{1}H-^{1}H COSY and the ^{1}H-^{31}P HMBC (**Figure A 4.3** and **Figure A 4.4**), respectively. The NMR data are listed in the **Table 4.11**.

The red labels in the ^{1}H and ^{31}P{^{1}H} in **Figure 4.5** (a) suggested a formation of the lithiated compound of the free PNNP ligand. These signals corresponded to the NMR solution of the lithiated product formed by a reaction of PNNP ligand with 1.0 equiv. LiMe which will be discussed in **section 4.3.7.2**. Moreover, the conversion of [Co^{I}(PNNP)(CH$_3$)] to the corresponding dearomatized complex [Co^{I}(dPNNP)] was further monitored by NMR measurements of the solution of [Co^{I}(PNNP)(CH$_3$)] when it was left at room temperature. for 2 days and 4 days. The NMR studies (**Figure 4.5**, b and c) showed that the [Co^{I}(PNNP)(CH$_3$)] gradually converted to [Co^{I}(dPNNP)] and remained in the solution upon leaving it for 4 days. The ^{31}P{^{1}H} NMR spectrum of the solution left for 2 days showed two new phosphorus peaks (green dots) at 48.65 ppm and 66.84 ppm which corresponded to the two distinct phosphorus atoms in [Co^{I}(dPNNP)] and are in agreement with the proton signals (green dots) in the ^{1}H NMR spectrum **Figure 4.5** c.

Moreover, the conversion of the [Co^{I}(PNNP)(CH$_3$)] to [Co^{I}(dPNNP)] in the solution could be observed by a colour change from an initial deep black of the methyl intermediate to deep green in toluene. The sharp NMR signals and normal chemical shifts indicate that both of these complexes adopt low spin, d^8 electronic states. The solid state X-ray structure (**Figure 4.11**) confirmed the diamagnetic nature of the Co(I) complex in a solution by the identity of low-spin d^8 distorted square planar complex with spin state S= 0.

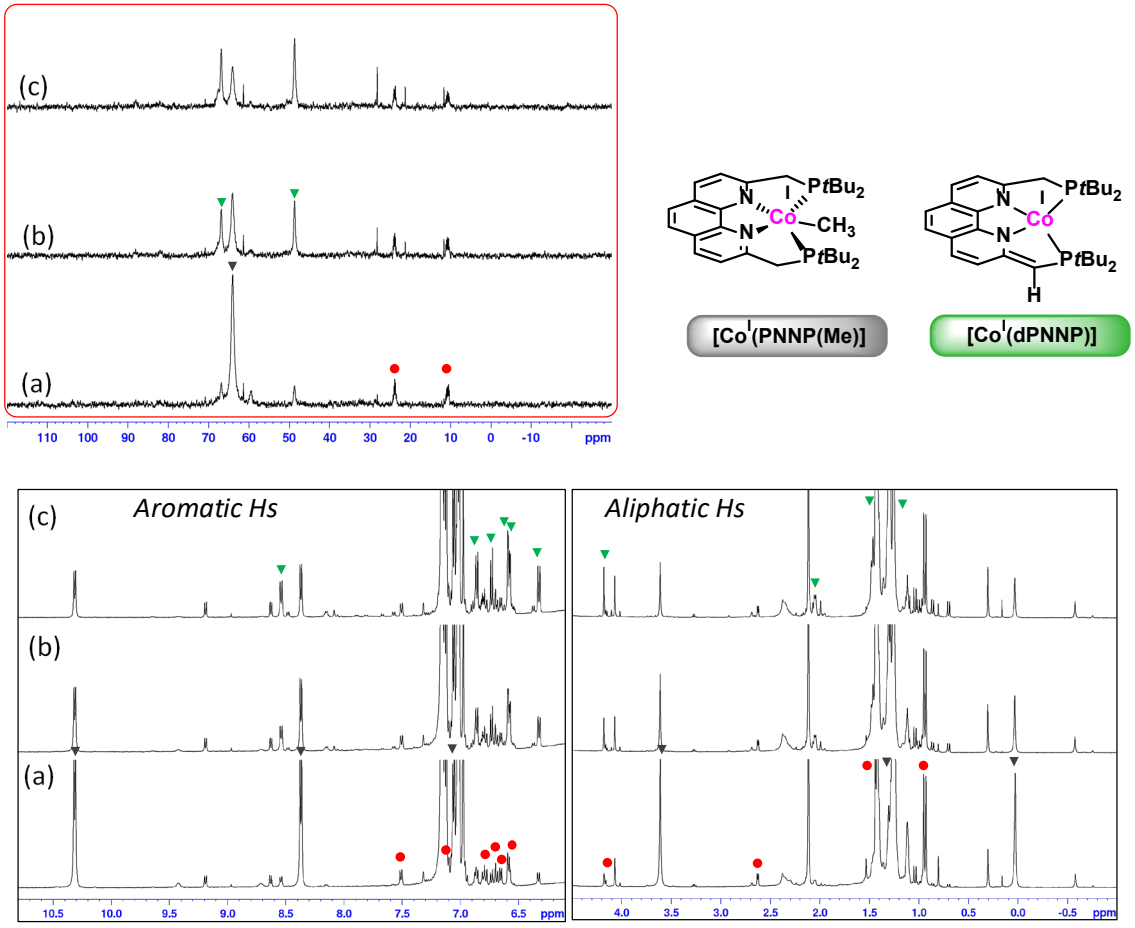

Figure 4.5. $^{31}P\{^{1}H\}$ NMR spectrum (red, frame) and ^{1}H NMR spectrum (black frame) of a solution of the [Co(PNNP)(Me)] in C_6D_6 left under Ar for (a) 30 min, (b) 2 days and (c) 4 days.

According to the NMR studies, the methyl intermediate [Co^{I}(PNNP)(CH$_3$)] was stable in the solution for at least for 30 min which then selectively formed the dearomatized [Co^{I}(dPNNP)] complex as proposed in **Scheme 4.8** via elimination of CH_4 by MLC reactivity. Furthermore, the assignments of protons and phosphorus atoms in the structure of [Co^{I}(dPNNP)] were confirmed by multi-nuclear NMR and 2D NMR characterization of the independently isolated [Co^{I}(dPNNP)] by ^{1}H, $^{1}H\{^{31}P\}$, $^{13}C\{^{1}H\}$, ^{13}C-DEPT, $^{31}P\{^{1}H\}$, ^{1}H-^{1}H COSY, ^{1}H-$^{31}P\{^{1}H\}$ HMBC and ^{1}H-^{13}C-DEPT correlation and LIFDI mass spectrometry (**Figure A 4.5**). Furthermore, the structure of [Co^{I}(dPNNP)] complex was confirmed by the X-ray crystal structure as shown in **Figure 4.11**.

Structural characterization of the independently synthesized [Co^{I}(dPNNP)] by NMR spectroscopy

The [Co^{I}(dPNNP)] was synthesized following the method as mentioned in **section 4.3.6** by a reaction of the Co^{II}(PNNP)Cl_2 with LiMe in toluene at -77 ^{0}C.

The NMR data as well as the structural assignments of this complex are listed in **Table 4.12.** The $^{31}P\{^{1}H\}$ NMR spectrum (**Figure 4.6**, red frame) exhibited two singlets corresponding to the two chemically inequivalent phosphorus atoms in the dearomatized [Co(dPNNP)]. In the ^{1}H NMR spectrum (**Figure 4.6**, black frame), the aromatic protons showed a doublet signal (labelled as Phen-*H*) which corresponded to the six different protons (H_3, H_4, H_5, H_6, H_7 and H_8) of the phenanthroline ligand. In the aliphatic region, the singlet peak at 4.17 ppm with integration ratio of 1 relative to that of a Phen-*H* proton in the Co(dPNNP)] is assigned to the C*H*P*t*Bu_2. This singlet is in agreement with the methine proton of the dearomatized Ru(II) complex at δ 4.35.[318] The CH_3 protons (labelled as $PC(CH_3)_3$) displayed two doublet signals at δ 1.43 and 1.31 with ^{2}J(H,P) = 9.71 Hz and 9.61 Hz, respectively. Moreover, the doublet signal for CH_2P*t*Bu_2 at δ 2.05 ppm also coupled to the nearby phosphorus with ^{2}J(H,P) = 5.89 Hz. These three doublet peaks due to coupling with phosphorus became singlets in the $^{1}H\{^{31}P\}$ NMR spectrum (**Figure 4.6** black in set, b).

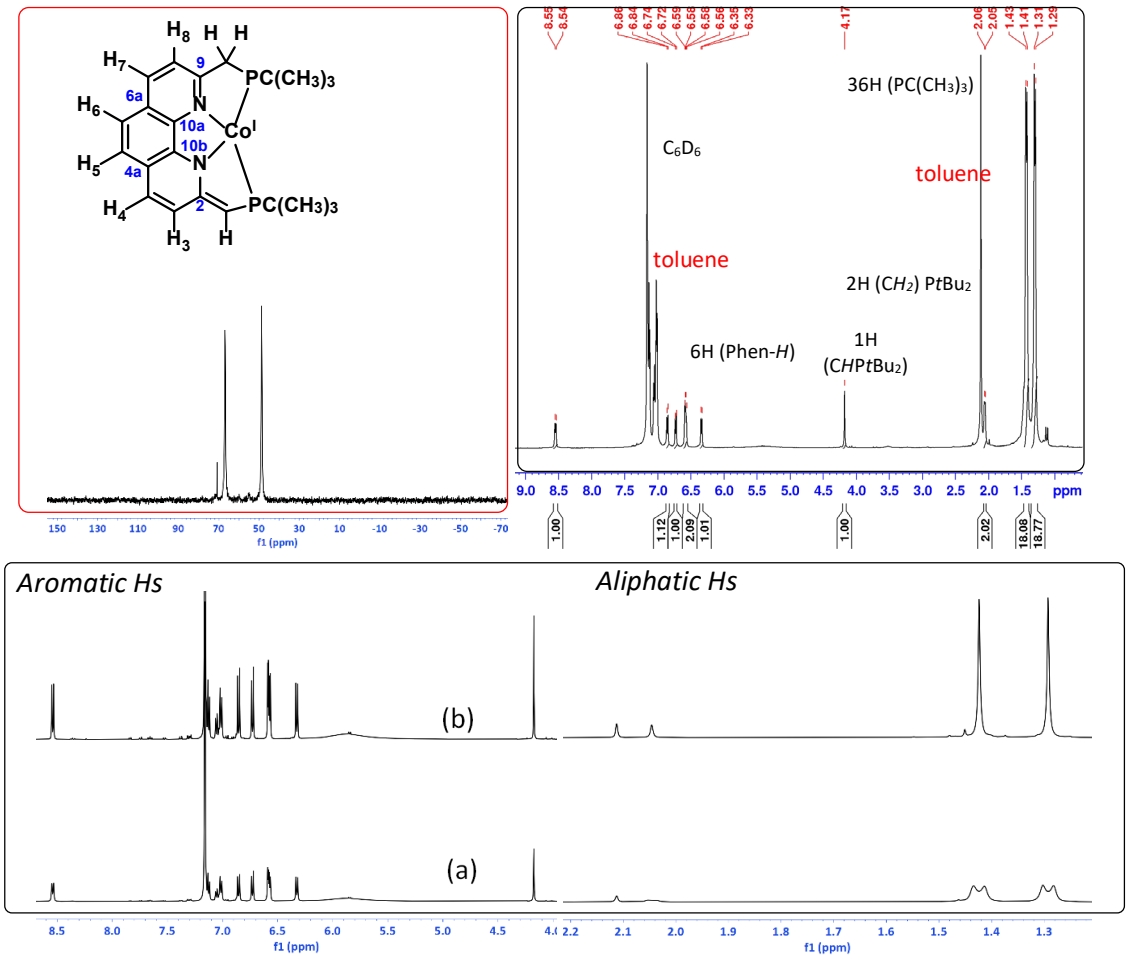

Figure 4.6. $^{31}P\{^{1}H\}$ NMR spectrum (red inset), ^{1}H NMR spectrum (black in set, a) compared to $^{1}H\{^{31}P\}$ NMR spectrum (black inset, b) of the dearomatized complex, [Co^{I}(dPNNP)] in C_6D_6.

The 2D ^{1}H-^{1}H COSY NMR spectrum (**Figure 4.7**, a) confirmed that there were proton-proton correlation peaks of the Phen-Hs but the two geminal protons in the C*H*$_2$P*t*Bu$_2$ appeared as a doublet at δ 2.05 ppm ($^{2}J_{H,P}$ = 5.89). In contrast to this, the C*H*$_2$P*t*Bu$_2$ in the Ru(II) analogue with a hydride ligand displayed two distinct proton signals as a doublet of doublet peak at δ 2.82 and 3.12 due to coupling to one proton with the same $^{2}J_{H,H}$ = 16.9 Hz and one phosphorus nucleus with respective $^{2}J_{H,P}$ = 7.8 Hz and 8.0 Hz in the ^{1}H NMR spectrum. [318] Therefore, the appearance of one peak for the two geminal protons (C*H*$_2$P*t*Bu$_2$) and also the two proton signals of CH_3 in $PC(CH_3)_3$ groups suggested that the structure of [Co^{I}(dPNNP)] with no axial ligand has higher symmetry than that of the Ru analogue containing a hydride ligand in an axial position. This number of proton signals in the ^{1}H NMR spectrum of [Co^{I}(dPNNP)] corresponded to the C_s symmetry of the X-ray crystal structure which revealed a distorted square planar geometry (see below, **Figure 4.11**).

The ^{1}H-^{31}P HMBC spectrum (**Figure 4.7**, b) showed cross peaks between the CH_3 protons in $PC(CH_3)_3$ groups and the two distinct P signals in the [Co^{I}(dPNNP)].

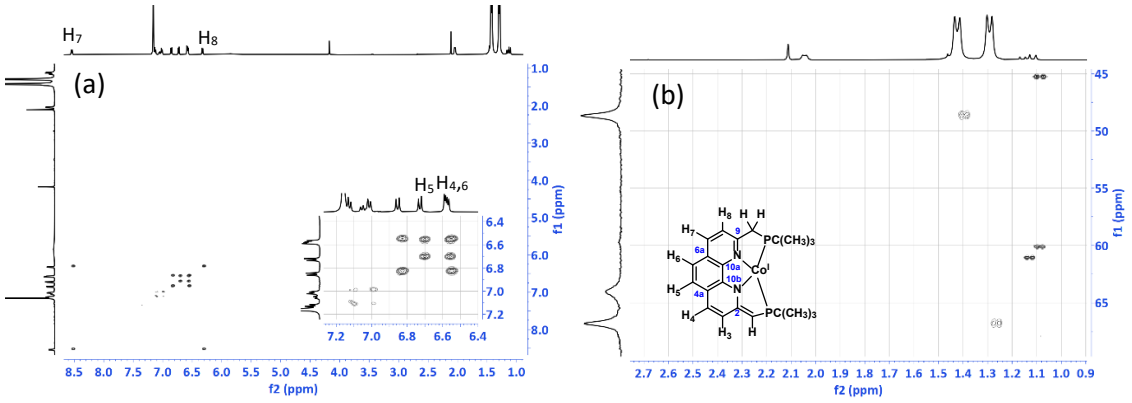

Figure 4.7. ^{1}H-^{1}H COSY NMR spectrum (a) and ^{1}H-$^{31}P\{^{1}H\}$ HMBC spectrum (b) of the dearomatized complex, [Co^{I}(dPNNP)] in C_6D_6, inset showed the expanded region of the Phen-*H*s correlations.

The assignment of carbon signals as labelled in the $^{13}C\{^{1}H\}$ NMR spectrum (**Figure 4.8**) for the structure of [Co(dPNNP)] was supported by the ^{13}C DEPT and 2D ^{1}H-^{13}C DEPT HSQC experiments. The quaternary carbons of this complex are labelled in blue in the structure which corresponded to the signals as labelled by Phen-C, C_2 (169.34 ppm) and C_{4a} (118.92 ppm) in the $^{13}C\{^{1}H\}$ NMR spectrum (**Figure 4.8**) in the aromatic region and the ^{13}C DEPT spectrum (**Figure 4.9**, purple inset, b) in aromatic region. The assigned C2a and C4a signals are consistent with the $^{13}C\{^{1}H\}$ NMR data reported for the Ru(II) analogue with a hydride ligand. [318] Moreover, the $^{13}C\{^{1}H\}$ NMR data allowed the identification of the proton attached to the carbons (Phen-(C)H) in the [Co(dPNNP)] by the ^{1}H-^{13}C DEPT HSQC experiment and proton correlations in the 2D ^{1}H-^{1}H COSY experiment. In the $^{13}C\{^{1}H\}$ NMR spectrum (**Figure 4.8**, inset) of [Co(dPNNP)], the Phen-(C_3)H and Phen-(C_8)H at δ 120.62 and 124.96 displayed doublet signals with ^{3}J(C,P) = 12.17 and 6.32 Hz, respectively. These data corresponded to the doublet of doublet carbon signals for Phen-(C_3)H at δ 121.21 (^{3}J(C,P) = 14.1 Hz and ^{5}J(C,P) = 1.7 Hz and Phen-(C_8)H at δ 119.80 with ^{3}J(C,P) = 7.9 Hz and ^{5}J(C,P) = 2.7 Hz in the Ru analogue. The ^{1}H-^{13}C DEPT HSQC spectrum (**Figure 4.10**) showed a cross peak of Phen-(C_3)H to the proton signal at δ 6.86 and a correlation of Phen-(C_8)H to the H peak at δ 6.35. This data was supported the assignment of two proton signals in the six of Phen-H protons. The other four carbon and attached proton nuclei for Phen-(C)H could then be further identified by the ^{1}H-^{13}C DEPT HSQC spectrum supported by the 2D ^{1}H-^{1}H COSY spectrum (**Figure 4.7**). From these correlations, the protons attached to carbon in Phen-(C)H were all assigned in the structure and labelled in the ^{1}H-^{13}C DEPT HSQC spectrum and the 2D ^{1}H-^{1}H COSY spectrum.

For the assignment of aliphatic carbons in the structure, the $^{13}C\{^{1}H\}$ NMR spectrum in the aliphatic region showed five different signals as labelled in the spectrum which were consistent

with the data in literature. [318]. The doublet peak of the methine (labelled as CHP*t*Bu$_2$) at δ 78.36 with ^{1}J(C,P) = 45.98 Hz is consistent with the same carbon in the Ru(II) analogue which appeared as dd at δ 82.2 (^{1}J(C,P) = 45.2 Hz and ^{3}J(C,P) = 3.2 Hz. The ^{13}C DEPT spectrum (**Figure 4.9**, purple inset, b) confirmed the CH_2 carbon for CH_2P*t*Bu$_2$ by showing the peak in negative phase. Moreover, the quaternary carbons (P(*C*(CH$_3$)$_3$)$_2$ at δ 35.67 did not show in the ^{13}C DEPT spectrum in the aliphatic region (**Figure 4.9**, purple inset, b).

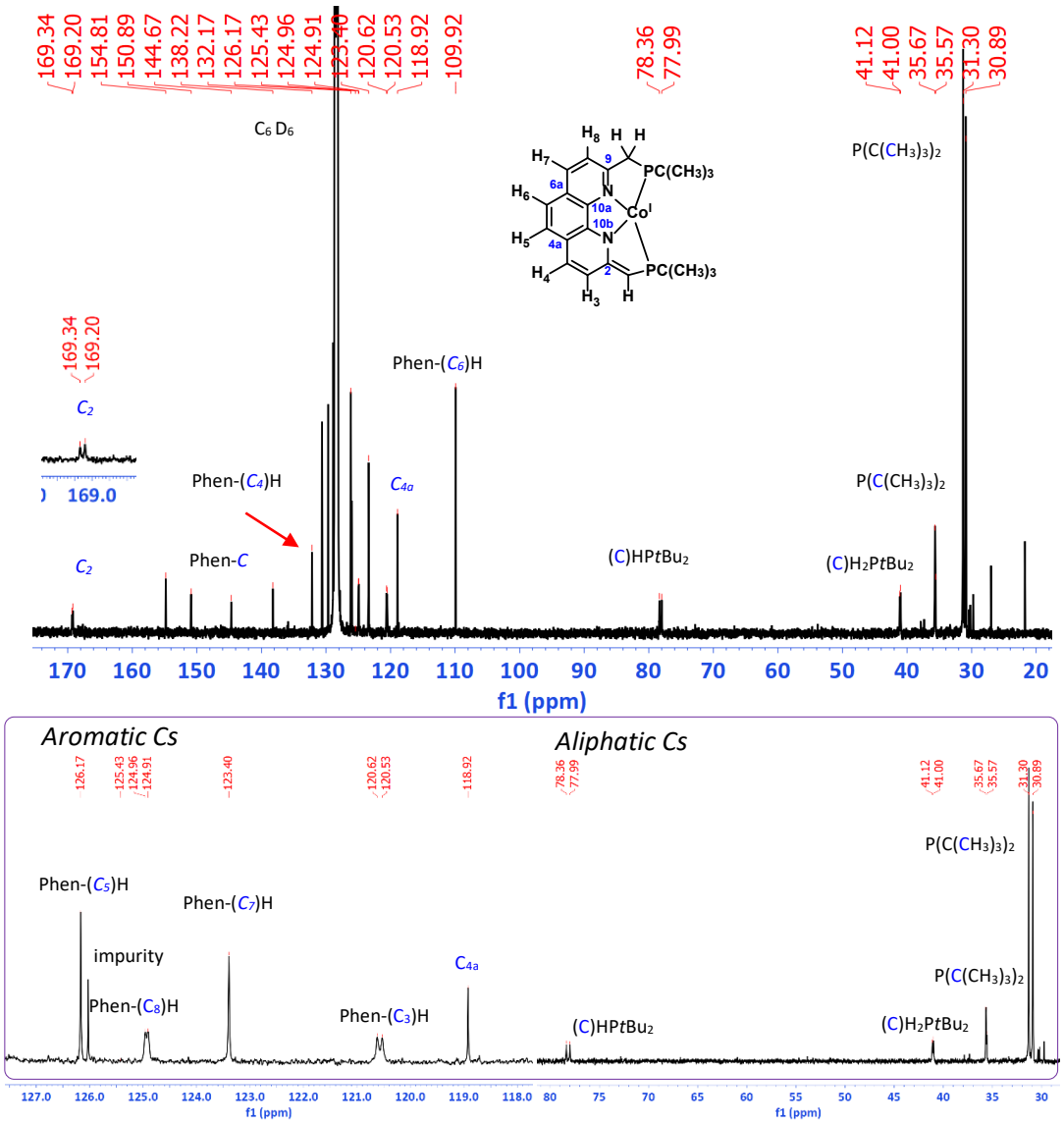

Figure 4.8. $^{13}C\{^{1}H\}$ NMR spectrum of the dearomatized complex, [Co(dPNNP)] in C_6D_6, inset showed the expansion of aromatic and aliphatic carbon signals.

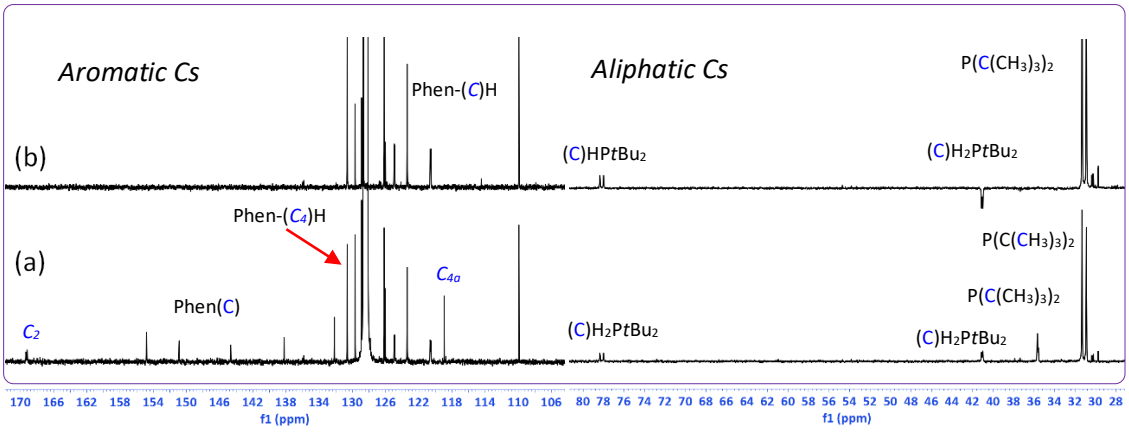

Figure 4.9. $^{13}C\{^{1}H\}$ NMR spectrum of the dearomatized complex, [Co(dPNNP)] in C_6D_6 (a) compared to the ^{13}C DEPT spectrum of this complex (b).

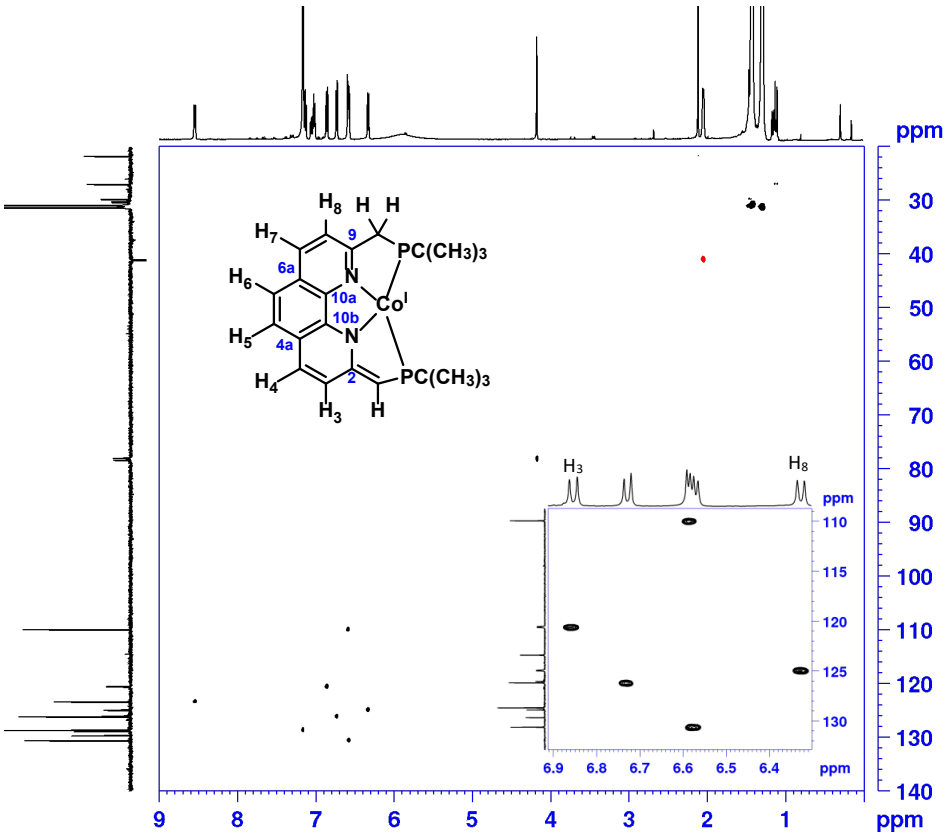

Figure 4.10. ^{1}H-^{13}C DEPT spectrum of the dearomatized complex, [Co(dPNNP)] in C_6D_6

Table 4.11. Assignment of hydrogen and phosphorus-atoms of [Co^{I}(PNNP)(Me)].

Assigned atom	δ (ppm)	J (Hz) and (multiplicity)	Integration
Phen-H_2	10.31	$^{3}J_{H,H}$ = 7.36, d	2H
Phen-H_1	8.37	$^{3}J_{H,H}$ = 7.32, d	2H
Phen-H_3	overlap	-	-
CH_2PtBu_2	3.61	br	4H
$PC(CH_3)_3$	1.25	br	36H
Co-CH_3	0.03	s	3H
P	64.01	s	-

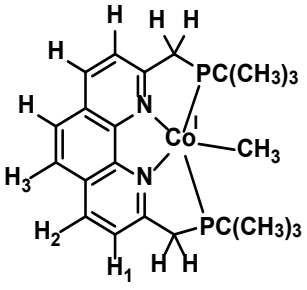

Table 4.12. Assignment of hydrogen, carbon and phosphorus-atoms of dearomatized [Co^{I}(dPNNP)] complex.

Assigned Atom	Labels	δ (ppm)	J (Hz) and (multiplicity)	Integration
Phen-(C)H$_7$		8.55 (123.40)	$^{3}J_{H,H}$ = 7.94, d, (s)	1H
Phen-(C)H$_3$		6.85 (120.62)	$^{3}J_{H,H}$ = 8.92, d ($J_{C,P}$ = 12.17, d)	1H
Phen-(C)H$_5$		6.73 (126.17)	$^{3}J_{H,H}$ = 7.93, d, (s)	1H
Phen-(C)H$_6$		6.58 (109.92)	$^{3}J_{H,H}$ = 7.59, d, (s)	1H
Phen-(C)H$_4$		6.57 (132.17)	$^{3}J_{H,H}$ = 8.88, d (s)	1H
Phen-(C)H$_8$		6.34 (124.96)	$^{2}J_{H,H}$ = 17.8, d ($J_{C,P}$ 6.32, d)	1H
(C)HP*t*Bu$_2$		4.17 (78.36)	s, ($^{1}J_{C,P}$ 45.98, d)	1H
(C)H$_2$P*t*Bu$_2$		2.06 (41.12)	$^{2}J_{H,P}$ = 5.89, d ($^{1}J_{C,P}$ 14.54, d)	2H
PC(CH$_3$)$_3$		1.42 (30.89)	$^{3}J_{H,P}$ = 9.71, d (br)	18H
PC(CH$_3$)$_3$		1.30 (31.30)	$^{3}J_{H,P}$ = 9.61, d (br)	18H
PC(CH$_3$)$_3$		35.57	br	-
PC(CH$_3$)$_3$		35.67	br	-
C$_2$	**Phen-Cq**	169.34	$J_{C,P}$ 18.50, d	-
C$_{4a}$		118.92	s	-
C$_{6a}$		154.84	s	-
C$_9$		150.89	s	-
C$_{10a}$		144.67	s	-
C$_{10b}$		138.22	s	-
P		66.83	s	1P
P		48.67	s	1P

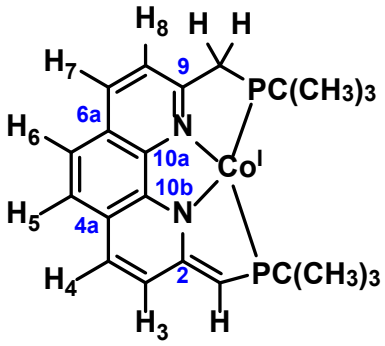

4.3.6.2 LIFDI mass spectrometry of [Co^{I}(dPNNP)]

The LIFDI-MS of the complex (**Figure A 4.5**) showed molecular peaks at *m/z* = 554.23845 which corresponded to the neutral [Co^{I}(dPNNP)]. The isotopic distribution patterns calculated for [$C_{30}H_{45}N_2P_2Co$] showed the parent ion at m/z = 554.23742

4.3.6.3 X-ray crystal structure of [Co^{I}(dPNNP)]

The crystal structure of this complex revealed a distorted square planar geometry, where the Co(I) metal centre coordinates to the tetradentate PNNP ligand. The sum of the angles at Co is 360.24° indicating almost perfect planarity, although one of the phosphine ligands is slightly above the ideal plane. The phenanthroline and C1 occupy the same plane but the saturated C12 lies out of the plane. The bond length C1-C2 of 1.363(3) is consistent with a double bond while C11-C12 and C2-C3 are considerably longer at 1.478(2) and 1.453 (3) Å consistent with a single bond. The two P-C distances to the phenanthroline differ markedly (P1-C12 1.858(2) and P2-C1 1.780(2) Å).

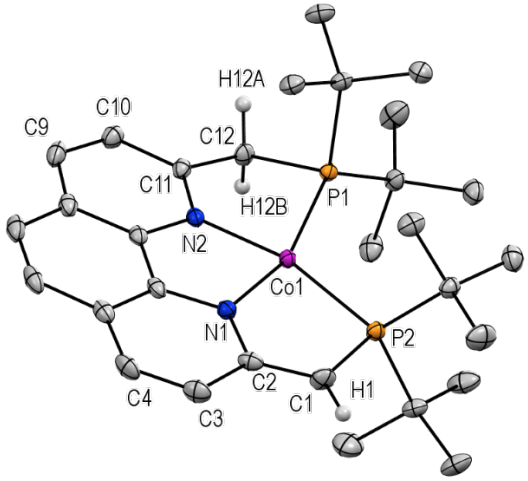

Figure 4.11. X-ray crystal structure of the cation of [Co^{I}(dPNNP)]. All hydrogen atoms apart from H1, H12A and H12B are omitted for clarify. Thermal ellipsoids are shown at the 50% probability level.

Table 4.13. Selected bond distances (Å) and bond angles (deg) in the [Co^{I}(dPNNP)] complex.

atom	atom	bond lengths (Å)	atom	atom	atom	bond angles (deg)
Co1	P1	2.2400(5)	P1	Co1	P2	115.172(19)
Co1	P2	2.2989(5)	N1	Co1	P1	160.93(5)
Co1	N1	1.9233(15)	N1	Co1	P2	81.91(5)
Co1	N2	1.9204(14)	N2	Co1	P1	81.97(5)
C2	C1	1.363(3)	N2	Co1	P2	162.86(5)
C11	C12	1.478(2)	N2	Co1	N1	81.19(6)
C2	C3	1.453(3)	C11	C12	P1	107.64(12)
C4	C3	1.351(3)	C2	C1	P2	115.28(14)
C11	C10	1.404(2)				
C10	C9	1.369(3)				
P2	C1	1.780(2)				
P1	C12	1.858(2)				

4.3.7 Synthesis and characterization of [Co^{I}(mPNNP)]

Following the successful selective synthesis of dearomatized [Co^{I}(dPNNP)] (**Scheme 4.8**), its reaction was then investigated with 4 bar of H_2. A solution of [Co^{I}(PNNP)(CH_3)] in C_6D_6 was left in a J Young NMR tube under Ar for 2 days to attain the dearomatized [Co^{I}(dPNNP)] (**Scheme 4.9,** green label). The solution was evacuated prior to adding 4 bar of H_2, and progress of reaction of the [Co^{I}(dPNNP)] under H_2 was then monitored over 4 days. The ^{1}H and $^{31}P\{^{1}H\}$ NMR studies suggested selective conversion of the dearomatized [Co^{I}(dPNNP)] to the hydrogenated product [Co^{I}(mPNNP)] via the dihydrogen complex (in brackets) as indicated by dashed arrows. The hydrogenated product with the orange label was initially formed in the reaction mixture which finally converted to the hydrogenated product for [Co^{I}(mPNNP)] as shown the structure with brown label. However, the dihydrogen complex was not observed in the ^{1}H NMR spectrum of the reaction mixture within 30 min of reaction time.

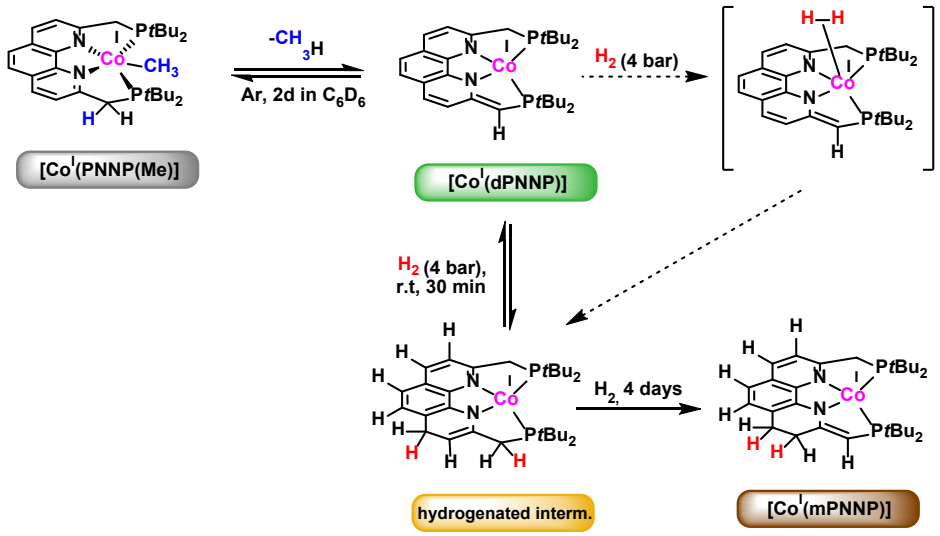

Scheme 4.9. Possible routes (solid black arrows) of [Co^{I}(dPNNP)] in C_6D_6 under 4 bar of H_2 for the formation of the hydrogenated intermediate (orange label) and [Co(mPNNP)] (brown label), dash black arrows indicating the formation of the hydrogenated intermediate (orange label) product via the η^2-H_2 complex.

4.3.7.1 The NMR studies of conversion of [Co^{I}(dPNNP)] under H_2 to [Co^{I}(mPNNP)]

The $^{31}P\{^{1}H\}$ NMR spectrum (**Figure 4.12** a, red frame) and the ^{1}H NMR spectrum (**Figure 4.12** a, black frame) of the solution of [Co^{I}(PNNP)(CH_3)], which was left in C_6D_6 under Ar for 2 days, showed the mixture of [Co^{I}(dPNNP)] and [Co^{I}(PNNP)(CH_3)] as labelled by black and green dots, respectively. After leaving it under 4 bar of H_2 for 1 hour, the $^{31}P\{^{1}H\}$ NMR spectrum (**Figure 4.12** b, red frame) showed the appearance of two new phosphorus peaks (orange dots) which corresponded to the proton signals in the ^{1}H NMR spectrum (**Figure 4.12** b, black frame) suggesting that the hydrogenated intermediate (orange label) was initially formed in the

reaction. After leaving the solution under H_2 overnight, the hydrogenated intermediate was converted to the hydrogenated [Co^{I}(mPNNP)] product as labelled with brown dots in the ^{1}H NMR and ^{31}P{^{1}H} NMR spectrum (**Figure 4.12** d). Moreover, the hydrogenated intermediate (orange label) depleted concomitantly with complete generation of the [Co^{I}(mPNNP)] upon leaving a solution under H_2 for 4 days (**Figure 4.12** f).

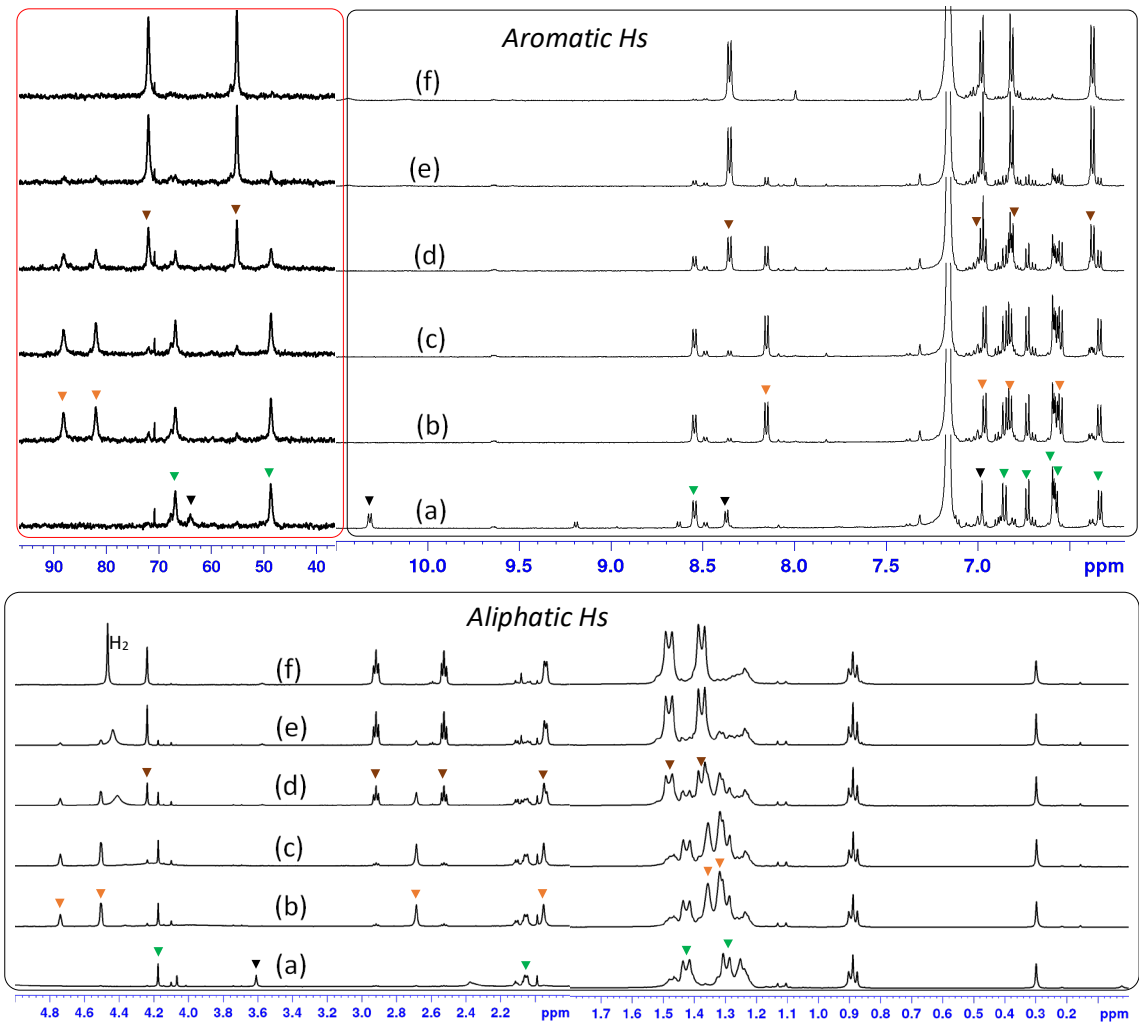

Figure 4.12. ^{31}P{^{1}H} NMR spectrum (red frame), ^{1}H NMR spectrum (black frame) of a solution of the [Co(PNNP)(Me)] in C_6D_6 left under Ar for 2 days (a), this solution under 4 bar of H_2 for 30 min (b), 1 h (c), overnight (d), 2 days (e) and 4 days (f). The peak labels correspond to the signals of each complex in **Scheme 4.9**.

The structural characterization of [Co^{I}(mPNNP)] in the solution left for 4 days under H_2 was further supported by multinuclear NMR techniques including ^{1}H, ^{1}H{^{31}P}, ^{31}P{^{1}H}, ^{13}C{^{1}H}, ^{13}C-DEPT and 2D NMR correlation techniques such as ^{1}H-^{1}H COSY, ^{1}H-^{31}P{^{1}H} HMBC and ^{1}H-^{13}C-DEPT correlation spectroscopy.

Structural characterization of [Co^{I}(mPNNP)] by NMR spectroscopy

The $^{31}P\{^{1}H\}$ NMR spectrum (**Figure 4.13**) displayed two sharp phosphorus peaks at δ 71.98 and 55.12 ppm which is consistent with the modification of the phen moiety giving rise to two chemically different P atoms. The assignment of hydrogen atoms in the structure corresponds to the labelled signals in the ^{1}H NMR spectrum (**Figure 4.14**). The assignment of the aromatic Phen-*H* protons (H_5, H_6, H_7 and H_8) was supported by the 2D ^{1}H-^{1}H COSY experiments (**Figure 4.15**) showing the correlation between these aromatic signals as labelled in the structure. For the aliphatic protons in the ^{1}H NMR, the singlet signal at δ 4.24 corresponded to the methine protons (C*H*P*t*Bu$_2$), and three different protons of CH_2 groups appeared as two triplet signals (2.53 ppm and 2.92 ppm) and one doublet signal were observed. The ^{1}H-^{1}H COSY experiments supported the two triplet signals coupling to each other which showed the correlation between these two proximal CH_2 protons (Phen-C*H*$_2$). Another CH_2 group (C*H*$_2$P*t*Bu$_2$) corresponded to the doublet signal at δ 1.94 with the $^{2}J(H,P)$ = 7.21 Hz. Among these three pairs of CH_2 protons, only the doublet signal of (C*H*$_2$P*t*Bu$_2$) became the singlet peak in the $^{1}H\{^{31}P\}$ NMR spectrum **(Figure 4.16** b, inset). Moreover, it also showed that the two doublet peaks of P(C(CH$_3$)$_3$)$_2$ in the ^{1}H NMR spectrum changed to a singlet signal in the $^{1}H\{^{31}P\}$ NMR spectrum (**Figure 4.16** b). That these proton signals coupled to the nearby phosphorus atom was confirmed by the ^{1}H-$^{31}P\{^{1}H\}$ HMBC experiment. The spectrum (**Figure 4.17**) showed the cross peaks between the two different phosphorus peaks and proton signals of P(C(CH$_3$)$_3$)$_2$. This result confirmed that the doublet peak was split by the neighboring phosphorus.

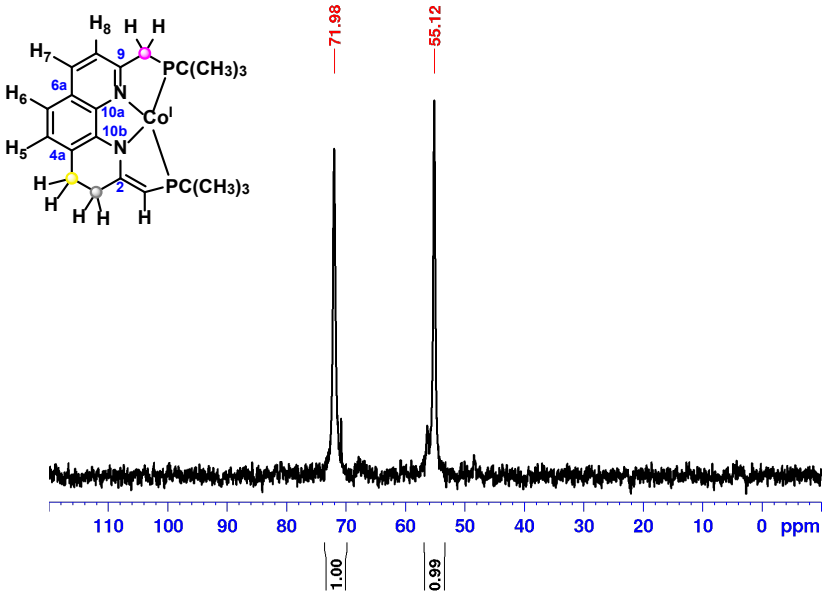

Figure 4.13. $^{31}P\{^{1}H\}$ NMR spectrum of a solution of the [Co(dPNNP)] in C_6D_6 leaving under 4 bar of H_2 for 4 days, resulting in conversion to [Co(mPNNP)].

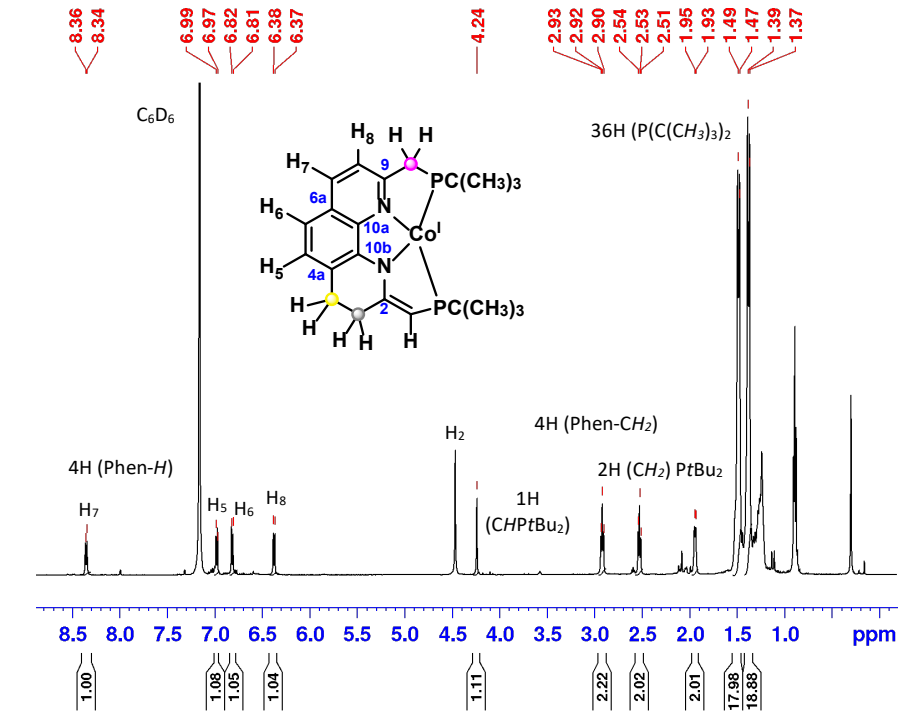

Figure 4.14. ^{1}H NMR spectrum of a solution of the [Co(dPNNP)] in C_6D_6 leaving under 4 bar of H_2 for 4 days.

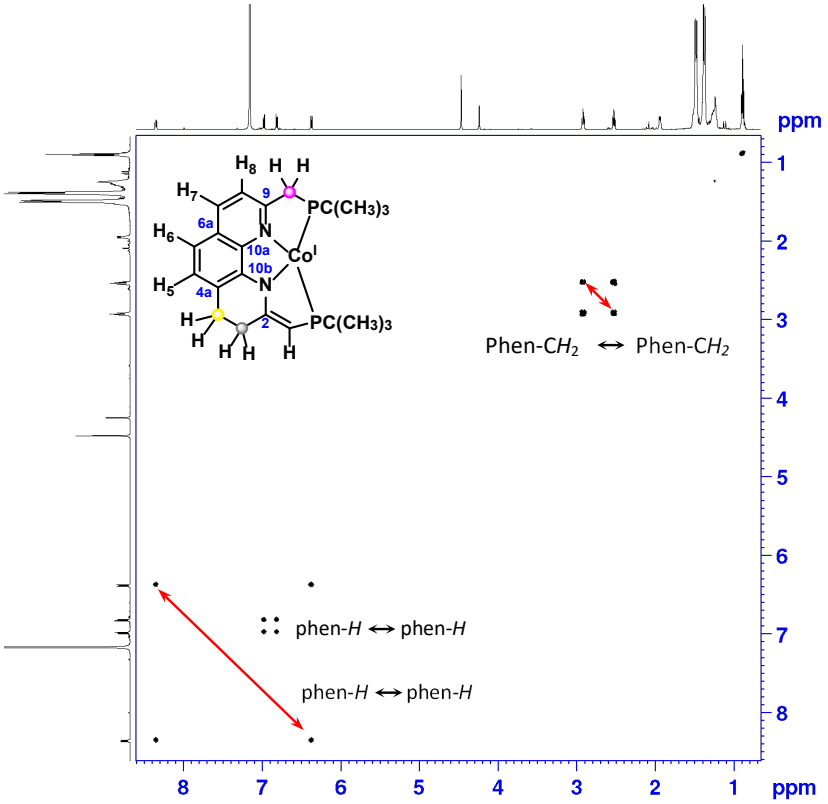

Figure 4.15. ^{1}H-^{1}H COSY NMR spectrum of a solution of the [Co(dPNNP)] in C_6D_6 leaving under 4 bar of H_2 for 4 days.

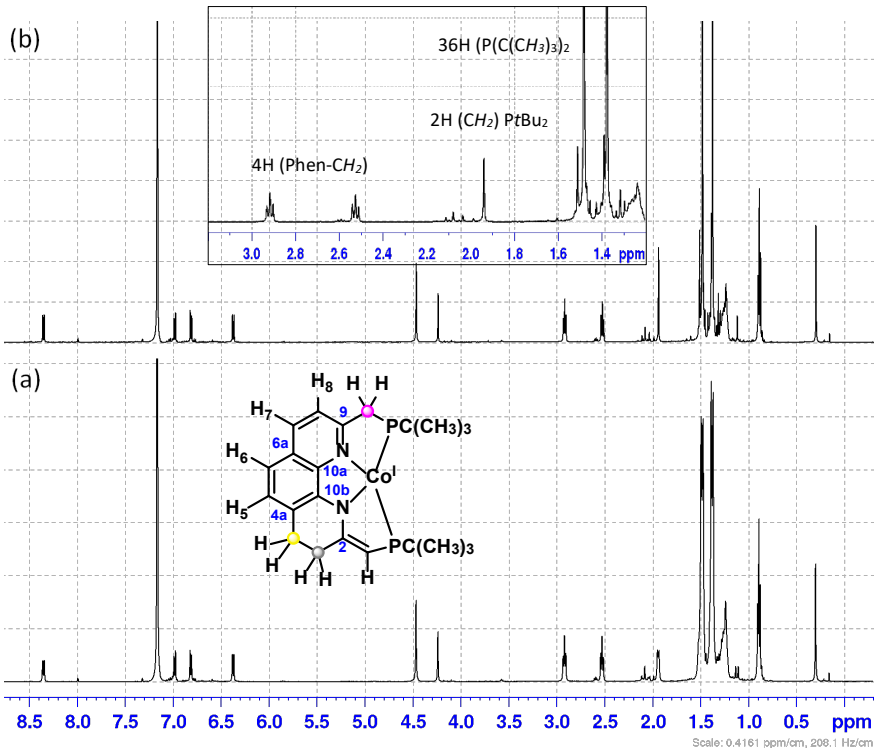

Figure 4.16. ^{1}H NMR spectrum of a solution of the [Co(dPNNP)] in C_6D_6 left under 4 bar of H_2 for (a) 4 days compared to (b) the $^{1}H\{^{31}P\}$ NMR of this solution.

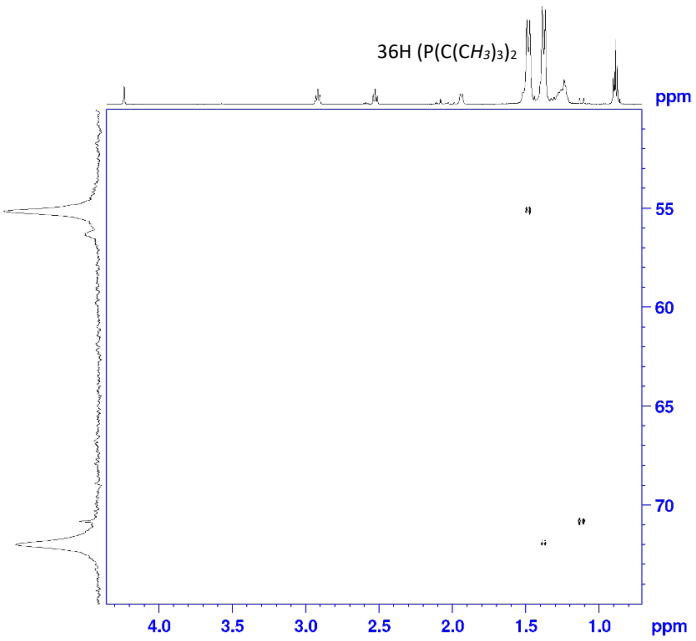

Figure 4.17. ^{1}H-$^{31}P\{^{1}H\}$ HMBC spectrum of a solution of the [Co(dPNNP)] in C_6D_6 leaving under 4 bar of H_2 for 4 days.

Furthermore, the assignment of carbon atoms in the structure of the [Co(mPNNP)] was supported by the $^{13}C\{^{1}H\}$ NMR spectrum (**Figure 4.18**, grey inset) and the ^{13}C-DEPT experiment (**Figure 4.18**, purple inset). The three distinct CH_2 groups in the ^{13}C-DEPT spectrum as labeled in

pink, grey and yellow dots in the structure corresponded to the negative phase of the carbon signal (at δ 26.29, 27.39 and 40.17 ppm) as identified by the same colour as that in the structure for [Co(mPNNP)]. Furthermore, the ^{1}H-^{13}C DEPT HSQC spectrum (**Figure 4.19**) showed cross peaks between these carbon and protons which further confirmed that each carbon for these CH_2 moieties of Phen-CH_2 in the complex is attached to two protons (**Figure 4.19 b**, inset). The doublet pattern of CH_2tBu_2 signal indicated that the carbon coupled to one phosphorus atom with the ^{1}J(C,P) = 13.51 Hz. Moreover, the quaternary carbon atoms (P(*C*)*t*Bu_2) at δ 35.59 and 35.09 ppm coupled to the nearby phosphorus with ^{1}J(C,P) = 6.25 Hz and 9.37 Hz, respectively. However, the PC(*C*H_3)$_3$ carbons showed two broad signals in the ^{13}C{^{1}H} and ^{13}C-DEPT spectra. Moreover, the ^{1}H-^{13}C-DEPT spectrum (**Figure 4.19**, a) displayed a correlation peak between singlet of methine proton (labelled as CHP*t*Bu_2) at δ 4.21 in the ^{1}H NMR spectrum and the doublet carbon signal at δ 87.25 with a large ^{1}J(C,P) = 40.40 Hz. This chemical shift and coupling constant value for the methine signal in the [Co(mPNNP)] is also consistent with the ^{1}J(C,P) value in the Ru(II) complex with the same modification of PNNP ligand which appeared at δ = 91.55 with ^{1}J(C,P) = 38.0 Hz.[318] Based on the NMR spectroscopic data of the Ru analogue reported in the literature, the assignment of aromatic carbon of the [Co(mPNNP) in the ^{13}C{^{1}H} spectrum was identified as the same order as the chemical shifts of carbon signals assigned for the Ru complex. The doublet carbon signal labelled as Phen-C_8 at δ 121.94 (^{3}J(C,P) = 6.1 Hz) corresponded to the same carbon signal in the Ru complex displaying at 118.31 with ^{3}J(C,P) = 8.0 Hz.

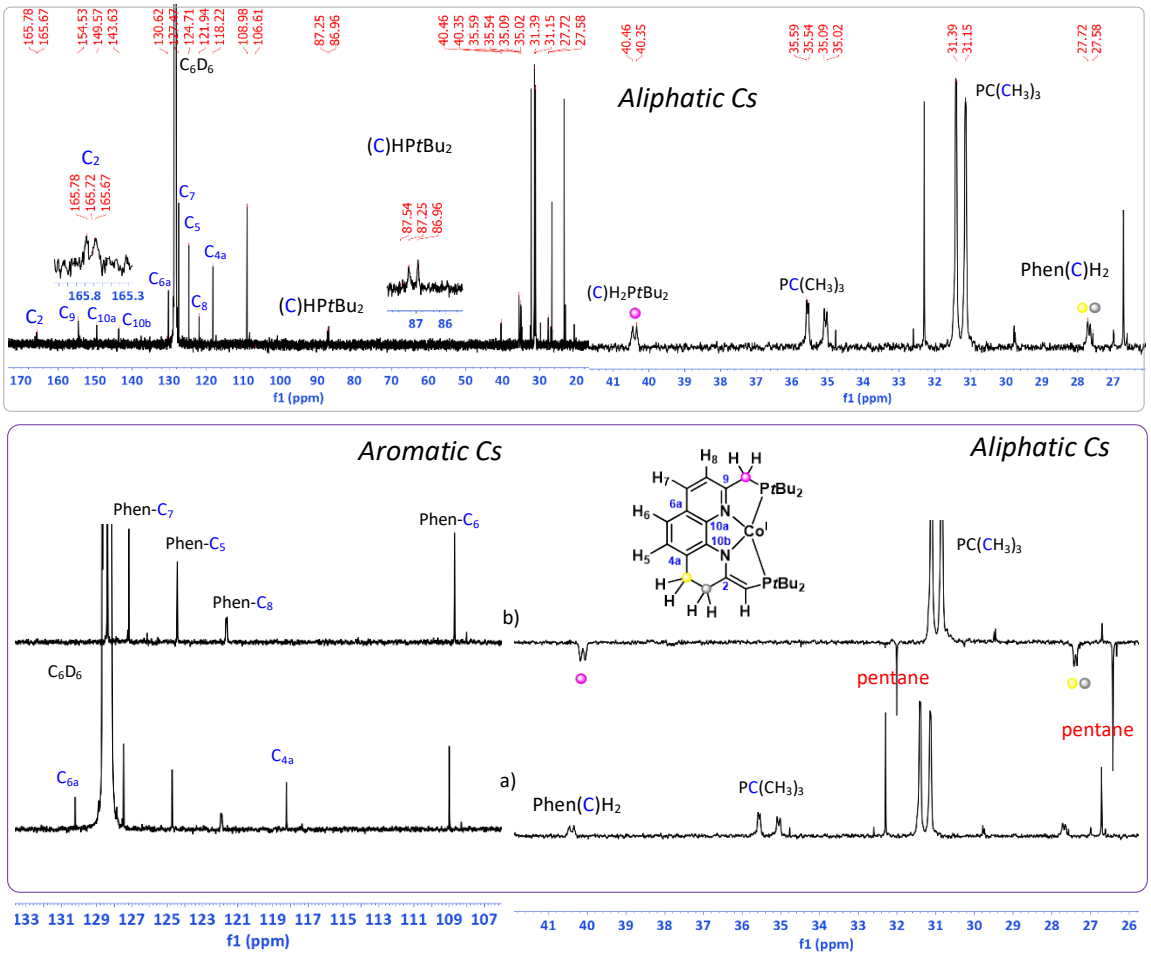

Figure 4.18. $^{13}C\{^1H\}$ NMR spectrum (grey inset) of a solution of the [Co(dPNNP)] in C_6D_6 leaving under 4 bar of H_2 for 4 days, ^{13}C-DEPT spectrum (purple inset, b) of this solution compared to the carbon signals in the $^{13}C\{^1H\}$ NMR spectrum (a).

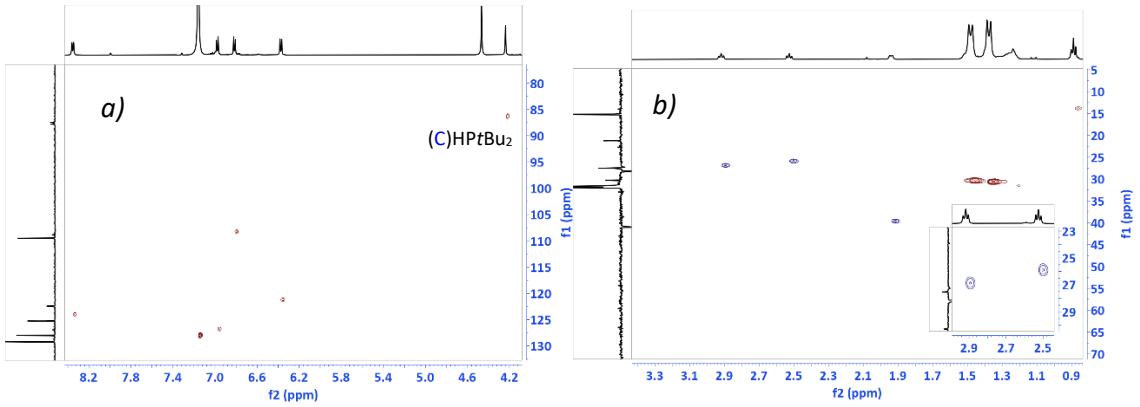

Figure 4.19. ^1H-^{13}C DEPT spectrum in aromatic region (a) and aliphatic region (b) of a solution of the [Co(dPNNP)] in C_6D_6 after leaving under 4 bar of H_2 for 4 days, inset showed the cross peaks of the Phen-CH_2 group in the complex.

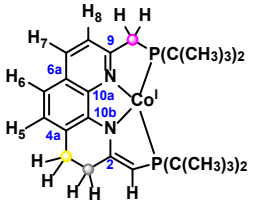

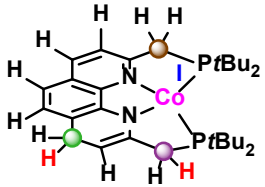

Table 4.14. Assignment of hydrogen, carbon and phosphorus-atoms of [Co(mPNNP)] and its isomers.

Assigned atom	NMR data for [Co^{I}(mPNNP)] in C_6D_6			NMR data for hydrogenated intermediate in C_6D_6			
	δ (ppm)	J (Hz) and multiplicity	Integration		δ (ppm)	J (Hz) and multiplicity	Integration
Phen-(C)H$_7$	8.35 (127.47)	$^{3}J_{H,H}$ = 8.25, d, (s)	1H	Phen-H	8.15	$^{3}J_{H,H}$ = 8.38, d	1H
Phen-(C)H$_5$	6.98 (124.71)	$^{3}J_{H,H}$ = 7.77, d (*s*)	1H	Phen-H	6.96	$^{3}J_{H,H}$ = 7.94, d	1H
Phen-(C)H$_6$	6.82 (108.98)	$^{3}J_{H,H}$ = 7.69, d, (s)	1H	Phen-H	6.82	$^{3}J_{H,H}$ = 8.02, d	1H
Phen-(C)H$_8$	6.38 (121.94)	$^{3}J_{H,H}$ = 8.20, d, ($J_{C,P}$ = 6.12, d)	1H	Phen-H	6.55	$^{3}J_{H,H}$ = 8.34, d	1H
(C)HP*t*Bu$_2$	4.24 (87.25)	s, ($^{1}J_{C,P}$ 40.40, d)	1H	***H***C(C(CH$_2$PtBu$_2$))	4.74	t (br)	1H
Phen-(C)H$_2$	2.92 (27.72)	$^{3}J_{H,H}$ = 7.15, t ($J_{C,P}$ = 8.31, d)	2H	Phen-CH$_2$ (green)	4.50	d (br)	2H
	2.53 (27.58)	$^{3}J_{H,H}$ = 7.10, t ($J_{C,P}$ d)	2H	(C)H$_2$P*t*Bu$_2$ (purple)	2.68	br	2H
(C)H$_2$P*t*Bu$_2$	1.94 (40.46)	$^{2}J_{H,P}$ = 7.21, d ($^{1}J_{C,P}$ 13.51, d)	2H	(C)H$_2$P*t*Bu$_2$ (brown)	1.97	br	2H
PC(*CH*$_3$)$_3$	1.48 (31.15)	$^{3}J_{H,P}$ = 10.23, d (br)	18H	PC(CH$_3$)$_3$	1.39	br	overlap
PC(*CH*$_3$)$_3$	1.38 (31.39)	$^{3}J_{H,P}$ = 10.23, d (br)	18H	PC(CH$_3$)$_3$	1.29	br	overlap
P*C*(CH$_3$)$_3$	35.59	$^{1}J_{C,P}$ 6.25,d	-	P	81.97	s	1P
P*C*(CH$_3$)$_3$	35.09	$^{1}J_{C,P}$ 9.37,d	-	P	89.63	s	1P
Phen-*C2*	165.72	$J_{C,P}$ 12.72, d	-	**NMR data for unidentified intermediate in C_6D_6**			
Phen-*C9*	154.53	s	-	Phen-H	8.02	$^{3}J_{H,H}$ = 8.03, d	1H
Phen-*C10a*	149.57	s	-	Phen-H	6.60	d (overlap)	2H
Phen-*C10b*	143.63	s	-	Phen-H	6.61 6.47	$^{3}J_{H,H}$ = 8.21, d $^{3}J_{H,H}$ = 7.87, d	1H
Phen-*C6a*	130.62	s	-	P	72.89	s	1P
Phen-*C4a*	118.22	s	-	P	78.34	s	1P
P	71.98	s	1P				
P	55.12	s	1P				

4.3.7.2 Reaction of free PNNP ligand with 1.0 equiv. LiMe

A reaction (**Scheme 4.10**) of the free PNNP ligand with 1.0 equiv. LiMe (1.6 M) in Et_2O under the same reaction conditions as that of the $[Co^{II}(PNNP)Cl_2]$ complex was then examined to confirm that the dearomatized (dPNNP) ligand and hydrogenated (mPNNP) ligand could be formed by the cooperative reaction with a cobalt metal centre. It was evidenced that LiMe reacted with the free PNNP ligand possibly by deprotonation of the one of the protons at $CH_2P(C(CH_3)_3)_2$ resulting in a formation of the unidentified lithiated product.

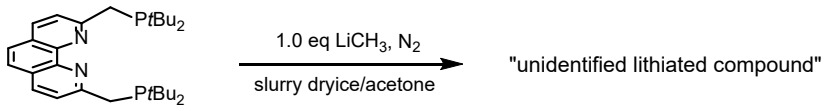

Scheme 4.10. Reaction scheme of the PNNP with 1.0 eq LiMe for a generation of unidentified lithiated compound.

In the $^{31}P\{^1H\}$ NMR spectrum (**Figure A 4.6** b, red frame), the two P atoms in the lithiated ligand coupled to the two different ^{7}Li nuclei (I = 3/2) resulting in complicated signals at δ 10.70 and 24.09 (red dots). The ^{1}H NMR spectrum (**Figure A 4.6** b, black frame) of the solution showed the 6 peaks in the aromatic region which corresponds to the dearomatized PNNP ligand. Furthermore, the hydrogenation of the lithiated analogue of dearomatized ligand was tested by leaving a solution of the lithiated compound under 4 bar of H_2 overnight. It was found that there was no hydrogenated product formed in the solution. However, conversion of this compound to unidentified species with no lithium (yellow dots) was observed as shown in the ^{1}H and $^{31}P\{^1H\}$ NMR spectrum (**Figure A 4.6** c) black and red in set, respectively.

Moreover, we also observed that the same lithiated compound was formed in a reaction of the $[Co^{II}(PNNP)(MeCN)][BF_4]_2$ complex with 1.0 eq LiMe with no generation of the [Co(dPNNP)] under the same conditions. However, a reaction of the $[Co^{II}(PNNP)Cl_2]$ with 1.0 equiv LiMe generated the dearomatized [Co(dPNNP)] as the main product with a small amount of the lithiated ligand (**Figure 4.5**). This evidence suggested that the coordinated Cl^- ligands in the $[Co^{II}(PNNP)Cl_2]$ inhibited a lithiation of the PNNP ligand in the complex possibly via a precipitation of LiCl salt from the solution mixture. The lack of conversion of the lithiated compound to the hydrogenated analogue upon leaving it under H_2, confirmed that the lithiated analogue of the dearomatized ligand did not react with H_2 in the absence of cobalt metal centre. The hydrogenated [Co(mPNNP)] complex was formed via metal-ligand cooperation. As a consequence, this evidence indicated that the cobalt centre was required to interact with H_2 to form the η^2-H_2 intermediate (**Scheme 4.9**) prior to adding to the C=C double bond of the phenanthroline scaffold of the dearomatized [Co(dPNNP)].

4.3.7.3 Reaction of the [Co^{I}(dPNNP)] under D_2

To understand the mechanism of a formation of the hydrogenated product, a deuterium labelled experiment of the dearomatized complex, [Co(dPNNP)], was performed. The ^{1}H NMR spectrum (**Figure 4.20** b, black frame) and ^{31}P{^{1}H} NMR spectrum (**Figure 4.20** b, red frame) measured after reaction of [Co(dPNNP)] with D_2 showed the aromatic protons and phosphorus signals at similar chemical shift values to those of the hydrogenated [Co^{I}(mPNNP)] complex (**Figure 4.20** c, brown dots). Therefore, it suggested formation of the deuterated [Co^{I}(mPNNP)] as shown the structure in **Figure 4.20**. The ^{1}H NMR spectrum in aliphatic region clearly showed the disappearance of the two triplet proton signals (Phen-CH_2) in the hydrogenated [Co^{I}(mPNNP)] (**Figure 4.20** b, black frame) and displayed two new broad signals as labelled by blue dots in the spectrum which corresponded to the two proton atoms in the structure. Moreover, the integration ratio of these two proton peaks became 1:1 ratio compared to an integral aromatic signal in the deuterated [Co^{I}(mPNNP)]. Thus, the deuterium labelled experiment of this complex supported that the hydrogenated product formed by the addition of H_2 to the double bond in the dearomatized ring of the phenanthroline ligand. The full ^{1}H NMR spectrum of this solution under D_2 (black in set, b) was demonstrated in **Figure A 4.7.**

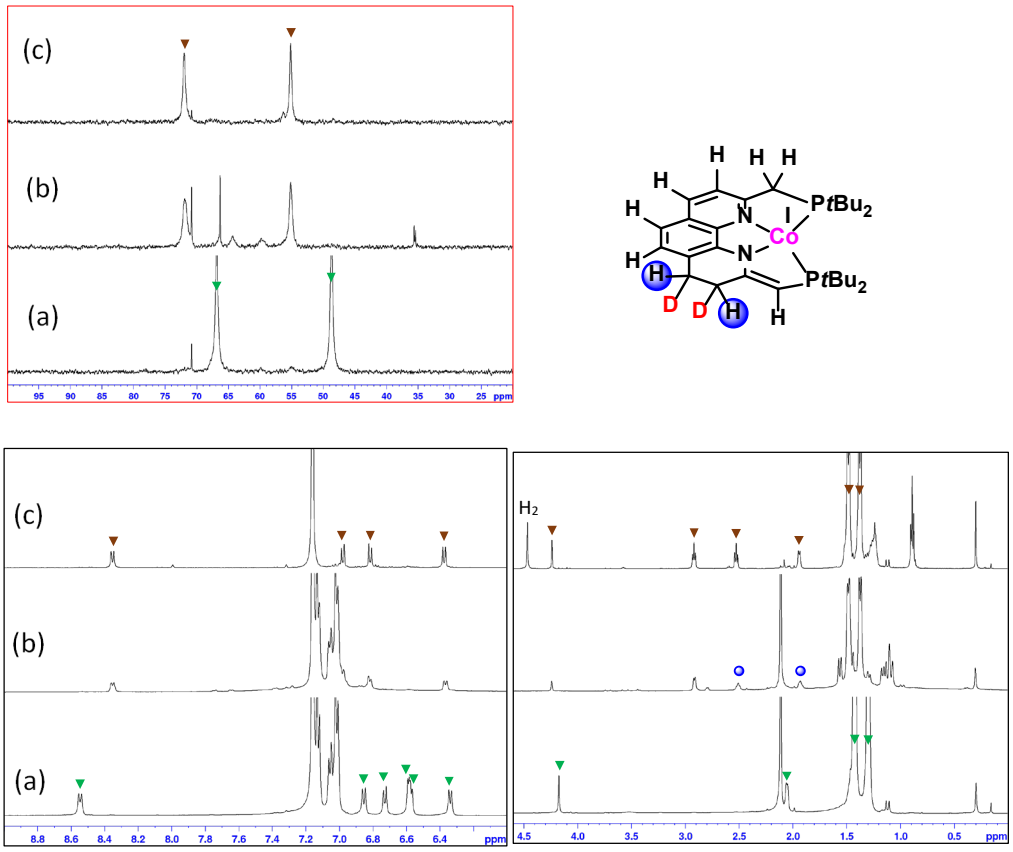

Figure 4.20. $^{31}P\{^{1}H\}$ NMR spectrum (red frame) and ^{1}H NMR spectrum (black frame) of (a) a solution of [Co(dPNNP)] in C_6D_6 left under Ar, (b) this solution under 4 bar of D_2 for 1 month, compared to (c) that of a solution of the [Co(dPNNP)] in C_6D_6 leaving under 4 bar of H_2 for 4 days.

4.3.8 Reaction of $[Co^{II}(PNNP)(MeCN)][BF_4]_2$ with 2.0 eq of $NaBEt_3H$ in toluene

Following the preparation of the Co(I) hydride supported by a pincer PNP ligand as reported by Chirik et al.[216] An effort was made to synthesize cobalt hydride complexes in this series by reacting $[Co^{II}(PNNP)(MeCN)][BF_4]_2$ with 2.0 equiv. $NaBEt_3H$. The NMR studies of this mixture at the initial reaction (30 min) suggested that the monohydride cobalt complex for $[Co^{I}(PNNP)(H)]$ was be able to generate in situ with formation of the hydrogenated complexes as shown in the structures with brown and orange labels and an unidentified product (blue label) (**Scheme 4.11**). The $[Co^{I}(PNNP)(H)]$ complex was eventually converted to these hydrogenated products upon leaving the solution at room temperature under Ar overnight. We postulated that the hydrogenated complexes were possibly formed via the η^2-H_2 complex in **Scheme 4.11** (dashed black arrows). Furthermore, it was observed that the hydrogenated complex (orange label) was also generated when the solution of $[Co^{I}(dPNNP)]$ was left in C_6D_6 under 4 bar of H_2 for 30 min as indicated by the blue arrows, and was discussed previously in section **4.3.7.1**. The η^2-H_2

complex was also assumed as intermediate by the interaction between the Co centre in the dearomatized [Co(dPNNP)] complex and molecular H_2 prior to the generation of the hydrogenated intermediate labelled in orange. The orange intermediate eventually changed to only the hydrogenated [Co(mPNNP)] (brown label) with no unidentified species (blue label) remaining when the solution was left for 4 days.

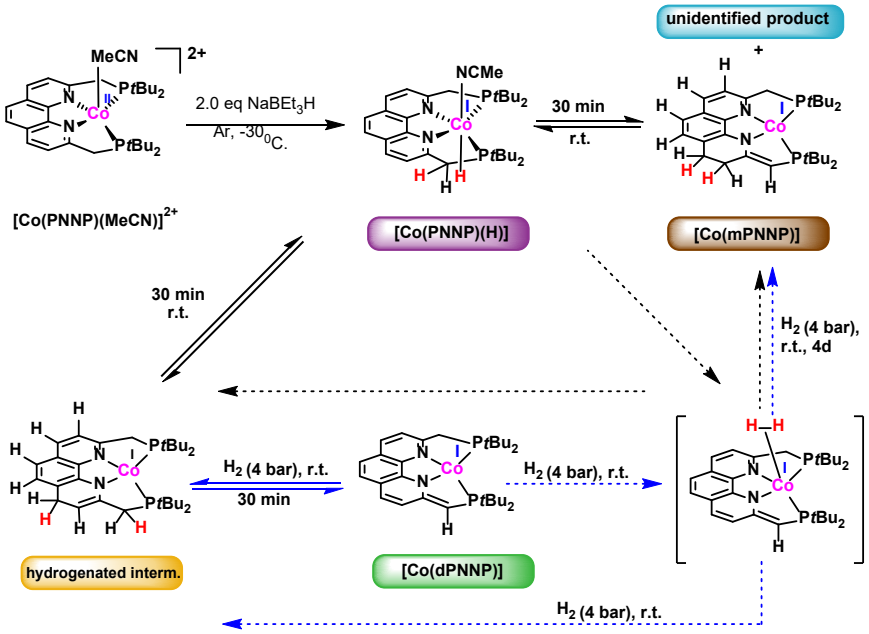

Scheme 4.11. Possible routes (solid black arrows) for the formation of hydrogenated complexes, [Co(mPNNP)] (brown label), hydrogenated intermediate (orange label) and unidentified product (blue label), and dashed black arrows indicating the formation of these hydrogenated product via the η^2-H_2 complex. The solid and dashed blue arrows represented a reaction of [Co(dPNNP)] under 4 bar of H_2 as shown previously in **Scheme 4.9**.

4.3.8.1 The NMR evidence of [Co^{I}(PNNP)(H)] by in situ generation

The NMR studies of this mixture at the initial reaction suggested that the monohydride cobalt complex for [Co^{I}(PNNP)(H)] (with purple label) was generated in situ with a mixture of the hydrogenated complexes (structure shown with orange and brown label) and unidentified product in the solution. The $^{31}P\{^{1}H\}$ NMR spectrum (**Figure 4.21**, red in set) and ^{1}H NMR spectrum (**Figure 4.21**, black in set) of the solution at initial reaction time was recorded at 30 min after adding $NaBHEt_3$ showing a triplet hydride signal (green in set) at δ -23.73 with $^{2}J(H,P)$ = 53.55 Hz and the integration of 1 relative to that of one of the aromatic protons. The single peak at δ 132.85 in the $^{31}P\{^{1}H\}$ spectrum (**red frame**) correlated with the triplet H^-signal. The appearance of only one phosphorus signal indicated that two phosphine arms in the [Co(PNNP)(H)] are chemically equivalent with no structural modification of the phenanthroline ligand. The Phen-*H* peaks for the hydride complex were indicated by purple dot in the ^{1}H NMR spectrum (black

frame). One of them overlapped with the solvent residue peak as identified in the 2D ^{1}H-^{1}H COSY spectrum (**Figure 4.22**) by showing a cross peak (purple arrow) with the Phen-*H* of the hydride complex at δ 7.48. However; one singlet signal of aromatic proton and aliphatic proton signals for the hydride complex could not be identified in the ^{1}H NMR spectrum due to complicated and overlapping peaks in this region. The number of NMR signals was consistent with the structure of [Co(PNNP)(H)] with higher symmetry than the structure of the hydrogenated complexes with modified PNNP ligand (orange and brown labels).

The hydrogenated intermediate as shown in the structure with the orange label also formed in the reaction. The assignment of protons and phosphorus atoms was indicated by orange dots in the NMR spectrum. The ^{31}P{^{1}H} NMR spectrum (red frame) exhibited two phosphorus signals which corresponded to the proton peaks with four different Phen-H protons in the aromatic region and the three distinct CH_2 protons (as labelled by green, purple and brown dots) in the ^{1}H NMR spectrum in aliphatic region (black in set). The broad signal at δ 4.63 corresponded to ***H***C(C(CH_2P*t*Bu_2)) in the hydrogenated intermediate with integration ratio of 1 relative to the three CH_2 protons. Based on this NMR evidence, this intermediate could be another isomer of the hydrogenated [Co(mPNNP)] complex as shown in the structure (brown label). Moreover, there was an unidentified product formed in this reaction as indicated by blue dots in the ^{31}P{^{1}H} and ^{1}H NMR spectrum. This species could not be identified due to the lack of obvious proton signals in the aliphatic region.

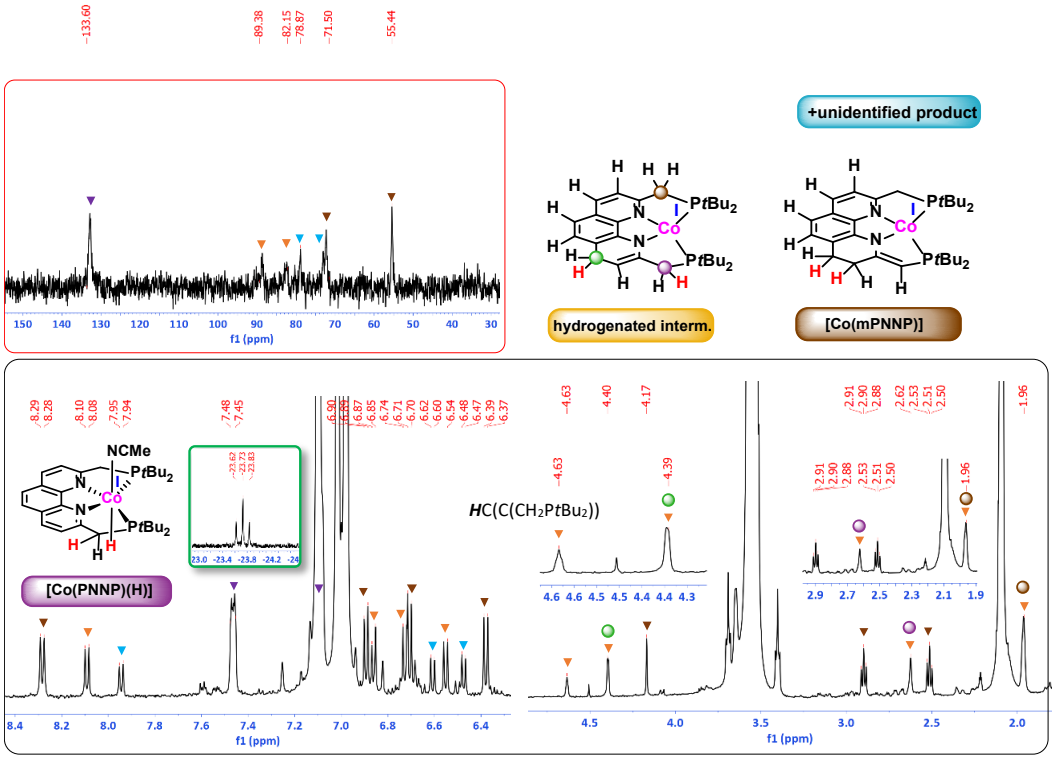

Figure 4.21 ^{1}H NMR spectrum (black frame) and ^{31}P{^{1}H} NMR spectrum (red frame) of a reaction mixture of [Co^{II}(PNNP)(MeCN)][BF$_4$]$_2$ with 2.0 equiv. NaBEt$_3$H in tol-d$_8$ left for 30 min under Ar. The NMR signals with purple labels for [Co^{I}(PNNP)(H)], orange labels for the hydrogenated intermediate, brown labels for [Co^{I}(mPNNP)] and blue labels for unidentified product.

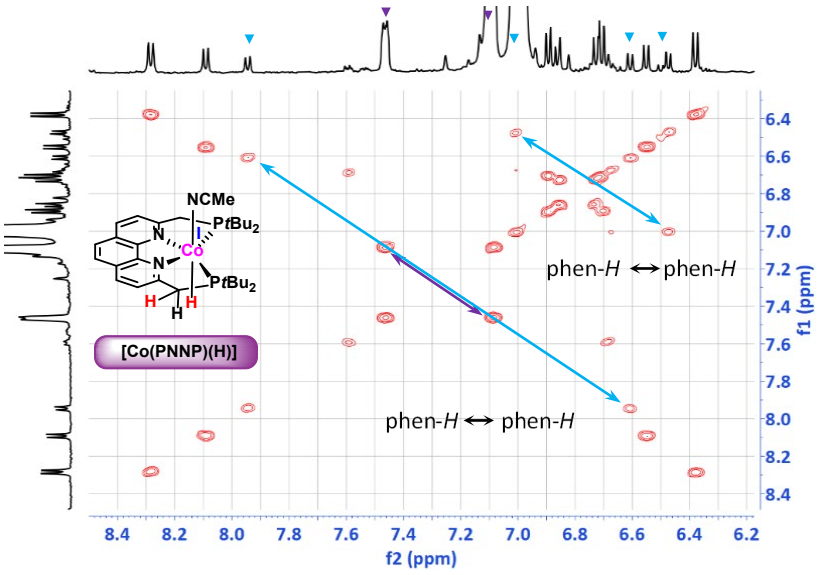

Figure 4.22. ^{1}H-^{1}H COSY NMR spectrum of a reaction mixture of [Co^{II}(PNNP)(MeCN)][BF$_4$]$_2$ with 2.0 equiv. NaBEt$_3$H in tol-d$_8$ left for 30 min under Ar. The black arrow showed the correlation between two protons as labelled by purple colour in the spectrum for the NMR signal of [Co^{I}(PNNP)(H)].

The $^{1}H\{^{31}P\}$ NMR spectrum in aromatic region for these complexes (**Figure A 4.8** b, red frame) showed well-resolved peaks as labelled by the same colour as those labels for the structure. The Phen-H signal (purple dot) in the [Co^{I}(PNNP)(H)] displayed sharper doublet signals in the $^{1}H\{^{31}P\}$ NMR spectrum suggesting the coupling to phosphorus in the hydride complex. The weak singlet hydride signal was observed in the $^{1}H\{^{31}P\}$ NMR spectrum (**Figure A 4.8**, green frame (b)) possibly due to a decomposition of this complex upon recording the spectrum at room temperature.. The $^{1}H\{^{31}P\}$ NMR data also supported the assignment to CH_2 protons in the structure of the hydrogenated intermediate (orange label). The broad CH_2 signals (purple and brown dots) and two broad methyl protons for $P(C(C\boldsymbol{H}_3)_3)_2$ in the complex suggested that these protons are close to phosphorus. In contrast to this, the ***H***C(C(CH_2P*t*Bu_2)) signal in this complex at δ 4.63 and the Phen-C***H***$_2$ (green dot) with the integration ratio of 1:2 remained the same as those in the ^{1}H NMR spectrum (black Iframe a). This indicated that these ***H***C(C(CH_2P*t*Bu_2)) and Phen-C***H***$_2$ protons are further away from the P atoms resulting in no coupling to the nearby phosphorus.

The progress of reaction was subsequently monitored after leaving it overnight, the ^{1}H NMR spectrum (**Figure 4.23** b, black frame) showed the disappearance of the proton signals (purple label), triplet hydride signal (green frame, b) and the phosphorus peaks at δ 132.85 in the $^{31}P\{^{1}H\}$ spectrum (**Figure 4.23** b, red frame) concomitant with generation of the two hydrogenated complexes (orange and brown labels) and unidentified products (**blue label**). However, an unidentified species (blue dots) with comparable amount to the hydrogenated complex, [Co(mPNNP)] species still could not be identified by the ^{1}H and $^{31}P\{^{1}H\}$ NMR data. However, it was assumed to be one of products formed by hydrogenation reaction of the dearomatized complex, [Co(dPNNP)] complex since it showed the same number of resonance peaks for aromatic protons (4 different peaks) as that of the [Co(mPNNP)] complex and a hydrogenated complex (orange label). The NMR data of all hydrogenated products including [Co(mPNNP)], the hydrogenated intermediate and unidentified product are listed in **Table 4.14**.

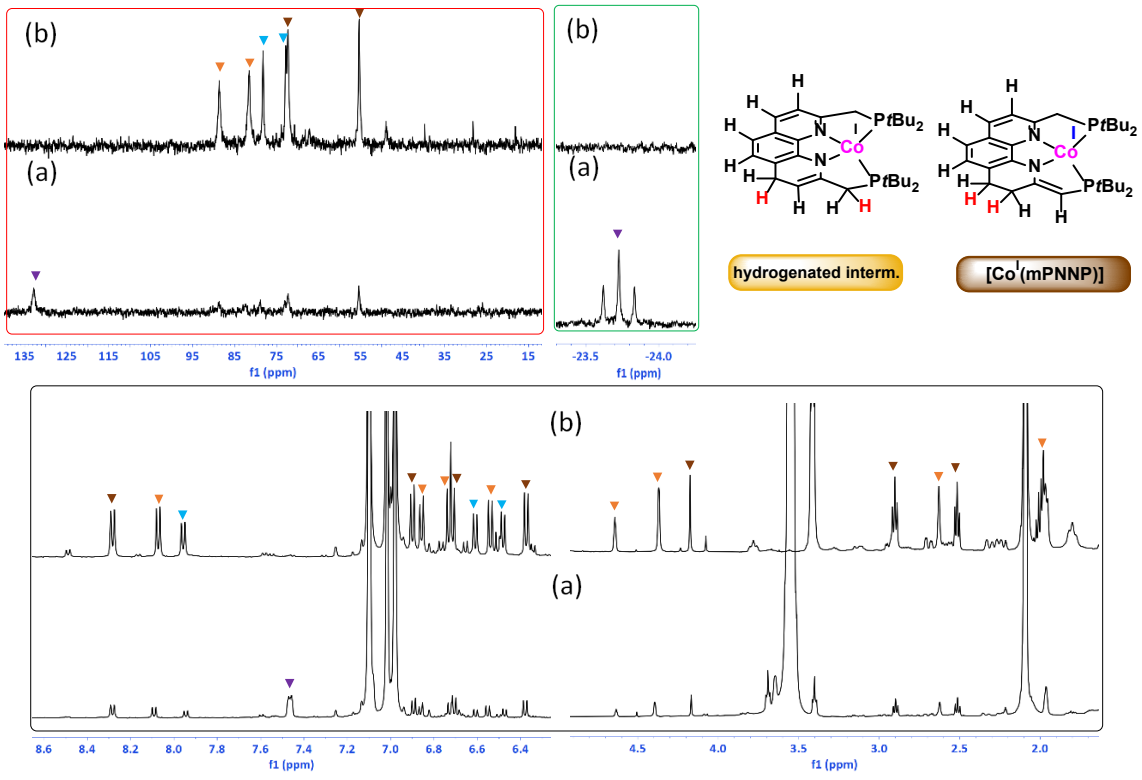

Figure 4.23. ^{1}H NMR spectrum (black frame) and $^{31}P\{^{1}H\}$ NMR spectrum (red frame) of a reaction mixture of [Co^{II}(PNNP)(MeCN)][BF_4]$_2$ with 2.0 equiv. $NaBEt_3H$ in tol-d_8 left (a) for 30 min and (b) overnight under Ar. The NMR signals with purple labels for [Co^{I}(PNNP)(H)], orange labels for hydrogenated intermediate and blue labels for unidentified product.

The $^{1}H\{^{31}P\}$ NMR spectrum (**Figure A 4.9** b) of the solution leaving under Ar overnight suggested that the unidentified species labelled by blue dots in the ^{1}H NMR spectrum (**Figure 4.23** b, black

in set) also has two distinct $PC(CH_3)_3$ which correspond to the four different of Phen-H proton peaks. The appearance of two different *t*Bu protons labelled as $PC(CH_3)_3$ in the ^1H NMR spectrum also agrees with the signals in the [Co(mPNNP)] and the hydrogenated intermediate with orange label. Moreover, the in situ generation of the hydride complex by reacting the $[Co^{II}(PNNP)(MeCN)]^{2+}$ with 2.0 equiv. $NaBEt_3H$ in C_6D_6 was also achieved under similar conditions to the reaction in Tol-d_8. The formation of the same species in the reaction mixture was also observed as labelled in the $^{31}P\{^1H\}$ and ^1H NMR spectrum (**Figure A 4.10** and **Figure A 4.11**, respectively).

4.3.9 Reaction of $[Co^{II}(PNNP)Cl_2]$ with 2.0 equiv $NaBEt_3H$ in toluene-d_8 under Ar

Reaction of $[Co^{II}(PNNP)Cl_2]$ with 2.0 equiv of $NaBEt_3H$ in tol-d_8, did not generate the anticipated hydride $[Co^{I}(PNNP)(H)(Cl)]^-$ species (as shown in the bracket, **Scheme 4.12**) in the solution. Nevertheless, apart from the hydride complex, the formation of the same species (hydrogenated complexes with orange and brown labels and unidentified product with blue label) as those generated by a reaction of the $[Co^{II}(PNNP)(MeCN)][BF_4]$ with 2.0 eq $NaBEt_3H$ was observed under the same conditions at a reaction time of 30 min. This high reactivity of the "not observed hydride intermediate" $[Co^{I}(PNNP)(H)(Cl)]^-$ was possibly due to the instability of the negatively charged species. This resulted in a fast elimination of Cl^- to form the mixture of hydrogenated products in the solution at room temperature. It was found that the hydrogenated intermediate (orange label) was converted to [Co(mPNNP)] and unidentified product upon leaving the reaction mixture at room temperature. under Ar for 3 days.

4.3.9.1 Isolation of [Co(dPNNP)] from reaction of $[Co^{II}(PNNP)Cl_2]$ with 1.0 equiv. $NaBEt_3H$ in toluene

The isolation of the dearomatized $[Co^{I}(dPNNP)]$ as a deep green powder was achieved by reacting $[Co^{II}(PNNP)Cl_2]$ with 1.0 equiv. $NaBEt_3H$ in toluene-d_8 at -30 ^{0}C. The reaction mixture of $[Co^{II}(PNNP)Cl_2]$ complex with 1.0 equiv. $NaBEt_3H$ was left in a vial for 5 min prior to filter through cotton and celite to remove undesired paramagnetic species. The similar colour change from deep purple to deep brown upon warming it up to room temperature. was observed to that on reacting with 2.0 equiv. of $NaBEt_3H$ in C_6D_6 or tol-d_8. By accident, precipitation of deep green solid from a deep brown solution at -77 ^{0}C (in dry ice/acetone bath) allowed us to isolate this complex and characterize it by NMR spectroscopy. This solid was characterized in C_6D_6 solution under Ar by NMR techniques including ^1H, $^{31}P\{1H\}$, 2D COSY and ^1H-$^{31}P\{^1H\}$ HMBC experiments (**Figure A 4.12-Figure A 4.14**). Its NMR characteristics corresponded to the data for [Co(dPNNP)] (listed in **Table 4.12**) which is selectively formed in a reaction of $[Co^{II}(PNNP)Cl_2]$ with 1.0 equiv. LiMe in toluene as discussed in the section **4.3.6.1**.

4.3.9.2 NMR studies of reaction of [Co(PNNP)Cl$_2$] with 2.0 equiv NaBEt$_3$H in C$_6$D$_6$

From the $^{31}P\{^1H\}$ NMR spectrum (**Figure A 4.15** b), the initial reaction by mixing the [Co(PNNP)Cl$_2$] with 2.0 equiv NaBEt$_3$H in C$_6$D$_6$ at 30 min caused generation of the dearomatized [Co(dPNNP)], hydrogenated species [Co(mPNNP)] and the unidentified hydrogenated complex (blue label). However, the hydrogenated intermediate (orange label) was not observed in the solution mixture. According to this evidence, conversion of this hydrogenated intermediate to the [Co(dPNNP)], [Co(mPNNP)] and the unidentified hydrogenated complex is faster in C$_6$D$_6$ solution than in tol-d$_8$. The MLC dearomatization chemistry as observed by a formation of the [Co(dPNNP)] indicates the acidity of the methylene proton, and anionic charater of nitrogen atom suggest a heterolytic C-H bond cleavage of the proposed Co(I) hydride complex resulting in a liberation of H$_2$.

Moreover, the brown solid obtained from a reaction of the [Co^{II}(PNNP)Cl$_2$] with 2.0 equiv NaBEt$_3$H in C$_6$D$_6$ was recrystallized in toluene/pentane under Ar to obtain a single crystal (brown needle) for X-ray crystallographic determination. The X-ray structure (**Figure 4.24**) revealed the crystals to be [Co^{II}(mPNNP)Cl] as shown in **Scheme 4.12** (inset), and the complex was supposed to be a paramagnetic species due to Co(II) oxidation state with d^7 configuration. Thus it was not one of the products characterized by the NMR technique as shown in the ^1H and $^{31}P\{^1H\}$ NMR spectrum (**Figure 4.26** d). However, this paramagnetic species could be formed in the reaction mixture as proposed in **Scheme 4.13** which caused the broad signals in the ^1H NMR spectrum (**Figure A 4.16**). The [Co^{II}(dPNNP)Cl] was formed in the reaction of [Co^{II}(PNNP)Cl$_2$] with 2.0 equiv NaBEt$_3$H by a deprotonation of one proton in the benzylic group to liberate H$_2$ and a precipitation of the NaCl salt. This first deprotonation step was observed in the [(^{tBu}PNP)Co^{II}Cl$_2$] complex treated with excess LiMe resulting in a formation of the dearomatized [(^{tBu}dPNP)Co^{II}Cl] analogue via a production of CH$_4$ and a precipitation of LiCl salt as proposed by Chirik et al.[216] The [Co^{II}(dPNNP)Cl] formed in the solution was then further reduced by NaBEt$_3$H to furnish the dearomatized [Co^{I}(dPNNP)] with a loss of Cl$^-$. This reduced Co(I) species was then hydrogenated to obtained the product of [Co^{I}(mPNNP)] as observed by the NMR studies. Therefore, in our observation, it can be inferred that NaBEt$_3$H can acts as a hydride source and reducing reagent. The previous literature reported that one electron reduction of cobalt dichloride complexes, (^{iPr}PNP)CoCl$_2$,[216] (^{Cy}APDI)CoCl$_2$ and (^{iPr}APDI)CoCl$_2$[323] can be achieved by reacting with 1.0 equiv of the NaBEt$_3$H to form the corresponding cobalt monochloride compounds.

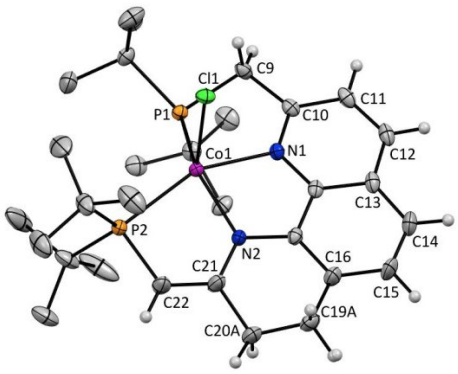

Figure 4.24. X-ray crystal structure of [Co^{II}(mPNNP)Cl] complex.

Table 4.15. Selected bond lengths (Å) and angles (deg) for [Co^{II}(mPNNP)Cl] (RNP 1812).

atom	atom	bond lengths (Å)	atom	atom	atom	bond angles/deg
Cl1	Co1	2.3179(5)	Cl1	Co1	P1	97.225(18)
Co1	N1	2.1525(15)	Cl1	Co1	P2	105.065(19)
Co1	N2	1.9999(15)	N1	Co1	Cl1	89.84(4)
Co1	P1	2.5446(5)	N1	Co1	P1	73.92(4)
Co1	P2	2.5068(5)	N1	Co1	P2	157.39(4)
			N2	Co1	Cl1	115.32(5)
			N2	Co1	N1	77.75(6)
			N2	Co1	P1	136.35(5)
			N2	Co1	P2	80.49(4)
			P2	Co1	P1	119.690(18)

Furthermore, the dearomatized [Co^{I}(dPNNP)] (as shown the structure with green label in **Scheme 4.12**) in the reaction mixture was converted to the hydrogenated [Co(mPNNP)] and unidentified product under 4 bar of H_2 (black arrow) The formation of hydrogenated products was also proposed via the dihydrogen complex as indicated by black dashed arrows in the reaction scheme. Moreover, the dearomatized [Co^{I}(dPNNP)] complex was generated in the solution mixture after leaving at room temperature. under Ar for 3 days. It could be inferred that the hydrogenated complexes (brown or orange label) liberated a H_2 molecule via the dihydrogen complex intermediate to eventually form [Co^{I}(dPNNP)] as shown by dashed green pathways.

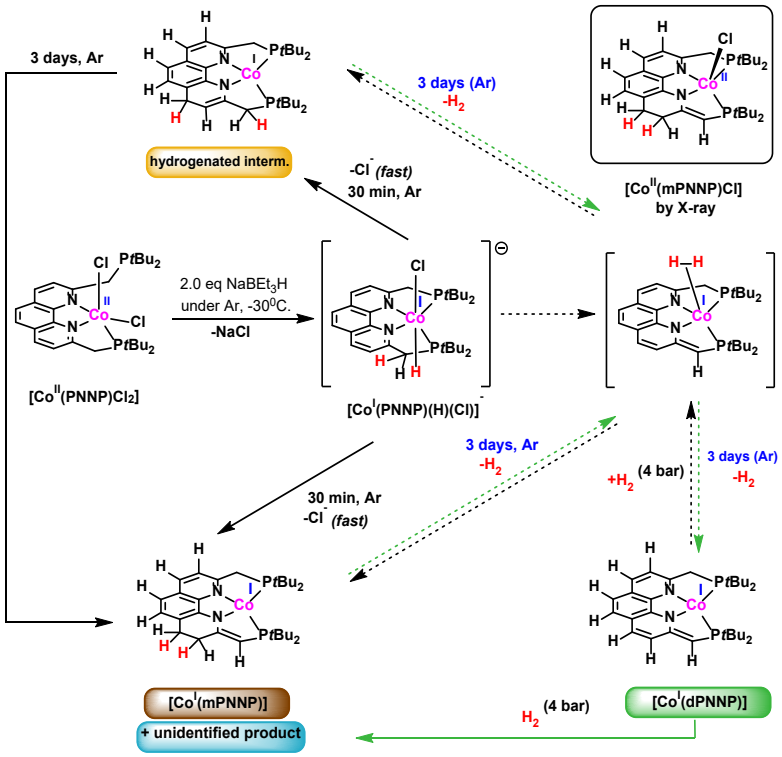

Scheme 4.12. Possible routes for the formation of hydrogenated complexes, [Co(mPNNP)] (brown label), hydrogenated intermediate (orange label), unidentified product (blue label) and dearomatized [Co(dPNNP)] (green label) by reaction of $[Co^{II}(PNNP)Cl_2]$ with 2.0 eq of $NaBEt_3H$ in toluene-d_8. Dashed black arrows indicate the formation of these hydrogenated product via the η^2-H_2 complex, solid green arrow show a reaction of [Co(dPNNP)] under 4 bar of H_2 and the dashed green arrows represent the generation of [Co(dPNNP)] in the solution leaving under Ar for 3 days.

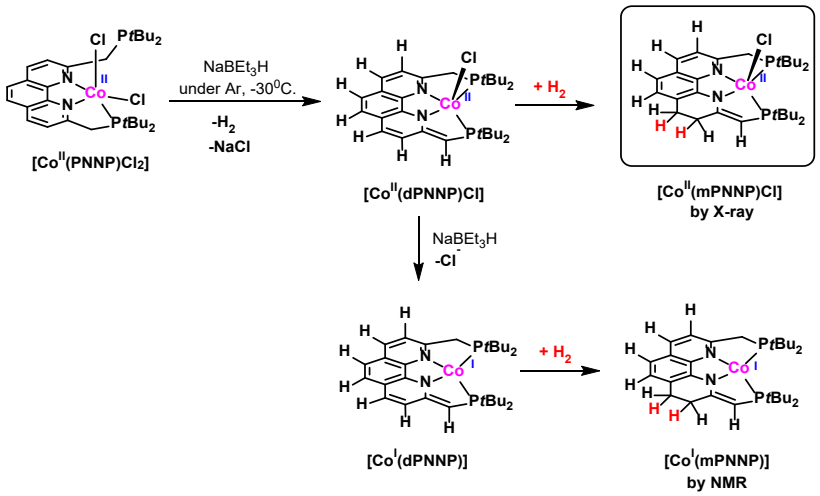

Scheme 4.13. Possible pathway for a generation of the $[Co^{II}(mPNNP)Cl]$ observed by the X-ray and the $[Co^{I}(mPNNP)]$ by NMR by a reaction of the $[Co^{II}(PNNP)Cl_2]$ with 2.0 eq of $NaBEt_3H$.

4.3.9.3 NMR studies of reaction of the [Co(PNNP)Cl$_2$] with 2.0 equiv NaBEt$_3$H

As mentioned previously, the initial reactions (30 min) of [Co(PNNP)(MeCN)][BF$_4$]$_2$ and [Co(PNNP)Cl$_2$] with NaBEt$_3$H generated the same species (the hydrogenated complexes with orange and brown labels and unidentified species with blue label) but a hydride complex was not observed from [Co(PNNP)Cl$_2$]. The ^{1}H NMR spectrum (**Figure 4.25** b, black frame) and the ^{31}P{^{1}H} NMR spectrum (**Figure 4.25** b, red frame) of the solution of [Co(PNNP)Cl$_2$] with NaBEt$_3$H showed that no triplet hydride signal and no singlet phosphorus signal around δ 135 were observed.

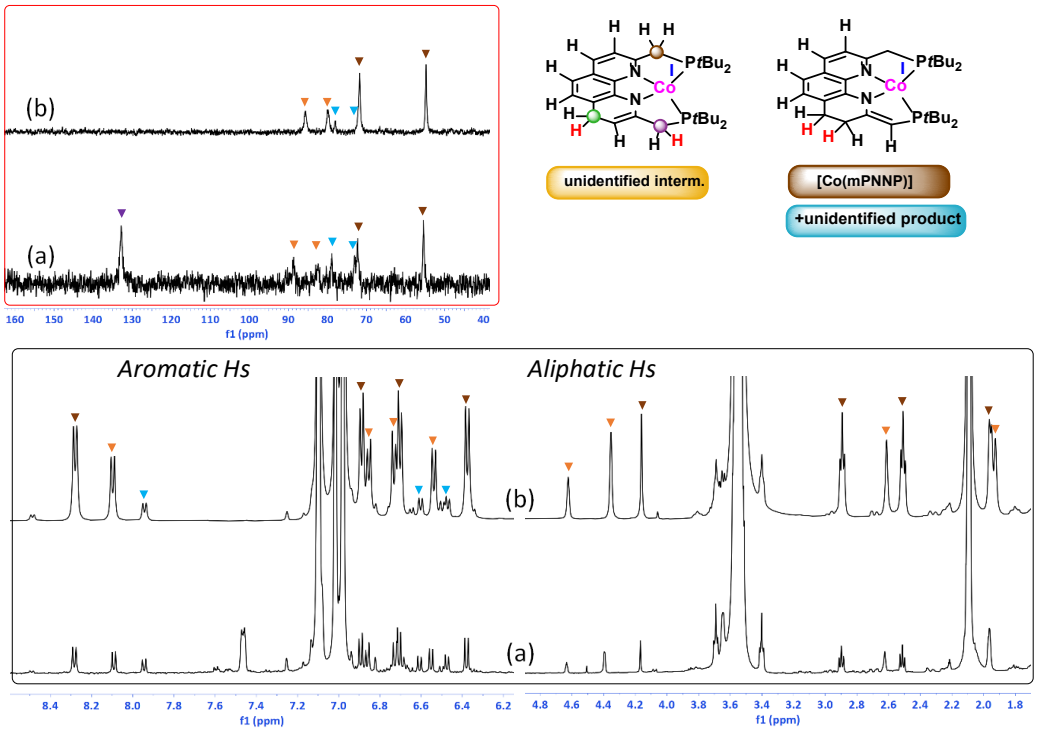

Figure 4.25. ^{1}H NMR spectrum (black frame) and ^{31}P{^{1}H} NMR spectrum (red frame) of (a) a reaction mixture of [Co^{II}(PNNP)(MeCN)][BF$_4$]$_2$ with 2.0 equiv. NaBEt$_3$H in tol-d$_8$ left under Ar for 30 min compared to (b) reaction mixture of [Co^{II}(PNNP)Cl$_2$] complex under similar conditions. The NMR signals for each complex were indicated by purple labels for [Co^{I}(PNNP)(H)], orange and blue labels for unidentified intermediates and brown labels for [Co^{I}(mPNNP)].

The solution was left at room temperature. under Ar and was monitored by NMR spectroscopy. It was observed that [Co(mPNNP)] withrelatively smaller amount of dearomatized [Co(dPNNP)] and the unidentified product were formed in the solution when it was left for 3 days (**Figure 4.26**, b). The disappearance of the NMR signals (orange labels) confirmed the transformation of the hydrogenated intermediate (orange label) to the mixture of [Co(mPNNP)], [Co(dPNNP)] and unidentified product (blue label). Moreover, the generation of the dearomatized complex concomitant with the disappearance of the hydrogenated complex (orange labels) suggested a

loss of H_2 from the hydrogenated complex via the η^2-H_2 complex as proposed in **Scheme 4.12** by the dashed green arrows. Another possible way to obtain the [Co(dPNNP)] would be liberation of H_2 form the hydrogenated [Co(mPNNP)] or the unidentified product. In the case of the Ru analogue [318], the hydrogenation of the dearomatized complex is a reversible process. Heating the solution of hydrogenated complex led to a regeneration of the dearomatized derivative with a liberation of a H_2 molecule. From our findings, the addition of H_2 to a solution of the dearomatized complex initially formed a hydrogenated complex (orange label) and this complex was subsequently converted to the [Co(mPNNP)] together with the unidentified product (blue label). Therefore, we believe that the dearomatized [Co(dPNNP)] complex in this reaction mixture left under Ar for 3 days is generated by dehydrogenation of the hydrogenated Co complex (orange label).

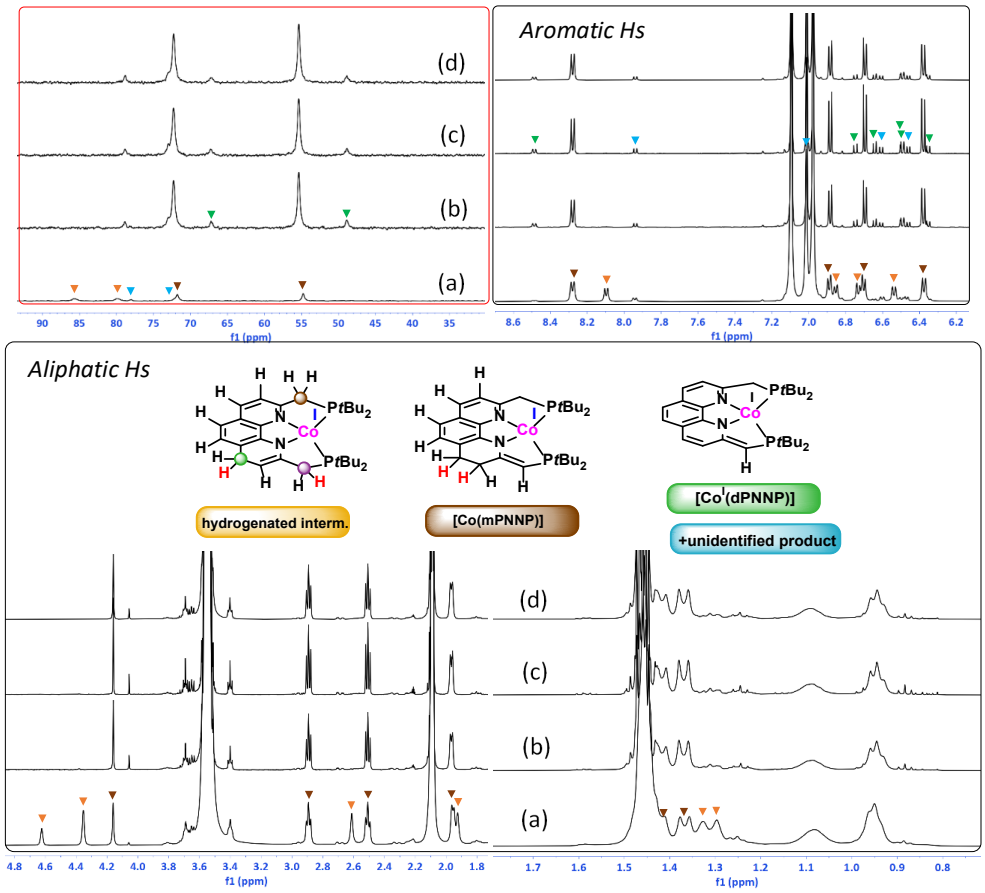

Figure 4.26. $^{31}P\{^1H\}$ NMR spectrum (red frame) and ^1H NMR spectrum (black frame) of a reaction mixture of [Co^{II}(PNNP)Cl$_2$] with 2.0 equiv. NaBEt$_3$H in tol-d_8 left under Ar for (a) 30 min, (b) 3 days, (c) 5 days, (d) 6 days. The NMR signals for each complex were indicated by brown labels for the [Co^{I}(mPNNP)], green labels for the [Co(dPNNP)], orange labels for the hydrogenated intermediate and blue labels for the unidentified product.

The low-temperature NMR studies of the solution mixture at 223 K

The $^{31}P\{^{1}H\}$ NMR and ^{1}H NMR spectrum (**Figure 4.27** a, red and black frame, respectively) of the solution of the [Co(PNNP)Cl_2] with 2.0 equiv $NaBEt_3H$ left under Ar at room temperature. for 6 days displayed the peaks corresponded to the mixture of [Co(mPNNP)], [Co(dPNNP) and unidentified product. At low temperature, the NMR peaks (**Figure 4.27** b) of these species became much sharper and were shifted from the peaks at room temperature. This result suggested that these hydrogenated complexes exhibit fluxional behaviour in a solution.

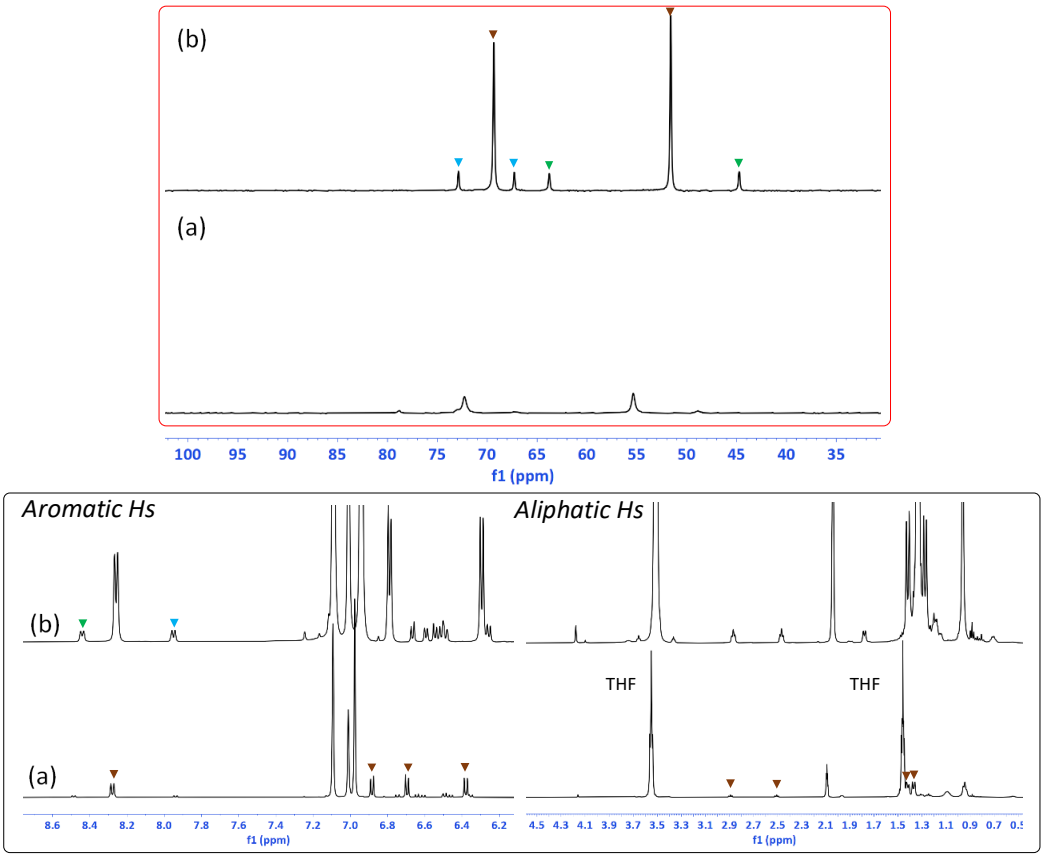

Figure 4.27. $^{31}P\{^{1}H\}$ NMR spectrum (red frame) and ^{1}H NMR spectrum (black frame) of a reaction mixture of [Co^{II}(PNNP)Cl_2] with 2.0 equiv. $NaBEt_3H$ in tol-d_8 left under Ar for 6 days recorded (a) at 298 K and (b) at 223 K.

NMR studies of reaction of [Co^{II}(PNNP)Cl$_2$] with 2.0 equiv NaBEt$_3$H in C$_6$D$_6$ under H$_2$

Furthermore, the hydrogenation of the dearomatized [Co^{I}(dPNNP)] complex generated by a reaction mixture of [Co^{II}(PNNP)Cl$_2$] with 2.0 equiv. NaBEt$_3$H in C$_6$D$_6$ was carried out under 4 bar of H$_2$. This solution was degassed under vacuum prior to adding 4 bar of H$_2$. After leaving a reaction mixture under H$_2$ for 1 h, the signals of [Co^{I}(dPNNP)] labelled as green squares in the ^{1}H and ^{31}P{^{1}H} NMR spectra (**Figure 4.28** b) disappeared indicating that this complex could react with H$_2$ to form a mixture of two products. The ^{31}P{^{1}H} NMR spectrum (red frame) showed the two distinct signals of phosphorus nuclei in the [Co^{I}(mPNNP)] as labelled with brown dots and the unidentified product (blue dots). The presence of this unidentified species in the solution under H$_2$ supported the hypothesis that this product was one of hydrogenated complexes generated by a reaction of the [Co^{II}(PNNP)(MeCN)]$^{2+}$ or [Co(PNNP)Cl$_2$] with 2.0 equiv. NaBEt$_3$H in the solution under Ar as discussed in the section **4.3.8** and **4.3.9**, respectively.

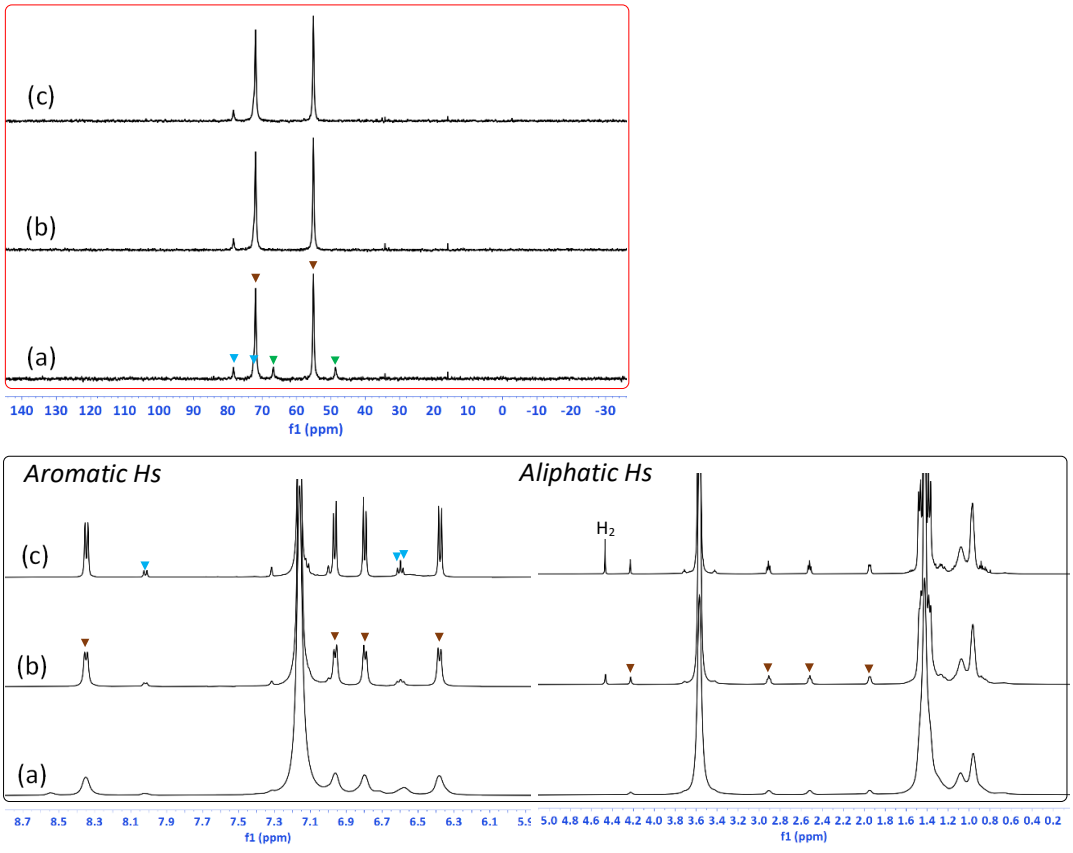

Figure 4.28. ^{31}P{^{1}H} NMR spectrum (red frame), ^{1}H NMR spectrum (black frame) of a reaction mixture of the [Co^{II}(PNNP)Cl$_2$] with 2.0 equiv. NaBEt$_3$H in C$_6$D$_6$ left under Ar for (a) 30 min, (b) this solution under 4 bar of H$_2$ for 1 h and (c) overnight.

4.3.10 Comparison of X-ray crystallographic data

The X-ray structure of the dearomatized [Co^{I}(dPNNP)] and the corresponding [Co^{I}(PNNP)]$^{+}$ (**Figure 4.29**) as well as the hydrogenated [Co^{II}(mPNNP)Cl] with the [Co^{II}(PNNP)Cl]$^{+}$ analogue (**Figure 4.30**) allow comparison between changes in bond distances and bond angles of the modified PNNP ligand in the [Co^{I}(dPNNP)], the [Co^{II}(mPNNP)Cl] and unmodified PNNP in their Co(I) and Co(II) analogue. The X-ray data of these complexes are listed in **Table 4.16.**

X-ray crystallographic analysis of the [Co^{I}(dPNNP)] and [Co^{I}(PNNP)][PF$_6$]

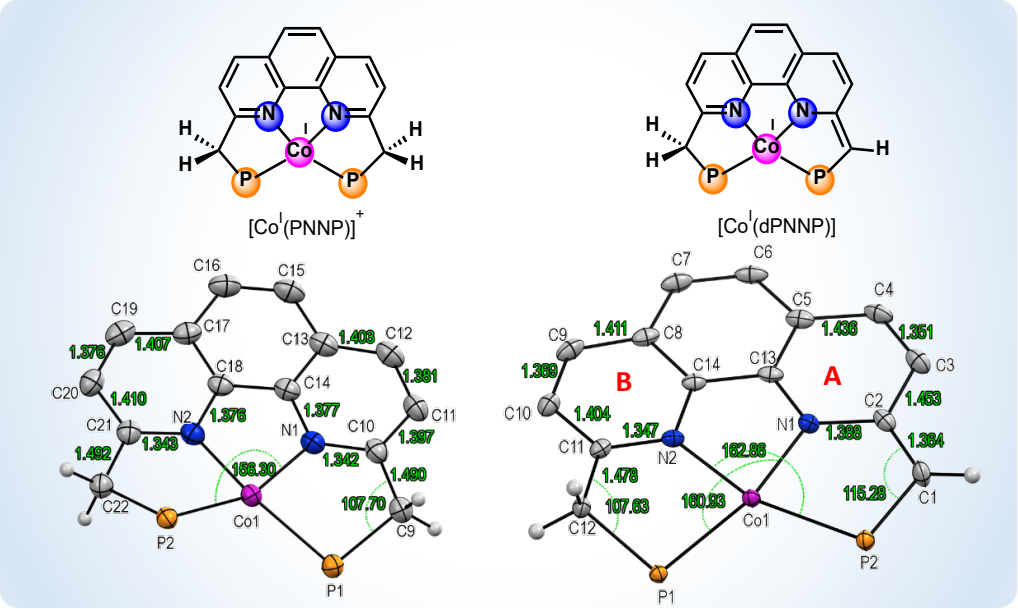

Figure 4.29. Comparison of X-ray crystal structure of (a) the unmodified [Co^{I}(PNNP)][PF$_6$], (b) dearomatized [Co^{I}(dPNNP)].

The alteration of C-C bond lengths in pyridine ring A in the [Co^{I}(dPNNP)] clearly showed dearomatization as compared to the pyridine ring B. The C2-N1 in the ring A becomes longer than the C11-N2 in the aromatic pyridine ring B, while the two C-N bond length (C10-N1 and C21-N2) length in the unmodified PNNP ligand of the [Co^{I}(PNNP)]$^{+}$ almost similar. The difference in the C-N bond distances between ring A and ring B confirmed the anionic nature of the dearomatized pyridine. Moreover, the Co-P bond lengths in the [Co^{I}(dPNNP)] are distinct as compared to those two similar Co-P bond distances in the unmodified [Co^{I}(PNNP)]$^{+}$. The shorter of the benzylic C-C bond distance of C1-C2 (1.363(3) Å) than that of C11-C12 (1.478(2) Å) indicate the C=C double bond, and the distinct between these two bond length also support the presence of anionic chelate. In contrast to this, the benzylic C-C bond of C9-C10 (1.490(3) Å) and C21-C22 (1.492(3) Å) in the neutral pyridine rings of unmodified PNNP are very similar in distance.

The anionic character of the dearomatized PNNP corresponded to the modified pincer ligand in the ^{tBu}mPNPCo^{I}N$_2$.[216]

Moreover, the structure of [Co^{I}(dPNNP)] shows a geometry closer to ideal square planar with the N2-Co1-P2 angle of 162.86(5) Å, while the N1-Co1-P2 angle of 156.30(6) Å was found in the [Co^{I}(PNNP)]. This reduced distortion found in the [Co^{I}(dPNNP)] is possibly due to containing of the C_{sp2} in the dearomatized ligand with the C2-C1-P2 angle of 115.28(14) deg which is almost ideal trigonal planar geometry. For the distorted planar four-coordinated [Co^{I}(^{tBu}PNP)N$_2$] pincer complex, the P-Co-P bond angle is found to be 169.688(16) Å.[216]

X-ray crystallographic analysis of the [Co^{II}(mPNNP)Cl] and [Co^{II}(PNNP)Cl$_2$]

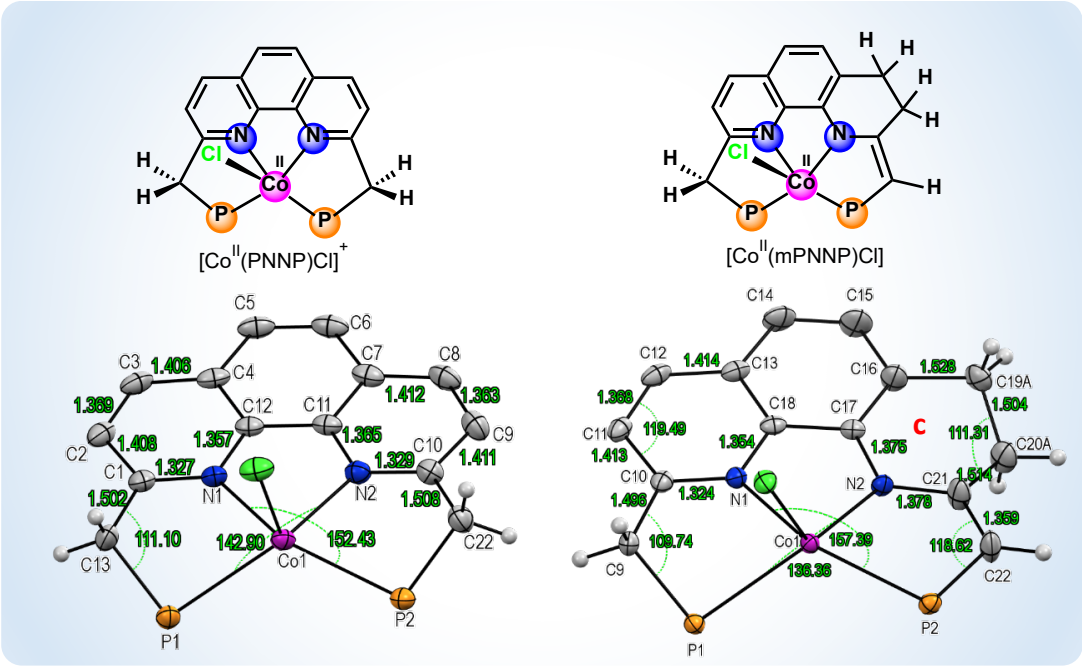

Figure 4.30. Comparison of X-ray crystal structure of (a) the unmodified cobalt(II) complex, [Co^{II}(PNNP)Cl][BAr$^{F}_4$] and (b) the hydrogenated [Co^{II}(mPNNP)Cl] complex.

The X-ray structure revealed that both of the [Co^{II}(mPNNP)Cl] and the unmodified Co(II) analogue showed a distorted square pyramidal geometry. The much longer of C21-N2 (1.378(2) Å) in the ring C than the distance in C10-N1 (1.324(2) Å) indicate the anionic modified ligand as observed in the dearomatized [Co^{I}(dPNNP)]. The similar change in bond distance between the shorter endocyclic C=C double bond (C21-C-22, 1.359(3) Å) and the C-C single bond (C9-C10, 1.496(3) Å), was also observed in the [Co^{II}(mPNNP)Cl] which confirmed dearomatization of the PNNP ligand. Moreover, the C-C bond distances C16-C19A (1.527(7) Å), C19A-C20A (1.504(10) Å and C20A-C21 (1.515(4) Å) in the pyridine ring C are more elongated than those in the unmodified [Co^{II}(PNNP)Cl]$^{+}$ and longer than C2-C3 (1.369(4) Å), C3-C4 (1.406(4) Å), and C4-C5 (1.436(3) Å) in ring A of the dearomatized [Co^{I}(dPNNP)]. The two C-C single bonds with sp^3

hybridization in heterocycle C are more flexible and lifted up from the basal plane of the two conjugated aromatic rings in the mPNNP ligand to accommodate angles close to tetrahedral. Moreover, a coordinated Cl^- ligand causes more distortion of the idealized metal-ligand square planar by showing the N1-Co1-P2 and the N2-Co1-P1 of 157.39(4) deg and 136.35(5) deg, respectively. The Co-N(amido) bond length also changed which is significantly shorter than that of the Co-N bonds with neutral N atoms of the aromatic phenanthroline ligand as labelled with brown color and underline. The shorter Co-N (amido) bond compared to other Co-N bonds supported a negative charged character resulting in a formation of a stronger electrostatic interaction with the cationic Co(II) centre. However, a difference in the two Co-N bond distances in the [Co^I(dPNNP)] was not observed.

Table 4.16. Lists of bond lengths (Å) and bond angles (deg) of each complex for comparison.

	[Co^I(PNNP)][PF_6]	**[Co^I(dPNNP)]**	**[Co^{II}(PNNP)Cl]$^+$**	**[Co^{II}(mPNNP)Cl]**
bond length (Å)				
Co1-P1	2.2518(6)	2.2400(5)	2.5502(8)	2.5446(5)
Co1 P2	2.2674(6)	2.2989(5)	2.5119(9)	2.5068(5)
Co1 N1	1.9091(17)	1.9233(15)	2.151(2)	2.1525(15)
Co1 N2	1.9013(18)	1.9204(14)	2.126(2)	2.0000(15)
C2-C1		1.363(3)		1.359(3) (C21-C22)
			1.507(4) (C10-C22)	1.496(3) (C9-C10)
C11-C12		1.478(2)	1.501(4)(C1-C13)	
C2-C3		1.453(3)		
C4-C3		1.351(3)		
C4-C5		1.436(3)		
C11-C10		1.404(2)	1.411(4) (C10-C9)	1.413(2)
C10-C9	1.490(3)	1.369(3)	1.363(5) C8-C9	1.368(3) (C11-C12)
C21-C22	1.492(3)			
C20A-C21				1.514(4)
C19A-C20A				1.504(10)
C16-C19A				1.527(7)
P2-C22	1.858(2)	1.8583(17) (P1-C12)	1.851(3) (P1-C13)	1.8531(18) (P1-C9)
P1-C9	1.855(2)	1.7799(19) (P2-C1)	1.845(3) (P2-C22)	1.786(2)P2-C22
bond angle (deg)				
N1-Co1-P2	156.30(6)			157.39(4)
N1-Co1-P1		160.93(5)		136.35(5) N2-Co1-P1
N2-Co1-P2		162.86(5)		
C11-C12-P1		107.64(12)		
C2-C1-P2		115.28(14)		

As a general overview, the X-ray structure of [Co(dPNNP)] complex showed a distorted square planar geometry where the dearomatized structure of PNNP ligand coordinated to the Co(I)

metal centre as L_3X type ligand. The alteration in C-C bonds in the pyridine ring confirmed a dearomatized structure. In contrast, the [Co^{II}(mPNNP)Cl] with hydrogenated PNNP ligand with one Cl^- coordinated at metal centre adopt a distorted square pyramidal complex with d^7-Co(II) metal centre and showed more distorted structure due to a coordinated Cl^- and the C-C single bond in the modified ligand.

4.3.11 UV-Vis/magnetic measurements and CV characterisation

The electronic, magnetic and redox properties for the Co(II) and Co(I) complexes in solution are discussed in this section. The UV-Vis spectroscopic data for [Co^{II}(PNNP)(MeCN)][BF_4]$_2$ [Co^{II}(PNNP)Cl][BAr^F_4], [Co^{II}(PNNP)Cl_2] and [Co^{I}(PNNP)][PF_6] are summarized in **Table 4.17** and the electrochemical data of the [Co^{II}(PNNP)(MeCN)][BF_4]$_2$ and [Co^{II}(PNNP)Cl_2] in this series characterized by cyclic voltammetry (CV) are summarized in **Table 4.18**.

Table 4.17. UV-Vis spectroscopic data of the [Co^{II}(PNNP)(MeCN)][BF_4]$_2$, [Co^{II}(PNNP)Cl][BAr^F_4], [Co^{II}(PNNP)Cl_2] and [Co^{I}(PNNP)][PF_6] in a solution.

compound	Concentration (M)	λ_{max} (nm)	ε (M^{-1} cm^{-1})	Assigned band
[Co^{II}(PNNP)(MeCN)][BF_4]$_2$ in MeCN	$1.5x10^{-4}$	2 bands (< 300 nm)		π-π* (L)
		355	2350	CT
		405	1493	CT
		456	910	CT
		645 (tail)	208	d-d transition
[Co^{II}(PNNP)Cl_2] in DCM	$5.75x10^{-4}$	358	2220	CT
		425	1470	CT
		495	616	CT
		735	16	d-d transition
[Co^{II}(PNNP)Cl_2] in 4% v/v DCM/MeCN	$5.75x10^{-4}$	514	235	d-d transition
		590	185	d-d transition
		640	182	d-d transition
[Co^{II}(PNNP)Cl][BAr^F_4] in MeCN	$4.81x10^{-4}$	529	170	d-d transition
		607	160	d-d transition
		655	180	d-d transition
[Co^{I}(PNNP)][PF_6] in MeCN	$1.25\ x10^{-4}$	358	3248	CT
		443	1824	CT
		704	2064	CT
		922	1992	CT
[Co^{I}(dPNNP)] in toluene	$1.00\ x10^{-4}$	344	18960	CT
		436	9250	CT
		468	8470	CT
		642	3990	CT
		892	3280	CT
		998	4720	CT

UV-Vis absorption and magnetic properties of the cobalt(II) complexes

The UV-Vis spectrum of the $[Co^{II}(PNNP)(MeCN)][BF_4]_2$ displayed two absorption bands in the UV region at λ < 300 nm (**Figure A 4.17**) which were assigned as π-π^* ligand-centred transitions in the complex.[251] The intense bands (**Figure 4.31** a) at wavelength ranging from 320 nm to 460 nm (ε = 910-2350 $M^{-1}cm^{-1}$) in the $[Co^{II}(PNNP)(MeCN)][BF_4]_2$ were assigned to charge transfer transitions in the metal complexes containing phenanthroline-based ligand. The CT band in the five-coordinated $[Co^{II}(PN)_2(MeCN)][BF_4]_2$ displayed CT at 450 nm with ε = 902 $M^{-1}\,cm^{-1}$ which is similar in intensity to the band at 456 nm (ε = 910 $M^{-1}\,cm^{-1}$). However, two more CT transitions were observed in the $[Co^{II}(PNNP)(MeCN)][BF_4]_2$ with relatively higher molar absorptivity possibly as a result of the extended π conjugation system in the phenanthroline ligand compared to pyridine ligands in the $[Co^{II}(PN)_2(MeCN)][BF_4]_2$. The very weak low-energy band centred at 645 nm (ε = 208 $M^{-1}\,cm^{-1}$) was then assigned as a d-d transition. The molar extinction of d-d transition band in this complex is consistent with the d-d transition in five-coordinated Co(II) complex (as listed in **Table 2.14**, **chapter 2**).

The complex $[Co^{II}(PNNP)(MeCN)][BF_4]_2$ is a paramagnetic species in solution with a magnetic moment of 2.42 Bohr Magneton from spin and orbital angular momentum indicating a low-spin, Co(II) d^7 complex with one unpaired electron (S = 1/2). The magnetic moment of this complex is consistent with the value for the five-coordinate Co(II) complex (~2.83 B.M.) reported in the literature.[324] The large magnetic moment is observed because of an orbital contribution associated with the energy proximity of d_{yz} and d_{xz}. In contrast, the low-spin Co(II), d^7 $Co^{II}(PN)_2(MeCN)][BF_4]_2$ with similar structural geometry exhibits the relatively small effective magnetic moment (μ= 1.64 B.M.) due to magnetic spin only momentum with one unpaired electron.

The complex $[Co^{II}(PNNP)Cl_2]$ is not soluble in MeCN, therefore, the UV-Vis spectrum of this complex was recorded in 4% v/v DCM in MeCN (**Figure 4.31** a, pink curve). Multiple absorption bands were observed in the visible region at 514, 590 and 640 nm with extinction coefficients between 180-235 $M^{-1}\,cm^{-1}$ suggesting a characteristic of the d-d transitions of a five- or four-coordinate Co(II) complex.[235] Moreover, the absorption of $[Co(PNNP)Cl_2]$ in 4% v/v DCM in MeCN was completely different from the solution of this complex in DCM (**Figure 4.31** b, blue curve) suggesting a mixture of pseudo tetrahedral and the five-coordinated $[Co(PNNP)Cl]^+$ complex in 4% v/v DCM/MeCN solution. The UV-Vis spectrum (**Figure 4.31** a, red) of $[Co^{II}(PNNP)Cl][BAr^F{}_4]$ showed similar absorption bands to those observed for $[Co(PNNP)Cl_2]$ in 4% v/v DCM in MeCN (**Figure 4.31** a, pink) which confirmed the existence of $[Co^{II}(PNNP)Cl]^+$ formed by dissociation of a Cl^- ligand in $[Co^{II}(PNNP)Cl_2]$. This $[Co^{II}(PNNP)Cl]^+$ species might form a mixture of 4- and 5-

coordinate complex in the solution. Generation of the mixture of 4- and 5-coordinated species was also evidenced in the UV-Vis studies of the five-coordinated $[Co^{II}cis\text{-}(PN)_2Cl]^+$ and the $[Co^{II}(PN)_2Cl_2]$ as discussed in the **section 2.5.4.2** and **2.5.4.3**, respectively. These multiple bands were also observed in the solution of the $CoCl_2$ in MeCN solution (**Figure 4.31**, b, green) which contributed to the $^4T_1(P) \leftarrow {}^4A_2(F)$ transition in the tetrahedral Co(II) d^7complex.

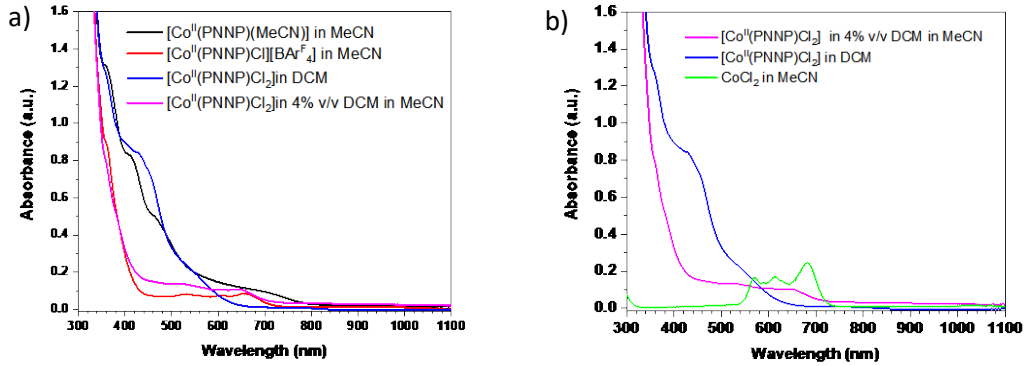

Figure 4.31. The UV-Vis spectrum (a) of $[Co^{II}(PNNP)(MeCN)][BF_4]_2$ ($5.75x10^{-4}$ M in MeCN) compared to the spectrum of $[Co^{II}(PNNP)Cl][BAr^F{}_4]$ ($4.81x10^{-4}$ M) in MeCN (red) $[Co^{II}(PNNP)Cl_2]$ ($5.75x10^{-4}$ M) in 4% v/v DCM in MeCN (pink), and the solution in DCM (blue). The UV-Vis spectrum (b) of $[Co^{II}(PNNP)Cl_2]$ in solution compared to the spectrum of $CoCl_2$ precursor ($5.75x10^{-4}$ M) in MeCN (green).

The UV-Vis spectrum of $[Co(PNNP)Cl_2]$ in DCM solution displayed CT bands at similar wavelengths to the CT tansitions in the $[Co(PNNP)(MeCN)]^{2+}$: however; the d-d transion in the $[Co(PNNP)Cl_2]$ in DCM at 735 nm showed very weak intensity (16 $M^{-1}\,cm^{-1}$). The higher ε value of d-d transition in the $[Co^{II}(PNNP)(MeCN)][BF_4]_2$ than that of $[Co^{II}(PNNP)Cl_2]$ may possibly be due to overlapping with a CT band.

Magnetic susceptibility measurements for $[Co^{II}(PNNP)Cl][BAr^F{}_4]$ yielded the magnetic moment of 4.87 Bohr Magneton suggested that it is a paramagnetic compound in solution showing a high spin configuration with three unpaired electrons (S=3/2). The μ_{eff} = 4.87 B.M. for $[Co^{II}(PNNP)Cl][BAr^F{}_4]$ corresponded to spin and orbital angular momentum of three unpaired electrons in 5-coordinate, Co(II), d^7complexes.[325, 326] This value is in the range 4.70-5.00 B.M. which are general for a high spin cobalt (II) system.

UV-Vis absorption and magnetic properties of the cobalt(I) complexes

The UV-Vis spectrum of cobalt (I) complexes (**Figure 4.32**) is completely distinct from those for the Co(II) complexes. The $[Co^{I}PNNP]^{+}$ and $[Co^{I}(dPNNP)]$ showed deep green color solutions in MeCN and toluene, respectively and exhibited various intense absorption bands in the UV-Vis and near IR regions. These bands with large molar absorptivity (1990-3250 M^{-1} cm^{-1}) for $[Co^{I}PNNP]^{+}$ and with considerably greater ε values (3280-18960 M^{-1} cm^{-1}) for $[Co^{I}dPNNP]$ contributed to charge transfer transitions. It was found that the complex with anionic dPNNP ligand showed more prominent CT character with relatively higher ε values. The intense CT bands are consistent with the UV-Vis spectrum of Co(I) complexes with a terpyridine-amine ligand at 572 and 685 nm (ε = 1738 and 1570 M^{-1} cm^{-1}) exhibiting intense absorption in the visible and near IR regions. The two CT bands were assigned to the respective intraligand charge transfer (ILCT) and metal-to-ligand charge transfer (MLCT) transitions.[327, 328]

The magnetic susceptibility measurement for $[Co^{I}(PNNP)][PF_6]$ complex gave μ_{eff} = 4.34 B.M. which suggested a high spin, d^8, Co(I) complex containing two unpaired electrons (S=1).[329] The difference in spin state between the low-spin $[Co^{I}(dPNNP)]$ and the high-spin $[Co^{I}(PNNP)][PF_6]$ complex may possibly be due to the different degree in distortion from the ideal square planar structure as observed in the X-ray crystal structure of these two complexes (**Figure 4.29**). The structure of $[Co^{I}(PNNP)][PF_6]$ shows more distorted square planar geometry with the N1-Co1-P2 angle of 156.30(6) Å, while the $[Co^{I}(dPNNP)]$ has the same bond angle of N2-Co1-P2 angle = 162.86(5) Å.

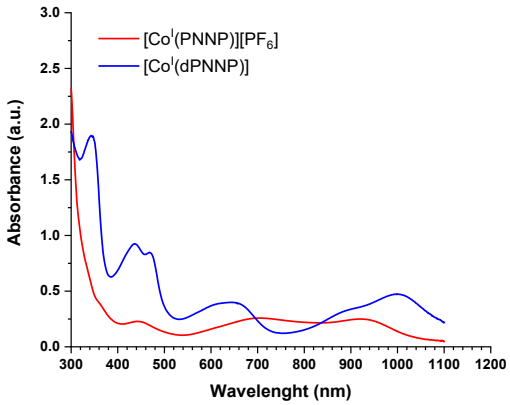

Figure 4.32. The UV-Vis spectrum of $[Co^{I}(PNNP)][PF_6]$ ($1.25x10^{-4}$ M in MeCN, red) and the spectrum of $[Co^{I}(dPNNP)]$ ($1.00x10^{-4}$ M in toluene, blue).

The CV characterization of the $[Co^{II}(PNNP)(MeCN)][BF_4]_2$ and $[Co^{II}(PNNP)Cl_2]$

The cyclic voltammogram for $[Co^{II}(PNNP)Cl_2]$ was recorded in 8% v/v CH_2Cl_2 in MeCN with 0.1 M $TBAPF_6$ as electrolyte solution. A small amount of DCM is needed to dissolve the complex for CV measurements.

Table 4.18. Electrochemical characterization data of the $[Co^{II}(PNNP)(MeCN)][BF_4]_2$ and the $[Co^{II}(PNNP)Cl_2]$ in acetonitrile solution containing 0.1 M $TBAPF_6$.

complex	$E_{1/2}$ (ΔE_p, mV)			
	$Co^{III/II}$	$Co^{II/I}$ (ΔE_p)	Co(I/0) or Co^{I}(phen/phen$^{\bullet-}$)	E_{pa} of phen/phen$^{\bullet-}$
PNNP ligand	-	-	-	0.59,0.79
$[Co^{II}(PNNP)Cl_2]$	E_{pa} 0.25 E_{pc} -0.10	-1.17 (100)	-1.67	-2.01
$[Co^{II}(PNNP)(MeCN)][BF_4]_2$	-	-1.00(71)	-1.84 (74) -2.48 V	-

The CV (**Figure 4.33**) of $[Co^{II}(PNNP)(MeCN)][BF_4]_2$ showed two fully reversible redox processes at -1.00 V and -1.84 V. The first reversible wave at -1.00 V (ΔE_p = 70 mV) is tentatively assigned to a metal-centred reduction of Co(II) to Co(I) couple which appeared in potential near to the redox couple of Co(II/I) in the previous series. However, the second reversible wave at the potential -1.8 V vs $Fc^{0/+}$ could possibly be attributed to a Co(I/0) redox couple or to a ligand reduction of $phen^{0/-}$ wave. This second redox couple around -2.0 V vs $Fc^{0/+}$ was tentatively assigned to a ligand based reduction in transition metal complexes containing polypyridyl ligands.[330-334] The irreversible reduction at E_{pc} = -2.5 V could then be a metal-centred reduction of $Co^{I/0}$ couple which corresponded to the characteristic of metal-centred reduction in the bis-chelating pyridine phosphine, $[Co^{II}(PN)_2(MeCN)]^{2+}$ complex (**section 2.5.5.1**, **Chapter 2**). However, a reduction of Co(I) to Co(0) appeared at much more negative potential at -2.48 V possibly due to more electron density in radical anion of the phen ligand which is reduced prior to the metal-centred reduction of Co(I) to Co(0) in this complex.

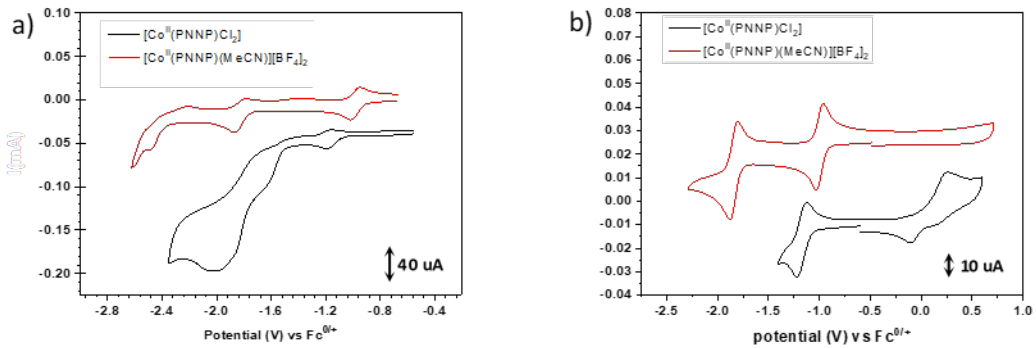

Figure 4.33. Cyclic voltammogram (a) of $[Co^{II}(PNNP)Cl_2]$ complex (1 mM, 8% v/v DCM in CH_3CN) with 0.1 M $TBAPF_6$ at the scan rate 100 mV/s, black curve. Compared to the CV of $[Co^{II}(PNNP)MeCN][BF_4]_2$ 1 mM, in CH_3CN (red); (b) CVs in the potential window of Co(III/II) and Co(II/I) in the complexes.

Upon scanning to negative direction (**Figure 4.33** a), the CV of $[Co^{II}(PNNP)Cl_2]$ showed a first quasi-reversible redox process at -1.17 V vs $Fc^{0/+}$ with ΔE_p = 100 mV which was assigned to a metal-centred Co(II/I) redox couple. The irreversible reduction waves at more negative potential -1.67 V are tentatively assigned to the ligand-centred reduction concomitant with a loss of chloride ligand in this complex. According to the previous literature, an irreversible reduction wave around -2.6 V vs $Fc^{0/+}$ for a pincer cobalt (II) amido complexes containing a Cl^- ligand was assigned to be a dissociation of chloride following one-electron transfer from the electrode to the complex.[335] Moreover, we also assumed that the irreversible wave could be possibly due to a chloride ligand loss after a stepwise two electron reduction at the metal-centred Co(II/I) redox couple and ligand-centred reduction to form $[Co^{I}(PNNP^{\bullet-})(MeCN)(Cl)]^-$ species. This evidence is similar to the previous literature reported that ligand-centred reduction of $[Ru^{II}(bpy)(tpy)(Cl)]^+$ complex at -1.91 V vs $Fc^{0/+}$ resulted in Cl^- loss to give $[Ru^{II}(bpy)(tpy^-)(MeCN)]^+$.[336]. The CVs in **Figure 4.33** b showed the Co(III/II) couple in the $[Co^{II}(PNNP)Cl_2]$ upon sweeping potential to positive direction, while the Co(III/II) couple in the MeCN analogue was not observed. This suggested that Cl^- ligands in $[Co^{II}(PNNP)Cl_2]$ could stabilize the higher Co(III) oxidation state.

4.3.12 Electrocatalytic H_2 evolution and electroreduction of CO_2

CV studies of the [Co^{II}(PNNP)Cl$_2$] and [Co^{II}(PNNP)(MeCN)] using TFA as H$^+$ source

The CV responses of these two complexes under catalytic conditions showed similar current increases at E_{cat} -1.21 V near the Co(II/I) couple upon increasing the concentration of TFA acid as shown in **Figure 4.34 a** for the $[Co^{II}(PNNP)(MeCN)]^{2+}$ and **Figure 4.34 b** for the $[Co^{II}(PNNP)Cl_2]$. The higher current density at similar reduction potential (**Figure 4.34 c**) near the second redox couple in these two complexes suggested more rapidly catalyzed reaction but much higher overpotential is required compared to the first catalytic process operated via a metal-centred Co(II/I) couple. The plot of i_{cat}/i_p at Co(II/I) couple versus concentration of TFA (**Figure 4.34 d**) indicated that the $[Co^{II}(PNNP)Cl_2]$ catalyzed H^+ reduction with faster catalytic rate than the corresponding MeCN complex.

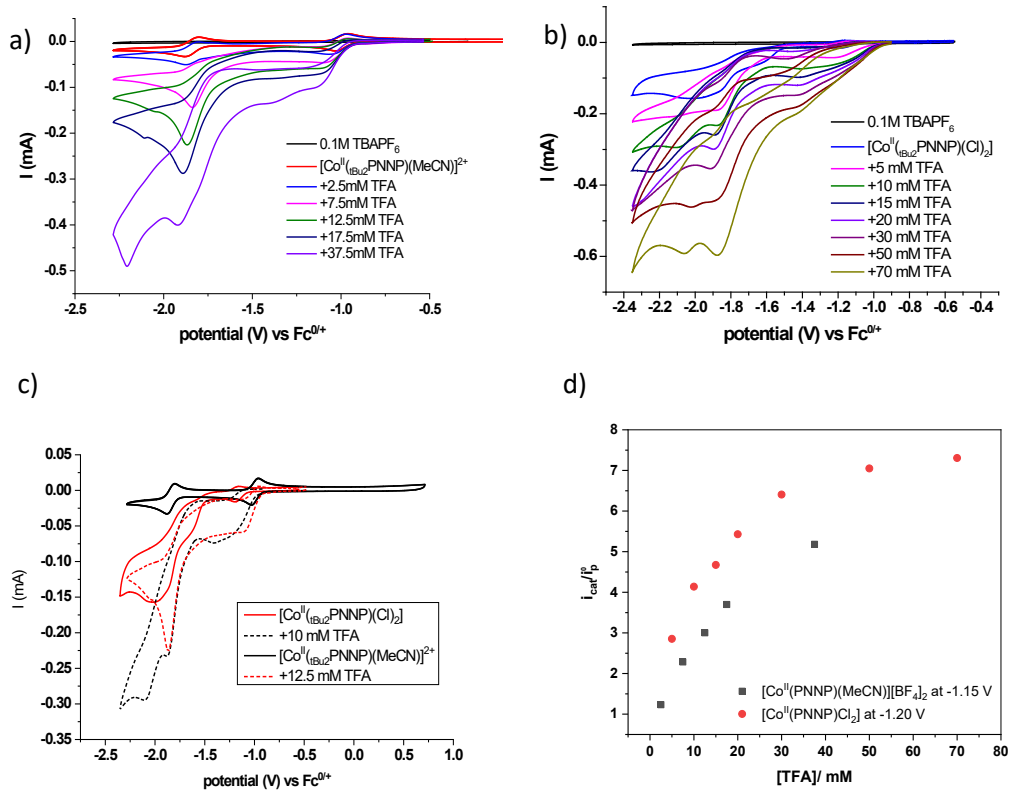

Figure 4.34. CVs at scan rate 100 mV/s of (a) $[Co^{II}(PNNP)Cl_2]$ and (b) $[Co^{II}(PNNP)(Cl)_2]$ (1 mM) in CH_3CN with 0.1 M $TBAPF_6$ upon titration with TFA acid, (c) comparison between CVs of these two complex under catalytic condition using TFA as H^+ source, and (d) plot of i_{cat}/i_p for each complex against the acid concentrations.

The control experiment (**Figure A 4.18**) of the free ligand with 50 mM TFA did not show current enhancement over the same potential window as that of the complex under the similar conditions. This confirmed that the enhancement of current at the potentials -1.21 V and -1.9 V corresponds to catalytic waves for H_2 evolution operated by the complex

The data for overpotential determination of these two complexes are listed in **Table 4.19**. The $E_{1/2}^{cat} = -1.03$ V was obtained for the $[Co^{II}(PNNP)(MeCN)][BF_4]_2$ which is slightly more positive than the $E_{1/2}^{cat}$ .of -1.06 V for the $[Co^{II}(PNNP)Cl_2]$. This corresponded to the overpotential of 290 mV for $[Co^{II}(PNNP)Cl_2]$ and 260 mV for $[Co^{II}(PNNP)(MeCN)][BF_4]_2$. The overpotential of $[Co^{II}(PNNP)Cl_2]$ for H_2 evolution is considerably decreased by 200 mV as compared to the cobalt(II) analogue supported by bis-chelating P,N ligand. The lowering in overpotential observed in this series is possibly due to using more extended π-electron system of phenanthroline ligand resulting in stabilization of Co (I) intermediate.

Table 4.19. Catalytic potential and overpotential for each complex (0.5 mM) in acetonitrile containing 0.1 M $TBAPF_6$ acidified with TFA acid.

Complex	[TFA]/ mM	E_{cat} (V)	$E_{cat/2}$ (V)	η (mV)
$[Co^{II}(PNNP)Cl_2]$	50	-1.21	-1.06	290
$[Co^{II}(PNNP)(MeCN)][BF_4]_2$	37.5	-1.15	-1.03	260

Overpotential (η) = $E_{cat/2}$-$E^0_{HA/H2}$, $E^0_{HA/H2}$ for TFA acid in MeCN = -0.77

Electrochemical CO_2 reduction activity of $[Co^{II}(PNNP)Cl_2]$ and $[Co^{II}(PNNP)(MeCN)][BF_4]_2$ in saturated-CO_2 acetonitrile solution

The electrocatalytic reduction of CO_2 by the $[Co^{II}(PNNP)Cl_2]$ and $[Co^{II}(PNNP)MeCN]^{2+}$ complexes were also examined by CV technique in CO_2-saturated acetonitrile solution containing 0.1 M $TBAPF_6$. The CV studies of $[Co^{II}(PNNP)Cl_2]$ was performed in 8% v/v DCM in MeCN due to lack of solubility in MeCN solution. In this work, external H^+ source with different pKa such as H_2O (pKa = 38-41 in MeCN [61] and 2,2,2-trifluoroethanol (TFE, pKa = 35.4 in MeCN) was used for screening their electrocatalytic CO_2 reduction activity in CH_3CN. These acids are commonly used as proton sources for electrocatalytic CO_2 reduction in organic media as reported in the literature.[61, 337, 338]

CV studies of CO_2 reduction activity of the $[Co^{II}(PNNP)Cl_2]$

CV measurements of the $[Co^{II}(PNNP)Cl_2]$ complex in CO_2-saturated CH_3CN exhibited no current enhancement: however; a large positive shift of the Co(II/I) redox couple and Co(I/0) or phen/$phen^{\bullet-}$ reduction potential could possibly imply formation of a CO_2 adduct (**Figure 4.35**). It could be assumed that two Cl^- losses following uptake one electron led to a generation of available binding site for CO_2 molecule. The loss of two Cl^- ligands is consistent with a chemical reduction of the $[Co^{II}(PNNP)Cl_2]$ complex with $NaBH_4$ in MeOH to give the corresponding $[Co^{I}(PNNP)]^+$ species which was confirmed by X-ray crystal structure as shown in **section 4.3.5**. A much more positive shift of Co(II/I) redox wave of the $[Co^{II}(PNNP)Cl_2]$ was observed when H^+

(0.9 M TFE) was added to the solution, although there was no change in the current near Co(I/0) or phen/phen$^{\bullet-}$ reduction potential. A large shift of Co(II/I) couple indicated that H^+ could stabilize the CO_2-Co(I) intermediate formed by one electron reduction of the $[Co^{II}(PNNP)Cl_2]$.

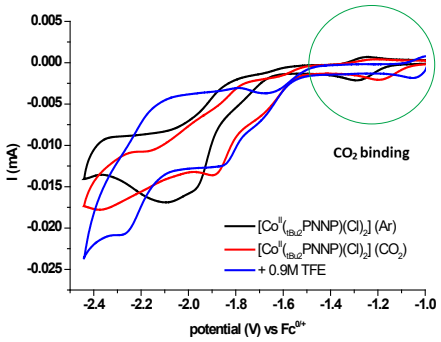

Figure 4.35 CVs of $[Co^{II}(PNNP)Cl_2]$ (1mM) at the scan rate 100 mV/s in CH_3CN containing 0.1 M $TBAPF_6$ under Ar, compared with the CO_2-saturated solution and addition of 0.9 M TFE.

CV studies of CO_2 reduction activity of $[Co^{II}(PNNP)(MeCN)][BF_4]_2$

Interestingly, the CV of $[Co^{II}(PNNP)(MeCN)]^{2+}$ exhibited maximum current enhancement at -2.33 V in CO_2 -saturated solution with no additional H^+ source (**Figure 4.36**). Moreover, a small increase in current and a loss of reversibility at the second reversible wave of Co(I/0) or Co^{I}(phen/phen$^{\bullet-}$) couple indicated formation of a CO_2 adduct as observed in the dichloride analogue. The positive shift of redox couples in these two complexes in the presence of CO_2 suggested the binding of CO_2 could occur at the reduced metal centre supported by the tetradentate PNNP ligand. The CO_2 binding at the reduced Co(0) intermediate formed after two single electron reduction processes of the corresponding Co(II) complex was also generally observed in the cobalt catalyst for CO_2 reduction.[114, 116]

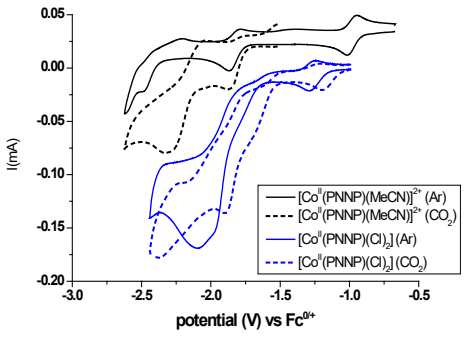

Figure 4.36. Cyclic voltammograms (CVs) of $[Co^{II}(PNNP)Cl_2]$ (1 mM) at the scan rate 100mV/s in CH_3CN containing 0.1 M $TBAPF_6$ under Ar, and the complex in CO_2-saturated solution, compared to the $[Co^{II}(PNNP)(MeCN)]^{2+}$ under similar conditions.

According to this evidence, we assumed that a strong interaction between reduced Co(0) metal centre and electrophilic CO_2 molecule concomitant with transformation of CO_2 to CO as product could happen. The CV response of $[Co^{II}(PNNP)(MeCN)]^{2+}$ in the solution with proton source (TFE or H_2O) shows similar current enhancement (**Figure 4.37**) In the case of using TFE as proton source, a slight increase in i_{cat} at the potential -2.28 V was obtained as shown in **Figure 4.37** b exhibiting i_{cat}/i_p = 4.1 as summarized in **Table 4.20.** A control experiment with $[Co^{II}(PNNP)(MeCN)]^{2+}$ and 2% water in acetonitrile solution with no CO_2 exhibited no increase in the current near to Co(I/0) redox couple (in **Figure 4.37** c). This evidence proved that the increase of current at this potential originated from CO_2 reduction activity of the complex.

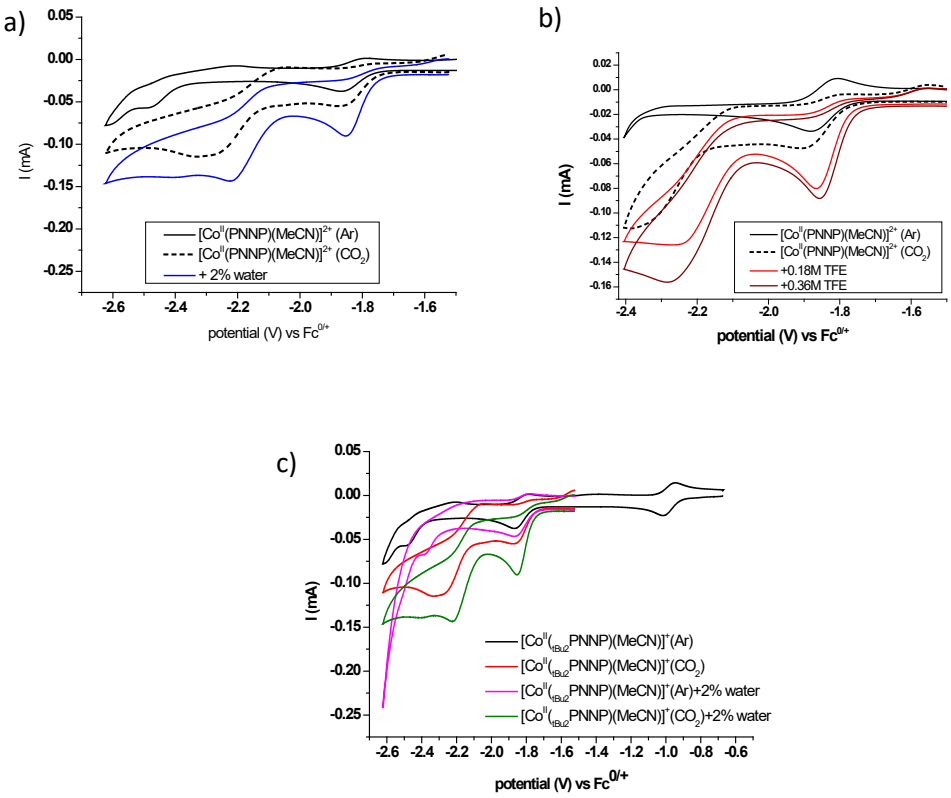

Figure 4.37. CVs of $[Co^{II}(PNNP)(MeCN)]^{2+}$ (1 mM) at the scan rate 100mV/s in CH_3CN containing 0.1 M $TBAPF_6$ under Ar, compared with the CO_2-saturated solution and addition of 2% water (a), and upon adding 0.36 M TFE (b), CVs of the complex in CO_2-saturated CH_3CN solution with 2% water compared to the CV of this complex with 2% water under Ar.

Table 4.20. Electrochemical data from CV measurements and conditions for the studies of electrocatalytic CO_2 reduction activity of each complex.

H^+ source	**$[Co^{II}(PNNP)Cl_2]$**		**$[Co^{II}(PNNP)MeCN)][BF_4]_2$**	
	[acid] (M)	i_{cat}/i_p (E_{cat})	[acid] (M)	i_{cat}/i_p (E_{cat})
TFE	0.9	~1 (-1.85 V)	0.36	4.1 (-2.28 V), 3.1 (-1.86 V)
H_2O	-		2%	3.1 (-2.29 V) 2.9 (-1.85 V)

.

4.4 Conclusion

Synthesis, UV-Vis/CV characterisation and magnetic properties

The novel Co(II) complexes supported by the tetradentate phosphino based phenanthroline ligand including the $[Co^{II}(PNNP)Cl_2]$, $[Co^{II}(PNNP)Cl][BAr^F{}_4]$ and $[Co^{II}(PNNP)(MeCN)][BF_4]_2$ were successfully synthesized in high percent yield. All of these complexes were structurally characterized by X-ray crystallographic determination. The UV-Vis studies of the $[Co^{II}(PNNP)Cl_2]$, $Co^{II}(PNNP)Cl][BAr^F{}_4]$ and $[Co^{II}(PNNP)(MeCN)][BF_4]_2$ indicate the more intense CT transitions in the visible region compared to the Co(II) complex supported by bis chelating P,N ligands, $[Co^{II}(PN)_2MeCN]$.

Furthermore, the new Co(I) complexes: $[Co^{I}PNNP][PF_6]$ and $[Co^{I}(dPNNP)]$ were isolated and structurally characterised by X-ray crystallographic technique. These two complexes with coordination number four adopt a distorted square planar geometry. The Co(I) complexes display CT transitions with intense absorption bands over the range from visible to near IR regions (340-1000 nm). The magnetic properties of $[Co^{I}PNNP][PF_6]$ in solution indicate a paramagnetic species with two unpaired electrons which is in agreement with a high spin, distorted square planar geometry, accounting for the lack of NMR spectrum. In contrast, the dearomatized $[Co^{I}(dPNNP)]$ complex containing the anionic ligand with the similar geometry is a diamagnetic species exhibiting a low spin, Co(I), d^8 electron configuration.

The redox properties in the $[Co^{II}(PNNP)(MeCN)][BF_4]_2$ display two fully reversible couple of the first Co(II/I) wave and the second redox couple which was tentatively assigned as the ligand-centred reduction in the complex. The most negative reduction potential was assigned to the Co(I/0) couple. The $[Co^{II}(PNNP)Cl_2]$ show quasi-reversible Co(III/II) and Co(II/I) couple. Moreover, the different second reduction process between the reversible couple in the $[Co^{II}(PNNP)(MeCN)][BF_4]_2$ and irreversible wave in the $[Co^{II}(PNNP)Cl_2]$ possibly due to a chemical reaction (Cl^- loss) occur following a sequential two electron reduction of the $[Co^{II}(PNNP)Cl_2]$.By changing the bis-P,N chelating phosphino based pyridine to the PNNP tetradentate phosphino based phenanthroline causes a positive shift of Co(II/I) redox couple in the $[Co^{II}(PNNP)Cl_2]$ by 130 mV from the Co(II/I) couple in the $[Co^{II}(PN)_2Cl_2]$. This demonstrates that the reduced Co(I) species with the dichloride ligands can be greatly stabilized by more π-conjugated system in the $[Co^{II}(PNNP)Cl_2]$.

Reactions with $NaBH_4$, $NaBEt_3H$ and LiMe

The reaction of $[Co^{II}(PNNP)Cl_2]$ with $NaBH_4$ causes formation of the corresponding $[Co^{I}(PNNP)]^+$ species as characterized by the X-ray structure. The reaction of $[Co^{II}(PNNP)Cl_2]$ with relatively stronger hydride reagent ($NaBEt_3H$) generates a mixture of products including the dearomatized $[Co^{I}(dPNNP)]$, $[Co^{I}(mPNNP)]$, hydrogenated intermediate and an unidentified product (**Scheme 4.13**). A hydride intermediate would be expected to form at the initial reaction time but was not observed in the NMR studies of the $[Co^{II}(PNNP)Cl_2]$ with 2.0 eq $NaBEt_3H$. The hydride analogue of $[Co^{II}(PNNP)(MeCN)][BF_4]_2$ was observed and is more stable than the expected $[Co^{I}(PNNP)(H)(Cl)]^-$. The MLC reactivity by elimination of H_2 from the hydride chloride complex is faster than H_2 liberation from $[Co^{I}(PNNP)(H)(MeCN)]$ as a result of more electron density at the metal centre containing a Cl^- ligand. The dearomatized $[Co^{I}(dPNNP)]$ is found to be the product formed by this MLC H_2 elimination. A reversible H_2 elimination/addition for the dearomatized $[Co^{I}(dPNNP)]$ complex possibly leads to formation of the hydrogenated [CoI(mPNNP)] and its isomers such as the hydrogenated intermediate and unidentified products in the solution. One of the hydrogenated $[Co^{II}(mPNNP)Cl]$ products was confirmed by X-ray crystallography indicating that $NaBEt_3H$ could act as a reducing agent to form the $[Co^{I}(mPNNP)]$ as evidenced in the NMR studies.

Reaction of the $[Co^{II}(PNNP)Cl_2]$ with 1.0 eq LiMe is an approach for selective preparation of the dearomatized [Co(dPNNP)] which is generated by an irreversible loss of methane from $[Co^{I}(PNNP)Me]$ (**Scheme 4.8**). Moreover, the clean conversion of [Co(dPNNP)] to the corresponding hydrogenated [Co(mPNNP)] was achieved by adding 4 bar of H_2. The hydrogenated intermediate was postulated to form via an η^2-H_2 complex which then converted to [Co(mPNNP)].

The X-ray comparison between the $[Co^{I}(dPNNP)]$ and $[Co^{II}(mPNNP)Cl]$

The X-ray structure of [Co(dPNNP)] complex confirmed the dearomatized structure of PNNP ligand and corresponded to a diamagnetic species of [Co(dPNNP)] with a low-spin, d^8 configuration and a distorted square planar geometry. In contrast, $[Co^{II}(mPNNP)Cl]$ with the hydrogenated PNNP ligand with one Cl^- coordinated at metal centre adopts a distorted square pyramidal complex with d^7-Co(II) metal centre resulting in a paramagnetic species exhibiting broad NMR signals. The modified PNNP ligands in the solid-structure of these two complexes include an anionic nitrogen of the dearomatized pehnanthroline ring.

H_2 evolution and CO_2 reduction activity

The new Co(II) complexes supported by the more conjugated π system of the tetradentate phenanthroline ligand could catalyze H_2 evolution at lower overpotential than the Co(II) catalysts supported by bis P,N chelating ligands. This lowering in overpotential could be achieved possibly due to a stabilization of Co(I) intermediate by conjugated π-electron system of phenanthroline ligand. Moreover, a chemical reduction of the $[Co^{II}(PNNP)Cl_2]$ and $[Co^{II}(PNNP)(MeCN)][BF_4]_2$ suggested a liberation of H_2 via a metal-ligand cooperativity of the corresponding cobalt hydride complex. The CO_2 reduction activity of the $[Co^{II}(PNNP)(MeCN)][BF_4]_2$ in the presence of H^+ source (TFE or H_2O) occurs at the doubly reduced species. This might involve a ligand-centred based CO_2 reduction activity.

Chapter 5

5.1 Concluding remarks and future work

5.1.1 Cobalt complexes supported by the P,N and PNNP ligand/s and their reactivity

In this thesis, we show that the PN and PNNP ligands can stabilize cobalt metal centres in various oxidation states (oxidation number from +1 to +3). In Chapter 2, we show that successful isolation and full characterisation of the new Co(II) complexes: $[Co^{II}(PN)_2(MeCN)][BF_4]_2$, $[Co^{II}$*cis*-$(PN)_2Cl][PF_6]$, $[Co^{II}(PN)_2Cl_2]$ and two novel cobalt(III) hydride complexes with bis-P,N chelating ligands, $[Co^{III}(PN)_2(H)(MeCN)][PF_6]_2$ and $[Co^{III}(PN)_2(H)(Cl)][PF_6]$ can be achieved under mild reaction conditions using $NaBH_4$ in a MeOH solution under N_2 at room temperature. The hydride ligand can be greatly stabilized by the Co(III) oxidation state with the right combination of the strong field P,N chelating ligands. These two hydride complexes are low-spin, d^6 diamagnetic species exhibiting sharp and well-separated NMR signals. The structural characterisation in solution corresponds to the solid-state X-ray structure which reveals a distorted octahedral geometry where the H^- is *trans* to the axial Cl^- or MeCN and *cis* to the two chemically equivalent P atoms in their structure. Moreover, $[Co^{III}$*cis*-$(PN)_2Cl_2][PF_6]$ is easily prepared through the oxidation of the $[Co^{II}(PN)_2Cl_2]$ by the air bubbling of the MeOH solution. The solid-state structure of $[Co^{III}$*cis*-$(PN)_2Cl_2][PF_6]$ reveals the *cis*-configuration between the two phosphorus atoms, while, the 2P atoms in the two Co(III) hydride complexes are *trans* to each another. The *trans* configuration of those two phosphoruses cause a rigid structure of the hydride complexes in a solution. They show a well-resolved triplet H^- signal with $^2J_{cis\ H.P} = \sim 60$ Hz at δ -19.05 for $[Co^{III}(PN)_2(H)(Cl)]^+$.

Chapter 4 demonstrates the synthesis and characterisation of novel cobalt complexes with the PNNP ligand. From the view of ligand synthesis, the two ligands are easy to prepare with moderate percentage yield (59% for the PN ligand and 34% for the PNNP ligand). The method for PNNP ligand preparation is less complicated than the preparation of PN ligand due to purification by recrystallisation instead of distillation under high vacuum condition for the P,N ligand. Interestingly, the isolable cobalt complexes with the PNNP ligand are found to be different from the complexes supported by the two PN ligands. Most of compounds which were successfully isolated are cobalt(I) complexes, while the Co(III) hydride with the PNNP ligand are relatively more reactive compared to the Co(III)-H complexes with the PN ligands. Furthermore, these PNNP complexes exhibit very different reactivity showing three types of reaction that are not observed with the complexes with bis-PN ligands: firstly, chemical reduction to low spin Co^I complexes, and secondly, dearomatization via metal-ligand cooperation, thirdly hydrogenation

of the ligand associated with dearomatization. This reactivity is reminiscent of the work of the Milstein and Chirik groups summarized in the introduction (chapter 4).

5.1.2 Electronic/magnetic properties and redox chemistry

We demonstrate that the PN and PNNP ligand/s can stabilize various oxidation state of cobalt complexes. The UV-Vis spectrum of Co(I), Co(II) and Co(III) complexes are completely different due to distinct electronic structure and geometry of the complexes. The electronic properties of the Co(II) complexes with P,N ligands by UV-Vis characterisation are very important to elucidate the lability of $[Co^{II}(PN)_2Cl_2]$ and $[Co^{II}$*cis*-$(PN)_2Cl][PF_6]$. The intense and multiple d-d transitions, which ascribed to the 4- or 5-coordinate species formed in a solution by a dissociation of a Cl^- or a PN ligand from the solid-state structure, are typically found in the UV-Vis spectrum. These complexes are expected to be a high spin, Co(II), d^7 with three unpaired-electrons, while the $[Co^{II}(PN)_2(MeCN)][BF_4]_2$ is a low-spin, Co(II), d^7 with one unpaired electron. Unlike the labile Co(II) complexes containing Cl^- ligand/s, the MeCN analogue is stable in a solution exhibiting a CT band in the UV-Vis spectrum with no extra d-d transitions belong to 4-coordinate species that would be formed by ligand exchange. The Co(III) complexes are all diamagnetic, d^6, low spin complexes. These complexes including the Co(III) hydrides are six-coordinate with distorted octahedral geometry exhibiting the same structure both in a solution and in a solid state. They show a CT band in the visible region.

The UV-Vis studies of $[Co^{II}(PNNP)Cl_2]$, $[Co^{II}PNNP)Cl][BAr^F{}_4]$ and $[Co^{II}(PNNP)(MeCN)][BF_4]_2$ indicate the more intense CT transitions in the visible region compared to the Co(II) complex supported by bis chelating P,N ligands, $[Co^{II}(PN)_2MeCN]$. $[Co^{II}(PNNP)Cl_2]$ in a MeCN solution is labile, showing Cl^- loss from the complex in the solid state. The $[Co^{II}(PNNP)Cl]^+$ is the most likely species formed in the solution. However, the MeCN derivative, $[Co^{II}(PNNP)(MeCN)][BF_4]_2$ is stable in a solution displaying CT bands in the visible regions with a tail absorption band at 645 nm for a d-d transition.

The ground state electronic structure of the Co(II) complexes: $[Co^{II}(PN)_2(MeCN)][BF_4]_2$ and $[Co^{II}(PNNP)(MeCN)][BF_4]_2$ with an axial MeCN ligand is low-spin (S=1/2). Changing from a MeCN to π-donor Cl^- ligand/s cause an alteration of Co(II) spin state from the low-spin to high-spin complexes (S=3/2) as observed in $[Co^{II}(PN)_2Cl_2]$ and $[Co^{II}(PNNP)(Cl)][BAr^F{}_4]$. We have shown that $[Co^{II}$*cis*-$(PN)_2Cl][PF_6]$ and $[Co^{II}(PN)_2Cl_2]$ are more labile than the low-spin, $[Co^{II}(PN)_2(MeCN)][BF_4]_2$ complex. The similar trend for lability of the Co(II) complexes with the PNNP ligand is observed where the high-spin $[Co^{II}(PNNP)(Cl)][BAr^F{}_4]$ is more labile than the low-spin $[Co^{II}(PNNP)(MeCN)][BF_4]_2$. Therefore, the ground state electronic structure of these Co(II) complexes greatly affects their lability in a solution. The electronic properties of Co(I) complexes:

$[Co^{I}(PNNP)][PF_6]$ and $[Co^{I}(dPNNP)]$ exhibit prominent CT transitions in the visible and near IR regions. The CT bands in the Co(I) complexes are more intense exhibiting relatively large ε values than those observed in the Co(II) analogues.

Furthermore, the replacement of an axial Cl^- ligand by MeCN can alter their electronics and reduction mechanism at the electrode. The first electron transfer to the dicationic complex $[Co^{III}(PN)_2(H)(MeCN)]^{2+}$ requires a less negative potential than that for the corresponding mono cationic $[Co^{III}(PN)_2(H)(Cl)]^+$ by 380 mV via a distinct reduction mechanism. An irreversible Cl^- loss from the reduced $[Co^{II}(PN)_2(H)(Cl)]^0$ species occurs following one-electron transfer to the $[Co^{III}(PN)_2(H)(Cl)]^+$ (E_qC_i pathway) while, a reversible MeCN dissociation is observed from the singly reduced $[Co^{II}(PN)_2(H)(MeCN)]^+$ via an E_rC_r pathway resulting in generation of $[Co^{II}(PN)_2(H)]^+$. Moreover, the first irreversible redox couple for Co(III/II)-H in the hydride $[Co^{III}(PN)_2(H)(Cl)]^+$ appears at much more negative potential by 1.06 V as compared to the quasi-reversible Co(III/II) couple in the $[Co^{III}$*cis*-$(PN)_2Cl_2]^+$ suggesting that the hydride ligand causes high electron density at the metal center. A similar trend is observed for the second electron transfer to the hydride complex which requires much more negative reduction potential as compared to that for the corresponding $[Co^{III}$*cis*-$(PN)_2Cl_2]^+$.

Changing the bis-PN chelating phosphino-based pyridine to the PNNP tetradentate phosphino-based phenanthroline causes a positive shift of Co(II/I) redox couple in the $[Co^{II}(PNNP)Cl_2]$ by 130 mV from the Co(II/I) couple in the $[Co^{II}(PN)_2Cl_2]$. This demonstrates that the reduced Co(I) species with the dichloride ligands can be greatly stabilized by more π-conjugated system in the $[Co^{II}(PNNP)Cl_2]$.

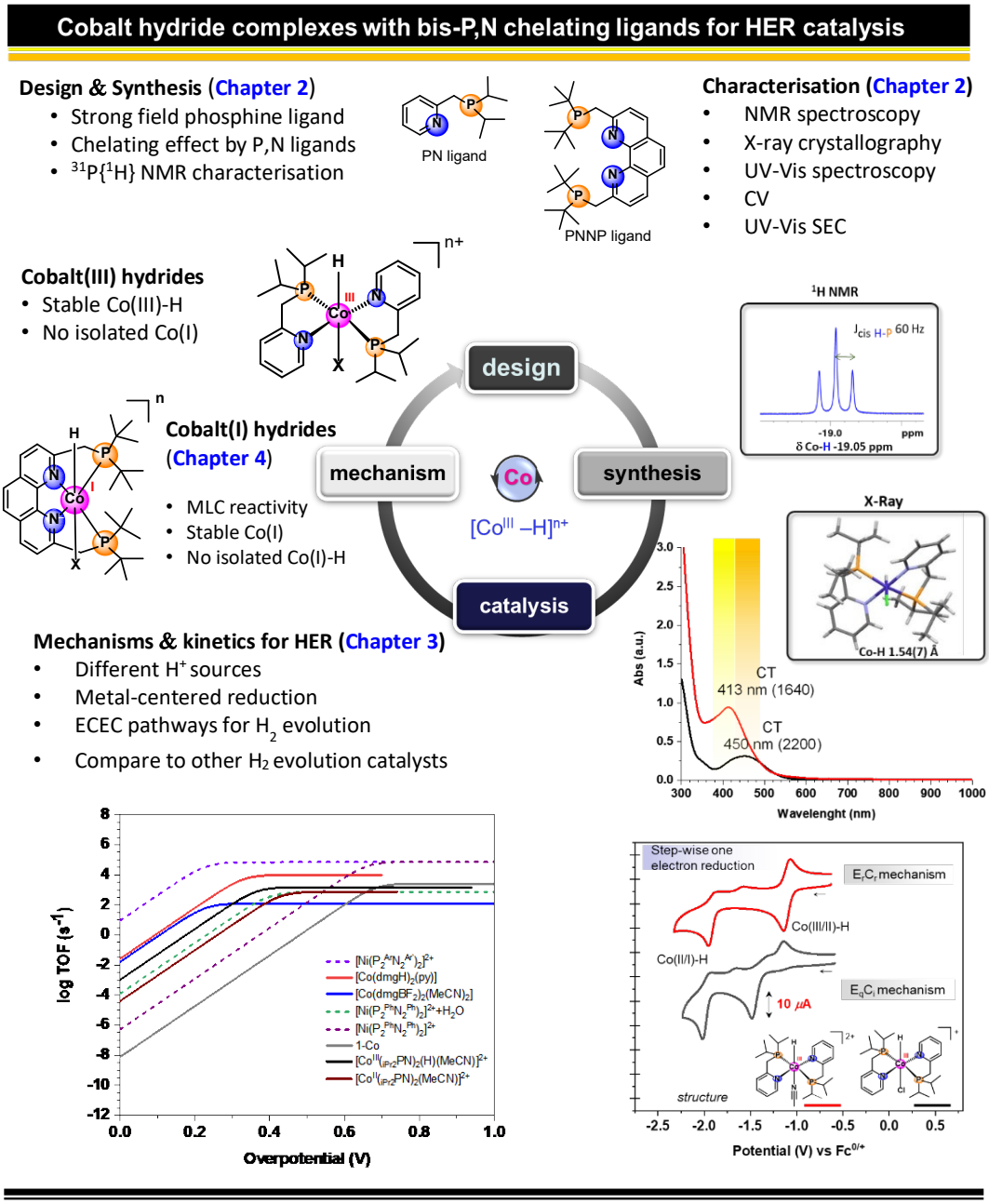

5.1.3 Metal-ligand cooperation

Chapter 4 demonstrates very different reactivity for Co(PNNP) complexes compared to Co(PN)2 complexes of chapters 2 and 3. Especially significant is the selective synthesis of the dearomatized [Co^{I}(dPNNP)] by reaction of [Co^{II}(PNNP)Cl$_2$] with LiMe. This selective formation can be achieved due to an irreversible loss of methane from the [Co^{I}(PNNP)Me]. Moreover, the clean conversion of [Co(dPNNP)] to the corresponding hydrogenated [Co(mPNNP)] was obtained by adding 4 bar of H_2. These are decisive examples of metal-ligand cooperation (MLC). The initial formation of the hydrogenated intermediate was proposed via MLC reactivity of η^2-H_2 complex. This dihydrogen complex may contribute to formation of various hydrogenated

products as observed in a reaction of the $[Co^{II}(PNNP)(MeCN)][BF_4]_2$ and the $[Co^{II}(PNNP)Cl_2]$ with $NaBEt_3H$.

The reaction of $[Co^{II}(PNNP)(MeCN)][BF_4]_2$ with $NaBEt_3H$ suggested liberation of H_2 from the reactive Co(I)-H intermediate. The H-H bond making between the H^- ligand and acidic hydrogen of the benzylic arm in the $[Co^{I}(PNNP)(H)(X)]^n$ (X = Cl (n = -1) or MeCN (n = 0)) resulted in formation of $[Co^{I}(dPNNP)]$ as a minor product with a mixture of three hydrogenated products such as the $[Co^{I}(mPNNP)]$ and the two isomers. It indicated these hydrogenated complexes were produced via distinct pathways for H_2 addition to the $[Co^{I}(dPNNP)]$ by metal-ligand cooperation.

A selective formation of the $[Co^{I}(dPNNP)]$ via MLC reactivity of the $[Co^{I}(PNNP)(Me)]$

- *The $[Co^{I}(PNNP)(Me)]$ generated by a reaction of $[Co^{II}(PNNP)Cl_2]$ with 1.0 eq. LiMe*

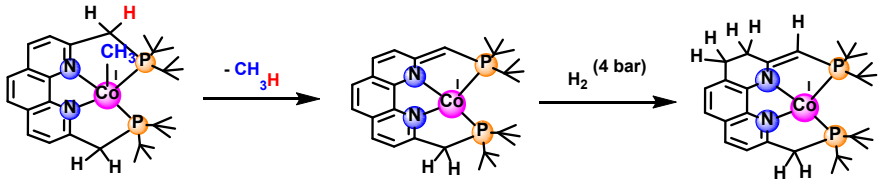

$[Co^{I}(PNNP)(Me)]$ $[Co^{I}(dPNNP)]$ $[Co^{I}(mPNNP)]$

- *The $[Co^{I}(PNNP)(H)(X)]^n$ formed by a reaction of the Co(II) analogue with 2.0 eq. $NaBEt_3H$*

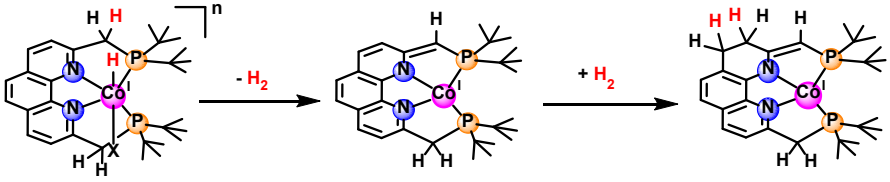

$[Co^{I}(PNNP)(H)(X)]^n$
X = Cl (n= -1) or MeCN (n = 0)

$[Co^{I}(dPNNP)]$

$[Co^{I}(mPNNP)]$
+ 2 isomers

5.1.4 H^+ and CO_2 reduction electrocatalysis

We present the detailed mechanisms for cobalt-catalysed H_2 evolution in Chapter 3. The CV studies of the $[Co^{III}(PN)_2(H)(Cl)]^+$ using different proton sources show H^+ reduction pathways via distinct mechanisms that operate at different reduction potentials. By using TFA acid, $[Co^{III}(PN)_2(H)(Cl)]^+$ catalyses H_2 evolution via ECEC pathways showing catalytic current near the Co(II/I) and Co(III/II)-H couple. This confirmed that the relatively more reduced Co(II)-H species is required for H_2 evolution. The UV-Vis SEC result and scan rate variation analysis indicated that the H_2 evolution step proceeds by protonation of the $[Co^{II}(PN)_2(H)]^+$ via a heterolytic pathway. Using weak CH_3COOH acid as H^+ source requires a doubly reduced Co(I)-H hydride intermediate, thus more negative potential is needed for the catalytic H_2 evolution. The kinetic studies show

that H_2 evolution by $[Co^{III}(PN)_2(H)(MeCN)]^{2+}$ and $[Co^{II}(PN)_2(MeCN)]^{2+}$ is typically dependent on acid concentration by first order catalytic rate reaction. By FOWA plots, the k_{cat} of 1560±6 M^{-1} s^{-1} was obtained for the hydride complex which is about double k_{cat} for $[Co^{II}(PN)_2(MeCN)]^{+}$. The catalytic Tafel plot showed that $[Co^{III}(PN)_2(H)(MeCN)][PF_6]_2$ is a more efficient catalyst than the Co(II) by reaching the TOF_{max} value at relatively lower overpotential. Moreover, their TOF_0 values are in between the TOF_0 of cobaloximes and the $[Ni(P^{Ph}_2N^{Ph}_2)_2]^{2+}$ HER electrocatalyst containing a basic amine group for assisting H^+ transfer to the metal centre. The two electrocatalysts are among the best molecular HECs and have been used as the catalysts in many heterogeneous systems (as shown in chapter 1). We thus assumed that a protonation at a pyridine ring in the $[Co^{II}(PN)_2(MeCN)][BF_4]_2$ and $[Co^{II}$*cis*$-(PN)_2Cl]^{+}$ could mediate formation of the resulting Co(III)-H species by transfer of H^+ to the reduced Co(I) metal centre. We also suggested that protonation of the reduced Co(I) species to generate Co(III)-H species might be the catalytic rate-determining step as suggested by the higher k_{cat} value of $[Co^{III}(PN)_2(H)(MeCN)][PF_6]_2$ than that for $[Co^{II}(PN)_2(MeCN)][BF_4]_2$.

Moreover, for the development of previous HECs based on polypyridyl ligands as discussed in introduction, the extended-π conjugated system can stabilize the Co(I) oxidation state. We applied this approach for the development of our HECs by changing the bis-chelating phosphino based pyridine to the tetradentate phosphino based phenanthroline. By this ligand modification, a positive shift of Co(II/I) redox couple in the $[Co^{II}(PNNP)Cl_2]$ by 130 mV from the Co(II/I) couple in the $[Co^{II}(PN)_2Cl_2]$ is obtained. $[Co^{II}(PNNP)Cl_2]$ catalyses H^+ reduction at lower overpotential than the reaction operated by $[Co^{III}$*cis*$-(PN)_2Cl_2][PF_6]$ by 230 mV. $[Co^{II}(PNNP)(MeCN)][BF_4]_2$ catalyzes H^+ reduction at the lowest overpotential (260 mV) among the HECs in this study and $[Co^{II}(PNNP)Cl_2]$ operates at a comparable overpotential of 290 mV. This demonstrates that the reduced Co(I) species with the dichloride ligands can be greatly stabilized by more π-conjugated system in the $[Co^{II}(PNNP)Cl_2]$.

Moreover, liberation of H_2 via a metal-ligand cooperation might be a possible pathway for H^+ reduction, and MLC cooperation might involve CO_2-catalyzed reduction by the complexes in this series. The preliminary studies of CO_2 reduction activity of the $[Co^{III}$*cis*$-(PN)_2Cl_2)][PF_6]$ and the $[Co^{III}(PN)_2(H)(Cl)][PF_6]$ proved the role of the hydride intermediate for conversion of CO_2 to possible $HCOOH/HCOO^-$ by showing the current increase near the doubly reduced Co(I)-H without the addition of external H^+ source to the catalytic system. However, a proton source is required for $[Co^{III}$*cis*$-(PN)_2Cl_2][PF_6]$ for CO_2 reduction activity at the Co(0) couple. This suggested that formation of a Co(I)-H intermediate by protonation of the reduced Co(0) species would be necessary for CO_2 reduction catalysis by the complexes in this series.

5.1.5 Future perspectives to the development of electrocatalysts for solar fuels production

We have shown that the new Co(II) complexes supported by the more conjugated π system of the tetradentate phenanthroline ligand could catalyze H_2 evolution at lower overpotential than the Co(II) catalysts supported by bis P,N chelating ligands. This lowering in overpotential could be achieved possibly due to a stabilization of Co(I) intermediate by the conjugated π-electron system of the phenanthroline ligand. Moreover, electrocatalytic H^+ reduction of the Co(II) complexes with the PNNP ligand is assumed to proceed by metal-ligand cooperation. The high reactivity of Co(III) hydride intermediates in this series and a liberation of H_2 via MLC reactivity would accelerate catalytic rates at lower overpotential compared to the catalysed reaction with a metal base reactivity. This MLC reactivity is particularly relevant to the development of efficient HECs to obtain a catalyst with high TOF but low overpotential. Therefore, the structural design of a future cobalt catalyst by using a phenanthroline core or other conjugated macrocyclic rings to stabilize a reduced Co(I) state would be a good choice of the ligand to obtain a catalyst that could operate at low overpotential. Variation of alkyl substituents on the two phosphorus atoms of the PNNP ligand to alter electronic properties of the CoPNNP complexes would be useful to understand their catalytic activity in more detail.

In terms of structural stability of cobalt catalysts, chelating ligands are crucial to stabilize Co(II) complexes with no ligand exchange in a solution. Our work has shown that the bidentate P,N and a Cl^- ligand in $[Co(PN)_2Cl_2]$ can dissociate while $[Co(PNNP)Cl_2]$ with the tetradentate PNNP can exchange only a Cl^- ligand without a completely loss of the PNNP ligand. Therefore, a tetradentate ligand would be more suitable than a bidentate ligand in order to obtain more stable Co(II) complexes. Furthermore, avoiding use of the $CoCl_2$ precursor for complexation with a suitable chelate ligand would be suggested because a π-donor Cl^- ligand might give a high-spin, Co(II), d^7 complex resulting in a labile complex. This would complicate the catalytic HER reaction by establishing a new equilibrium by Cl^- loss or ligand exchange. The generated complex might be inactive or active species for the catalytic reaction. The active intermediate might cause H_2 evolution via different pathways and H_2 molecule will be evolved from another catalytic cycle.

5.2 Future work

Chapter 2 and Chapter 3

- X-ray crystal structure of the $[Co^{III}(PN)_2(H)(MeCN)][PF_6]_2$ will be necessary to confirm the structural characterization and to compare to the solid state structure of the corresponding $[Co^{III}(PN)_2(H)(Cl)][PF_6]$. A single crystal of the $[Co^{III}(PN)_2(H)(MeCN)][PF_6]_2$ might be achieved by using new preparation methods to obtain reproducible and reasonable amounts of $[Co^{III}(PN)_2(H)(MeCN)][PF_6]_2$. A reaction of the $[Co^{III}(PN)_2(H)(Cl)]^+$ analogue with $NaBAr^F{}_4$ in MeCN solution might be promising way to afford the desired amount of the complex.
- Variation of the concentration of the catalyst at a certain TFA concentration will further support the second-order catalytic rate constant (k_{cat}, $M^{-1}\,s^{-1}$) for $Co^{III}(PN)_2(H)(MeCN)][PF_6]_2$ and $[Co^{III}(PN)_2(H)(MeCN)][PF_6]_2$
- To gain more reliable mechanism for H_2 evolution catalysed by the $[Co^{III}$*cis*$-(PN)_2Cl_2]$ and the $[Co^{III}(PN)_2(H)(Cl)][PF_6]$, adding an extra equivalent of the PN ligand to the catalytic system of this complex would lead to increases in catalytic currents at Co(II/I) couple monitored by CV technique.
- Characterisation of possible products ($HCOOH/HCOO^-$, CO or H_2) by bulk electrolysis of the $[Co^{III}(PN)_2(H)(Cl)][PF_6]$ in a CO_2 saturated MeCN solution at E_{app} ~ -2.0 V vs $Fc^{0/+}$ will be the highest priority to investigate mechanism for electroreduction of CO_2 reduction. The most likely product would be $HCOO^-$ produced by a bulk electrolysis of the $[Co^{III}(PN)_2(H)(Cl)][PF_6]$ in the solution without H^+ source.

Chapter 4

- Improved mass spectrometric and analytical data are required
- The reduction mechanism of the $[Co^{II}(PNNP)(MeCN)][BF_4]_2$ at the second reversible redox couple will be further identified as ligand-centered reduction if the Zn analogue, $[Zn^{II}(PNNP)(MeCN)]^{2+}$ with a redox-inactive metal centre shows a redox couple at similar reduction potential.
- The detailed mechanistic investigation of H_2 evolution catalysed by the $[Co^{II}(PNNP)(MeCN)][BF_4]_2$ complexes in this series might prove the intrinsic properties of the H^+ or CO_2 reduction activity of the complexes in this series via metal ligand cooperation

Appendix to Chapter 2

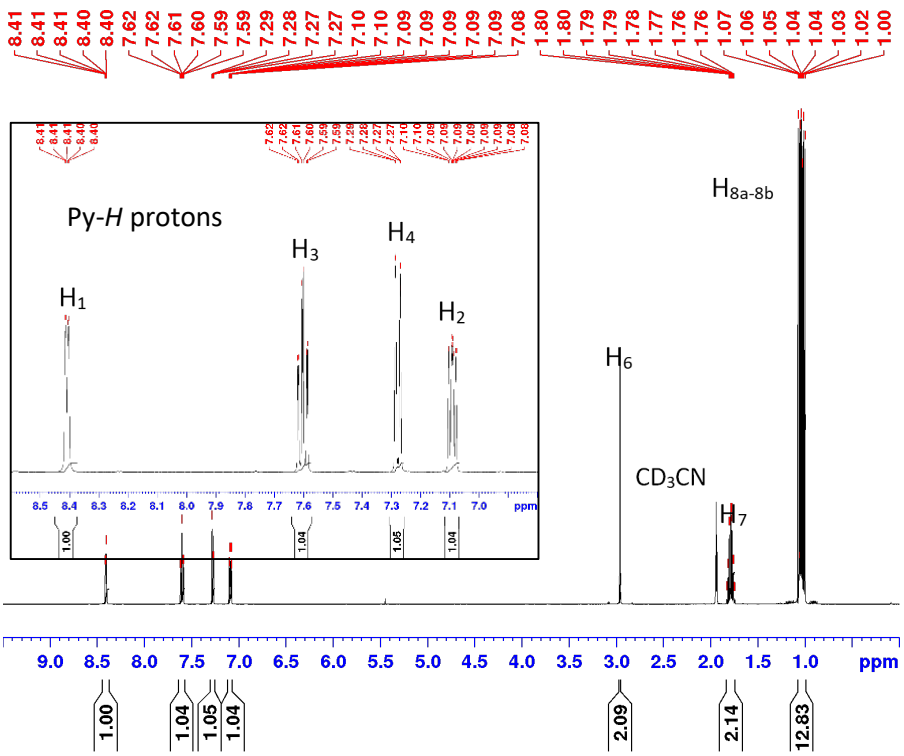

Figure A 2.1. ^{1}H NMR spectrum of the PN ligand in CD_3CN, inset show expansion of signals in aromatic region of pyridine protons.

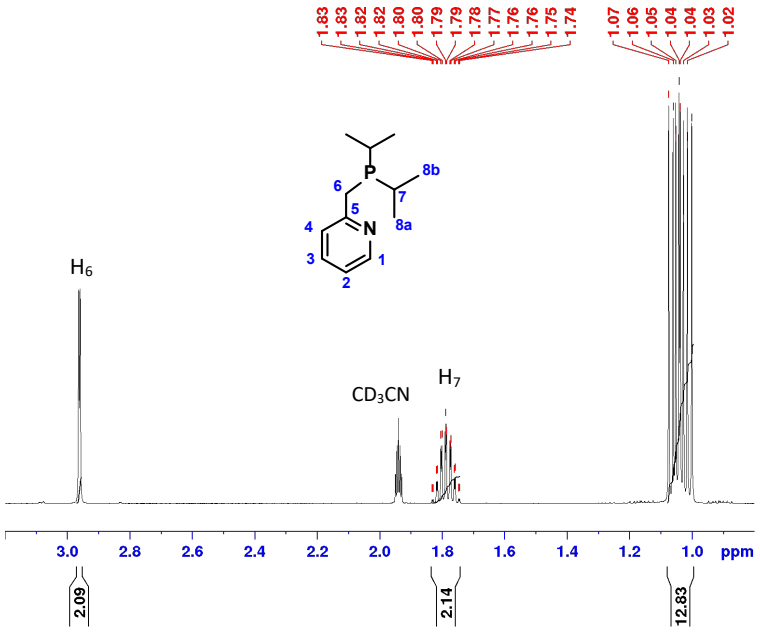

Figure A 2.2. ^{1}H NMR spectrum of the PN ligand in CD_3CN (aliphatic region).

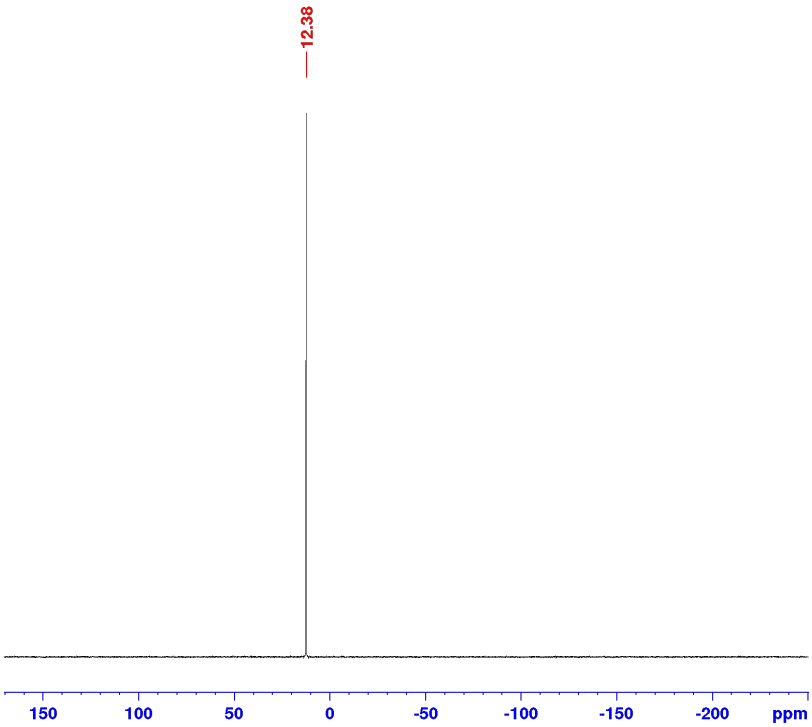

Figure A 2.3. $^{31}P\{^{1}H\}$ NMR spectrum of the PN ligand in CD_3CN.

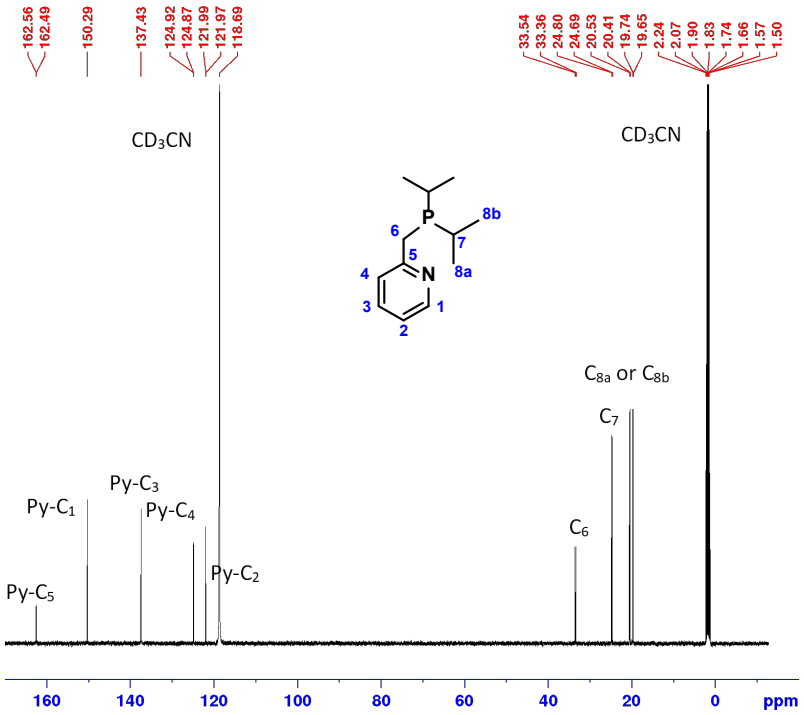

Figure A 2.4. $^{13}C\{^{1}H\}$ NMR spectrum of the PN ligand in CD_3CN.

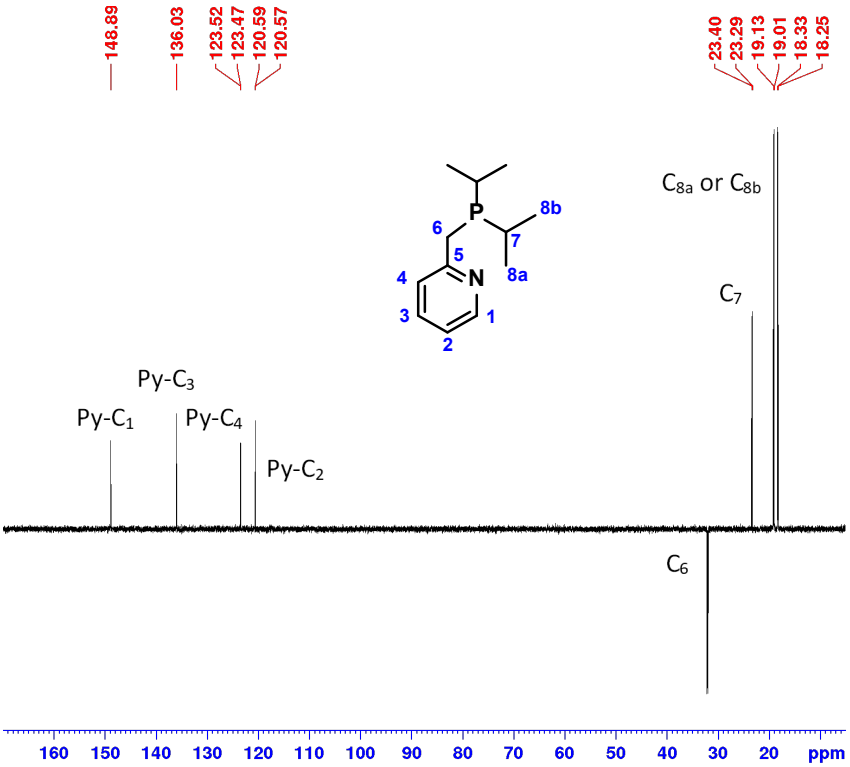

Figure A 2.5. ^{13}C-DEPT NMR spectrum of the PN ligand in CD_3CN.

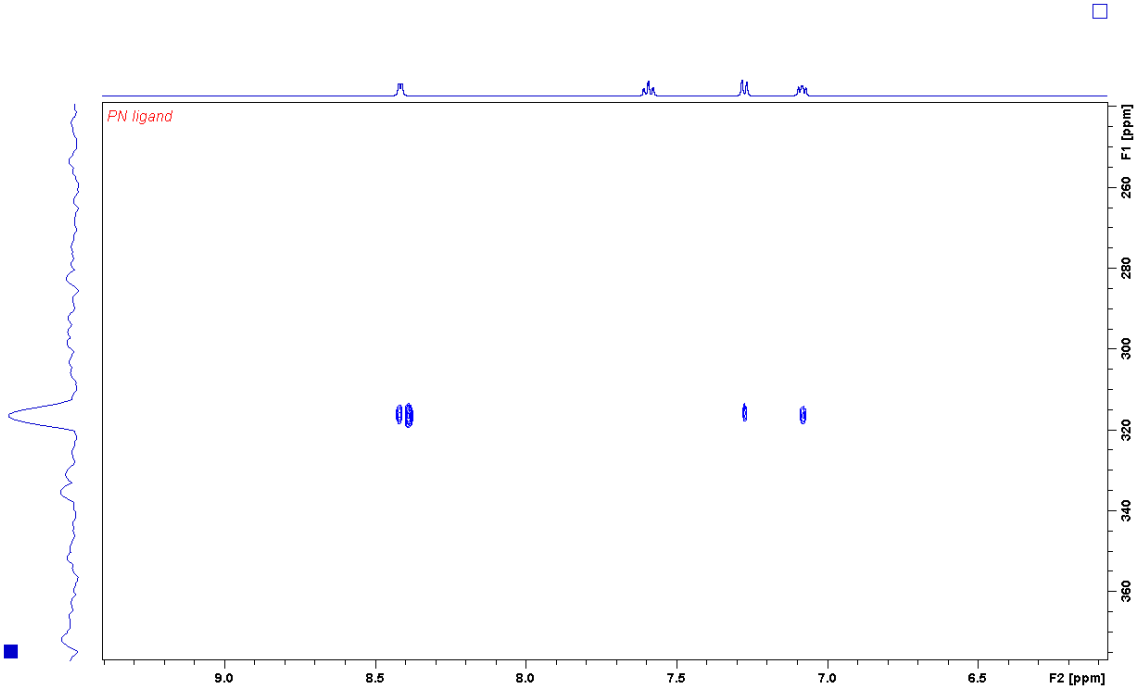

Figure A 2.6. ^{1}H-^{15}N HMBC spectrum of the PN ligand in CD_3CN.

a)

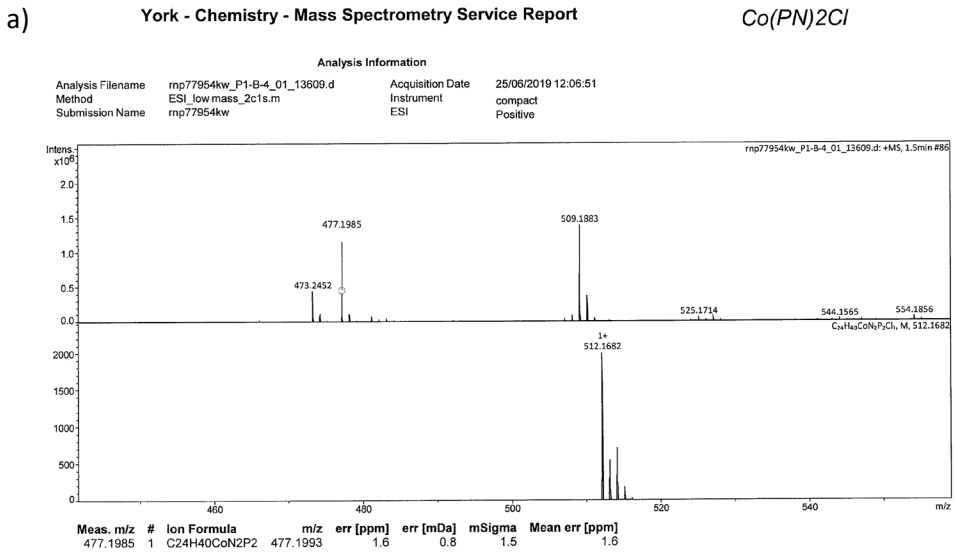

b)

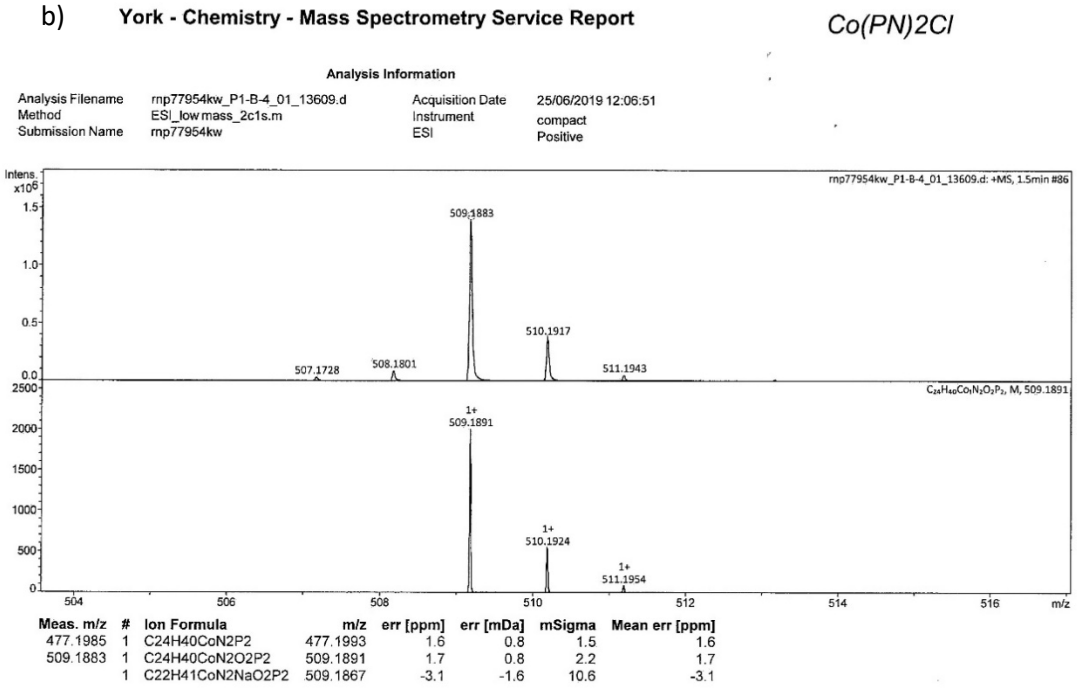

Figure A 2.7. (a) ESI-Mass spectrometry (positive ion mode in THF) of $[Co^{II}cis\text{-}(PN)_2Cl][PF_6]$ (top) and the calculated peak at m/z = 512.1682 for $[C_{24}H_{40}CoN_2P_2Cl]^+$ (bottom). (b) Experimental (top) and simulated isotope distribution patterns (b) of the peak at m/z = 509.1883 for the $[Co^{I}(PN)_2O_2]^+$.

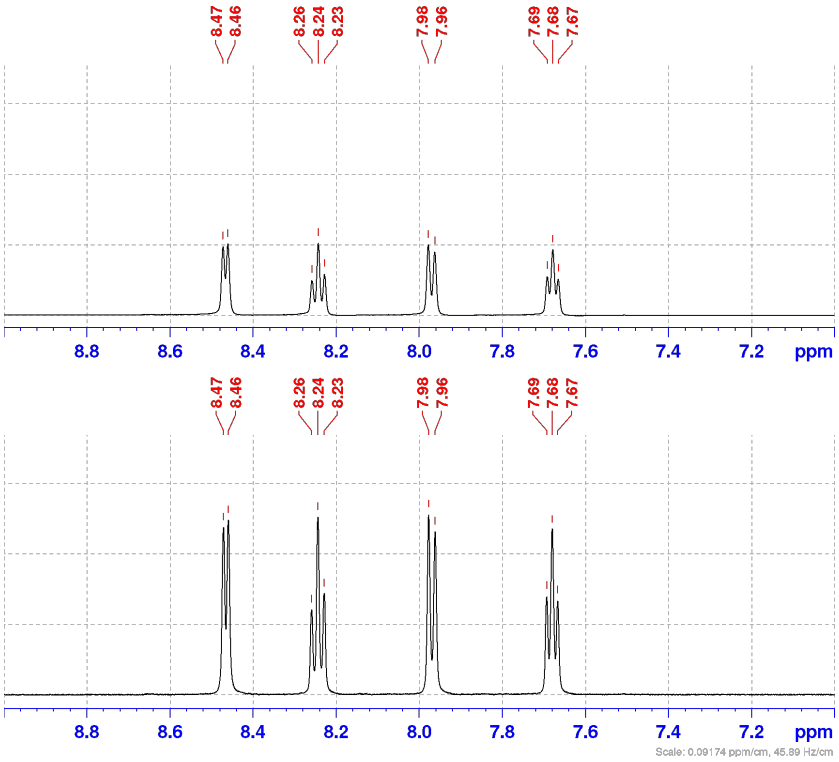

Figure A 2.8. ^{1}H NMR spectrum in aromatic region (bottom) and the $^{1}H\{^{31}P\}$ NMR spectrum (top) of the $[Co^{III}cis\text{-}(PN)_2Cl_2][PF_6]$ in acetone-d_6 at 223 K.

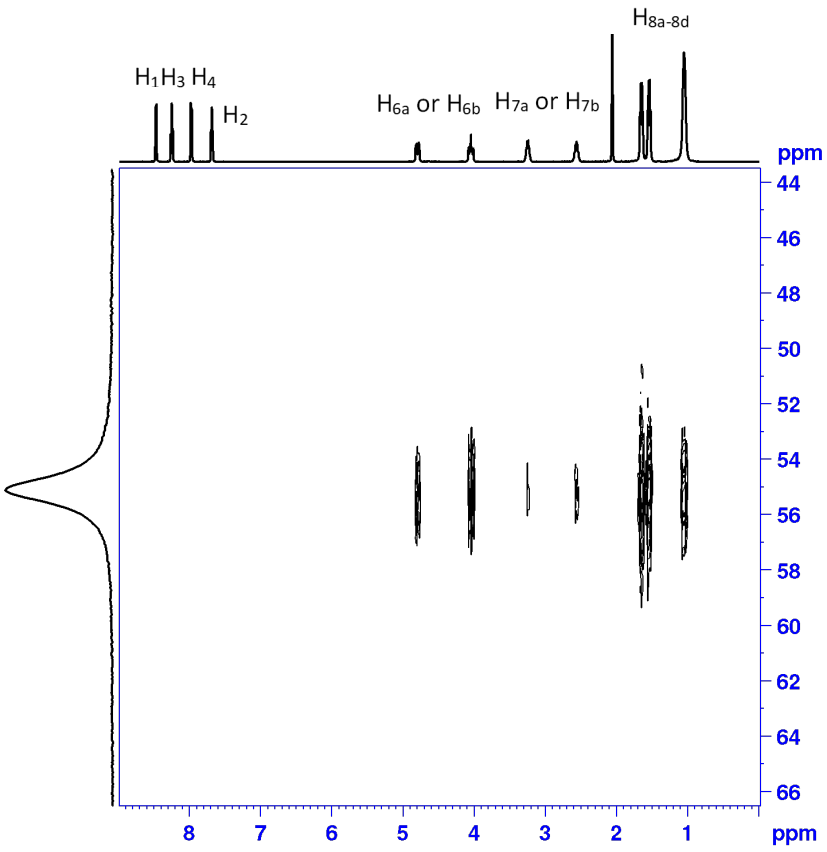

Figure A 2.9. $^{1}H\text{-}^{31}P\{^{1}H\}$ HMBC correlation of $[Co^{III}cis\text{-}(PN)_2Cl_2][PF_6]$ in acetone-d_6 at 223 K.

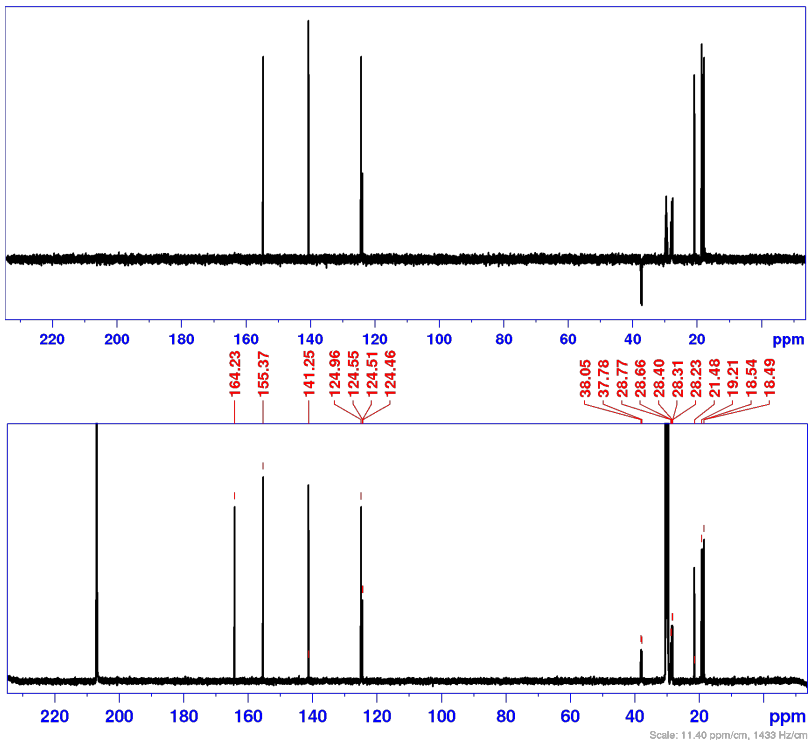

Figure A 2.10. ^{13}C-DEPT NMR spectrum of the [Co^{III}cis-(PN)$_2$Cl$_2$][PF$_6$] in acetone-d$_6$ at 223 K.

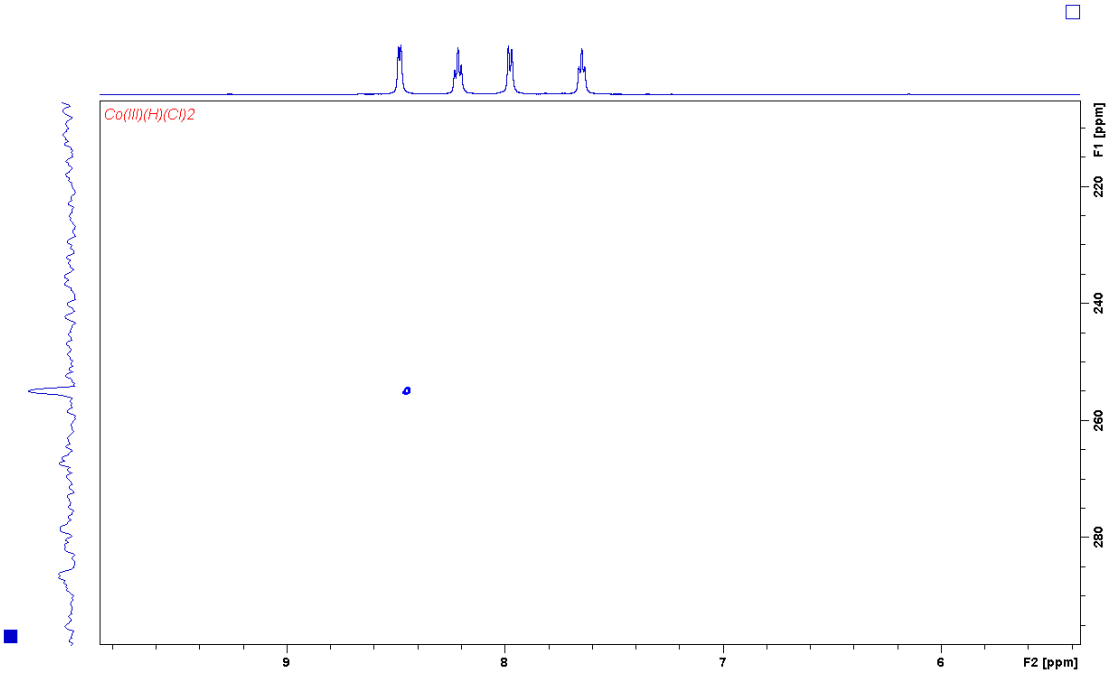

Figure A 2.11. ^{1}H-^{15}N HMBC spectrum of the [Co^{III}cis-(PN)$_2$Cl$_2$][PF$_6$] in CD$_3$CN.

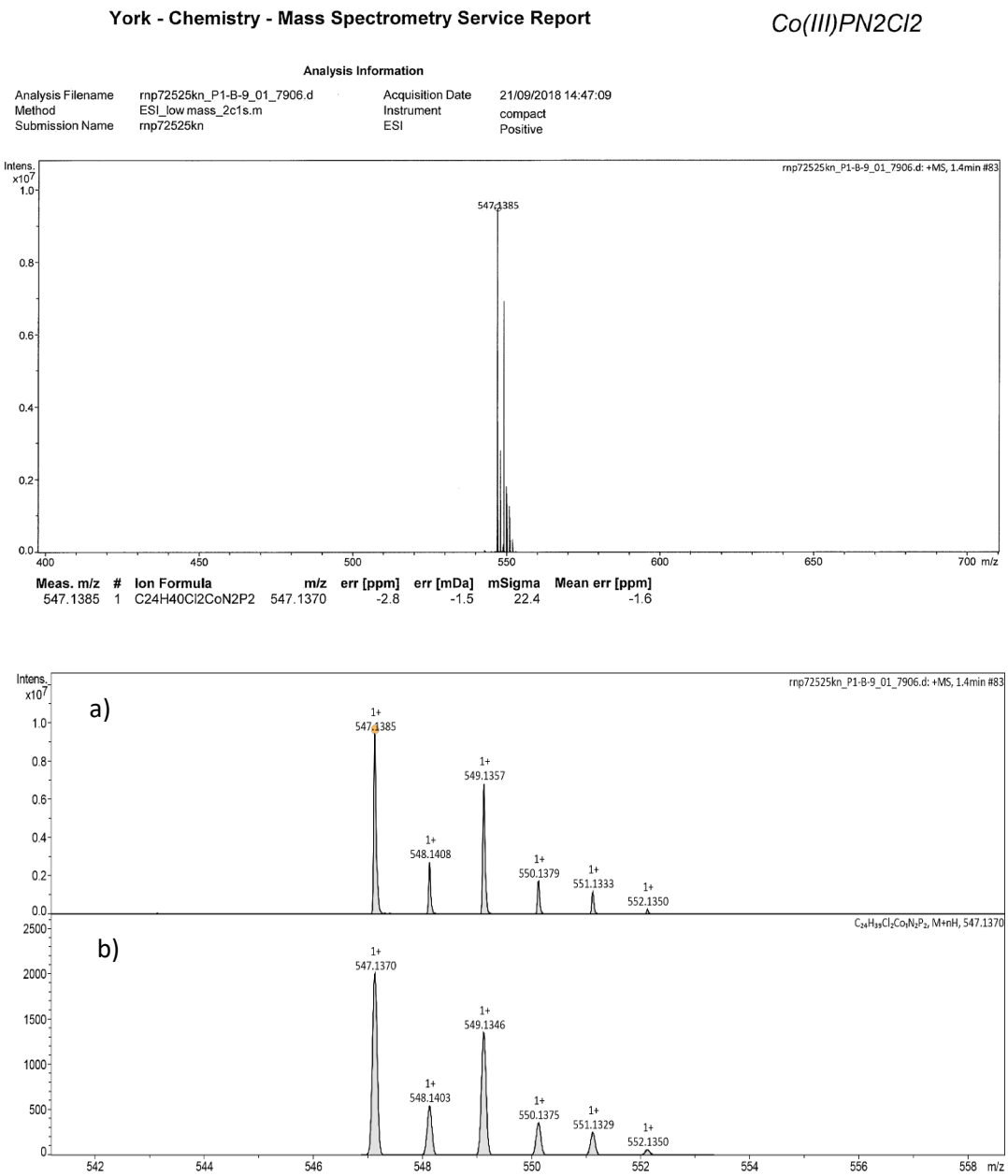

Figure A 2.12. ESI-Mass spectrometry (positive ion mode in MeCN) of the $[Co^{III}$*cis*-$(PN)_2Cl_2][PF_6]$ complex (top). Bottom: experimental (a) and simulated isotope distribution patterns (b) of the peak at m/z = 547.1385.

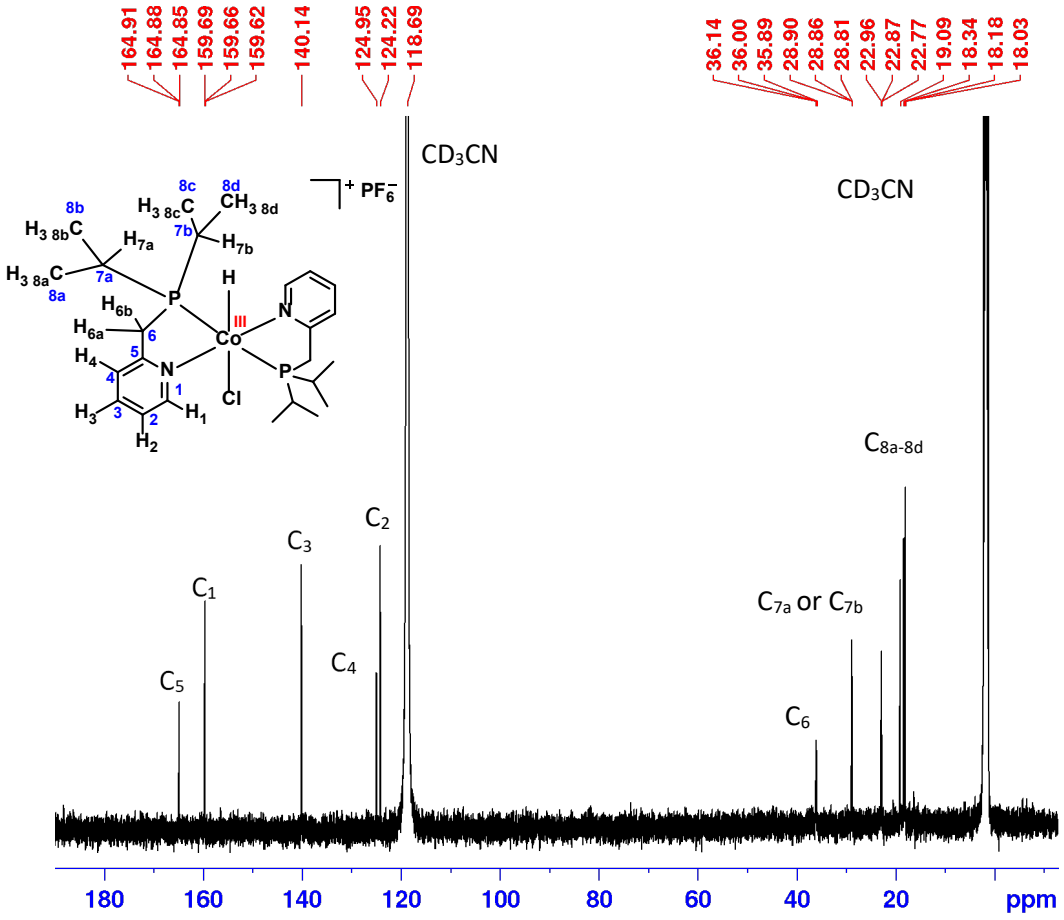

Figure A 2.13. $^{13}C\{^{1}H\}$ NMR spectrum of the $[Co^{III}(PN)_2(H)(Cl)\ ][PF_6]$ in CD_3CN at room temperature.

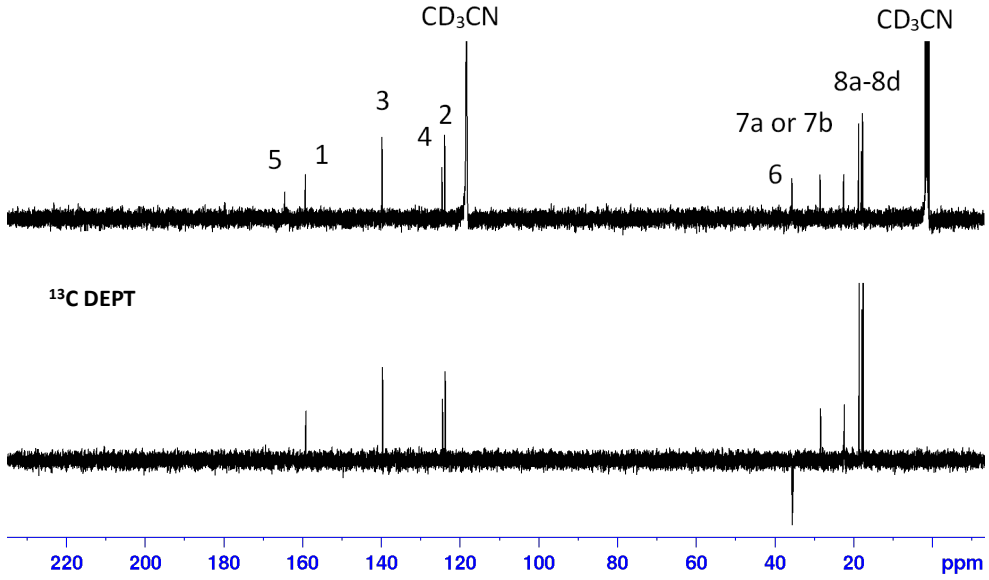

Figure A 2.14. $^{13}C\{^{1}H\}$ NMR spectra (top) and ^{13}C DEPT experiment (bottom) of the $[Co^{III}(PN)_2(H)(Cl)][PF_6]$ in CD_3CN at room temperature.

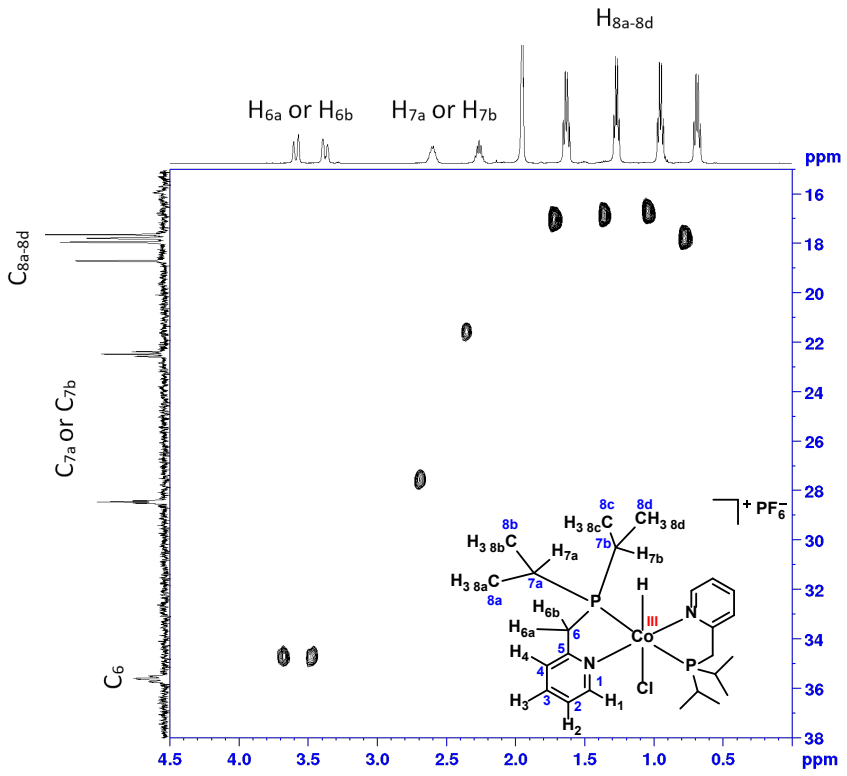

Figure A 2.15. ^{1}H-$^{13}C\{^{1}H\}$ HSQC spectrum of the $[Co^{III}(PN)_2(H)(Cl)][PF_6]$ in CD_3CN at room temperature (aliphatic protons).

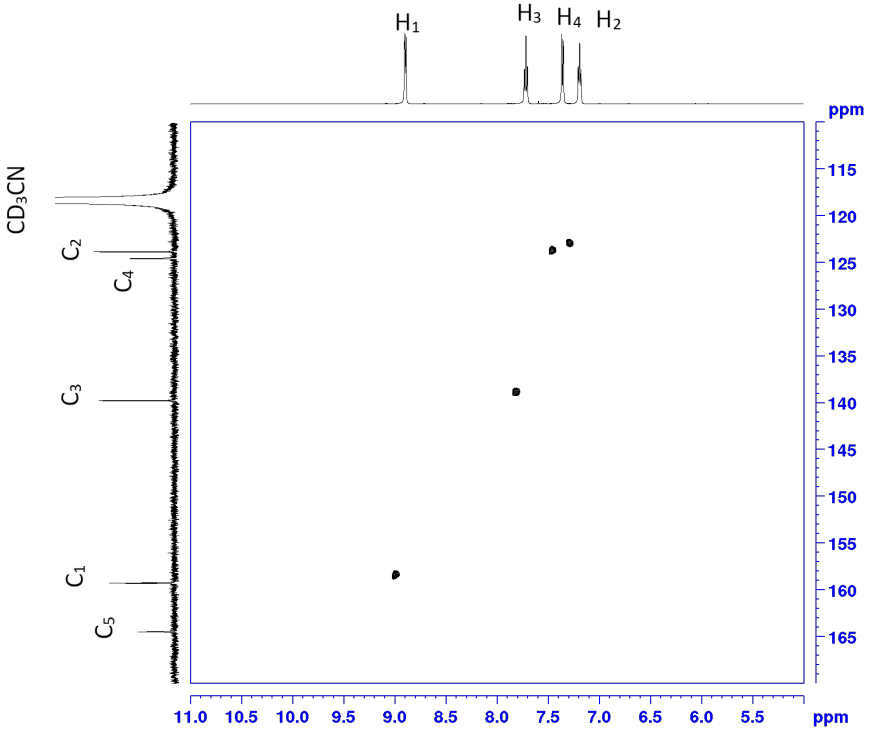

Figure A 2.16. ^{1}H-$^{13}C\{^{1}H\}$ HSQC NMR spectrum of the $[Co^{III}(PN)_2(H)(Cl)][PF_6]$ in CD_3CN at room temperature (aromatic protons).

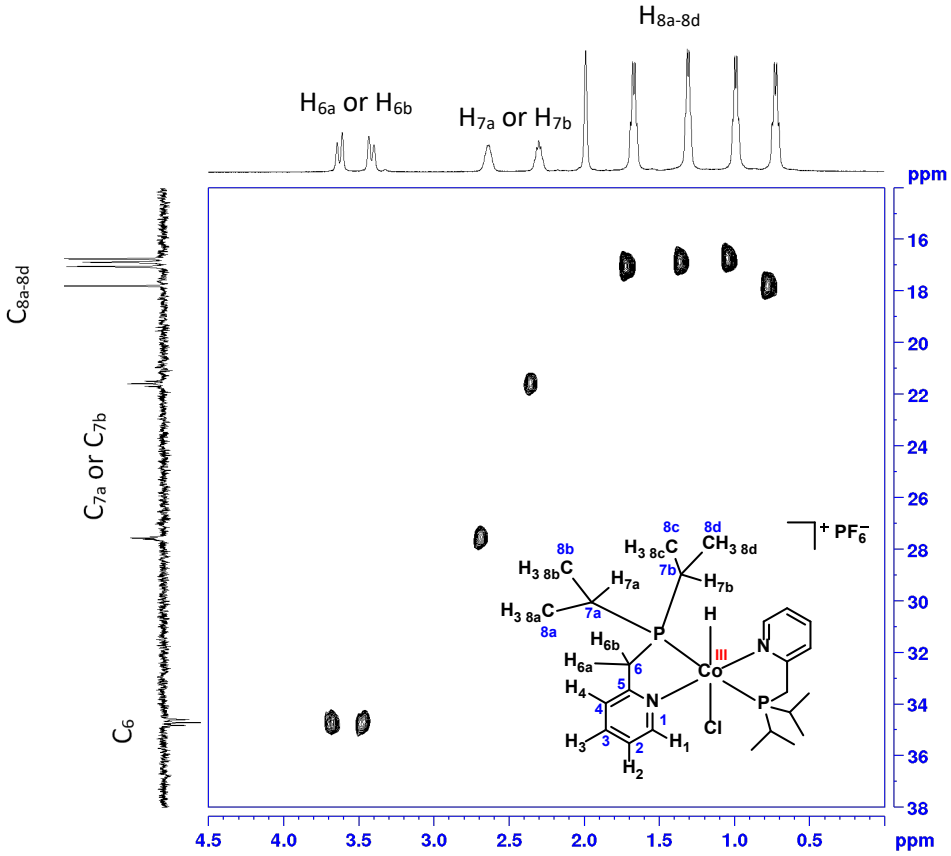

Figure A 2.17. ^{1}H-^{13}C DEPT correlation spectroscopy of the $[Co^{III}(PN)_2(H)(Cl)][PF_6]$ in CD_3CN at room temperature (aliphatic protons).

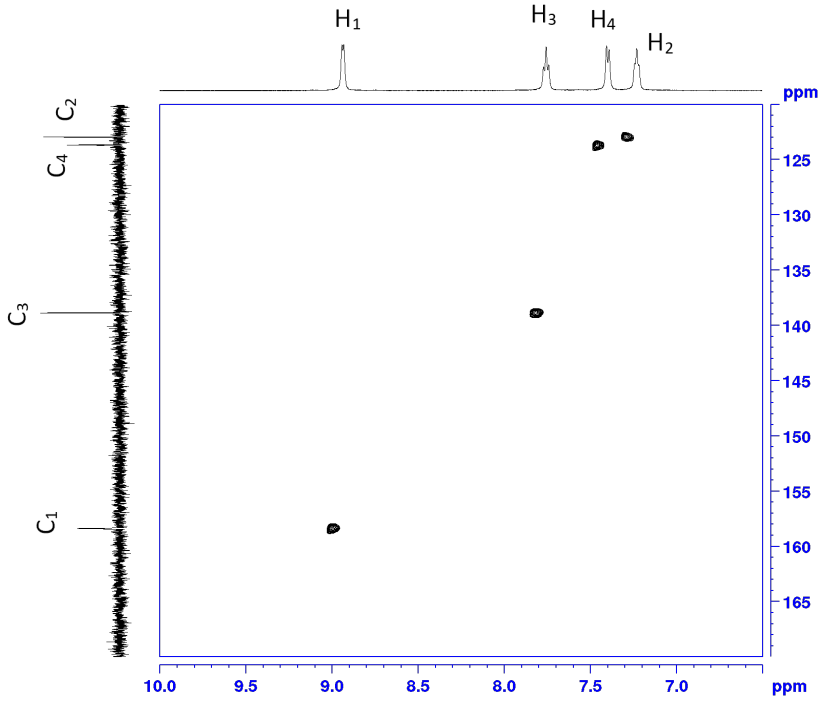

Figure A 2.18. ^{1}H-^{13}C DEPT correlation spectroscopy of $[Co^{III}(PN)_2(H)(Cl)][PF_6]$ in CD_3CN at room temperature (aromatic protons).

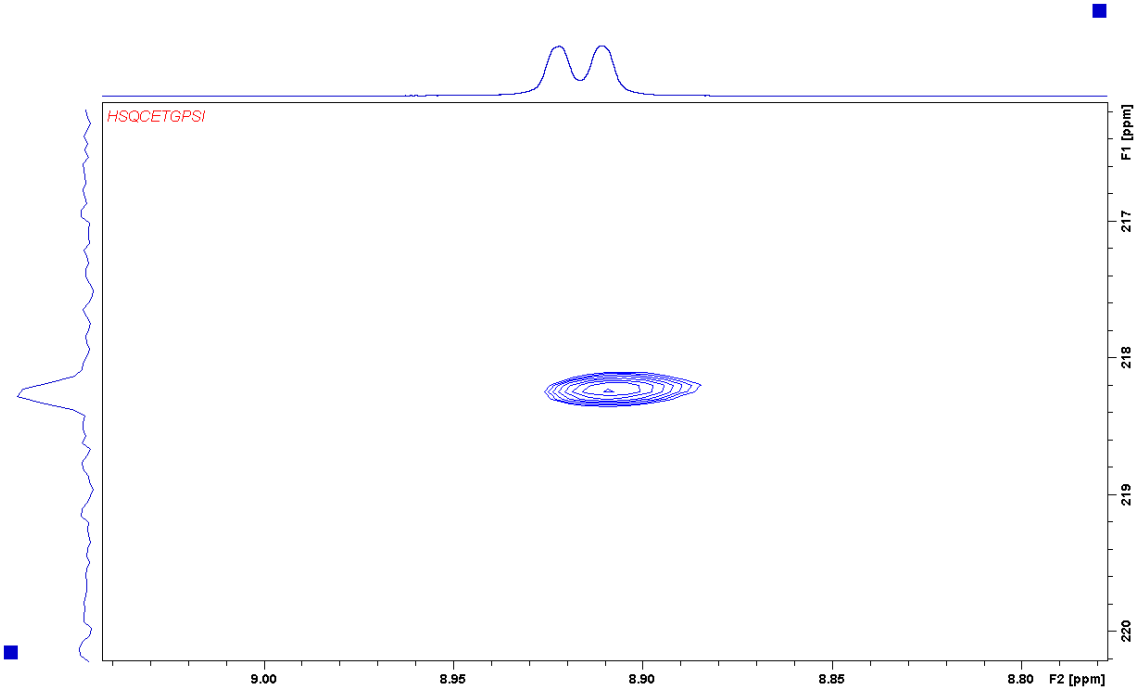

Figure A 2.19. ^{1}H-^{15}N HMBC spectrum of the $[Co^{III}(PN)_2(H)(Cl)][PF_6]$ in CD_3CN.

KW039

York - Chemistry - Mass Spectrometry Service Report

Analysis Information Acquisition Date 13/03/2017 14:27:48

Analysis Filename	rnp63694kw_P1-C-2_01_3544.d
Method	800p_lcms_2c1s.m
Submission Name	RNP63694KW
Instrument	micrOTOF
ESI	Positive

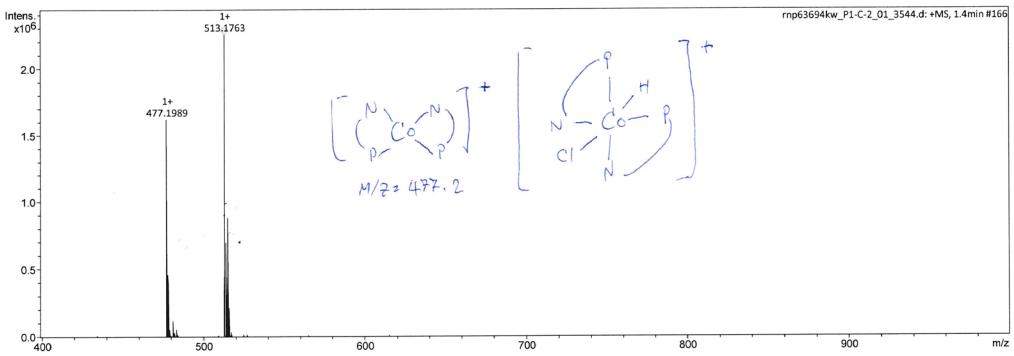

Meas. m/z	#	Ion Formula	m/z	err [ppm]	err [mDa]	mSigma	Mean err [ppm]
513.176335	1	C24H41ClCoN2P2	513.175997	0.7	0.3	23.7	0.2

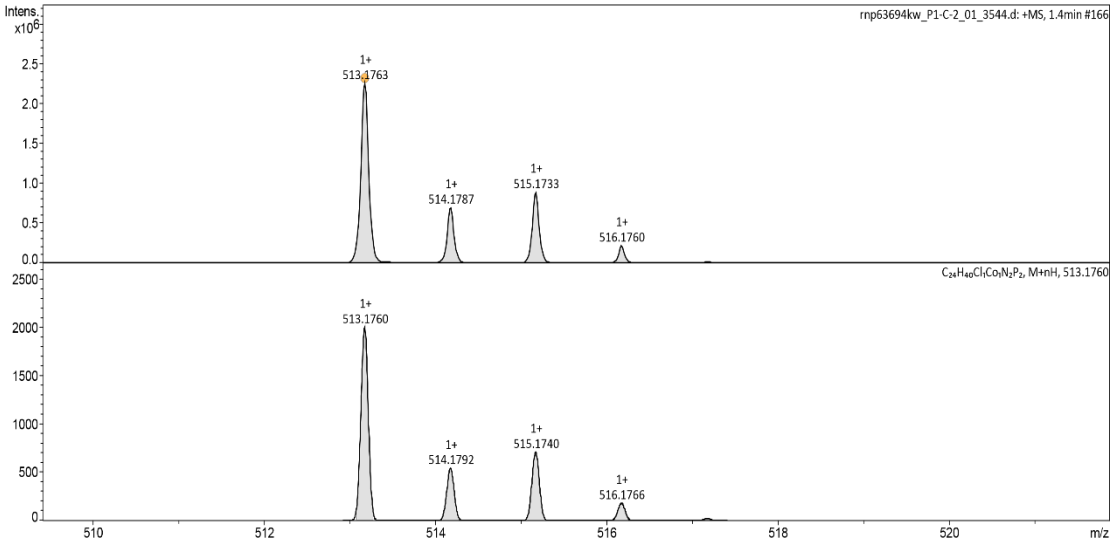

Figure A 2.20. ESI-Mass spectrometry (positive ion mode in MeCN) of the $[Co^{III}(PN)_2H)(Cl)][PF_6]$ complex(top). Bottom: experimental (a) and simulated isotope distribution patterns (b) of the peak at m/z = 513.1763 for $[Co^{III}(PN)_2H)(Cl)]^+$.

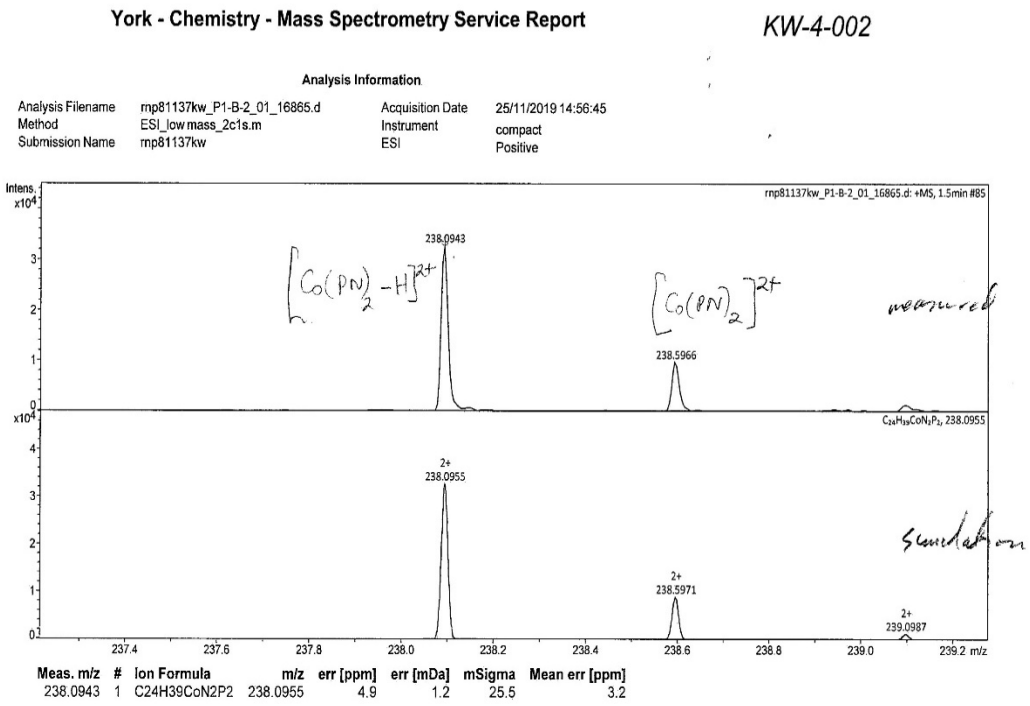

Figure A 2.21. ESI-Mass spectrometry (positive ion mode in acetone) of $[Co^{II}(PN)_2(MeCN)]^{2+}$, observed spectrum (top) and simulated spectrum (bottom).

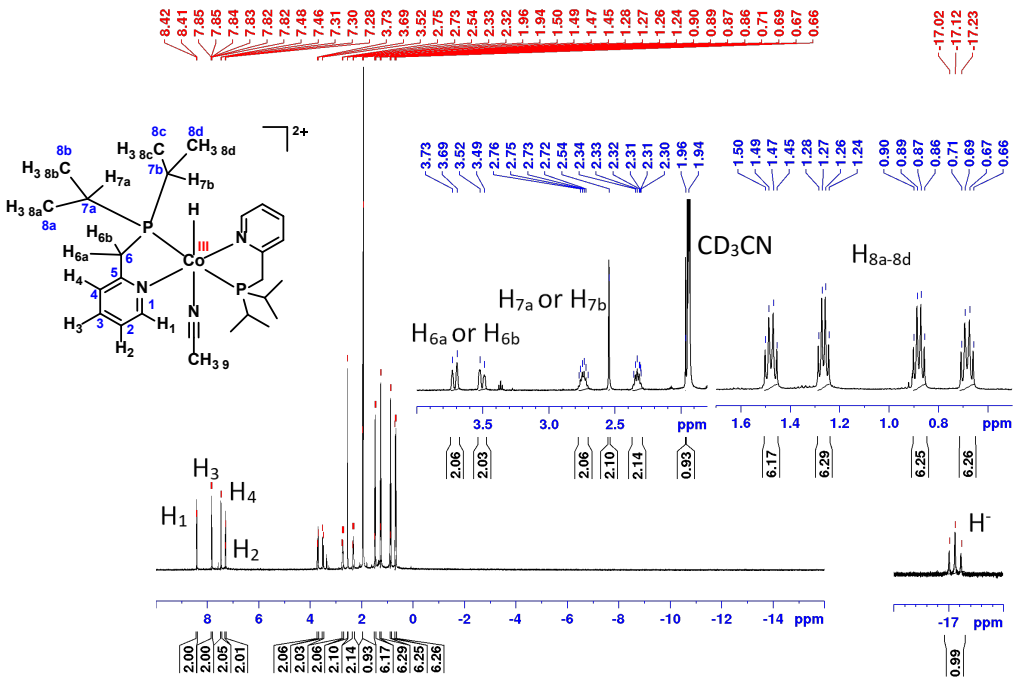

Figure A 2.22. ^1H NMR spectrum of $[Co^{III}(PN)_2(H)(MeCN)]^{2+}$ in CD_3CN at room temperature.

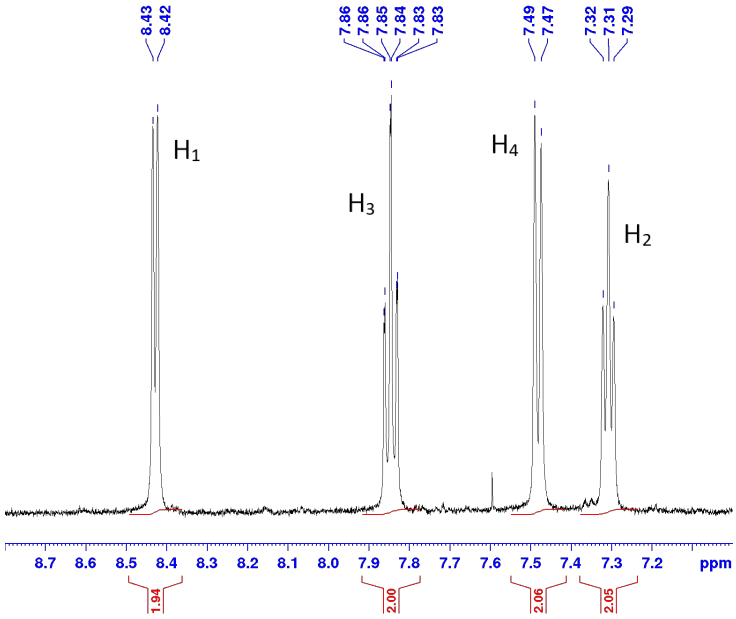

Figure A 2.23. ^{1}H NMR spectrum (aromatic protons) of $[Co^{III}(PN)_2(H)(MeCN)]^{2+}$ in CD_3CN at room temperature.

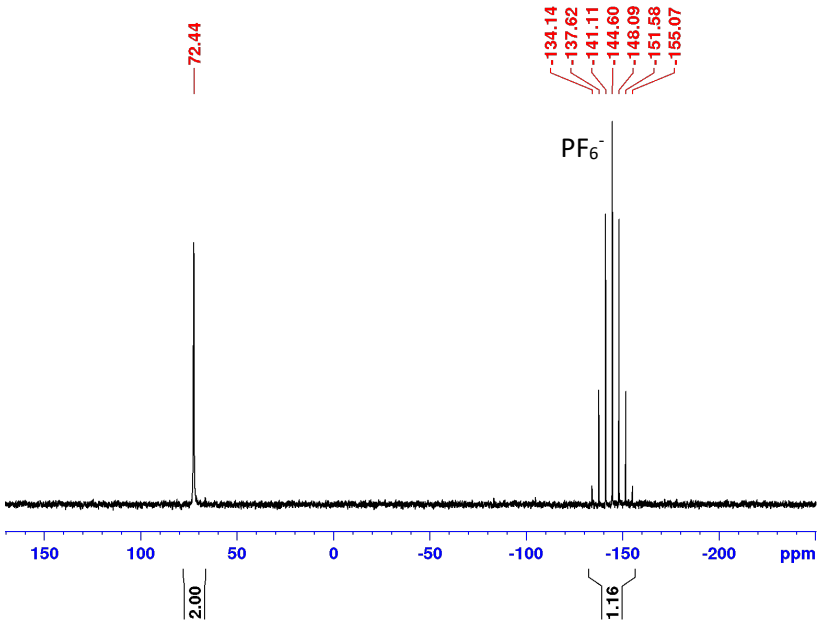

Figure A 2.24. $^{31}P\{^{1}H\}$ NMR spectrum of $[Co^{III}(PN)_2(H)(MeCN)]^{2+}$ in CD_3CN at room temperature.

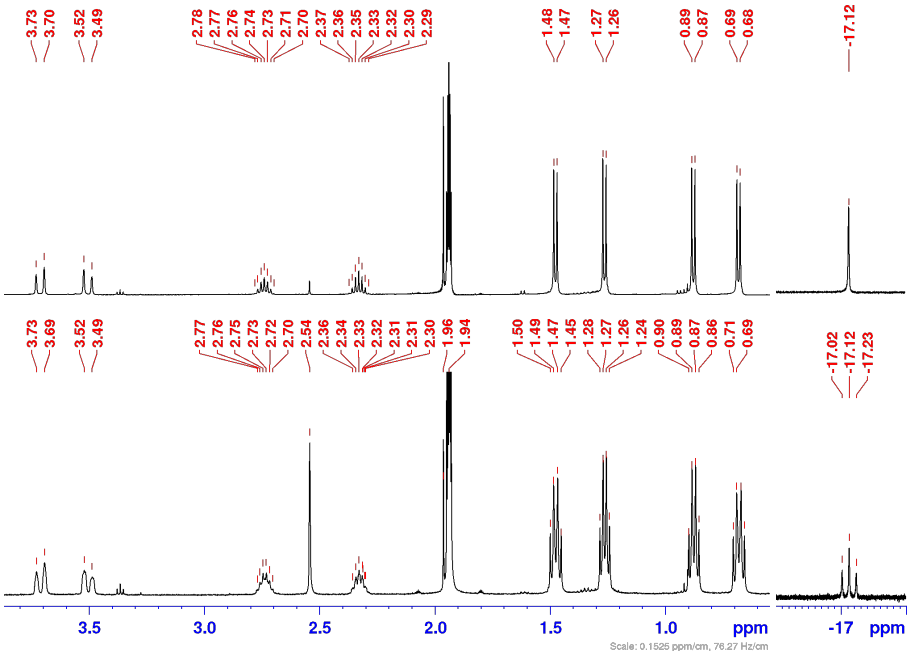

Figure A 2.25. ^{1}H NMR spectrum (aliphatic protons and hydride signal) of the $[Co^{III}(PN)_2(H)(MeCN)][PF_6]_2$ in CD_3CN at room temperature (bottom) compared to the $^{31}P\{^{1}H\}$ (top).

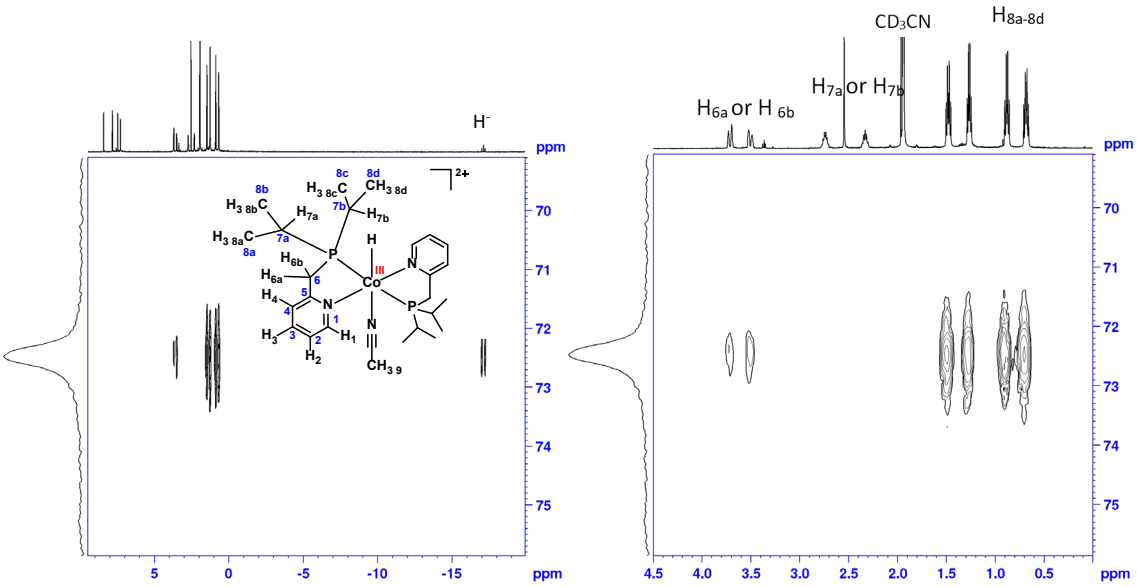

Figure A 2.26. ^{1}H-$^{31}P\{^{1}H\}$ HMBC correlation of $[Co^{III}(PN)_2(H)(MeCN)]^{2+}$at room temperature in CD_3CN showing the whole spectrum (left), and the aliphatic region (right).

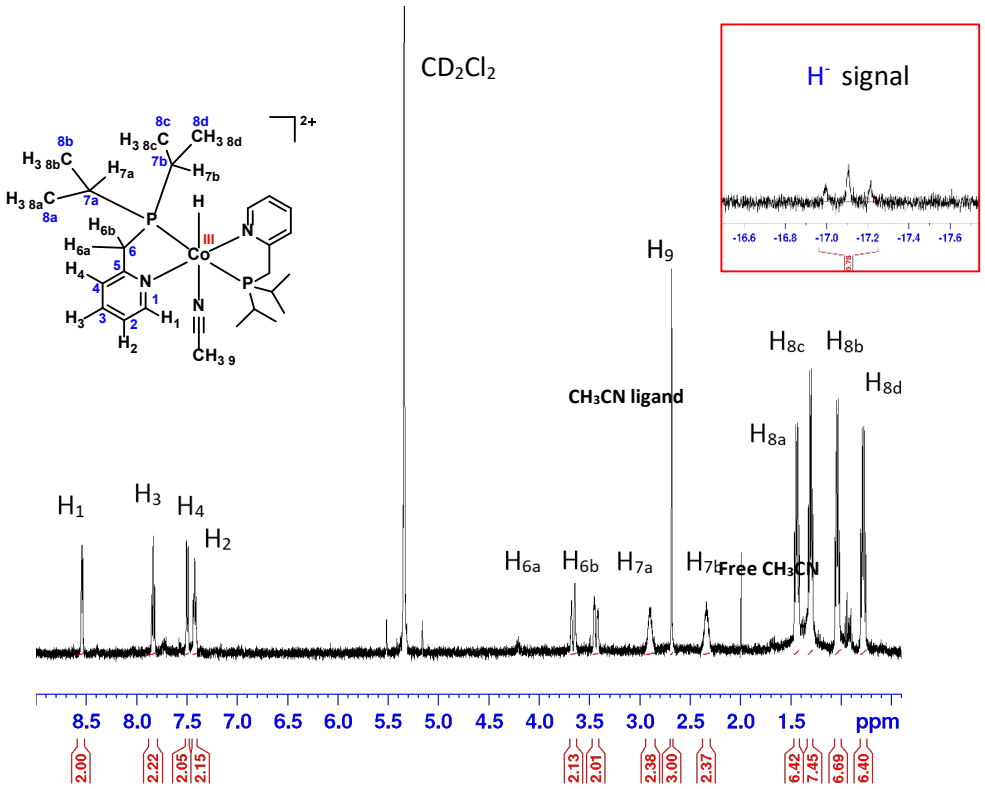

Figure A 2.27. ^{1}H NMR spectrum of $[Co^{III}(PN)_2(H)(MeCN)]^{2+}$ in CD_2Cl_2, inset showed the H^- signal.

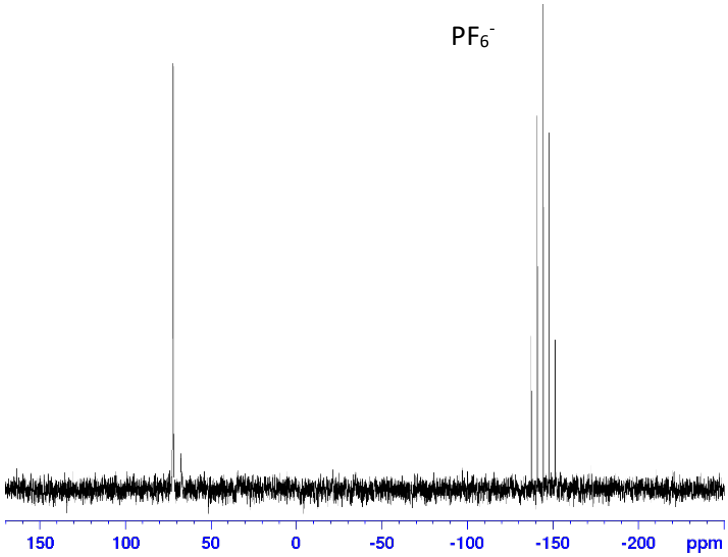

Figure A 2.28. $^{31}P\{^{1}H\}$ NMR spectrum of $[Co^{III}(PN)_2(H)(MeCN)]^{2+}$ in CD_2Cl_2, with the PF_6^- counter anion.

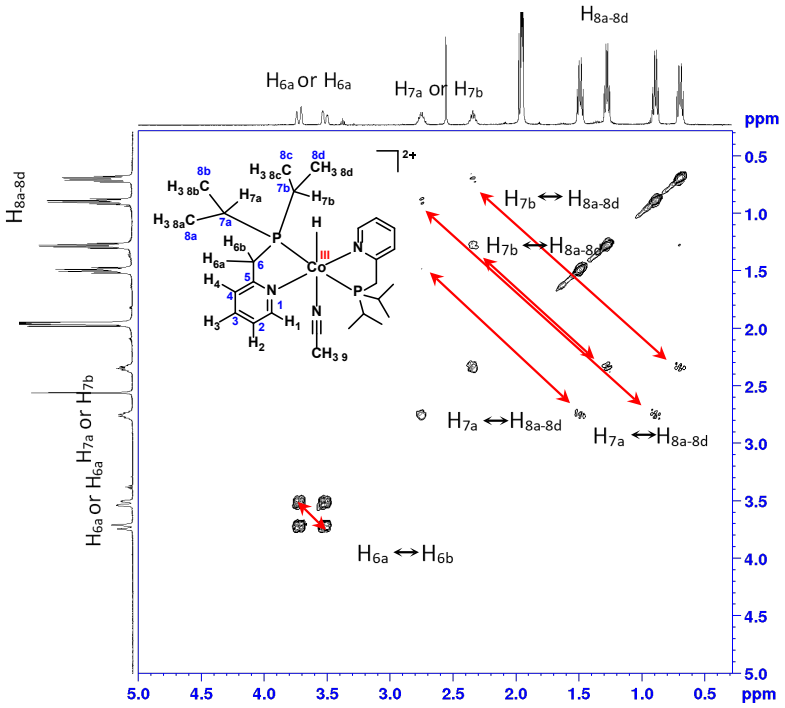

Figure A 2.29. ^{1}H-^{1}H COSY NMR correlation of $[Co^{III}(PN)_2(H)(MeCN)]^{2+}$ at room temperature in CD_3CN (aliphatic protons), the red arrows showed the correlation between two protons as labelled in the spectrum.

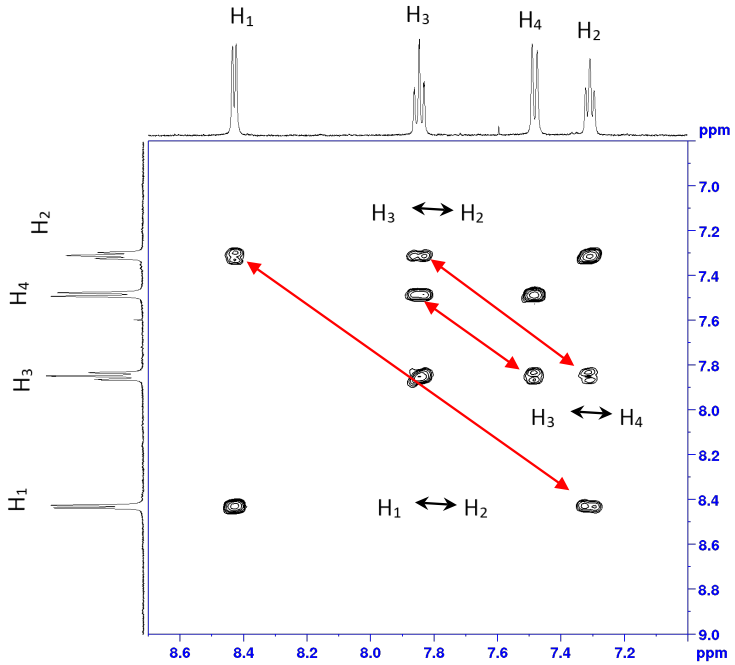

Figure A 2.30. ^{1}H-^{1}H COSY NMR correlation of $[Co^{III}(PN)_2(H)(MeCN)]^{2+}$at room temperature in CD_3CN (aromatic protons), the red arrows showed the correlation between two protons as labelled in the spectrum.

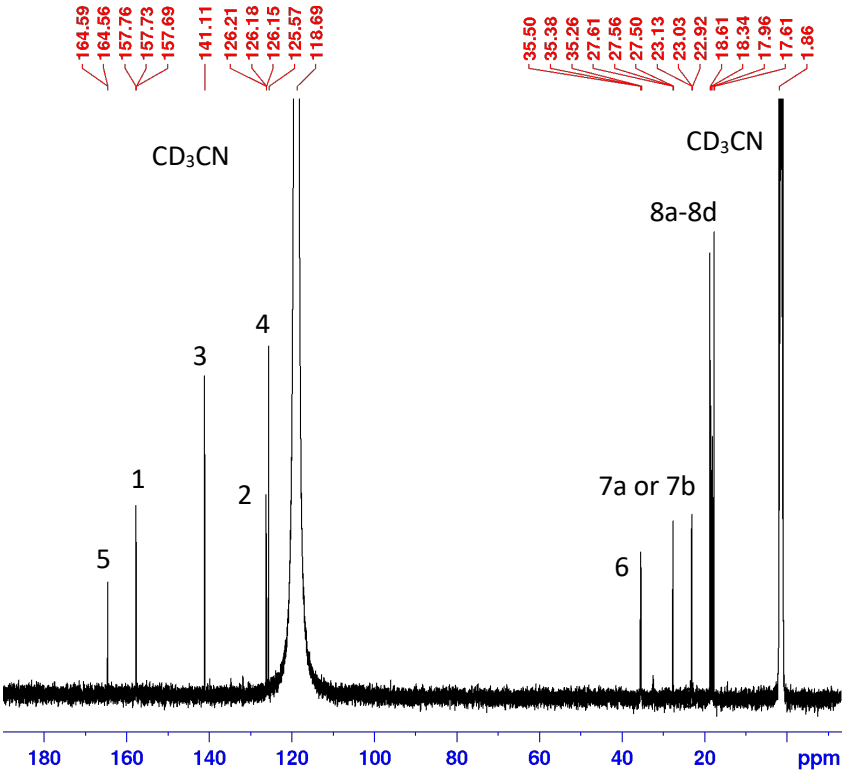

Figure A 2.31. $^{13}C\{^{1}H\}$ NMR spectrum of the $[Co^{III}(PN)_2(H)(MeCN)]^{2+}$ at room temperature in CD_3CN

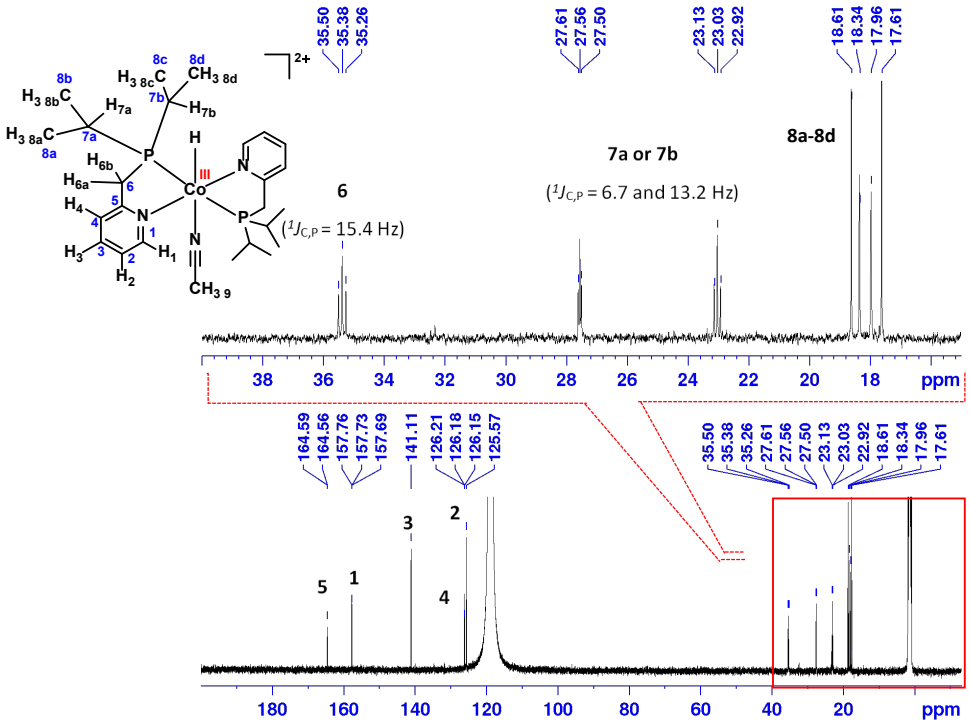

Figure A 2.32. $^{13}C\{^{1}H\}$ NMR spectrum of $[Co^{III}(PN)_2(H)(MeCN)]^{2+}$ at room temperature in CD_3CN.

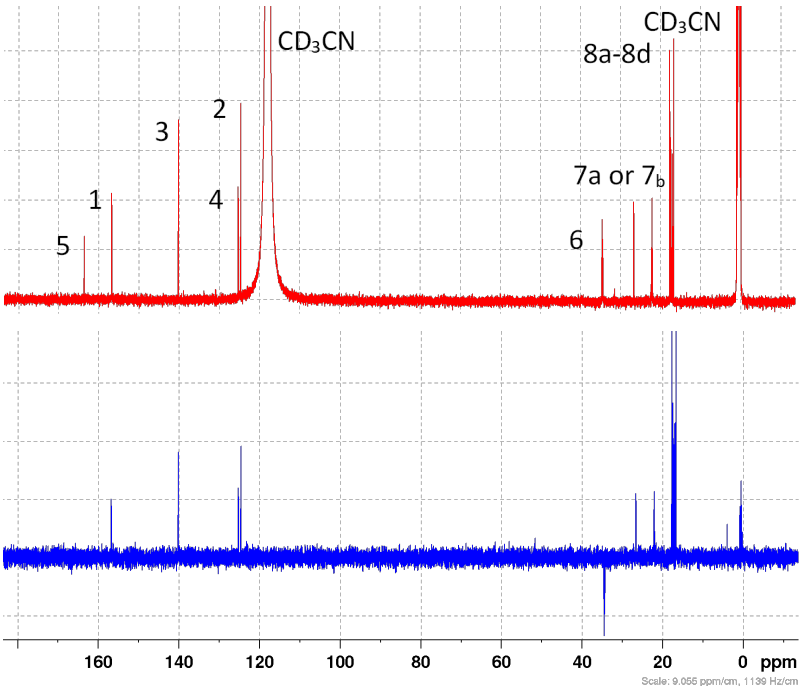

Figure A 2.33. $^{13}C\{^{1}H\}$ NMR spectra (top) and ^{13}C DEPT experiment (bottom) of $[Co^{III}(PN)_2(H)(MeCN)]^{2+}$ at room temperature in CD_3CN.

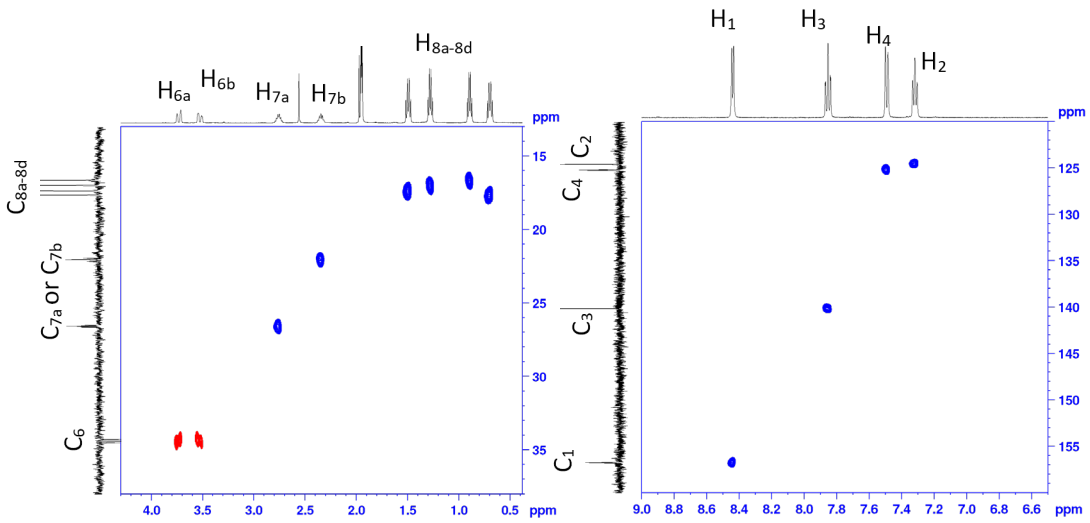

Figure A 2.34. ^{1}H-^{13}C DEPT correlation spectroscopy of $[Co^{III}(PN)_2(H)(MeCN)]^{2+}$ at room temperature in CD_3CN showing aliphatic protons(left) and aromatic protons (right).

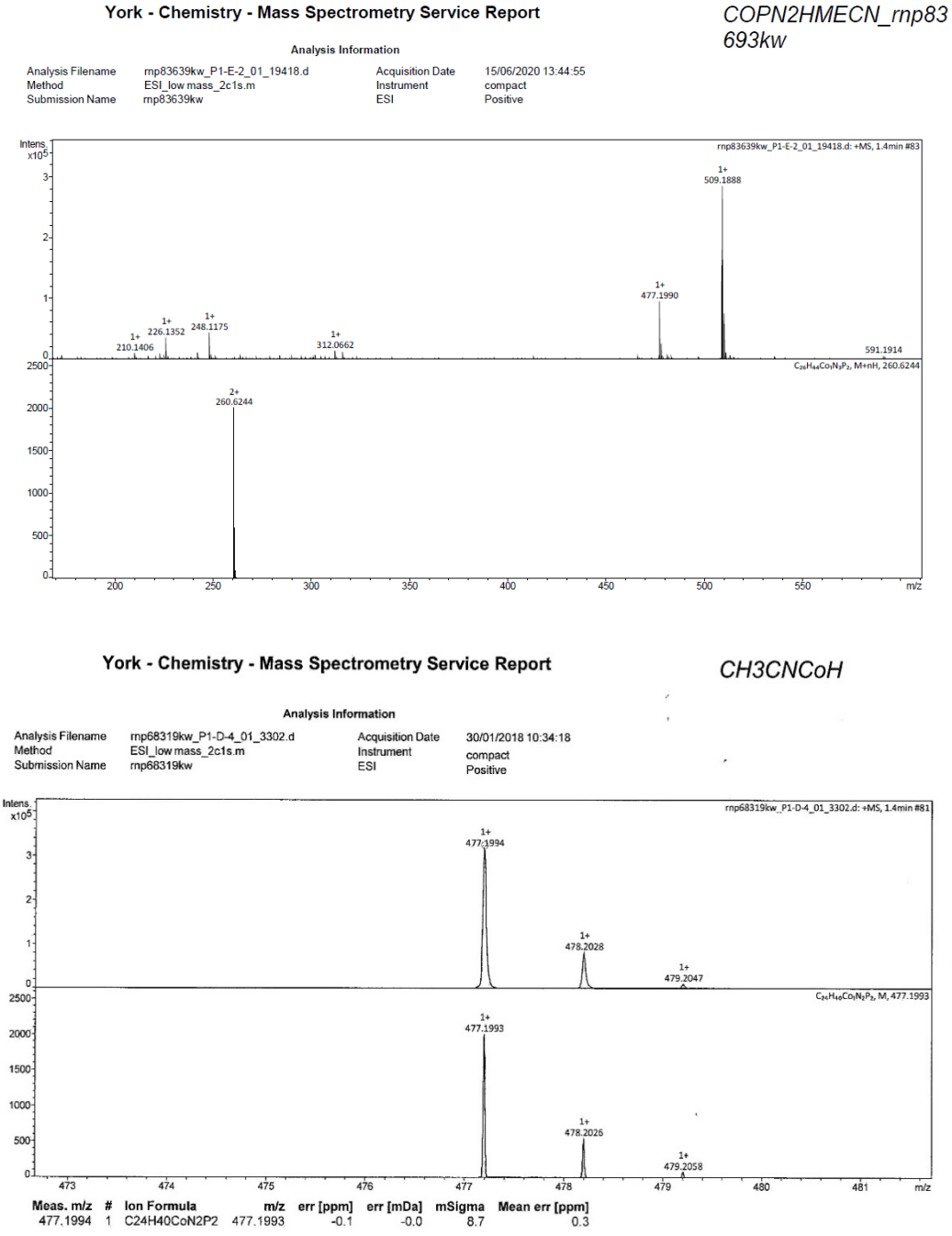

Figure A 2.35. ESI-Mass spectrometry (positive ion mode in MeCN) of $[Co^{III}(PN)_2(H)(MeCN)][PF_6]$ (top). Bottom: experimental (a) and simulated isotope distribution patterns (b) of the peak at m/z = 477.1994 for $[Co^{I}(PN)_2]^+$.

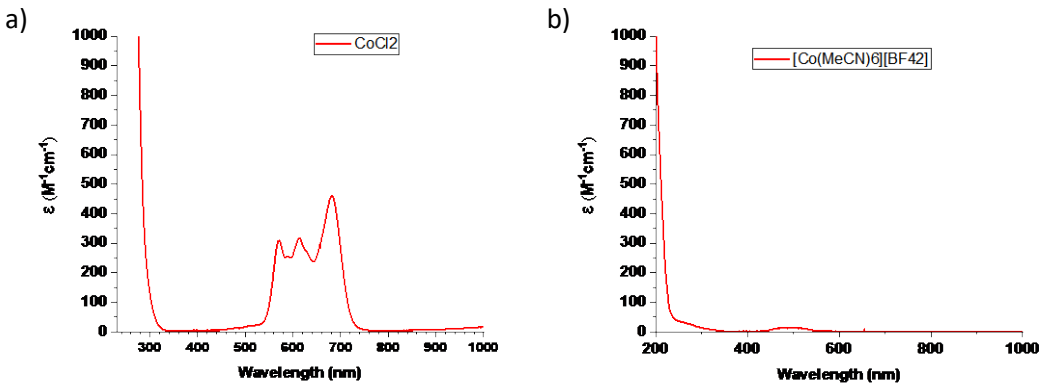

Figure A 2.36. UV-Vis spectrum of the $CoCl_2$ anhydrous ($5.75x10^{-4}$ M) in CH_3CN and the $[Co^{II}(MeCN)_6][BF_4]_2$ complex ($5.75x10^{-4}$ M) in CH_3CN (b).

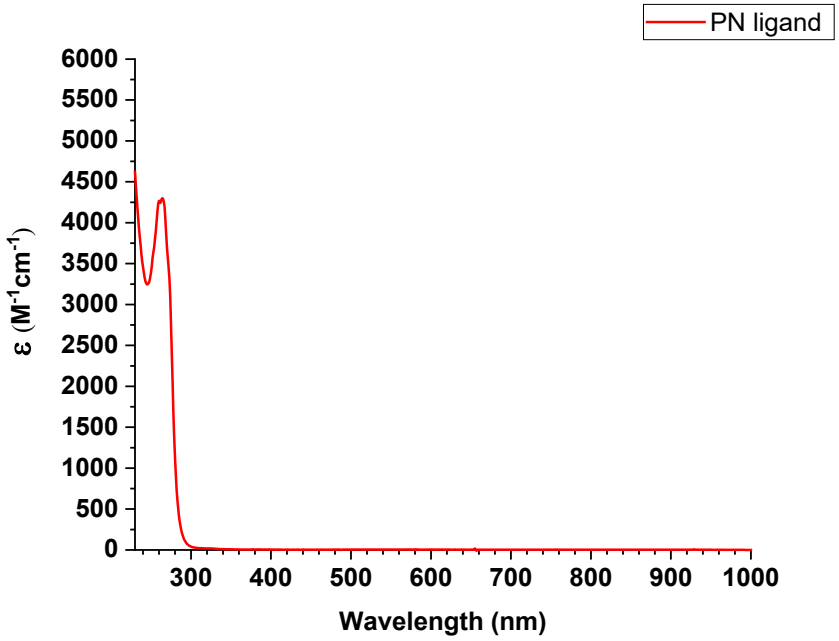

Figure A 2.37. UV-Vis spectrum of the PN ligand ($5.75x10^{-4}$ M) in CH_3CN.

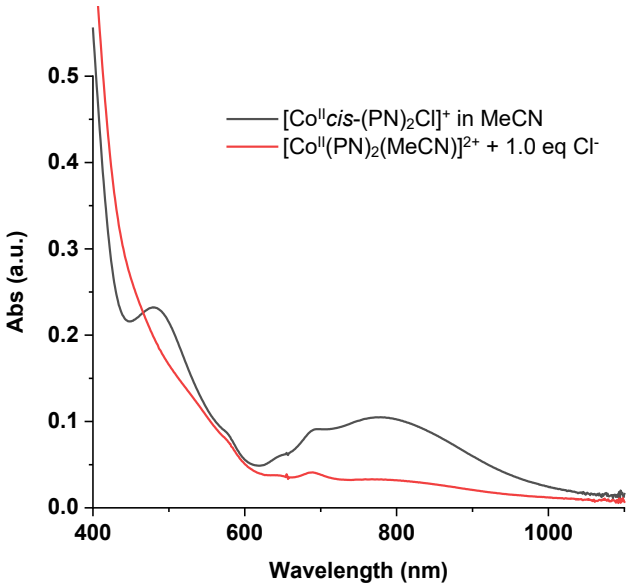

Figure A 2.38. The UV-Vis spectrum of independently synthesized $[Co^{II}cis\text{-}(PN)_2Cl][PF_6]$ ($5.75x10^{-5}$ M in MeCN, black solid) and the spectrum of the $[Co^{II}(PN)_2(MeCN)]^{2+}$ with 1.0 equiv. Cl^- in MeCN.

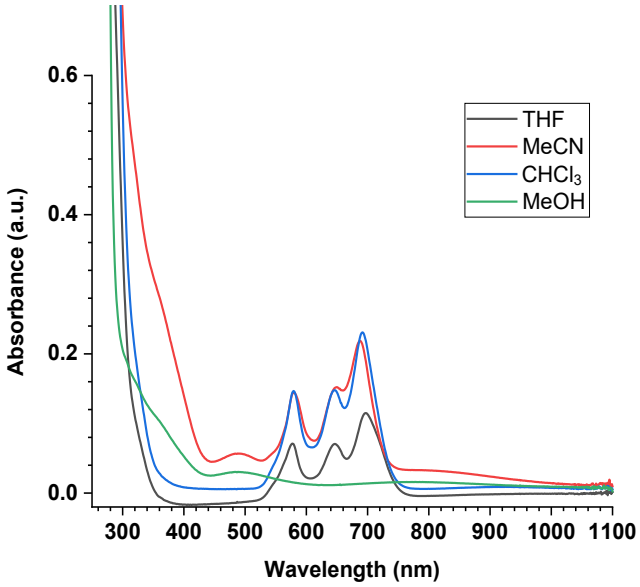

Figure A 2.39. UV-Vis spectrum of the $[Co^{II}(PN)Cl_2]$ complex ($5.75x10^{-4}$ M) in different solvents.

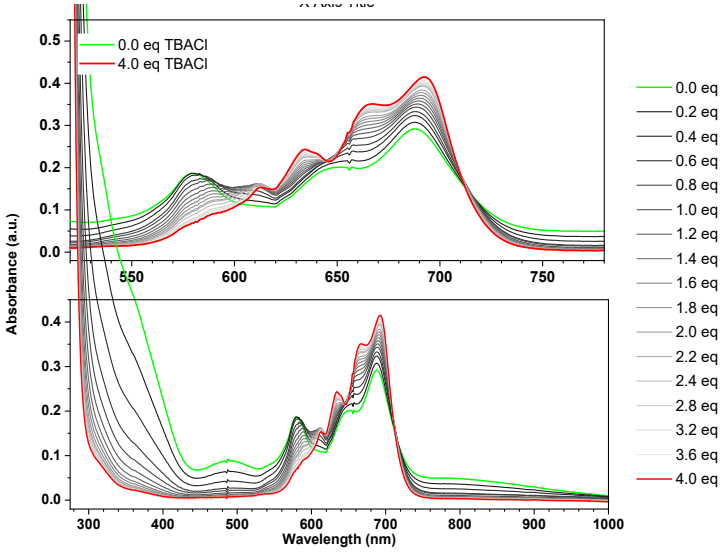

Figure A 2.40. UV-Vis spectral changes of the $[Co^{II}(PN)_2Cl_2]$ ($5.75x10^{-4}$ M, in CH_3CN) upon addition of TBACl from 0 to 4.0 equiv.

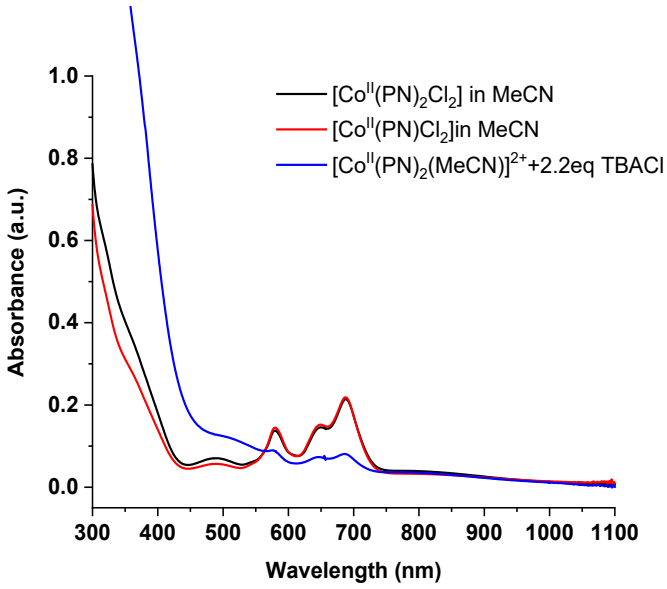

Figure A 2.41. The UV-Vis spectrum of the $[Co^{II}(PN)_2Cl_2]$ ($5.75x10^{-5}$ M in MeCN, black), independently synthesized $[Co^{II}(PN)Cl_2]$ (red) and the spectrum of $[Co^{II}(PN)_2(MeCN)]^{2+}$ with 2.2 eq TBACl under the similar conditions.

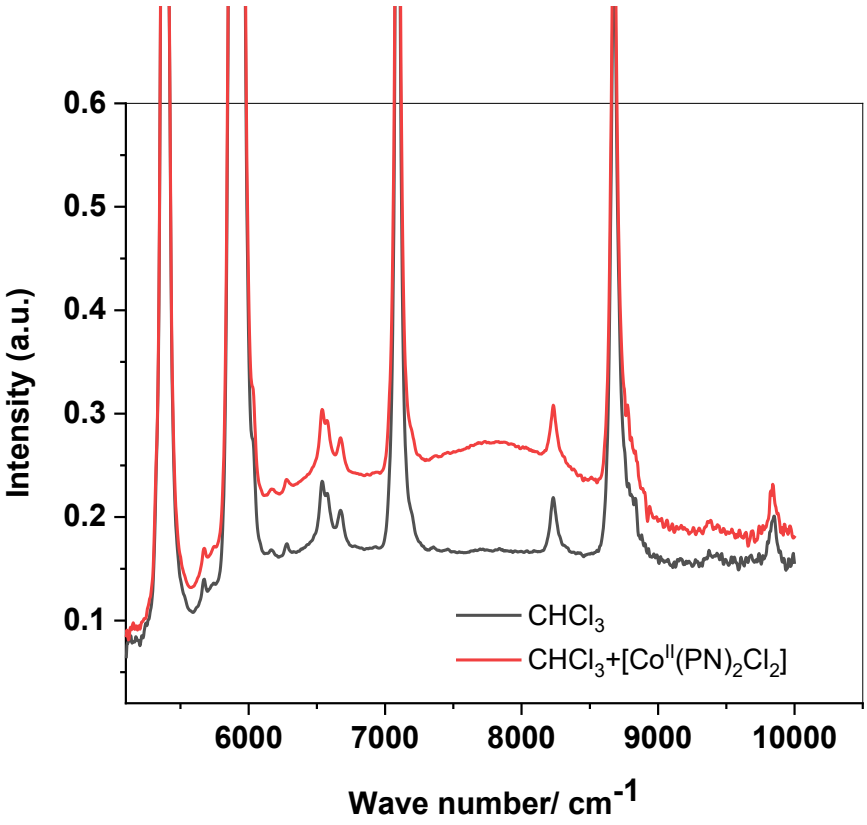

Figure A 2.42. The NIR spectrum of the $[Co^{II}(PN)_2Cl_2]$ (in $CHCl_3$, red), and the spectrum $CHCl_3$ with no complex (black).

Appendix to Chapter 3

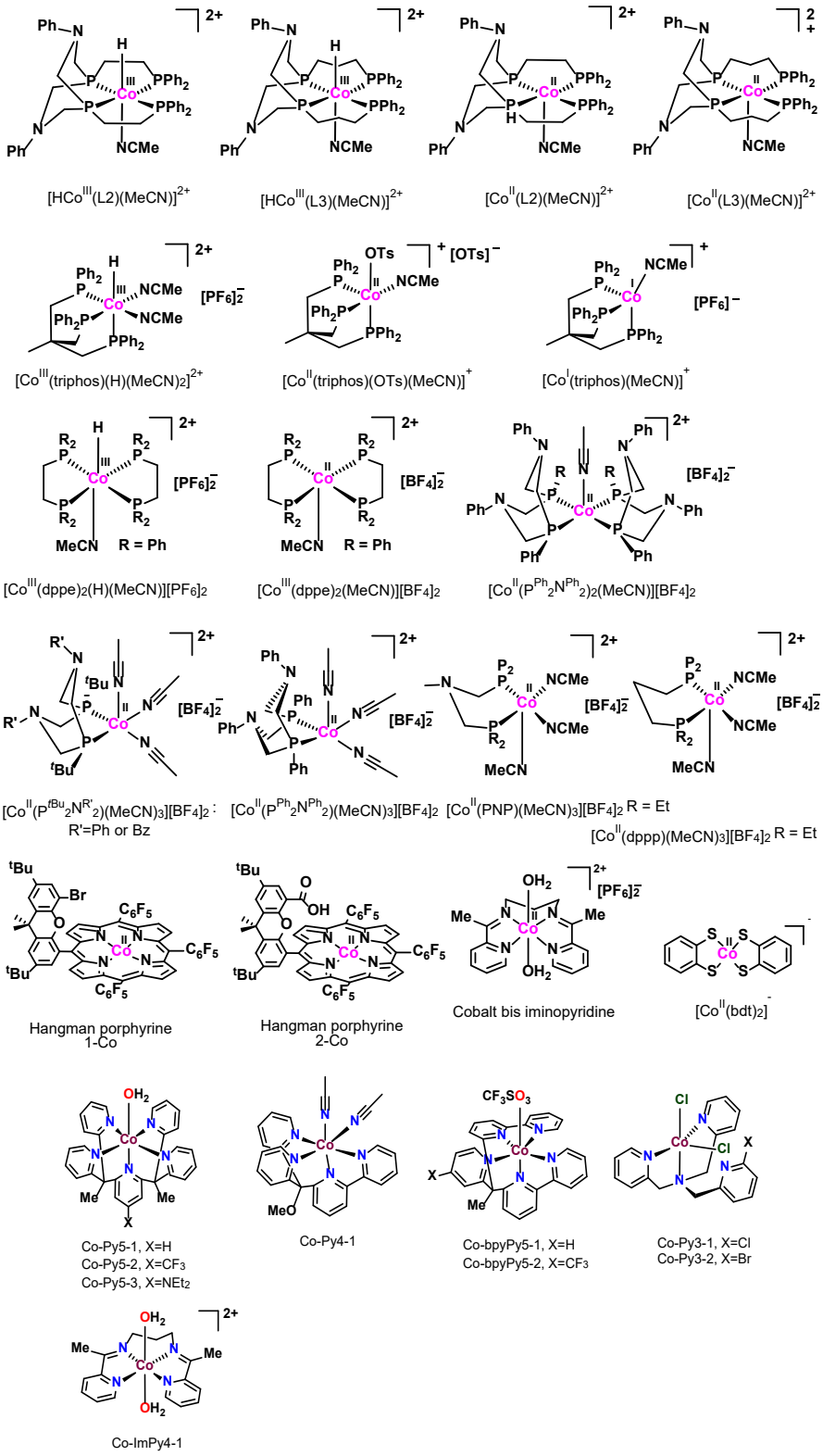

Chart A 3.1. The structures of cobalt complexes with different ligand scaffolds for electrocatalytic hydrogen evolution in the literatures.

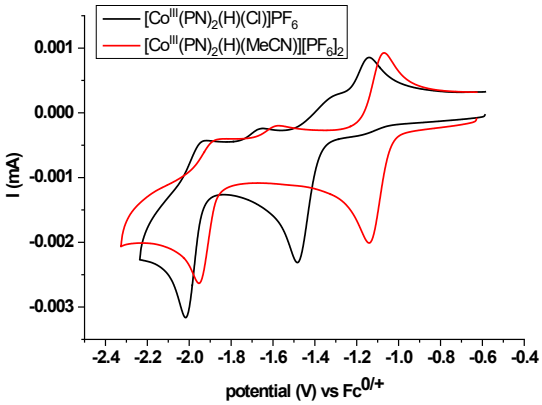

Figure A 3.1. CVs of the $[Co^{III}(PN)_2(H)(Cl)][PF_6]$ (1 mM) in CH_3CN with 0.1 M $TBAPF_6$, compared to the hydride derivative containing CH_3CN ligand at scan rate 100 mVs^{-1}.

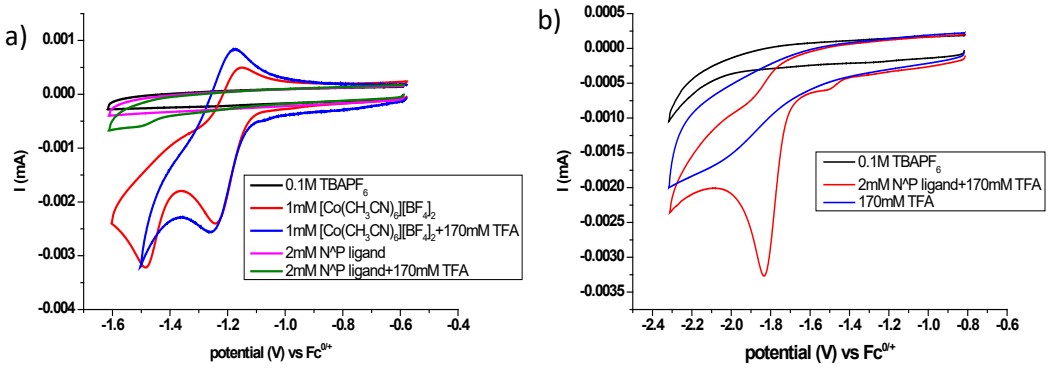

Figure A 3.2. (a) CVs of the PN ligand (2 mM) and $[Co(CH_3CN)_6][BF_4]_2$ (1mM) in the absence and presence of 170 mM TFA in CH_3CN containing 0.1 M $TBAPF_6$ and (b) scanning to more negative potential . Scan rate 100 mVs^{-1}.

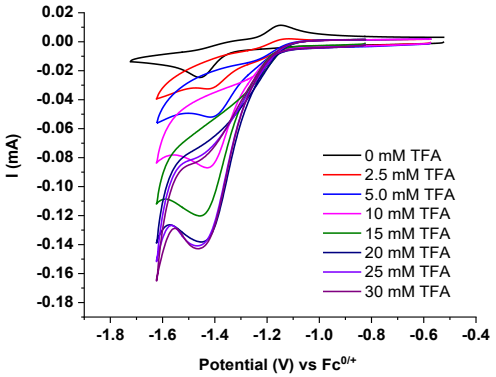

Figure A 3.3. CVs of $[Co^{III}(PN)_2(H)(Cl)][PF_6]$ (1 mM) in CH_3CN with 0.1 M $TBAPF_6$ at 100 mV s^{-1} in the presence of various concentrations of CF_3COOH at Co(III/II)-H.

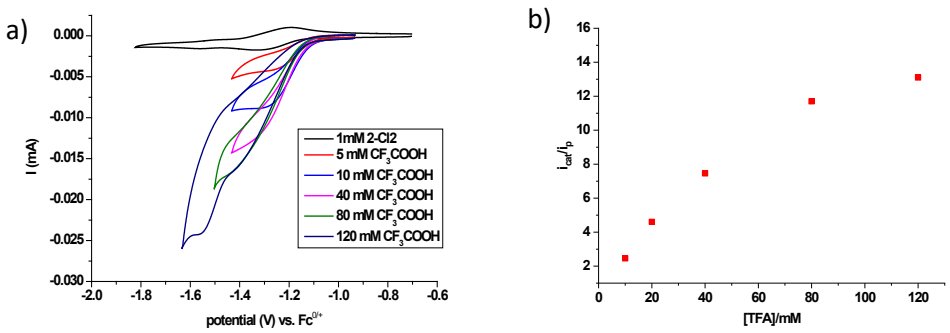

Figure A 3.4.a) Cyclic voltammograms of $Co^{II}(PN)_2Cl_2$ (1 mM) in CH_3CN with 0.1 M $TBAPF_6$ at 100 mV s^{-1} in the presence of various concentrations of CF_3COOH, b) plot of i_{cat}/i_p taken from the peak currents, in CH_3CN with 0.1 M $TBAPF_6$ versus the concentration of TFA acid at 100 mV s^{-1}.

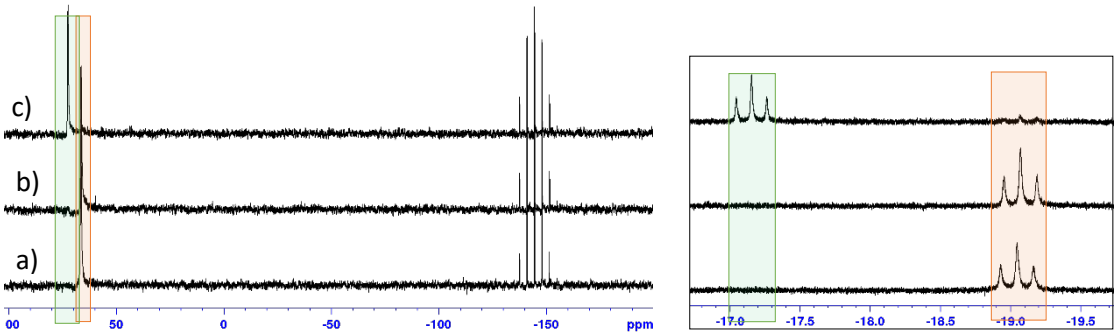

Figure A 3.5. $^{31}P\{^1H\}$ NMR spectra of $[Co^{III}(PN)_2(H)(Cl)][PF_6]$ at room temperature (in CD_3CN), a) in the presence of 0.0 equiv CF_3COOH, b) 10.0 equiv CF_3COOH left for 30 min **and c)** 10.0 equiv CF_3COOH left for 2 days. Inset shows the ^1H NMR of these solutions in hydride region and the orange and green labels indicated the signals of the $[Co^{III}(PN)_2(H)(Cl)][PF_6]$ and $[Co^{III}(PN)_2(H)(MeCN)]^{2+}$, respectively.

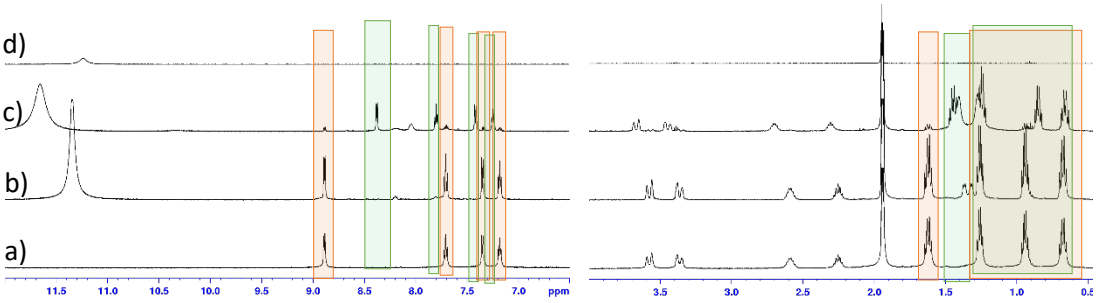

Figure A 3.6. ^1H NMR spectra of $[Co^{III}(PN)_2(H)(Cl)][PF_6]$ in CD_3CN, **a)** in the presence of 0.0 equiv CF_3COOH, **b) 1**0.0 equiv CF_3COOH left for 30 min and **c)** 10.0 equiv CF_3COOH left for 2 days, **d)** a solution of 10.0 equiv CF_3COOH in CD_3CN. Orange labels and green labels indicate the signals of the $[Co^{III}(PN)_2(H)(Cl)][PF_6]$ and $[Co^{III}(PN)_2(H)(MeCN)]^{2+}$, respectively.

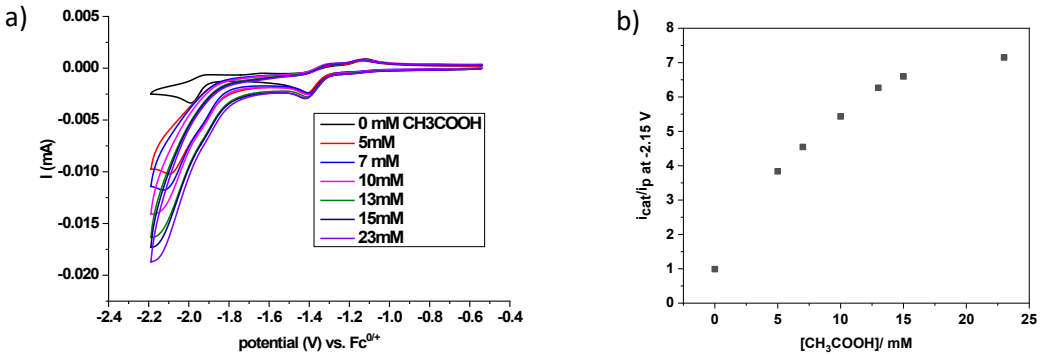

Figure A 3.7. (a) CVs of $[Co^{III}(PN)_2(H)(Cl)][PF_6]$ (1mM) in CH_3CN with 0.1 M $TBAPF_6$ at 100 mV s^{-1} in the presence of various concentrations of CH_3COOH. (b) plot of i_{cat}/i_p of the complex taken from the peak current versus the concentration of acetic acid.

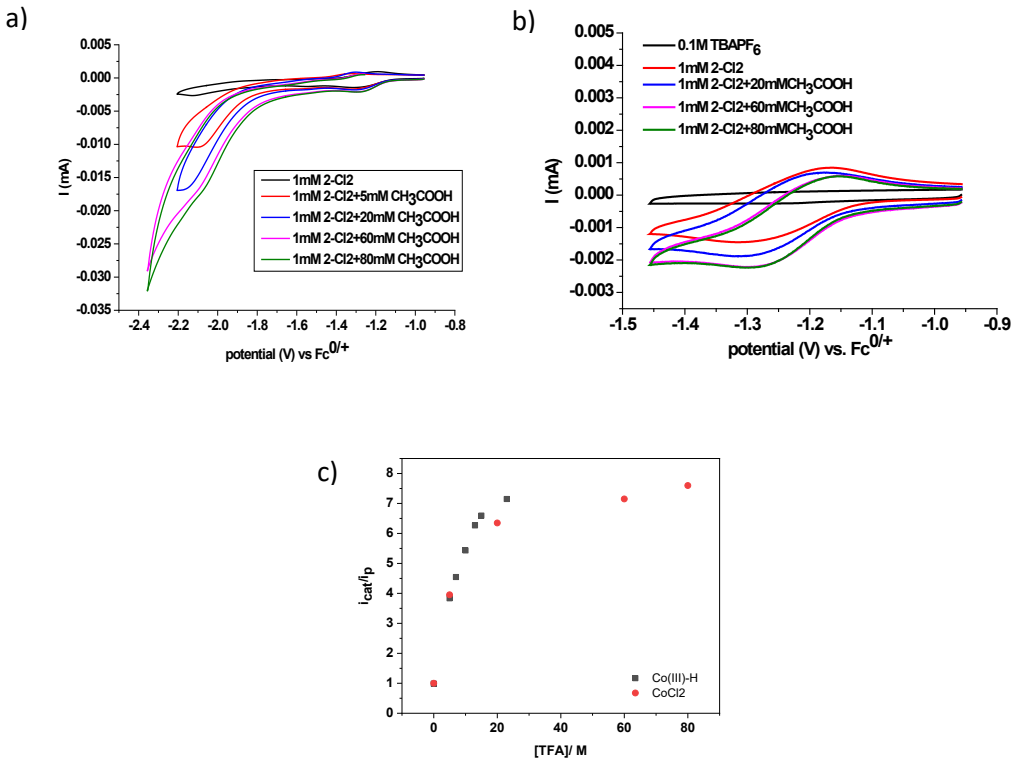

Figure A 3.8. CVs of a) $Co^{II}PN_2Cl_2$ (1 mM), b) redox wave of Co(II/I), in CH_3CN with 0.1 M $TBAPF_6$ at 100 mV s^{-1} upon tritration with CH_3COOH, c) plot of i_{cat}/i_p of the complex taken from the peak current versus the concentration of acetic acid compared to that of the hydride derivatives.

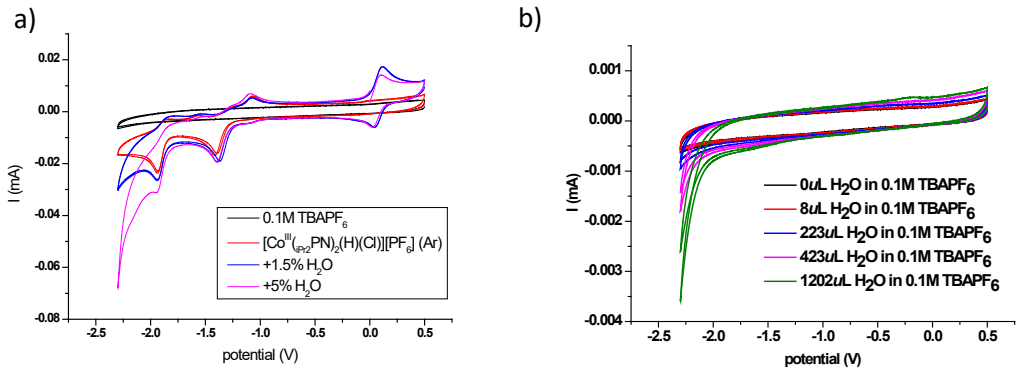

Figure A 3.9. CVs of $[Co^{III}(PN)_2(H)(Cl)][PF_6]$ (1 mM) in CH_3CN with 0.1 M $TBAPF_6$ at 100 mV s^{-1} in the presence of various concentrations of H_2O (a), CVs of background (0.1 M $TBAPF_6$) with no complex at 100 mV s^{-1} in the presence of various concentrations of water, (b).

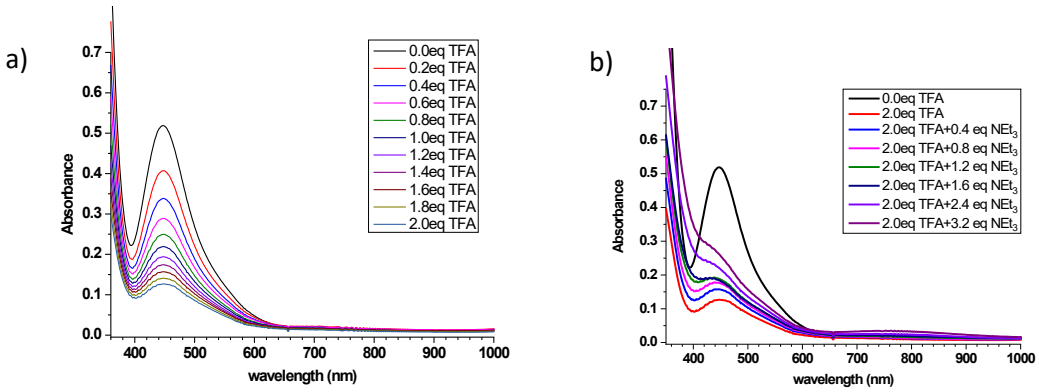

Figure A 3.10. (a) UV-Vis spectral changes of $[Co^{II}(PN)_2(MeCN)][BF_4]_2$ ($5.75x10^{-4}$ M, in CH_3CN) upon addition of TFA acid, (b) the solution with 2.0 equiv TFA upon addition of NEt_3.

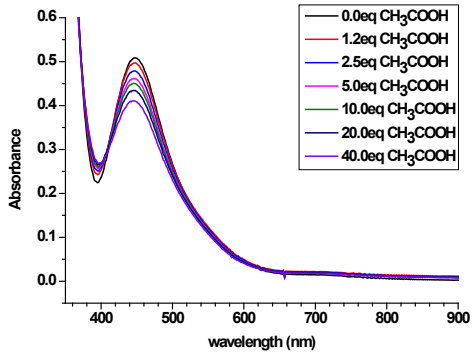

Figure A 3.11. UV-Vis spectral changes of $[Co^{II}(PN)_2(MeCN)][BF_4]_2$ ($5.75x10^{-4}$ M, in CH_3CN) upon addition of CH_3COOH from 0 to 40.0 equiv.

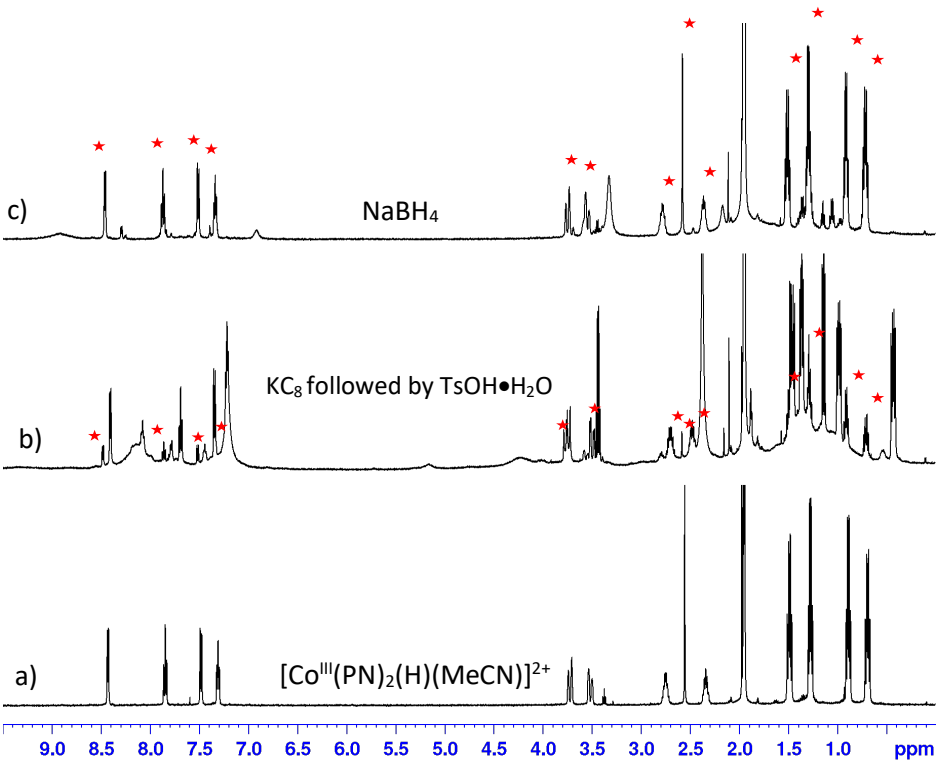

Figure A 3.12. ^{1}H NMR spectra of (a) $[Co^{III}(PN)_2(H)(MeCN)]^{2+}$ 16.8 mM in CD_3CN, (b) products formed by protonation with $TsOH•H_2O$ following a reduction of $[Co^{II}(PN)_2(MeCN)]^{2+}$ with KC_8, (c) products obtained by a reaction of the $[Co^{II}(PN)_2(MeCN)]^{2+}$ complex with $NaBH_4$. Red asterisks signals of $[Co^{III}(PN)_2(H)(MeCN)]^{2+}$.

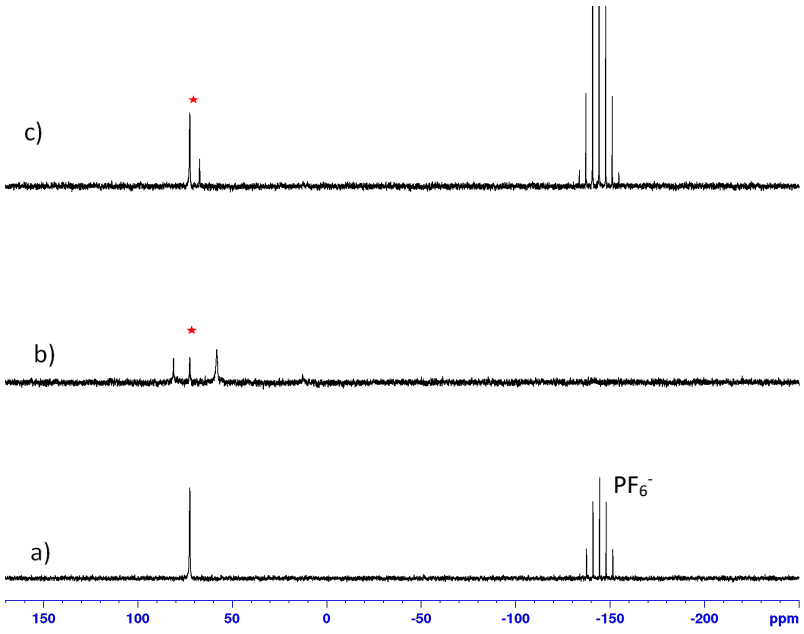

Figure A 3.13. $^{31}P\{^{1}H\}$ NMR spectra of (a) $[Co^{III}(PN)_2(MeCN)(H)]^{2+}$ 16.8 mM in CD_3CN, (b) products formed by protonation by $TsOH•H_2O$ following reduction of $[Co^{II}(PN)_2(MeCN)]^{2+}$ with KC_8, (c) products obtained by a reaction of the $[Co^{II}(PN)_2(MeCN)]^{2+}$ complex with $NaBH_4$. Red asterisks signals of $[Co^{III}(PN)_2(H)(MeCN)]^{2+}$.

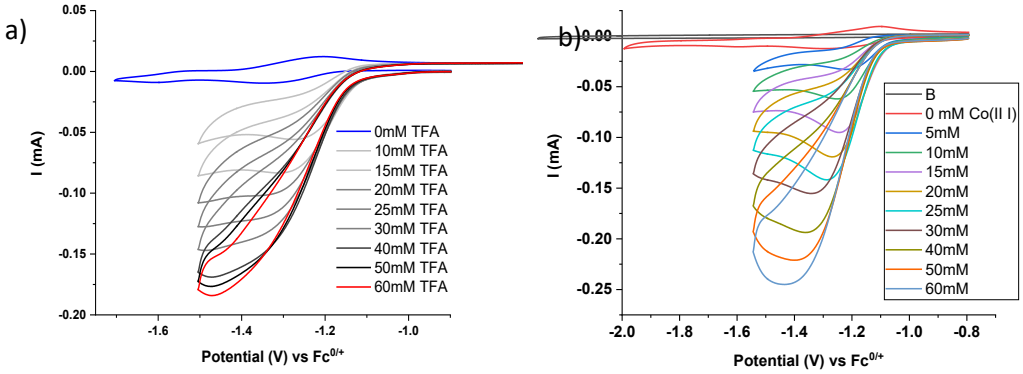

Figure A 3.14. CVs titration of (a) [Co^{III}*cis*-$(PN)_2Cl_2$][PF_6].and (b) [Co^{II}*cis*-$(PN)_2Cl$][PF_6] with TFA acid (0-60 mM). Conditions: 1 mM of the complex in CH_3CN with 0.1 M $TBAPF_6$ at scan rate of 100 mV s^{-1}.

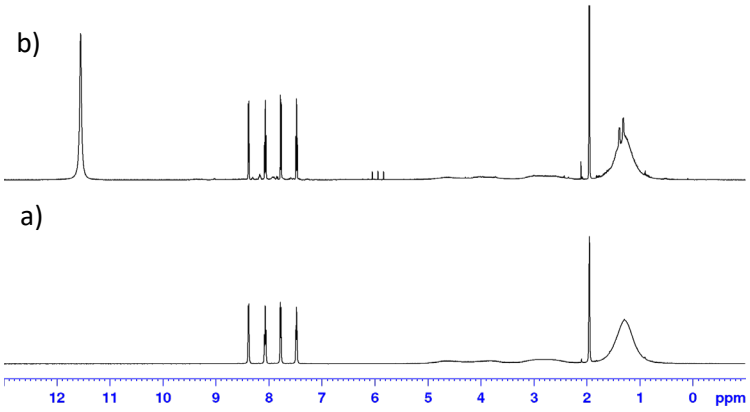

Figure A 3.15. ^{1}H NMR of [Co^{III}*cis*-$(PN)_2Cl_2$]PF_6 16.8 mM in CD_3CN in the absence (a) and in the presence (b) of 10 equiv. of TFA.

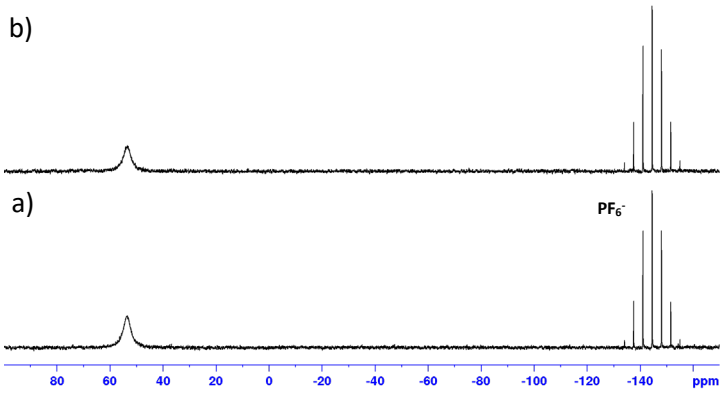

Figure A 3.16. $^{31}P\{^1H\}$ NMR spectra of [Co^{III}*cis*-$(PN)_2Cl_2$]PF_6 16.8 mM in CD_3CN in the absence (a) and in the presence (b) of 10 equiv. of TFA**.**

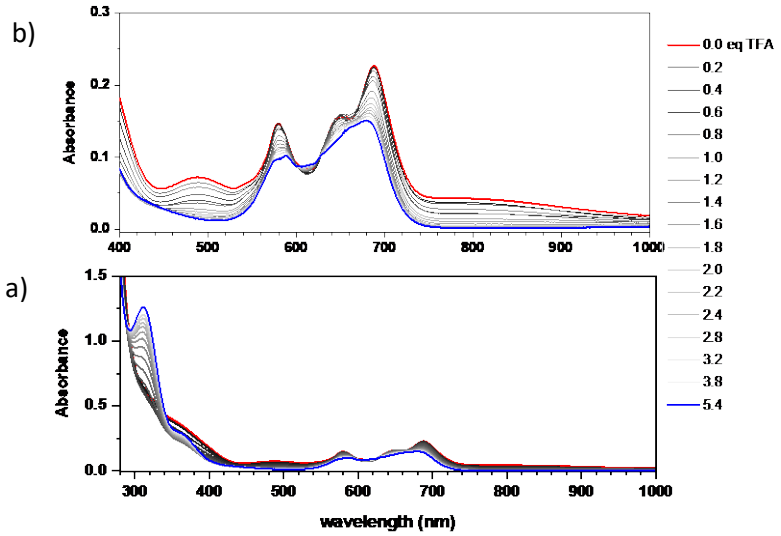

Figure A 3.17. (a) UV-Vis spectral changes of $[Co^{II}(PN)_2Cl_2]$ ($5.75x10^{-4}$ M, in CH_3CN) upon addition of TFA, (b) d-d transition bands in the visible region ranging from 400-800 nm.

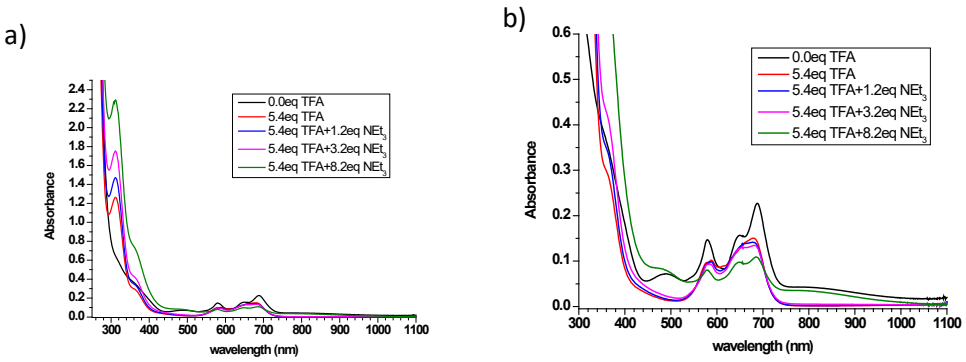

Figure A 3.18. UV-Vis spectral changes of $[Co^{II}(PN)_2Cl_2]$ ($5.75x10^{-4}$ M, in CH_3CN) (a) with 5.4 equiv TFA upon addition of NEt_3, (b) d-d transition bands in the visible region ranging from 400-800 nm.

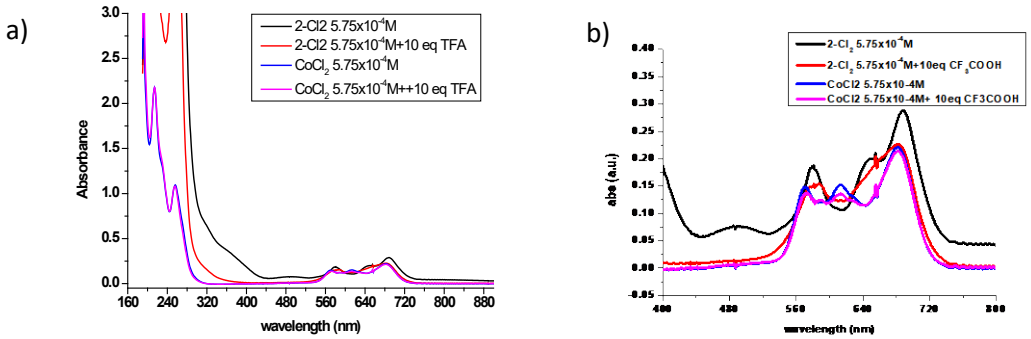

Figure A 3.19. (a) UV-Vis spectral changes of $[Co^{II}(PN)_2Cl_2]$ ($5.75x10^{-4}$ M, in CH_3CN) with 10 equiv TFA acid compared to that of precursor $CoCl_2$ in the same conditions, (b) d-d transition bands in the visible region ranging from 400-800 nm.

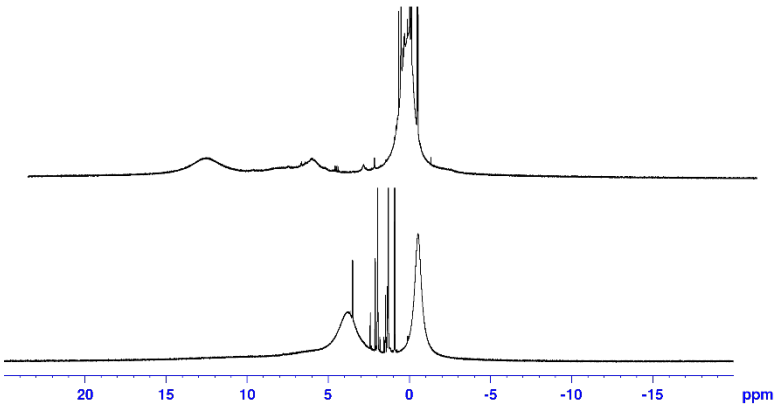

Figure A 3.20. ^{1}H NMR spectra of $[Co^{II}(PN)_2Cl_2]$ 21.6 mM in CD_3CN in the absence (bottom) and in the presence (top) of 6.8 eq trifluoroacetic acid.

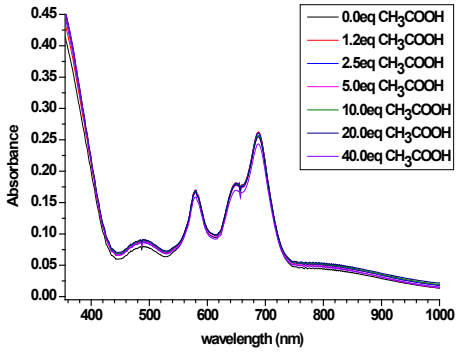

Figure A 3.21. (a) UV-Vis spectral changes of $[Co^{II}(PN)_2Cl_2]$ ($5.75x10^{-4}$ M, in CH_3CN) upon addition of CH_3COOH acid from 0 to 40.0 equiv.

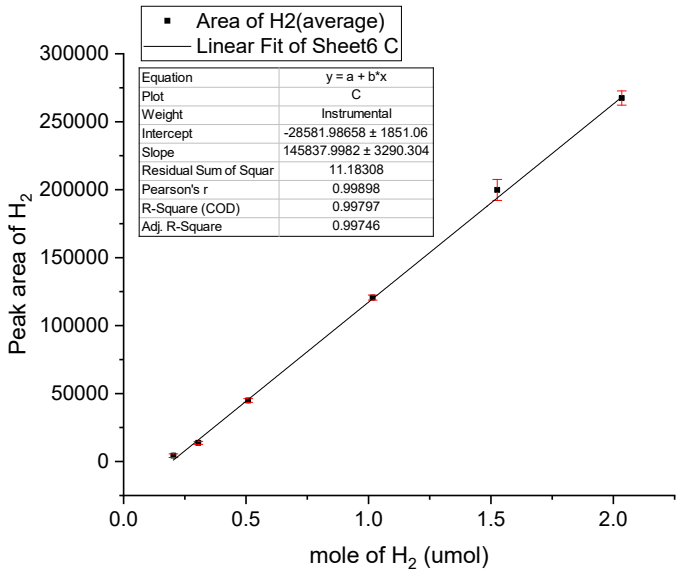

Figure A 3.22. Calibration curve for H_2 determination.

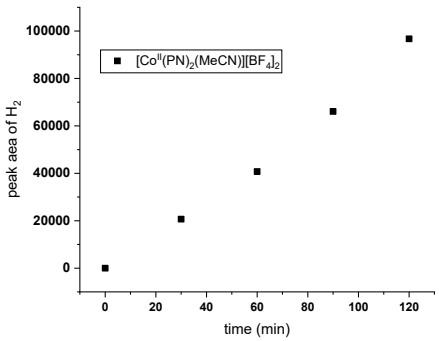

Figure A 3.23. Plot of peak area of H_2 evolved during the course of electrolysis of 0.9 mM $[Co^{II}(PN)_2(MeCN)][BF_4]_2$ (black) in CH_3CN solution containing 0.1 M $TBAPF_6$ in the presence of 60 mM of TFA at E_{app} = -1.33.

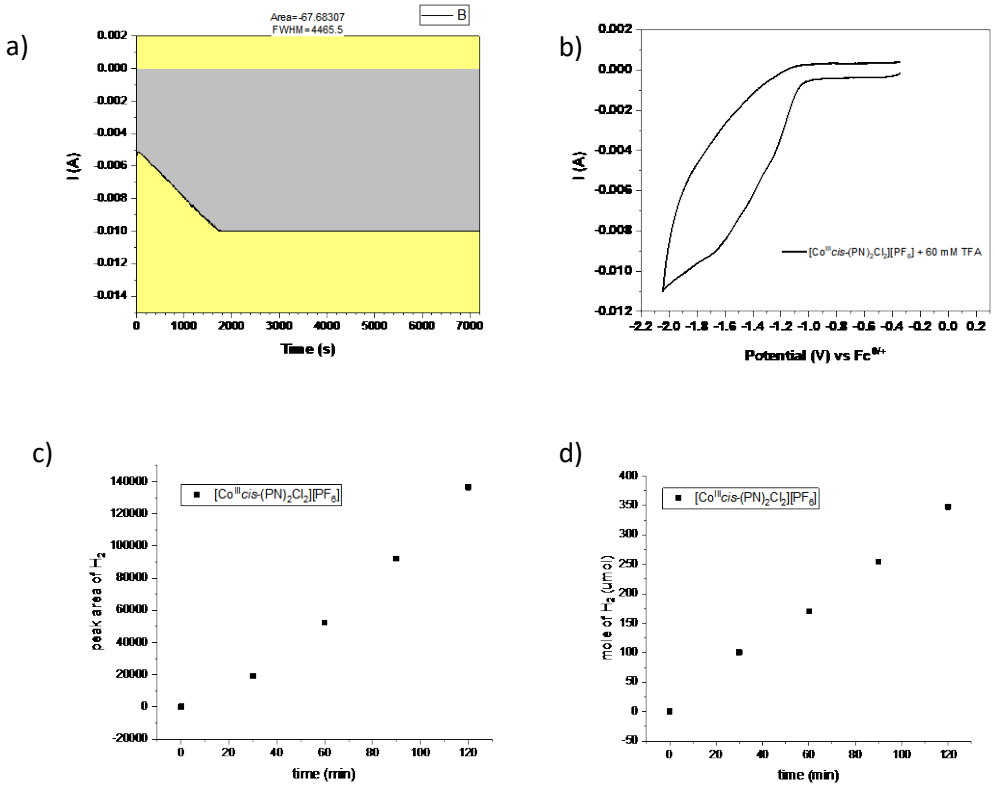

Figure A 3.24. (a) Controlled potential electrolysis of 0.9 mM $[Co^{III}cis\text{-}(PN)_2Cl_2]PF_6$ in CH_3CN solution containing 0.1 M $TBAPF_6$ in the presence of 60 mM of TFA at E_{app} = -1.48 V vs $Fc^{0/+}$ for 2h. (b) the CV of this complex in the same solution recorded before electrolysis, right. Plot of peak area (c) experimental number of moles of of H_2 (d) against bulk electrolysis time.

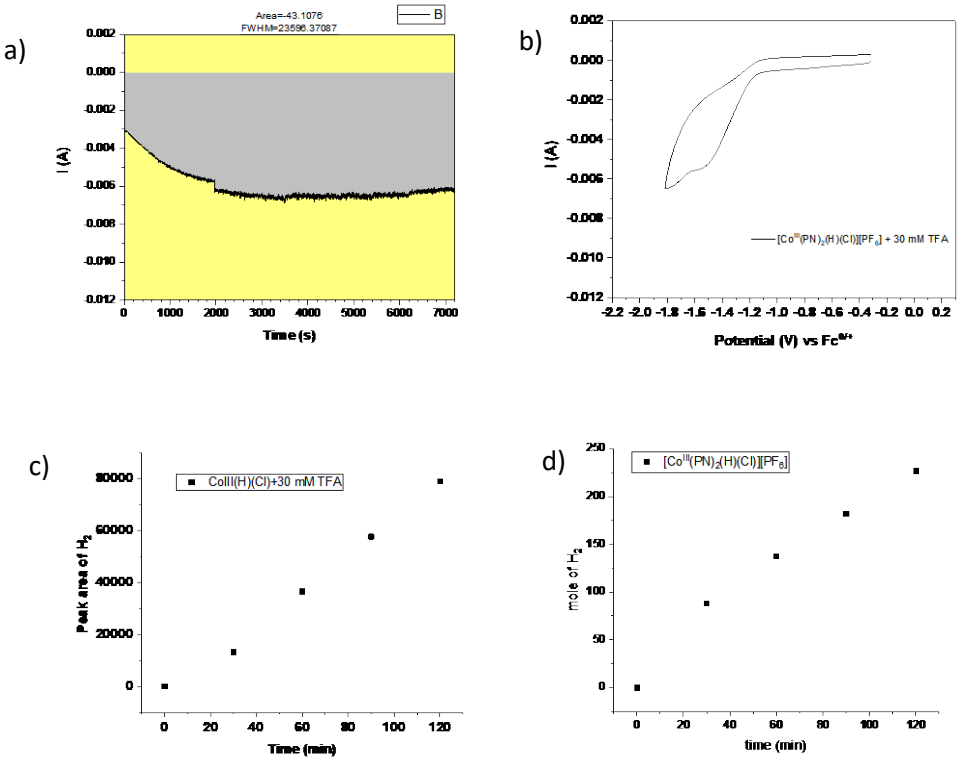

Figure A 3.25. (a) Controlled potential electrolysis of 0.9 mM $[Co^{III}(PN)_2(H)(Cl]PF_6$ in CH_3CN solution containing 0.1 M $TBAPF_6$ in the presence of 30 mM of TFA at E_{app} = -1.50 V vs $Fc^{0/+}$ for 2h, (b) the CV of this complex in the same solution recorded before electrolysis, right. Plot of peak area (c) experimental number of moles of of H_2 (d) against bulk electrolysis time.

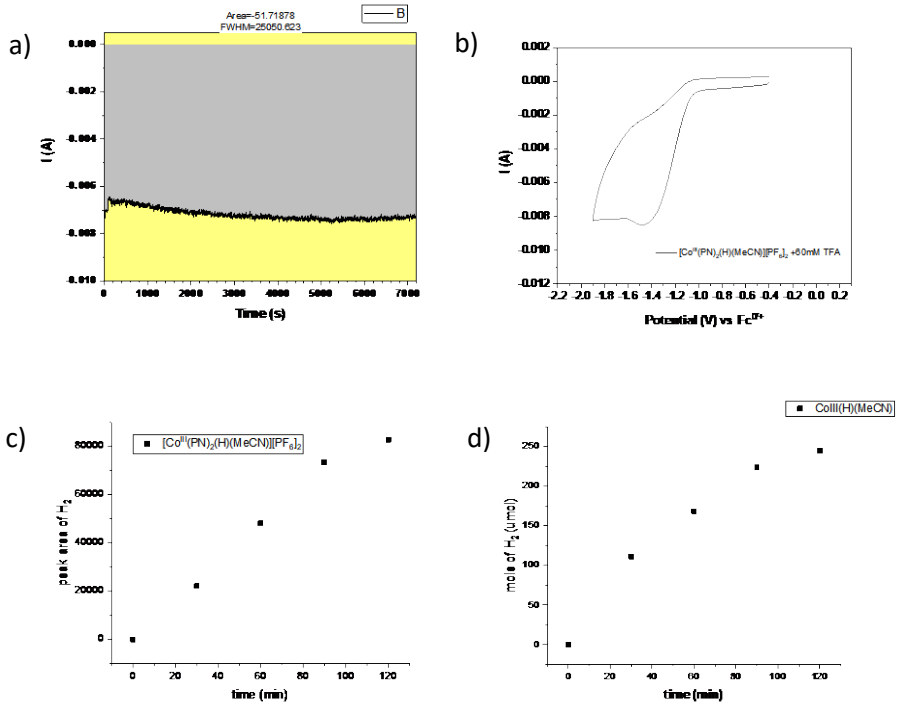

Figure A 3.26. (a) Controlled potential electrolysis of 0.9 mM $[Co^{III}(PN)_2(H)(MeCN)][PF_6]_2$ in CH_3CN solution containing 0.1 M $TBAPF_6$ in the presence of 60 mM of TFA at Eapp = -1.40 V vs $Fc^{0/+}$ for 2h, (b) the CV of this complex in the same solution recorded before electrolysis. Plot of peak area (c) experimental number of moles of of H_2 (d) against bulk electrolysis time.

Benchmarking HER catalysts and comparison to other catalysts

Overpotential ($\eta_{cat/2}$) for the $[Co^{III}(PN)_2(H)(Cl)][PF_6]$ in MeCN by using TFA as H^+ source can be determined as the following equation:

$$\eta_{cat/2} = E_{cat/2} - E^0_{HA/H2}\ ;\ (E^0_{HA/H2} = -0.77\ V \text{ for TFA in MeCN})$$
$$= 1.31 - 0.77$$
$$= 540\ mV$$

Therefore, the overpotential as listed in the **Table A 3.1** for other catalysts can be determined by the same calculation by using $E^0_{HA/H2}$ = -0.53 and -1.42 V for $TsOH{\cdot}H_2O$ and CH_3COOH, respectively.

Table A 3.1. Overpotentials (V vs. $Fc^{0/+}$) of $[Co^{III}(PN)_2(H)(Cl)][PF_6]$ in the presence of 5 equiv of various acids in CH_3CN containing 0.1 M $TBAPF_6$.

Acids	**$TsOH{\bullet}H_2O$**	**CF_3COOH**	**CH_3COOH**
pK_a	8.6	12.65	23.51
$E^0(HA/H_2)$ in CH_3CN	-0.5354V	-0.774V	-1.4151
i_{cat} (mA)	0.087	0.007	0.084
E_{cat} (V)	-1.55	-1.41	-2.03
$E_{cat/2}$ (V)	-1.39	-1.31	-1.89
Over potential (η)	860 m V	540 mV	470 mV

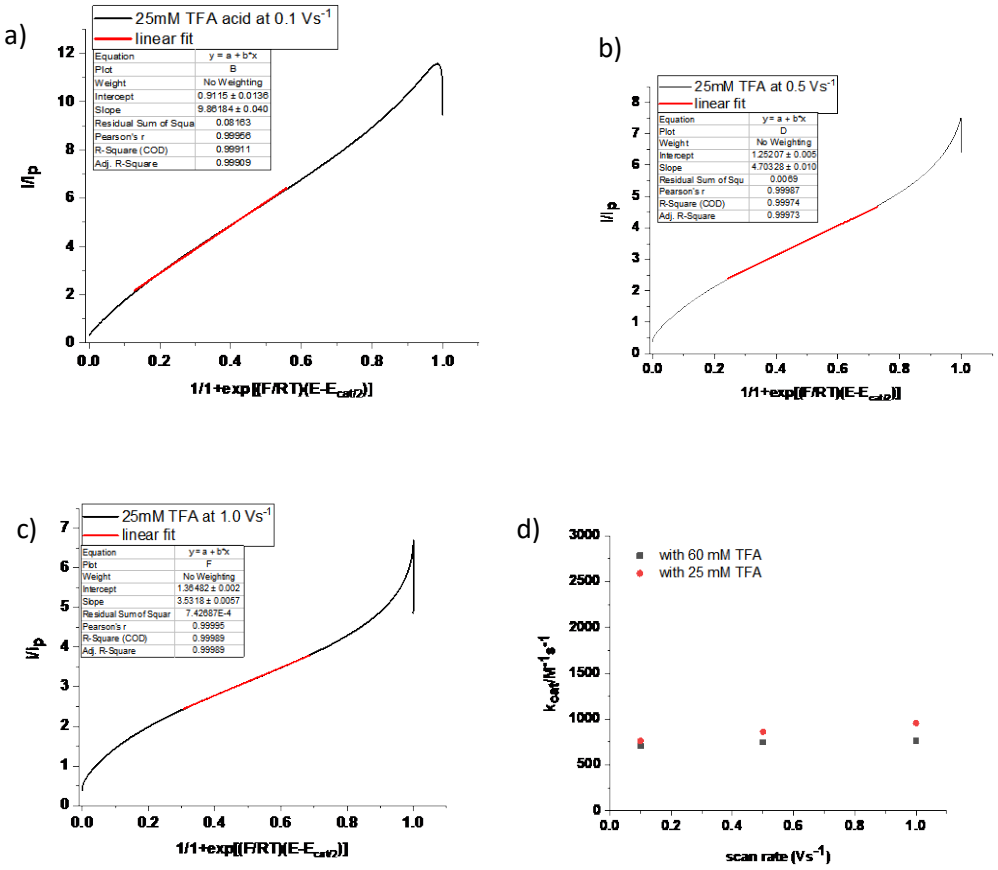

Figure A 3.27. FOWA plots and linear fit for $[Co^{II}(PN)_2(MeCN)][BF_4]_2$ complex (1mM in MeCN with 0.1 M $TBAPF_6$) with 25 mM TFA at different scan rates: (a) 0.1 , (b) 0.5 , (c) 1 V s^{-1}, (d) k_{cat} values from the FOWA plot for the complex with 25 mM TFA (red dot) and 60 mM TFA (black square) at different scan rates.

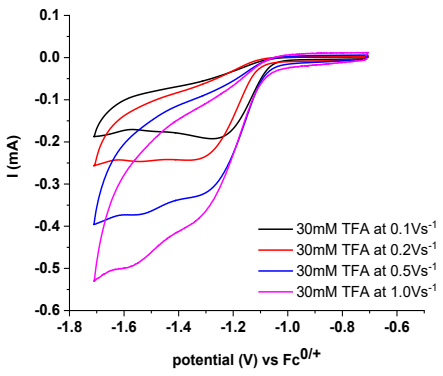

Figure A 3.28. CVs of $[Co^{III}(PN)_2(H)(MeCN)][PF_6]_2$ complex (1 mM) in CH_3CN containing 0.1 M $TBAPF_6$ with 30 mM TFA acid at various scan rates from 0.1 to 1.0 V s^{-1}.

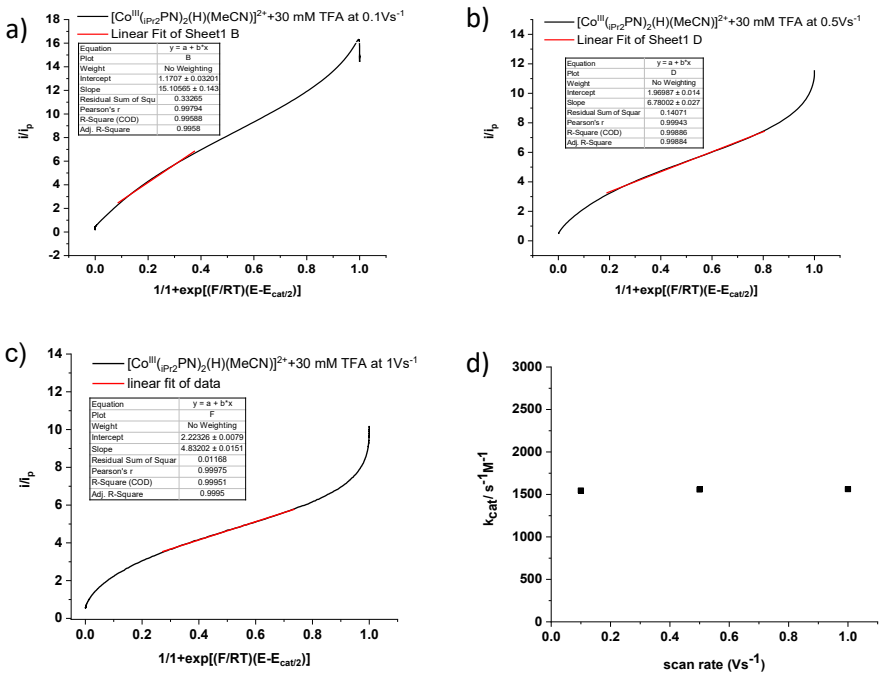

Figure A 3.29. FOWA plots and linear fit for $[Co^{III}(PN)_2(H)(MeCN)][PF_6]_2$ complex (1mM in MeCN with 0.1 M $TBAPF_6$) with 30 mM TFA at different scan rates: (a) 0.1, (b) 0.5, (c) 1 V s^{-1}, (d), k_{cat} values from the FOWA plot for the complex at different scan rates.

Appendix to chapter 4

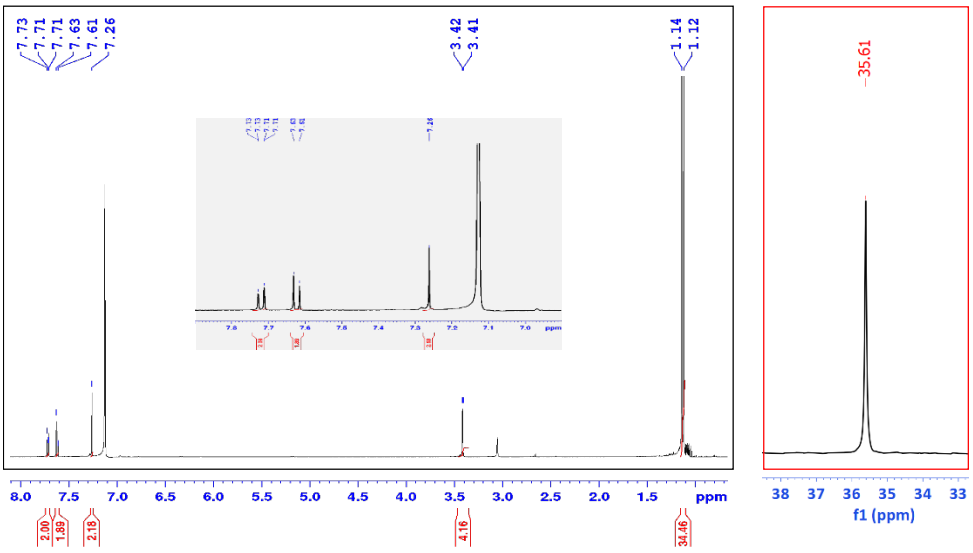

Figure A 4.1. ^{1}H NMR spectrum (black inset) and $^{31}P\{^{1}H\}$ NMR spectrum (red in set) of PNNP ligand in C_6D_6.

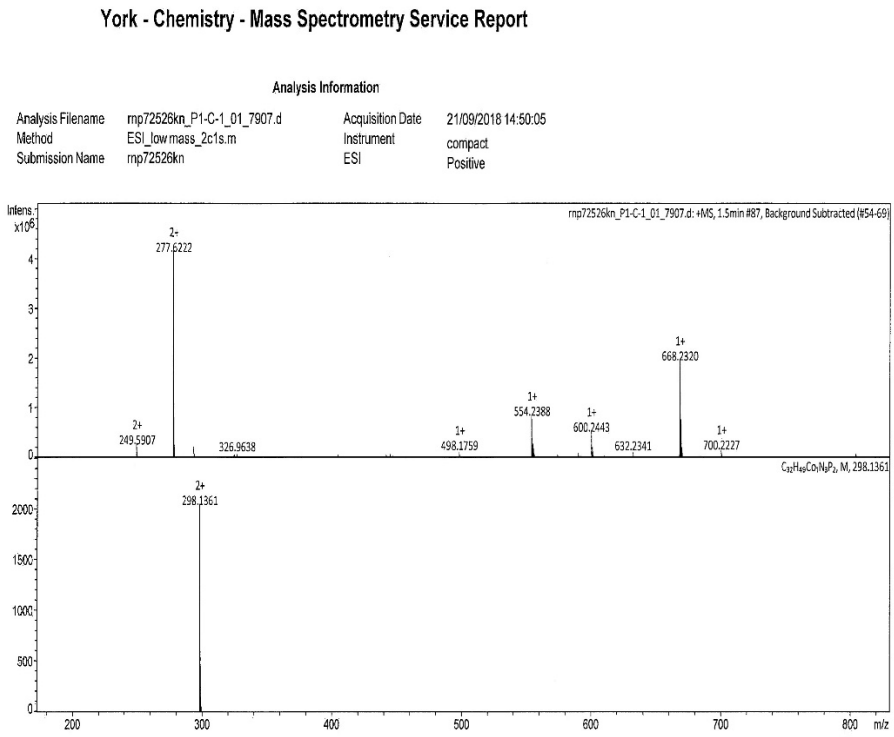

Figure A 4.2. ESI-Mass spectrum (positive ion mode in MeCN) of the $[Co^{II}(PNNP)(MeCN)][BF_4]_2$ complex (top) and the calculated ion peak at m/z = 298.1361 for $[C_{32}H_{49}CoN_3P_2]^{2+}$ (bottom).

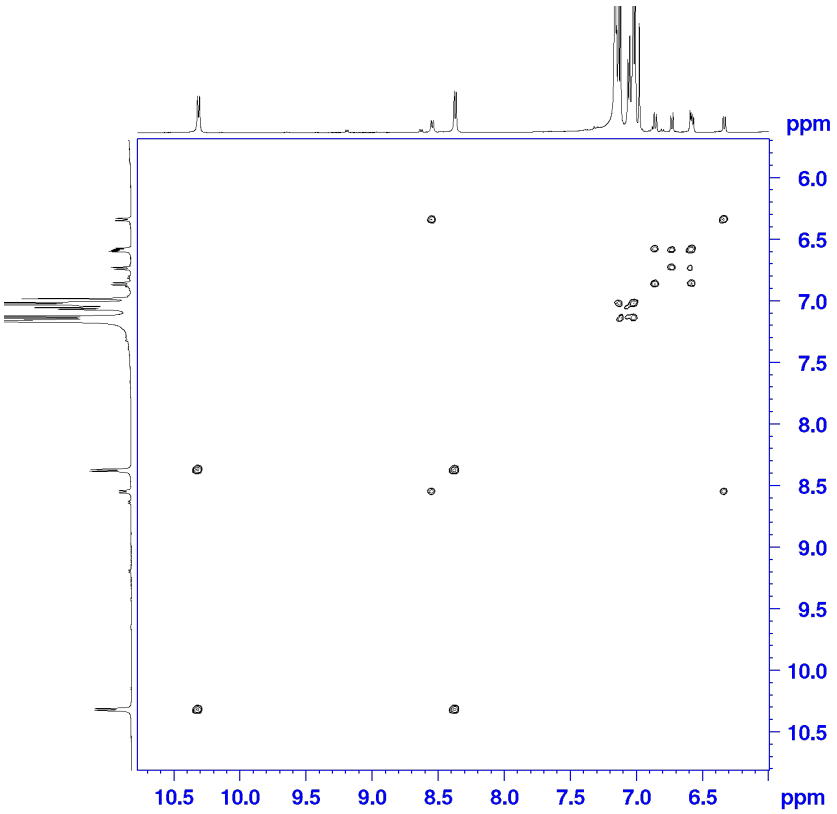

Figure A 4.3. ^{1}H-^{1}H COSY NMR spectrum (aromatic region) of a solution of the [Co(PNNP)(Me)] in C_6D_6 left under Ar for 2 days.

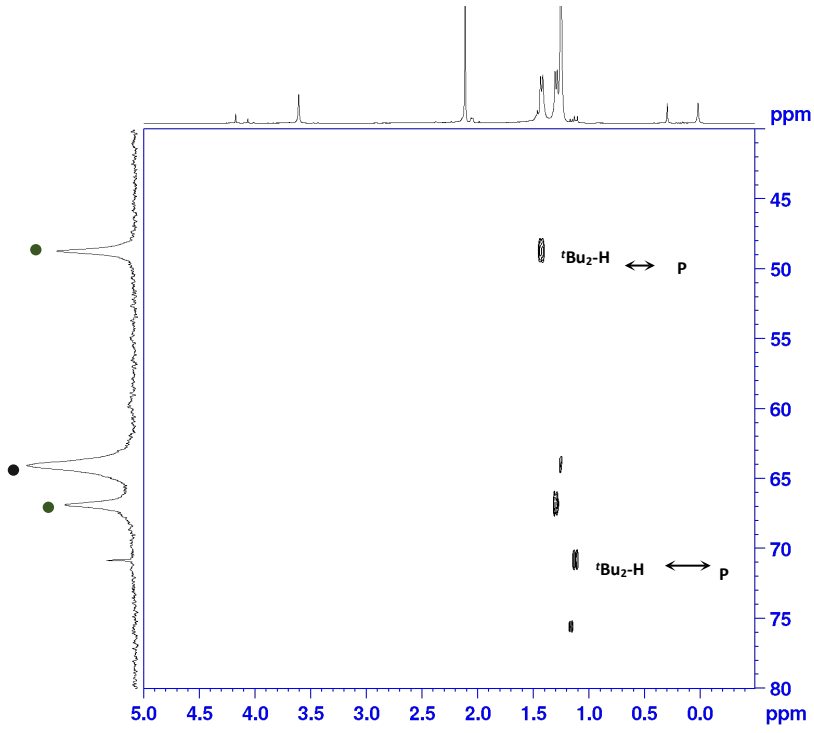

Figure A 4.4. ^{1}H-^{31}P{^{1}H} HMBC spectrum of a solution of the [Co(PNNP)(Me)] in C_6D_6 left under Ar for 2 days.

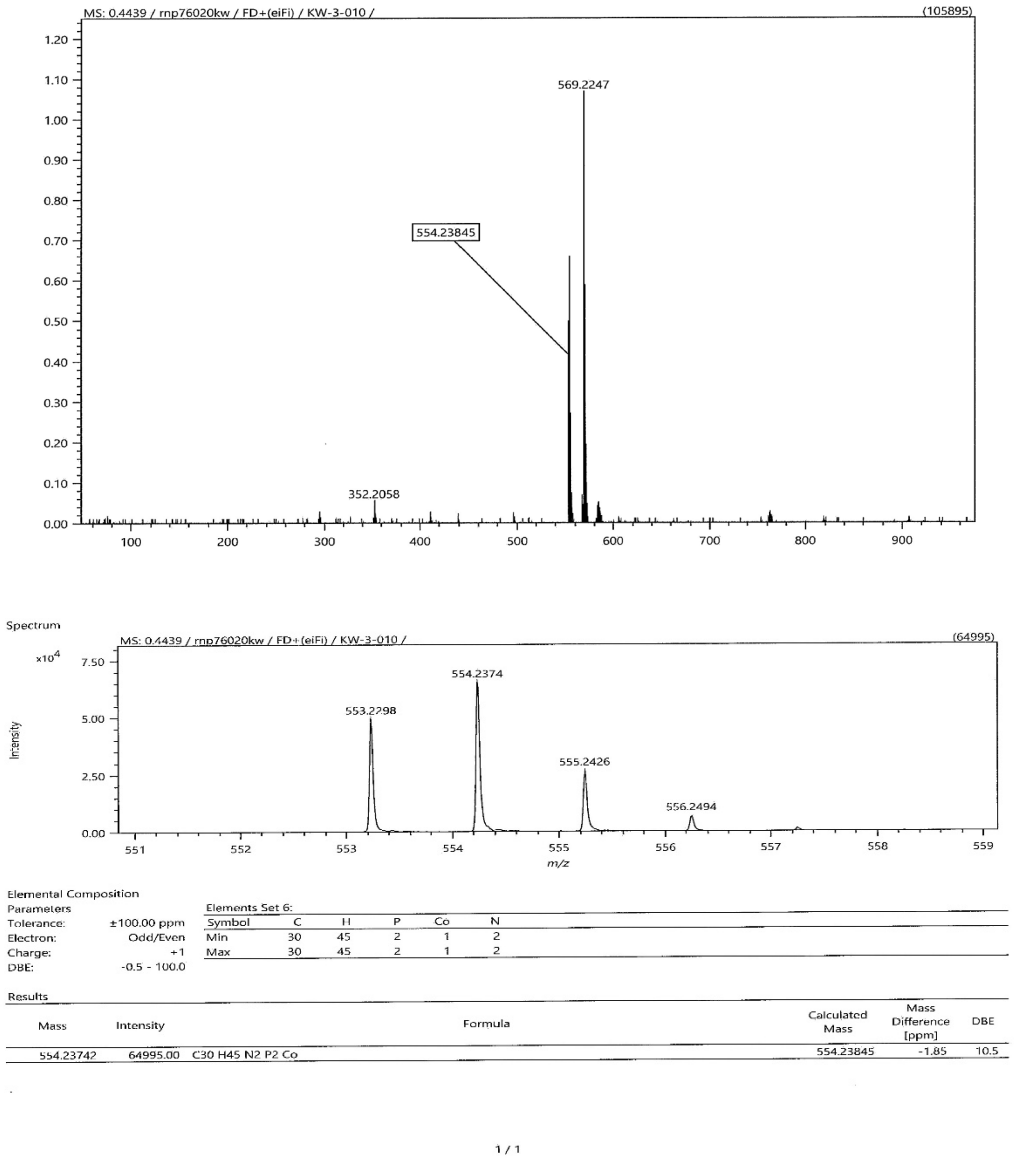

Figure A 4.5. LIFDI Mass spectra (in toluene) of [Co^{I}(dPNNP)] (top), the expansion of the peak at m/z = 554.23742 for [$C_{30}H_{45}N_2P_2Co$] (bottom).

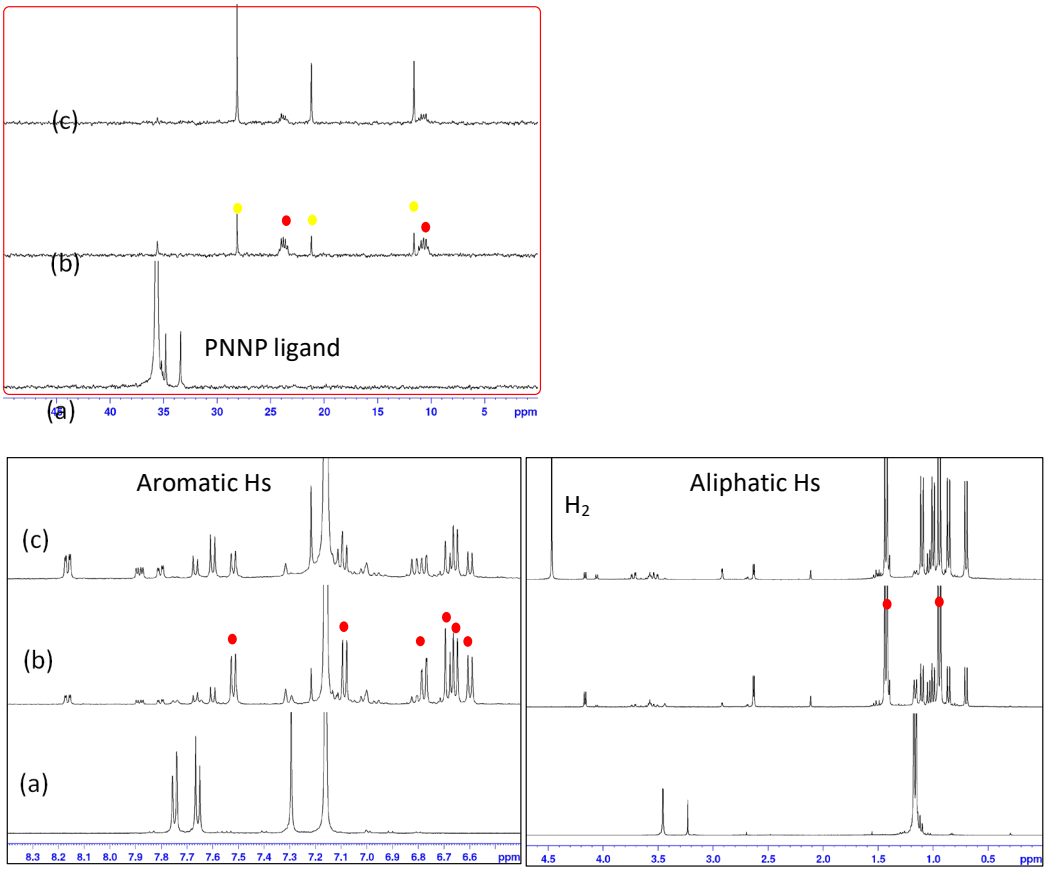

Figure A 4.6. $^{31}P\{^{1}H\}$ NMR spectrum (red in set) and ^{1}H NMR spectrum (black in set) of a solution of the free PNNP ligand in C_6D_6 (a), compared to a solution of lithiated ligand C_6D_6 (b), this solution left under 4 bar of H_2 for overnight (c).

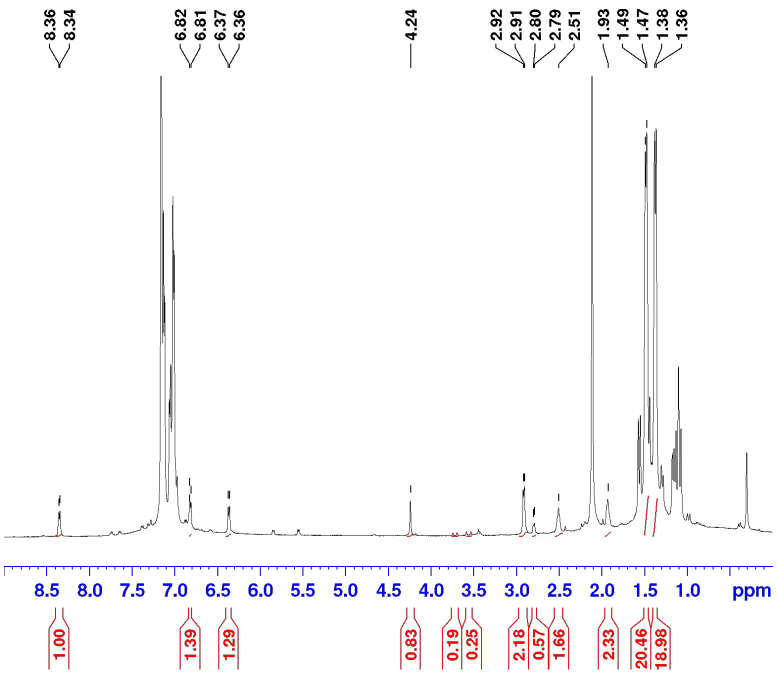

Figure A 4.7. ^{1}H NMR spectrum of a solution of the [Co(dPNNP)] in C_6D_6 left under D_2 for 1 month.

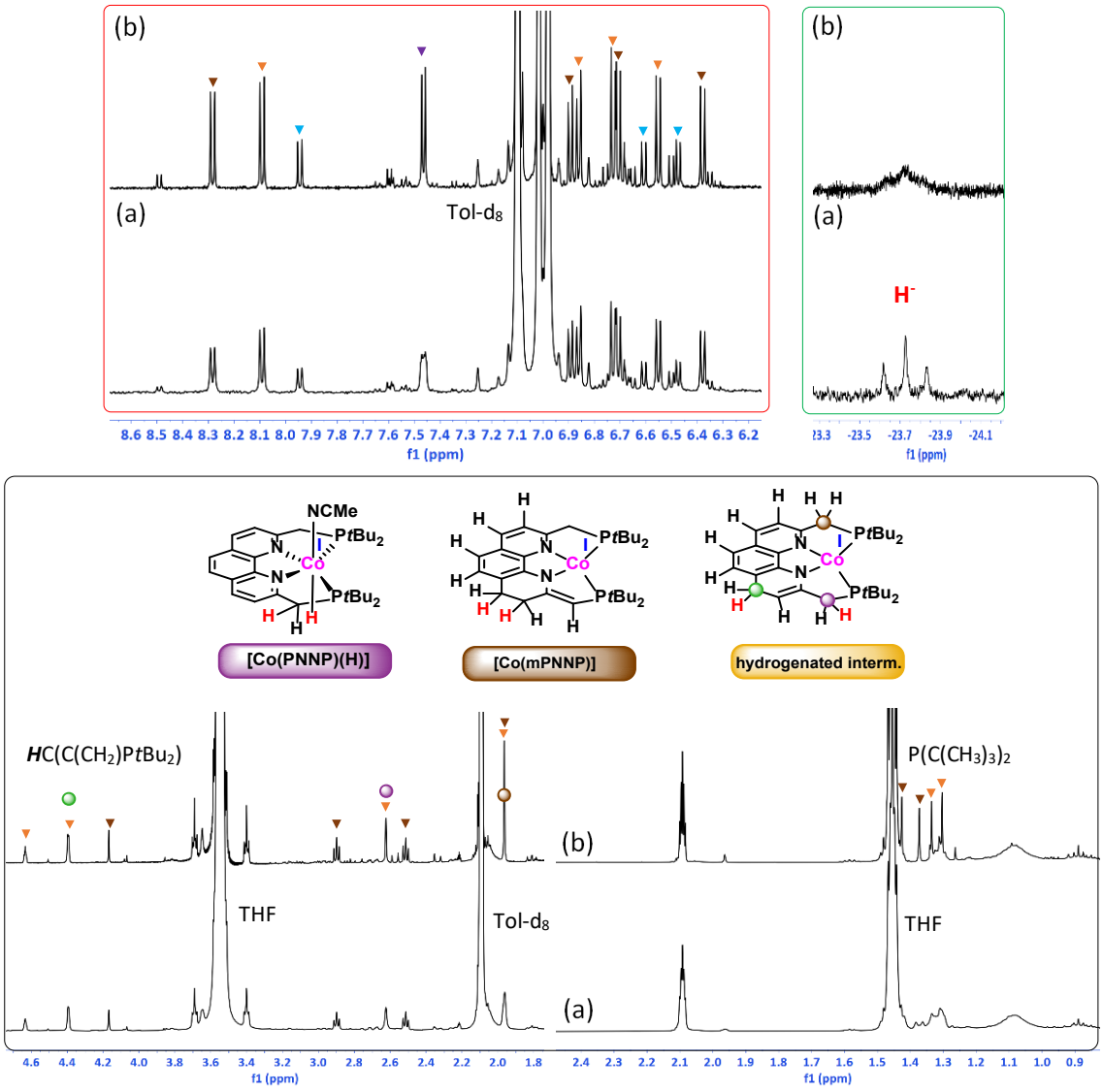

Figure A 4.8. (a) The ^{1}H NMR spectrum and (b) $^{1}H\{^{31}P\}$ NMR spectrum of a reaction mixture of $[Co^{II}(PNNP)(MeCN)][BF_4]_2$ with 2.0 equiv. $NaBEt_3H$ in tol-d_8 left for 1 hour under Ar. The purple labels represented the signals for $[Co^{I}(PNNP)(H)]$, orange labels for hydrogenated intermediate, brown labels for $[Co^{I}(mPNNP)]$ and blue labels for unidentified product. Note that the spectra at right are expanded vertically much less than the spectra at left.

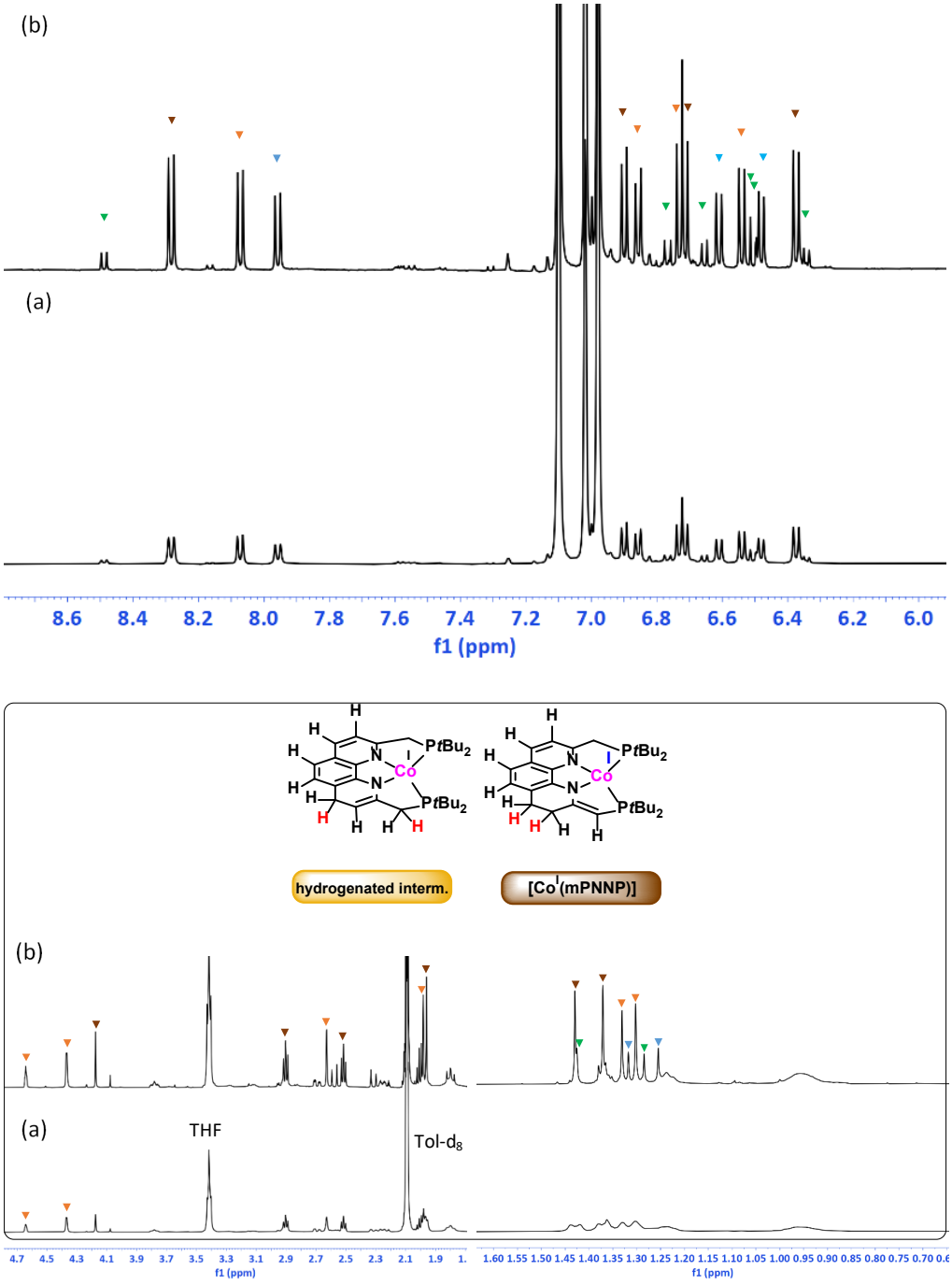

Figure A 4.9. The ^{1}H NMR spectrum (a) and ^{1}H{^{31}P} NMR spectrum (b) of a reaction mixture of [Co^{II}(PNNP)(MeCN)][BF$_4$]$_2$ with 2.0 equiv. NaBEt$_3$H in tol-d$_8$ left for overnight under Ar. The NMR signals with green labels for [Co^{I}(dPNNP)], brown labels for [Co(mPNNP)], orange labels for hydrogenated intermediate and blue labels for unidentified product.

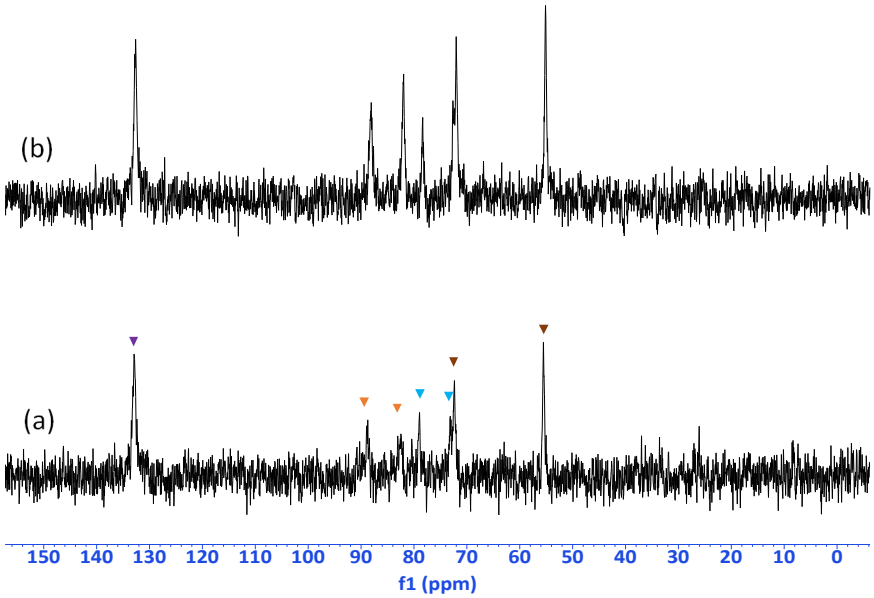

Figure A 4.10. $^{31}P\{^{1}H\}$ NMR spectrum of a reaction mixture of $[Co^{II}(PNNP)(MeCN)]^{2+}$ with 2.0 equiv. $NaBEt_3H$ in tol-d_8 left for 30 min (a) and in C6D6 for 30 min (b)

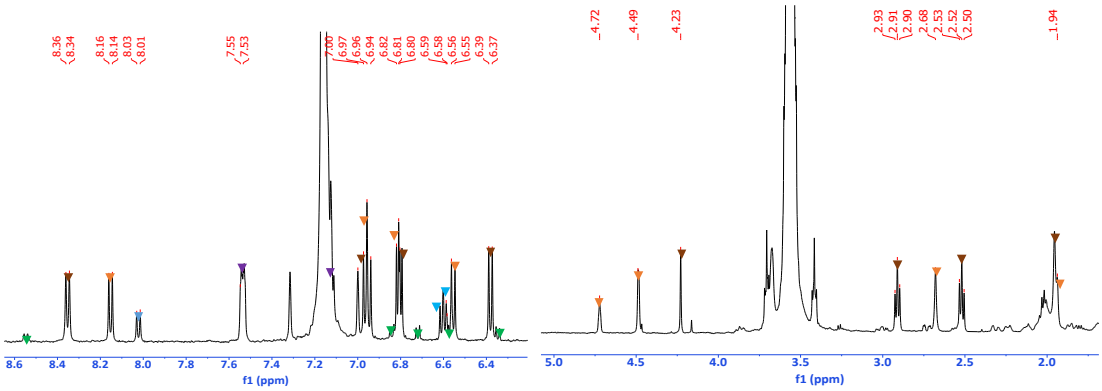

Figure A 4.11. ^{1}H NMR spectrum of a reaction mixture of $[Co^{II}(PNNP)(MeCN)]^{2+}$ with 2.0 equiv. $NaBEt_3H$ leaving under Ar for 30 min in C_6D_6.

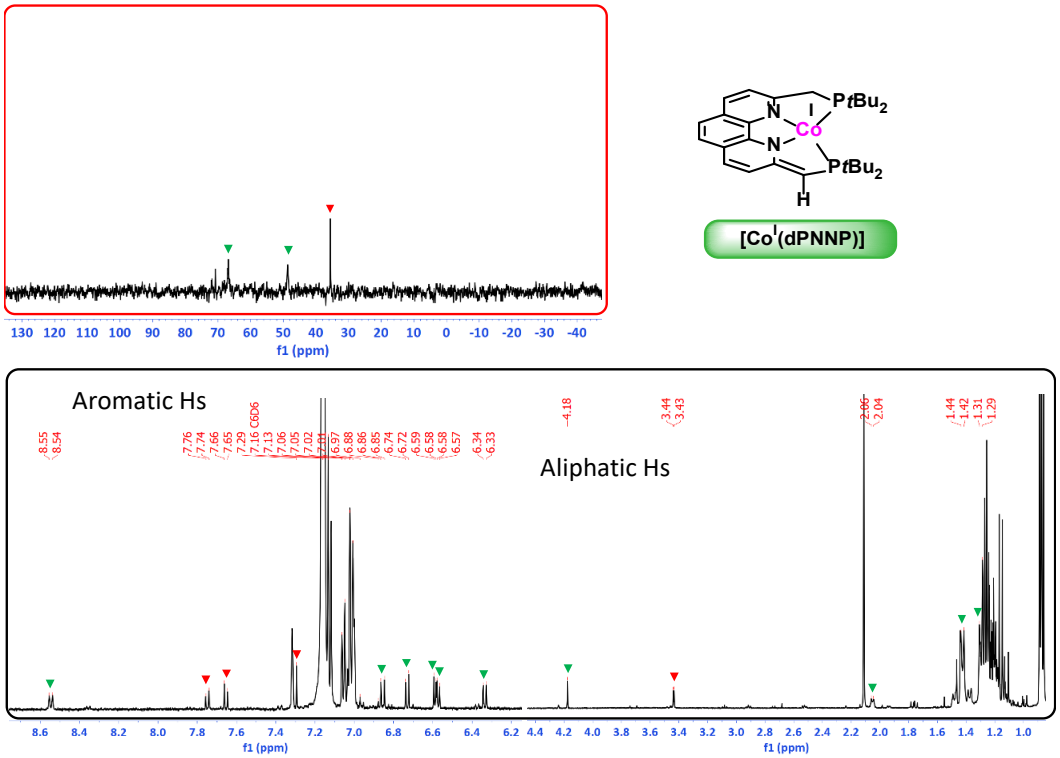

Figure A 4.12. $^{31}P\{^{1}H\}$ NMR spectrum (red in set), ^{1}H NMR spectrum (black inset) of the dearomatized complex, [Co^{I}(dPNNP)] in C_6D_6.

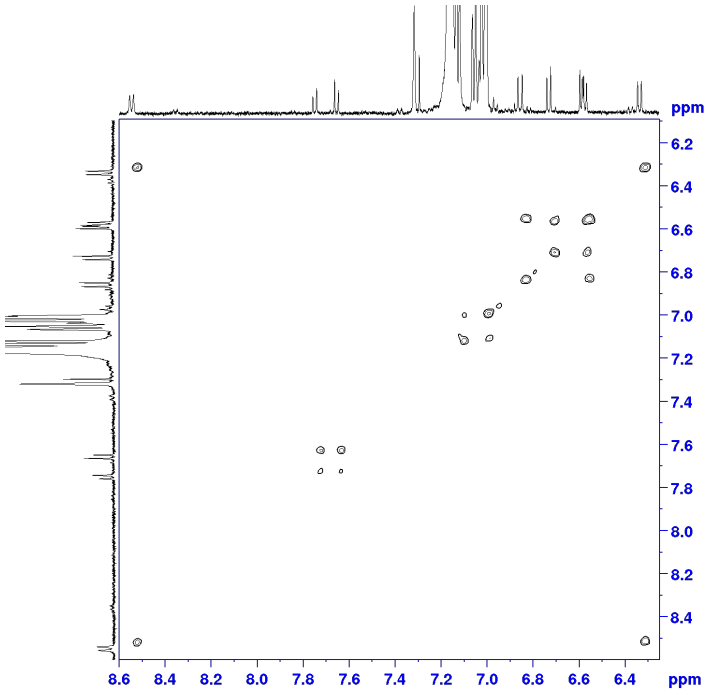

Figure A 4.13. ^{1}H-^{1}H COSY NMR correlation (aromatic protons) of the dearomatized complex, [Co^{I}(dPNNP)] in C_6D_6.

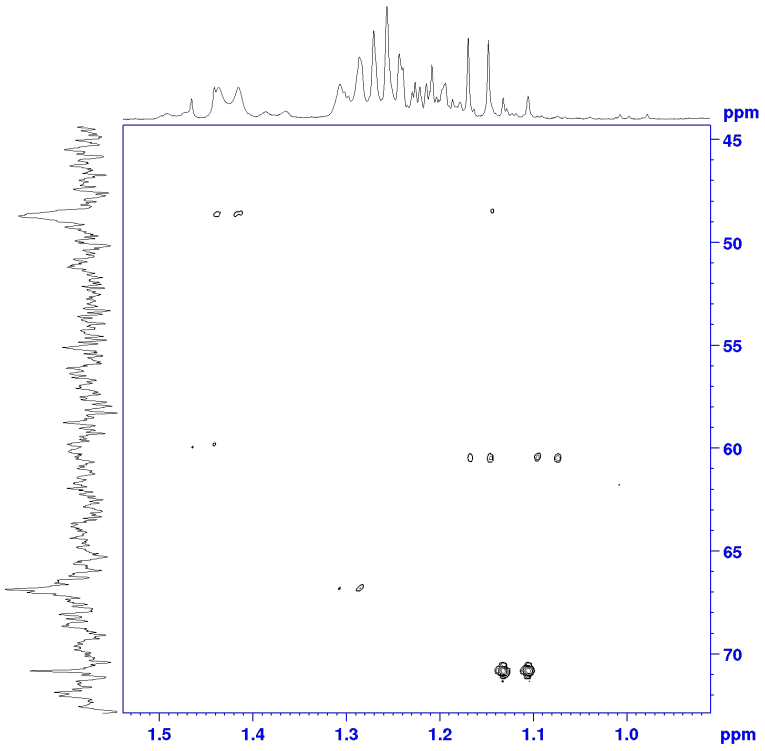

Figure A 4.14. ^{1}H-$^{31}P\{^{1}H\}$ HMBC spectrum of the dearomatized complex, [Co^{I}(dPNNP)] in C_6D_6.

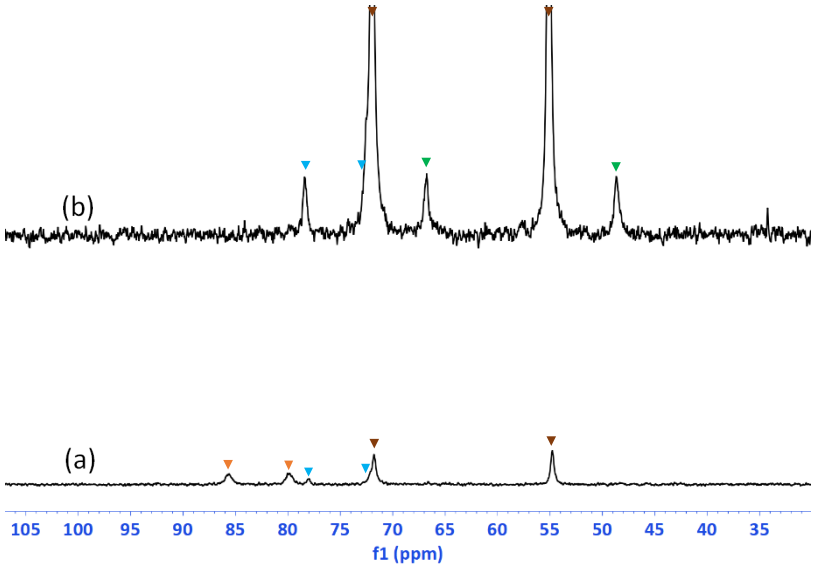

Figure A 4.15. $^{31}P\{^{1}H\}$ NMR spectrum of a reaction mixture of [Co^{II}(PNNP)Cl$_2$] with 2.0 equiv. NaBEt$_3$H in tol-d$_8$ (a) compared to the reaction in C_6D_6 (b) under Ar for 30 min.

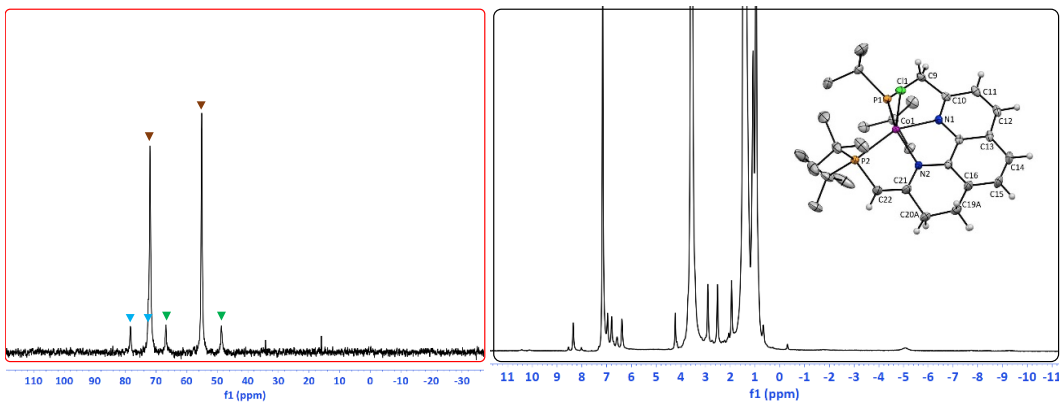

Figure A 4.16. $^{31}P\{^{1}H\}$ NMR spectrum (red inset) and ^{1}H NMR spectrum of the solid isolated from a reaction of the [Co(PNNP)Cl_2] with 2.0 equiv $NaBEt_3H$ in C_6D_6, inset showed the X-ray structure of the [Co^{II}(mPNNP)Cl] which was obtained from the recrystallisation of this solid in toluene/pentane.

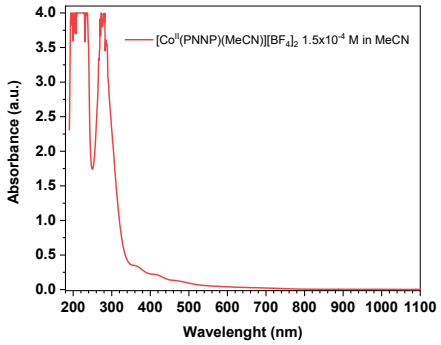

Figure A 4.17. The absorption spectrum of the [Co^{II}(PNNP)(MeCN)][BF_4]$_2$ complex ($1.5x10^{-4}$ M) in MeCN.

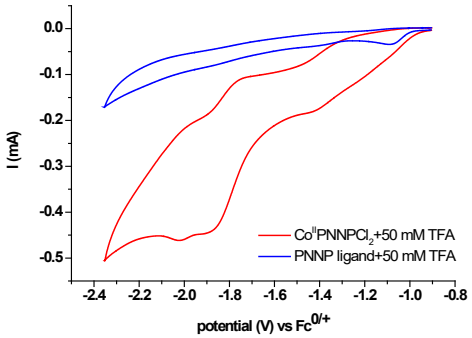

Figure A 4.18. CV of a solution of the free PNNP ligand (1 mM) with 50 mM TFA acid in acetonitrile solution containing 0.1 M $TBAPF_6$ compared to the CVs of [Co^{II}(PNNP)Cl_2] under the same catalytic conditions at a scan rate of 100 mV/s.

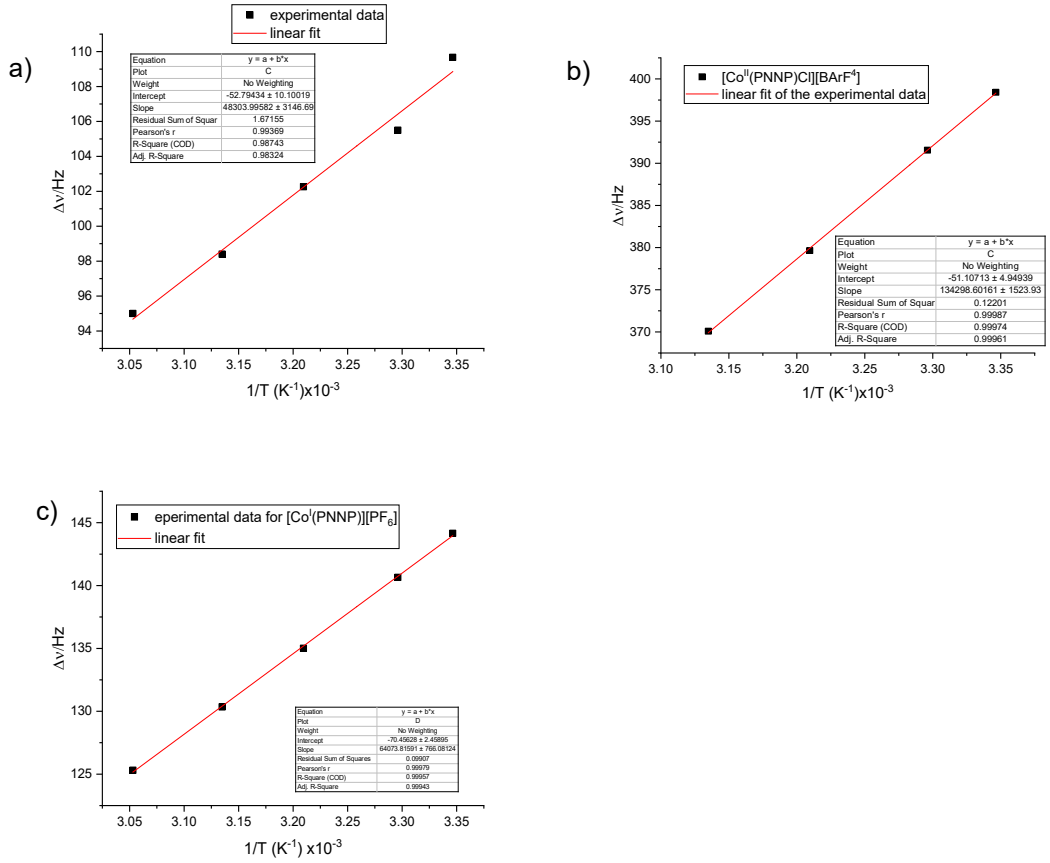

Figure A 4.19. Chemical shift change of THF reference with temperature by Evans method for (a) $[Co^{II}(PNNP)(MeCN)][BF_4]_2$ (b) $[Co^{II}(PNNP)(Cl)][BArF^4]$ and (c) $[Co^{I}(PNNP)][PF_6]$ in CD_3CN.

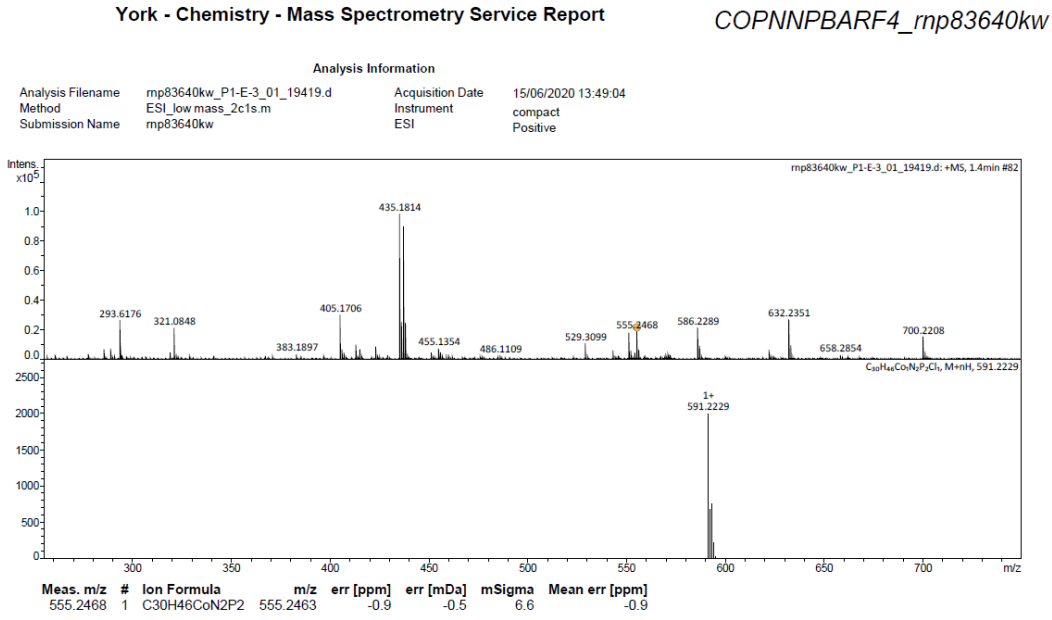

Figure A 4.20. ESI-Mass spectrum (positive ion mode in MeCN) of the $[Co^{II}(PNNP)Cl][BArF^4]$ complex at m/z = 555.2468 for $[C_{30}H_{46}CoN_2P_2]^+$ (top) and the calculated ion peak at m/z = 591.2229 for $[C_{30}H_{46}CoN_2P_2Cl]^+$ (bottom).

Abbreviations

T	Absolute temperature (K)
MeCN	Acetonitrile
E_{app}	Applied potential
i_{pa}	Anodic peak current
E_{pa}	Anodic peak potential
PNP	A pincer bis(phosphino)pyridine
PNNP ligand	2,9-bis(di-*tert*-butylphosphino)-methyl)-1,1-phenanthroline
br	board
B.M.	Bohr Magneton
cald	Calculated or theoretical value
cat	catalyst
E_{cat}	Catalytic peak potential
k_{cat}	Catalytic rate constant
i_{cat}	Catalytic peak current
i_{pc}	Cathodic peak current
E_{pc}	Cathodic peak potential
δ	chemical shift
Δf	Chemical shift difference (Hz)
COSY	correlation spectroscopy
J	Coupling constant (Hz)
CO2RR	CO_2 reduction reaction
CO2RRc	CO_2 reduction catalysts
CODs	Carbon monoxide Dehydrogenase
CVs	Cyclic voltammograms
CT	Charge transfer
Cs	carbon atoms
Cy	cyclohexyl
dPNNP	Dearomatized PNNP ligand
THF-d_8	Deuterated tetrahydrofuran
DCM	Dichloro methane
PN ligand	2-(diisopropylphosphino-methyl) pyridine
DPPMP	diphenylphosphinomethylpyridine
DEPT	distortionless enhancement by polarisation transfer
d	doublet
ddd	Doublet of doublet of doublet
DSPEC	dye-sensitized photoelectrochemical cell
ET	Electron Transfer
eV	Electron volt
equiv.	equivalents
ESI-MS	electrospray ionisation mass spectroscopy
PS*	Excited state photosensitizer
$Fc^{0/+}$	ferrocene/ferrocenium
FOWA	Foot of the Wave Analysis
$E^{0'}(cat^{n+/0})$	Formal potential for an electrocatalyst
FDH	Formic acid Dehydrogenase

GaP	Gallium phosphide
GC analysis	Gas chromatography analysis
GC	Glassy carbon electrode
$E_{1/2}$	Half wave potential
$E_{cat/2}$	Half wave potential for catalysis
HECs	Hydrogen evolution catalysts
HER	Hydrogen evolution reaction
HMBC	heteronuclear multiple bond correlation
Hs	Hydrogen atoms
HSQC	heteronuclear single quantum coherence
InP	Indium phosphide
iPr	iso propyl
LIF-DI	liquid injection field desorption ionisation
C_i	Irreversible chemical step
E_i	Irreversible electron transfer
μ	Magnetic moment (B.M.)
TOFmax	Maximun turnover frequency
m	multiplet
mPNNP	Modified PNNP ligand
M	molar
ε	Molar absorptivity ($M^{-1}cm^{-1}$)
χ_M	Molar susceptibility
Me	methyl
MLC	Metal-ligand cooperation
MOF	Metal Organic Framework
min.	minutes
i_p	Non-catalytic current
NHE	normal hydrogen electrode
n-BuOH	Normal buthanol
K_{obs}	Observed catalytic rate constant
η	Overpotential
PS^+	Oxidized photosensitizer
Ox	Oxidized species
OECs	Oxygen evolving catalysts
ΔE_p	Peak-to-peak separation potential
%FE	Percent Faradaic Efficiency
PEC	photoelectrochemical
PFE	Protein Film Electrochemistry
Py	pyridine
NPP	2-pyridylbis(diphenylphosphino)metane
PS	photosensitizer
E_q	Quasi-reversible electron transfer
PS^-	Reduced photosensitizer
Red	Reduced species
PV-EC	Photovoltaic-Electrochemical
PXRD	Powder X-Ray Diffraction
q	quartet

RE	Reference electrode
E_r	Reversible electron transfer
RHE	Reversible Hydrogen Electrode
SEA	Sacrificial Electron Acceptor
SEC	saturated calomel electrode
SED	Sacrificial electron donor
ν	Scan rate
SED^+	Oxidized Sacrificial electron donor
sept	septet
s	singlet
$NaBAr^F_4$	Sodium tetrakis[3,5-bis(trifluoromethyl)phenyl]borate
TPP	Tetraphenylporphyrin
TBACl	Tetrabutylammonium choride
$TBAPF_6$	Tetrabutylammonium hexafluorophosphate
TDHPP	5,10,15,20-tetrakis(2',6'-dihydroxyphenyl)-porphyrin
tBu	tertiary butyl
$TsOH•H_2O$	*p*-toluenesulfonic acid monohydrate
α	Transfer coefficient
TFE	2,2,2-trifluoroethanol
TFA	trifluoroacetic acid
THF	tetrahydrofuran
TCD	Thermal conductivity detector
TOF	Turnover frequency
TOF_0	Turnover frequency at zero overpotential
TON	Turnover number
E^0_{HA}	Thermodynamic potential for proton reduction
t	triplet
UV-Vis SEC	Ultra-violet-Visible spectroelectrochemistry
Virtual q	Virtual quartet
Virtual t	Virtual triplet
VLA-SCs	Visible Light Absorbing Semiconductors
WE	Working electrode
WOCs	Water oxidation catalysts

References

1. Chu, S.; Majumdar, A., Opportunities and challenges for a sustainable energy future. *Nature* **2012,** *488*, 294-303.

2. Turner, J. A., Sustainable Hydrogen Production. *Science* **2004,** *305*, 972.

3. Balzani, V.; Credi, A.; Venturi, M., Photochemical Conversion of Solar Energy. *ChemSusChem* **2008,** *1*, 26-58.

4. Purchase, R. L.; de Groot, H. J. M., Biosolar cells: global artificial photosynthesis needs responsive matrices with quantum coherent kinetic control for high yield. *Interface Focus* **2015,** *5*, 20150014.

5. Yan, Z.; Hitt, J. L.; Turner, J. A.; Mallouk, T. E., Renewable electricity storage using electrolysis. *Proc. Natl. Acad. Sci. U. S. A.* **2019**, 201821686.

6. Petroleum, B., BP Statistical Review of world energy 2015. *Br. Pet* **2017,** *66*, 1-52.

7. Barber, J., Photosynthetic energy conversion: natural and artificial. *Chem. Soc. Rev.* **2009,** *38*, 185-196.

8. Woolerton, T. W.; Sheard, S.; Chaudhary, Y. S.; Armstrong, F. A., Enzymes and bio-inspired electrocatalysts in solar fuel devices. *Energ. Environ. Sci.* **2012,** *5*, 7470-7490.

9. Lewis, N. S., Research opportunities to advance solar energy utilization. *Science* **2016,** *351*, aad1920.

10. Roger, I.; Shipman, M. A.; Symes, M. D., Earth-abundant catalysts for electrochemical and photoelectrochemical water splitting. *Nat. Rev. Chem.* **2017,** *1*, 0003.

11. White, J. L.; Baruch, M. F.; Pander, J. E.; Hu, Y.; Fortmeyer, I. C.; Park, J. E.; Zhang, T.; Liao, K.; Gu, J.; Yan, Y.; Shaw, T. W.; Abelev, E.; Bocarsly, A. B., Light-Driven Heterogeneous Reduction of Carbon Dioxide: Photocatalysts and Photoelectrodes. *Chem. Rev.* **2015,** *115*, 12888-12935.

12. Chang, X.; Wang, T.; Gong, J., CO_2 photo-reduction: insights into CO_2 activation and reaction on surfaces of photocatalysts. *Energ. Environ. Sci.* **2016,** *9*, 2177-2196.

13. Tu, W.; Zhou, Y.; Zou, Z., Photocatalytic Conversion of CO_2 into Renewable Hydrocarbon Fuels: State-of-the-Art Accomplishment, Challenges, and Prospects. *Adv. Mater.* **2014,** *26*, 4607-4626.

14. McEvoy, J. P.; Brudvig, G. W., Water-Splitting Chemistry of Photosystem II. *Chem. Rev.* **2006,** *106*, 4455-4483.

15. Liu, X.; Inagaki, S.; Gong, J., Heterogeneous Molecular Systems for Photocatalytic CO_2 Reduction with Water Oxidation. *Angew. Chem. Int. Ed.* **2016,** *55*, 14924-14950.

16. Dalle, K. E.; Warnan, J.; Leung, J. J.; Reuillard, B.; Karmel, I. S.; Reisner, E., Electro- and Solar-Driven Fuel Synthesis with First Row Transition Metal Complexes. *Chem. Rev.* **2019,** *119*, 2752-2875.

17. Alstrum-Acevedo, J. H.; Brennaman, M. K.; Meyer, T. J., Chemical Approaches to Artificial Photosynthesis. 2. *Inorg. Chem.* **2005,** *44*, 6802-6827.

18. Zhang, B.; Sun, L., Artificial photosynthesis: opportunities and challenges of molecular catalysts. *Chem. Soc. Rev.* **2019,** *48*, 2216-2264.

19. Kim, J. H.; Hansora, D.; Sharma, P.; Jang, J.-W.; Lee, J. S., Toward practical solar hydrogen production – an artificial photosynthetic leaf-to-farm challenge. *Chem. Soc. Rev.* **2019,** *48*, 1908-1971.

20. Walter, M. G.; Warren, E. L.; McKone, J. R.; Boettcher, S. W.; Mi, Q.; Santori, E. A.; Lewis, N. S., Solar Water Splitting Cells. *Chem. Rev.* **2010,** *110*, 6446-6473.

21. Kang, D.; Kim, T. W.; Kubota, S. R.; Cardiel, A. C.; Cha, H. G.; Choi, K.-S., Electrochemical Synthesis of Photoelectrodes and Catalysts for Use in Solar Water Splitting. *Chem. Rev.* **2015,** *115*, 12839-12887.

22. Zhang, N.; Long, R.; Gao, C.; Xiong, Y., Recent progress on advanced design for photoelectrochemical reduction of CO_2 to fuels. *Sci. China Mater.* **2018,** *61*, 771-805.

23. Ran, J.; Zhang, J.; Yu, J.; Jaroniec, M.; Qiao, S. Z., Earth-abundant cocatalysts for semiconductor-based photocatalytic water splitting. *Chem. Soc. Rev.* **2014,** *43*, 7787-7812.

24. Chen, X.; Shen, S.; Guo, L.; Mao, S. S., Semiconductor-based Photocatalytic Hydrogen Generation. *Chem. Rev.* **2010,** *110*, 6503-6570.

25. Maeda, K., Metal-Complex/Semiconductor Hybrid Photocatalysts and Photoelectrodes for CO_2 Reduction Driven by Visible Light. *Adv. Mater.* **2019,** *31*, 1808205.

26. Iwase, A.; Yoshino, S.; Takayama, T.; Ng, Y. H.; Amal, R.; Kudo, A., Water Splitting and CO_2 Reduction under Visible Light Irradiation Using Z-Scheme Systems Consisting of Metal Sulfides, CoO_x-Loaded $BiVO_4$, and a Reduced Graphene Oxide Electron Mediator. *J. Am. Chem. Soc.* **2016,** *138*, 10260-10264.

27. Fujishima, A.; Honda, K., Electrochemical Photolysis of Water at a Semiconductor Electrode. *Nature* **1972,** *238*, 37-38.

28. Hagfeldt, A.; Boschloo, G.; Sun, L.; Kloo, L.; Pettersson, H., Dye-Sensitized Solar Cells. *Chem. Rev.* **2010,** *110*, 6595-6663.

29. Schmidt, M.; Contakes, S. M.; Rauchfuss, T. B., First Generation Analogues of the Binuclear Site in the Fe-Only Hydrogenases: $Fe_2(\mu\text{-}SR)_2(CO)_4(CN)_2^{2-}$. *J. Am. Chem. Soc.* **1999,** *121*, 9736-9737.

30. Li, L.; Duan, L.; Wen, F.; Li, C.; Wang, M.; Hagfeldt, A.; Sun, L., Visible light driven hydrogen production from a photo-active cathode based on a molecular catalyst and organic dye-sensitized p-type nanostructured NiO. *Chem. Commun.* **2012,** *48*, 988-990.

31. Kaeffer, N.; Massin, J.; Lebrun, C.; Renault, O.; Chavarot-Kerlidou, M.; Artero, V., Covalent Design for Dye-Sensitized H_2-Evolving Photocathodes Based on a Cobalt Diimine–Dioxime Catalyst. *J. Am. Chem. Soc.* **2016,** *138*, 12308-12311.

32. Kamata, R.; Kumagai, H.; Yamazaki, Y.; Sahara, G.; Ishitani, O., Photoelectrochemical CO_2 Reduction Using a Ru(II)–Re(I) Supramolecular Photocatalyst Connected to a Vinyl Polymer on a NiO Electrode. *Acs. Appl. Mater. Interfaces.* **2019,** *11*, 5632-5641.

33. Kumagai, H.; Sahara, G.; Maeda, K.; Higashi, M.; Abe, R.; Ishitani, O., Hybrid photocathode consisting of a $CuGaO_2$ p-type semiconductor and a Ru(II)–Re(I) supramolecular

photocatalyst: non-biased visible-light-driven CO_2 reduction with water oxidation. *Chem. Sci.* **2017,** *8*, 4242-4249.

34. Cedeno, D.; Krawicz, A.; Moore, G. F., Hybrid photocathodes for solar fuel production: coupling molecular fuel-production catalysts with solid-state light harvesting and conversion technologies. *Interface Focus* **2015,** *5*, 1-10.

35. Arai, T.; Sato, S.; Kajino, T.; Morikawa, T., Solar CO_2 reduction using H_2O by a semiconductor/metal-complex hybrid photocatalyst: enhanced efficiency and demonstration of a wireless system using $SrTiO_3$ photoanodes. *Energ. Environ. Sci.* **2013,** *6*, 1274-1282.

36. Roy, S.; Huang, Z.; Bhunia, A.; Castner, A.; Gupta, A. K.; Zou, X.; Ott, S., Electrocatalytic Hydrogen Evolution from a Cobaloxime-Based Metal–Organic Framework Thin Film. *J. Am. Chem. Soc.* **2019,** *141*, 15942-15950.

37. Zheng, D.; Zhang, Y.; Liu, X.; Wang, J., Coupling natural systems with synthetic chemistry for light-driven enzymatic biocatalysis. *Photosynth. Res.* **2020,** *143*, 221-231.

38. Svetlitchnyi, V.; Peschel, C.; Acker, G.; Meyer, O., Two Membrane-Associated NiFeS-Carbon Monoxide Dehydrogenases from the Anaerobic Carbon-Monoxide-Utilizing Eubacterium Carboxydothermus hydrogenoformans. *J. Bacteriol.* **2001,** *183*, 5134-5114.

39. Lubitz, W.; Ogata, H.; Rüdiger, O.; Reijerse, E., Hydrogenases. *Chem. Rev.* **2014,** *114*, 4081-4148.

40. Jones, A. K.; Sillery, E.; Albracht, S. P. J.; Armstrong, F. A., Direct comparison of the electrocatalytic oxidation of hydrogen by an enzyme and a platinum catalyst. *Chem. Commun.* **2002**, 866-867.

41. Nicolet, Y.; Piras, C.; Legrand, P.; Hatchikian, C. E.; Fontecilla-Camps, J. C., Desulfovibrio desulfuricans iron hydrogenase: the structure shows unusual coordination to an active site Fe binuclear center. *Structure* **1999,** *7*, 13-23.

42. Volbeda, A.; Charon, M.-H.; Piras, C.; Hatchikian, E. C.; Frey, M.; Fontecilla-Camps, J. C., Crystal structure of the nickel–iron hydrogenase from Desulfovibrio gigas. *Nature* **1995,** *373*, 580-587.

43. De Lacey, A. L.; Fernández, V. M.; Rousset, M.; Cammack, R., Activation and Inactivation of Hydrogenase Function and the Catalytic Cycle: Spectroelectrochemical Studies. *Chem. Rev.* **2007,** *107*, 4304-4330.

44. Lubitz, W.; Reijerse, E.; van Gastel, M., [NiFe] and [FeFe] Hydrogenases Studied by Advanced Magnetic Resonance Techniques. *Chem. Rev.* **2007,** *107*, 4331-4365.

45. Vincent, K. A.; Parkin, A.; Armstrong, F. A., Investigating and Exploiting the Electrocatalytic Properties of Hydrogenases. *Chem. Rev.* **2007,** *107*, 4366-4413.

46. Siegbahn, P. E. M.; Tye, J. W.; Hall, M. B., Computational Studies of [NiFe] and [FeFe] Hydrogenases. *Chem. Rev.* **2007,** *107*, 4414-4435.

47. Schilter, D.; Camara, J. M.; Huynh, M. T.; Hammes-Schiffer, S.; Rauchfuss, T. B., Hydrogenase Enzymes and Their Synthetic Models: The Role of Metal Hydrides. *Chem. Rev.* **2016,** *116*, 8693-8749.

48. Woolerton, T. W.; Sheard, S.; Reisner, E.; Pierce, E.; Ragsdale, S. W.; Armstrong, F. A., Efficient and Clean Photoreduction of CO_2 to CO by Enzyme-Modified TiO_2 Nanoparticles Using Visible Light. *J. Am. Chem. Soc.* **2010,** *132*, 2132-2133.

49. Zhang, L.; Can, M.; Ragsdale, S. W.; Armstrong, F. A., Fast and Selective Photoreduction of CO_2 to CO Catalyzed by a Complex of Carbon Monoxide Dehydrogenase, TiO_2, and Ag Nanoclusters. *ACS Catal.* **2018,** *8*, 2789-2795.

50. Reisner, E.; Fontecilla-Camps, J. C.; Armstrong, F. A., Catalytic electrochemistry of a [NiFeSe]-hydrogenase on TiO_2 and demonstration of its suitability for visible-light driven H_2 production. *Chem. Commun.* **2009**, 550-552.

51. Armstrong, F. A.; Belsey, N. A.; Cracknell, J. A.; Goldet, G.; Parkin, A.; Reisner, E.; Vincent, K. A.; Wait, A. F., Dynamic electrochemical investigations of hydrogen oxidation and production by enzymes and implications for future technology. *Chem. Soc. Rev.* **2009,** *38*, 36-51.

52. Chaudhary, Y. S.; Woolerton, T. W.; Allen, C. S.; Warner, J. H.; Pierce, E.; Ragsdale, S. W.; Armstrong, F. A., Visible light-driven CO_2 reduction by enzyme coupled CdS nanocrystals. *Chem. Commun.* **2012,** *48*, 58-60.

53. Parkin, A.; Goldet, G.; Cavazza, C.; Fontecilla-Camps, J. C.; Armstrong, F. A., The Difference a Se Makes? Oxygen-Tolerant Hydrogen Production by the [NiFeSe]-Hydrogenase from Desulfomicrobium baculatum. *J. Am. Chem. Soc.* **2008,** *130*, 13410-13416.

54. Vincent, K. A.; Li, X.; Blanford, C. F.; Belsey, N. A.; Weiner, J. H.; Armstrong, F. A., Enzymatic catalysis on conducting graphite particles. *Nat. Chem. Biol.* **2007,** *3*, 761-762.

55. Miller, M.; Robinson, W. E.; Oliveira, A. R.; Heidary, N.; Kornienko, N.; Warnan, J.; Pereira, I. A. C.; Reisner, E., Interfacing Formate Dehydrogenase with Metal Oxides for the Reversible Electrocatalysis and Solar-Driven Reduction of Carbon Dioxide. *Angew. Chem. Int. Ed.* **2019,** *58*, 4601-4605.

56. Mersch, D.; Lee, C.-Y.; Zhang, J. Z.; Brinkert, K.; Fontecilla-Camps, J. C.; Rutherford, A. W.; Reisner, E., Wiring of Photosystem II to Hydrogenase for Photoelectrochemical Water Splitting. *J. Am. Chem. Soc.* **2015,** *137*, 8541-8549.

57. Sokol, K. P.; Robinson, W. E.; Oliveira, A. R.; Zacarias, S.; Lee, C.-Y.; Madden, C.; Bassegoda, A.; Hirst, J.; Pereira, I. A. C.; Reisner, E., Reversible and Selective Interconversion of Hydrogen and Carbon Dioxide into Formate by a Semiartificial Formate Hydrogenlyase Mimic. *J. Am. Chem. Soc.* **2019,** *141*, 17498-17502.

58. Wilson, A. D.; Shoemaker, R. K.; Miedaner, A.; Muckerman, J. T.; DuBois, D. L.; DuBois, M. R., Nature of hydrogen interactions with Ni(II) complexes containing cyclic phosphine ligands with pendant nitrogen bases. *Proc. Natl. Acad. Sci.* **2007,** *104*, 6951-6956.

59. Bullock, R. M.; Appel, A. M.; Helm, M. L., Production of hydrogen by electrocatalysis: making the H–H bond by combining protons and hydrides. *Chem. Commun.* **2014,** *50*, 3125-3143.

60. Felton, G. A. N.; Glass, R. S.; Lichtenberger, D. L.; Evans, D. H., Iron-Only Hydrogenase Mimics. Thermodynamic Aspects of the Use of Electrochemistry to Evaluate Catalytic Efficiency for Hydrogen Generation. *Inorg. Chem.* **2006,** *45*, 9181-9184.

61. McCarthy, B. D.; Martin, D. J.; Rountree, E. S.; Ullman, A. C.; Dempsey, J. L., Electrochemical Reduction of Brønsted Acids by Glassy Carbon in Acetonitrile—Implications for Electrocatalytic Hydrogen Evolution. *Inorg. Chem.* **2014,** *53*, 8350-8361.

62. Smith, S. E.; Yang, J. Y.; DuBois, D. L.; Bullock, R. M., Reversible Electrocatalytic Production and Oxidation of Hydrogen at Low Overpotentials by a Functional Hydrogenase Mimic. *Angew. Chem. Int. Ed.* **2012,** *51*, 3152-3155.

63. Benson, E. E.; Kubiak, C. P.; Sathrum, A. J.; Smieja, J. M., Electrocatalytic and homogeneous approaches to conversion of CO_2 to liquid fuels. *Chem. Soc. Rev.* **2009,** *38*, 89-99.

64. Saveant, J. M.; Vianello, E., Potential-sweep chronoamperometry: Kinetic currents for first-order chemical reaction parallel to electron-transfer process (catalytic currents). *Electrochim. Acta* **1965,** *10*, 905-920.

65. Wang, J.-W.; Liu, W.-J.; Zhong, D.-C.; Lu, T.-B., Nickel complexes as molecular catalysts for water splitting and CO_2 reduction. *Coord. Chem. Rev.* **2019,** *378*, 237-261.

66. Appel, A. M.; Bercaw, J. E.; Bocarsly, A. B.; Dobbek, H.; DuBois, D. L.; Dupuis, M.; Ferry, J. G.; Fujita, E.; Hille, R.; Kenis, P. J. A.; Kerfeld, C. A.; Morris, R. H.; Peden, C. H. F.; Portis, A. R.; Ragsdale, S. W.; Rauchfuss, T. B.; Reek, J. N. H.; Seefeldt, L. C.; Thauer, R. K.; Waldrop, G. L., Frontiers, Opportunities, and Challenges in Biochemical and Chemical Catalysis of CO_2 Fixation. *Chem. Rev.* **2013,** *113*, 6621-6658.

67. Artero, V.; Chavarot-Kerlidou, M.; Fontecave, M., Splitting Water with Cobalt. **2011,** *50*, 7238-7266.

68. Jurss, J. W.; Khnayzer, R. S.; Panetier, J. A.; El Roz, K. A.; Nichols, E. M.; Head-Gordon, M.; Long, J. R.; Castellano, F. N.; Chang, C. J., Bioinspired Design of Redox-active Ligands for Multielectron Catalysis: Effects of Positioning Pyrazine Reservoirs on Cobalt for Electro- and Photocatalytic Generation of Hydrogen from Water. *Chem. Sci.* **2015,** *6*, 4954-4972.

69. Zee, D. Z.; Chantarojsiri, T.; Long, J. R.; Chang, C. J., Metal–Polypyridyl Catalysts for Electro- and Photochemical Reduction of Water to Hydrogen. *Acc. Chem. Res.* **2015,** *48*, 2027-2036.

70. Queyriaux, N.; Jane, R. T.; Massin, J.; Artero, V.; Chavarot-Kerlidou, M., Recent developments in hydrogen evolving molecular cobalt(II)–polypyridyl catalysts. *Coord. Chem. Rev.* **2015,** *304-305*, 3-19.

71. Zhao, X.; Wang, P.; Long, M., Electro- and Photocatalytic Hydrogen Production by Molecular Cobalt Complexes With Pentadentate Ligands. *Comments Inorg. Chem.* **2017,** *37*, 238-270.

72. Thoi, V. S.; Sun, Y.; Long, J. R.; Chang, C. J., Complexes of Earth-Abundant Metals for Catalytic Electrochemical Hydrogen Generation under Aqueous Conditions. *Chem. Soc. Rev.* **2013,** *42*, 2388-2400.

73. Eckenhoff, W. T.; Eisenberg, R., Molecular systems for light driven hydrogen production. *Dalton. Trans.* **2012,** *41*, 13004-13021.

74. Berardi, S.; Drouet, S.; Francàs, L.; Gimbert-Suriñach, C.; Guttentag, M.; Richmond, C.; Stoll, T.; Llobet, A., Molecular artificial photosynthesis. *Chem. Soc. Rev.* **2014,** *43*, 7501-7519.

75. Bhugun, I.; Lexa, D.; Savéant, J.-M., Catalysis of the Electrochemical Reduction of Carbon Dioxide by Iron(0) Porphyrins: Synergystic Effect of Weak Brönsted Acids. *J. Am. Chem. Soc.* **1996,** *118*, 1769-1776.

76. Wiedner, E. S.; Chambers, M. B.; Pitman, C. L.; Bullock, R. M.; Miller, A. J. M.; Appel, A. M., Thermodynamic Hydricity of Transition Metal Hydrides. *Chem. Rev.* **2016,** *116*, 8655-8692.

77. Ryan, O. B.; Tilset, M.; Parker, V. D., Chemical and electrochemical oxidation of group 6 cyclopentadienylmetal hydrides. First estimates of 17-electron metal-hydride cation-radical thermodynamic acidities and their decomposition of 17-electron neutral radicals. *J. Am. Chem. Soc.* **1990,** *112*, 2618-2626.

78. Berning, D. E.; Noll, B. C.; DuBois, D. L., Relative Hydride, Proton, and Hydrogen Atom Transfer Abilities of $[HM(diphosphine)_2]PF_6$ Complexes (M = Pt, Ni). *J. Am. Chem. Soc.* **1999,** *121*, 11432-11447.

79. Ciancanelli, R.; Noll, B. C.; DuBois, D. L.; DuBois, M. R., Comprehensive Thermodynamic Characterization of the Metal−Hydrogen Bond in a Series of Cobalt-Hydride Complexes. *J. Am. Chem. Soc.* **2002,** *124*, 2984-2992.

80. Price, A. J.; Ciancanelli, R.; Noll, B. C.; Curtis, C. J.; DuBois, D. L.; DuBois, M. R., $HRh(dppb)_2$, a Powerful Hydride Donor. *Organometallics* **2002,** *21*, 4833-4839.

81. Waldie, K. M.; Ostericher, A. L.; Reineke, M. H.; Sasayama, A. F.; Kubiak, C. P., Hydricity of Transition-Metal Hydrides: Thermodynamic Considerations for CO_2 Reduction. *ACS Catal.* **2018,** *8*, 1313-1324.

82. Curtis, C. J.; Miedaner, A.; Ellis, W. W.; DuBois, D. L., Measurement of the Hydride Donor Abilities of $[HM(diphosphine)_2]^+$ Complexes (M = Ni, Pt) by Heterolytic Activation of Hydrogen. *J. Am. Chem. Soc.* **2002,** *124*, 1918-1925.

83. Ostericher, A. L.; Waldie, K. M.; Kubiak, C. P., Utilization of Thermodynamic Scaling Relationships in Hydricity To Develop Nickel Hydrogen Evolution Reaction Electrocatalysts with Weak Acids and Low Overpotentials. *ACS Catal.* **2018,** *8*, 9596-9603.

84. Kang, P.; Cheng, C.; Chen, Z.; Schauer, C. K.; Meyer, T. J.; Brookhart, M., Selective Electrocatalytic Reduction of CO_2 to Formate by Water-Stable Iridium Dihydride Pincer Complexes. *J. Am. Chem. Soc.* **2012,** *134*, 5500-5503.

85. Helm, M. L.; Stewart, M. P.; Bullock, R. M.; DuBois, M. R.; DuBois, D. L., A Synthetic Nickel Electrocatalyst with a Turnover Frequency Above 100,000 s^{-1} for H_2 Production. *Science* **2011,** *333*, 863-866.

86. Bhugun, I.; Lexa, D.; Savéant, J.-M., Homogeneous Catalysis of Electrochemical Hydrogen Evolution by Iron(0) Porphyrins. *J. Am. Chem. Soc.* **1996,** *118*, 3982-3983.

87. Razavet, M.; Artero, V.; Fontecave, M., Proton Electroreduction Catalyzed by Cobaloximes: Functional Models for Hydrogenases. *Inorg. Chem.* **2005,** *44*, 4786-4795.

88. Liu, T.; Guo, M.; Orthaber, A.; Lomoth, R.; Lundberg, M.; Ott, S.; Hammarström, L., Accelerating proton-coupled electron transfer of metal hydrides in catalyst model reactions. *Nat. Chem.* **2018,** *10*, 881-887.

89. Kurtz, D. A.; Dempsey, J. L., Proton-Coupled Electron Transfer Kinetics for the Photoinduced Generation of a Cobalt(III)-Hydride Complex. *Inorg. Chem.* **2019,** *58*, 16510-16517.

90. Kohler, L.; Niklas, J.; Johnson, R. C.; Zeller, M.; Poluektov, O. G.; Mulfort, K. L., Molecular Cobalt Catalysts for H_2 Generation with Redox Activity and Proton Relays in the Second Coordination Sphere. *Inorg. Chem.* **2019,** *58*, 1697-1709.

91. O'Hagan, M.; Ho, M.-H.; Yang, J. Y.; Appel, A. M.; DuBois, M. R.; Raugei, S.; Shaw, W. J.; DuBois, D. L.; Bullock, R. M., Proton Delivery and Removal in $[Ni(P^{R2}N^{R'2})_2]^{2+}$ Hydrogen Production and Oxidation Catalysts. *J. Am. Chem. Soc.* **2012,** *134*, 19409-19424.

92. Thammavongsy, Z.; Mercer, I. P.; Yang, J. Y., Promoting proton coupled electron transfer in redox catalysts through molecular design. *Chem. Commun.* **2019,** *55*, 10342-10358.

93. Rakowski DuBois, M.; DuBois, D. L., The roles of the first and second coordination spheres in the design of molecular catalysts for H_2 production and oxidation. *Chem. Soc. Rev.* **2009,** *38*, 62-72.

94. Kilgore, U. J.; Roberts, J. A. S.; Pool, D. H.; Appel, A. M.; Stewart, M. P.; DuBois, M. R.; Dougherty, W. G.; Kassel, W. S.; Bullock, R. M.; DuBois, D. L., $[Ni(P^{Ph2}N^{C6H4X2})_2]^{2+}$ Complexes as Electrocatalysts for H_2 Production: Effect of Substituents, Acids, and Water on Catalytic Rates. *J. Am. Chem. Soc.* **2011,** *133*, 5861-5872.

95. Whipple, D. T.; Kenis, P. J. A., Prospects of CO_2 Utilization via Direct Heterogeneous Electrochemical Reduction. *J. Phys. Chem. Lett.* **2010,** *1*, 3451-3458.

96. Li, Y.; Chan, S. H.; Sun, Q., Heterogeneous catalytic conversion of CO_2: a comprehensive theoretical review. *Nanoscale* **2015,** *7*, 8663-8683.

97. Elgrishi, N.; Chambers, M. B.; Wang, X.; Fontecave, M., Molecular polypyridine-based metal complexes as catalysts for the reduction of CO_2. *Chem. Soc. Rev.* **2017,** *46*, 761-796.

98. Hawecker, J.; Lehn, J.-M.; Ziessel, R., Electrocatalytic reduction of carbon dioxide mediated by $Re(bipy)(CO)_3Cl$ (bipy = 2,2'-bipyridine). *J. Chem. Soc., Chem. Commun.* **1984**, 328-330.

99. Atoguchi, T.; Aramata, A.; Kazusaka, A.; Enyo, M., Cobalt(II)–tetraphenylporphyrin–pyridine complex fixed on a glassy carbon electrode and its prominent catalytic activity for reduction of carbon dioxide. *J. Chem. Soc., Chem. Commun.* **1991**, 156-157.

100. Costentin, C.; Drouet, S.; Robert, M.; Savéant, J.-M., A Local Proton Source Enhances CO_2 Electroreduction to CO by a Molecular Fe Catalyst. *Science* **2012,** *338*, 90-94.

101. Chen, Z.; Kang, P.; Zhang, M.-T.; Meyer, T. J., Making syngas electrocatalytically using a polypyridyl ruthenium catalyst. *Chem. Commun.* **2014,** *50*, 335-337.

102. Thoi, V. S.; Kornienko, N.; Margarit, C. G.; Yang, P.; Chang, C. J., Visible-Light Photoredox Catalysis: Selective Reduction of Carbon Dioxide to Carbon Monoxide by a Nickel N-Heterocyclic Carbene–Isoquinoline Complex. *J. Am. Chem. Soc.* **2013,** *135*, 14413-14424.

103. Schneider, J.; Jia, H.; Kobiro, K.; Cabelli, D. E.; Muckerman, J. T.; Fujita, E., Nickel(II) macrocycles: highly efficient electrocatalysts for the selective reduction of CO_2 to CO. *Energ. Environ. Sci.* **2012,** *5*, 9502-9510.

104. Smieja, J. M.; Sampson, M. D.; Grice, K. A.; Benson, E. E.; Froehlich, J. D.; Kubiak, C. P., Manganese as a Substitute for Rhenium in CO_2 Reduction Catalysts: The Importance of Acids. *Inorg. Chem.* **2013,** *52*, 2484-2491.

105. Bourrez, M.; Molton, F.; Chardon-Noblat, S.; Deronzier, A., [Mn(bipyridyl)$(CO)_3$Br]: An Abundant Metal Carbonyl Complex as Efficient Electrocatalyst for CO_2 Reduction. *Angew. Chem. Int. Ed.* **2011,** *50*, 9903-9906.

106. Sampson, M. D.; Nguyen, A. D.; Grice, K. A.; Moore, C. E.; Rheingold, A. L.; Kubiak, C. P., Manganese Catalysts with Bulky Bipyridine Ligands for the Electrocatalytic Reduction of Carbon Dioxide: Eliminating Dimerization and Altering Catalysis. *J. Am. Chem. Soc.* **2014,** *136*, 5460-5471.

107. Bourrez, M.; Orio, M.; Molton, F.; Vezin, H.; Duboc, C.; Deronzier, A.; Chardon-Noblat, S., Pulsed-EPR Evidence of a Manganese(II) Hydroxycarbonyl Intermediate in the Electrocatalytic Reduction of Carbon Dioxide by a Manganese Bipyridyl Derivative. *Angew. Chem. Int. Ed.* **2013,** *53*, 240-243.

108. Bhugun, I.; Lexa, D.; Saveant, J.-M., Ultraefficient selective homogeneous catalysis of the electrochemical reduction of carbon dioxide by an iron(0) porphyrin associated with a weak Broensted acid cocatalyst. *J. Am. Chem. Soc.* **1994,** *116*, 5015-5016.

109. Bhugun, I.; Lexa, D.; Savéant, J.-M., Catalysis of the Electrochemical Reduction of Carbon Dioxide by Iron(0) Porphyrins. Synergistic Effect of Lewis Acid Cations. *J. Phys. Chem.* **1996,** *100*, 19981-19985.

110. Hammouche, M.; Lexa, D.; Momenteau, M.; Saveant, J. M., Chemical catalysis of electrochemical reactions. Homogeneous catalysis of the electrochemical reduction of carbon dioxide by iron("0") porphyrins. Role of the addition of magnesium cations. *J. Am. Chem. Soc.* **1991,** *113*, 8455-8466.

111. Costentin, C.; Robert, M.; Savéant, J.-M.; Tatin, A., Efficient and selective molecular catalyst for the CO_2-to-CO electrochemical conversion in water. *Proc. Natl. Acad. Sci.* **2015,** *112*, 6882-6886.

112. Fesseler, J.; Jeoung, J.-H.; Dobbek, H., How the [$NiFe_4S_4$] Cluster of CO Dehydrogenase Activates CO_2 and NCO^-. *Angew. Chem. Int. Ed.* **2015,** *54*, 8560-8564.

113. Jeoung, J.-H.; Dobbek, H., Carbon Dioxide Activation at the Ni,Fe-Cluster of Anaerobic Carbon Monoxide Dehydrogenase. *Science* **2007,** *318*, 1461-1464.

114. Chapovetsky, A.; Welborn, M.; Luna, J. M.; Haiges, R.; Miller, T. F.; Marinescu, S. C., Pendant Hydrogen-Bond Donors in Cobalt Catalysts Independently Enhance CO_2 Reduction. *ACS Cent. Sci.* **2018,** *4*, 397-404.

115. Chapovetsky, A.; Do, T. H.; Haiges, R.; Takase, M. K.; Marinescu, S. C., Proton-Assisted Reduction of CO_2 by Cobalt Aminopyridine Macrocycles. *J. Am. Chem. Soc.* **2016,** *138*, 5765-5768.

116. Chabolla, S. A.; Yang, J. Y., For CO_2 Reduction, Hydrogen-Bond Donors Do the Trick. *ACS Cent. Sci.* **2018,** *4*, 315-317.

117. Jeletic, M. S.; Mock, M. T.; Appel, A. M.; Linehan, J. C., A Cobalt-Based Catalyst for the Hydrogenation of CO_2 under Ambient Conditions. *J. Am. Chem. Soc.* **2013,** *135*, 11533-11536.

118. Peters, J. W.; Schut, G. J.; Boyd, E. S.; Mulder, D. W.; Shepard, E. M.; Broderick, J. B.; King, P. W.; Adams, M. W. W., [FeFe]- and [NiFe]-hydrogenase diversity, mechanism, and maturation. *BBA-Mol. Cell. Res.* **2015,** *1853*, 1350-1369.

119. Fontecilla-Camps, J. C.; Volbeda, A.; Cavazza, C.; Nicolet, Y., Structure/Function Relationships of [NiFe]- and [FeFe]-Hydrogenases. *Chem. Rev.* **2007,** *107*, 4273-4303.

120. Tard, C.; Pickett, C. J., Structural and Functional Analogues of the Active Sites of the [Fe]-, [NiFe]-, and [FeFe]-Hydrogenases. *Chem. Rev.* **2009,** *109*, 2245-2274.

121. Wang, M.; Chen, L.; Sun, L., Recent Progress in Electrochemical Hydrogen Production with Earth-abundant Metal Complexes as Catalysts. *Energ. Environ. Sci.* **2012,** *5*, 6763-6778.

122. McKone, J. R.; Marinescu, S. C.; Brunschwig, B. S.; Winkler, J. R.; Gray, H. B., Earth-abundant Hydrogen Evolution Electrocatalysts. *Chem. Sci.* **2014,** *5*, 865-878.

123. Liu, T.; Darensbourg, M. Y., A Mixed-Valent, Fe(II)Fe(I), Diiron Complex Reproduces the Unique Rotated State of the [FeFe]Hydrogenase Active Site. *J. Am. Chem. Soc.* **2007,** *129*, 7008-7009.

124. Gloaguen, F.; Lawrence, J. D.; Rauchfuss, T. B., Biomimetic Hydrogen Evolution Catalyzed by an Iron Carbonyl Thiolate. *J. Am. Chem. Soc.* **2001,** *123*, 9476-9477.

125. Esmieu, C.; Raleiras, P.; Berggren, G., From protein engineering to artificial enzymes – biological and biomimetic approaches towards sustainable hydrogen production. *Sustain. Energy Fuels* **2018,** *2*, 724-750.

126. Zhao, X.; Georgakaki, I. P.; Miller, M. L.; Yarbrough, J. C.; Darensbourg, M. Y., H/D Exchange Reactions in Dinuclear Iron Thiolates as Activity Assay Models of Fe−H_2ase. *J. Am. Chem. Soc.* **2001,** *123*, 9710-9711.

127. Barton, B. E.; Rauchfuss, T. B., Terminal Hydride in [FeFe]-Hydrogenase Model Has Lower Potential for H_2 Production Than the Isomeric Bridging Hydride. *Inorg. Chem.* **2008,** *47*, 2261-2263.

128. Barton, B. E.; Olsen, M. T.; Rauchfuss, T. B., Aza- and Oxadithiolates Are Probable Proton Relays in Functional Models for the [FeFe]-Hydrogenases. *J. Am. Chem. Soc.* **2008,** *130*, 16834-16835.

129. Curtis, C. J.; Miedaner, A.; Ciancanelli, R.; Ellis, W. W.; Noll, B. C.; Rakowski DuBois, M.; DuBois, D. L., $[Ni(Et_2PCH_2NMeCH_2PEt_2)_2]^{2+}$ as a Functional Model for Hydrogenases. *Inorg. Chem.* **2003,** *42*, 216-227.

130. Rakowski Dubois, M.; Dubois, D. L., Development of Molecular Electrocatalysts for CO_2 Reduction and H_2 Production/Oxidation. *Acc. Chem. Res.* **2009,** *42*, 1974-1982.

131. DuBois, D. L.; Bullock, R. M., Molecular Electrocatalysts for the Oxidation of Hydrogen and the Production of Hydrogen – The Role of Pendant Amines as Proton Relays. *Eur. J. Inorg. Chem.* **2011,** *2011*, 1017-1027.

132. Sommer, C.; Adamska-Venkatesh, A.; Pawlak, K.; Birrell, J. A.; Rüdiger, O.; Reijerse, E. J.; Lubitz, W., Proton Coupled Electronic Rearrangement within the H-Cluster as an Essential Step in the Catalytic Cycle of [FeFe] Hydrogenases. *J. Am. Chem. Soc.* **2017,** *139*, 1440-1443.

133. Stewart, M. P.; Ho, M.-H.; Wiese, S.; Lindstrom, M. L.; Thogerson, C. E.; Raugei, S.; Bullock, R. M.; Helm, M. L., High Catalytic Rates for Hydrogen Production Using Nickel Electrocatalysts with Seven-Membered Cyclic Diphosphine Ligands Containing One Pendant Amine. *J. Am. Chem. Soc.* **2013,** *135*, 6033-6046.

134. Helm, M. L.; Stewart, M. P.; Bullock, R. M.; DuBois, M. R.; DuBois, D. L., A Synthetic Nickel Electrocatalyst with a Turnover Frequency Above 100,000 s^{-1} for hydrogen Production. Science: 2011; Vol. 333, pp 863-866.

135. Horvath, S.; Fernandez, L. E.; Soudackov, A. V.; Hammes-Schiffer, S., Insights into proton-coupled electron transfer mechanisms of electrocatalytic H_2 oxidation and production. *Proc. Natl. Acad. Sci.* **2012,** *109*, 15663-15668.

136. Hu, X.; Brunschwig, B. S.; Peters, J. C., Electrocatalytic Hydrogen Evolution at Low Overpotentials by Cobalt Macrocyclic Glyoxime and Tetraimine Complexes. *J. Am. Chem. Soc.* **2007,** *129*, 8988-8998.

137. Wang, H.; Lu, Y.; Mijangos, E.; Thapper, A., Photo-Induced Water Oxidation Based on a Mononuclear Cobalt(II) Complex. *Chin. J. Chem .* **2014,** *32*, 467-473.

138. Gloaguen, F.; Rauchfuss, T. B., Small molecule mimics of hydrogenases: hydrides and redox. *Chem. Soc. Rev.* **2009,** *38*, 100-108.

139. Graham, D. J.; Nocera, D. G., Electrocatalytic H_2 Evolution by Proton-Gated Hangman Iron Porphyrins. *Organometallics* **2014,** *33*, 4994-5001.

140. Baffert, C.; Artero, V.; Fontecave, M., Cobaloximes as Functional Models for Hydrogenases. 2. Proton Electroreduction Catalyzed by Difluoroborylbis(dimethylglyoximato)cobalt(II) Complexes in Organic Media. *Inorg. Chem.* **2007,** *46*, 1817-1824.

141. Kaeffer, N.; Chavarot-Kerlidou, M.; Artero, V., Hydrogen Evolution Catalyzed by Cobalt Diimine–Dioxime Complexes. *Acc. Chem. Res.* **2015,** *48*, 1286-1295.

142. Solis, B. H.; Hammes-Schiffer, S., Theoretical Analysis of Mechanistic Pathways for Hydrogen Evolution Catalyzed by Cobaloximes. *Inorg. Chem.* **2011,** *50*, 11252-11262.

143. Rose, M. J.; Gray, H. B.; Winkler, J. R., Hydrogen Generation Catalyzed by Fluorinated Diglyoxime–Iron Complexes at Low Overpotentials. *J. Am. Chem. Soc.* **2012,** *134*, 8310-8313.

144. Zhang, W.; Lai, W.; Cao, R., Energy-Related Small Molecule Activation Reactions: Oxygen Reduction and Hydrogen and Oxygen Evolution Reactions Catalyzed by Porphyrin- and Corrole-Based Systems. *Chem. Rev.* **2017,** *117*, 3717-3797.

145. Lee, C. H.; Dogutan, D. K.; Nocera, D. G., Hydrogen Generation by Hangman Metalloporphyrins. *J. Am. Chem. Soc.* **2011,** *133*, 8775-8777.

146. Bediako, D. K.; Solis, B. H.; Dogutan, D. K.; Roubelakis, M. M.; Maher, A. G.; Lee, C. H.; Chambers, M. B.; Hammes-Schiffer, S.; Nocera, D. G., Role of pendant proton relays and proton-coupled electron transfer on the hydrogen evolution reaction by nickel hangman porphyrins. *Proc. Natl. Acad. Sci.* **2014,** *111*, 15001.

147. Roubelakis, M. M.; Bediako, D. K.; Dogutan, D. K.; Nocera, D. G., Proton-coupled electron transfer kinetics for the hydrogen evolution reaction of hangman porphyrins. *Energ. Environ. Sci.* **2012,** *5*, 7737-7740.

148. Fisher, B. J.; Eisenberg, R., Electrocatalytic reduction of carbon dioxide by using macrocycles of nickel and cobalt. *J. Am. Chem. Soc.* **1980,** *102*, 7361-7363.

149. Collin, J. P.; Jouaiti, A.; Sauvage, J. P., Electrocatalytic properties of (tetraazacyclotetradecane)nickel(2+) and Ni_2(biscyclam)$^{4+}$ with respect to carbon dioxide and water reduction. *Inorg. Chem.* **1988,** *27*, 1986-1990.

150. Karunadasa, H. I.; Chang, C. J.; Long, J. R., A molecular molybdenum-oxo catalyst for generating hydrogen from water. *Nature* **2010,** *464*, 1329-1333.

151. McNamara, W. R.; Han, Z.; Yin, C.-J.; Brennessel, W. W.; Holland, P. L.; Eisenberg, R., Cobalt-Dithiolene Complexes for The Photocatalytic and Electrocatalytic Reduction of Protons in Aqueous Solutions. *Proc. Natl. Acad. Sci.* **2012,** *109*, 15594-15599.

152. Tatematsu, R.; Inomata, T.; Ozawa, T.; Masuda, H., Electrocatalytic Hydrogen Production by a Nickel(II) Complex with a Phosphinopyridyl Ligand. *Angew. Chem. Int. Ed.* **2016,** *55*, 5247-5250.

153. McNamara, W. R.; Han, Z.; Alperin, P. J.; Brennessel, W. W.; Holland, P. L.; Eisenberg, R., A Cobalt–Dithiolene Complex for the Photocatalytic and Electrocatalytic Reduction of Protons. *J. Am. Chem. Soc.* **2011,** *133*, 15368-15371.

154. Gan, L.; Groy, T. L.; Tarakeshwar, P.; Mazinani, S. K. S.; Shearer, J.; Mujica, V.; Jones, A. K., A Nickel Phosphine Complex as a Fast and Efficient Hydrogen Production Catalyst. *J. Am. Chem. Soc.* **2015,** *137*, 1109-1115.

155. Lacy, D. C.; McCrory, C. C. L.; Peters, J. C., Studies of Cobalt-Mediated Electrocatalytic CO_2 Reduction Using a Redox-Active Ligand. *Inorg. Chem.* **2014,** *53*, 4980-4988.

156. Nie, W.; McCrory, C. C. L., Electrocatalytic CO_2 reduction by a cobalt bis(pyridylmonoimine) complex: effect of acid concentration on catalyst activity and stability. *Chem. Commun.* **2018,** *54*, 1579-1582.

157. Jeffrey, J. C.; Rauchfuss, T. B., Metal complexes of hemilabile ligands. Reactivity and structure of dichlorobis(o-(diphenylphosphino)anisole)ruthenium(II). *Inorg. Chem.* **1979,** *18*, 2658-2666.

158. Espinet, P.; Soulantica, K., Phosphine-pyridyl and related ligands in synthesis and catalysis. *Coord. Chem. Rev.* **1999,** *193-195*, 499-556.

159. Jansen, A.; Pitter, S., Synthesis of Hemilabile P,N Ligands: ω-2-Pyridyl-n-alkylphosphines. *Monatsh. Chem.* **1999,** *130*, 783-794.

160. Newkome, G. R., Pyridylphosphines. *Chem. Rev.* **1993,** *93*, 2067-2089.

161. Slone, C. S.; Weinberger, D. A.; Mirkin, C. A., The Transition Metal Coordination Chemistry of Hemilabile Ligands. **1999,** *48*, 233-350.

162. Carroll, M. P.; Guiry, P. J., P,N ligands in asymmetric catalysis. *Chem. Soc. Rev.* **2014,** *43*, 819-833.

163. Moldes, I.; de la Encarnación, E.; Ros, J.; Alvarez-Larena, Á.; Piniella, J. F., Ruthenium(II) Complexes Containing both Arene and Functionalized Phosphines. Synthesis and Catalytic Activity for The Hydrogenation of Styrene and Phenylacetylene. *J. Organomet. Chem.* **1998,** *566*, 165-174.

164. Caballero, A.; Jalón, F. A.; Manzano, B. R.; Espino, G.; Pérez-Manrique, M.; Mucientes, A.; Poblete, F. J.; Maestro, M., Ruthenium Arene Derivatives with PN Hemilabile Ligands. P−C Cleavage and Phosphine to Phosphinite Transformation. *Organometallics* **2004,** *23*, 5694-5706.

165. Langer, R.; Gese, A.; Gesevičius, D.; Jost, M.; Langer, B. R.; Schneck, F.; Venker, A.; Xu, W., Formation of Different Isomers of Phosphine–Imidazolyl and –Pyridyl Ruthenium(II) Complexes Affecting the Catalyst Activity in the Acceptorless Dehydrogenation of Alcohols. *Eur. J. Inorg. Chem.* **2015,** *2015*, 696-705.

166. Iida, K.; Miura, T.; Ando, J.; Saito, S., The Dual Role of Ruthenium and Alkali Base Catalysts in Enabling a Conceptually New Shortcut to N-Unsubstituted Pyrroles through Unmasked α-Amino Aldehydes. *Org. Lett.* **2013,** *15*, 1436-1439.

167. Wei, S.; Pedroni, J.; Meißner, A.; Lumbroso, A.; Drexler, H.-J.; Heller, D.; Breit, B., Development of an Improved Rhodium Catalyst for Z-Selective Anti-Markovnikov Addition of Carboxylic Acids to Terminal Alkynes. *Chemistry – A European Journal* **2013,** *19*, 12067-12076.

168. Mague, J. T.; Hawbaker, S. W., 2-pyridylbis(diphenylphosphino)methane chemistry. Synthesis and Structures of $[Cu(\mu-\eta^2:\eta^1(Ph_2P)_2-CHC_5H_4N)(THF)]_2(BF_4)_2$ and $[Ni(Ph_2PCH_2C_5H_4N)_2]$-$[NiCl_4]\cdot 0.85CH_2Cl_2$ and $[Ni(Ph_2PCH_2C_5H_4N)_2]$-$[NiCl_4]\cdot 0.85CH_2Cl_2$. *J. Chem. Crystallogr.* **1997,** *27*, 603-608.

169. Rummelt, S. M.; Zhong, H.; Léonard, N. G.; Semproni, S. P.; Chirik, P. J., Oxidative Addition of Dihydrogen, Boron Compounds, and Aryl Halides to a Cobalt(I) Cation Supported by a Strong-Field Pincer Ligand. *Organometallics* **2019,** *38*, 1081-1090.

170. Schaefer, B. A.; Margulieux, G. W.; Small, B. L.; Chirik, P. J., Evaluation of Cobalt Complexes Bearing Tridentate Pincer Ligands for Catalytic C–H Borylation. *Organometallics* **2015,** *34*, 1307-1320.

171. Zhang, L.; Zuo, Z.; Leng, X.; Huang, Z., A Cobalt-Catalyzed Alkene Hydroboration with Pinacolborane. *Angew. Chem. Int. Ed.* **2014,** *53*, 2696-2700.

172. Srimani, D.; Mukherjee, A.; Goldberg, A. F. G.; Leitus, G.; Diskin-Posner, Y.; Shimon, L. J. W.; Ben David, Y.; Milstein, D., Cobalt-Catalyzed Hydrogenation of Esters to Alcohols: Unexpected Reactivity Trend Indicates Ester Enolate Intermediacy. *Angew. Chem. Int. Ed.* **2015,** *54*, 12357-12360.

173. Zhang, L.; Huang, Z., Synthesis of 1,1,1-Tris(boronates) from Vinylarenes by Co-Catalyzed Dehydrogenative Borylations–Hydroboration. *J. Am. Chem. Soc.* **2015,** *137*, 15600-15603.

174. Semproni, S. P.; Atienza, C. C. H.; Chirik, P. J., Oxidative Addition and C–H Activation Chemistry with a PNP Pincer-Ligated Cobalt Complex. *Chem. Sci.* **2014,** *5*, 1956.

175. Obligacion, J. V.; Semproni, S. P.; Chirik, P. J., Cobalt-Catalyzed C–H Borylation. *J. Am. Chem. Soc.* **2014,** *136*, 4133.

176. Neely, J. M.; Bezdek, M. J.; Chirik, P. J., Insight into Transmetalation Enables Cobalt-Catalyzed Suzuki–Miyaura Cross Coupling. *ACS Cent. Sci.* **2016,** *2*, 935-942.

177. Scheuermann, M. L.; Semproni, S. P.; Pappas, I.; Chirik, P. J., Carbon Dioxide Hydrosilylation Promoted by Cobalt Pincer Complexes. *Inorg. Chem.* **2014,** *53*, 9463-9465.

178. Shaffer, D. W.; Johnson, S. I.; Rheingold, A. L.; Ziller, J. W.; Goddard, W. A.; Nielsen, R. J.; Yang, J. Y., Reactivity of a Series of Isostructural Cobalt Pincer Complexes with CO2, CO, and H+. *Inorg. Chem.* **2014,** *53*, 13031-13041.

179. Mukherjee, A.; Srimani, D.; Chakraborty, S.; Ben-David, Y.; Milstein, D., Selective Hydrogenation of Nitriles to Primary Amines Catalyzed by a Cobalt Pincer Complex. *J. Am. Chem. Soc.* **2015,** *137*, 8888-8891.

180. Müller, G.; Klinga, M.; Leskelä, M.; Rieger, B., Iron and Cobalt Complexes of a Series of Tridentate P, N, P Ligands — Synthesis, Characterization, and Application in Ethene Polymerization Reactions. *Z. Anorg. Allg. Chem.* **2002,** *628*, 2839-2846.

181. Chen, L.; Ai, P.; Gu, J.; Jie, S.; Li, B.-G., Stereospecific Polymerization of 1,3-butadiene Catalyzed by Cobalt Complexes Bearing N-containing diphosphine PNP Ligands. *J. Organomet. Chem.* **2012,** *716*, 55-61.

182. Dahlhoff, W. V.; Dick, T. R.; Ford, G. H.; Kelly, W. S. J.; Nelson, S. M., Stereochemical Control in the Choice of Donor Atoms in Metal Complexes of a 'Bifunctional' Bidentate Ligand. *Journal of the Chemical Society A: Inorganic, Physical, Theoretical* **1971**, 3495-3499.

183. Mague, J. T.; Krinsky, J. L., Synthetic and Structural Studies of the Coordination Behavior of 2-Pyridylbis(diphenylphosphino)methane. *Inorg. Chem.* **2001,** *40*, 1962-1971.

184. Kobayashi, M.; Shimizu, S., Cobalt Proteins. *Eur. J. Biochem.* **1999,** *261*, 1-9.

185. Taube, H., Rates and Mechanisms of Substitution in Inorganic Complexes in Solution. *Chem. Rev.* **1952,** *50*, 69-126.

186. Cotton, F. A.; Goodgame, D. M. L.; Goodgame, M., The Electronic Structures of Tetrahedral Cobalt(II) Complexes. *J. Am. Chem. Soc.* **1961,** *83*, 4690-4699.

187. Kooistra, T. M.; Hekking, Koen F. W.; Knijnenburg, Q.; de Bruin, B.; Budzelaar, Peter H. M.; de Gelder, R.; Smits, Jan M. M.; Gal, Anton W., Cobalt Chloride Complexes of N_3 and N_4 Donor Ligands. *Eur. J. Inorg. Chem.* **2003,** *2003*, 648-655.

188. Kal, S.; Filatov, A. S.; Dinolfo, P. H., Electrocatalytic Proton Reduction by a Dicobalt Tetrakis-Schiff Base Macrocycle in Nonaqueous Electrolyte. *Inorg. Chem.* **2014,** *53*, 7137-7145.

189. Böttcher, A.; Takeuchi, T.; Hardcastle, K. I.; Meade, T. J.; Gray, H. B.; Cwikel, D.; Kapon, M.; Dori, Z., Spectroscopy and Electrochemistry of Cobalt(III) Schiff Base Complexes. *Inorg. Chem.* **1997,** *36*, 2498-2504.

190. Meghdadi, S.; Amirnasr, M.; Habibi, M. H.; Amiri, A.; Ghodsi, V.; Rohani, A.; Harrington, R. W.; Clegg, W., Synthesis, Structure, and Electrochemistry of Pyridinecarboxamide Cobalt(III) Complexes; The Effect of Bridge Substituents on The Redox Properties. *Polyhedron* **2008,** *27*, 2771-2778.

191. Ray, M.; Mukherjee, R. N., Cobalt(III) Complexes Using In-plane Tetradentate Pyridinecarboxamide Ligands and Two Monodentate Axial Ligands: Spectroelectrochemical Correlation. *Polyhedron* **1992,** *11*, 2929-2937.

192. Jahn, H. A.; Teller, E.; Donnan, F. G., Stability of Polyatomic Molecules in Degenerate Electronic States - I—Orbital Degeneracy. *P. ROY. SOC. A-MATH. PHY.* **1937,** *161*, 220-235.

193. Drew, M. G. B.; McCann, M.; Nelson, S. M., The Crystal Structures of Iron(II) and Cobalt(II) Complexes of a 30-Membered Macrocyclic Ligand: Observation of Jahn-Teller Distortion in a Six-Coordinate Low-Spin Cobalt(II) Complex. *Inorg. Chim. Acta* **1980,** *41*, 213-219.

194. Kissinger, P. T.; Heineman, W. R., Cyclic Voltammetry. *J. Chem. Educ.* **1983,** *60*, 702.

195. Mabbott, G. A., An Introduction to Cyclic Voltammetry. *J. Chem. Educ.* **1983,** *60*, 697.

196. Bard, A. J.; Faulkner, L. R., *Electrochemical Methods: Fundamentals and Applications*. John Wiley & Sons: 2001; Vol. 2.

197. Savéant, J.-M., Molecular Catalysis of Electrochemical Reactions. Mechanistic Aspects. *Chem. Rev.* **2008,** *108*, 2348-2378.

198. Lee, K. J.; Elgrishi, N.; Kandemir, B.; Dempsey, J. L., Electrochemical and Spectroscopic Methods for Evaluating Molecular Electrocatalysts. *Nat. Rev. Chem.* **2017,** *1*, 0039.

199. Savéant, J.-M., *Elements of Molecular and Biomolecular Electrochemistry: An Electrochemical Approach to Electron Transfer Chemistry*. 2 ed.; John Wiley & Sons, Inc.: Hoboken, New Jersey, 2006.

200. Elgrishi, N.; Rountree, K. J.; McCarthy, B. D.; Rountree, E. S.; Eisenhart, T. T.; Dempsey, J. L., A Practical Beginner's Guide to Cyclic Voltammetry. *J. Chem. Educ.* **2018,** *95*, 197-206.

201. Pavlishchuk, V. V.; Addison, A. W., Conversion Constants for Redox Potentials Measured versus Different Reference Electrodes in Acetonitrile Solutions at 25°C. *Inorg. Chim. Acta* **2000,** *298*, 97.

202. Lee, J. Electrochemical Sensing of Oxygen Gas in Ionic Liquids on Screen Printed Electrodes. 2014.

203. Elgrishi, N.; McCarthy, B. D.; Rountree, E. S.; Dempsey, J. L., Reaction Pathways of Hydrogen-Evolving Electrocatalysts: Electrochemical and Spectroscopic Studies of Proton-Coupled Electron Transfer Processes. *ACS Catal.* **2016,** *6*, 3644-3659.

204. Savéant, J. M.; Xu, F., First- and Second-Order Chemical-Electrochemical Mechanisms: Extraction of Standard Potential, Equilibrium and Rate Constants from Linear Sweep Voltammetric Curves. *J. Electroanal. Chem. Interfacial Electrochem.* **1986,** *208*, 197.

205. Nicholson, R. S.; Shain, I., Theory of Stationary Electrode Polarography. Single Scan and Cyclic Methods Applied to Reversible, Irreversible, and Kinetic Systems. *Anal. Chem.* **1964,** *36*, 706-723.

206. Wiedner, E. S.; Roberts, J. A. S.; Dougherty, W. G.; Kassel, W. S.; DuBois, D. L.; Bullock, R. M., Synthesis and Electrochemical Studies of Cobalt(III) Monohydride Complexes Containing Pendant Amines. *Inorg. Chem.* **2013,** *52*, 9975-9988.

207. Wiedner, E. S.; Bullock, R. M., Electrochemical Detection of Transient Cobalt Hydride Intermediates of Electrocatalytic Hydrogen Production. *J. Am. Chem. Soc.* **2016,** *138*, 8309-8318.

208. Koelle, U.; Paul, S., Electrochemical Reduction of Protonated Cyclopentadienylcobalt Phosphine Complexes. *Inorg. Chem.* **1986,** *25*, 2689-2694.

209. Pilloni, G.; Schiavon, G.; Zotti, G.; Zecchin, S., Electrochemistry of Coordination Compounds XV. Paramagnetic Hydrido Complexes of Cobalt(II), Rhodium(II) and Iridium(II). *J. Organomet. Chem.* **1977,** *134*, 305-318.

210. Bianchini, C.; Mealli, C.; Meli, A.; Peruzzini, M.; Zanobini, F., A stable .Eta.2-Dihydrogen Complex of Cobalt. Role of The Hydrogen-Hydrogen Interaction in Hydrogen Transfer from Metal to Alkene. *J. Am. Chem. Soc.* **1988,** *110*, 8725-8726.

211. Bianchini, C.; Mealli, C.; Peruzzini, M.; Zanobini, F., Reversible Uptake of Hydrogen and Nitrogen at Cobalt in The Solid State. Influence of The Counter Anion on The Formation of Classical Dihydride vs. Nonclassical .Eta.2-Dihydrogen Forms of $[(PP_3)CoH_2]^+$. *J. Am. Chem. Soc.* **1992,** *114*, 5905-5906.

212. Heinekey, D. M.; van Roon, M., Dihydride Complexes of the Cobalt and Iron Group Metals: An Investigation of Structure and Dynamic Behavior. *J. Am. Chem. Soc.* **1996,** *118*, 12134-12140.

213. Camus, A.; Cocevar, C.; Mestroni, G., Cobalt Complexes of 2,2'-Bipyridine and 1,10-Phenanthroline: II. Reactions with Molecular Hydrogen and Conjugated Dienes in The Presence of Tertiary Phosphines. *J. Organomet. Chem.* **1972,** *39*, 355-364.

214. Schrauzer, G. N.; Holland, R. J., Hydridocobaloximes. *J. Am. Chem. Soc.* **1971,** *93*, 1505-1506.

215. Khaskin, E.; Diskin-Posner, Y.; Weiner, L.; Leitus, G.; Milstein, D., Formal Loss of an H radical by A Cobalt Complex via Metal–Ligand Cooperation. *Chem. Commun.* **2013,** *49*, 2771-2773.

216. Semproni, S. P.; Milsmann, C.; Chirik, P. J., Four-Coordinate Cobalt Pincer Complexes: Electronic Structure Studies and Ligand Modification by Homolytic and Heterolytic Pathways. *J. Am. Chem. Soc.* **2014,** *136*, 9211-9224.

217. Ai, W.; Zhong, R.; Liu, X.; Liu, Q., Hydride Transfer Reactions Catalyzed by Cobalt Complexes. *Chem. Rev.* **2019,** *119*, 2876-2953.

218. Robinson, S. J. C.; Heinekey, D. M., Hydride & Dihydrogen Complexes of Earth Abundant Metals: Structure, Reactivity, and Applications to Catalysis. *Chem. Commun.* **2017,** *53*, 669-676.

219. Perutz, R. N.; Procacci, B., Photochemistry of Transition Metal Hydrides. *Chem. Rev.* **2016,** *116*, 8506-8544.

220. Dempsey, J. L.; Brunschwig, B. S.; Winkler, J. R.; Gray, H. B., Hydrogen Evolution Catalyzed by Cobaloximes. *Acc. Chem. Res.* **2009,** *42*, 1995-2004.

221. Varma, S.; Castillo, C. E.; Stoll, T.; Fortage, J.; Blackman, A. G.; Molton, F.; Deronzier, A.; Collomb, M.-N., Efficient Photocatalytic Hydrogen Production in Water using A Cobalt(III) Tetraaza-Macrocyclic Catalyst: Electrochemical Generation of The Low-Valent Co(I) Species and its Reactivity toward Proton Reduction. *PCCP* **2013,** *15*, 17544-17552.

222. Letko, C. S.; Panetier, J. A.; Head-Gordon, M.; Tilley, T. D., Mechanism of the Electrocatalytic Reduction of Protons with Diaryldithiolene Cobalt Complexes. *J. Am. Chem. Soc.* **2014,** *136*, 9364-9376.

223. Du, P.; Schneider, J.; Luo, G.; Brennessel, W. W.; Eisenberg, R., Visible Light-Driven Hydrogen Production from Aqueous Protons Catalyzed by Molecular Cobaloxime Catalysts. *Inorg. Chem.* **2009,** *48*, 4952-4962.

224. Marinescu, S. C.; Winkler, J. R.; Gray, H. B., Molecular Mechanisms of Cobalt-Catalyzed Hydrogen Evolution. *Proc. Natl. Acad. Sci.* **2012,** *109*, 15127.

225. Fang, M.; Wiedner, E. S.; Dougherty, W. G.; Kassel, W. S.; Liu, T.; DuBois, D. L.; Bullock, R. M., Cobalt Complexes Containing Pendant Amines in the Second Coordination Sphere as Electrocatalysts for H_2 Production. *Organometallics* **2014,** *33*, 5820-5833.

226. Loliger, J.; Scheffold, R., Paramagnetic Moment Measurements by NMR. A Micro technique. *J. Chem. Educ.* **1972,** *49*, 646.

227. Ostfeld, D.; Cohen, I. A., A Cautionary Note on The Use of The Evans Method for Magnetic Moments. *J. Chem. Educ.* **1972,** *49*, 829.

228. Dolomanov, O. V.; Bourhis, L. J.; Gildea, R. J.; Howard, J. A. K.; Puschmann, H., OLEX2: A Complete Structure Solution, Refinement and Analysis Program. *J. Appl. Crystallogr.* **2009,** *42*, 339-341.

229. Sheldrick, G. M., Integrated Space-Group and Crystal-Structure Determination. *ACTA. CRYSTALLOGR. B.* **2015,** *71*, 3-8.

230. Sheldrick, G. M., Crystal Structure Refinement with SHELXL. *ACTA. CRYSTALLOGR. C.* **2015,** *71*, 3-8.

231. Coucouvanis, D., *Inorganic Syntheses*. John Wiley & Sons, Inc.: 2002; Vol. 33.

232. J.W., A.; B.E., M., *NMR and chemistry: An introduction to modern NMR spectroscopy*. 4 ed.; Stanley Thornes Ltd: 2000.

233. Fackler, J. P.; Fetchin, J. A.; Mayhew, J.; Seidel, W. C.; Swift, T. J.; Weeks, M., Chemical Exchange in "Virtually Coupled" Systems. Metal-Ion-Induced Relaxation of Methyl-Phosphorus Coupling in Phosphine Complexes. *J. Am. Chem. Soc.* **1969,** *91*, 1941-1947.

234. D. Han; B. Andres; Spannenberg, A.; Beweries, T., Synthesis and Coordination Chemistry of the PPN Ligand 2-[bis-(diiso-propyl-phosphanyl)methyl]-6-Methyl-pyridine. *ACTA. CRYSTALLOGR. C.* **2017,** *C73*, 917-922.

235. A.B.P., L., *Inorganic electronic spectroscopy*. 2 ed.; Elsevier Science: 1984.

236. Ramírez-Delgado, V.; Morales León, R. E.; Hernández-Ayala, L. F.; Ramírez Coutiño, V. A.; Rodríguez, F. J.; Osorio-Monreal, G.; García-Ramos, J. C.; Flores-Alamo, M.; Ruiz-Azuara, L.; Ortiz-Frade, L., First Example of Bridge Mono-Coordination Mode for The Ligand 1,8-Bis-(2-pyridyl)-3,6-dithiaoctane (pdto) in A Co(II) Tetrahedral Complex. *Polyhedron* **2014,** *74*, 72-78.

237. Sénèque, O.; Campion, M.; Giorgi, M.; Le Mest, Y.; Reinaud, O., Funnel Complexes with CoII and NiII: New Probes into the Biomimetic Coordination Ability of the Calix[6]arene-Based Tris(imidazole) System. *Eur. J. Inorg. Chem.* **2004,** *2004*, 1817-1826.

238. Chan, S. L.-F.; Lam, T. L.; Yang, C.; Yan, S.-C.; Cheng, N. M., A Robust and Efficient Cobalt Molecular Catalyst for CO_2 Reduction. *Chem. Commun.* **2015,** *51*, 7799-7801.

239. Chang, K.; Mei, Z.; Wang, T.; Kang, Q.; Ouyang, S.; Ye, J., MoS_2/Graphene Cocatalyst for Efficient Photocatalytic H_2 Evolution under Visible Light Irradiation. *ACS nano* **2014,** *8*, 7078-7087.

240. Stubbert, B. D.; Peters, J. C.; Gray, H. B., Rapid Water Reduction to H_2 Catalyzed by a Cobalt Bis(iminopyridine) Complex. *J. Am. Chem. Soc.* **2011,** *133*, 18070-18073.

241. West, R. J.; Lincoln, S. F., Exchange of Acetonitrile on Complexes of Nickel(II) and Cobalt(II) Formed with 2,2',2''-triaminotriethylamine, and 2,2',2''-tri(N,N-dimethylamino)triethylamine. *Inorg. Chem.* **1973,** *12*, 494-497.

242. Tordin, E.; List, M.; Monkowius, U.; Schindler, S.; Knör, G., Synthesis and Characterisation of Cobalt, Nickel and Copper Complexes with Tripodal 4N Ligands as Novel Catalysts for The Homogeneous Partial Oxidation of Alkanes. *Inorg. Chim. Acta* **2013,** *402*, 90-96.

243. Chakraborty, B.; Paine, T. K., Synthesis and Characterization of Cobalt(II)–Salicylate Complexes Derived from N4-Donor Ligands: Stabilization of A Hexameric Water Cluster in The Lattice Host of A Cobalt(III)–Salicylate Complex. *Inorg. Chim. Acta* **2011,** *378*, 231-238.

244. Jiang, F.; Siegler, M. A.; Sun, X.; Jiang, L.; Fonseca Guerra, C.; Bouwman, E., Redox Interconversion between Cobalt(III) Thiolate and Cobalt(II) Disulfide Compounds. *Inorg. Chem.* **2018,** *57*, 8796-8805.

245. Wang, J.; Li, C.; Zhou, Q.; Wang, W.; Hou, Y.; Zhang, B.; Wang, X., A Polypyridyl Co(II) Complex-Based Water Reduction Catalyst with Double H_2 Evolution Sites. *Catal. Sci. Technol.* **2016,** *6*, 8482-8489.

246. Jacobsen, G. M.; Yang, J. Y.; Twamley, B.; Wilson, A. D.; Bullock, R. M.; Rakowski DuBois, M.; DuBois, D. L., Hydrogen Production using Cobalt-Based Molecular Catalysts Containing A Proton Relay in The Second Coordination Sphere. *Energ. Environ. Sci.* **2008,** *1*, 167-174.

247. Wiedner, E. S.; Yang, J. Y.; Dougherty, W. G.; Kassel, W. S.; Bullock, R. M.; DuBois, M. R.; DuBois, D. L., Comparison of Cobalt and Nickel Complexes with Sterically Demanding Cyclic Diphosphine Ligands: Electrocatalytic H_2 Production by $[Co(P^{tBu2}N^{Ph2})(CH_3CN)_3](BF_4)_2$. *Organometallics* **2010,** *29*, 5390-5401.

248. Land, J. M.; Stubbs, J. A.; Wrobleski, J. T., Synthesis and Characterization of Cobalt(II) Halide and Pseudohalide Complexes of 4-N,N-Dimethylaminopyridine. *Inorg. Chem.* **1977,** *16*, 1955-1958.

249. Goodgame, M.; Hayward, P. J., Hydrated Complexes of Manganese(II) and Cobalt(II) Halides with Heterocyclic Ligands. *J. Chem. Soc. A. Inorg. phys. theor.* **1971**, 3406-3409.

250. Singh Pannu, A. P.; Kapoor, P.; Hundal, G.; Kapoor, R.; Corbella, M.; Aliaga-Alcalde, N.; Singh Hundal, M., Magneto-Structural Studies of Two New Cobalt(II)-N,N-Diisobutylisonicotinamide Compounds: $[CoLCl_2]_n$ and $[Co(L)_2(H_2O)_4][CoLBr_3]_2{\cdot}2H_2O$. *Dalton. Trans.* **2011,** *40*, 12560-12569.

251. Garai, M.; Dey, D.; Yadav, H. R.; Maji, M.; Choudhury, A. R.; Biswas, B., Synthesis and Phosphatase Activity of A Cobalt(II) Phenanthroline Complex. *J. Chem. Sci.* **2017,** *129*, 1513-1520.

252. Lo, W. K. C.; Castillo, C. E.; Gueret, R.; Fortage, J.; Rebarz, M.; Sliwa, M.; Thomas, F.; McAdam, C. J.; Jameson, G. B.; McMorran, D. A.; Crowley, J. D.; Collomb, M.-N.; Blackman, A.

G., Synthesis, Characterization, and Photocatalytic H_2-Evolving Activity of a Family of $[Co(N_4Py)(X)]^{n+}$ Complexes in Aqueous Solution. *Inorg. Chem.* **2016,** *55*, 4564-4581.

253. Khan, S.; Roy, S.; Bhar, K.; Mitra, P.; Slawin, A.; Kumar Ghosh, B., Syntheses, Structures, and Properties of Two Mononuclear Cobalt(III) Azido Complexes Containing A Tetradentate N-Donor Schiff Base as End-capping Ligand. *Transition Met. Chem.* **2011,** *36*, 99-106.

254. Collomb, M.-N.; Deronzier, A.; Gorgy, K.; Lepretre, J.-C.; Pecaut, J., Electrochemical Properties of $[Fe^{III}(L)_2Cl_2][PF_6]$ and $[Fe_2^{III,III}O(L)_4Cl_2][PF_6]_2$ [L=2,2′-bipyridine (bpy) and 4,4′-dimethyl-2,2′-bipyridine (dmbpy)]. Crystal Structures of The dmbpy Derivatives. *New J. Chem.* **1999,** *23*, 785-790.

255. **AJ, B.**; LR, F., Electrochemical methods: Fundamentals and Application. **John wiley & sons** Hoboken

NJ, **2001**; Vol. 2.

256. Savéant, J.-M., Elements of Molecular and Biomolecular Electrochemistry : An Electrochemical Approach to Electron Transfer Chemistry. Wiley: 2006.

257. Wiedner, E. S.; Brown, H. J. S.; Helm, M. L., Kinetic Analysis of Competitive Electrocatalytic Pathways: New Insights into Hydrogen Production with Nickel Electrocatalysts. *J. Am. Chem. Soc.* **2016,** *138*, 604-616.

258. Bhattacharjee, A.; Andreiadis, E. S.; Chavarot-Kerlidou, M.; Fontecave, M.; Field, M. J.; Artero, V., A Computational Study of the Mechanism of Hydrogen Evolution by Cobalt(Diimine-Dioxime) Catalysts. *19*, 15166-15174.

259. Sun, Y.; Bigi, J. P.; Piro, N. A.; Tang, M. L.; Long, J. R.; Chang, C. J., Molecular Cobalt Pentapyridine Catalysts for Generating Hydrogen from Water. *J. Am. Chem. Soc.* **2011,** *133*, 9212-9215.

260. King, A. E.; Surendranath, Y.; Piro, N. A.; Bigi, J. P.; Long, J. R.; Chang, C. J., A Mechanistic Study of Proton Reduction Catalyzed by A Pentapyridine Cobalt Complex: Evidence for Involvement of An Anation-based Pathway. *Chem. Sci.* **2013,** *4*, 1578-1587.

261. Call, A.; Codolà, Z.; Acuña-Parés, F.; Lloret-Fillol, J., Photo- and Electrocatalytic H_2 Production by New First-Row Transition-Metal Complexes Based on an Aminopyridine Pentadentate Ligand. **2014,** *20*, 6171-6183.

262. Dempsey, J. L.; Winkler, J. R.; Gray, H. B., Kinetics of Electron Transfer Reactions of H_2-Evolving Cobalt Diglyoxime Catalysts. *J. Am. Chem. Soc.* **2010,** *132*, 1060-1065.

263. Dempsey, J. L.; Winkler, J. R.; Gray, H. B., Mechanism of H_2 Evolution from a Photogenerated Hydridocobaloxime. *J. Am. Chem. Soc.* **2010,** *132*, 16774-16776.

264. Lazarides, T.; McCormick, T.; Du, P.; Luo, G.; Lindley, B.; Eisenberg, R., Making Hydrogen from Water Using a Homogeneous System Without Noble Metals. *J. Am. Chem. Soc.* **2009,** *131*, 9192-9194.

265. Szajna-Fuller, E.; Bakac, A., Catalytic Generation of Hydrogen with Titanium Citrate and a Macrocyclic Cobalt Complex. **2010,** *2010*.

266. Solis, B. H.; Hammes-Schiffer, S., Substituent Effects on Cobalt Diglyoxime Catalysts for Hydrogen Evolution. *J. Am. Chem. Soc.* **2011,** *133*, 19036-19039.

267. Muckerman, J. T.; Fujita, E., Theoretical Studies of the Mechanism of Catalytic Hydrogen Production by a Cobaloxime. *Chem. Commun.* **2011,** *47*, 12456-12458.

268. Solis, B. H.; Yu, Y.; Hammes-Schiffer, S., Effects of Ligand Modification and Protonation on Metal Oxime Hydrogen Evolution Electrocatalysts. *Inorg. Chem.* **2013,** *52*, 6994-6999.

269. Rountree, E. S.; McCarthy, B. D.; Eisenhart, T. T.; Dempsey, J. L., Evaluation of Homogeneous Electrocatalysts by Cyclic Voltammetry. *Inorg. Chem.* **2014,** *53*, 9983-10002.

270. Roberts, J. A. S.; Bullock, R. M., Direct Determination of Equilibrium Potentials for Hydrogen Oxidation/Production by Open Circuit Potential Measurements in Acetonitrile. *Inorg. Chem.* **2013,** *52*, 3823-3835.

271. Appel, A. M.; Helm, M. L., Determining the Overpotential for a Molecular Electrocatalyst. *ACS Catal.* **2014,** *4*, 630-633.

272. Savéant, J. M., *Elements of Molecular and Biomolecular Electrochemistry*. 2006.

273. Costentin, C.; Drouet, S.; Robert, M.; Savéant, J.-M., Turnover Numbers, Turnover Frequencies, and Overpotential in Molecular Catalysis of Electrochemical Reactions. Cyclic Voltammetry and Preparative-Scale Electrolysis. *J. Am. Chem. Soc.* **2012,** *134*, 11235-11242.

274. Costentin, C.; Savéant, J.-M., Multielectron, Multistep Molecular Catalysis of Electrochemical Reactions: Benchmarking of Homogeneous Catalysts. *ChemElectroChem* **2014,** *1*, 1226-1236.

275. Artero, V.; Saveant, J.-M., Toward the Rational Benchmarking of Homogeneous H_2-evolving Catalysts. *Energ. Environ. Sci.* **2014,** *7*, 3808-3814.

276. Chao, T.-H.; Espenson, J. H., Mechanism of Hydrogen Evolution from Hydridocobaloxime. *J. Am. Chem. Soc.* **1978,** *100*, 129-133.

277. Jacques, P.-A.; Artero, V.; Pécaut, J.; Fontecave, M., Cobalt and nickel diimine-dioxime complexes as molecular electrocatalysts for hydrogen evolution with low overvoltages. *Proc. Natl. Acad. Sci.* **2009,** *106*, 20627.

278. McCrory, C. C. L.; Uyeda, C.; Peters, J. C., Electrocatalytic Hydrogen Evolution in Acidic Water with Molecular Cobalt Tetraazamacrocycles. *J. Am. Chem. Soc.* **2012,** *134*, 3164-3170.

279. Nippe, M.; Khnayzer, R. S.; Panetier, J. A.; Zee, D. Z.; Olaiya, B. S.; Head-Gordon, M.; Chang, C. J.; Castellano, F. N.; Long, J. R., Catalytic Proton Reduction with Transition Metal Complexes of the Redox-active Ligand bpy2PYMe. *Chem. Sci.* **2013,** *4*, 3934-3945.

280. Tong, L.; Kopecky, A.; Zong, R.; Gagnon, K. J.; Ahlquist, M. S. G.; Thummel, R. P., Light-Driven Proton Reduction in Aqueous Medium Catalyzed by a Family of Cobalt Complexes with Tetradentate Polypyridine-Type Ligands. *Inorg. Chem.* **2015,** *54*, 7873-7884.

281. Rodenberg, A.; Orazietti, M.; Probst, B.; Bachmann, C.; Alberto, R.; Baldridge, K. K.; Hamm, P., Mechanism of Photocatalytic Hydrogen Generation by a Polypyridyl-Based Cobalt Catalyst in Aqueous Solution. *Inorg. Chem.* **2015,** *54*, 646-657.

282. Bigi, J. P.; Hanna, T. E.; Harman, W. H.; Chang, A.; Chang, C. J., Electrocatalytic Reduction of Protons to Hydrogen by a Water-compatible Cobalt Polypyridyl Platform. *Chem. Commun.* **2010,** *46*, 958-960.

283. Anxolabéhère-Mallart, E.; Costentin, C.; Fournier, M.; Robert, M., Cobalt-Bisglyoximato Diphenyl Complex as a Precatalyst for Electrocatalytic H_2 Evolution. *J. Phys. Chem. C* **2014,** *118*, 13377-13381.

284. Efros, L. L.; Thorp, H. H.; Brudvig, G. W.; Crabtree, R. H., Towards a Functional Model of Hydrogenase: Electrocatalytic Reduction of Protons to Dihydrogen by a Nickel Macrocyclic Complex. *Inorg. Chem.* **1992,** *31*, 1722-1724.

285. Solis, B. H.; Hammes-Schiffer, S., Computational Study of Anomalous Reduction Potentials for Hydrogen Evolution Catalyzed by Cobalt Dithiolene Complexes. *J. Am. Chem. Soc.* **2012,** *134*, 15253-15256.

286. Wiedner, E. S.; Appel, A. M.; DuBois, D. L.; Bullock, R. M., Thermochemical and Mechanistic Studies of Electrocatalytic Hydrogen Production by Cobalt Complexes Containing Pendant Amines. *Inorg. Chem.* **2013,** *52*, 14391-14403.

287. Roy, S.; Sharma, B.; Pécaut, J.; Simon, P.; Fontecave, M.; Tran, P. D.; Derat, E.; Artero, V., Molecular Cobalt Complexes with Pendant Amines for Selective Electrocatalytic Reduction of Carbon Dioxide to Formic Acid. *J. Am. Chem. Soc.* **2017,** *139*, 3685-3696.

288. Benson, E. E.; Sampson, M. D.; Grice, K. A.; Smieja, J. M.; Froehlich, J. D.; Friebel, D.; Keith, J. A.; Carter, E. A.; Nilsson, A.; Kubiak, C. P., The Electronic States of Rhenium Bipyridyl Electrocatalysts for CO_2 Reduction as Revealed by X-ray Absorption Spectroscopy and Computational Quantum Chemistry. *Angew. Chem. Int. Ed.* **2013,** *52*, 4841-4844.

289. Keith, J. A.; Grice, K. A.; Kubiak, C. P.; Carter, E. A., Elucidation of the Selectivity of Proton-Dependent Electrocatalytic CO_2 Reduction by fac-Re(bpy)$(CO)_3$Cl. *J. Am. Chem. Soc.* **2013,** *135*, 15823-15829.

290. Shimoda, T.; Morishima, T.; Kodama, K.; Hirose, T.; Polyansky, D. E.; Manbeck, G. F.; Muckerman, J. T.; Fujita, E., Photocatalytic CO_2 Reduction by Trigonal-Bipyramidal Cobalt(II) Polypyridyl Complexes: The Nature of Cobalt(I) and Cobalt(0) Complexes upon Their Reactions with CO_2, CO, or Proton. *Inorg. Chem.* **2018,** *57*, 5486-5498.

291. Franco, F.; Fernández, S.; Lloret-Fillol, J., Advances in the Electrochemical Catalytic Reduction of CO_2 with Metal Complexes. *Curr. Opin. Electrochem.* **2019,** *15*, 109-117.

292. Dey, S.; Ahmed, M. E.; Dey, A., Activation of Co(I) State in a Cobalt-Dithiolato Catalyst for Selective and Efficient CO_2 Reduction to CO. *Inorg. Chem.* **2018,** *57*, 5939-5947.

293. DuBois, D. L.; Miedaner, A., Synthesis, Characterization, and Electrochemical Studies of Iron, Cobalt, and Nickel Complexes of Polyphosphine Ligands. *Inorg. Chem.* **1986,** *25*, 4642-4650.

294. Kaeffer, N.; Morozan, A.; Fize, J.; Martinez, E.; Guetaz, L.; Artero, V., The Dark Side of Molecular Catalysis: Diimine–Dioxime Cobalt Complexes Are Not the Actual Hydrogen Evolution Electrocatalyst in Acidic Aqueous Solutions. *ACS Catal.* **2016,** *6*, 3727-3737.

295. Ghachtouli, S. E.; Guillot, R.; Brisset, F.; Aukauloo, A., Cobalt-Based Particles Formed upon Electrocatalytic Hydrogen Production by a Cobalt Pyridine Oxime Complex. *ChemSusChem* **2013,** *6*, 2226-2230.

296. Queyriaux, N.; Sun, D.; Fize, J.; Pécaut, J.; Field, M. J.; Chavarot-Kerlidou, M.; Artero, V., Electrocatalytic Hydrogen Evolution with a Cobalt Complex Bearing Pendant Proton Relays: Acid Strength and Applied Potential Govern Mechanism and Stability. *J. Am. Chem. Soc.* **2020,** *142*, 274-282.

297. Klug, C. M.; Cardenas, A. J. P.; Bullock, R. M.; O'Hagan, M.; Wiedner, E. S., Reversing the Tradeoff between Rate and Overpotential in Molecular Electrocatalysts for H_2 Production. *ACS Catal.* **2018,** *8*, 3286-3296.

298. Maher, A. G.; Passard, G.; Dogutan, D. K.; Halbach, R. L.; Anderson, B. L.; Gagliardi, C. J.; Taniguchi, M.; Lindsey, J. S.; Nocera, D. G., Hydrogen Evolution Catalysis by a Sparsely Substituted Cobalt Chlorin. *ACS Catal.* **2017,** *7*, 3597-3606.

299. Madden, C.; Vaughn, M. D.; Díez-Pérez, I.; Brown, K. A.; King, P. W.; Gust, D.; Moore, A. L.; Moore, T. A., Catalytic Turnover of [FeFe]-Hydrogenase Based on Single-Molecule Imaging. *J. Am. Chem. Soc.* **2012,** *134*, 1577-1582.

300. Du, P.; Eisenberg, R., Catalysts Made of Earth-abundant Elements (Co, Ni, Fe) for Water Splitting: Recent Progress and Future Challenges. *Energ. Environ. Sci.* **2012,** *5*, 6012-6021.

301. Francke, R.; Schille, B.; Roemelt, M., Homogeneously Catalyzed Electroreduction of Carbon Dioxide—Methods, Mechanisms, and Catalysts. *Chem. Rev.* **2018,** *118*, 4631-4701.

302. Dub, P. A.; Ikariya, T., Catalytic Reductive Transformations of Carboxylic and Carbonic Acid Derivatives Using Molecular Hydrogen. *ACS Catal.* **2012,** *2*, 1718-1741.

303. Werkmeister, S.; Junge, K.; Beller, M., Catalytic Hydrogenation of Carboxylic Acid Esters, Amides, and Nitriles with Homogeneous Catalysts. *Org. Process Res. Dev* **2014,** *18*, 289-302.

304. Werkmeister, S.; Neumann, J.; Junge, K.; Beller, M., Pincer-Type Complexes for Catalytic (De)Hydrogenation and Transfer (De)Hydrogenation Reactions: Recent Progress. *Chem. Eur. J.* **2015,** *21*, 12226-12250.

305. Filonenko, G. A.; van Putten, R.; Hensen, E. J. M.; Pidko, E. A., Catalytic (de)hydrogenation promoted by non-precious metals – Co, Fe and Mn: recent advances in an emerging field. *Chem. Soc. Rev.* **2018,** *47*, 1459-1483.

306. Liu, W.; Sahoo, B.; Junge, K.; Beller, M., Cobalt Complexes as an Emerging Class of Catalysts for Homogeneous Hydrogenations. *Acc. Chem. Res.* **2018,** *51*, 1858-1869.

307. Junge, K.; Wendt, B.; Cingolani, A.; Spannenberg, A.; Wei, Z.; Jiao, H.; Beller, M., Cobalt Pincer Complexes for Catalytic Reduction of Carboxylic Acid Esters. *Chem. Eur. J.* **2017,** *24*, 1046-1052.

308. Morales-Morales, D., The Chemistry of PCP Pincer Phosphinite Transition Metal Complexes. 2007; pp 151-179.

309. Milstein, D., Metal–ligand Cooperation by Aromatization–dearomatization as a Tool in Single Bond Activation. *Phil. Trans. R. Soc. A.* **2015,** *373*, 1-10.

310. Gnanaprakasam, B.; Balaraman, E.; Ben-David, Y.; Milstein, D., Synthesis of Peptides and Pyrazines from β-Amino Alcohols through Extrusion of H_2 Catalyzed by Ruthenium Pincer Complexes: Ligand-Controlled Selectivity. *Angew. Chem.* **2011,** *123*, 12448-12452.

311. Feller, M.; Gellrich, U.; Anaby, A.; Diskin-Posner, Y.; Milstein, D., Reductive Cleavage of CO_2 by Metal–Ligand-Cooperation Mediated by an Iridium Pincer Complex. *J. Am. Chem. Soc.* **2016,** *138*, 6445-6454.

312. Oren, D.; Diskin-Posner, Y.; Avram, L.; Feller, M.; Milstein, D., Metal–Ligand Cooperation as Key in Formation of Dearomatized Ni^{II}–H Pincer Complexes and in Their Reactivity toward CO and CO_2. *Organometallics* **2018,** *37*, 2217-2221.

313. Khusnutdinova, J. R.; Milstein, D., Metal–Ligand Cooperation. *Angew. Chem. Int. Ed.* **2015,** *54*, 12236-12273.

314. van der Vlugt, J. I.; Reek, J. N. H., Neutral Tridentate PNP Ligands and Their Hybrid Analogues: Versatile Non-Innocent Scaffolds for Homogeneous Catalysis. *Angew. Chem. Int. Ed.* **2009,** *48*, 8832-8846.

315. Gunanathan, C.; Gnanaprakasam, B.; Iron, M. A.; Shimon, L. J. W.; Milstein, D., "Long-Range" Metal−Ligand Cooperation in H_2 Activation and Ammonia-Promoted Hydride Transfer with a Ruthenium−Acridine Pincer Complex. *J. Am. Chem. Soc.* **2010,** *132*, 14763-14765.

316. Gunanathan, C.; Shimon, L. J. W.; Milstein, D., Direct Conversion of Alcohols to Acetals and H_2 Catalyzed by an Acridine-Based Ruthenium Pincer Complex. *J. Am. Chem. Soc.* **2009,** *131*, 3146-3147.

317. Balaraman, E.; Gnanaprakasam, B.; Shimon, L. J. W.; Milstein, D., Direct Hydrogenation of Amides to Alcohols and Amines under Mild Conditions. *J. Am. Chem. Soc.* **2010,** *132*, 16756-16758.

318. Langer, R.; Fuchs, I.; Vogt, M.; Balaraman, E.; Diskin-Posner, Y.; Shimon, L. J. W.; Ben-David, Y.; Milstein, D., Stepwise Metal–Ligand Cooperation by a Reversible Aromatization/Deconjugation Sequence in Ruthenium Complexes with a Tetradentate Phenanthroline-Based Ligand. *Chem. Eur. J.* **2013,** *19*, 3407-3414.

319. Stepowska, E.; Jiang, H.; Song, D., Reversible H_2 splitting between Ru(II) and a Remote Carbanion in a Zwitterionic Compound. *Chem. Commun.* **2010,** *46*, 556-558.

320. Khaskin, E.; Diskin-Posner, Y.; Weiner, L.; Leitus, G.; Milstein, D., Formal Loss of an H radical by A Cobalt Complex via Metal-Ligand Cooperation. *Chem. Commun.* **2013,** *49*, 2771-2773.

321. Addison, A. W.; Rao, T. N.; Reedijk, J.; van Rijn, J.; Verschoor, G. C., Synthesis, Structure, and Spectroscopic Properties of Copper(II) Compounds Containing Nitrogen–sulphur Donor Ligands; the Crystal and Molecular Structure of Aqua [1,7-bis(N-methylbenzimidazol-2'-yl)-2,6-dithiaheptane]copper(II) perchlorate. *J. Chem. Soc., Dalton Trans.* **1984**, 1349-1356.

322. Zhang, L.; Zuo, Z.; Wan, X.; Huang, Z., Cobalt-Catalyzed Enantioselective Hydroboration of 1,1-Disubstituted Aryl Alkenes. *J. Am. Chem. Soc.* **2014,** *136*, 15501-15504.

323. Bowman, A. C.; Milsmann, C.; Bill, E.; Lobkovsky, E.; Weyhermüller, T.; Wieghardt, K.; Chirik, P. J., Reduced N-Alkyl Substituted Bis(imino)pyridine Cobalt Complexes: Molecular and Electronic Structures for Compounds Varying by Three Oxidation States. *Inorg. Chem.* **2010,** *49*, 6110-6123.

324. Dey, S.; Wayland, B. B.; Zdilla, M. J., Solution and Solid State Properties for Low-Spin Cobalt(II) Dibenzotetramethyltetraaza[14]annulene [(tmtaa)Co^{II}] and the Monopyridine Complex. *Inorg. Chem.* **2019,** *58*, 1224-1233.

325. Yamami, M.; Tanaka, M.; Sakiyama, H.; Koga, T.; Kobayashi, K.; Miyasaka, H.; Ohba, M.; Ōkawa, H., Dinuclear Complexes of Mn^{II}, Co^{II} and Zn^{II} Triply Bridged by Carboxylate Groups: Structures, Properties and Catalase-like Function *J. Chem. Soc., Dalton Trans.* **1997**, 4595-4602.

326. Singh, V. P.; Singh, S.; Katiyar, A., Synthesis, Physico-chemical Studies of Manganese(II), Cobalt(II), Nickel(II), Copper(II) and Zinc(II) Complexes with Some p-substituted Acetophenone Benzoylhydrazones and their Antimicrobial Activity. *J. Enzyme. Inhib. Med. Chem.* **2009,** *24*, 577-588.

327. Lewandowska-Andralojc, A.; Baine, T.; Zhao, X.; Muckerman, J. T.; Fujita, E.; Polyansky, D. E., Mechanistic Studies of Hydrogen Evolution in Aqueous Solution Catalyzed by a Tertpyridine–Amine Cobalt Complex. *Inorg. Chem.* **2015,** *54*, 4310-4321.

328. Hu, X.; Cossairt, B. M.; Brunschwig, B. S.; Lewis, N. S.; Peters, J. C., Electrocatalytic Hydrogen Evolution by Cobalt Difluoroboryl-diglyoximate Complexes. *Chem. Commun.* **2005**, 4723-4725.

329. Gray, H. B.; Billig, E., The Electronic Structures of Square-Planar Metal Complexes. III. High-Spin Planar Cobalt(I) and Iron(I). *J. Am. Chem. Soc.* **1963,** *85*, 2019-2020.

330. Ferreira, H.; Conradie, M. M.; Conradie, J., Electrochemical and Electronic Properties of a Series of Substituted Polypyridine Ligands and their Co(II) Complexes. *Inorg. Chim. Acta* **2019,** *486*, 26-35.

331. Chen, Z.; Concepcion, J. J.; Brennaman, M. K.; Kang, P.; Norris, M. R.; Hoertz, P. G.; Meyer, T. J., Splitting CO_2 into CO and O_2 by a Single Catalyst. *Proc. Natl. Acad. Sci.* **2012,** *109*, 15606.

332. Elgrishi, N.; Chambers, M. B.; Artero, V.; Fontecave, M., Terpyridine complexes of first row transition metals and electrochemical reduction of CO_2 to CO. *PCCP* **2014,** *16*, 13635-13644.

333. Kershaw Cook, L. J.; Tuna, F.; Halcrow, M. A., Iron(II) and cobalt(II) complexes of tris-azinyl analogues of 2,2′:6′,2′′-terpyridine. *Dalton. Trans.* **2013,** *42*, 2254-2265.

334. Ferreira, H.; Conradie, M. M.; Conradie, J., Cyclic voltammetry data of polypyridine ligands and Co(II)-polypyridine complexes. *Data in Brief* **2019,** *22*, 436-445.

335. Lagaditis, P. O.; Schluschaß, B.; Demeshko, S.; Würtele, C.; Schneider, S., Square-Planar Cobalt(III) Pincer Complex. *Inorg. Chem.* **2016,** *55*, 4529-4536.

336. Chen, Z.; Chen, C.; Weinberg, D. R.; Kang, P.; Concepcion, J. J.; Harrison, D. P.; Brookhart, M. S.; Meyer, T. J., Electrocatalytic reduction of CO_2 to CO by polypyridyl ruthenium complexes. *Chem. Commun.* **2011,** *47*, 12607-12609.

337. Riplinger, C.; Carter, E. A., Influence of Weak Brønsted Acids on Electrocatalytic CO_2 Reduction by Manganese and Rhenium Bipyridine Catalysts. *ACS Catal.* **2015,** *5*, 900-908.

338. Ngo, K. T.; McKinnon, M.; Mahanti, B.; Narayanan, R.; Grills, D. C.; Ertem, M. Z.; Rochford, J., Turning on the Protonation-First Pathway for Electrocatalytic CO_2 Reduction by Manganese Bipyridyl Tricarbonyl Complexes. *J. Am. Chem. Soc.* **2017,** *139*, 2604-2618.